
ADVANCES IN NANOCOMPOSITE TECHNOLOGY

Edited by **Abbas Hashim**

INTECHWEB.ORG

Advances in Nanocomposite Technology

Edited by Abbas Hashim

Published by InTech

Janeza Trdine 9, 51000 Rijeka, Croatia

Copyright © 2011 InTech

All chapters are Open Access articles distributed under the Creative Commons Non Commercial Share Alike Attribution 3.0 license, which permits to copy, distribute, transmit, and adapt the work in any medium, so long as the original work is properly cited. After this work has been published by InTech, authors have the right to republish it, in whole or part, in any publication of which they are the author, and to make other personal use of the work. Any republication, referencing or personal use of the work must explicitly identify the original source.

Statements and opinions expressed in the chapters are these of the individual contributors and not necessarily those of the editors or publisher. No responsibility is accepted for the accuracy of information contained in the published articles. The publisher assumes no responsibility for any damage or injury to persons or property arising out of the use of any materials, instructions, methods or ideas contained in the book.

Publishing Process Manager Romina Krebel

Technical Editor Teodora Smiljanic

Cover Designer Jan Hyrat

Image Copyright Handy Widiyanto, 2010. Used under license from Shutterstock.com

First published July, 2011

Printed in Croatia

A free online edition of this book is available at www.intechopen.com
Additional hard copies can be obtained from orders@intechweb.org

Advances in Nanocomposite Technology, Edited Abbas Hashim

p. cm.

ISBN 978-953-307-347-7

INTECH OPEN ACCESS
PUBLISHER

INTECH open

free online editions of InTech
Books and Journals can be found at
www.intechopen.com

Contents

Preface IX

Part 1 Electronic Applications 1

- Chapter 1 **Solar Nanocomposite Materials 3**
Zhengdong Cheng
- Chapter 2 **Conducting Polymer-Metal
Nanocomposite Coating on Fibers 47**
Syuji Fujii, Mizuho Kodama, Soichiro Matsuzawa,
Hiroyuki Hamasaki, Atsushi Ohtaka and Yoshinobu Nakamura
- Chapter 3 **Electroplated Nanocomposites of High
Wear Resistance for Advanced Systems Application 73**
Ioury Timoshkov, Victor Kurmashev and Vadim Timoshkov
- Chapter 4 **Nanocomposite Thin Films Resulting from Au Nanoclusters
Dispersed in a Titanium Oxide Dielectric Matrix:
the Surface Plasmon Resonance Effect 89**
M. Torrell, L. Cunha, M.I. Vasilevskiy, E. Alves,
N.P. Barradas, A. Cavaleiro and F. Vaz
- Chapter 5 **Comparative Study of Membranes Obtained
from PA6 and PA66/Natural Clay Nanocomposites 115**
Amanda M. D. Leite, Edcleide M. Araújo,
Vanessa da N. Medeiros, Rene A. da Paz and Hélio de L. Lira

Part 2 Material Nanocomposites 131

- Chapter 6 **Clay-Containing Polysulfone Nanocomposites 133**
Priscila Anadão
- Chapter 7 **Processing and Characterization of Alumina / Chromium
Carbide Ceramic Nanocomposite 147**
Jow-Lay Huang and Pramoda K. Nayak

- Chapter 8 **Environmentally-Safe Polymer-Metal Nanocomposites with Most Favorable Distribution of Catalytically Active and Biocide Nanoparticles** 175
A. Alonso, J. Macanás, G.L. Davies,
Y.K. Gun'ko, M. Muñoz and D.N. Muraviev
- Chapter 9 **Silicate Glass-Based Nanocomposite Scintillators** 201
Martin Nikl, Daniel Nižňanský, Jakub Ruzicka,
Carla Cannas and Takayuki Yanagida
- Chapter 10 **Atomic Scale Study of Deformation and Failure Mechanisms in Ceramic-Reinforced Metal-Matrix Composites** 227
Avinash M. Dongare and Bruce LaMattina
- Chapter 11 **Functionalized Graphene Nanocomposites** 247
Paula A. A. P. Marques, Gil Gonçalves,
Sandra Cruz, Nuno Almeida, Manoj K. Singh,
José Grácio and Antonio C.M. Sousa
- Part 3 Human and Bioapplications** 273
- Chapter 12 **Biofunctional Composites of Polysaccharides Containing Inorganic Nanoparticles** 275
Ana L. Daniel-da-Silva and Tito Trindade
- Chapter 13 **Applications of Antimicrobial Polymer Nanocomposites in Food Packaging** 299
Aryou Emamifar
- Chapter 14 **Functional Polymer Nanocomposite Materials from Microfibrillated Cellulose** 319
Philippe Tingaut, Christian Eyholzer and Tanja Zimmermann
- Chapter 15 **Versatile Nanocomposite Formulation System of Non-Steroidal Anti-Inflammatory Drugs of the Arylalkanoic Acids** 335
Mohamed R. Berber, Inas H. Hafez, Keiji Minagawa,
Takeshi Mori and Masami Tanaka
- Chapter 16 **Dendrimers in Anti-HIV Therapy** 361
Volha Dzmitruk, Dzmitry Shcharbin,
Elzbieta Pedziwiatr-Werbicka and Maria Bryszewska

Preface

Major improvements in functional and structural properties in material application are achieved by using composite material made with nanoscale components. Nowadays, for many industries nanocomposites are of great importance. The growing demand for nanocomposite material is showing a promising future. The use of such material is strongly influencing the industry of automotive, aerospace, food products, medicine and pharmacy, as well as material for engineering applications.

In order to accelerate growth of this promising field of technology, taking into account the recent research and studies, this book is considered the appropriate way of communicating the advances in nanocomposite materials to the scientists. The interdisciplinary scientific achievements will create valuable links for the experts worldwide, and will strengthen the approach to build scientific excellence in this field. This will stimulate technology transfer and will create valuable input from international projects for industry with special focus on the use of nanocomposite material.

Material nanocomposites have transformed the research strategy in the field of composite system performance and have led to the expansion of the spectrum of application of the commodity materials to more advanced high end applications.

Today, a number of successful system applications can be achieved in electronic applications, ceramic nanocomposites, functioning of nanopolymers and human and bio-applications. The nanocomposite technology is demanded worldwide, it has changed and it will continue to change the quality of life in the future.

In recent years, many new techniques have been employed to overcome the scientific problems. This includes more advanced material modification protocols, development of stable structure modification and altogether new nanocomposites synthesis technologies. The composite material properties have to be compared to the required property models and to be able to predict the properties of the similar systems in advance. The recently developed models as well as methods focusing on the real nanocomposite morphologies have proven to be very helpful. Though a remarkable research focus lies on these material systems, there is also a need to give some attention to environmentally friendly nanocomposite systems and to develop methods to achieve proper production techniques.

InTech Publisher's initiative is to contribute to the scientific community by focusing on the aims and objectives of up-to-date technologies.

One of such initiatives is the book "Advances in Nanocomposite Technology", in the field of nano scale materials. It contains 16 chapters divided in three sections.

Section one deals with the preparation and characterization of nanocomposite materials for electronic applications and studies: the new modification of solar cells, conducting polymer-metal nanocomposite, advanced systems application, surface plasmon resonance effect and comparative study of membranes obtained from natural clay nanocomposites. Five chapters in this section are focusing on the most recent individual technologies and research in electronic applications.

Polymer nanocomposites are an area of substantial scientific interest, the technology of emerging industrial practice. The dispersion of low loadings inorganic particles in the nanosize scale in organic polymers is a challenge for the preparation of new composite materials to enhanced mechanical, gas barrier and flame retardant properties. A homogenous dispersion of nanoparticles is believed to constrict better properties. Polymer-clay nanocomposite is one of the new forms of composite in polymer matrixes. The dispersed phase is the silicate constituted by one dimensional nanoparticle.

The incorporation of few percents of nano-sized particles makes great property changes and formerly unachievable property combinations possible. The achievable advantages of these nanocomposites are improved mechanical properties, surface properties, decreased permeability to gases, water and hydrocarbons, higher thermal stability and heat distortion, higher chemical resistance, smooth surface appearance and higher thermal conductivity.

In section two (Material Nanocomposites) the advanced research of polymer nanocomposite material and polymer-clay, ceramic, silicate glass-based nanocomposite and the functionality of graphene nanocomposites is presented.

The Human and Bioapplications section is describing how nanostructures are synthesized and draw attention on wide variety of nanostructures available for biological research and treatment applications. Focusing on the assembly of nanostructures with biological molecules could lead to the design of multi-functional nanosystems.

This section includes five chapters experiencing the unique properties of nanostructures provided along with the current applications of nanocomposites in biology and medicine. Some applications include the use of natural polysaccharides and their biofunctioning, antimicrobial polymer for food packaging and functional polymer for microfibrillated cellulose. This final section of the book also describes the progressing research in passive and active targeted-drug delivery, addressing the non-

steroidal anti-inflammatory drugs of the Arylalkanoic acids. The last chapter is about dendrimers as new class of nanoparticles for drug and gene delivery.

We believe that this book offers broad examples of existing developments in nanocomposite technology research and an excellent introduction to nanoelectronics, nanomaterial applications and bionanocomposites.

InTech Publisher and myself as the editor hope that this book will be supportive for the current research and prove to be very useful for the scientific community.

Dr. Abbass Hashim

Material and Engineering Research Institute
Sheffield Hallam University
UK

Part 1

Electronic Applications

Solar Nanocomposite Materials

Zhengdong Cheng

Artie McFerrin Department of Chemical Engineering

And the Materials Science and Engineering program

And the Professional Program in Biotechnology

Texas A&M University, College Station, Texas

USA

1. Introduction

The energy from the sun that strikes the earth is a gigantic 3×10^{24} J a year, or about 10,000 times more than what the global population currently consumes (M. Gratzel, 2007; B. Li, et al., 2006). World energy consumption is 5.0×10^{20} J and is expected to grow about 2% each year for the next 25 years (Us_Energy_Information_Administration, 2010). Covering 0.1% of the earth's surface with solar cells at an efficiency of 10% would provide the current energy needs of the whole world (B. Li, et al., 2006). However, the electricity generated from solar cells today is less than 0.1% of the world's total energy demand (P. V. Kamat, 2007). The first generation photovoltaic devices (PV) are based on single- or multi-crystalline p-n junction silicon cells. They are commercially available for installation with market share of about 85% and deliver power with 15% efficiency, but suffer from high cost of manufacturing and installation. There are high purity requirements for the silicon crystals, high fabrication temperatures and a large amount of material is needed for a wafer-based cell. The second generation PV devices use polycrystalline semiconductor thin films, mostly based on CdTe, having a market share of 15% (S. Ruhle, et al., 2010). Thin films of CuInGaSe₂ (CIGS) bring down the cost but their efficiency needs to improve for practical applications. The third generation devices will be based on nanocomposites (nano-structured semiconductors, organic-inorganic hybrid assemblies, and molecular assemblies), aiming to deliver high efficiency at an economically viable cost (P. V. Kamat, 2007). Nanostructure offers spatial quantum confinement for the tailor of the optical properties of semiconductor nanomaterials. The use of multi-components offers a high degree of flexibility for altering and controlling properties and functionalities of nanocomposites.

Nanocomposites are developed for superior device performance. In solar energy harvest and conversion, nanocomposites are utilized to overcome limits of single materials in solar spectrum response (band gap engineering), transport of electrons or holes (defect engineering), reaction of electrons or holes with chemicals (catalyst engineering), and reduce of costs (economic consideration).

2. History of solar nanocomposites

The first modern PV solar cells, silicon (Si) p/n, were developed by Chapin *et al.* at Bell laboratories in 1954 (D. M. Chapin, et al., 1954). These so called *first generation solar cells* cost

about \$4/W due to the materials used (the high quality and low defect single crystal Si, the strengthened low-iron glass cover sheet, and encapsulants). They are quickly used in space exploration. Considerable domestic use begun in 1978 when NASA installed a 3.5 kW system in a 16-home India village in Papago reservation, Arizona. Apart from regular use in power calculator, traffic signs, clocks and other small appliances, the use of solar cells has grow slowly although steadily (L. M. Goncalves, et al., 2008). The first amorphous Si cell (a-Si) appeared in 1976 right after the first oil shock (D. E. Carlson & C. R. Wronski, 1976). The high absorption rate of a-Si comparing to crystal silicon make it be a thin film technology. The thin film technology based solar cells are often called the *second generation solar cells*. They aimed at lower cost than the first generation. Among the three thin film technologies (a-Si, CdTe and Cu(In,Ga)Se₂), Cu(In,Ga)Se₂ (CIGS) cells have the best future due to higher efficiencies, confirmed maximum efficiency of 19.2% in 1999 (M. A. Contreras, et al., 1999; M. A. Green, et al., 2008) and low manufacturing energy consumption. Both first and second generation solar cells are based on single junction devices, for which the calculated thermodynamic efficiency limits (33.7%) is called Shockley-Queisser limit (W. Shockley & H. J. Queisser, 1961). Six junction (6J) cell (AlInGaP/InGaP/AlInGaAs/InGaAs/InGaAs/Ge) has a predicted maximum efficiency of 57% (M. Bosi & C. Pelosi, 2007). A theoretical limit for infinity-layer cell is 68% (A. Devos, 1980). In space applications where cost is not the major problem, multi-junction cells have replaced Si cells. The second generation solar cells and multi-layer semiconductor stack cells are still under development.

1883	Vogel	Ag-dye
1954	Chapin <i>et al.</i>	Si-p/n
1972	Fujishima &Hoda	TiO ₂ water splitting
1976	Carlson <i>et al.</i>	a-Si
1976	Matsumura <i>et al.</i>	ZnO-DSSC
1984	Serpone <i>et al.</i>	QDSSC
1991	Gratzel <i>et al.</i>	TiO ₂ -DSSC
1999	Contreras <i>et al.</i>	CIGS 19% efficiency

Table 1. History of solar nanocomposites

Historically, photographic films were particularly insensitive to mid-spectrum and red light due to wide band gap of the silver halide grains range from 2.7 eV to 3.2 eV (Fig.1) which has negligible absorption at wavelengths longer than 460nm (M. Gratzel, 2001). In 1883, Vogel discovered (W. West, 1974) that silver halide emulsion could be sensitized by adding a dye to extend the photosensitivity to longer wavelength. Four years later, this concept of dye enhancement was carried over to photoelectrochemistry cells by Moser using erythrosine on silver halide electrodes (M. Gratzel, 2001). It was later recognized that that the dye should be adsorbed on the semiconductor electrodes in a closely packed monolayer for maximum efficiency (R. C. Nelson, 1965), and electron transfer to be the prevalent

mechanism for the sensitization (K. Hauffe, et al., 1970). Photoelectrochemistry became a thriving research field on the foundation laid down by the work of Brattain and Garret (W. H. Brattain & C. G. B. Garrett, 1955) and subsequently Gerischer (H. Gerische, 1966) who took the first detailed electrochemical and photochemical studies of the semiconductor-electrolyte interface.

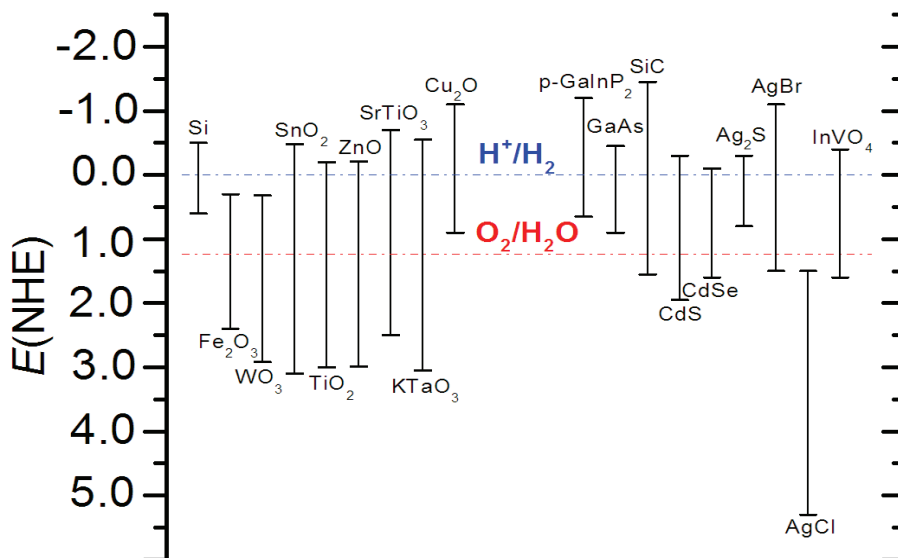


Fig. 1. Band gaps of semiconductors.

The oil crisis in 1973 fueled a rapid research on photoelectrochemical cells (K. Kalyanasundaram, 1985). TiO₂ became the favored semiconductor for water photolysis following its use by Fujishima and Honda in 1972 (A. Fujishima & K. Honda, 1972). The solution to the problem that narrow-bandgap semiconductors for efficient absorption of sunlight are unstable against photo-corrosion came in the separation of optical absorption and charge-generating functions. An electron transfer sensitizer is used to absorb the visible light and inject charge carriers across the semiconductor-electrolyte junction into a substrate with a wide bandgap, which is stable. This concept leads to the development of *dye-sensitized solar cells* (DSSC) in 1991 (B. Oregan & M. Gratzel, 1991) (Matsumura *et al.* developed ZnO-DSSC in 1976 (H. Tsubomura, et al., 1976)). In DSSC, the semiconductor is in the *mesoscopic* state (M. Gratzel, 2001): minutely structured with an enormous internal surface area (percolating nanoporous networks). The semiconductor (TiO₂, ZnO, SnO₂, CdSe etc.) films are made up of arrays of tinny crystals measuring a few nanometers across, which are interconnected to allow electronic conduction to take place. This structure has a much larger surface area (over a thousand times) available for dye chemisorption than a flat, unstructured electrode. The photocurrent in standard sunlight increased 10³-10⁴ times when passing from a single crystal to a nano-crystalline electrode. A overall power conversion efficiency of 10.4% has been obtained for DSSC (M. A. Green, et al., 2008; M. K. Nazeeruddin, et al., 2001). The record efficiency of DSSC is 12% for small cells and about 9% minimodules (A. Hagfeldt, et al., 2010).

The successful of DSSC has rekindled interest in tandem cells for water splitting by visible light. Tandem cells are needed for two reasons. First, most metal oxide semiconductors (such as WO_3 , Fe_2O_3 and TiO_2) can only reduce or oxidize water, not both. Secondly, most of the oxide semiconductors only absorb UV light. With DSSC can efficiently utilize the visible light and TiO_2 can reduce water, TiO_2 DSSC are used as bottom electrode to absorb the visible light and reduce water to hydrogen gas, which is in couple to the top electrode, either crystalline WO_3 (C. Santato, et al., 2001) or Fe_2O_3 (S. U. M. Khan & J. Akikusa, 1999) to absorb the blue part of the sunlight. This configuration is in close analogy to the "Z-scheme" of the photosynthesis of the green plants adsorbing complementary parts of the solar spectrum, where one photosystem oxidizes water to oxygen and the other generate the compound NADPH used in fixation of carbon dioxide. At present, the overall conversion efficiency from standard solar light to chemical energy is 4.5%.

Further the idea of sensitization, but using quantum dots (QDs) instead of dye to be attached to the semiconductor oxide matrix as light absorbers, we see the birth of the quantum dots sensitized solar cells (QDSCs) in 1984 (N. Serpone, et al., 1984). Comparing to DSSC, QDSSC has higher absorption, greater stability, wider tunable responsible wavelength range, and importantly the possibility to exploit *multiple exciton* generation and utilize *hot electrons* whose energy is higher than the low limit of conduction band (A. J. Nozik, 2002). The solar efficiency of liquid junction QDSSCs has reach 4.9% at present (G. Hodes, 2008; Q. X. Zhang, et al., 2011). The name of the *third generation solar cells* are given to devices (M. A. Green, 2003) aim to overcome the Shockley-Queisser limit of single junction or single band gap devices (33.7%), even the limit of an infinite stack of band gaps that perfectly matched to the solar spectrum (68%), and large-scale implementation. In principle, sunlight can be converted to electricity at efficiency close to Carnot limit of 93%. QDSSCs are very promising third generation solar cells due to their potential of achieving competitive cost-efficiency ratio. DSSCs are second generation solar cells with the possibility to become third generation devices if the efficiency can be largely improved.

3. PV cells

3.1 Dye Sensitized Solar Cells

DSSCs differ from conventional semiconductor devices in that they separate the function of light absorption from charge carrier transport, which solves the instability problem of narrow bandgap semiconductors using the concept very close to compositing. Dye sensitizer absorbs the incident sunlight (Fig.2 (M. Gratzel, 2004)) and exploits the light energy to induce vectorial electron transfer reaction. DSSC has the following advantages comparing with the Si based photovoltaics (D. Wei, 2010). (1) It is not sensitive to the defects in semiconductors such as defects in Si. It was found that the charge transport of photo-generated electrons passing the nanocrystalline particles and grain boundaries is highly efficient (U. Wurfel, et al., 2008). (2) The semiconductor-electrolyte interface (SEI) is easy to form and it is cost effective for production. (3) It is possible to realize the direct energy transfer from photons to chemical energy using nanoporous structures that offer a enormous surface area (1000 fold enhancement comparing a monolyer) for the adsorption of dye molecules. Other names for DSSC are dye-sensitized nanostructured solar cells, mesoscopic injection solar cells, nanosolar cells, the artificial leaves, or Gratzel cells (A. Hagfeldt, et al., 2010). (4) It is a *cheaper* alternative to silicon solar cells.

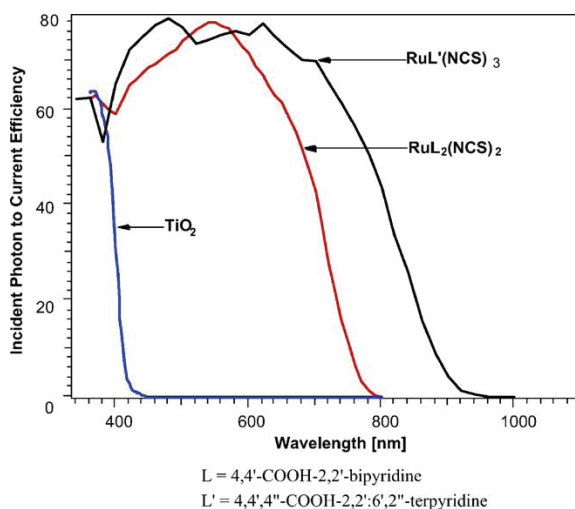


Fig. 2. Sensitization effect. DSSCs can convert visible light into electricity while TiO_2 only cannot.

Because of the encapsulation problem posed by liquid in the conventional wet DSSC, much work has also been done on an all solid DSSC (U. Bach, et al., 1998). To construct a full solid-state DSSC, a solid p-type conductor should be chosen to replace the liquid electrolyte. The redox levels of the dye and p-type materials have to be adapted carefully to result in an electron in the conduction band of n-type semiconductors (e.g., TiO_2 , ZnO (H. Tsubomura, et al., 1976), SnO_2 , SrTiO_3) and a hole localized on the p-type conductor (e.g., CuI (K. Tennakone, et al., 1998), CuSCN (B. Oregan & D. T. Schwartz, 1995)). Solid DSSC has also been fabricated using TiO_2 and conducting *polymers* (polypyrrole (K. Murakoshi, et al., 1998) and polyaniline (S. Ameen, et al., 2009)) and low bandgap polymer (W. S. Shin, et al., 2007). Solid state DSSCs based on ionic liquids were also reported to enhance the conversion efficiency (P. Wang, et al., 2003), and the non-volatile character of ionic liquids offers the easy packaging for printable DSSCs.

Plastic and solid state DSSCs incorporating single walled carbon nanotubes (SWNT) have been fabricated (N. Ikeda & T. Miyasaka, 2007). When employing SWNT as conducting scaffolds in a TiO_2 based DSSC, the photoconversion efficiency can be boosted by a factor of 2 (A. Kongkanand, et al., 2007). Graphene was also introduced to the study of DSSC recently. Transparent, conductive and ultrathin graphene films are used as an alternative to the ubiquitously employed metal oxides window electrodes in DSSCs (X. Wang, et al., 2008). In terms of publications, ZnO is so far the runner up to TiO_2 , mainly attributed to the relative ease of synthesizing highly crystalline ZnO with various morphologies, such as nanoparticles, nanowires, nanorods, nanotubes, tetrapods, nanoflowers, nanosheets and branched nanostructures. Nanostructured ZnO has been synthesized via a wide range of techniques. Historically, ZnO was one of the first semiconductors used in DSSCs (H. Tsubomura, et al., 1976). The band gap of ZnO is similar to TiO_2 (Fig.1). ZnO has higher electron mobility than TiO_2 , which should favor electron transport. However, ZnO is not chemically stable; it dissolves under both acidic and basic conditions. Other metal oxides used in DSSCs include SnO_2 , SrTiO_3 and others.

DSSC is the only solar cell that can offer both flexibility and transparency. Solid state and printable DSSCs will have a promising future for the development of efficient and flexible optoelectronics (S. Gunes & N. S. Sariciftci, 2008). Their efficiency is comparable to amorphous silicon solar cells but with a much lower cost, longer lasting and work at wide angles. Also, DSSCs work more efficiently in indoor light because dye absorbs diffuse sunlight and fluorescent lighting (D. Wei, 2010).

A challenging but realizable *goal* for the present DSSC technology is to achieve efficiencies above 15%. It requires developing dye-electrolyte systems that give efficient regeneration of the oxidized dye at a driving force of 0.2-0.4 V (A. Hagfeldt, et al., 2010). DSSC is a good example of a system where the function of the overall device is better than predicted from the sum of the properties of its components (A. Hagfeldt, et al., 2010). The nanostructured TiO₂ electrode does not conduct any electrical current and itself is a very good insulator. The conventional N3 dye dissolved in a solution degrades after a few hours under light. But when these are brought together in a well-working device, the solar cell conducts electrical current up to 20 mA/cm² and the dye will be stable for more than 15 years in outdoor solar radiation. Therefore, the photovoltaic function is the emergent property of the device that is made of the individual entities of the semiconductor, the sensitizer and the electrolytes.

The future directions for the development of DSSCs include (1) organic dyes that can extend light absorption into the near infrared with good photo and thermal stability (K. Kalyanasundaram & M. Gratzel, 1998), (2) synthesis and modification of various types of TiO₂, or other semiconductors, nanomaterials (X. B. Chen & S. S. Mao, 2006), and (3) modification of the physical properties of TiO₂ nanostructures to extend optical absorption into the visible region (X. B. Chen, et al., 2005; S. U. M. Khan, et al., 2002).

3.2 Quantum Dots Sensitized Solar Cells

The concept of Quantum dot (QD) sensitized solar cells (QDSSCs) is borrowed from the photoelectrochemical Gratzel's cells, the dye sensitized solar cells (DSSC) (B. Oregan & M. Gratzel, 1991). Due to the similar size of QDs and the nanocrystals of the metal oxide semiconductors, *all QDSSCs are nanocomposites* in tend to optimize the solar spectrum response of the resulted materials.

Quantum dot sensitizers for solar cells have several promising advantages over dye sensitizers: (1) Tunable energy gaps (S. Gorer & G. Hodes, 1994). The band gaps can be simply adjusted by changing the size and shape of QDs, and well match the solar spectrum. Also, there is a wider band gap range of semiconductor than dyes. (2) Large absorption coefficient (typically by a factor of 5 (G. Hodes, 2008)) (I. Moreels, et al., 2007). The high extinction property of bulk semiconductors are preserved at the nanoscale (W. W. Yu, et al., 2003). (3) Multiple electron-hole pair production per photon utilizing hot electrons (V. I. Klimov, 2006; A. J. Nozik, 2002; R. D. Schaller & V. I. Klimov, 2004; Y. Takeda & T. Motohiro). Other advantages include superior resistance towards photobleaching over organometallic or organic dyes (G. Hodes, 2008), low cost and easy to synthesis. In addition, the production of QDs is significantly cheaper compared to their bulk counterparts since their synthesis takes place at significantly lower temperatures and with solution-based approaches.

In spite of the above advantages of QDs compared with dyes, the best reported efficiencies of QDSSCs are still lower than that of DSSCs. Large improvement in efficiency of QDSSCs, comparable to DSSCs, is expected. The main differences between these two types of solar

cells are (G. Hodes, 2008) : (1) Multiple layer absorption of QDs on the mesoporous oxide surface compared to a monolayer of absorbed dye might hindrance the electron transfer rate from the QD to the oxide. (2) Different electrolytes are used (I. Mora-Sero & J. Bisquert, 2010). The polyiodide electrolyte used in DSSC might be also beneficial to QDSSC. However, the choice of electrolyte will depend on the specific adsorbing semiconductor used, and no optimized electrolyte system has been obtained. (3) The presence of considerable surface charge traps on absorbed QDs which increases recombination. Passivation of surface states on the QDs can be done, after deposition of the QDs to the oxide, by coating the QDs with suitable band-aligned semiconductor shell or by adsorbing long chain organic passivating molecules onto the QDs. Passivation of the QD-Oxide interface might be pre-deposition of a buffer layer or small molecules on the oxide before QD deposition. Wide band gap semiconductor ZnS has coated on the surface of CdS QDs that were *grown* in situ on TiO₂ inverse opal and led to a higher efficiency due to the decrease of QD surface traps (L. J. Diguna, et al., 2007b).

A recent study presented CdS QDSSC based on a mesoporous TiO₂ film with remarkable stability using I⁻/I₃⁻ electrolyte (M. Shalom, S. Dor, et al., 2009). Chemical Bath Deposition (CBD) was used to *deposit* the CdS QDs within the porous network. A thin coating of the QD sensitized film with an *amorphous TiO₂ layer* has improved the performance and photostability of the solar cell, which confirmed the hypothesis that the coating passivates QD surface states which act as hole traps and are responsible for photodegradation of the device. In addition, this coating decreased the recombination of electrons from the CdS QDs and the mesoporous TiO₂ into the electrolyte solution. A total light to electric power conversion efficiency of 1.24% was achieved.

The conduction and valence bands levels of QDs play an important role in dictating capture of photogenerated electrons and holes at the interface. Both CdSe and CdTe QDs bind strongly to TiO₂ through a linker molecule, and inject electrons into TiO₂ with an ultrafast rate under bandgap excitation. CdTe has a more negative conduction band (-1.25V vs NHE, normal hydrogen electrode) compared to CdSe (-1.2V vs NHE) and hence injects electrons into TiO₂ nanoparticles at a faster rate. The reactivity of photogenerated holes with the sulfide electrolyte, however, determines their suitability in QDSSCs (J. H. Bang & P. V. Kamat, 2009). CdSe remains regenerative during the operation of QDSSC as the photogenerated holes are scavenged by S²⁻ ions. A maximum Incident Photo to Charge conversion efficiency (IPCE) of 70% shows the suitability of this system in a photoelectrochemical solar cell. The scenario is, however, different for CdTe-based QDSC. The formation of a CdS shell and the inability to scavenge photogenerated holes make CdTe a poor candidate for QDSCs. A series of other redox couples were used in the photoelectrochemical cells as a replacement of the S²⁻/S_n²⁻, none of them seems to provide the required photostability for the CdTe QD electrodes; most of them immediately corrode CdTe QDs even under ambient conditions. Despite the fast electron injection rate was observed, it has a poor external quantum efficiency (3%) (J. H. Bang & P. V. Kamat, 2009). The difference in the performance of these two systems has been understood based on the position of their valence bands (0.53V in CdSe and 0.1V in CdTe). The energy levels of valence bands are such that redox couples such as a sulfide/polysulfide couple (-0.5V) scavenge holes only from CdSe and *not* from CdTe. This failure to scavenge photogenerated holes results in the degradation of CdTe. Hence, the choice of CdTe for the operation of QDSSCs (*i.e.*, photoelectrochemical cells) currently poses a serious challenge.

There are generally two methods adopted to realize QDs sensitizers over mesoporous TiO₂ films: (1) direct growth of the QDs on the TiO₂ photoanode surface by chemical bath deposition (CBD) or by successive ionic layer adsorption and reaction (SILAR); (2) pre-synthesized colloidal QDs attached to the electrode surface directly or with the aid of bifunctional linker molecules. These methods sometimes are combined in order to achieve co-sensitized deposition (L. Yin & C. Ye, 2011; Q. X. Zhang, et al., 2011). For example, CdSe can be pre-synthesized in a colloidal form with different shapes and sizes that may be directly attached to the wide band gap semiconductors (the electron-transport matrix) (S. Gimenez, et al., 2009; N. Guijarro, et al., 2009) or through bifunctional linker molecules (H. J. Lee, et al., 2008; I. Mora-Sero, et al., 2008; I. Robel, et al., 2006). It has also been directly grown on the surface on a wide gap semiconductor by CBD (L. J. Diguna, et al., 2007a; O. Niitsoo, et al., 2006; Q. Shen, et al., 2008), SILAR (H. Lee, et al., 2009) or electrodeposition (C. Levy-Clement, et al., 2005).

In QDSSC, the diameter of QDs anchored on the photoanode generally ranges from 3 to 8 nm, much larger than that of dyes. For the normal nanoparticle-based TiO₂ film, its inner pores are much easier to be blocked while depositing QDs. Other factors such as TiO₂ morphology, surface area, inner pore structure etc. will strongly influence the QDs loading and cell performance. Of course, optical confinement and light scattering effect to improve the light absorption efficiency are also necessary. Aiming at improving the efficient assembly of the QDs onto the TiO₂ photoanode, the influence of structural properties of various TiO₂ photoanodes on the photovoltaic performance of CdS/CdSe- QDSSCs has been systematically investigated (Q. X. Zhang, et al., 2011). The results revealed that unlike conventional DSSCs, the main contribution of the scattering layer to QDSSCs is adjusting the aperture distribution of TiO₂ working electrode for CdS/CdSe deposition, extending the light path length and decreasing the electron recombination. In the meantime, an introduction of large size 300 nm TiO₂ particles into the photoanode can achieve a wider pore size distribution from several nanometers to over 50 nanometers for effective CdS/CdSe coverage on the surface of TiO₂ photoanodes as well as facilitating the polysulfide electrolyte penetration in the TiO₂ films. A double-layer photoanodic structure can give 4.92% of light-to-electricity conversion efficiency with 0.15 cm² of photoactive area, which is among the best results for the QDSSCs.

To harvest as much as possible the solar energy, combination of the absorber materials with varied band gap (*nanocomposite absorbers*) have been tested (V. Gonzalez-Pedro, et al., 2010; Y. L. Lee & Y. S. Lo, 2009; O. Niitsoo, et al., 2006). An interesting study shows that CdS and CdSe QDs have a complementary effect in light harvesting and the performance of a QDs co-sensitized solar cell is strongly dependent on the order of CdS and CdSe respected to the TiO₂ (**Fig.3 a&b**. TiO₂/CdS(3)/CdSe(4) means TiO₂ nanoporous film was deposited CdS QDs by 3 CBD cycles followed by deposition of CdSe by 4 CBD cycles) (Y. L. Lee & Y. S. Lo, 2009). In the cascade structure of TiO₂/CdS/CdSe electrode, the re-organization of energy levels (**Fig.3c**) between CdS and CdSe forms a stepwise structure of band-edge levels which is advantageous to the electron injection and hole-recovery of CdS and CdSe QDs. An energy conversion efficiency of 4.22% is achieved using a TiO₂/CdS/CdSe/ZnS electrode, under the illumination of one sun (AM1.5, 100 mW cm⁻²). The present of CdS between TiO₂ and CdSe does not inhibit the transport of excited electron from CdSe to TiO₂, but it is not the case when you switch CdS and CdSe. In the long-wavelength region where only CdSe can be photoexcited, the IPCE increment of the TiO₂/CdS/CdSe device, with respect to that

of TiO_2/CdSe , indicates that the presence of CdS between TiO_2 and CdSe should take the responsibility for the performance enhancement of the $\text{TiO}_2/\text{CdS}/\text{CdSe}$ device (**Fig.3b**).

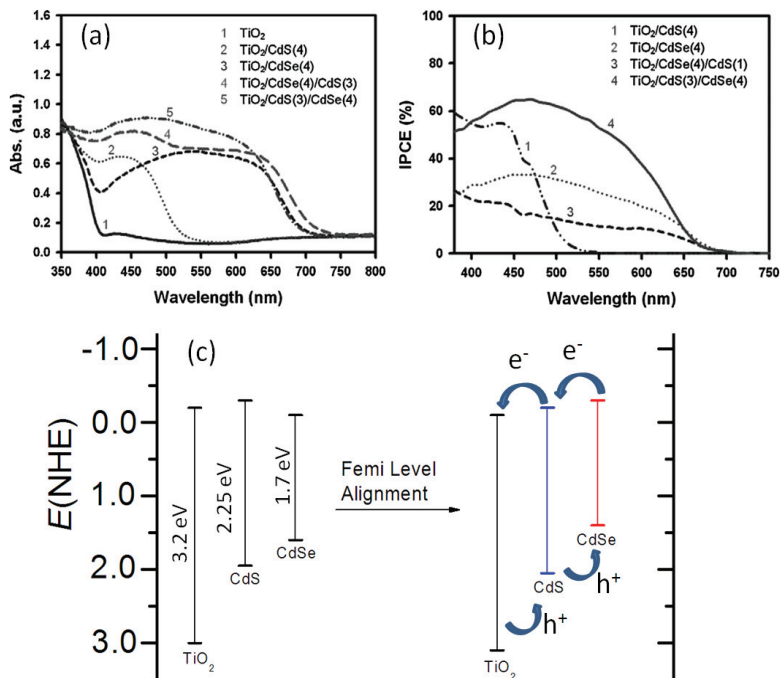


Fig. 3. Femi level alignment.

That is, the presence of CdS is helpful to the collection of excited electrons from CdSe to TiO_2 , which takes major contribution to the cosensitization effect of the $\text{TiO}_2/\text{CdS}/\text{CdSe}$ device. On the other hand, when CdS is deposited on TiO_2/CdSe , the IPCE of the $\text{TiO}_2/\text{CdSe}/\text{CdS}$ device is lower than that of TiO_2/CdSe and TiO_2/CdS devices, which means that introduction a CdSe layer between TiO_2 and CdS is detrimental to the transport of excitons and, therefore, the co-sensitization effect cannot be achieved. The band edges of TiO_2 , CdS, and CdSe in bulk are schematically shown in **Fig.3c**. When CdS and CdSe were brought in contact as a cascade structure, the energy levels difference (Fermi level difference if they follow Fermi-Dirac statistic) between CdS and CdSe causes the electrons flow from CdS (higher level) to CdSe (lower level). Such electron transfer is known as the *Fermi level alignment* if the material can be described by Fermi-Dirac distribution. The redistribution of the electrons between CdS and CdSe is supposed to trigger a downward and upward shift of the band edges, respectively, for CdS and CdSe. Therefore, the resulting band edges for the $\text{TiO}_2/\text{CdS}/\text{CdSe}$ device are inferred to have a stepwise structure as shown in **Fig.3c**. Both the conduction and valence bands edges of the three materials increase in the order: $\text{TiO}_2 < \text{CdS} < \text{CdSe}$. That is, the insertion of a CdS layer between TiO_2 and CdSe elevates the conduction band edge of CdSe, giving a higher driving force for the injection of excited electrons out of CdSe layer. This is why a higher IPCE was obtained for the $\text{TiO}_2/\text{CdS}/\text{CdSe}$

device in the long-wavelength region, compared with the TiO₂/CdSe device. When both CdS and CdSe are photoexcited under white light illumination, the stepwise structure of the band edges is advantageous not only to the electron injection but also to the hole-recovery for both the inner CdS and outer CdSe layers. On the contrary, in the TiO₂/CdSe/CdS device, the conduction and valence bands edges of intermediate CdSe will be higher respected to those of CdS. In such an energy structure, energy barriers exist for injecting an excited electron from outer CdS layer and transferring a hole out of inner CdSe, which causes a low IPCE of the TiO₂/CdSe/CdS device.

It is possible to design both injection and recombination in QDSSC by the appropriate use of *molecular dipoles* and conformal coatings via *energy level alignment* (E. M. Barea, et al., 2010; M. Shalom, S. Ruhle, et al., 2009). Mesoporous TiO₂ electrodes were coated with "in situ" grown CdSe semiconductor nanocrystals by CBD. Surface modification of the CdSe sensitized electrodes by conformal ZnS coating and grafting of molecular dipoles (DT) has been explored to both increase the injection from QDs into the TiO₂ matrix and reduce the recombination of the QD sensitized electrodes. Different sequences of both treatments have been tested aiming at boosting the energy conversion efficiency of the devices. The obtained results showed that the most favorable sequence of the surface treatment (DT+ZnS) led to a dramatic 600% increase of photovoltaic performance compared to the reference electrode (without modification), and efficiency 1.60% under full 1 sun illumination was obtained (E. M. Barea, et al., 2010).

Ag₂S has an energy band gap of $E_g \sim 1.1\text{eV}$ (Fig.1), which is equal to the optimal band-gap of 1.13 eV for a PV cells (A. Marti & G. L. Araujo, 1996). Ag₂S QDs were synthesized using successive ionic layer adsorption and reaction (SILAR) deposition (A. Tubtimtae, et al., 2010). A 0.1 M AgNO₃ ethanol solution was prepared by dissolving AgNO₃ crystals in ethanol, then stirring vigorously for 30 min. A TiO₂ electrode was dipped into the 25°C AgNO₃ solution for 1 min, washed with ethanol, then dipped into a 0.1 M Na₂S methanol solution for 3 min. The two-step procedure forms one SILAR cycle, and was repeated several times. The assembled Ag₂S-QD solar cells yield a best power conversion efficiency of 1.70% and a short-circuit current of 1.54 mA/cm² under 10.8% sun. The solar cells have a maximal external quantum efficiency (EQE) of 50% at $\lambda=530\text{ nm}$ and an average EQE about 42% over the spectral range of 400–1000 nm. The effective photovoltaic range covers the visible and near infrared spectral regions and is 2–4 times broader than that of the cadmium chalcogenide systems, the CdS and CdSe. The results show that Ag₂S QDs can be used as a highly efficient and broadband sensitizer for solar cells.

To increase the light absorption and raise the photoelectric conversion efficiency, porous oxide semiconductor is frequently used as one of the electrodes. One dimensional nanomaterials, such as nanotubes (D. R. Baker & P. V. Kamat, 2009; A. Kongkanand, et al., 2008), nanowires and nanorods (A. Belaidi, et al., 2008), and inverted opals (L. J. Diguna, et al., 2007a; K. Shankar, et al., 2009) are also excellent candidates (K. Shankar, et al., 2009; Y. Tak, et al., 2009). QD-SSC was designed and prepared by using CdS/CdSe co-sensitized TiO₂ nanotubes (TNT) on Ti wire and a highly active Cu₂S counter electrode (Fig.4). By optimizing the CdSe deposition time and length of nanotubes, a best efficiency of 3.18% was obtained under AM1.5 illumination (100mW cm⁻²). It is revealed that there are several advantages of this fibrous QD-SSC based on TNT: (1) the conflict between illumination and opaque electrodes is effectively solved, in contrast to the situation based on Ti foil; (2) many more kinds of counter electrodes can be selected, giving the possibility of better photovoltaic performance and (3) it is flexible, of low serial resistance and easily weaved and integrated.

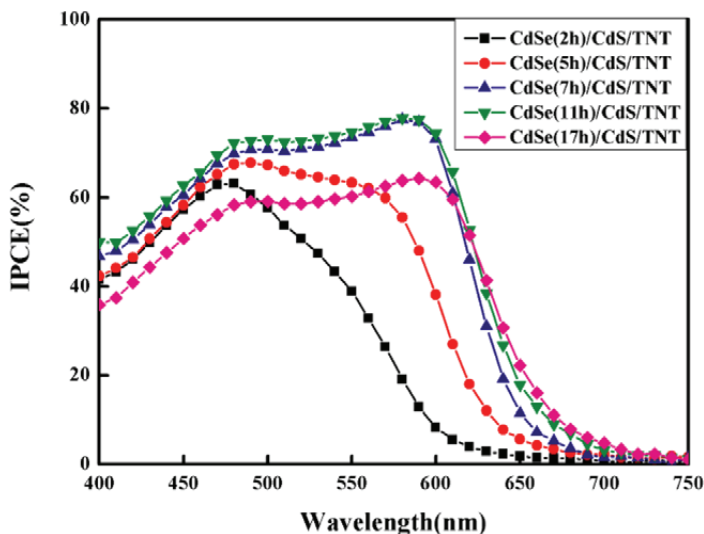


Fig. 4. Fibrous CdS/CdSe QDs co-sensitized solar cells based on ordered TiO₂ nanotube arrays.

Therefore, the fibrous QD-SSC is expected to have a potential application in the future (S. Q. Huang, et al., 2010).

In summary, nanocomposite QDSSCs work through two beneficial effects, (1) broaden spectral absorption range and (2) interaction between different absorbing parts reducing the overall recombination. QDSSCs have experienced rapid growth over the past two decades, and hold promising advantages over DSSCs. To achieve efficiency higher than the current record of 4.9%, the future directions in QDSSCs include (1) developing strategies to organize ordered assemblies of two or more components (QDs and other semiconductors, metals, polymers) on electrode surfaces (J. Chen, et al., 2009), and gaining thorough understanding of the charge separation and transport (M. Shalom, S. Ruhle, et al., 2009); (2) developing new QDs that can harvest infrared photons to broaden the photo-response in the solar spectrum; (3) developing techniques to harvest hot (W. A. Tisdale, et al., 2010) or multiple charge carriers generated in QDs (A. J. Nozik, 2002); (4) synthesis and modification of various type of TiO₂, or other semiconductors, nanomaterials (X. B. Chen & S. S. Mao, 2006; Y. J. Lin, et al., 2009), and (5) modification of the physical properties of TiO₂ nanostructures to extend optical absorption into the visible region (X. B. Chen, et al., 2005; S. U. M. Khan, et al., 2002).

3.3 Polymer-inorganic PV cells

Polymer-based photovoltaic (PV) devices are of great interest, because they can be used to fabricate low-cost, light weight, large-area, and flexible solar cells using inexpensive painting or simple printing (Q. Q. Qiao, et al., 2008; M. K. Siddiki, et al., 2010). Hybrid polymer-based PV devices consisting of a conjugated polymer (p-type semiconductor) and inorganic semiconductors (n-type) have attracted attention as promising alternatives for future PV devices, since they combine the unique properties of inorganic semiconductors (e.g., high electron mobility and stability) with the good film-forming properties of conjugated polymers. Meanwhile, the size, shape, and optoelectronic properties of inorganic

semiconductor nanocrystals can be tailored during the synthesis process before the organic phase is incorporated. Conjugated polymers offer an attractive approach for increasing solar cell efficiencies because their band gaps and energy levels can be engineered by modifying their chemical structure (M. K. Siddiki, et al., 2010).

The highest theoretical energy conversion coefficient for a single-junction polymer solar cell is about 10-13% for a polymer with a band gap of 1.5 eV (M. C. Scharber, et al., 2006). Multi-junction structures have appeared as a promising solution to achieve higher efficiency. Currently, a maximum 7.9% efficiency has been obtained (M. K. Siddiki, et al., 2010). New materials for broad spectrum light harvesting, highly efficient interfacial layer materials as both protection and recombination layer, and novel device designs are needed to increase the efficiency for large scale applications.

Tandem solar cells, in which two solar cells with different absorption characteristics are linked to use a wider range of the solar spectrum, has been fabricated with each layer processed from solution with the use of bulk heterojunction materials comprising semiconducting polymers and fullerene derivatives (J. Y. Kim, et al., 2007). A transparent titanium oxide (TiO_x) layer separates and connects the front cell and the back cell. The TiO_x layer serves as an electron transport and collecting layer for the first cell and as a stable foundation that enables the fabrication of the second cell to complete the tandem cell architecture. An inverted structure was used with the low band-gap polymer-fullerene composite as the charge-separating layer in the front cell and the high band-gap polymer composite as that in the back cell. Power-conversion efficiencies of more than 6% were achieved at illuminations of 200 mW/cm².

4. Solar hydrogen production via water splitting

In the various strategies for solar energy conversion, solar fuel or solar hydrogen conversion is attractive in that the harvested energy can be stored in chemical bonds. Since electricity only can be generated during day time by PV cells, large scale use of solar energy requires an efficient *energy storage* solution. Hydrogen is a “fuel of the future” because of its abundance and zero greenhouse gas emissions (S. Combs, 2008; G. W. Crabtree, et al., 2004). The splitting of water with sunlight to produce hydrogen is the basis for one of the most promising new energy industries, both in terms of high projected growth and low environmental footprint. Both water and sunlight are abundant resources, while hydrogen is a unique energy carrier since its oxidation leads to production of the starting material (water).

Once produced, hydrogen is the best transportation fuel, the most versatile, most efficient, most environmentally compatible, safest and most cost effective fuel to society (J. A. Turner, 1999; T. N. Veziroglu & F. Barbir, 1992). Prototypes of a number of hydrogen fuel cell devices are already on the market, including uses in cell phones, and even a self-sustained, hydrogen-operated house (D. Biello, 2008). The largest market segment is hydrogen use for transportation. Several cities, including Chicago and Vancouver, are already testing buses running on hydrogen in their public transit fleets, with plans to convert entire fleets to hydrogen. The hydrogen distribution infrastructure is also rapidly developing, with 74 hydrogen refueling stations already operational in the U.S. and Canada, and 43 more planned in the immediate future. The size of the current market (\$1.5B) is limited to uses mandating the exploration of alternative energies. Efficient catalysts for solar hydrogen

production would make it possible to compete for the over \$500B per year the US spends on oil.

Currently, most of the hydrogen is produced from methane-steam reforming (E. Kikuchi, et al., 2000), which consumes energy and produces green house gases emissions, mainly, carbon dioxide (W. Dougherty, et al., 2009). In contrast, the photoelectrochemical water-splitting process is a zero-emission process that only uses freely available solar energy (A. Currao, 2007). The problems of direct photochemical conversion of solar energy into hydrogen fall into the following categories: (1) inefficient use of solar spectrum for the generation of excitons (Wide bandgap semiconductors TiO_2 , SrTiO_3 , KTaO_3 that can split water directly use only UV wavelengths 4% of the total energy), (2) exciton recombination, and (3) inefficient use of dissociated electrons and holes in catalysis. Ever since the discovery of water-splitting by Fujishima and Honda in 1972 (A. Fujishima & K. Honda, 1972), numerous studies have discussed these issues heavily to find a strong candidate material that overcomes these problems. The properties, size, geometry and compositions of materials are the keys to modify the material activity to improve hydrogen production (M. Ni, et al., 2007). Many tested semiconductors are either unstable in aqueous solution (CdS), or their band gap is too large to use light efficiently (SnO_2) (M. Matsuoka, et al., 2007). TiO_2 is chosen as the most stable semiconductor in water, but its large bandgap (3.2 eV) results in poor solar energy conversion. Currently, the use of visible light responsive quantum dots (including CdS, CdSe and PdSe) to improve the efficiency of TiO_2 -based photovoltaics is an area of active exploration (T. Lopez-Luke, et al., 2008).

The advantage of photo-electro-chemical water splitting over water electrolyzing using solar PV cells. The current commercially available electrolyzers have electricity to hydrogen conversion efficiencies of up to 85%. To achieve a current density of about $1\text{A}/\text{cm}^2$ that is normally used in electrolyzers, a cell voltage of 1.9V is required. Since the thermodynamic potential required for water splitting is 1.23eV, the energy conversion efficiency has an upper limit of $1.23/1.9=65\%$ for the electrolyzers. Therefore, the PV-electrolyzer efficiency is limited to $\sim 8\%$ (O. Khaselev, et al., 2001; R. Van De Krol, et al., 2008). On the other hand, solar hydrogen production via direct photocatalytical reaction can be much higher, for example 16.8% for using a single semiconductor (A. B. Murphy, et al., 2006). Other advantages include the avoid of the significant fabrication and systems costs involved with the use of separate electrolyzers that are wired to p-n junction solar cells, and the easiness that an electric field can be created at a semiconductor-liquid junction (A. Heller, 1981).

Photoelectrochemical splitting of water involves the use of a semiconductor to convert solar energy into electrochemical energy and using it to split water. Advanced concepts in solar-fuel conversion share much in common with many third-generation concepts for solar cells. Suitable photo-electrode materials for efficient solar hydrogen generation have to fulfill the following requirement: (1) strong (visible) light absorption, (2) high chemical stability, (3) suitable band edge positions to enable reduction/oxidation of water, (4) efficient charge transport in the semiconductor, (5) low overpotential for the reduction/oxidation reaction, and (6) low cost (R. Van De Krol, et al., 2008).

The first requirement is related to solar spectrum and energy requirement for chemical reaction. The minimum band gap of the semiconductor for photo water splitting is determined by the energy required to split water (1.23 eV), plus the thermodynamic loss ($\sim 0.4\text{eV}$) (M. F. Weber & M. J. Dignam, 1986), and the over-potentials that are required to

ensure sufficient fast reaction kinetics ($\sim 0.3\text{--}0.4\text{eV}$) (J. R. Bolton, et al., 1985; A. B. Murphy, et al., 2006). So, the low limit of band gap is 1.9 eV, which corresponding to light wavelength of 650 nm, in the lower energy red portion of the visible spectra. Since the sunlight intensity drops rapidly below 400 nm (corresponding to 3.1 eV), the suitable band gap for the semiconductors is 1.9–3.1eV, which is in the visible range of the solar spectrum. Murphy *et al.* predicted a maximum efficiency of 16.8% for a hypothetically idea material with a band gap of 2.03eV (A. B. Murphy, et al., 2006), which exceeds the 10% target by 2018 set the U.S. Department of Energy for photoelectrochemical hydrogen production (Us_Department_of_Energy, 2007). Higher efficiencies can be obtained using a multiple band gap system. *Nanocomposites are needed to construct a system to meet the requirement of visible-light absorption.*

The second requirement excludes non-protected direct use of most non-oxide semiconductors, such as Si, GaAs, GaP, CdS, which either dissolve or form a thin oxide film that prevent electron transfer across the semiconductor-electrolyte interface. For thermodynamic stability, a semiconductor's reductive and oxidative decomposition potentials must be more negative than the semiconductor's conduction band-edge for water reduction or more positive than the semiconductor valence band-edge potential for water oxidation, respectively (O. Khaselev & J. A. Turner, 1998b). Photo generated holes are able to oxidize most metal oxides, but photo-corrosion can be avoided if the charge transfer across the interface to oxidize water is faster than the decomposition reaction. TiO_2 and SnO_2 show excellent stability over a wide range of pH values and applied potential, while ZnO always decomposes and the stability of Fe_2O_3 depends on the present of dopants, pH, and oxygen stoichiometry (R. Shinar & J. H. Kennedy, 1982). Generally speaking, wide bandgap metal oxides semiconductors are stable against photo-corrosion and small band gap semiconductors are not, in contradiction to the first requirement. This is the so called "duality principle" limitation of photoelectrolysis (N. S. Lewis, 2001). Therefore, *nanocomposites are needed to solve the photo-corrosion problem.*

Fig.1 shows the band-edge positions of various semiconductors. For photo water splitting, the conduction and valence band edges should straddle the reduction and oxidation potential of water: the conduction edge should above $E_{\text{red}}(\text{H}^+/\text{H}_2)$ and the valence edge should below $E_{\text{ox}}(\text{OH}/\text{O}_2)$. Most non-oxide semiconductors are able to reduce, but not oxidize water; and most oxide semiconductors are able to oxidize, but not reduce water. After photo-excitation and charge separation in an n-type semiconductor, holes in the VB diffuse to the semiconductor-liquid interface to oxidize water. The large difference between the VB of oxide semiconductors ($\sim 3\text{eV}$ vs NHE, *cf.* Fig.1) and the oxygen evolution reaction (OER) potential (1.23 eV vs NHE) indicate, much of the excess energy ($\sim 1.77\text{eV}$) is wasted by thermal relaxation. Therefore, the efficiencies converting sunlight to O_2 of most photoanodes are very low.

Wide band gap metal oxide semiconductors absorb only a small portion of the solar spectrum (UV part). By using a tandem cell approach, the remaining part of the spectrum can be used to provide the additional bias voltage required for the reduction reaction. For example, a *separated* DSSC was used to provide a bias voltage to WO_3 or Fe_2O_3 photo-anode (involving two separated devices). An efficiency of 4.5% was achieved for WO_3 photo-anode (M. Gratzel, 2001), which is close to the theoretical efficiency WO_3 (A. B. Murphy, et al., 2006). Using highly efficient dendritic $\alpha\text{-Fe}_2\text{O}_3$ photo-anodes, overall solar-to-hydrogen efficient 2.2% are reached (A. Kay, et al., 2006). A *monolithic* tandem cell (involving only a

single-device) based on a p-type CaInP_2 photo-cathode biased by a GaAs p-n junction solar cell was fabricated, and the solar-to-chemical conversion efficiency is 12.4% (O. Khaselev & J. A. Turner, 1998a). The shortcomings of this device are *high cost* and severe photo-corrosion problem. Amorphous silicon (a-Si) is much cheaper than GaAs-based materials. The a-Si/ WO_3 hybrid photo-electrodes show solar-to-hydrogen conversion efficiencies of 1% in out-door test (E. L. Miller, et al., 2005). A particular challenge for such device fabrication is to deposit the metal oxides at sufficiently low temperatures ($<300^\circ\text{C}$) to avoid degradation of the underlying a-Si junctions.

In the *composite particle systems*, a hetero-junction forms between two component-particles. Due to the different energetic positions of the conduction and valences edges, the electrons are transported to one component-particle, while the holes move to the other one. The effective charge separation in such systems limits the recombination of photo-excitons; hence improve the sun-to-hydrogen conversion efficiency. In the *mixed-particle systems*, this concept is taken a step further by perform the oxidation and reduction of water on two different particles that are not in direct contact. To ensure a complete redox reaction at each individual particle, a redox mediator, for example I-/ IO_3^- (K. Sayama, et al., 2001), is used to transport electrons from the oxygen evolving particles to their hydrogen evolving counterparts.

Even though several semiconductors have band-edge positions that are appropriate for water reduction or oxidation, the kinetics of these reactions on the bare semiconductor surface generally limit the efficiency. Addition of a *co-catalyst* to the surface can improve the reaction kinetics. Pt is the frequently used co-catalyst for hydrogen evolution reaction (HER). Noble metals and transition metals, such as Au, Ag, Cu and Ni, can be also effective and cheaper (N. Alenzi, et al., 2010; M. G. Walter, et al., 2010). On the other hand RuO_2 , IrO_2 can be effective co-catalysts for OER (M. G. Walter, et al., 2010). When the noble metals are loaded to the surface of a semiconductor, they act as electron traps because their lower Fermi energy level than the semiconductor, facilitating electron-hole separation and promotes interfacial electron transfer process (V. Subramanian, et al., 2001). In addition, surface plasmon resonances of noble metal particles, which can be excited by visible light, increase the electric field around metal particles and thus enhance the surface electron excitation and electron-hole separation on noble metal-doped semiconductor particles (Y. M. Cho & W. Y. Choi, 2002; E. Kowalska, et al., 2010). The role played by the co-catalyst is extremely important. It improves overall photocatalytical activity of the water splitting. In many cases, the photo-catalyst is only able to evolve either hydrogen or oxygen gas, not both at the same time. If only hydrogen (oxygen) evolves, a sacrificial electron donor (acceptor) must be present to ensure the stoichiometric consumption of electrons and holes. The sacrificial systems are of considerable interest because they permit the study of electrode reactions. Methanol is almost always used as a sacrificial electron donor (hole scavenger) (E. L. Miller, et al., 2005).

4.1 CdS

CdS is a fascinating visible light-driven photocatalyst for water splitting having a band-gap energy of 2.4 eV. Its CB and VB positions are very suitable for HER and OER, respectively. However, CdS is very unstable toward photocorrosion due to serious self oxidation of the photogenerated holes in the valence band ($2\text{h}^+_{\text{vb}} + \text{CdS} \rightarrow \text{Cd}^{2+} + \text{S}$). CdS nanocrystals, nanowires, and nanorods were synthesized and used to study photo

hydrogen production using sacrificial reagents under visible light irradiation (N. Bao, et al., 2007; J. S. Jang, et al., 2007; Y. Li, et al., 2009). A high quantum yield of about 60% measured (N. Z. Bao, et al., 2008) at 420 nm was obtained for hydrogen production over nanoporous CdS nanostructures attributed the high efficiency to the efficient charge separation, fast transport of the photo-generated carriers, and fast photochemical reaction at the CdS/electrolyte interface.

Among the CdS composites, CdS-TiO₂ has attracted the most extensive research (X. B. Chen, et al., 2010; T. Y. Peng, et al., 2008). Both the conduction and valence band edges of CdS are at more negative potentials than those of TiO₂ (cf. Fig.1). Under visible-light irradiation, the photogenerated electrons in the CdS particles quickly transfer to TiO₂ particles, whereas photogenerated holes stay in CdS. This facilitates the electron-hole separation and prevents the charge recombination, improving the photocatalytical activity.

CdS-Au-TiO₂ heterojunction was developed where CdS, TiO₂ and the electro-transfer medium Au were all spatially fixed. This three-component system exhibits a high photocatalytical activity, far exceeding those of the single- and two-component systems, as a result of vectorial electron transfer driven by the excitation of both TiO₂ and CdS (H. Tada, et al., 2006). General speaking, a *Z-scheme* water splitting involve two step photo-excitation under visible light irradiation mimicking the nature photosynthesis of green plants (K. Sayama, et al., 2002). The Z-scheme system consisted of a H₂-evolution photocatalyst (PS1), an O₂-evolution photocatalyst (PS2), and a reversible redox mediator (Ox/Red) which acts separately as electro donor (PS1) and acceptor (PS2) for the respective half reaction and which is different from irreversible sacrificial reagents used in conventional systems. CdS-Au-TiO₂ is an all-solid-state Z scheme (PS1:CdS, PS2:TiO₂ and Au is the electro-transfer system). The electron supply from TiO₂ to CdS via Au restricts the self-decomposition of CdS due to the oxidation of surface S²⁻ ions by the photogenerated holes in CdS. In a Z-scheme system, H₂ and O₂ are evolved separately from two different photocatalysts, which restrains the back-reaction of water decomposition to some extent.

In the CdS, TiO₂ and Pt system (H. Park, et al., 2008), the direct particle to particle contact of CdS and TiO₂, and the photodeposition of Pt on the TiO₂ particle surface which resulted in the vectorial electron transfer of CdS → TiO₂ → Pt were necessary to achieve efficient charge separation and transfer, hence the observed highest photoactivity of the CdS/(Pt-TiO₂) hybrid catalyst. The photocatalytic activity of CdS could be enhanced significantly by loading a small amount of a noble metal sulfide (PdS, Rh₂S₃, Ru₂S₃), as well as a noble metal (Pt, Pd, Ru, Rh) (H. J. Yan, et al., 2009). Moreover, co-deposition of Pt with other noble metal sulfides on CdS demonstrated further enhanced photoactivity in hydrogen production; the photocatalytical activity of CdS co-deposited with Pt and PdS was greater than those of Pt/CdS and PdS/CdS. This synergistic effect between the Pt and PdS cocatalysts could be explained by the fact that the two cocatalysts may facilitate separation of the photogenerated electrons and holes on the photocatalyst.

Nanostructured Ag₂S/CdS were synthesized by a two-step precipitation method with Ag₂S (cf. Fig.1) (S. H. Shen, et al., 2010), the photoactivity was evaluated by hydrogen evolution from aqueous solution containing Na₂S/Na₂SO₃ as a hole scavenger under simulated solar light (AM1.5). When the concentration of Ag₂S was 5% by weight, Ag₂S/CdS showed the highest photocatalytical activity for hydrogen evolution due to the efficient electron-hole separation, with the solar-hydrogen energy conversion efficiency approximately 0.7%.

The transition-metal sulfides have also been developed as novel cocatalysts. The CdS activity was enormously increased by loading with MoS₂, even higher than that of Pt-loaded CdS under the same reaction conditions (X. Zong, et al., 2010). The better coupling between the structures and electronic configurations of MoS₂ and CdS together, and the formation of junctions between CdS and MoS₂, improved the charge separation and were mainly responsible for the high activity of this MoS₂/CdS catalyst. The MoS₂ activated the photocatalyst by reducing the electrochemical proton reduction overpotential (F. A. Frame & F. E. Osterloh, 2010).

CdSe and CdS have been used to co-sensitize nitrogen doped TiO₂ (N:TiO₂) (J. Hensel, M. Canin, et al., 2010). The CdSe/CdS/N:TiO₂ electrodes has much higher photoelectrochemical (PEC) response as well as incident photon to charge efficiency (IPCE) than the CdSe/CdS/TiO₂ electrodes. This was attributed to increased hole transport from CdS to oxygen vacancy levels introduced into the TiO₂ upon nitrogen doping. This increased hole transport reduces undesired electron hole recombination in the CdS layer that otherwise tends to reduce PEC performance. The results demonstrate the importance of engineering the band structure of metal oxide nanocomposite structures for PEC and other applications.

In a heterostructure where a CdSe seed encapsulated in a CdS rod which is tipped with a Pt particle (Fig.5) (L. Amirav & A. P. Alivisatos, 2010), the holes were three-dimensionally confined to the CdSe seed while the delocalized electrons were transferred to the metal tip, so the electrons were separated from the holes over three different components and by the tunable physical length of the CdS rod. By tuning the nanorod heterostructure length and the size of the seed, the hydrogen production activity was significantly increased compared to that of the unseeded rods. This structure was highly active for hydrogen production with an apparent quantum yield of 20% at 450 nm wave length. There was also a demonstrated improved stability compare to CdS rods without CdSe seeding. Among all the systems studied involving CdS so far, this heterostructure yielded the *highest* hydrogen production activity, 40,000 μmol/h/g (X. B. Chen, et al., 2010).

To improve their photocatalytical stability and photoactivity, sulfides, such as CdS, have been intercalated into the layers of some layered metal oxide. The photocatalytical activities for hydrogen evolution of CdS-intercalated composites were superior to those of CdS alone or to a physical mixture of CdS and the metal oxides (W. F. Shangguan, 2007). The improvement was attributed to the quick transfer of the photogenerated electrons from CdS to the metal oxides through the layered nanostructure.

4.2 AgCl/AgBr

Thin silver chloride (AgCl) layers evolve oxygen under UV/vis illumination in aqueous solution under appropriate conditions. AgCl deposited on a conducting support photocatalyzes the oxidation of water to O₂ in the presence of a small excess of silver ions in solution. The light sensitivity in the visible part of the spectrum is due to self-sensitization caused by reduced silver clusters which has CB significantly positive that that of AgCl (D. Schurch, et al., 2002). Considerable improvement of sensitivity has been observed with AgBr sensitized AgCl photoanodes. Similar to CdS and CdSe, the bandgap edges of AgBr straddle the HER and OER potentials (*cf.* Fig.1). The AgCl photoanode was combined with hydrogen-producing semiconductors, a platinized silicon solar cell or platinized p-GaInP₂ to reduce water to hydrogen. Direct water splitting use AgBr only has not been performed yet.

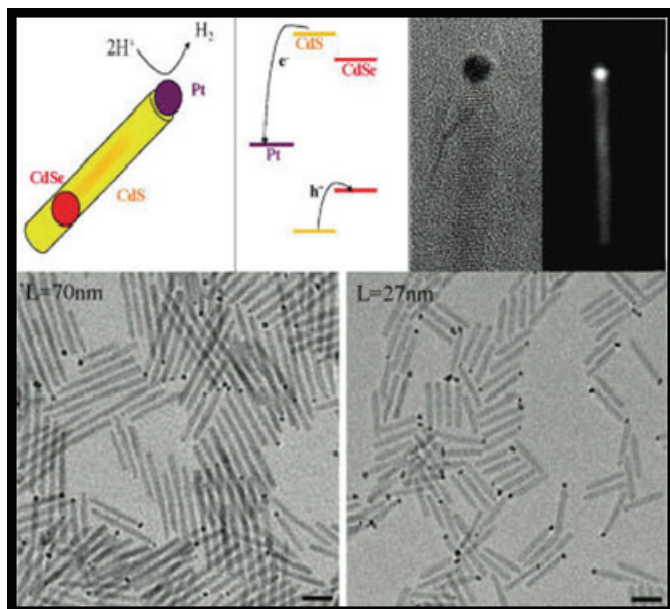


Fig. 5. Heterostructure of CdSe-CdS-Pt.

4.3 InVO₄

InVO₄ has band gap of about 2.0 eV (Fig.1) and was found to be a new visible light responding photocatalyst for water decomposition (J. H. Ye, et al., 2002). The photocatalyst showed activity to visible light in a wide wavelength range up to 600 nm. The photocatalytical water splitting activity increases significantly by loading NiO as a co-catalyst. The evolution rate of H₂ from water has achieved about 5 μmol/(g·h) under visible light (λ>420nm) of a 300W Xe arc lamp.

The mesoporous photocatalyst InVO₄ was synthesized by the template-directing self-assembling method (L. X. Xu, et al., 2006). The crystal structure of InVO₄ could be controlled by changing the calcination temperature. Compared with the anatase TiO₂ and conventional InVO₄, the mesoporous InVO₄ was more responsive toward visible light. The evolution rate of H₂ from water over the mesoporous InVO₄ achieved 1836 μmol/(g·h) under UV light irradiation, which was much higher than the anatase TiO₂ and conventional InVO₄.

4.4 CdSe

Nanocomposite materials based on visible-light-absorbing CdSe QDs and N-doped TiO₂ nanoparticles and nanowire arrays with properties tailored for PEC hydrogen generation. The experiments demonstrated that the synergistic effect of sensitization *and* elemental doping significantly enhances the photoelectrochemical activities of the TiO₂ nanostructured photoanodes (Fig.6) (J. Hensel, G. M. Wang, et al., 2010). These composite nanostructures show enhanced overall charge transport and improved PEC performance when the relevant band gap states are properly aligned and utilized. Enhanced electron-hole separation and hole transfer/transport through the oxygen vacancy states, V_o, mediated by N-doping has

been proposed to explain the observed experimental results. Such nanocomposite structures simultaneously enhance visible light absorption and interfacial charge transfer. The results provide useful insights for developing new nanostructures tailored for PEC hydrogen generation and other applications via controlled band engineering.

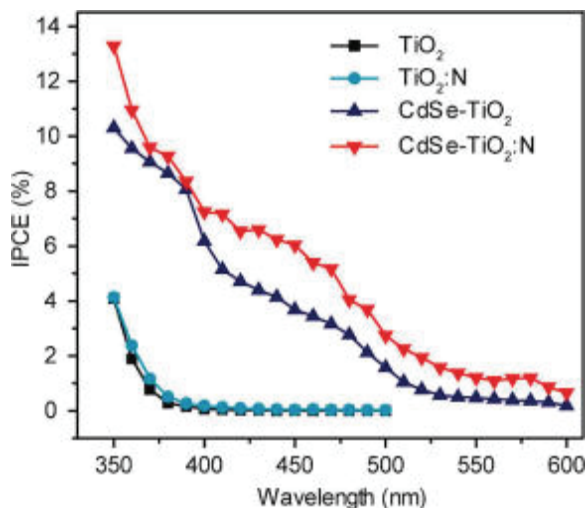


Fig. 6. Synergy of CdSe QDs sensitization and N-doping of TiO₂.

Under visible light irradiation, CdSe-nanoribbons photocatalyze H₂ evolution from aqueous sodium sulfite/sulfide solution with a quantum efficiency of 9.2% at 440 nm, whereas bulk CdSe is not active for the reaction. Photoelectrochemical measurements show that the activity of nano-CdSe is caused by a raised flatband potential (-0.55 V, NHE) which follows from the increased bandgap (2.7 eV) of this quantum confined material. In the presence of a sulfide ion, the flatband potential is fixed to -0.43 V (NHE), slightly below the sulfide redox potential (-0.48 V, NHE). When the nanoribbons are chemically linked to MoS₂ nanoplates that were obtained by exfoliation and ultrasonication of bulk MoS₂, the activity increases almost four times, depending on the mass percentage of MoS₂. Cyclic voltammetry reveals that the enhancement from the MoS₂ nanoplates is due to a reduction of the H₂ evolution overpotential (F. A. Frame & F. E. Osterloh, 2010). In contrast, chemical linkage of Pt nanoparticles to the nanoribbons does not affect the photocatalytical activity.

4.5 Eosin Y sensitized CuO-TiO₂

It has been demonstrated that the dye-sensitized CuO/TiO₂ can be used as photocatalyst for hydrogen production from Diethanolamine-H₂O mixture with high quantum efficiencies under visible light irradiation ($\lambda > 420$ nm). Eosin Y sensitized CuO/TiO₂ photocatalysts were very active and stable for hydrogen generation. The addition of CuO strongly improved the adsorption capability of TiO₂ toward eosin dye. The electrons excited from the sensitizer molecules by the visible light injected into the conduction band (CB) of both TiO₂ and CuO, the electrons in CB of TiO₂ subsequently transferred to CB of CuO, which resulted in a build-up of excess electrons in the conduction band of CuO. Consequently, the accumulation of excess electrons in CuO causes a negative shift in the Fermi level of CuO

which gains the required overvoltage necessary for sufficient water reduction reaction. As a result, the significant enhancement of apparent quantum yield and a good stability was obtained over the dye-sensitized 1.0 wt% CuO/TiO₂ photocatalyst. The function of CuO is to help the charge separation and to act as a water reduction site. In the presence of triethanolamine, acetonitrile and triethylamine, the photocatalyst can catalyze hydrogen evolution over 120 h. The highest quantum efficiency obtained was about 5.1%.

4.6 MoS₂

Molybdenum disulfide (MoS₂) is a layered semiconductor that exhibits both quantum confinement and excellent catalytic activity for HER when nanostructured (J. Bonde, et al., 2008; T. F. Jaramillo, et al., 2007). In the bulk, its conduction band sits below the HER potential (J. P. Wilcoxon & G. A. Samara, 1995) and its band gap of 1.2 eV is too small to drive water splitting without a bias. Nanostructured MoS₂ could potentially alleviate these limitations while further improving charge transport by minimizing the distance of travel for photogenerated charge carriers. In addition, MoS₂ is a material that has previously exhibited excellent photocatalytic stability (H. Tributsch & J. C. Bennett, 1977) and is a highly scalable, widely used industrial catalyst (R. R. Chianelli, et al., 2006) and solid lubricant (C. Muratore & A. A. Voevodin, 2009).

MoS₂ nanostructures were synthesized and their electrochemical activity was investigated for hydrogen evolution and photoelectrochemical water splitting (Z. B. Chen, et al., 2010). MoS₂ nanoparticles were made using a reverse micelle encapsulation method and exhibit quantum confinement of the indirect band gap up to 1.8 eV. A MoS₂ double-gyroid bi-continuous structure was made using an evaporation induced self assembly method. Both nanostructures exhibit improved activity for the hydrogen evolution reaction versus bulk MoS₂. Photoelectrochemical activity was also observed in both nanostructures (Z. B. Chen, et al., 2010).

UV-light irradiation to TiO₂ in an aqueous ethanol solution of (NH₄)₂MoS₄ under deaerated conditions has yielded molybdenum (IV) sulfide nanoparticles on a TiO₂ surface (MoS₂/TiO₂). In HCOOH aqueous solutions, the MoS₂/TiO₂ system exhibits a high level of photocatalytic activity for H₂ generation (S. Kanda, et al., 2011).

4.7 WO₃

WO₃ has been suggested as a candidate material for PEC hydrogen production as earlier as 1976 (G. Hodes, et al., 1976). It can be fabricated using low-cost processes, such as anodic oxidation, chemical vapor deposition, sol-gel as well as reactive sputtering (N. Gaillard, et al., 2010). In the case of integration over low-cost amorphous silicon-based solar cells to form hybrid-photo-electrode (HPE) device, reactive sputtering is of great interest because of its low deposition temperature capabilities (from 200°C to 300°C). From an electrochemical point of view, tungsten oxide corrosion resistance in acidic solutions has been already demonstrated (M. A. Petit & V. Plichon, 1996) and its excellent behavior as a device under various PEC operations has been widely reported (C. G. Granqvist, 2000; C. Santato, et al., 2001). Due to its wide band gap (2.6eV), tungsten oxide framework or optoelectronic properties modification using foreign element incorporation such as silicon, molybdenum or nitrogen became of great interest. However, no modified tungsten oxide-based thin film material has yet surpassed pure WO₃ PEC performances, with a saturation photocurrent density of approximately 3.0 mAcm⁻² in acidic solution under AM1.5G illumination (R.

Solarska, et al., 2010), which is only 50% of the theoretical value based on pure WO₃ bandgap (6% STH efficiency) (Z. B. Chen, et al., 2010), assuming a complete collection and conversion to electronic current of photogenerated electron hole pairs. Thus, improvement of tungsten oxide-based PEC devices performances is theoretically possible.

Polycrystalline WO₃ thin films for photoelectrochemical hydrogen production were investigated using photoelectron spectroscopy and inverse photoemission. A careful study has minimized X-ray and electron beam-induced degradation and combined ultraviolet photoelectron spectroscopy and inverse photoemission determined the surface positions of the valence and conduction band edges, respectively, and the work function (i.e., the position of the vacuum level). This allows to paint a completely experiment-based picture of the WO₃ surface level positions, which are of central relevance for the photoelectrochemical activity of such surfaces (L. Weinhardt, et al., 2008). It was found that the WO₃ surface to be wide gap (3.28±0.14) eV and n-type, with the conduction band minimum 0.39±0.10 eV above the Fermi level and 0.31±0.11 eV above the H⁺/H₂ reduction potential. The valence band maximum is 2.89±0.10 eV below the Fermi level and 1.74±0.11 eV below the H₂O/O₂ oxidation potential (L. Weinhardt, et al., 2008).

In both PV and PEC cells, improved performance and higher conversion efficiency can be obtained using diode structures combining suitable n-type photoanodes and p-type photocathodes which lead to efficient electron-hole separation (M. Gratzel, 2001; O. Khaselev & J. A. Turner, 1998a; A. J. Nozik, 1976). A p-Cu₂O (band gap 2.0eV)/n-WO₃ (band gap 2.6eV) coupling system was developed to avoid back reaction of the photo-induced charges (C. C. Hu, et al., 2008), and resulted in higher photocatalytical hydrogen production. Mo incorporation in the entire WO₃ film (WO₃-Mo) results in poor PEC performances, most likely due to defects that trap photo generated charge earners. However, compared to a pure WO₃, a 20% increase of the photocurrent density at 16 V vs SCE is observed for WO₃-Mo based PEC electrode if the Mo incorporation is limited to the near-surface region of the WO₃ film. The resulting WO₃/WO₃-Mo bilayer structure is formed by epitaxial growth of the WO₃-Mo top layer on the WO₃ bottom layer, which allows an optimization of the electronic structure induced by Mo incorporation while maintaining good crystallographic properties (N. Gaillard, et al., 2009). The WO₃-Mo films were found in a recent study (M. Bar, et al., 2010) to be n-type with an electronic surface band gap of 3.27±0.15 eV. The conduction band minimum (valence band maximum) is 0.64±0.10 eV above (2.63±0.10 eV below) the Fermi level and at most 0.38±0.11 eV above the H⁺/H₂ reduction potential (at least 1.66±0.11 eV below the H₂O/O₂ oxidation potential). The conduction band of WO₃:Mo is shifted upwards (further away from the reduction potential compared to WO₃) while maintaining a valence band position which is still sufficiently low with respect to the oxidation potential) for PEC operation. The findings suggest an explanation why WO₃:Mo/WO₃ bilayer structures show improved photoelectrochemical performance compared to respective single layer photoanodes (M. Bar, et al., 2010). The bilayer approach, i.e., the deliberate decoupling of the tailored electrode surface from its bulk properties may open a new promising route for the development of next-generation PEC materials.

A new device integration scheme was presented recently to increase photocurrent density using highly textured substrates (HTS) (N. Gaillard, et al., 2010), which were obtained by anisotropic etching of [100] silicon substrates in KOH solution. A very good coverage of WO₃ onto the silicon pyramids and a photocurrent doubling is observed when compared to WO₃ deposited on flat silicon substrates.

4.8 Fe_2O_3

Early studies identified haematite ($\alpha\text{-Fe}_2\text{O}_3$) as potential photoanode material for water splitting (J. H. Kennedy & K. W. Frese, 1977; J. H. Kennedy & M. Anderman, 1983; R. K. Quinn, et al., 1976). Recent work has focused on developing films that could be used as part of tandem photoelectrolysis cells, in which high energy photons are used to drive the oxidation of water by photogenerated holes at the Fe_2O_3 surface, and lower energy photons transmitted through the oxide are harvested by a solar cell that applies a bias voltage to the photoelectrolysis cell. Recent optimization of the morphology and doping of nano-structured thin films of Fe_2O_3 have resulted in substantial improvements in the photocurrent response (I. Cesar, et al., 2009; S. Saremi-Yarahmadi, K. G. U. Wijayantha, et al., 2009; S. Saremi-Yarahmadi, A. A. Tahir, et al., 2009).

Photoelectrochemical Impedance Spectroscopy (PEIS) has been used to characterize the kinetics of electron transfer and recombination taking place during oxygen evolution at illuminated polycrystalline $\alpha\text{-Fe}_2\text{O}_3$ electrodes prepared by aerosol-assisted chemical vapor deposition from a ferrocene precursor (K. G. U. Wijayantha, et al., 2011). The complex potential dependence of the rate constants for these two processes highlights the non-ideal nature of the $\alpha\text{-Fe}_2\text{O}_3$ -electrolyte interface arising from photogenerated surface species. Efficient water splitting in a tandem photoelectrochemical cell using $\alpha\text{-Fe}_2\text{O}_3$ as a photoanode requires that the photocurrent onset should be as close to the flatband potential as possible, about 0.8 V negative of the reversible oxygen electrode potential. A positive displacement of the photocurrent onset represents a loss of free energy and hence of efficiency. Clearly this means that accumulation of positive surface charge associated with Fermi level pinning and changes in surface composition must be avoided as far as possible. Since the accumulation of electronic and ionic surface charge appears to be associated with sluggish hole transfer kinetics, it should be possible to overcome the effects by using a suitable surface catalyst for the oxygen evolution reaction. The PEIS analysis also shows that the limiting factor determining the performance of the $\alpha\text{-Fe}_2\text{O}_3$ photoanode is electron-hole recombination in the bulk of the oxide. The minimization of the loss of holes can be achieved at least in part by growing nano-structured thin films in such a way that the dimensions are comparable with the width of the space charge region (J. Brillet, et al., 2010; F. Le Formal, et al., 2010). Other promising approaches include using oriented nanorod arrays (R. Van De Krol, et al., 2008), or a host-guest structure in which small $\alpha\text{-Fe}_2\text{O}_3$ particles are deposited on a porous oxide substrate such as WO_3 (K. Sivula, et al., 2009).

To improve the optoelectronic properties of iron oxide as a photoelectrode, hematite ($\alpha\text{-Fe}_2\text{O}_3$) thin films were doped with titanium using atmospheric pressure chemical vapor deposition (APCVD) for synthesis (P. Zhang, et al., 2011). The films were prepared by pyrolysis of $\text{Fe}(\text{CO})_5$ and TiCl_4 precursors on fluorine-doped tin oxide (FTO) substrates and found to have a polycrystalline morphology with faceted particulates about 20 to 50 nm in size with a preferred crystallographic growth along the [110] direction (direct band gap with a value of ~ 2.1 eV). The performance of the photoanodes was measured as a function of titanium concentration. A maximum efficiency was observed at about 0.8 atom% Ti in hematite. The Incident Photon-to-current Conversion Efficiency (IPCE) to hydrogen was measured in alkaline electrolyte. Under an applied bias of 0.6 V vs. Ag/AgCl at 400 nm the IPCE for water splitting in alkaline solution was found to be 27.2%, the highest efficiency reported for Ti doped hematite photoanodes. The IPCE of the Ti doped hematite sample at the lower bias (6% at 0.4 V vs. Ag/AgCl) is relatively low which is associated with a large

photocurrent onset potential (0.2V), which suggested a high density of trap states located below the conduction band edge.

An experimental study of the influence of gold nanoparticles on an α -Fe₂O₃ photoanodes for photoelectrochemical water splitting is described (E. Thimsen, et al., 2011). A relative enhancement in the water splitting efficiency at photon frequencies corresponding to the *plasmon resonance* in gold was observed. This relative enhancement was observed only for electrode geometries with metal particles that were localized at the semiconductor-electrolyte interface consistent with the observation that minority carrier transport to the electrolyte is the most significant impediment to achieving high efficiencies in this system.

4.9 Ternary oxides

The oxides are privileged materials for the water photo-splitting owing to their chemical inertness in aqueous electrolytes. For oxides without partially filled d-levels, an empirical relationship was found between the flat band potential (V_{cb}) and energy gap E_g : $V_{cb,VNHE} = 2.94 - E_g$ (D. E. Scaife, 1980). Oxides having an optical gap around 1.4 eV are particularly interesting for the terrestrial applications but most of them have either unsuitable potential V_{cb} for hydrogen evolution reaction. Rewriting the equation, $E_g = 2.94 - V_{cb,VNHE}$, we see that for suitable $V_{cb,VNHE}$ (~ -0.5 eV), the band gaps will be very wide (>3 eV). They absorb only in the UV region because of their large forbidden band (E_g) and the quantum yields are generally low.

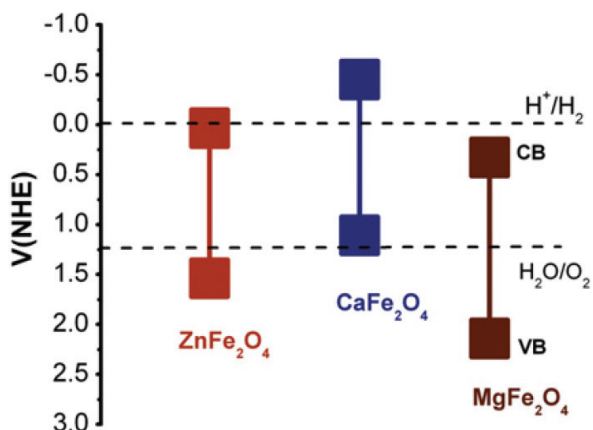


Fig. 7. Band gaps of spinels.

Ternary oxides CuMO_2 crystallizing in the delafossite structure begins to receive interest in the field of the photoelectrochemistry owing to their interesting properties of band gap modulation and pH-insensitivity of the electronic bands (A. Derbal, et al., 2008). The delafossite CuFeO_2 has been prepared by thermal decomposition from various salts. The polarity of generated voltage is positive indicating that the materials exhibit p-type conductivity whereas the electroneutrality is achieved by oxygen insertion. CuFeO_2 is a narrow band gap semiconductor with an optical gap of 1.32 eV. The oxide was characterized photoelectrochemically; its conduction band (-1.09 V-RHE) is located below that of SnO_2 (-0.86 V-RHE) at pH 13.5, more negative than the $\text{H}_2\text{O}/\text{H}_2$ level leading to a

thermodynamically favorable H_2 evolution under visible irradiation. The sensitizer $CuFeO_2$, working as an electron pump, is stable towards photocorrosion by hole consumption reactions involving the reducing agents X^{2-} (i.e., $S_2O_3^{2-}$ and SO_3^{2-}). The photoactivity was dependent the precursor and the best performance (1160 $\mu\text{mol/hg}$) was obtained in $S_2O_3^{2-}$ (pH 13.5) over $CuFeO_2$ synthesized from nitrate with a mass ratio ($CuFeO_2/SnO_2$) equal to unity. A quantum yield of 0.5% was obtained under polychromatic light (A. Derbal, et al., 2008).

The physical properties and photoelectrochemical characterization of the spinel $ZnFe_2O_4$ have been investigated for the hydrogen production under visible light (S. Boumaza, et al., 2010). The forbidden band was found to be 1.92 eV and the transition is indirectly allowed. The electrical conduction occurs by small polaron hopping with activation energy of 0.20 eV. p -type conductivity is evidenced from positive thermopower and cathodic photocurrent. The flat band potential (-0.33 VNHE) determined from the capacitance measurements is suitably positioned with respect to H^+/H_2 level. Hence, $ZnFe_2O_4$ was found to be an efficient photocatalyst for hydrogen generation under visible light. The photoactivity increases significantly when the spinel is combined with a wide band gap semiconductor. The best performance with a hydrogen rate evolution of 410,688 $\mu\text{mol/hg}$ concurs over the hetero-system $ZnFe_2O_4/SrTiO_3$ in $Na_2S_2O_3$ (0.025 M) solution, which is the *record high* among all the photocatalysts studied so far (X. B. Chen, et al., 2010).

Nanocrystalline photocatalysts of spinel $MgFe_2O_4$, $ZnFe_2O_4$ and orthorhombic $CaFe_2O_4$ oxides were synthesized (at low temperature about 973 K) by microwave sintering, in one sixtieth of the time required to that of the conventional method (R. Dom, et al., 2011). A significantly improved crystallinity was obtained for the samples irradiated for longer duration of time (10-100 min). The theoretically computed electronic structure of the MFe_2O_4 (M: Ca, Zn, Mg) systems was respectively correlated with the experimental results obtained from their structural and photocatalytical characterization. The photocatalytical performance was found to be affected by surface area and crystallinity of the photocatalyst. The density functional theory (DFT) calculations of MFe_2O_4 lattices revealed that M-ion controllably affects the density of states of the Fe- d orbitals near the Fermi level. Consequently they play an important role in determining the band-energetics and thus the visible light photocatalytical activity for methylene blue degradation (Fig.7).

4.10 Water splitting systems

Over the past several decades, a number of photocatalysts have been successfully developed to construct an overall water-splitting system for simultaneous hydrogen and oxygen generation in the absence of sacrificial reagents (Z. G. Zou, et al., 2001). Among which $(Ga_{1-x}Zn_x)(N_{1-x}O_x)$ has been proven as the most promising (X. B. Chen, et al., 2010; K. Maeda, et al., 2008). Steady and stoichiometric H_2 and O_2 evolutions were found to evolve with a quantum yield of 5.9% in the range of 420-400 nm.

A Z-scheme system has been designed for overall water splitting into H_2 and O_2 using a two-step photoexcitation (R. Abe, et al., 2001). It was composed of an IO_3^-/I^- shuttle redox mediator and two different photocatalysts: Pt-loaded anatase TiO_2 for H_2 evolution and rutile TiO_2 for O_2 evolution. Under UV irradiation, simultaneous gas evolution of H_2 (180 $\mu\text{mol/h}$) and O_2 (90 $\mu\text{mol/h}$) was observed from a basic (pH=11) NaI aqueous suspension of these two different TiO_2 photocatalysts. The advantage of this system was that H_2 gas was evolved only over the Pt- TiO_2 -anatase photocatalyst and that O_2 gas was evolved over the

TiO₂-rutile photocatalyst only, even from a mixture of IO₃⁻ and I⁻ in a basic aqueous solution. Therefore, the undesirable backward reaction, H₂O formation from H₂ and O₂ on Pt particles, was suppressed. Among the various Z-scheme systems studied, the (Pt/ZrO₂-TaON)-(Pt/WO₃)-(IO₃⁻/I⁻) system showed the highest photocatalytical activity for overall water splitting with a quantum efficiency of ca. 6.3% at 420.5 nm (X. B. Chen, et al., 2010). In this Z-scheme overall water splitting system, the H₂ and IO₃⁻ production took place over the Pt/ZrO₂-TaON photocatalyst; meanwhile, the IO₃⁻ reduction and water oxidation to O₂ took place over Pt-WO₃ under visible-light irradiation (K. Maeda, et al., 2010).

An overall water-splitting system driven by a Z-scheme inter-particle electron transfer between H₂ and O₂ photocatalysts (Ru/SrTiO₃:Rh-BiVO₄) without a redox mediator is shown in Fig.8 (Y. Sasaki, et al., 2009). The undesirable reactions and negative effects by an electron mediator were excluded. Although the activity of a Z-scheme overall water splitting system is quite low and only a little higher than that achieved by conventional pure water-splitting systems using one single photocatalyst, these results provided a promising approach to constructing efficient overall water splitting systems.

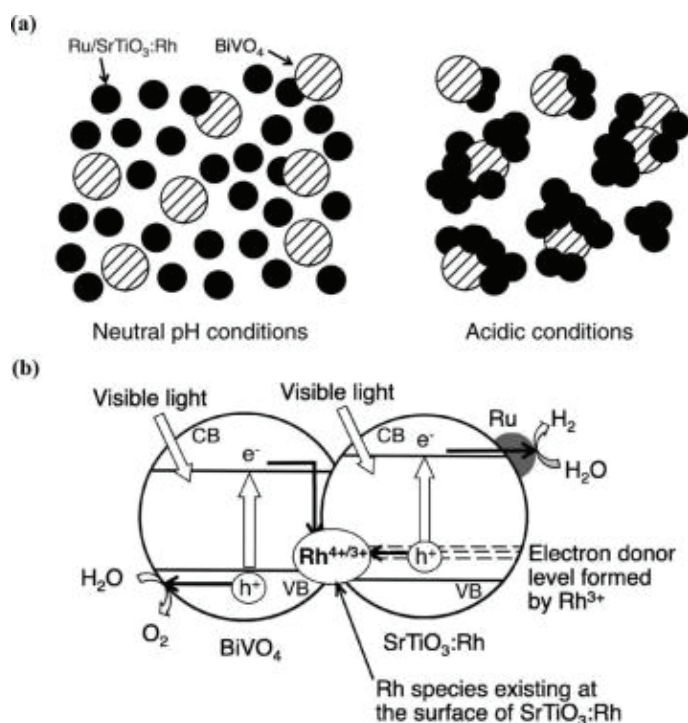


Fig. 8. Z-scheme water splitting without a redox mediator.

In summary, the research directions in solar hydrogen production via water splitting includes: (1) standardization of the photocatalyst characterization (Z. B. Chen, et al., 2010), (2) development of efficient narrow band gap semiconductors for visible light harvest (Z. B. Chen, et al., 2010; R. Dom, et al., 2011; J. H. Ye, et al., 2002), (3) construction of nanocomposites to enhance photogenerated charge separation and transfer (L. Amirav & A.

P. Alivisatos, 2010; J. Hensel, G. M. Wang, et al., 2010; H. Tada, et al., 2006), improve energy conversion efficiency (Y. L. Lee & Y. S. Lo, 2009), and realize hydrogen evolution reaction (M. Bar, et al., 2010), (4) development of inexpensive, effective and stable catalyst for HER and OER (M. G. Walter, et al., 2010) and to host them in well defined and tailored locations, (5) establishment of nanostructures to control charge movement and light absorption pathways which might allow the use of less expensive catalyst with lowered catalytic activities (X. B. Chen & S. S. Mao, 2006; E. Thimsen, et al., 2011; M. G. Walter, et al., 2010), and (6) improvement of the efficiency of the overall water splitting systems (K. Maeda, et al., 2008; K. Maeda, et al., 2010) through a better understanding of the reaction kinetics and carry out of scale-up study from lab to industry applications.

5. Photocatalytic degradation for cleanup of water and air, generation of electricity and hydrogen

Presently, the available efficiency for water splitting for simultaneous hydrogen and oxygen production under visible-light irradiation is still quite low due to fast charge recombination and backward reactions. To achieve enhanced and sustainable hydrogen production, the continual addition of electron donors is required to make up half of the water-splitting reaction to reduce H_2O to H_2 . These sacrificial electron donors can irreversibly consume photogenerated holes, thus prohibiting undesirable charge recombination. Lowering cost for solar-to- H_2 energy conversion, polluting byproduct from industries (e.g., H_2S from nature gas wells, azodyes) and low-cost renewable biomass from animals or plants are preferential sacrificial electron donors (e.g. bio-ethanol, organic acids, saccharides) in water-splitting (or even electricity generation (M. Antoniadou & P. Lianos, 2010)) systems (V. M. Daskalaki, et al., 2010; P. Lianos, 2010). At little or no cost, they could be exploited to accomplish both the tasks of hydrogen production and waste treatment and biomass reforming simultaneously (X. B. Chen, et al., 2010). Such an admirable goal for the practical application of water-splitting systems is especially interesting in light of worldwide energy and environmental concerns.

In photocatalytical degradation of molecules, the holes generation by the photon can react with surface adsorbed H_2O to produce $\cdot\text{OH}$ radicals (hydroxyl ions acts as hole scavengers assisting electro-hole separation and preventing recombination), or directly oxidize the molecules into their radicals. In aerated systems, the conduction band electrons are usually scavenged by O_2 to yield superoxide radical anions $\cdot\text{O}_2$. By this ways, both the O_2 and the molecules are activated. The subsequent radical reactions usually have low or no barriers, resulting in the facile oxidative degradation of the molecules. Fig.9 illustrated the energy levels of semiconductors. We can see that some band gaps straddle the $\cdot\text{O}_2/\text{O}_2$ and $\cdot\text{OH}/\text{OH}^-$ potentials (TiO_2 , SnO_2 , ZnO and KTaO_3). TiO_2 has established itself as the so far most successful photocatalyst for heterogeneous photocatalytical degradation of organic wastes, because it is stable in most chemical environments, seems nontoxic, can be easily synthesized and deposited as thin mesoporous film by soft chemistry techniques, like the sol-gel process. In addition, it is commercially available at very reasonable prices. TiO_2 is used as white pigment in all kinds of products, ranging from paints to tooth pastes. ZnO is the second broadly studied semiconductor after TiO_2 .

The strategies used to improve the properties for TiO_2 and other semiconductors for solar hydrogen production via water splitting should be applicable here to photocatalytical degradation of organic wastes, such as doping TiO_2 for visible absorption, nanocomposites

for improvement of charge separation and transfer, co-catalyst sensitization (C. C. Chen, et al., 2010; P. Lianos, 2010).

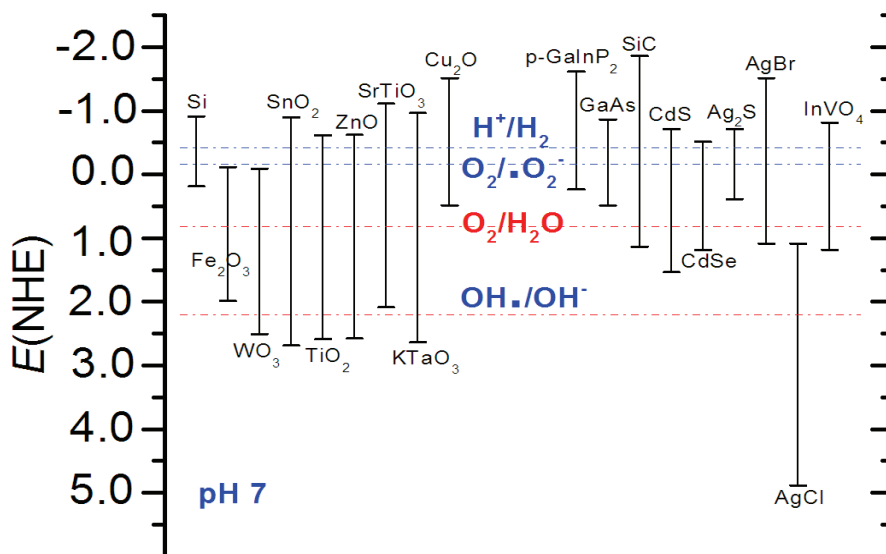


Fig. 9. Energetics of semiconductors at pH 7 for photocatalytic applications.

In the conventional photocatalysis process, the semiconductor is *directly excited* by light to initiate the degradation reaction (X. Chen & S. S. Mao, 2007; M. R. Hoffmann, et al., 1995; D. Ravelli, et al., 2009). However, a wide range of organic pollutants were found to be efficiently degraded on the surface of semiconductor, TiO_2 , ZnO and others, via the **electron injection** of excited organic dyes or other color species (hence the name semiconductor-mediated photodegradation, SMPD (C. C. Chen, et al., 2010)). (1) Sensitizer degradation on dye-sensitized-semiconductor. Various organic *dye* pollutants have strong visible absorption, and themselves have been successfully degraded in the TiO_2 aqueous suspensions under visible irradiation (which is harvested by themselves) and in the presence of O_2 (T. X. Wu, et al., 1998). (2) Co-pollutants degradation by dye-sensitized-semiconductor. The organic radicals or active oxygen species formed using solar energy harvest by one kind of dye molecules can attack the other co-existing pollutants (dye, or pesticides that they might not need to harvest light by themselves) to drive their decontamination under visible light irradiation (D. Chatterjee & A. Mahata, 2001, 2004). (3) Pollutant degradation by QDots-sensitized-semiconductor. The surface modification by using more tolerant color species, such as inorganic metal complexes, noble metal nanoparticles and Qdots, can be conducted to construct stable photocatalysis systems, which are able to degrade even colorless pollutants under visible light irradiation, whereas color species themselves are regenerated and remain undegraded at the end of the degradation reaction (H. Kisch, et al., 1998; W. Zhao, et al., 2008). (4) The organic pollutants with appropriate redox potential (such as halogenated pollutants) can be reductively decontaminated by electrons injected into the conduction band (dehalogenation) (Y. M. Cho, et al., 2001; H. Kyung, et al., 2005).

Depositing an insulating Al_2O_3 shell (nanometers thick) on TiO_2 resulted in a significant retardation in the charge recombination dynamics (up to a 10-fold) (J. R. Durrant, et al., 2006). The rate constant for the SMPD of RhB in an Al_2O_3 -modified TiO_2 system was nearly five-fold higher than that on pure TiO_2 (D. Zhao, et al., 2008). Very recently showed that introducing a thin Al_2O_3 layer on TiO_2 enhanced the visible light activities for the dechlorination of CCl_4 (W. Kim, et al., 2009). Measurements of time-resolved diffuse reflectance spectra of bare TiO_2 and $\text{Al}_2\text{O}_3/\text{TiO}_2$ in suspensions observed an increase in the average lifetime of the separated charges by about 3 times in $\text{Al}_2\text{O}_3/\text{TiO}_2$. In these systems, the dyes (RhB or Ruthenium bipyridyl complexes with carboxylate anchoring groups) were preferably adsorbed on the Al_2O_3 , and the electrons injected into the TiO_2 by tunneling through the porous Al_2O_3 layer. On the other hand, the presence of the Al_2O_3 layer increases the physical separation between the injected electrons and the oxidized dye, thereby retarding the charge recombination reactions. But, the electron acceptors (such as O_2 and CCl_4) are still able to scavenge the conduction band electrons.

Silver nanoparticles have plasmon resonance absorption in the visible region. Irradiation on silver nanoparticles with various sizes and shapes on TiO_2 by a monochromatic visible light caused selective removal of the Ag particles due to the selective Plasmon absorption of the nanoparticles (Y. Ohko, et al., 2003). Ag nanoparticles were loaded on the surface of AgCl to constitute a plasmon-based photocatalyst with strong absorption in the visible region, and methyl orange dye was decomposed very rapidly under visible light irradiation on this plasmonic photocatalyst (P. Wang, et al., 2008). Au-deposited TiO_2 has been reported to exhibit enhanced photodegradation of Methylene Blue under visible light irradiation because of the increased absorption in the visible range (X. Z. Li & F. B. Li, 2001).

Combining TiO_2 with carbonaceous nanomaterials is being increasingly investigated as a means to increase photocatalytic activity, and demonstrations of enhancement are plentiful, which was reviewed recently on nanocarbon- TiO_2 photocatalysts, covering activated carbon, carbon doping, carbon nanotubes, [60]-fullerenes, graphene, thin layer carbon coating, nanometric carbon black and more recently developed morphologies. Mechanisms of enhancement, synthesis routes and future applications are summarized and discussed. New insight and enhanced photocatalytic activity may be provided by novel nanocarbon- TiO_2 systems (R. Leary & A. Westwood, 2011).

One approach to achieve visible light photo activity is to couple TiO_2 by a narrow band gap semiconductor such as CdS, InVO_4 (Fig.9). Visible-light-activated photocatalytic Ag/ InVO_4 - TiO_2 thin films were developed through a sol-gel method from the TiO_2 sol containing Ag and InVO_4 . The photocatalytic activities of Ag/ InVO_4 - TiO_2 thin films were investigated based on the oxidation decomposition of methyl orange in aqueous solution. The Ag and InVO_4 co-doped thin films significantly enhanced the methyl orange photodegradation under visible light irradiation (L. Ge, et al., 2006).

The visible light photocatalytic activities of platinumized WO_3 (Pt/WO_3) was studied on the degradation of aquatic pollutants and the role of main photooxidants. The presence of Pt on WO_3 is known to facilitate the *multi-electron* reduction of O_2 , which enables O_2 to serve as an electron acceptor despite the insufficient reduction potential of the conduction band electrons in WO_3 for the one-electron reduction of O_2 (cf. Fig.9). The concurrent oxidative reactions occurring on WO_3 were markedly enhanced in the presence of Pt and accompanied the production of OH radicals under visible light, which was confirmed by both a fluorescence method (using a chemical trap) and a spin trap method. The generation of OH

radicals mainly comes from the reductive decomposition of H_2O_2 that is produced in situ from the reduction of O_2 on Pt/ WO_3 . The rate of in situ production of H_2O_2 under visible light was significantly faster with Pt/ WO_3 than WO_3 . Six substrates that were tested for the visible light ($\lambda > 420$ nm) induced degradation on Pt/ WO_3 included dichloroacetate (DCA), 4-chlorophenol (4-CP), tetramethylammonium (TMA), arsenite (As(III)), methylene blue (MB), and acid orange 7 (A07). The degradation (or conversion) of all six substrates was successfully achieved with Pt/ WO_3 and the role of OH radicals in Pt/ WO_3 photocatalysis seemed to be different depending on the kind of substrate. In the presence of tert-butyl alcohol (TBA: OH radical scavenger), the photocatalytical degradation was markedly reduced for 4-CP or completely inhibited for DCA and TMA whereas that of As(III), MB, and A07 was little affected. Pt/ WO_3 photocatalyst that oxidizes various substrates under visible light with a sufficient photostability can be applied for solar water treatment (J. Kim, et al., 2010).

The photocatalytical decomposition of acetaldehyde over $CaFe_2O_4$ (CFO)/ WO_3 based composite photocatalysts under visible light irradiation was carried out. The photocatalytical activity of WO_3 was improved by simply mixing with CFO, and 5 wt % CFO coupled WO_3 showed the optimized performance. Ag and ITO coating on the CFO particle surface obviously promoted the photocatalytical activity of the CFO/ WO_3 composite. The CFO/Ag (or ITO)/ WO_3 composite photocatalyst could completely decompose acetaldehyde under visible light irradiation (Z. F. Liu, et al., 2009).

A review of patents on the application of titanium dioxide photocatalysis for air treatment was presented (Y. Paz, 2011). A comparison between water treatment and air treatment reveals that the number of scientific publications dedicated to photocatalytical air treatment is significantly lower than the number of scientific manuscripts dedicated to photocatalytical water treatment, yet the situation is reversed upon comparing relevant patents. This indicates a growing interest in the implementation of photocatalysis for air treatment purposes, which surpasses that of water treatment. The review analyzed the various patents in the area of air treatment, while differentiating between indoor air treatment and outdoor air treatment. Specific efforts were made to characterize the main challenges and achievements en-route for successful implementation, which were categorized according to mass transport, adsorption of contaminants, quantum efficiency, deactivation, and, no less important, the adherence and the long term stability of the photocatalyst.

In summary, future research in photocatalytical degradation should include, (1) systematic study on visible and solar light activated photocatalysts to achieve high efficiency (S. Ahmed, et al., 2010; C. C. Chen, et al., 2010), (2) catalyst immobilization strategy to provide cost-effective solid-liquid separation (M. N. Chong, et al., 2010; R. Leary & A. Westwood, 2011), (3) improvement in the photocatalytical operation for wider pH range, and (4) effective design of photocatalytical reaction system.

6. Conclusion

The discovery and utilization of solar composite materials have a long history which was dated back to 1800s. Accelerated development has taken place in recent decades, with a great promise to solve the global energy, environmental and social problems. Along with the relative maturing of dye sensitized solar cells, quantum dots solar energy harvesting is predicted to be the future technology to be developed, in the forms of QDSSC, solar hydrogen production via water splitting, and photocatalytical degradation of pollutants or

biomass in conjunction with fuel or electricity generation. In the effort to improve device efficiency and achieve commercialization, further research should be carried on to tailor the nanostructures, to control the charge separation and transportation, to effectively use inexpensive cocatalysts, and to study the reaction kinetics and their large scale realization.

7. References

- Abe, R., Sayama, K., Domen, K., & Arakawa, H. (2001). A New Type of Water Splitting System Composed of Two Different TiO_2 Photocatalysts (Anatase, Rutile) and a I^{3-}/I^- Shuttle Redox Mediator. *Chemical Physics Letters*, Vol. 344, No. 3-4, pp. 339-344, 0009-2614.
- Ahmed, S., Rasul, M. G., Martens, W. N., Brown, R., & Hashib, M. A. (2010). Heterogeneous Photocatalytic Degradation of Phenols in Wastewater: A Review on Current Status and Developments. *Desalination*, Vol. 261, No. 1-2, pp. 3-18, 0011-9164.
- Alenzi, N., Liao, W. S., Cremer, P. S., Sanchez-Torres, V., Wood, T. K., Ehlig-Economides, C., et al. (2010). Photoelectrochemical Hydrogen Production from Water/Methanol Decomposition Using Ag/TiO_2 Nanocomposite Thin Films. *International Journal of Hydrogen Energy*, Vol. 35, No. 21, pp. 11768-11775, 0360-3199.
- Ameen, S., Akhtar, M. S., Kim, G. S., Kim, Y. S., Yang, O. B., & Shin, H. S. (2009). Plasma-Enhanced Polymerized Aniline/ TiO_2 Dye-Sensitized Solar Cells. *Journal of Alloys and Compounds*, Vol. 487, No. 1-2, pp. 382-386, 0925-8388.
- Amirav, L., & Alivisatos, A. P. (2010). Photocatalytic Hydrogen Production with Tunable Nanorod Heterostructures. *Journal of Physical Chemistry Letters*, Vol. 1, No. 7, pp. 1051-1054, 1948-7185.
- Antoniadou, M., & Lianos, P. (2010). Production of Electricity by Photoelectrochemical Oxidation of Ethanol in a Photofuelcell. *Applied Catalysis B-Environmental*, Vol. 99, No. 1-2, pp. 307-313, 0926-3373.
- Bach, U., Lupo, D., Comte, P., Moser, J. E., Weissortel, F., Salbeck, J., et al. (1998). Solid-State Dye-Sensitized Mesoporous TiO_2 Solar Cells with High Photon-to-Electron Conversion Efficiencies. *Nature*, Vol. 395, No. 6702, pp. 583-585, 0028-0836.
- Baker, D. R., & Kamat, P. V. (2009). Photosensitization of TiO_2 Nanostructures with Cds Quantum Dots: Particulate Versus Tubular Support Architectures. *Advanced Functional Materials*, Vol. 19, No. 5, pp. 805-811, 1616-301X.
- Bang, J. H., & Kamat, P. V. (2009). Quantum Dot Sensitized Solar Cells. A Tale of Two Semiconductor Nanocrystals: Cdse and Cdte. *Acs Nano*, Vol. 3, No. 6, pp. 1467-1476, 1936-0851.
- Bao, N., Shen, L., Takata, T., Domen, K., Gupta, A., & Yanagisawa, K. (2007). Facile Cd-Thiourea Complex Thermolysis Synthesis of Phase-Controlled Cds Nanocrystals for Photocatalytic Hydrogen Production under Visible Light. *Journal of Physical Chemistry C*, Vol. 111, No. pp. 17527-17534.
- Bao, N. Z., Shen, L. M., Takata, T., & Domen, K. (2008). Self-Templated Synthesis of Nanoporous Cds Nanostructures for Highly Efficient Photocatalytic Hydrogen Production under Visible. *Chemistry of Materials*, Vol. 20, No. 1, pp. 110-117, 0897-4756.
- Bar, M., Weinhardt, L., Marsen, B., Cole, B., Gaillard, N., Miller, E., et al. (2010). Mo Incorporation in Wo_3 Thin Film Photoanodes: Tailoring the Electronic Structure for

- Photoelectrochemical Hydrogen Production. *Applied Physics Letters*, Vol. 96, No. 3, pp. 032107, 0003-6951.
- Barea, E. M., Shalom, M., Gimenez, S., Hod, I., Mora-Sero, I., Zaban, A., et al. (2010). Design of Injection and Recombination in Quantum Dot Sensitized Solar Cells. *Journal of the American Chemical Society*, Vol. 132, No. 19, pp. 6834-6839, 0002-7863.
- Belaidi, A., Dittrich, T., Kieven, D., Tornow, J., Schwarzburg, K., & Lux-Steiner, M. (2008). Influence of the Local Absorber Layer Thickness on the Performance of ZnO Nanorod Solar Cells. *Physica Status Solidi-Rapid Research Letters*, Vol. 2, No. 4, pp. 172-174, 1862-6254.
- Biello, D. (2008). Inside the Solar-Hydrogen House: No More Power Bills--Ever. *Scientific American*. Retrieved from <http://www.scientificamerican.com/article.cfm?id=hydrogen-house>
- Bolton, J. R., Strickler, S. J., & Connolly, J. S. (1985). Limiting and Realizable Efficiencies of Solar Photolysis of Water. *Nature*, Vol. 316, No. 6028, pp. 495-500, 0028-0836.
- Bonde, J., Moses, P. G., Jaramillo, T. F., Nørskov, J. K., & Chorkendorff, I. (2008). Hydrogen Evolution on Nano-Particulate Transition Metal Sulfides. *Faraday Discussions*, Vol. 140, No. pp. 219-231, 1364-5498.
- Bosi, M., & Pelosi, C. (2007). The Potential of III-V Semiconductors as Terrestrial Photovoltaic Devices. *Progress in Photovoltaics*, Vol. 15, No. 1, pp. 51-68, 1062-7995.
- Boumaza, S., Boudjemaa, A., Bouguelia, A., Bouarab, R., & Trari, M. (2010). Visible Light Induced Hydrogen Evolution on New Hetero-System ZnFe₂O₄/SrTiO₃. *Applied Energy*, Vol. 87, No. 7, pp. 2230-2236, 0306-2619.
- Brattain, W. H., & Garrett, C. G. B. (1955). Experiments on the Interface between Germanium and an Electrolyte. *Bell System Technical Journal*, Vol. 34, No. 1, pp. 129-176, 0005-8580.
- Brillet, J., Gratzel, M., & Sivula, K. (2010). Decoupling Feature Size and Functionality in Solution-Processed, Porous Hematite Electrodes for Solar Water Splitting. *Nano Letters*, Vol. 10, No. 10, pp. 4155-4160, 1530-6984.
- Carlson, D. E., & Wronski, C. R. (1976). Amorphous Silicon Solar-Cell. *Applied Physics Letters*, Vol. 28, No. 11, pp. 671-673, 0003-6951.
- Cesar, I., Sivula, K., Kay, A., Zboril, R., & Gratzel, M. (2009). Influence of Feature Size, Film Thickness, and Silicon Doping on the Performance of Nanostructured Hematite Photoanodes for Solar Water Splitting. *Journal of Physical Chemistry C*, Vol. 113, No. 2, pp. 772-782, 1932-7447.
- Chapin, D. M., Fuller, C. S., & Pearson, G. L. (1954). A New Silicon P-N Junction Photocell for Converting Solar Radiation into Electrical Power. *Journal of Applied Physics*, Vol. 25, No. 5, pp. 676-677, 0021-8979.
- Chatterjee, D., & Mahata, A. (2001). Demineralization of Organic Pollutants on the Dye Modified TiO₂ Semiconductor Particulate System Using Visible Light. *Applied Catalysis B-Environmental*, Vol. 33, No. 2, pp. 119-125, 0926-3373.
- Chatterjee, D., & Mahata, A. (2004). Evidence of Superoxide Radical Formation in the Photodegradation of Pesticide on the Dye Modified TiO₂ Surface Using Visible Light. *Journal of Photochemistry and Photobiology a-Chemistry*, Vol. 165, No. 1-3, pp. 19-23, 1010-6030.
- Chen, Z.B., Kibsgaard, J. & Jaramillo, T.F., (2010) Nanostructuring MoS₂ for Photoelectrochemical Water Splitting. *Solar Hydrogen and Nanotechnology V*,

- Proceedings of the SPIE-The International Society for Optical Engineering*, Vol 7770, pp 7770-K1-K7,0277-768X
- Chen, C. C., Ma, W. H., & Zhao, J. C. (2010). Semiconductor-Mediated Photodegradation of Pollutants under Visible-Light Irradiation. *Chemical Society Reviews*, Vol. 39, No. 11, pp. 4206-4219, 0306-0012.
- Chen, J., Zhao, D. W., Song, J. L., Sun, X. W., Deng, W. Q., Liu, X. W., et al. (2009). Directly Assembled Cdse Quantum Dots on Tio₂ in Aqueous Solution by Adjusting Ph Value for Quantum Dot Sensitized Solar Cells. *Electrochemistry Communications*, Vol. 11, No. 12, pp. 2265-2267, 1388-2481.
- Chen, X., & Mao, S. S. (2007). Titanium Dioxide Nanomaterials: Synthesis, Properties, Modifications, and Applications. *Chemical Reviews*, Vol. 107, No. 7, pp. 2891-2959, 0009-2665.
- Chen, X. B., Lou, Y. B., Samia, A. C. S., Burda, C., & Gole, J. L. (2005). Formation of Oxynitride as the Photocatalytic Enhancing Site in Nitrogen-Doped Titania Nanocatalysts: Comparison to a Commercial Nanopowder. *Advanced Functional Materials*, Vol. 15, No. 1, pp. 41-49, 1616-301X.
- Chen, X. B., & Mao, S. S. (2006). Synthesis of Titanium Dioxide (Tio₂) Nanomaterials. *Journal of Nanoscience and Nanotechnology*, Vol. 6, No. 4, pp. 906-925, 1533-4880.
- Chen, X. B., Shen, S. H., Guo, L. J., & Mao, S. S. (2010). Semiconductor-Based Photocatalytic Hydrogen Generation. *Chemical Reviews*, Vol. 110, No. 11, pp. 6503-6570, 0009-2665.
- Chen, Z. B., Jaramillo, T. F., Deutsch, T. G., Kleiman-Shwarstein, A., Forman, A. J., Gaillard, N., et al. (2010). Accelerating Materials Development for Photoelectrochemical Hydrogen Production: Standards for Methods, Definitions, and Reporting Protocols. *Journal of Materials Research*, Vol. 25, No. 1, pp. 3-16, 0884-2914.
- Chianelli, R. R., Siadati, M. H., De la Rosa, M. P., Berhault, G., Wilcoxon, J. P., Bearden, R., et al. (2006). Catalytic Properties of Single Layers of Transition Metal Sulfide Catalytic Materials. *Catalysis Reviews-Science and Engineering*, Vol. 48, No. 1, pp. 1-41, 0161-4940.
- Cho, Y. M., Choi, W. Y., Lee, C. H., Hyeon, T., & Lee, H. I. (2001). Visible Light-Induced Degradation of Carbon Tetrachloride on Dye-Sensitized Tio₂. *Environmental Science & Technology*, Vol. 35, No. 5, pp. 966-970, 0013-936X.
- Cho, Y. M., & Choi, W. Y. (2002). Visible Light-Induced Reactions of Humic Acids on Tio₂. *Journal of Photochemistry and Photobiology a-Chemistry*, Vol. 148, No. 1-3, pp. 129-135, 1010-6030.
- Chong, M. N., Jin, B., Chow, C. W. K., & Saint, C. (2010). Recent Developments in Photocatalytic Water Treatment Technology: A Review. *Water Research*, Vol. 44, No. 10, pp. 2997-3027, 0043-1354.
- Combs, S. (2008). The Energy Report (Chapter 22). Retrieved from <http://window.state.tx.us/specialrpt/energy>
- Contreras, M. A., Egaas, B., Ramanathan, K., Hiltner, J., Swartzlander, A., Hasoon, F., et al. (1999). Progress toward 20% Efficiency in Cu(in,Ca)Se-2 Polycrystalline Thin-Film Solar Cells. *Progress in Photovoltaics*, Vol. 7, No. 4, pp. 311-316, 1062-7995.
- Crabtree, G. W., Dresselhaus, M. S., & Buchanan, M. V. (2004). The Hydrogen Economy. *Physics Today*, Vol. 57, No. 12, pp. 39-44, 0031-9228.
- Currao, A. (2007). Photoelectrochemical Water Splitting. *CHIMIA International Journal for Chemistry*, Vol. 61, No, pp. 815-819.

- Daskalaki, V. M., Antoniadou, M., Puma, G. L., Kondarides, D. I., & Lianos, P. (2010). Solar Light-Responsive Pt/Cds/TiO₂ Photocatalysts for Hydrogen Production and Simultaneous Degradation of Inorganic or Organic Sacrificial Agents in Wastewater. *Environmental Science & Technology*, Vol. 44, No. 19, pp. 7200-7205, 0013-936X.
- Derbal, A., Omeiri, S., Bouguelia, A., & Trari, M. (2008). Characterization of New Heterosystem CuFeO₂/SnO₂ Application to Visible-Light Induced Hydrogen Evolution. *International Journal of Hydrogen Energy*, Vol. 33, No. 16, pp. 4274-4282, 0360-3199.
- DeVos, A. (1980). Detailed Balance Limit of the Efficiency of Tandem Solar Cells. *Journal of Physics D: Applied Physics*, Vol. 13, No. 5, pp. 839-846.
- Diguna, L. J., Shen, Q., Kobayashi, J., & Toyoda, T. (2007a). High Efficiency of CdSe Quantum-Dot-Sensitized TiO₂ Inverse Opal Solar Cells. *Applied Physics Letters*, Vol. 91, No. 2, pp. 023116, 0003-6951.
- Diguna, L. J., Shen, Q., Kobayashi, J., & Toyoda, T. (2007b). High Efficiency of CdSe Quantum-Dot-Sensitized TiO₂ Inverse Opal Solar Cells. *Applied Physics Letters*, Vol. 91, No. 2, pp, 0003-6951.
- Dom, R., Subasri, R., Radha, K., & Borse, P. H. (2011). Synthesis of Solar Active Nanocrystalline Ferrite, MFe₂O₄ (M: Ca, Zn, Mg) Photocatalyst by Microwave Irradiation. *Solid State Communications*, Vol. 151, No. 6, pp. 470-473, 0038-1098.
- Dougherty, W., Kartha, S., Rajan, C., Lazarus, M., Bailie, A., Runkle, B., et al. (2009). Greenhouse Gas Reduction Benefits and Costs of a Large-Scale Transition to Hydrogen in the USA. *Energy Policy*, Vol. 37, No. 1, pp. 56-67, 0301-4215.
- Durrant, J. R., Haque, S. A., & Palomares, E. (2006). Photochemical Energy Conversion: From Molecular Dyads to Solar Cells. *Chemical Communications*, Vol. 31, pp. 3279-3289, 1359-7345.
- Frame, F. A., & Osterloh, F. E. (2010). CdSe-MoS₂: A Quantum Size-Confined Photocatalyst for Hydrogen Evolution from Water under Visible Light. *Journal of Physical Chemistry C*, Vol. 114, No. 23, pp. 10628-10633, 1932-7447.
- Fujishima, A., & Honda, K. (1972). Electrochemical Photolysis of Water at a Semiconductor Electrode. *Nature*, Vol. 238, No, pp. 37-38.
- Fujishima, A., & Honda, K. (1972). Electrochemical Photolysis of Water at a Semiconductor Electrode. *Nature*, Vol. 238, No. 5358, pp. 37-38, 0028-0836.
- Gaillard, N., Kaneshiro, J., Miller, E. L., Weinhardt, L., Bar, M., Heske, C., et al. (2009). Surface Modification of Tungsten Oxide-Based Photoanodes for Solar-Powered Hydrogen Production. In *Compound Semiconductors for Energy Applications and Environmental Sustainability*, ShahedipourSandvik, F., Schubert, E. F., Bell, L. D., Tilak, V. & Bett, A. W. (Eds.), (Vol. 1167), pp. 109-114 Materials Research Society, 0272-9172, Warrendale.
- Gaillard, N., Chang, Y., Kaneshiro, J., Deangelis, A., & Miller, E. L. (2010). Status of Research on Tungsten Oxide-Based Photoelectrochemical Devices at the University of Hawai'i. In *Solar Hydrogen and Nanotechnology V*, Idriss, H. & Wang, H. (Eds.), (Vol. 7770), pp. 77700V-77701, 0277-786X 978-0-8194-8266-2.
- Ge, L., Xu, M. X., & Fang, H. B. (2006). Preparation and Characterization of Silver and Indium Vanadate Co-Doped TiO₂ Thin Films as Visible-Light-Activated

- Photocatalyst. *Journal of Sol-Gel Science and Technology*, Vol. 40, No. 1, pp. 65-73, 0928-0707.
- Gerische, H. (1966). Electrochemical Behavior of Semiconductors under Illumination. *Journal of the Electrochemical Society*, Vol. 113, No. 11, pp. 1174-1182, 0013-4651.
- Gimenez, S., Mora-Sero, I., Macor, L., Guijarro, N., Lana-Villarreal, T., Gomez, R., et al. (2009). Improving the Performance of Colloidal Quantum-Dot-Sensitized Solar Cells. *Nanotechnology*, Vol. 20, No. 29, pp. 0957-4484.
- Goncalves, L. M., Bermudez, V. D., Ribeiro, H. A., & Mendes, A. M. (2008). Dye-Sensitized Solar Cells: A Safe Bet for the Future. *Energy & Environmental Science*, Vol. 1, No. 6, pp. 655-667, 1754-5692.
- Gonzalez-Pedro, V., Xu, X. Q., Mora-Sero, I., & Bisquert, J. (2010). Modeling High-Efficiency Quantum Dot Sensitized Solar Cells. *Acs Nano*, Vol. 4, No. 10, pp. 5783-5790, 1936-0851.
- Gorer, S., & Hodes, G. (1994). Quantum-Size Effects in the Study of Chemical Solution Deposition Mechanisms of Semiconductor-Films. *Journal of Physical Chemistry*, Vol. 98, No. 20, pp. 5338-5346, 0022-3654.
- Granqvist, C. G. (2000). Electrochromic Tungsten Oxide Films: Review of Progress 1993-1998. *Solar Energy Materials and Solar Cells*, Vol. 60, No. 3, pp. 201-262, 0927-0248.
- Gratzel, M. (2001). Photoelectrochemical Cells. *Nature*, Vol. 414, No. 6861, pp. 338-344, 0028-0836.
- Gratzel, M. (2004). Conversion of Sunlight to Electric Power by Nanocrystalline Dye-Sensitized Solar Cells. *Journal of Photochemistry and Photobiology a-Chemistry*, Vol. 164, No. 1-3, pp. 3-14, 1010-6030.
- Gratzel, M. (2007). Photovoltaic and Photoelectrochemical Conversion of Solar Energy. *Philosophical Transactions of the Royal Society a-Mathematical Physical and Engineering Sciences*, Vol. 365, No. 1853, pp. 993-1005, 1364-503X.
- Green, M. A. (2003). *Third Generation Photovoltaics: Advanced Solar Energy Conversion*, Springer-Verlag, Berlin, Heidelberg.
- Green, M. A., Emery, K., Hishikawa, Y., & Warta, W. (2008). Solar Cell Efficiency Tables (Version 32). *Progress in Photovoltaics*, Vol. 16, No. 5, pp. 435-440, 1062-7995.
- Guijarro, N., Lana-Villarreal, T., Mora-Sero, I., Bisquert, J., & Gomez, R. (2009). Cdse Quantum Dot-Sensitized Tio₂ Electrodes: Effect of Quantum Dot Coverage and Mode of Attachment. *Journal of Physical Chemistry C*, Vol. 113, No. 10, pp. 4208-4214, 1932-7447.
- Gunes, S., & Sariciftci, N. S. (2008). Hybrid Solar Cells. *Inorganica Chimica Acta*, Vol. 361, No. pp. 581-588.
- Hagfeldt, A., Boschloo, G., Sun, L. C., Kloo, L., & Pettersson, H. (2010). Dye-Sensitized Solar Cells. *Chemical Reviews*, Vol. 110, No. 11, pp. 6595-6663, 0009-2665.
- Hauffe, K., Danzmann, H. J., Pusch, H., Range, J., & Volz, H. (1970). New Experiments on Sensitization of Zinc Oxide by Means of Electrochemical Cell Technique. *Journal of the Electrochemical Society*, Vol. 117, No. 8, pp. 993-999, 0013-4651.
- Heller, A. (1981). Conversion of Sunlight into Electrical-Power and Photoassisted Electrolysis of Water in Photoelectrochemical Cells. *Accounts of Chemical Research*, Vol. 14, No. 5, pp. 154-162, 0001-4842.
- Hensel, J., Canin, M., & Zhang, J. Z. (2010). Qd Co-Sensitized and Nitrogen Doped Tio₂ Nanocomposite for Photoelectrochemical Hydrogen Generation. In *Solar Hydrogen*

- and Nanotechnology V*, Idriss, H. & Wang, H. (Eds.), (Vol. 7770), pp. 777012 Spie-Int Soc Optical Engineering, 0277-786X 978-0-8194-8266-2, Bellingham.
- Hensel, J., Wang, G. M., Li, Y., & Zhang, J. Z. (2010). Synergistic Effect of Cdse Quantum Dot Sensitization and Nitrogen Doping of Tio₂ Nanostructures for Photoelectrochemical Solar Hydrogen Generation. *Nano Letters*, Vol. 10, No. 2, pp. 478-483, 1530-6984.
- Hodes, G., Cahen, D., & Manassen, J. (1976). Tungsten Trioxide as a Photoanode for a Photoelectrochemical Cell (Pec). *Nature*, Vol. 260, No. 5549, pp. 312-313, 0028-0836.
- Hodes, G. (2008). Comparison of Dye- and Semiconductor-Sensitized Porous Nanocrystalline Liquid Junction Solar Cells. *Journal of Physical Chemistry C*, Vol. 112, No. 46, pp. 17778-17787, 1932-7447.
- Hoffmann, M. R., Martin, S. T., Choi, W. Y., & Bahnemann, D. W. (1995). Environmental Applications of Semiconductor Photocatalysis. *Chemical Reviews*, Vol. 95, No. 1, pp. 69-96, 0009-2665.
- Hu, C. C., Nian, J. N., & Teng, H. (2008). Electrodeposited P-Type Cu₂o as Photocatalyst for H-2 Evolution from Water Reduction in the Presence of Wo₃. *Solar Energy Materials and Solar Cells*, Vol. 92, No. 9, pp. 1071-1076, 0927-0248.
- Huang, S. Q., Zhang, Q. X., Huang, X. M., Guo, X. Z., Deng, M. H., Li, D. M., et al. (2010). Fibrous Cds/Cdse Quantum Dot Co-Sensitized Solar Cells Based on Ordered Tio₂ Nanotube Arrays. *Nanotechnology*, Vol. 21, No. 37, pp. 375201, 0957-4484.
- Ikeda, N., & Miyasaka, T. (2007). Plastic and Solid-State Dye-Sensitized Solar Cells Incorporating Single-Wall Carbon Nanotubes. *Chemistry Letters*, Vol. 36, No. 3, pp. 466-467, 0366-7022.
- Jang, J. S., Joshi, U. A., & Lee, J. S. (2007). Solvothermal Synthesis of Cds Nanowires for Photocatalytic Hydrogen and Electricity Production. *Journal of Physical Chemistry C*, Vol. 111, No, pp. 13280-13287.
- Jaramillo, T. F., Jorgensen, K. P., Bonde, J., Nielsen, J. H., Horch, S., & Chorkendorff, I. (2007). Identification of Active Edge Sites for Electrochemical H-2 Evolution from Mos₂ Nanocatalysts. *Science*, Vol. 317, No. 5834, pp. 100-102, 0036-8075.
- Kalyanasundaram, K. (1985). Photoelectrochemical Cell Studies with Semiconductor Electrodes - a Classified Bibliography (1975 - 1983). *Solar Cells*, Vol. 15, No. 2, pp. 93-156, 0379-6787.
- Kalyanasundaram, K., & Gratzel, M. (1998). Applications of Functionalized Transition Metal Complexes in Photonic and Optoelectronic Devices. *Coordination Chemistry Reviews*, Vol. 177, No, pp. 347-414, 0010-8545.
- Kamat, P. V. (2007). Meeting the Clean Energy Demand: Nanostructure Architectures for Solar Energy Conversion. *Journal of Physical Chemistry C*, Vol. 111, No. 7, pp. 2834-2860, 1932-7447.
- Kanda, S., Akita, T., Fujishima, M., & Tada, H. (2011). Facile Synthesis and Catalytic Activity of Mos₂/Tio₂ by a Photodeposition-Based Technique and Its Oxidized Derivative Moo₃/Tio₂ with a Unique Photochromism. *Journal of Colloid and Interface Science*, Vol. 354, No. 2, pp. 607-610, 0021-9797.
- Kay, A., Cesar, I., & Gratzel, M. (2006). New Benchmark for Water Photooxidation by Nanostructured Alpha-Fe₂o₃ Films. *Journal of the American Chemical Society*, Vol. 128, No. 49, pp. 15714-15721, 0002-7863.

- Kennedy, J. H., & Frese, K. W. (1977). Photooxidation of Water at Alpha-Fe₂O₃ Electrodes. *Journal of the Electrochemical Society*, Vol. 124, No. 3, pp. C130-C130, 0013-4651.
- Kennedy, J. H., & Anderman, M. (1983). Photoelectrolysis of Water at Alpha-Fe₂O₃ Electrodes in Acidic Solution. *Journal of the Electrochemical Society*, Vol. 130, No. 4, pp. 848-852, 0013-4651.
- Khan, S. U. M., & Akikusa, J. (1999). Photoelectrochemical Splitting of Water at Nanocrystalline N-Fe₂O₃ Thin-Film Electrodes. *Journal of Physical Chemistry B*, Vol. 103, No. 34, pp. 7184-7189, 1089-5647.
- Khan, S. U. M., Al-Shahry, M., & Ingler, W. B. (2002). Efficient Photochemical Water Splitting by a Chemically Modified N-TiO₂. *Science*, Vol. 297, No. 5590, pp. 2243-2245, 0036-8075.
- Khaselev, O., & Turner, J. A. (1998a). A Monolithic Photovoltaic-Photoelectrochemical Device for Hydrogen Production Via Water Splitting. *Science*, Vol. 280, No. 5362, pp. 425-427, 0036-8075.
- Khaselev, O., & Turner, J. A. (1998b). Electrochemical Stability of P-GaInP₂ in Aqueous Electrolytes toward Photoelectrochemical Water Splitting. *Journal of the Electrochemical Society*, Vol. 145, No. 10, pp. 3335-3339, 0013-4651.
- Khaselev, O., Bansal, A., & Turner, J. A. (2001). High-Efficiency Integrated Multijunction Photovoltaic/Electrolysis Systems for Hydrogen Production. *International Journal of Hydrogen Energy*, Vol. 26, No. 2, pp. 127-132, 0360-3199.
- Kikuchi, E., Nemoto, Y., Kajiwara, M., Uemiyu, S., & Kojima, T. (2000). Steam Reforming of Methane in Membrane Reactors: Comparison of Electroless-Plating and Cvd Membranes and Catalyst Packing Modes. *Catalysis Today*, Vol. 56, No. 1-3, pp. 75-81, 0920-5861.
- Kim, J., Lee, C. W., & Choi, W. (2010). Platinized WO₃ as an Environmental Photocatalyst That Generates Oh Radicals under Visible Light. *Environmental Science & Technology*, Vol. 44, No. 17, pp. 6849-6854, 0013-936X.
- Kim, J. Y., Lee, K., Coates, N. E., Moses, D., Nguyen, T. Q., Dante, M., et al. (2007). Efficient Tandem Polymer Solar Cells Fabricated by All-Solution Processing. *Science*, Vol. 317, No. 5835, pp. 222-225, 0036-8075.
- Kim, W., Tachikawa, T., Majima, T., & Choi, W. (2009). Photocatalysis of Dye-Sensitized TiO₂ Nanoparticles with Thin Overcoat of Al₂O₃: Enhanced Activity for H₂ Production and Dechlorination of CCl₄. *Journal of Physical Chemistry C*, Vol. 113, No. 24, pp. 10603-10609, 1932-7447.
- Kisch, H., Zang, L., Lange, C., Maier, W. F., Antonius, C., & Meissner, D. (1998). Modified, Amorphous Titania - a Hybrid Semiconductor for Detoxification and Current Generation by Visible Light. *Angewandte Chemie-International Edition*, Vol. 37, No. 21, pp. 3034-3036, 1433-7851.
- Klimov, V. I. (2006). Detailed-Balance Power Conversion Limits of Nanocrystal-Quantum-Dot Solar Cells in the Presence of Carrier Multiplication. *Applied Physics Letters*, Vol. 89, No. 12, pp. 123118, 0003-6951.
- Kongkanand, A., Dominguez, R. M., & Kamat, P. V. (2007). Single Wall Carbon Nanotube Scaffolds for Photoelectrochemical Solar Cells. Capture and Transport of Photogenerated Electrons. *Nano Letters*, Vol. 7, No. 3, pp. 676-680, 1530-6984.
- Kongkanand, A., Tvrdy, K., Takechi, K., Kuno, M., & Kamat, P. V. (2008). Quantum Dot Solar Cells. Tuning Photoresponse through Size and Shape Control of CdSe-TiO₂

- Architecture. *Journal of the American Chemical Society*, Vol. 130, No. 12, pp. 4007-4015, 0002-7863.
- Kowalska, E., Mahaney, O. O. P., Abe, R., & Ohtani, B. (2010). Visible-Light-Induced Photocatalysis through Surface Plasmon Excitation of Gold on Titania Surfaces. *Physical Chemistry Chemical Physics*, Vol. 12, No. 10, pp. 2344-2355, 1463-9076.
- Kyung, H., Lee, J., & Choi, W. Y. (2005). Simultaneous and Synergistic Conversion of Dyes and Heavy Metal Ions in Aqueous TiO₂ Suspensions under Visible-Light Illumination. *Environmental Science & Technology*, Vol. 39, No. 7, pp. 2376-2382, 0013-936X.
- Le Formal, F., Gratzel, M., & Sivula, K. (2010). Controlling Photoactivity in Ultrathin Hematite Films for Solar Water-Splitting. *Advanced Functional Materials*, Vol. 20, No. 7, pp. 1099-1107, 1616-301X.
- Leary, R., & Westwood, A. (2011). Carbonaceous Nanomaterials for the Enhancement of TiO₂ Photocatalysis. *Carbon*, Vol. 49, No. 3, pp. 741-772, 0008-6223.
- Lee, H., Wang, M. K., Chen, P., Gamelin, D. R., Zakeeruddin, S. M., Gratzel, M., et al. (2009). Efficient Cdse Quantum Dot-Sensitized Solar Cells Prepared by an Improved Successive Ionic Layer Adsorption and Reaction Process. *Nano Letters*, Vol. 9, No. 12, pp. 4221-4227, 1530-6984.
- Lee, H. J., Yum, J. H., Leventis, H. C., Zakeeruddin, S. M., Haque, S. A., Chen, P., et al. (2008). Cdse Quantum Dot-Sensitized Solar Cells Exceeding Efficiency 1% at Full-Sun Intensity. *Journal of Physical Chemistry C*, Vol. 112, No. 30, pp. 11600-11608, 1932-7447.
- Lee, Y. L., & Lo, Y. S. (2009). Highly Efficient Quantum-Dot-Sensitized Solar Cell Based on Co-Sensitization of Cds/Cdse. *Advanced Functional Materials*, Vol. 19, No. 4, pp. 604-609, 1616-301X.
- Levy-Clement, C., Tena-Zaera, R., Ryan, M. A., Katty, A., & Hodes, G. (2005). Cdse-Sensitized P-CuscN/Nanowire N-Zno Heterojunctions. *Advanced Materials*, Vol. 17, No. 12, pp. 1512-1515, 0935-9648.
- Lewis, N. S. (2001). Light Work with Water. *Nature*, Vol. 414, No, pp. 589-590.
- Li, B., Wang, L. D., Kang, B. N., Wang, P., & Qiu, Y. (2006). Review of Recent Progress in Solid-State Dye-Sensitized Solar Cells. *Solar Energy Materials and Solar Cells*, Vol. 90, No. 5, pp. 549-573, 0927-0248.
- Li, X. Z., & Li, F. B. (2001). Study of Au/Au³⁺-TiO₂ Photocatalysts toward Visible Photooxidation for Water and Wastewater Treatment. *Environmental Science & Technology*, Vol. 35, No. 11, pp. 2381-2387, 0013-936X.
- Li, Y., Hu, Y., Peng, S., Lu, G., & Li, S. (2009). Nanorods by an Ethylenediamine Assisted Hydrothermal Method for Photocatalytic Hydrogen Evolution. *Journal of Physical Chemistry C* Vol. 113, No, pp. 9352-9358.
- Lianos, P. (2010). Production of Electricity and Hydrogen by Photocatalytic Degradation of Organic Wastes in a Photoelectrochemical Cell the Concept of the Photofuelcell: A Review of a Re-Emerging Research Field. *Journal of Hazardous Materials*, Vol. 185, No. 2-3, pp. 575-590, 0304-3894.
- Lin, Y. J., Zhou, S., Liu, X. H., Sheehan, S., & Wang, D. W. (2009). TiO₂/TiSi₂ Heterostructures for High-Efficiency Photoelectrochemical H₂O Splitting. *Journal of the American Chemical Society*, Vol. 131, No. 8, pp. 2772-2773, 0002-7863.

- Liu, Z. F., Zhao, Z. G., & Miyauchi, M. (2009). Efficient Visible Light Active $\text{CaFe}_2\text{O}_4/\text{WO}_3$ Based Composite Photocatalysts: Effect of Interfacial Modification. *Journal of Physical Chemistry C*, Vol. 113, No. 39, pp. 17132-17137, 1932-7447.
- Lopez-Luke, T., Wolcott, A., Xu, L. P., Chen, S. W., Wcn, Z. H., Li, J. H., et al. (2008). Nitrogen-Doped and Cdse Quantum-Dot-Sensitized Nanocrystalline TiO_2 Films for Solar Energy Conversion Applications. *Journal of physical Chemistry C*, Vol. 112, No. 4, pp. 1282-1292, 1932-7447.
- Maeda, K., Teramura, K., & Domen, K. (2008). Effect of Post-Calcination on Photocatalytic Activity of $(\text{Ga}_{1-x}\text{Zn}_x)(\text{N}_{1-x}\text{O}_x)$ Solid Solution for Overall Water Splitting under Visible Light. *Journal of Catalysis*, Vol. 254, No. 2, pp. 198-204, 0021-9517.
- Maeda, K., Higashi, M., Lu, D. L., Abe, R., & Domen, K. (2010). Efficient Nonsacrificial Water Splitting through Two-Step Photoexcitation by Visible Light Using a Modified Oxynitride as a Hydrogen Evolution Photocatalyst. *Journal of the American Chemical Society*, Vol. 132, No. 16, pp. 5858-5868, 0002-7863.
- Marti, A., & Araujo, G. L. (1996). Limiting Efficiencies for Photovoltaic Energy Conversion in Multigap Systems. *Solar Energy Materials and Solar Cells*, Vol. 43, No. 2, pp. 203-222, 0927-0248.
- Matsuoka, M., Kitano, M., Takeuchi, M., Tsujimaru, K., Anpo, M., & Thomas, J. M. (2007). Photocatalysis for New Energy Production - Recent Advances in Photocatalytic Water Splitting Reactions for Hydrogen Production. *Catalysis Today*, Vol. 122, No. 1-2, pp. 51-61, 0920-5861.
- Miller, E. L., Paluselli, D., Marsen, B., & Rocheleau, R. E. (2005). Development of Reactively Sputtered Metal Oxide Films for Hydrogen-Producing Hybrid Multijunction Photoelectrodes. *Solar Energy Materials and Solar Cells*, Vol. 88, No. 2, pp. 131-144, 0927-0248.
- Mora-Sero, I., Gimenez, S., Moehl, T., Fabregat-Santiago, F., Lana-Villareal, T., Gomez, R., et al. (2008). Factors Determining the Photovoltaic Performance of a Cdse Quantum Dot Sensitized Solar Cell: The Role of the Linker Molecule and of the Counter Electrode. *Nanotechnology*, Vol. 19, No. 42, pp. 0957-4484.
- Mora-Sero, I., & Bisquert, J. (2010). Breakthroughs in the Development of Semiconductor-Sensitized Solar Cells. *Journal of Physical Chemistry Letters*, Vol. 1, No. 20, pp. 3046-3052, 1948-7185.
- Moreels, I., Lambert, K., De Muynck, D., Vanhaecke, F., Poelman, D., Martins, J. C., et al. (2007). Composition and Size-Dependent Extinction Coefficient of Colloidal Pbse Quantum Dots. *Chemistry of Materials*, Vol. 19, No. 25, pp. 6101-6106, 0897-4756.
- Murakoshi, K., Kogure, R., Wada, Y., & Yanagida, S. (1998). Fabrication of Solid-State Dye-Sensitized TiO_2 Solar Cells Combined with Polypyrrole. *Solar Energy Materials and Solar Cells*, Vol. 55, No. 1-2, pp. 113-125, 0927-0248.
- Muratore, C., & Voevodin, A. A. (2009). Chameleon Coatings: Adaptive Surfaces to Reduce Friction and Wear in Extreme Environments. *Annual Review of Materials Research*, Vol. 39, No. pp. 297-324, 1531-7331.
- Murphy, A. B., Barnes, P. R. F., Randeniya, L. K., Plumb, I. C., Grey, I. E., Horne, M. D., et al. (2006). Efficiency of Solar Water Splitting Using Semiconductor Electrodes. *International Journal of Hydrogen Energy*, Vol. 31, No. 14, pp. 1999-2017, 0360-3199.
- Nazeeruddin, M. K., Pechy, P., Renouard, T., Zakeeruddin, S. M., Humphry-Baker, R., Comte, P., et al. (2001). Engineering of Efficient Panchromatic Sensitizers for

- Nanocrystalline TiO₂-Based Solar Cells. *Journal of the American Chemical Society*, Vol. 123, No. 8, pp. 1613-1624, 0002-7863.
- Nelson, R. C. (1965). Minority Carrier Trapping and Dye Sensitization. *Journal of Physical Chemistry*, Vol. 69, No. 3, pp. 714-&, 0022-3654.
- Ni, M., Leung, M. K. H., Leung, D. Y. C., & Sumathy, K. (2007). A Review and Recent Developments in Photocatalytic Water-Splitting Using TiO₂ for Hydrogen Production. *Renewable and Sustainable Energy Reviews*, Vol. 11, No. 3, pp. 401-425, 1364-0321.
- Niitsoo, O., Sarkar, S. K., Pejoux, C., Ruhle, S., Cahen, D., & Hodes, G. (2006). Chemical Bath Deposited CdS/Cdse-Sensitized Porous TiO₂ Solar Cells. *Journal of Photochemistry and Photobiology a-Chemistry*, Vol. 181, No. 2-3, pp. 306-313, 1010-6030.
- Nozik, A. J. (1976). P-N Photoelectrolysis Cells. *Applied Physics Letters*, Vol. 29, No. 3, pp. 150-153, 0003-6951.
- Nozik, A. J. (2002). Quantum Dot Solar Cells. *Physica E-Low-Dimensional Systems & Nanostructures*, Vol. 14, No. 1-2, pp. 115-120, 1386-9477.
- Ohko, Y., Tatsuma, T., Fujii, T., Naoi, K., Niwa, C., Kubota, Y., et al. (2003). Multicolour Photochromism of TiO₂ Films Loaded with Silver Nanoparticles. *Nature Materials*, Vol. 2, No. 1, pp. 29-31, 1476-1122.
- Oregan, B., & Gratzel, M. (1991). A Low-Cost, High-Efficiency Solar-Cell Based on Dye-Sensitized Colloidal TiO₂ Films. *Nature*, Vol. 353, No. 6346, pp. 737-740, 0028-0836.
- Oregan, B., & Schwartz, D. T. (1995). Efficient Photo-Hole Injection from Adsorbed Cyanine Dyes into Electrodeposited Copper(I) Thiocyanate Thin-Films. *Chemistry of Materials*, Vol. 7, No. 7, pp. 1349-1354, 0897-4756.
- Park, H., Choi, W., & Hoffmann, M. R. (2008). Effects of the Preparation Method of the Ternary CdS/TiO₂/Pt Hybrid Photocatalysts on Visible Light-Induced Hydrogen Production. *Journal of Materials Chemistry*, Vol. 18, No. 20, pp. 2379-2385, 0959-9428.
- Paz, Y. (2011). Application of TiO₂ Photocatalysis for Air Treatment: Patents' Overview. *Applied Catalysis B-Environmental*, Vol. 99, No. 3-4, pp. 448-460, 0926-3373.
- Peng, T. Y., Dai, K., Yi, H. B., Ke, D. N., Cai, P., & Zan, L. (2008). Photosensitization of Different Ruthenium(II) Complex Dyes on TiO₂ for Photocatalytic H₂ Evolution under Visible-Light. *Chemical Physics Letters*, Vol. 460, No. 1-3, pp. 216-219, 0009-2614.
- Petit, M. A., & Plichon, V. (1996). Electrochemical Behavior of WO₃ Films in H₃PO₄/H₂O Binary Mixtures. *Journal of the Electrochemical Society*, Vol. 143, No. 9, pp. 2789-2794, 0013-4651.
- Qiao, Q. Q., Xie, Y., & McLeskey, J. T. (2008). Organic/Inorganic Polymer Solar Cells Using a Buffer Layer from All-Water-Solution Processing. *Journal of Physical Chemistry C*, Vol. 112, No. 26, pp. 9912-9916, 1932-7447.
- Quinn, R. K., Nasby, R. D., & Baughman, R. J. (1976). Photoassisted Electrolysis of Water Using Single-Crystal Alpha-Fe₂O₃ Anodes. *Materials Research Bulletin*, Vol. 11, No. 8, pp. 1011-1017, 0025-5408.
- Ravelli, D., Dondi, D., Fagnoni, M., & Albini, A. (2009). Photocatalysis. A Multi-Faceted Concept for Green Chemistry. *Chemical Society Reviews*, Vol. 38, No. 7, pp. 1999-2011, 0306-0012.
- Robel, I., Subramanian, V., Kuno, M., & Kamat, P. V. (2006). Quantum Dot Solar Cells. Harvesting Light Energy with Cdse Nanocrystals Molecularly Linked to

- Mesoscopic TiO₂ Films. *Journal of the American Chemical Society*, Vol. 128, No. 7, pp. 2385-2393, 0002-7863.
- Ruhle, S., Shalom, M., & Zaban, A. (2010). Quantum-Dot-Sensitized Solar Cells. *Chemphyschem*, Vol. 11, No. 11, pp. 2290-2304, 1439-4235.
- Santato, C., Ulmann, M., & Augustynski, J. (2001). Photoelectrochemical Properties of Nanostructured Tungsten Trioxide Films. *Journal of Physical Chemistry B*, Vol. 105, No. 5, pp. 936-940, 1089-5647.
- Saremi-Yarahmadi, S., Wijayantha, K. G. U., Tahir, A. A., & Vaidhyanathan, B. (2009). Nanostructured Alpha-Fe₂O₃ Electrodes for Solar Driven Water Splitting: Effect of Doping Agents on Preparation and Performance. *Journal of Physical Chemistry C*, Vol. 113, No. 12, pp. 4768-4778, 1932-7447.
- Saremi-Yarahmadi, S., Tahir, A. A., Vaidhyanathan, B., & Wijayantha, K. G. U. (2009). Fabrication of Nanostructured Alpha-Fe₂O₃ Electrodes Using Ferrocene for Solar Hydrogen Generation. *Materials Letters*, Vol. 63, No. 5, pp. 523-526, 0167-577X.
- Sasaki, Y., Nemoto, H., Saito, K., & Kudo, A. (2009). Solar Water Splitting Using Powdered Photocatalysts Driven by Z-Schematic Interparticle Electron Transfer without an Electron Mediator. *Journal of Physical Chemistry C*, Vol. 113, No. 40, pp. 17536-17542, 1932-7447.
- Sayama, K., Mukasa, K., Abe, R., Abe, Y., & Arakawa, H. (2001). Stoichiometric Water Splitting into H₂ and O₂ Using a Mixture of Two Different Photocatalysts and an I³⁻/I⁻ Shuttle Redox Mediator under Visible Light Irradiation. *Chemical Communications*, Vol. 23, pp. 2416-2417, 1359-7345.
- Sayama, K., Mukasa, K., Abe, R., Abe, Y., & Arakawa, H. (2002). A New Photocatalytic Water Splitting System under Visible Light Irradiation Mimicking a Z-Scheme Mechanism in Photosynthesis. *Journal of Photochemistry and Photobiology a-Chemistry*, Vol. 148, No. 1-3, pp. 71-77, 1010-6030.
- Scaife, D. E. (1980). Oxide Semiconductors in Photoelectrochemical Conversion of Solar-Energy. *Solar Energy*, Vol. 25, No. 1, pp. 41-54, 0038-092X.
- Schaller, R. D., & Klimov, V. I. (2004). High Efficiency Carrier Multiplication in Pbse Nanocrystals: Implications for Solar Energy Conversion. *Physical Review Letters*, Vol. 92, No. 18, pp. 186601, 0031-9007.
- Scharber, M. C., Wuhlbacher, D., Koppe, M., Denk, P., Waldauf, C., Heeger, A. J., et al. (2006). Design Rules for Donors in Bulk-Heterojunction Solar Cells - Towards 10 % Energy-Conversion Efficiency. *Advanced Materials*, Vol. 18, No. 6, pp. 789-+, 0935-9648.
- Schurch, D., Currao, A., Sarkar, S., Hodes, G., & Calzaferri, G. (2002). The Silver Chloride Photoanode in Photoelectrochemical Water Splitting. *Journal of Physical Chemistry B*, Vol. 106, No. 49, pp. 12764-12775, 1520-6106.
- Serpone, N., Borgarello, E., & Gratzel, M. (1984). Visible-Light Induced Generation of Hydrogen from H₂s in Mixed Semiconductor Dispersions - Improved Efficiency through Inter-Particle Electron-Transfer. *Journal of the Chemical Society-Chemical Communications*, Vol. 6, pp. 342-344, 0022-4936.
- Shalom, M., Dor, S., Ruhle, S., Grinis, L., & Zaban, A. (2009). Core/Cds Quantum Dot/Shell Mesoporous Solar Cells with Improved Stability and Efficiency Using an Amorphous TiO₂ Coating. *Journal of Physical Chemistry C*, Vol. 113, No. 9, pp. 3895-3898, 1932-7447.

- Shalom, M., Ruhle, S., Hod, I., Yahav, S., & Zaban, A. (2009). Energy Level Alignment in Cds Quantum Dot Sensitized Solar Cells Using Molecular Dipoles. *Journal of the American Chemical Society*, Vol. 131, No. 29, pp. 9876-9877, 0002-7863.
- Shangguan, W. F. (2007). Hydrogen Evolution from Water Splitting on Nanocomposite Photocatalysts. *Science and Technology of Advanced Materials*, Vol. 8, No. 1-2, pp. 76-81, 1468-6996.
- Shankar, K., Basham, J. I., Allam, N. K., Varghese, O. K., Mor, G. K., Feng, X. J., et al. (2009). Recent Advances in the Use of TiO₂ Nanotube and Nanowire Arrays for Oxidative Photoelectrochemistry. *Journal of Physical Chemistry C*, Vol. 113, No. 16, pp. 6327-6359, 1932-7447.
- Shen, Q., Kobayashi, J., Diguna, L. J., & Toyoda, T. (2008). Effect of ZnS Coating on the Photovoltaic Properties of CdSe Quantum Dot-Sensitized Solar Cells. *Journal of Applied Physics*, Vol. 103, No. 8, pp. 0021-8979.
- Shen, S. H., Guo, L. J., Chen, X. B., Ren, F., & Mao, S. S. (2010). Effect of Ag₂S on Solar-Driven Photocatalytic Hydrogen Evolution of Nanostructured Cds. *International Journal of Hydrogen Energy*, Vol. 35, No. 13, pp. 7110-7115, 0360-3199.
- Shin, W. S., Kim, S. C., Lee, S. J., Jeon, H. S., Kim, M. K., Naidu, B. V. K., et al. (2007). Synthesis and Photovoltaic Properties of a Low-Band-Gap Polymer Consisting of Alternating Thiophene and Benzothiadiazole Derivatives for Bulk-Heterojunction and Dye-Sensitized Solar Cells. *Journal of Polymer Science Part a-Polymer Chemistry*, Vol. 45, No. 8, pp. 1394-1402, 0887-624X.
- Shinar, R., & Kennedy, J. H. (1982). Photoactivity of Doped Alpha-Fe₂O₃ Electrodes. *Solar Energy Materials*, Vol. 6, No. 3, pp. 323-335, 0165-1633.
- Shockley, W., & Queisser, H. J. (1961). Detailed Balance Limit of Efficiency of P-N Junction Solar Cells. *Journal of Applied physics*, Vol. 32, No. pp. 510-519.
- Siddiki, M. K., Li, J., Galipeau, D., & Qiao, Q. Q. (2010). A Review of Polymer Multijunction Solar Cells. *Energy & Environmental Science*, Vol. 3, No. 7, pp. 867-883, 1754-5692.
- Sivula, K., Le Formal, F., & Gratzel, M. (2009). WO₃-Fe₂O₃ Photoanodes for Water Splitting: A Host Scaffold, Guest Absorber Approach. *Chemistry of Materials*, Vol. 21, No. 13, pp. 2862-2867, 0897-4756.
- Solarska, R., Alexander, B. D., Braun, A., Jurczakowski, R., Fortunato, G., Stiefel, M., et al. (2010). Tailoring the Morphology of WO₃ Films with Substitutional Cation Doping: Effect on the Photoelectrochemical Properties. *Electrochimica Acta*, Vol. 55, No. 26, pp. 7780-7787, 0013-4686.
- Subramanian, V., Wolf, E., & Kamat, P. V. (2001). Semiconductor-Metal Composite Nanostructures. To What Extent Do Metal Nanoparticles Improve the Photocatalytic Activity of TiO₂ Films? *Journal of Physical Chemistry B*, Vol. 105, No. 46, pp. 11439-11446, 1089-5647.
- Tada, H., Mitsui, T., Kiyonaga, T., Akita, T., & Tanaka, K. (2006). All-Solid-State Z-Scheme in Cds-Au-TiO₂ Three-Component Nanojunction System. *Nature Materials*, Vol. 5, No. 10, pp. 782-786, 1476-1122.
- Tak, Y., Hong, S. J., Lee, J. S., & Yong, K. (2009). Fabrication of ZnO/Cds Core/Shell Nanowire Arrays for Efficient Solar Energy Conversion. *Journal of Materials Chemistry*, Vol. 19, No. 33, pp. 5945-5951, 0959-9428.

- Takeda, Y., & Motohiro, T. Requisites to Realize High Conversion Efficiency of Solar Cells Utilizing Carrier Multiplication. *Solar Energy Materials and Solar Cells*, Vol. 94, No. 8, pp. 1399-1405, 0927-0248.
- Tennakone, K., Kumara, G., Kottegoda, I. R. M., Wijayantha, K. G. U., & Perera, V. P. S. (1998). A Solid-State Photovoltaic Cell Sensitized with a Ruthenium Bipyridyl Complex. *Journal of Physics D-Applied Physics*, Vol. 31, No. 12, pp. 1492-1496, 0022-3727.
- Thimsen, E., Le Formal, F., Gratzel, M., & Warren, S. C. (2011). Influence of Plasmonic Au Nanoparticles on the Photoactivity of Fe₂O₃ Electrodes for Water Splitting. *Nano Letters*, Vol. 11, No. 1, pp. 35-43, 1530-6984.
- Tisdale, W. A., Williams, K. J., Timp, B. A., Norris, D. J., Aydil, E. S., & Zhu, X. Y. (2010). Hot-Electron Transfer from Semiconductor Nanocrystals. *Science*, Vol. 328, No. 5985, pp. 1543-1547, 0036-8075.
- Tributsch, H., & Bennett, J. C. (1977). Electrochemistry and Photochemistry of Mos₂ Layer Crystals .1. *Journal of Electroanalytical Chemistry*, Vol. 81, No. 1, pp. 97-111, 0022-0728.
- Tsubomura, H., Matsumura, M., Nomura, Y., & Amamiya, T. (1976). Dye Sensitized Zinc-Oxide - Aqueous-Electrolyte - Platinum Photocell. *Nature*, Vol. 261, No. 5559, pp. 402-403, 0028-0836.
- Tubtimtae, A., Wu, K. L., Tung, H. Y., Lee, M. W., & Wang, G. J. (2010). Ag₂S Quantum Dot-Sensitized Solar Cells. *Electrochemistry Communications*, Vol. 12, No. 9, pp. 1158-1160, 1388-2481.
- Turner, J. A. (1999). A Realizable Renewable Energy Future. *Science*, Vol. 285, No, pp. 687-689.
- US_Department_of_Energy (2007). Technical Plan, Hydrogen Production, Multi-Year Research, Development and Demonstration Plan: Planned Program Activities for 2005-2015. Retrieved from <http://www1.eere.energy.gov/hydrogenandfuelcells/mypp/index.html>
- US_Energy_Information_Administration (2010). International Energy Outlook 2010. Retrieved from [http://www.eia.doe.gov/oiaf/ieo/pdf/0484\(2010\).pdf](http://www.eia.doe.gov/oiaf/ieo/pdf/0484(2010).pdf)
- van de Krol, R., Liang, Y. Q., & Schoonman, J. (2008). Solar Hydrogen Production with Nanostructured Metal Oxides. *Journal of Materials Chemistry*, Vol. 18, No. 20, pp. 2311-2320, 0959-9428.
- Veziroglu, T. N., & Barbir, F. (1992). Hydrogen - the Wonder Fuel. *International Journal of Hydrogen Energy*, Vol. 17, No. 6, pp. 391-404, 0360-3199.
- Walter, M. G., Warren, E. L., McKone, J. R., Boettcher, S. W., Mi, Q. X., Santori, E. A., et al. (2010). Solar Water Splitting Cells. *Chemical Reviews*, Vol. 110, No. 11, pp. 6446-6473, 0009-2665.
- Wang, P., Zakeeruddin, S. M., Moser, J. E., & Gratzel, M. (2003). A New Ionic Liquid Electrolyte Enhances the Conversion Efficiency of Dye-Sensitized Solar Cells. *Journal of Physical Chemistry B*, Vol. 107, No. 48, pp. 13280-13285, 1520-6106.
- Wang, P., Huang, B. B., Qin, X. Y., Zhang, X. Y., Dai, Y., Wei, J. Y., et al. (2008). Ag@AgCl: A Highly Efficient and Stable Photocatalyst Active under Visible Light. *Angewandte Chemie-International Edition*, Vol. 47, No. 41, pp. 7931-7933, 1433-7851.
- Wang, X., Zhi, L. J., & Mullen, K. (2008). Transparent, Conductive Graphene Electrodes for Dye-Sensitized Solar Cells. *Nano Letters*, Vol. 8, No. 1, pp. 323-327, 1530-6984.

- Weber, M. F., & Dignam, M. J. (1986). Splitting Water with Semiconducting Photoelectrodes Efficiency Considerations. *International Journal of Hydrogen Energy*, Vol. 11, No. 4, pp. 225-232, 0360-3199.
- Wei, D. (2010). Dye Sensitized Solar Cells. *International Journal of Molecular Sciences*, Vol. 11, No. 3, pp. 1103-1113, 1422-0067.
- Weinhardt, L., Blum, M., Bar, M., Heske, C., Cole, B., Marsen, B., et al. (2008). Electronic Surface Level Positions of Wo_3 Thin Films for Photoelectrochemical Hydrogen Production. *Journal of Physical Chemistry C*, Vol. 112, No. 8, pp. 3078-3082, 1932-7447.
- West, W. (1974). First Hundred Years of Spectral Sensitization. *Photographic Science and Engineering*, Vol. 18, No. 1, pp. 35-48, 0031-8760.
- Wijayantha, K. G. U., Saremi-Yarahmadi, S., & Peter, L. M. (2011). Kinetics of Oxygen Evolution at Alpha- Fe_2O_3 Photoanodes: A Study by Photoelectrochemical Impedance Spectroscopy. *Physical Chemistry Chemical Physics*, Vol. 13, No. 12, pp. 5264-5270, 1463-9076.
- Wilcoxon, J. P., & Samara, G. A. (1995). Strong Quantum-Size Effects in a Layered Semiconductor - MoS_2 Nanoclusters. *Physical Review B*, Vol. 51, No. 11, pp. 7299-7302, 1098-0121.
- Wu, T. X., Liu, G. M., Zhao, J. C., Hidaka, H., & Serpone, N. (1998). Photoassisted Degradation of Dye Pollutants. V. Self-Photosensitized Oxidative Transformation of Rhodamine B under Visible Light Irradiation in Aqueous TiO_2 Dispersions. *Journal of Physical Chemistry B*, Vol. 102, No. 30, pp. 5845-5851, 1089-5647.
- Wurfel, U., Peters, M., & Hinscht, A. (2008). Detailed Experimental and Theoretical Investigation of the Electron Transport in a Dye Solar Cell by Means of a Three-Electrode Configuration. *Journal of Physical Chemistry C*, Vol. 112, No. 5, pp. 1711-1720, 1932-7447.
- Xu, L. X., Sang, L. X., Ma, C. F., Lu, Y. W., Wang, F., Li, Q. W., et al. (2006). Preparation of Mesoporous InVO_4 Photocatalyst and Its Photocatalytic Performance for Water Splitting. *Chinese Journal of Catalysis*, Vol. 27, No. 2, pp. 100-102, 0253-9837.
- Yan, H. J., Yang, J. H., Ma, G. J., Wu, G. P., Zong, X., Lei, Z. B., et al. (2009). Visible-Light-Driven Hydrogen Production with Extremely High Quantum Efficiency on Pt-Pds/Cds Photocatalyst. *Journal of Catalysis*, Vol. 266, No. 2, pp. 165-168, 0021-9517.
- Ye, J. H., Zou, Z. G., Oshikiri, M., Matsushita, A., Shimoda, M., Imai, M., et al. (2002). A Novel Hydrogen-Evolving Photocatalyst InVO_4 Active under Visible Light Irradiation. *Chemical Physics Letters*, Vol. 356, No. 3-4, pp. 221-226, 0009-2614.
- Yin, L., & Ye, C. (2011). Review of Quantum Dot Deposition for Extremely Thin Absorber Solar Cells. *Science of advanced materials*, Vol. 3, No, pp. 41-58.
- Yu, W. W., Qu, L. H., Guo, W. Z., & Peng, X. G. (2003). Experimental Determination of the Extinction Coefficient of Cdte, Cdse, and Cds Nanocrystals. *Chemistry of Materials*, Vol. 15, No. 14, pp. 2854-2860, 0897-4756.
- Zhang, P., Kleiman-Shwarsstein, A., Hu, Y. S., Lefton, J., Sharma, S., Forman, A. J., et al. (2011). Oriented Ti Doped Hematite Thin Film as Active Photoanodes Synthesized by Facile Apcvd. *Energy & Environmental Science*, Vol. 4, No. 3, pp. 1020-1028, 1754-5692.
- Zhang, Q. X., Guo, X. Z., Huang, X. M., Huang, S. Q., Li, D. M., Luo, Y. H., et al. (2011). Highly Efficient Cds/Cdse-Sensitized Solar Cells Controlled by the Structural

- Properties of Compact Porous TiO₂ Photoelectrodes. *Physical Chemistry Chemical Physics*, Vol. 13, No. 10, pp. 4659-4667, 1463-9076.
- Zhao, D., Chen, C., Wang, Y., Ma, W., Zhao, J., Rajh, T., et al. (2008). Enhanced Photocatalytic Degradation of Dye Pollutants under Visible Irradiation on Al(III)-Modified TiO₂: Structure, Interaction, and Interfacial Electron Transfer. *Environmental Science & Technology*, Vol. 42, No. 1, pp. 308-314, 0013-936X.
- Zhao, W., Sun, Y. L., & Castellano, F. N. (2008). Visible-Light Induced Water Detoxification Catalyzed by Pt-Ir Dye Sensitized Titania. *Journal of the American Chemical Society*, Vol. 130, No. 38, pp. 12566-12567, 0002-7863.
- Zong, X., Wu, G. P., Yan, H. J., Ma, G. J., Shi, J. Y., Wen, F. Y., et al. (2010). Photocatalytic H₂ Evolution on MoS₂/CdS Catalysts under Visible Light Irradiation. *Journal of Physical Chemistry C*, Vol. 114, No. 4, pp. 1963-1968, 1932-7447.
- Zou, Z. G., Ye, J. H., Sayama, K., & Arakawa, H. (2001). Direct Splitting of Water under Visible Light Irradiation with an Oxide Semiconductor Photocatalyst. *Nature*, Vol. 414, No. 6864, pp. 625-627, 0028-0836.

Conducting Polymer-Metal Nanocomposite Coating on Fibers

Syuji Fujii¹, Mizuho Kodama¹, Soichiro Matsuzawa²,
Hiroyuki Hamasaki¹, Atsushi Ohtaka¹ and Yoshinobu Nakamura^{1,3}

¹*Department of Applied Chemistry, Faculty of Engineering
Osaka Institute of Technology, Osaka*

²*Graduate School of Engineering Osaka Institute of Technology, Osaka*

³*Nanomaterials Microdevices Research Center, Osaka Institute of Technology, Osaka
Japan*

1. Introduction

Conducting polymers continue to be the focus of active research in diverse fields including electronics (Burroughes et al., 1988; Sailor et al., 1990; Gustafsson et al., 1992; Zhang et al., 1994), energy storage (Conway, 1991; Geniès, 1991; Li et al., 1991), catalysis (Andrieux et al., 1982; Bull et al., 1983; Hable et al., 1993), chemical sensing (Josowicz et al., 1986; Heller, 1992; Gardner et al., 1993; Kuwabata et al., 1994; Freund et al., 1995) and biochemistry (Miller, 1988; Guimard et al., 2007). Despite the promise of these new materials and their widespread study, the scope of commercial uses remains small and relatively few viable technologies have emerged from the laboratory proof-of-concept stage. Limitations of processability such as low mechanical strength, poor flexibility and high cost have prevented conducting polymers from making significant commercial impact. In order to improve the processability of the conducting polymers, several approaches have been developed over the years: (1) synthesis of soluble conducting polymers by the addition of bulky side chains along the backbone (Wang et al., 2003), (2) synthesis in the form of colloidal dispersions by dispersion and emulsion polymerizations (Armes, 1998; Chehimi et al., 2004), (3) the use of metastable mixtures of monomer and oxidant that enable processability followed by *in situ* polymerization initiated by solvent evaporation (Grimaldo et al., 2007) and (4) fabrication of composite consisting of conducting polymers and substrates with high workability (Niwa et al., 1984; Paoli et al., 1984; Niwa et al., 1987; Yosomiya et al., 1986; Gregory et al., 1989; Heisey et al., 1993; Kuhn et al., 1995; Kincal et al., 1998; Appel et al., 1996; Collins et al., 1996; Kaynak et al., 2002; Han et al., 1999; Han et al., 2001; Dong et al., 2004; Dong et al., 2004; Abidian et al., 2006; Oh et al., 1999; Kim et al., 2002; Huang et al., 2005).

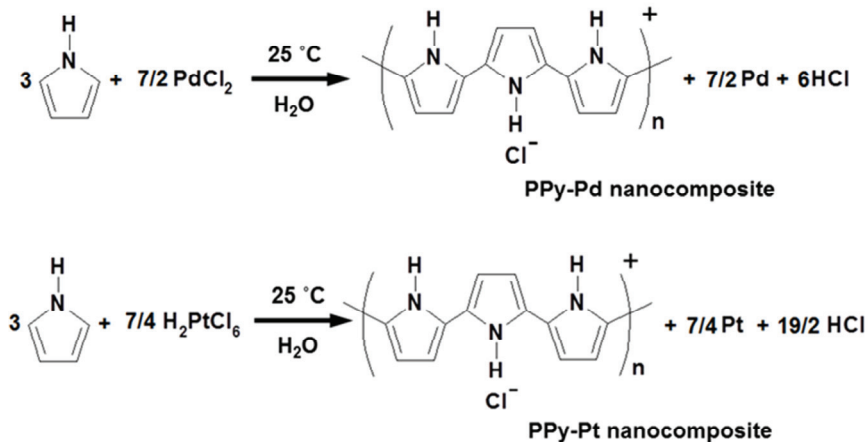
There have been numerous reports on the deposition of air-stable conducting organic polymers such as polypyrrole (PPy), polyaniline (PANI), or poly(3,4-ethylenedioxythiophene) (PEDOT) onto fibrous substrates (Gregory et al., 1989; Heisey et al., 1993; Kuhn et al., 1995; Kincal et al., 1998; Appel et al., 1996; Collins et al., 1996; Kaynak et al., 2002; Han et al., 1999; Han et al., 2001; Dong et al., 2004; Dong et al., 2004; Abidian et

al., 2006; Oh et al., 1999; Kim et al., 2002; Huang et al., 2005). The synthesis of conducting polymer-coated fibers has attracted much interest, due to the increasing applications of these fibers including microwave attenuation, static charge dissipation and electromagnetic interference shielding. Despite a significant amount of work on the synthesis and characterization of fibers coated with various conductive polymer shells and their corresponding hollow tubes, there is no report on conducting polymer-noble metal nanocomposite-coated fibers, to our best knowledge. The main benefit from the introduction of noble metal nanoparticles to fibrous surfaces is to avoid the spread of the nanoparticles to the environment. Conducting polymer-noble metal nanocomposites provide an exciting system to investigate the possibility of designing device functionality (Gangopadhyay et al., 2000) and also exhibit enhanced sensing and catalytic capabilities, compared with those of the pure conducting polymers (Tian et al., 1991; Drelinkiewicz et al., 2000; Kitani et al., 2001; Radford et al., 2001; Pillalamarri et al., 2005). The coating of such conducting polymer-metal nanocomposite on the substrates typically requires more than two steps including purification steps: (i) coating of the substrates with a conductive polymer and (ii) application of metal nanoparticles onto the conducting polymer shells.

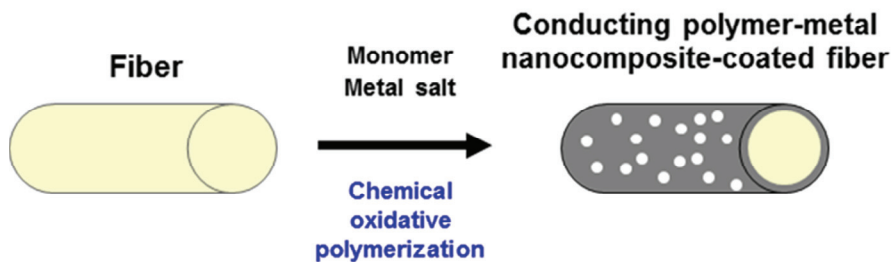
Recently, it was reported that conducting polymer-noble metal nanocomposites can be synthesized by a one-step chemical oxidative polymerization using metal salts as an oxidant (Scheme 1) (Selvan et al., 1998; Chen et al., 2005; Chen et al., 2005; Fujii et al., 2007; Freund et al., 2001; Fujii et al., 2010; Vasilyeva et al., 2008; Fujii et al., 2010). It was demonstrated that chemical oxidative polymerization using metal salts such as hydrogen tetrachloroaurate(III), silver nitrate (AgNO_3), palladium(II) chloride (PdCl_2), and hydrogen hexachloroplatinate(IV) (H_2PtCl_6), which act both as an oxidant and as a source of metal atoms, yielded well-dispersed metal nanoparticles in/on bulk conducting polymers. Selvan *et al.* (Selvan et al., 1998) polymerized pyrrole with tetrachloroauric acid as an oxidant in the presence of polystyrene-*b*-poly(2-vinylpyridine) copolymer micelles dispersed in toluene, which led to the fabrication of PPy-Au nanocomposites. Chen *et al.* (Chen et al., 2005; Chen et al., 2005) and the present authors (Fujii et al., 2007) have demonstrated a one-step facile and versatile synthetic route to PPy-Ag nanocomposites by chemical oxidative polymerization using AgNO_3 as an oxidant in aqueous media. Henry *et al.* (Henry et al., 2001) and the present authors (Fujii et al., 2010) suggested that PdCl_2 acts as an efficient oxidant for pyrrole to form PPy-Pd composite in aqueous media (Scheme 1). More recently, Vasilyeva *et al.* (Vasilyeva et al., 2008) described the synthesis of PPy-Pd nanocomposites via direct redox reaction between Pd(II) acetate and pyrrole in acetonitrile. We have succeeded in one-step synthesis of PANI-Ag (Fujii et al., 2010) and PPy-Au (Fujii et al., 2008) nanocomposites by chemical oxidative polymerization in aqueous media.

In the present work, a facile and new chemical approach is developed to enable nanoprecise coating of conducting polymer-noble metal nanocomposite on fibers without disrupting their morphological hierarchies: we describe the one-step facile coating of fibers with conducting polymer-noble metal nanocomposites by chemical oxidative polymerization using metal salts in aqueous media (Scheme 2). To the authors' knowledge, this is the first report of a one-step and one-pot coating of fibrous substrates with conducting polymer-metal nanocomposites. The pristine fibers and resulting composite fibers were extensively characterized with respect to fiber diameter, morphology and surface/bulk chemical compositions by optical microscopy and scanning/transmission electron microscopies, elemental analysis, energy dispersive X-ray spectroscopy, X-ray photoelectron spectroscopy and X-ray diffraction, respectively. Diacetate, polyamide, silk, cotton, viscose, wool and

glass fibers were used as a substrate. The nanocomposite-coated fibers functioned as an efficient catalyst for Suzuki-type coupling reactions in aqueous media for the formation of carbon-carbon bonds.



Scheme 1. Chemical oxidative polymerization of pyrrole using metal salts toward conducting polymer-metal nanocomposites.



Scheme 2. One-step facile syntheses of fibers coated with conducting polymer-noble metal nanocomposites in aqueous media.

2. Experimental

2.1 Materials

Unless otherwise stated, all materials were guaranteed reagent grade. Palladium(II) chloride (PdCl_2 , 99.9%), hydrogen hexachloroplatinatate(IV) hexahydrate, ($\text{H}_2\text{PtCl}_6 \cdot 6\text{H}_2\text{O}$, 99.9 %), dimethyl sulfoxide (DMSO, 99.9 %), *p*-methylphenylboronic acid (96%) and *p*-(trifluoromethyl)phenylboronic acid were obtained from Wako Chemicals. *p*-Bromotoluene (99%) and *p*-bromoanisole (97%) were obtained from Tokyo Chemical Industry Co., Japan. Sodium chloride (NaCl , 99.5%), hydrated ferric chloride ($\text{FeCl}_3 \cdot 6\text{H}_2\text{O}$) and aluminium oxide (activated, basic, Brockmann 1, standard grade, ~ 150 mesh, 58 \AA) were obtained from Sigma-Aldrich and were used without further purification. Pyrrole (Py, 98%) was also

obtained from Sigma-Aldrich and purified by passing through a column of the activated basic alumina prior to storage at $-15\text{ }^{\circ}\text{C}$ before use. Deionized water ($< 0.06\text{ }\mu\text{S cm}^{-1}$) was prepared using a deionized water producing apparatus (Advantec MFS RFD240NA: GA25A-0715) and used for syntheses and purifications of the nanocomposite-coated fibers. Polymeric fibers (AATCC Multifiber Adjacent Fabric [Style #1, Lot #800, Piece #1886-26]) were purchased from Testfabrics, Inc. (USA). The fiber samples were obtained as fabrics consisting of six kinds of polymeric fibers, namely spun diacetate, bleached cotton, spun polyamide (nylon 6,6), spun silk, spun viscose and worsted wool. As inorganic fibers, glass fibers were used: Quartz fiber filter (Lot No. 91210714, Grade QR-100, circles 21 mm) was purchased from Advantec®. Silica glass microfibre thimble (Cat No. 2812259, external diameter \times external length 25 mm \times 90 mm) was purchased from Whatman®. The fibers used in this study were used after washing using 2-propanol.

2.2 Synthesis of PPy and PPy-metal nanocomposite bulk powders

Chemical oxidative precipitation polymerization was conducted to obtain PPy-metal nanocomposites and PPy homopolymer bulk powders. The PPy-Pd nanocomposite bulk powder was synthesized as follows. PdCl_2 (0.154 g, 8.69×10^{-4} mol) and NaCl (0.102 g, 1.75×10^{-3} mol) were dissolved in deionized water (5.0 g) at $25\text{ }^{\circ}\text{C}$. This aqueous solution was injected via syringe into a stirred pyrrole aqueous solution (1.0 wt%, 5.0 g: pyrrole, 7.45×10^{-4} mol). The solid-state density of the PPy-Pd nanocomposite bulk powder was measured to be 2.708 g/cm^3 by helium pycnometry using a Micromeritics Accu Pyc 1330 instrument. The PPy-Pt nanocomposite bulk powder was also synthesized using $\text{H}_2\text{PtCl}_6 \cdot 6\text{H}_2\text{O}$ in the same manner. The PPy homopolymer bulk powder was synthesized as follows. $\text{FeCl}_3 \cdot 6\text{H}_2\text{O}$ (0.470 g, 1.74×10^{-3} mol) was dissolved in deionized water (5.0 g) at $25\text{ }^{\circ}\text{C}$. This aqueous solution was injected via syringe into the stirred pyrrole aqueous solution (1.0 wt%, 5.0 g: pyrrole, 7.45×10^{-4} mol). In all cases, the polymerization solutions were stirred (magnetic stirrer, 250 rpm) for 7 days at $25\text{ }^{\circ}\text{C}$ and the resulting black precipitates were washed several times with de-ionized water, followed by freeze-drying overnight.

2.3 Deposition of PPy-metal nanocomposite onto fibers

The following protocol was used for coating the fibers with a PPy-Pd nanocomposite overlayer at a pyrrole concentration of 100 wt% (based on the fibers). Pyrrole (0.01 g, 1.49×10^{-4} mol) was added by syringe to an aqueous media containing fiber (2.0 g, containing 0.01 g fiber) in a 13 mL screw-capped bottle and the system was left for 1 h with magnetic stirring. PdCl_2 oxidant (31 mg, 1.74×10^{-4} mol) and NaCl (31 mg, 5.22×10^{-4} mol) were dissolved in 1.0 g water and then added to the aqueous media containing the fiber. NaCl was added in order to dissolve PdCl_2 in the aqueous medium. The polymerization was allowed to proceed for 4 days at 300 rpm. Chemical oxidative polymerization of pyrrole proceeds with a reaction stoichiometry of 2.33 moles of electrons per mole of monomer (Armes et al., 1991). The Pd^{2+} /pyrrole molar ratio was adjusted to 1.17: two electrons are necessary to reduce one Pd(II) ion. In order to control the PPy-Pd nanocomposite loading on the fibers, the pyrrole concentration was systematically varied from 2 to 100 wt% with respect to the fiber. PPy-Pt nanocomposite coatings of fibers were also conducted by the chemical oxidative aqueous polymerization in the same manner using $\text{H}_2\text{PtCl}_6 \cdot 6\text{H}_2\text{O}$ as an oxidant; the ratio of pyrrole monomer and the weight of the fiber was adjusted to be the same with the 100 wt% system. The PPy-metal nanocomposite-coated fibers were subsequently purified by repeated ultrasonic cleaning in water (successive supernatants

were replaced with de-ionized water) in order to remove the unwanted inorganic by-products (water-soluble metal salts, NaCl and HCl).

2.4 Characterization of fibers and PPy-metal nanocomposite-coated fibers

Digital photography

Digital images were captured using a Ricoh Caplio R7 camera.

Optical microscopy

Fiber was placed on a microscope slide and observed using an optical microscope (Shimadzu Motic BA200) fitted with a digital system (Shimadzu Moticam 2000).

Transmission electron microscopy study

Examination of samples placed on carbon-coated copper grids was performed using a transmission electron microscope (TEM; Jeol JEM-2000EX).

Scanning electron microscopy study

Scanning electron microscopy (SEM; Keyence VE-8800, 12 kV) was conducted with Au sputter-coated (Elionix SC-701 Quick Coater) dried samples.

Energy dispersive X-ray spectroscopy study

Elemental analysis of the fibers was performed using a JSM-7001FA field emission scanning electron microscope equipped with an energy dispersive X-ray (EDX) microanalyzer operating at 15 kV.

Fourier transform infrared spectroscopy

The composition of the synthesized nanocomposite-coated fibers was studied using Fourier transform-infrared spectroscopy (FT-IR; Horiba Freexact-II FT-720) with samples dispersed in KBr discs at 20 scans per spectrum with 4 cm⁻¹ resolution.

Chemical composition

The PPy-metal nanocomposite and PPy loadings of the nanocomposite-coated fibers were determined by comparing the nitrogen contents determined by CHN elemental microanalysis (Yanaco CHN-Corder MT-5) with those of the PPy-metal and PPy bulk powders prepared by precipitation polymerization.

X-ray photoelectron spectroscopy study

For X-ray photoelectron spectroscopy (XPS) analyses, the dried powder samples were spread on an indium plate with a spatula and mounted onto sample stubs using conductive tape. XPS measurements were carried out using an XPS spectrometer (Axis Ultra) with a monochromated Al K α X-ray gun. The base pressure was < 1.0 \times 10⁻⁸ Torr. Pass energies of 80 eV and 20 eV were employed for the survey spectra and elemental core-line spectra, respectively. Quantification of the atomic percentage composition was obtained from high resolution spectra according to the manufacturer sensitivity factors. Spectra were aligned to the hydrocarbon component of the C 1s peak set at 285 eV.

X-ray diffraction measurement

Powder X-ray diffraction analysis of air-dried samples was performed with an X-ray diffractometer (XRD; Rigaku RINT 2200) using Ni-filtered Cu K α (1.54056 Å) radiation.

Conductivity measurements

The electrical conductivity of the dried samples was determined for pressed pellets (13 mm diameter, prepared at 300 kg cm⁻² for 16 min) at room temperature using a conventional four-point-probe technique with a resistivity meter (Loresta-GP MCP-T610, Mitsubishi Chemical Co.).

Contact angle measurements

Contact angles for water droplets (10 μ L) placed on pressed pellets prepared from dried PPy-Pd nanocomposite bulk powder, wool fiber and PPy-Pd nanocomposite-coated wool fiber (pelletized at 300 kgcm⁻² for 10 min using Shimadzu SSP-IOA hand press) were determined using an Excimer Simage02 apparatus at 25 °C.

2.5 Suzuki reaction in aqueous media using PPy-Pd nanocomposite-coated fibers as a catalyst

A typical procedure is given for the reaction of bromobenzene with *p*-methylphenylboronic acid. To a screw-capped vial with a stirring bar were added 0.5 mmol of bromobenzene, 0.75 mmol of *p*-methylphenylboronic acid, PPy-Pd nanocomposite-coated polyamide fiber (6.4 mg, 0.10 mol% of Pd), and 1.5 mol L⁻¹ aqueous potassium carbonate solution (1 mL). After stirring at 80 °C for 3 h, the reaction mixture was cooled to room temperature by immersing the vial in water (~20 °C). Subsequently, the aqueous phase was removed and the recovered catalyst was washed with water (5 \times 1.5 mL) and diethyl ether (5 \times 1.5 mL), which were then added to the aqueous phase. The aqueous phase was extracted five times with diethyl ether. The combined organic extracts were dried over MgSO₄, concentrated under reduced pressure, and purified by flash column chromatography on silica gel to give the desired product. The product was analyzed by ¹H NMR. ¹H NMR spectra in CDCl₃ were recorded with a 300 MHz NMR spectrometer (UNITY 300, Varian, Palo Alto, CA) using tetramethylsilane (δ = 0) as an internal standard. The same protocol was used for other Suzuki coupling reactions: the *p*-bromoacetophenone and *p*-methylphenylboronic acid system, the *p*-bromoanisole and *p*-methylphenylboronic acid system, and the *p*-bromotoluene and *p*-(trifluoromethyl)phenylboronic acid system.

3. Results and discussion

3.1 Characterization of fibrous substrates

The color of pristine polymeric fibers is white, because of light scattering at their surface. Optical microscopy and SEM studies indicated that diacetate, cotton and viscose fibers have 'flat-noodle' morphology: the diacetate fibers had wrinkles on their surfaces and the cotton fibers were twisted. Typical SEM images of the pristine fibers are shown in Figure 1. Diacetate fibers have number-average long-axis length of 27.9 \pm 1.8 μ m and short-axis length of 13.1 \pm 2.2 μ m. Cotton fibers have number-average long-axis length of 20.1 \pm 3.2 μ m and short-axis length of 6.5 \pm 1.0 μ m. Viscose fibers have number-average long-axis length of 18.8 \pm 1.9 μ m and short-axis length of 7.6 \pm 0.9 μ m. Polyamide, silk and wool fibers have cylindrical morphology. The number-average diameters of polyamide, silk and wool fibers were measured as 19.0 \pm 1.1 μ m, 11.7 \pm 0.7 μ m and 20.7 \pm 3.0 μ m, respectively (over 50 fibers were counted). On the surface of the wool fiber, cuticles were observed and a number-average height of the cuticle and a number-average distance between them were measured to be 830 nm and 9.74 μ m, respectively. All the inorganic fibers used in this study are white

	Nitrogen content (CHN%) / wt%	PPy-Pd loading (CHN %) ^{a)} / wt%	PPy loading (CHN %) ^{b)} / wt%	Pd loading ^{c)} / wt%	Shell thickness ^{d)} / nm	Conductivity of pellet ^{e)} / Scm ⁻¹
Diacetate fiber	~0	-	-	-	-	< 10 ⁻⁸
Cotton fiber	~0	-	-	-	-	< 10 ⁻⁸
Polyamide fiber	11.92	-	-	-	-	< 10 ⁻⁸
Silk fiber	~0	-	-	-	-	< 10 ⁻⁸
Viscose fiber	24.33	-	-	-	-	< 10 ⁻⁸
Wool fiber	15.25	-	-	-	-	< 10 ⁻⁸
PPy-Pd bulk powder	6.36	100	38.6	61.4	-	3.0 × 10 ¹
PPy bulk powder	16.49	-	100	-	-	4.7 × 10 ⁰
Diacetate/PPy-Pd (Py, 100 wt%)	0.27	4.3	1.7	2.6	98	3.1 × 10 ⁻⁶
Diacetate/PPy-Pd (Py, 20 wt%)	0.22	3.5	1.4	2.1	79	< 10 ⁻⁸
Diacetate/PPy-Pd (Py, 10 wt%)	< 0.22	< 3.5	< 1.4	< 2.1	< 79	< 10 ⁻⁸
Diacetate/PPy-Pd (Py, 5 wt%)	< 0.22	< 3.5	< 1.4	< 2.1	< 79	< 10 ⁻⁸
Diacetate/PPy-Pd (Py, 2 wt%)	< 0.22	< 3.5	< 1.4	< 2.1	< 79	< 10 ⁻⁸
Cotton/PPy-Pd (Py, 100 wt%)	0.33	5.2	2.0	3.2	78	9.0 × 10 ⁻⁵
Polyamide/PPy-Pd (Py, 100 wt%)	11.39	n.d.	n.d.	n.d.	n.d.	1.8 × 10 ⁻⁵
Silk/PPy-Pd (Py, 100 wt%)	0.22	3.5	1.4	2.1	55	6.0 × 10 ⁻⁶
Viscose/PPy-Pd (Py, 100 wt%)	23.91	n.d.	n.d.	n.d.	n.d.	7.4 × 10 ⁻⁶
Wool/PPy-Pd (Py, 100 wt%)	13.30	n.d.	n.d.	n.d.	n.d.	2.2 × 10 ⁻⁶

^{a)} Percentage mass of PPy-Pd nanocomposite loading on the fibers, as determined by nitrogen microanalyses (comparing to a nitrogen content of 6.36 % for PPy-Pd nanocomposite bulk powder).

^{b)} Percentage mass of PPy component loading on the fibers, as determined by nitrogen microanalysis (comparing to a nitrogen content of 16.49 % for PPy bulk powder).

^{c)} Calculated using the following equation: PPy-Pd loading (CHN %) - PPy loading (CHN %).

^{d)} Calculated assuming the smooth shell using PPy-Pd nanocomposite loading (CHN %) and densities of fibers and PPy-Pd nanocomposite (2.708 gcm⁻³)

^{e)} Pressed pellet conductivity at 25 °C determined using the conventional four-point probe technique.

Table 1. Summary of microanalytical data, PPy-Pd nanocomposite, PPy and Pd loadings, shell thickness and conductivities of the uncoated polymeric fibers and PPy-Pd nanocomposite-coated polymeric fibers.

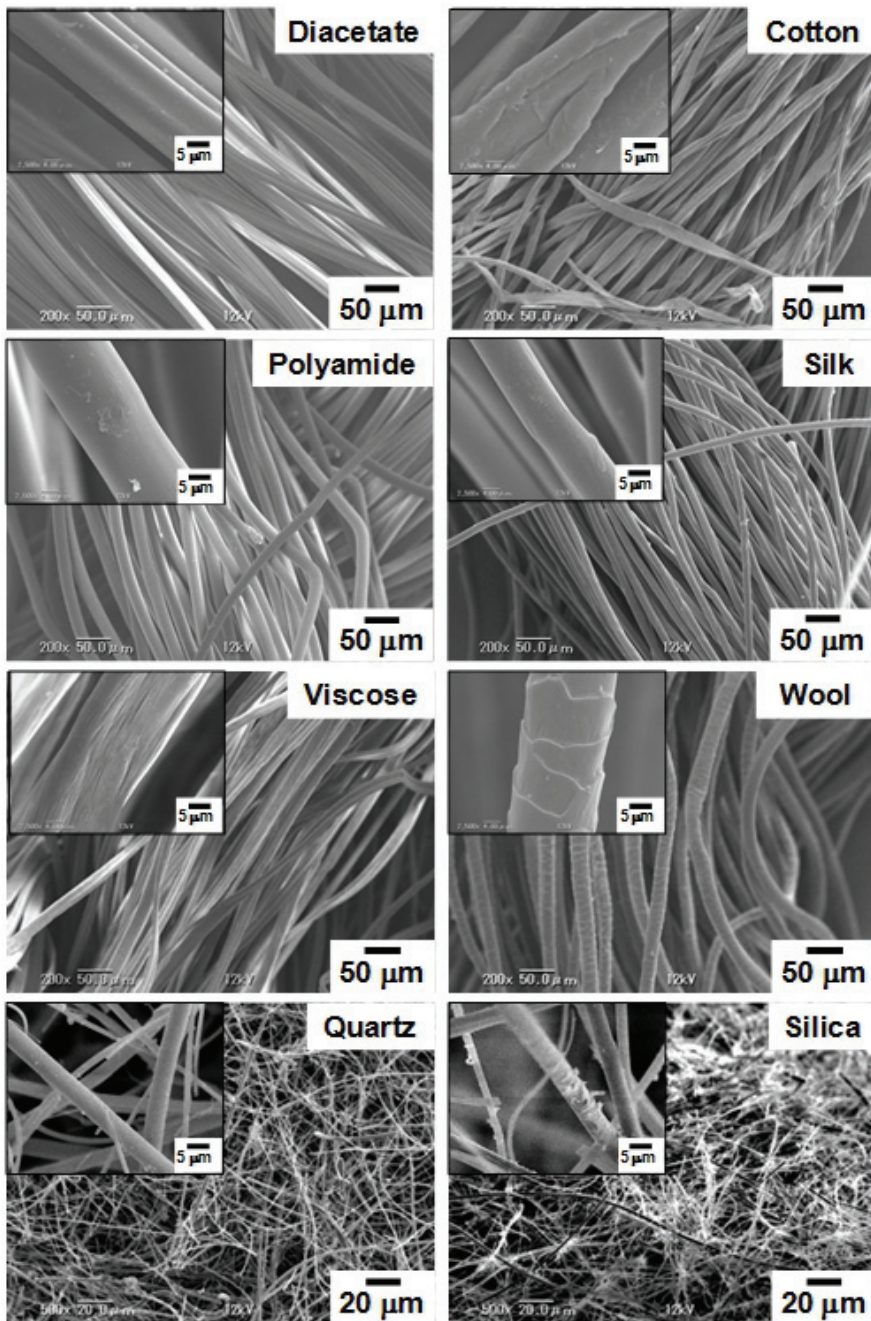


Fig. 1. SEM images of polymeric and inorganic fibers used in this study.

colored and have cylindrical morphology, which was confirmed by optical and SEM studies (Figure 1). The number-average diameters of the inorganic fibers were measured to be $1.2 \pm 0.5 \mu\text{m}$ (Quartz Fiber Filter) and $0.8 \pm 0.2 \mu\text{m}$ (Silica Glass Microfibre Thimbles) using the SEM images, respectively. Optical microscopy analyses confirmed that all the polymeric and inorganic fibers are well wetted with water and no bubble (larger than submicrometer) can be observed on their surfaces in aqueous media.

3.2 Conducting polymer-noble metal nanocomposite-coated fibers

3.2.1 Conducting polymer-metal nanocomposite coating on polymeric fibers

3.2.1.1 PPy-Pd nanocomposite-coated polymeric fibers

After addition of the PdCl_2 oxidant to the aqueous media containing polymeric fibers with dissolved pyrrole monomer, the polymerization system turned black within 10 min, which indicates the production of the PPy-Pd component. The color of the fibers changed from white to black, which suggests a deposition of black colored PPy-Pd nanocomposite on the fibers. The morphology of the synthesized fibers was assessed by optical microscopy. Optical microscopy indicated no signs of appreciable destruction of fibrous morphologies in all systems. SEM studies revealed that micrometer-sized fibers with surface nuclei ranging between 50 and 250 nm were obtained after chemical oxidative polymerization in all fiber systems (see Figure 2 inset). The nuclei on the surface seem to be due to the precipitation of PPy-Pd nanocomposite nuclei from the aqueous medium, which are then adsorbed by the fiber surfaces. Similar nuclei on the surface of the polymeric substrate were also observed in the case of PPy-Pd nanocomposite-coated polystyrene particles (Fujii et al., 2010). The pyrrole monomer was expected to polymerize exclusively in aqueous solution and/or on the fiber surface, because the ionic Pd^{2+} oxidant should not diffuse into the hydrophobic polymeric fibers; therefore, pyrrole polymerization within the fiber interior was highly unlikely. PPy-Pd nanocomposite component precipitated in the aqueous media and on the fiber surface should accumulate on the fiber surface in order to minimize interfacial free energy (Lovell et al., 1997; Okubo et al., 1999) and PPy-Pd nanocomposite-coated fibers with core-shell morphologies were expected.

A summary of the microanalytical data, PPy-Pd nanocomposite, PPy and Pd loadings, shell thickness and electrical conductivity of the uncoated fibers and the PPy-Pd nanocomposite-coated fibers is given in Table 1. Microanalytical studies indicate the PPy-Pd nanocomposite bulk powder consists of 38.6 wt% PPy and 61.4 wt% Pd components, which is in good agreement with the theoretical values calculated using the reaction scheme shown in Scheme 1 (PPy, 38.3 wt% and Pd, 61.7 wt%). This result indicates that the pyrrole was quantitatively polymerized with the Pd^{2+} oxidant. The percentage mass of the PPy-Pd nanocomposite loading on the composite fiber was determined by comparing the nitrogen content to that of the PPy-Pd composite bulk powder (N = 6.36%) synthesized in the absence of fibers. The percentage mass of the PPy component loading was also calculated by comparing the nitrogen content to that of chlorine-doped PPy homopolymer bulk powder prepared by chemical oxidative precipitation polymerization using FeCl_3 oxidant, assuming that the PPy component in the PPy-Pd nanocomposite and the PPy homopolymer have the same chemical structure. The PPy-Pd nanocomposite loadings (Py, 100 wt% systems) were measured to be ranging between 3.5 and 5.2 wt% and there was no large difference.

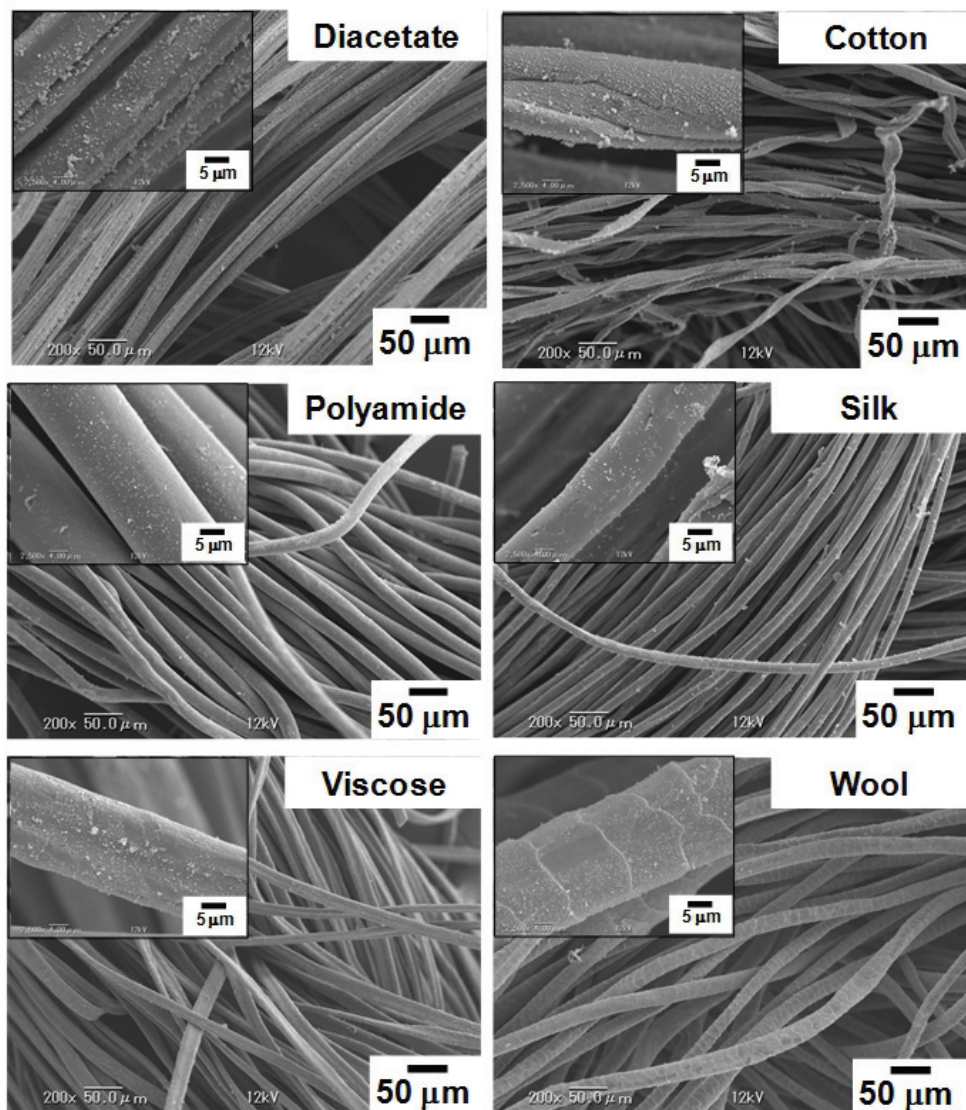


Fig. 2. SEM images of PPy-Pd nanocomposite-coated polymeric fibers (Py, 100 wt % based on fiber).

Considering that all the fibers have the similar diameters and specific surface areas, it is reasonable for the fibers to have the similar PPy-Pd nanocomposite loadings. These results also indicate the surface chemistry does not have a large effect on the PPy-Pd nanocomposite loading amount. The weight ratios of the PPy and Pd components in the nanocomposite-coated fibers were calculated to be around 39:61 for all the systems, which is again in good agreement with the theoretical values. These results indicate that the

polymeric fibers do not interfere with the chemical oxidative polymerization of pyrrole using Pd^{2+} .

The conductivities of pressed pellets of the PPy-Pd nanocomposite-coated fibers (Py, 100 wt% system) were measured to be in the order of 10^{-5} – 10^{-6} Scm^{-1} (Table 1), which are higher than those of the pristine fibers ($<10^{-8}$ Scm^{-1}). Although the conductivities of the PPy-Pd nanocomposite-coated fibers are relatively low, it is worth emphasizing that pressed pellets prepared from a heterogeneous admixture of 95 wt% polymeric fibers and 5 wt% PPy-Pd nanocomposite bulk powder had even lower electrical conductivity, which was below the lower limit for the four-point-probe set-up ($<10^{-8}$ S cm^{-1}). More efficient electrical conduction occurs in the PPy-Pd nanocomposite-coated fibers, because the electrons can flow with lower resistance between adjacent fibers via the conductive pathway provided by the PPy-Pd overlayers, without interference from the underlying electrically insulating fibrous cores. This result indicates that the composite fibers have lower percolation threshold comparing with the heterogeneous mixture of the polymeric fibers with PPy-Pd nanocomposite bulk powder. The same mechanism was also proposed in the conducting polymer-coated latex particles (Fujii et al., 2010; Lascelles et al., 1997; Okubo et al., 2001).

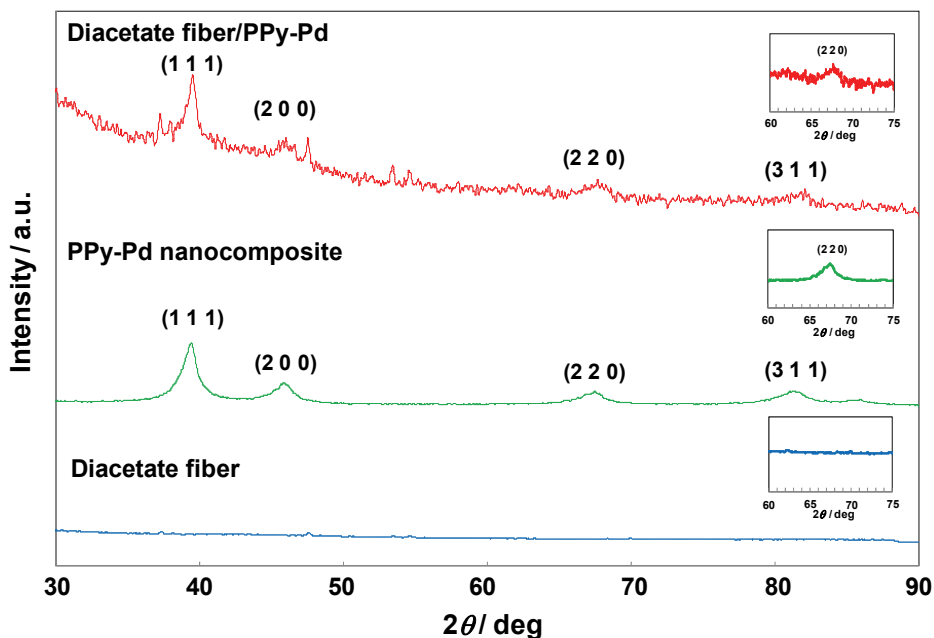


Fig. 3. XRD spectra obtained for PPy-Pd nanocomposite-coated diacetate fiber, PPy-Pd nanocomposite bulk powder and diacetate fiber.

FT-IR studies were conducted for the PPy-Pd nanocomposite-coated diacetate fibers (pyrrole 100 wt% system), the PPy-Pd nanocomposite bulk powder (synthesized by aqueous precipitation polymerization in the absence of polymeric fiber) and the uncoated diacetate fibers. The spectrum for the uncoated diacetate fibers shows the characteristic absorbances of carbonyl group at 1766 cm^{-1} and hydroxyl group in a range between 3100 and 3700 cm^{-1} .

The FT-IR spectrum of the PPy-Pd nanocomposite bulk powder, which shows characteristic bipolaron bands at 1196 and 934 cm^{-1} and broad bands at 1538 and 1043 cm^{-1} , indicates the formation of PPy in its doped state (Bjorklund et al., 1986). The spectrum for the PPy-Pd nanocomposite-coated diacetate fibers is very similar to that obtained for the pristine diacetate fibers. This is not particularly surprising, given that these composite fibers comprise more than 96% diacetate by mass and the diacetate component dominates the FT-IR spectrum.

In order to confirm the presence of a Pd component in the composite fibers, XRD studies were carried out. XRD patterns of the PPy-Pd nanocomposite-coated diacetate fibers (pyrrole 100 wt%), the PPy-Pd nanocomposite bulk powder and the diacetate fibers are shown in Figure 3. Four peaks at 39.5°, 45.1°, 67.4° and 82.1° 2θ , which correspond to the (111), (200), (220) and (311) lattice plane diffractions of Pd crystals, are clearly observed for the PPy-Pd nanocomposite-coated diacetate fibers and the PPy-Pd nanocomposite bulk powder. These peaks are in agreement with those reported for Pd nanoparticles (Zhang et al., 2008; Wen et al., 2008). There are no detectable peaks due to PdCl_2 (e.g. 16.7°, 28.7°, 37.6° and 56.0° 2θ), which provides unambiguous evidence that the reduction of Pd(II) to Pd(0) has taken place. On the other hand, only a very broad peak was observed at 18° for the amorphous diacetate fiber (data not shown).

In order to confirm the presence of Pd and PPy components on the fiber surface (~ 10 nm), XPS studies were carried out. Figure 4 shows the XPS survey spectra of the PPy-Pd nanocomposite-coated diacetate fibers (pyrrole 100 wt% system), the PPy-Pd nanocomposite bulk powder and the diacetate fibers. Signals due to Pd and N, in addition to those due to C and O, are clearly apparent for the PPy-Pd bulk powder and the PPy-Pd nanocomposite-coated diacetate fiber, which indicates the existence of PPy and Pd components on the fiber surface. Pd percentages on the surface were calculated to be 4.97 mol% and 6.39 mol% for the PPy-Pd nanocomposite-coated diacetate fiber and the bulk powder, respectively. The O 1s signal observed in the nanocomposite bulk powder spectrum should arise from the partial over-oxidation of the PPy backbone. A signal due to Cl 2p was also observed in the PPy-Pd nanocomposite bulk powder spectrum, which indicates that the cationic PPy chains are doped with chloride anions (from the PdCl_2 oxidant and NaCl): it was difficult to observe the Cl 2p signal in the PPy-Pd nanocomposite-coated fibers in the survey spectrum, but it can be detected in narrow scan spectrum. The Cl/N atomic ratios of the PPy-Pd bulk powder and the composite fibers were estimated from the XPS spectra to be 0.34 and 0.036 respectively. The Cl/N atomic ratio for the bulk powder accords well with that calculated based on the chemical structure shown in Scheme 1 (0.33). The lower Cl/N atomic ratio for the composite fibers might be due to the likelihood of surface degradation and concomitant loss of Cl dopant. The surface C/N atomic ratio of the PPy-Pd nanocomposite-coated diacetate was determined to be 3.13, which accords with that of the PPy-Pd nanocomposite bulk powder (3.29). These C/N ratios are in good agreement with the theoretical value calculated for PPy component (3.33). From the XPS results, it has been confirmed that the PPy-Pd nanocomposite coated the polymeric fiber substrates.

To map Pd element on synthesized composite diacetate fibers, EDX study was conducted. EDX image for Pd element of the PPy-Pd nanocomposite-coated diacetate fibers is depicted in Figure 5. The EDX image of the composite fibers revealed that Pd element existed homogeneously on the surface of PPy-Pd nanocomposite-coated diacetate fibers.

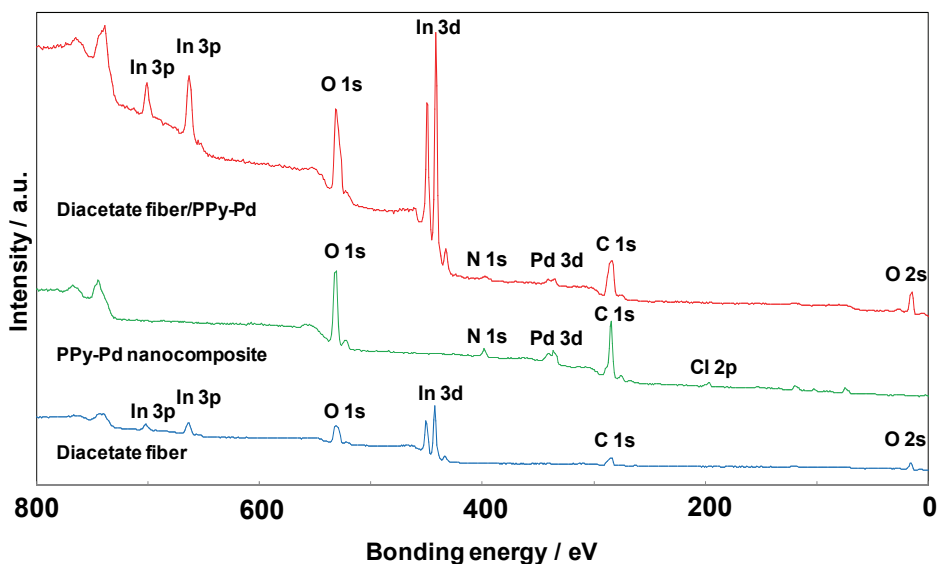


Fig. 4. XPS survey spectra obtained for PPy-Pd nanocomposite-coated diacetate fiber, PPy-Pd nanocomposite bulk powder and diacetate fiber.

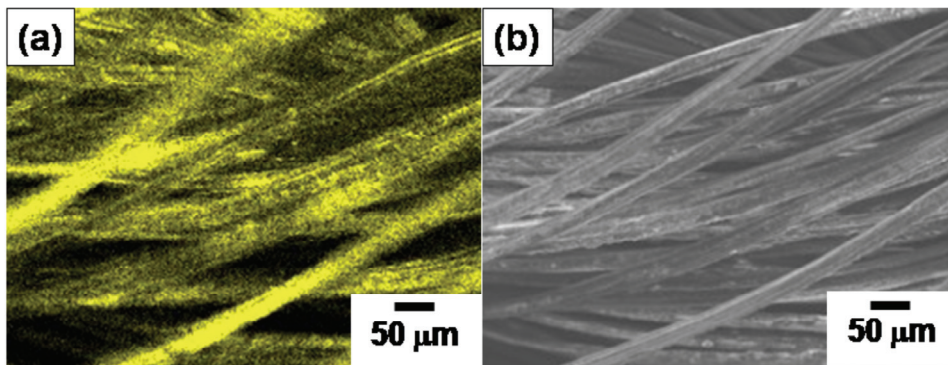


Fig. 5. (a) EDX image for Pd element and (b) SEM image of PPy-Pd nanocomposite-coated diacetate fiber.

Surface coating with PPy-Pd nanocomposite can also be confirmed by contact angle measurement studies. Contact angle measurement is an established technique for investigating surface hydrophilic/hydrophobic characters. The static contact angle for a sessile water drop on a pressed pellet of the fibers was measured. The contact angles for the pristine wool fibers and the PPy-Pd nanocomposite bulk powder were measured to be 141° and 60° , respectively. The contact angle for the PPy-Pd nanocomposite-coated wool fibers was 121° , which sits between the two contact angle values. This result can be explained by the PPy-Pd nanocomposite coating on the wool fibers, which will increase the hydrophilic character for the fiber surface.

The core-shell nature of the PPy-Pd nanocomposite-coated fibers has been readily verified by solvent extraction of the fiber core, followed by morphological examination of the insoluble PPy-Pd residues. DMSO was used for the extraction of diacetate and viscose fibers. Hot KOH aqueous solution (80 °C) and formic acid were used for the extraction of wool and polyamide fibers, respectively. Extraction of core component from the composite fibers using the solvents resulted in insoluble black residues: the composite fibers were dispersed in solvents for 24 h and were washed by replacing the solvents (five cycles) with pure solvents. Analysis of the black residues by FT-IR spectroscopy and CHN elemental microanalysis confirmed that these material were PPy-Pd nanocomposite and contained little core components. These results indicate that almost the core component was extracted from the original composite fibers. Examination of the black PPy-Pd nanocomposite residues by optical microscope revealed 'tubular' morphologies, with diameters corresponding to those of the original coated fibers (Figure 6). The solvent extraction experiment confirms that the composite fibers do possess a core-shell morphology, which is consistent with the XPS, EDX and contact angle results. Shell thicknesses were calculated to be ranging between 55 and 98 nm assuming the smooth shell surface using PPy-Pd nanocomposite loading% and densities of fibers and PPy-Pd nanocomposite (Table 1). The structure of PPy-Pd nanocomposite shell (pyrrole 100 wt%) was investigated using a TEM in detail (Figure 7). The TEM images revealed that there are two Pd size distributions in diacetate, polyamide and viscose systems (approximately 6 nm and 1.4 nm). The 6-nm Pd nanoparticles formed aggregates (50~250 nm), which were observed in bump-like projections on a fiber surface. Heterogeneous character of the continuous shell was composed of a more transparent host material (presumably the PPy polymer) with incorporated 1.4 nm-sized Pd nanoparticles that have a higher absorbance for TEM electrons (dark elements dispersed in the PPy matrix.). The mechanism resulting in these two Pd size distributions (6 nm and 1.4 nm) is not clear at this stage, and we are currently exploring the effect of the polymerization conditions on the Pd nanoparticle size distribution. An interesting characteristic of the conducting polymer tubes is that the transport rates of small molecules into the tube core are affected by the oxidation state of the conductive polymer (Abidian et al., 2006), a feature with potential application in many molecular uptake and release scenarios. The PPy-Pd nanocomposite loading was simply controlled by varying the amount of pyrrole monomer based on the fibrous substrates in the polymerization recipe: an increase of the pyrrole/diacetate fiber ratio increased the PPy-Pd nanocomposite loading. The chemical oxidative polymerization was conducted in the presence of diacetate fibers at various Py concentrations (2~20 wt% based on the fibers). As the fiber surface area available for PPy-Pd nanocomposite deposition was increased, the amount of free by-product PPy-Pd nuclei ranging between 50 and 250 nm were obtained after chemical oxidative polymerizations. The PPy-Pd loadings were lower than the theoretical values calculated from the polymerization reactions. The lower PPy-Pd loadings are due to the removal of free PPy-Pd by-products by washing with aqueous media prior to elemental analysis. Examination of the black PPy-Pd nanocomposite residues obtained after the extraction of diacetate from the composite fibers by optical microscope revealed 'tubular' morphology, with a diameter corresponding to that of the original composite fibers, at 20 wt% system (Figure 8). In the cases of the 10, 5 and 2 wt% systems, the PPy-Pd nanocomposite coating was relatively inhomogeneous, due to low PPy-Pd nanocomposite loadings, so that the shell cannot maintain complete tubular morphology and was partially broken. In these systems, two Pd nanoparticle size

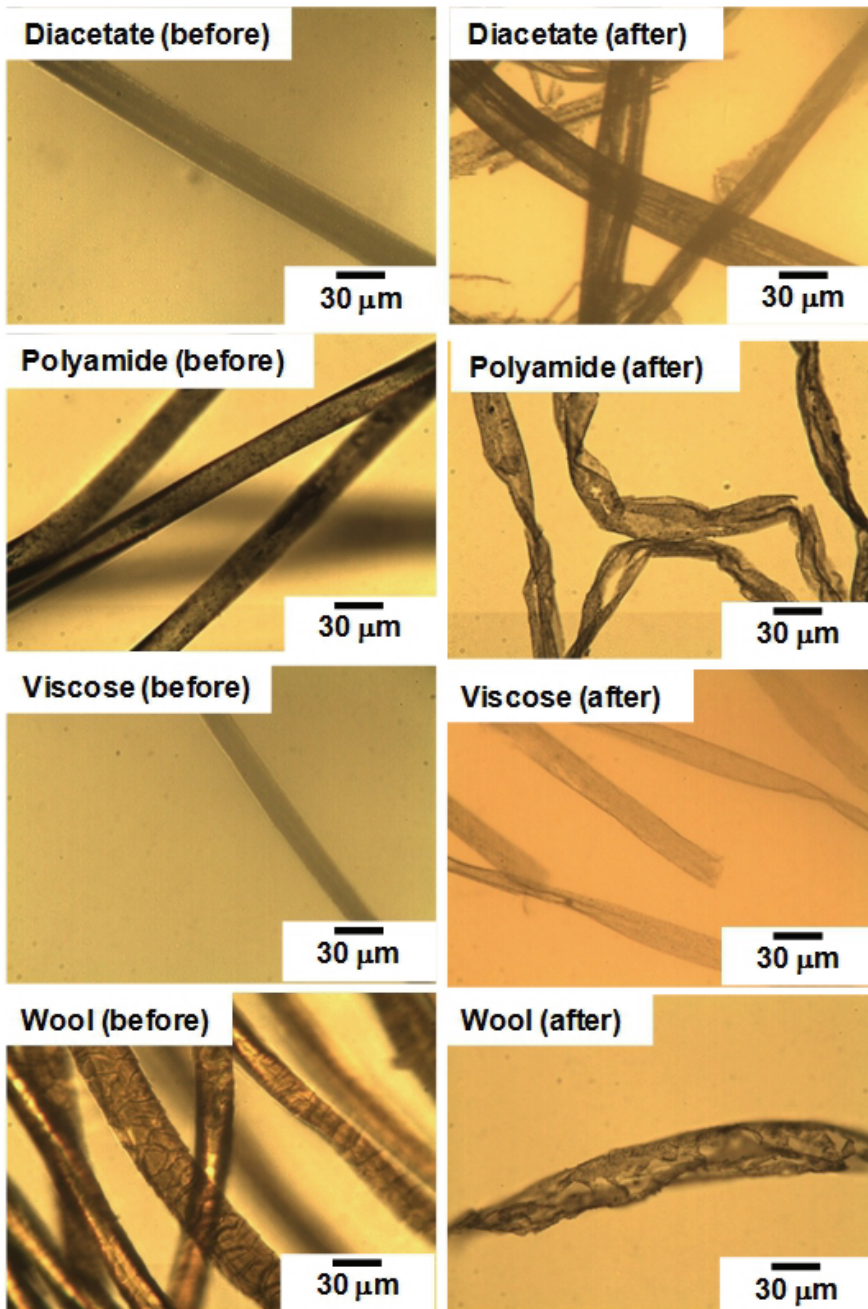


Fig. 6. Optical micrographs of PPy-Pd nanocomposite-coated polymeric fibers before and after extraction of fibers.

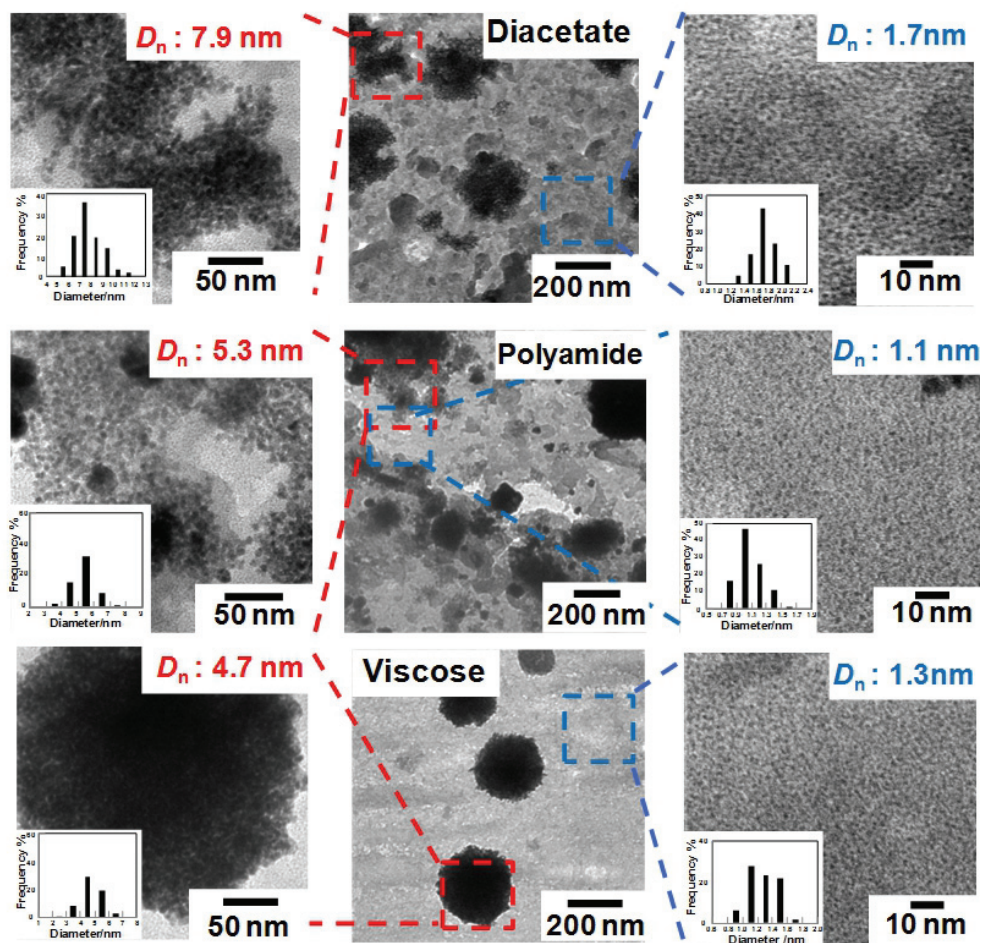


Fig. 7. TEM images of PPy-Pd nanocomposite-coated fibers after extraction of fibers. DMSO (for diacetate and viscose) and formic acid (for polyamide) were used for extraction of polymeric fibers.

distributions were again observed by TEM. Unfortunately, the conductivity was measured to be below $10^{-8} \text{ S cm}^{-1}$, which is lower measurable limit by our four-point-probe set-up, for PPy-Pd nanocomposite-coated diacetate fibers synthesized at Py concentrations of 20, 10, 5 and 2 wt%.

Finally, the deposition of PPy-Pd nanocomposite in a large scale was investigated. Nanocomposite coating can be conducted on woven cloth which consists of fibers, such as a T-shirt. Figure 9 shows digital camera images of a T-shirt before and after PPy-Pd nanocomposite coating by chemical oxidative polymerization in aqueous media at room temperature. In this system, Py concentration was set at 1.0 wt% based on the T-shirt. The color of the T-shirt changed from white to black after the chemical oxidative polymerization, which indicates the nanocomposite coating. The color of the T-shirt was not breached even

after five times sonication in aqueous media, which indicated that the fibers were firmly coated with the PPy-Pd nanocomposite. This synthetic route is advantageous because the reaction takes place in aqueous media at room temperature and production on an industrial scale is much more likely compared to a two-step synthetic route.

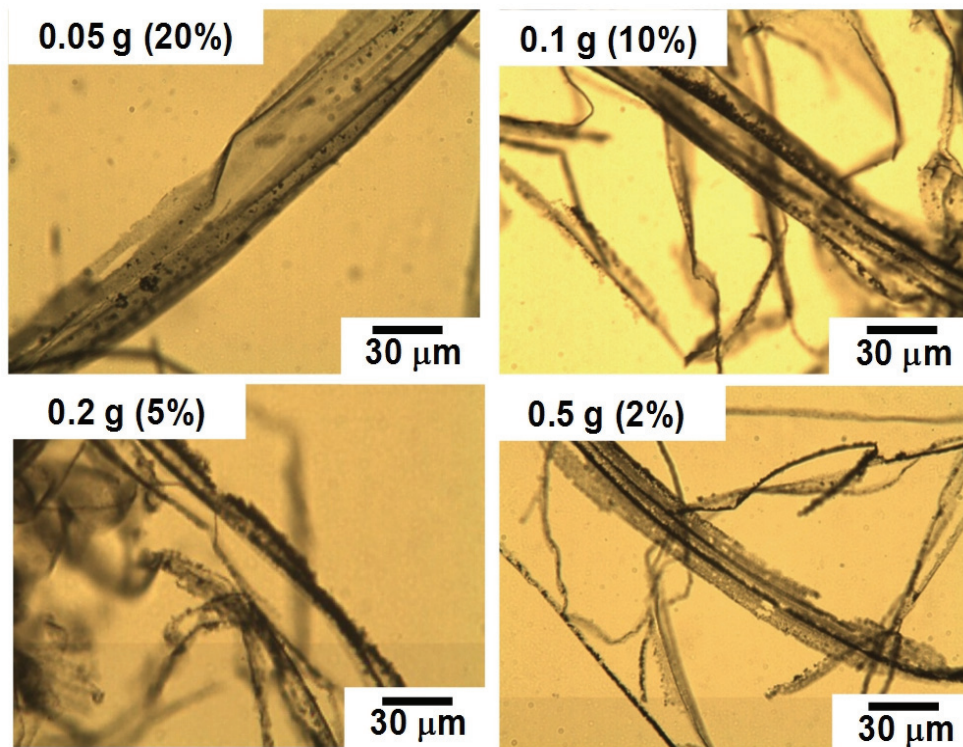


Fig. 8. Optical micrographs of PPy-Pd nanocomposite-coated diacetate fibers with various PPy-Pd nanocomposite loadings after extraction of diacetate fiber with DMSO.

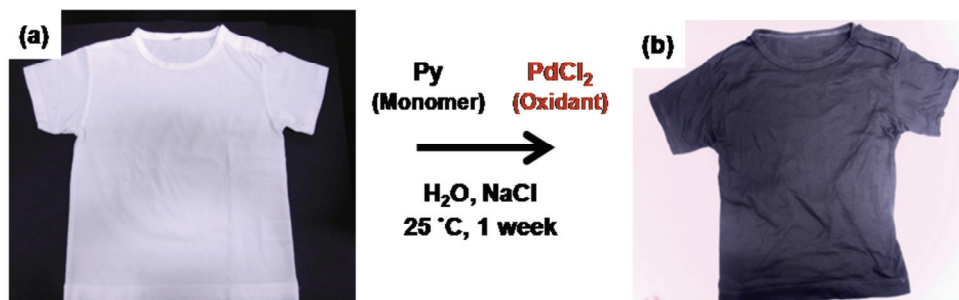


Fig. 9. Digital photographs of T-shirt (Cotton 100 %) before (a) and after (b) PPy-Pd nanocomposite coating.

3.2.1.2 PPy-Pt nanocomposite-coated polymeric fibers

The deposition of PPy-metal nanocomposite other than PPy-Pd nanocomposite on the polymeric fibers (diacetate, cotton, polyamide, silk, viscose and wool) has also been investigated. After addition of the $\text{H}_2\text{PtCl}_6 \cdot 6\text{H}_2\text{O}$ oxidant to the aqueous media containing fibers with dissolved pyrrole monomer, the polymerization system turned black within 10 min, which indicates the production of the PPy-Pt component. The morphology of the synthesized fibers was assessed by optical microscopy, which indicated no signs of appreciable destruction of morphologies in all fiber systems. The color of the fibers changed from white to black, which suggests a deposition of black colored PPy-Pt nanocomposite on the fibers. SEM studies revealed that micrometer-sized fibers with smooth surface were obtained after chemical oxidative polymerization in all fiber systems, which is different result comparing with those obtained for PPy-Pd nanocomposite coating system. 'Tubular' morphologies, with diameters corresponding to those of the original coated fibers, were observed using optical microscope after the extraction of core component from the composite fibers. This result confirms that the composite fibers do possess a core-shell morphology. The structure of PPy-Pt nanocomposite shell (pyrrole 100 wt%) was investigated using TEM in detail (Figure 10). The TEM image revealed the heterogeneous character of the shell is composed of a more transparent host PPy with incorporated Pt nanoparticles that have a higher absorbance for TEM electrons. The Pt nanoparticles have near-monodispersed size distributions and the number average diameters of the Pt nanoparticles were measured to be approximately 1 nm in all fiber systems. Other conducting polymer-metal nanocomposites such as PPy-silver, PANI-silver and PEDOT-Pd can also be deposited onto the fibers with maintaining fibrous morphology.

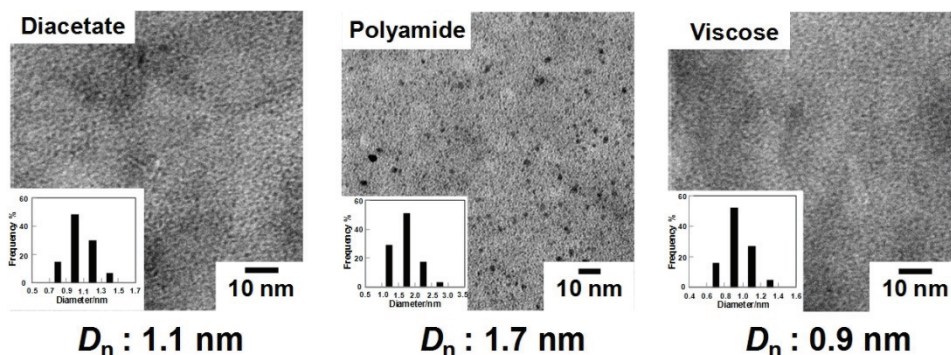


Fig. 10. TEM images of PPy-Pt nanocomposite-coated fibers after extraction of fibers. DMSO (for diacetate and viscose) and formic acid (for polyamide) were used for extraction of polymeric fibers.

3.2.2 Conducting polymer-metal nanocomposite coating on inorganic fibers

The deposition of PPy-Pd nanocomposite on the inorganic fibers has also been investigated. Here we used inorganic fibers made of silica and quartz. After chemical oxidative polymerization, the color of the fibers changed from white to black, which suggests a deposition of black colored PPy-Pd nanocomposite on the inorganic fibers. PPy-Pd

nanocomposite component precipitated in the aqueous media and on the fiber surface should accumulate on the fiber surface in order to minimize interfacial free energy (Lovell et al., 1997; Okubo et al., 1999). Interaction between silanol group on the fiber surface and cationic PPy should also play an important role for the PPy-Pd nanocomposite to deposit on the fiber surface (Maeda et al., 1994). SEM studies revealed that both quartz and silica fibers had submicrometer-sized dots (290 ~ 310 nm) on their surfaces and also the distinctive, micrometer-sized globular morphology of the PPy-Pd nanocomposite by-products with sizes between a few and 60 μm were formed as separate sub-phases (see Figure 11). The by-products seem to be the excessively precipitated PPy-Pd nanocomposites from the aqueous medium, which were entrapped between the fibers.

Nanocomposite coating can be easily scaled up: a microfiber thimble (2.5 cm in diameter and 9.0 cm in length) which consists of silica fibers was coated in its form. Digital camera images of the microfiber thimble before and after PPy-Pd nanocomposite coating by chemical oxidative polymerization in aqueous media at room temperature suggest that the color of the microfiber thimble changed from white to black, which indicates the nanocomposite coating. Using the microfiber thimbles, Pd-based catalytic reaction can be conducted in a continuous mode.

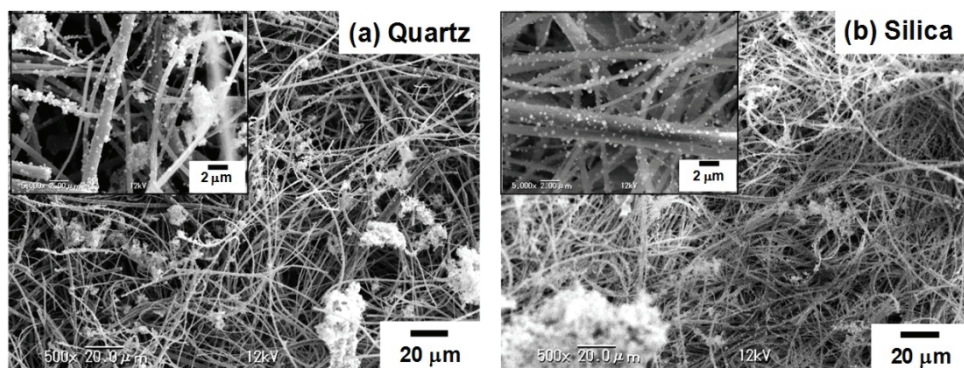
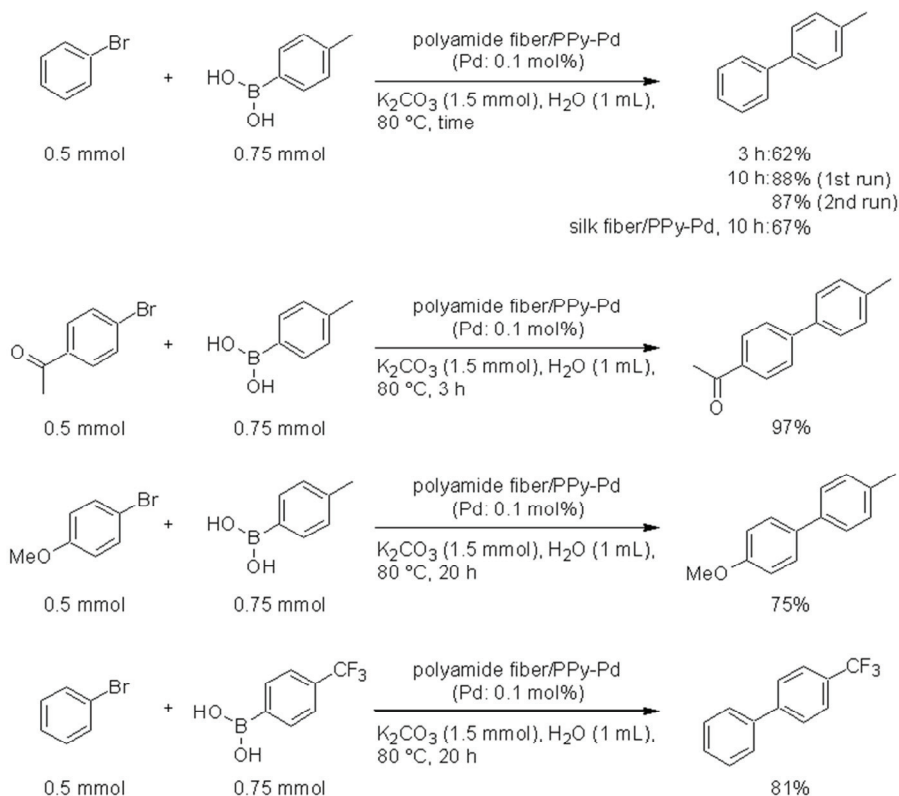


Fig. 11. SEM images of (a) quartz and (b) silica fibers after PPy-Pd nanocomposite coating (Py, 100 wt % based on fiber).

3.3 Suzuki coupling reactions using the conducting polymer-metal nanocomposite coated fibers as a catalyst

The Suzuki coupling reaction is an important and versatile method for the generation of unsymmetrical biaryls from aryl halides and arylboronic acids in a single step using Pd species as a catalyst (Miyaura et al., 1995; Hassan et al., 2002). The development of immobilized Pd catalysts and the use of aqueous media have been of great interest in recent organic chemistry (Lamblin et al., 2010). The simple recovery of catalysts by filtration and their reuses resulted in enhancing the economical evaluation of the reaction. At the same time, there is a prospect that the environmental pollution caused by residual metals in the waste fluid will be decreased. Pd nanoparticles are known to be effective catalysts for chemical transformations due to the high surface-to-volume ratio (Astruc et al., 2005; Moreno-Mañas et al., 2003). The common method to prepare Pd nanoparticles involves the

reduction of Pd(II) salt in the presence of stabilizers because they tend to precipitate or aggregate and lose their high catalytic activities. Hydrophilic polymers (Sawoo et al., 2009; Wei et al., 2008)- and hydrophobic polymers (Lyubimov et al., 2009)-stabilized Pd nanoparticles have high catalytic activity toward Suzuki coupling reaction in water.



Scheme 3. Representative Suzuki-cross coupling reactions performed using the PPy-Pd nanocomposite-coated fibers as a catalyst.

However, a significant decrease in catalytic activity is observed for recycling because of a significant leaching of Pd into the reaction solutions and a decrease of Pd surface area caused by Ostwald ripening during the reaction. There have been several reports showing conducting polymers can be used as a support for Pd catalyst (Choudary et al., 2006; Houdayer et al., 2005). Kantam *et al.* reported that PANI-supported Pd nanoparticles have high catalytic activity for Suzuki coupling reactions in water and were reused without loss of activity (Kantam et al., 2007). PANI nanofiber-supported Pd nanoparticles with low metal loading (0.05 mol%) are active catalysts for the Suzuki coupling reaction of aryl chlorides with arylboronic acids in water (Gallon et al., 2007). Recently, we have found PPy-Pd nanocomposite-coated polystyrene particles have high catalytic activity for Suzuki coupling reaction in water (Fujii et al., 2010). Encouraged by this result, we examined the Suzuki coupling reaction using the PPy-Pd nanocomposite-coated fibers in aqueous media.

The reaction of bromobenzene with *p*-methylphenylboronic acid was carried out in 1.5 mol L⁻¹ aqueous potassium carbonate solution in the presence of PPy-Pd nanocomposite-coated polyamide fiber (0.1 mol% of Pd) at 80 °C for 3 h to give 4-methylbiphenyl in 62 % yield. When the reaction time was extended to 10 h, the coupling product was obtained in 88% yield (Scheme 3). This result indicated that the PPy-Pd nanocomposite-coated polyamide fiber showed lower catalytic activity than the PPy-Pd nanocomposite-coated PS particles, probably due to smaller surface-to-volume ratio. After the reaction, the catalyst was recovered and reused under the same reaction conditions without significant loss of activity. 4-Bromoacetophenone (electron-deficient aryl bromide) also underwent the Suzuki coupling reaction with *p*-methylphenylboronic acid at 80 °C for 3 h to afford the corresponding product in 97% yield. Both *p*-bromoanisole (electron-rich aryl bromide) and *p*-(trifluoromethyl)phenylboronic acid (electron-deficient arylboronic acid) were reactive, affording the desired coupling products in 75% and 81% yields, respectively. These results indicate that the PPy-Pd nanocomposite-coated polyamide fibers are an effective catalyst for Suzuki reactions performed in aqueous media.

4. Conclusions

In summary, polymeric and inorganic fibers were successfully coated with an ultrathin layer of PPy-metal nanocomposite by aqueous chemical oxidative polymerization using metal salts as an oxidant in one step. The resulting composite fibers were extensively characterized using optical microscopy, SEM, TEM, XPS, XRD, FT-IR, elemental analysis, contact angle and electrical conductivity measurements. Extensive studies were conducted for the PPy-Pd nanocomposite-coated polymeric fibers. Good control over the PPy-Pd nanocomposite loading was demonstrated by simply varying the weight ratio of the fiber and pyrrole monomer. Optical microscopy study confirmed that the morphology of nanocomposite-coated fibers was not destroyed after PPy-Pd nanocomposite coating. SEM and TEM studies indicated the presence of PPy-Pd nanocomposite shells and revealed two Pd nanoparticle size distributions: 6.0-nm Pd nanoparticles forming 50-250 nm-sized Pd aggregates on the shell and 1.4-nm Pd nanoparticles dispersed in the shell. XPS studies provided an evidence for the presence of elemental Pd within/on the shell, in agreement with the TEM and contact angle measurement results. Solvent extraction of the fiber component led to the formation of PPy-Pd nanocomposite tubes, which also supported the core-shell morphology. Production of conducting polymer-metal nanocomposite-coated fibers in a large scale can be easily attained. The synthesized composite fibers were then tested for their catalytic activity in C-C bond formation. Suzuki coupling reactions performed in aqueous media demonstrated that PPy-Pd nanocomposite-coated fibers act as an efficient catalyst in organic chemistry. The advantages of a nanocomposite-coated fiber-based catalytic system are high activity, air and temperature stability and ease of separation. The fiber nanoengineering developed in this study provides a pathway to various practical hybrid materials with desired functions thanks to the rich varieties of natural/synthetic fibers, metals and conducting polymers.

5. Acknowledgments

We are grateful to Prof. Araki Masuyama of Osaka Institute of Technology for FT-IR studeis. Prof. Kensuke Akamatsu, Dr. Takaaki Tsuruoka and Prof. Hidemi Nawafune of Konan

University are thanked for the EDX and TEM studies. We are also grateful to Prof. Steven P. Armes of Sheffield University for the He pycnometry studies. Mr. Yuki Kono is thanked for his assistance in Suzuki coupling reaction experiments. This work was partially supported by the Core-to-Core Program [Project No.18004] from the Japan Society for the Promotion of Science. Financial support of this study from Iketani Science and Technology Foundation (No. 0191107-A) is gratefully acknowledged.

6. References

- Abidian, MR.; Kim, D.-H. & Martin, DC. (2006). Conducting-Polymer Nanotubes for Controlled Drug Release. *Advanced Materials*, Vol. 18, pp. 405-409
- Andrieux, CP.; Dumasbouchiat, JM. & Saveant, JM. (1982). Catalysis of Electrochemical Reactions at Redox Polymer Electrodes: Kinetic Model for Stationary Voltammetric Techniques. *Journal of Electroanalytical Chemistry and Interfacial Electrochemistry*, Vol. 131, pp. 1-35
- Appel, G.; Yfantis, A.; Göpel, W. & Schmeißer, D. (1996). Highly Conductive Polypyrrole Films on Non-Conductive Substrates. *Synthetic Metals*, Vol. 83, pp. 197-200
- Armes, SP.; Gottesfeld, S.; Beery, JG.; Garzon, F. & Agnew, SF. (1991). Conducting Polymer-Colloidal Silica Composites. *Polymer*, Vol. 32, pp. 2325-2330
- Armes, SP. (1998). Chapter 17 in *Handbook of Conducting Polymers*, Marcel Dekker Inc, Ed. Elsenbaumer, RL.; Reynolds, JR.; Skotheim, TA. & Armes, SP. Colloidal Dispersions of Conducting Polymers, pp. 423-435
- Astruc, D.; Lu, F. & Aranzaes, JR. (2005). Nanoparticles as Recyclable Catalysts: The Frontier between Homogeneous and Heterogeneous Catalysis. *Angewandte Chemie International Edition*, Vol. 44, pp. 7852-7872
- Bjorklund, RB. & Liedberg, B. (1986). Electrically Conducting Composites of Colloidal Polypyrrole and Methylcellulose. *Journal of the Chemical Society, Chemical Communications*, pp. 1293-1295
- Bull, RA.; Fan, F.-R. & Bard, AJ. (1983). Polymer Films on Electrodes. *Journal of the Electrochemical Society*, Vol. 130, pp. 1636-1638
- Burroughes, JH.; Jones, CA. & Friend, RH. (1988). New Semiconductor Device Physics in Polymer Diodes and Transistors. *Nature*, Vol. 335, pp. 137-141
- Chehimi, MM.; Azioune, A.; Bousalem, S.; Slimane, AB. & Yassar, A. (2004). Chapter 10 in *Colloidal Polymers: Synthesis and Characterization* (Surfactant Science Vol. 115) Marcel Dekker Inc, Edn. Elaissari, A.; Synthesis, Characterization, and Biomedical Applications of Conducting Polymer Particles, pp. 245-284
- Chen, A.; Kamata, K.; Nakagawa, M.; Iyoda, T.; Wang, H. & Li, X. (2005). Formation Process of Silver-Polypyrrole Coaxial Nanocables Synthesized by Redox Reaction between AgNO₃ and Pyrrole in the Presence of Poly(vinyl pyrrolidone). *The Journal of Physical Chemistry B*, Vol. 109, pp. 18283-18288
- Chen, A.; Wang, H. & Li, X. (2005). One-Step Process to Fabricate Ag-Polypyrrole Coaxial Nanocables. *Chemical Communications*, pp. 1863-1864
- Choudary, BM.; Roy, M.; Roy, S.; Kantam, ML.; Sreedhar, B. & Kumar, KV. (2006). Preparation, Characterization and Catalytic Properties of Polyaniline-Supported Metal Complexes. *Advanced Synthesis & Catalysis*, Vol. 348, pp. 1734-1742
- Collins, GE. & Buckley, LJ. (1996). Conductive Polymer-Coated Fabrics for Chemical Sensing. *Synthetic Metals*, Vol. 78, pp. 93-101

- Conway, BE. (1991). Transition from "Supercapacitor" to "Battery" Behavior in Electrochemical Energy Storage. *Journal of the Electrochemical Society*, Vol. 138, pp. 1539-1548
- Dong, H.; Nyame, V.; MacDiarmid, AG. & Jones, WE. Jr. (2004). Polyaniline/Poly(methyl methacrylate) Coaxial Fibers: The Fabrication and Effects of the Solution Properties on the Morphology of Electrospun Core Fibers. *Journal of Polymer Science Part B: Polymer Physics*, Vol. 42, pp. 3934-3942
- Dong, H.; Prasad, S.; Nyame, V. & Jones, WE. Jr. (2004). Sub-Micrometer Conducting Polyaniline Tubes Prepared from Polymer Fiber Templates. *Chemistry of Materials*, Vol. 16, pp. 371-373
- Drelinkiewicz, A.; Hasik, M. & Kloc, M. (2000). Pd/Polyaniline as the Catalysts for 2-Ethylanthraquinone Hydrogenation. The Effect of Palladium Dispersion. *Catalysis Letters*, Vol. 64, pp. 41-47
- Freund, MS. & Lewis, NS. (1995). A Chemically Diverse Conducting Polymer-Based "Electronic Nose". *Proceedings of the National Academy of Sciences of the United States of America*, Vol. 92, pp. 2652-2656
- Fujii, S.; Aichi, A.; Akamatsu, K.; Nawafune, H. & Nakamura, Y. (2007). One-Step Synthesis of Polypyrrole-Coated Silver Nanocomposite Particles and Their Application as a Coloured Particulate Emulsifier. *Journal of Materials Chemistry*, Vol. 17, pp. 3777-3779
- Fujii, S.; Mouri, M.; Aichi, A.; Akamatsu, K.; Nawafune, H. & Nakamura, Y. (2008). Synthesis of Polypyrrole-Gold Nanocomposite-Coated Polystyrene Latex Particles by Simultaneous Organic-Inorganic Deposition Method. *Journal of the Adhesion Society of Japan*, Vol. 44, pp. 12-18
- Fujii, S.; Matsuzawa, S.; Nakamura, Y.; Ohtaka, A.; Teratani, T.; Akamatsu, K.; Tsuruoka, T. & Nawafune, H. (2010). Synthesis and Characterization of Polypyrrole-Palladium Nanocomposite-Coated Latex Particles and Their Use as a Catalyst for Suzuki Coupling Reaction in Aqueous Media. *Langmuir*, Vol. 26, pp. 6230-6239
- Fujii, S.; Nishimura, Y.; Aichi, A.; Matsuzawa, S.; Nakamura, Y.; Akamatsu, K. & Nawafune, H. (2010). Facile One-Step Route to Polyaniline-Silver Nanocomposite Particles and Their Application as a Colored Particulate Emulsifier. *Synthetic Metals*, Vol. 160, pp. 1433-1437
- Gallon, BJ.; Kojima, RW.; Kaner, RB. & Diaconescu, PL. (2007). Palladium Nanoparticles Supported on Polyaniline Nanofibers as a Semi-Heterogeneous Catalyst in Water. *Angewandte Chemie International Edition*, Vol. 46, pp. 7251-7254
- Gangopadhyay, R. & De, A. (2000). Conducting Polymer Nanocomposites: A Brief Overview. *Chemistry of Materials*, Vol. 12, pp. 608-622
- Gardner, JW. & Bartlett, PN. (1993). Design of Conducting Polymer Gas Sensors: Modelling and Experiment. *Synthetic Metals*, Vol. 57, pp. 3665-3670
- Geniès, EM. (1991). *New Journal of Chemistry*, Vol. 15, pp. 373-377
- Gregory, RV.; Kimbrell, WC. & Kuhn, HH. (1989). Conductive Textiles. *Synthetic Metals*, Vol. 28, pp. 823-835
- Grimaldo, EB.; Hachey, S.; Cameron, CG. & Freund, MS. (2007). Metastable Reaction Mixtures for the in situ Polymerization of Conducting Polymers. *Macromolecules*, Vol. 40, pp. 7166-7170

- Guimard, NK.; Gomez, N. & Schmidt, CE. (2007). Conducting Polymers in Biomedical Engineering. *Progress in Polymer Science*, Vol. 32, pp. 876-921
- Gustafsson, G.; Cao, Y.; Treacy, GM.; Klavetter, F.; Colaneri, N. & Heeger, A. (1992). Flexible Light-Emitting Diodes Made from Soluble Conducting Polymers. *Nature*, Vol. 357, pp. 477-479
- Hable, CT. & Wrighton, MS. (1993). Electrocatalytic Oxidation of Methanol and Ethanol: a Comparison of Platinum-Tin and Platinum-Ruthenium Catalyst Particles in a Conducting Polyaniline Matrix. *Langmuir*, Vol. 9, pp. 3284-3290
- Han, C.-C.; Lee, J.-T.; Yang, R.-W.; Chang, H. & Han, C.-H. (1999). A New and Easy Method for Making Well-Organized Micrometer-Sized Carbon Tubes and Their Regularly Assembled Structures. *Chemistry of Materials*, Vol. 11, pp.1806-1813
- Han, C.-C.; Lee, J.-T.; Yang, R.-W. & Han C.-H. (2001). Formation Mechanism of Micrometer-Sized Carbon Tubes. *Chemistry of Materials*, Vol. 13, pp. 2656-2665
- Hassan, J.; Sevignon, M.; Gozzi, C.; Schulz, E. & Lemaire, M. (2002). Aryl-Aryl Bond Formation One Century after the Discovery of the Ullmann Reaction. *Chemical Reviews*, Vol. 102, pp. 1359-1469
- Heisey, CL.; Wightman, JP.; Pittman, EH. & Kuhn, HH. (1993). Surface and Adhesion Properties of Polypyrrole-Coated Textiles. *Textile Research Journal*, Vol. 63, pp.247-256
- Heller, A. (1992). Electrical Connection of Enzyme Redox Centers to Electrodes. *The Journal of Physical Chemistry*, Vol. 96, pp. 3579-3587
- Henry, MC.; Hsueh, C.-C.; Timko, BP. & Freund, MS. (2001). Reaction of Pyrrole and Chlorauric Acid a New Route to Composite Colloids. *Journal of the Electrochemical Society*, Vol. 148, pp. D155-D162
- Houdayer, A.; Schneider, R.; Billaud, D. & Ghanbaja, J. (2005). Heck and Suzuki-Miyaura Couplings Catalyzed by Nanosized Palladium in Polyaniline. *Applied Organometallic Chemistry*, Vol. 19, pp. 1239-1248
- Huang, J.; Ichinose, I. & Kunitake, T. (2005). Nanocoating of Natural Cellulose Fibers with Conjugated Polymer: Hierarchical Polypyrrole Composite Materials. *Chemical Communications*, pp. 1717-1719
- Josowicz, M. & Janata, J. (1986). Suspended Gate Field Effect Transistors Modified with Polypyrrole as Alcohol Sensor. *Analytical Chemistry*, Vol. 58, pp. 514-517
- Kantam, ML.; Roy, M.; Roy, S.; Sreedhar, B.; Madhavendra, SS.; Choudary, BM. & De, RL. (2007). Polyaniline Supported Palladium Catalyzed Suzuki-Miyaura Cross-Coupling of Bromo- and Chloroarenes in Water. *Tetrahedron*, Vol. 63, pp. 8002-8009
- Kaynak, A.; Wang, L.; Hurren, C. & Wang, X. (2002). Characterization of Conductive Polypyrrole Coated Wool Yarns. *Fibers and Polymers*, Vol. 3, pp. 24-30
- Kim, SM.; Kim HK.; Byun, SW.; Jeong, SH.; Hong YK.; Joo, JS.; Song, KT.; Kim, JK.; Lee, CJ. & Lee, JY. (2002). PET Fabric/Polypyrrole Composite with High Electrical Conductivity for EMI Shielding. *Synthetic Metals*, Vol. 126, pp. 233-239
- Kincal, D.; Kumar, A.; Child, AD. & Reynolds, JR. (1998). Conductivity Switching in Polypyrrole-Coated Textile Fabrics as Gas Sensors. *Synthetic Metals*, Vol. 92, pp. 53-56
- Kitani, A.; Akashi, T.; Sugimoto, K. & Ito, S. (2001). Electrocatalytic Oxidation of Methanol on Platinum Modified Polyaniline Electrodes. *Synthetic Metals*, Vol. 121, pp. 1301-1302

- Kuhn, HH.; Child, AD. & Kimbrell, WC. (1995). Toward Real Applications of Conductive Polymers. *Synthetic Metals*, Vol. 71, pp. 2139-2142
- Kuwabata, S. & Martin, CR. (1994). Mechanism of the Amperometric Response of a Proposed Glucose Sensor Based on a Polypyrrole-Tubule-Impregnated Membrane. *Analytical Chemistry*, Vol. 66, pp. 2757-2762
- Lamblin, M.; Nassar-Hardy, L.; Hierso, J.-C.; Fouquet, E. & Felpin, F.-X. (2010). Recyclable Heterogeneous Palladium Catalysts in Pure Water: Sustainable Developments in Suzuki, Heck, Sonogashira and Tsuji-Trost Reactions. *Advanced Synthesis & Catalysis*, Vol. 352, pp. 33-79
- Lascelles, SF. & Armes, SP. (1997). Synthesis and Characterization of Micrometre-Sized, Polypyrrole-Coated Polystyrene Latexes. *Journal of Materials Chemistry*, Vol. 7, pp. 1339-1347
- Li, F. & Albery, WJ. (1991). Electrochemical Polymerization of Poly(thiophene-3-ethyl acetate) – a New Candidate for a Rechargeable Battery Cathode. *Journal of Electroanalytical Chemistry and Interfacial Electrochemistry*, Vol. 302, pp. 279-284
- Lovell, PA. & El-Aasser, MS. (1997). *Emulsion Polymerization and Emulsion Polymers*. John Wiley and Sons, Chichester, UK
- Lyubimov, SE.; Vasil'ev, AA.; Korlyukov, AA.; Ilyin, MM.; Pisarev, SA.; Matveev, VV.; Chalykh, AE.; Zlotin, SG. & Davankov, VA. (2009). Palladium-Containing Hypercrosslinked Polystyrene as an Easy to Prepare Catalyst for Suzuki Reaction in Water and Organic Solvents. *Reactive & Functional Polymers*, Vol. 69, pp. 755-75
- Maeda, S. & Armes, SP. (1994). Preparation and Characterisation of Novel Polypyrrole-Silica Colloidal Nanocomposites. *Journal of Materials Chemistry*, Vol. 4, pp. 935-94
- Miller, LL. (1988). Electrochemically Controlled Release of Drug Ions from Conducting Polymers. *Molecular Crystals and Liquid Crystals*, Vol. 160, pp. 297-301
- Miyaura, N. & Suzuki, A. (1995). Palladium-Catalyzed Cross-Coupling Reactions of Organoboron Compounds. *Chemical Reviews*, Vol. 95, pp. 2457-2483
- Moreno-Mañas, M. & Pleixats, R. (2003). Formation of Carbon-Carbon Bonds under Catalysis by Transition-Metal Nanoparticles. *Accounts of Chemical Research*, Vol. 36, pp. 638-643
- Niwa, O. & Tamamura, T. (1984). Electrochemical Polymerization of Pyrrole on Polymer-Coated Electrodes. *Journal of the Chemical Society, Chemical Communications*, pp. 817-818
- Niwa, O.; Kakuchi, M. & Tamamura, T. (1987). Polypyrrole-Based Conducting Polymer Alloy Films: Physical Properties and Film Morphology. *Macromolecules*, Vol. 20, pp. 749-753
- Oh, KW.; Hong, KH. & Kim, SH. (1999). Electrically Conductive Textiles by *in situ* Polymerization of Aniline. *Journal of Applied Polymer Science*, Vol. 74, pp. 2094-210
- Okubo, M.; Izumi, J. & Takekoh, R. (1999). Production of Micron-Sized Monodispersed Core/Shell Composite Polymer Particles by Seeded Dispersion Polymerization. *Colloid and Polymer Science*, Vol. 277, pp. 875-880
- Okubo, M.; Fujii, S. & Minami, H. (2001). Production of Electrically Conductive, Core/Shell Polystyrene/Polyaniline Composite Particles by Chemical Oxidative Seeded Dispersion Polymerization. *Colloid and Polymer Science*, Vol. 279, pp. 139-145

- Paoli, M.-AD.; Waltman, RJ.; Diaz, AF. & Bargon, J. (1984). Conductive Composite From Poly(vinyl chloride) and Polypyrrole. *Journal of the Chemical Society, Chemical Communications*, pp. 1015-1016
- Pillalamarri, SK.; Blum, FD.; Tokuhira, AT. & Bertino, MF. (2005). One-Pot Synthesis of Polyaniline–Metal Nanocomposites. *Chemistry of Materials*, Vol. 17, pp. 5941-5944
- Radford, PT. & Creager, SE. (2001). Dual-Stream Flow Injection Method for Amplified Electrochemical Detection of Ferrocene Derivatives. *Analytica Chimica Acta*, Vol. 449, pp. 199-209
- Sailor, MJ.; Ginsburg, EJ.; Gorman, CB., Kumar, A.; Grubbs, RH. & Lewis, NS. (1990). Thin Films of n-Si/Poly-(CH₃)₂Si-Cyclooctatetraene: Conducting-Polymer Solar Cells and Layered Structures. *Science*, Vol. 249, pp. 1146-1149
- Sawoo, S.; Srimani, D.; Dutta, P.; Lahiri, R. & Sarkar, A. (2009). Size Controlled Synthesis of Pd Nanoparticles in Water and Their Catalytic Application in C-C Coupling Reactions. *Tetrahedron*, Vol. 65, pp. 4367-4374
- Selvan, ST.; Spatz, JP.; Klok, H.-A. & Möller, M. (1998). Gold–Polypyrrole Core–Shell Particles in Diblock Copolymer Micelles. *Advanced Materials*, Vol. 10, pp. 132–134
- Tian, ZQ.; Lian, YZ.; Wang, JQ.; Wang, SJ. & Li, WH. (1991). Electrochemical and XPS Studies on the Generation of Silver Clusters in Polyaniline Films. *Journal of Electroanalytical Chemistry and Interfacial Electrochemistry*, Vol. 308, pp. 357-363
- Vasilyeva, SV.; Vorotyntsev, MA.; Bezverkhyy, I.; Lesniewska, E.; Heintz, O. & Chassagnon, R. (2008). Synthesis and Characterization of Palladium Nanoparticle/Polypyrrole Composites. *The Journal of Physical Chemistry C*, Vol. 112, pp. 19878-19885
- Wang, G.; Swensen, J.; Moses, D. & Heeger, AJ. (2003). Increased Mobility from Regioregular Poly(3-hexylthiophene) Field-Effect Transistors. *Journal of Applied Physics*, Vol. 93, pp. 6137-6141
- Wei, G.; Zhang, W.; Wen, F.; Wang, Y. & Zhang, M. (2008). Suzuki Reaction within the Core-Corona Nanoreactor of Poly(N-isopropylacrylamide)-Grafted Pd Nanoparticle in Water. *The Journal of Physical Chemistry C*, Vol. 112, pp. 10827-10832
- Wen, F.; Zhang, W.; Wei, G.; Wang, Y.; Zhang, J.; Zhang, M. & Shi, L. (2008). Synthesis of Noble Metal Nanoparticles Embedded in the Shell Layer of Core–Shell Poly(styrene-co-4-vinylpyridine) Microparticles and Their Application in Catalysis. *Chemistry of Materials*, Vol. 20, pp. 2144–2150
- Yosomiya, R.; Hirata, M.; Haga, Y.; An, H. & Seki, M. (1986). Electrical Properties of Polypyrrole-Polymer Composite Films. *Die Makromolekulare Chemie, Rapid Communications*, Vol. 7, pp. 697-701
- Zhang, C.; Hoger, S.; Pakbaz, K.; Wudl, F. & Heeger, AJ. (1994). Improved Efficiency in Green Polymer Light-Emitting Diodes with Air-Stable Electrodes. *Journal of Electronic Materials*, Vol. 23, pp. 453-458
- Zhang, M. & Zhang, W. (2008). Pd Nanoparticles Immobilized on pH-Responsive and Chelating Nanospheres as an Efficient and Recyclable Catalyst for Suzuki Reaction in Water. *The Journal of Physical Chemistry C*, Vol. 112, pp. 6245-6252

Electroplated Nanocomposites of High Wear Resistance for Advanced Systems Application

Ioury Timoshkov, Victor Kurmashev and Vadim Timoshkov
Belarus State University of Informatics and Radioelectronics
Belarus

1. Introduction

Micro and nanosystems have become the integral part of human being. They help people to improve safety, health and quality of life. Such modern complex advanced systems and their production technologies require new types of material to be developed. These materials should be structured by shape and properties in nano and micro scale for fulfilment of requirements and further incorporation into the systems.

One of the approaches to solve the problem of wear and friction of mechanically moving and load carrying elements of micro and nano dimensions is the use of nanocomposite materials; in particular, codeposited metal and alloy with inert hard nanoparticles by electrochemical or electroless processes. Composite coatings have unique properties that not typical for each phase apart. Varying metal matrix and second dispersed phase the following properties of composite coatings can be improved: hardness, wear-resistance, coefficient of friction, and corrosion-resistance and exposure endurance to aggressive environments. Synthesis of composite coatings by electrolytic codeposition is promising in terms of its low cost, simplicity, and adaptability for different industrial processes. The most exciting applications of plated nanostructured materials are microelectromechanical systems (MEMS), roll-to-roll polymer and nanoimprint technologies. Friction, wear and failure resistance of functional layers are fundamental problems and determine their lifetime.

2. Nanocomposite plating process

Nanocomposite coatings containing ultra-fine particles were plated from sulphate, glycine, acetic, and Watts bathes. Soft magnetic (NiFe, CoFeP, CoP) and hard magnetic (CoNiP, CoW, CoP) alloys as well as conductive matrix of Cu and Ni were investigated. The thickness of the investigated deposits was up to 200 μm . Concentration of ultra-fine particles was varied from 0 to 10 $\text{g}\cdot\text{dm}^{-3}$ (dry substance). Diamond, alumina and aluminium monohydrate ultra-fine particles and BN microparticles were used (Fig. 1).

Average size of nanodiamond particles was 7 nm, alumina - 47 nm, aluminium monohydrate - 20 nm and boron nitride - 1 μm . Codeposition process was carried out in the electrolytic cell of flow type (Fig.2).

Nickel coatings are deposited from the bath: nickel sulfamic-acid water - 400-420 g/l, boric acid - 35-40 g/l, saccharin sodium salt - 0,5-1 g/l, surfactant - 0,2-2 g/l, ultra-dispersed particles - 2-10 g/l, temperature - 38-42 $^{\circ}\text{C}$, current density - 2,2-2,5 A/dm^2 , pH - 4,0-4,2.

Deposition rate is 30 $\mu\text{m}/\text{h}$. Optimal concentration of ultra-dispersed particles is defined experimentally: Al_2O_3 - 4,0 g/l; UDD - 2,0 g/l, AlOOH - 5,0 g/l

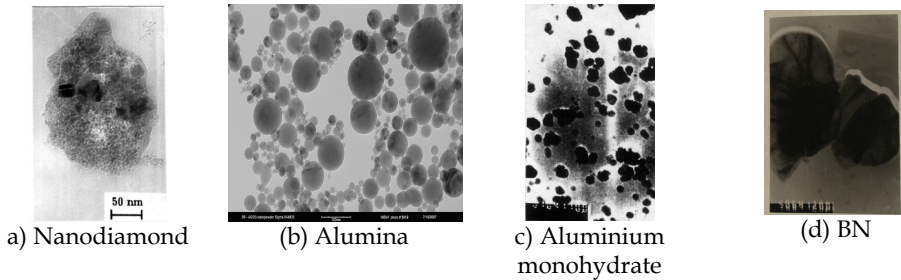


Fig. 1. Inert particles used for codeposition.

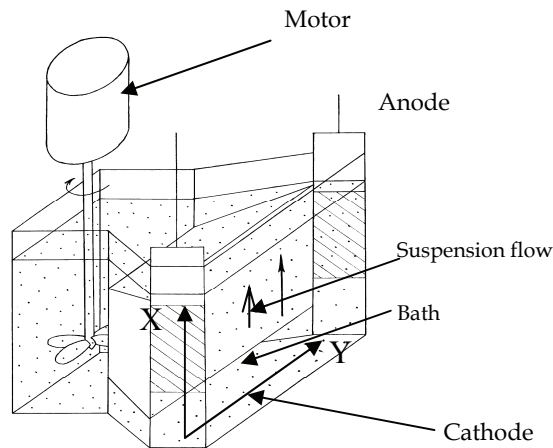


Fig. 2. Electrolytic cell for codeposition process.

The amount of codeposited particles was determined both by integral Coulometric analysis on express analyser AH-7529 (USSR) and by local Auger spectroscopy (PHI-660 Perkin Elmer Corp., USA). The Vickers microhardness of coatings was measured at a load of 0.5 N with MICROMET-II (Buehler-Met, CH). The structure of the deposits was explored by TEM (EM-125, USSR). The coefficient of friction and the wear were evaluated by a FRETTING II test machine (KU Leuven, BE). Wear volumes were estimated by RM600 laser profilometry (Rodenstok, D) after 100,000 fretting cycles.

3. Codeposition model of nanocomposite plating

In general, during the electrolytic codeposition, the suspended inert particles interact with the surface of the growing film due to hydrodynamic, molecular and electrostatic forces (Franssaer et al. 1992). This complex process results in the formation of composite coatings.

Auger profiles (Fig.3) and local X-ray analysis (Fig.4) demonstrate that ultra-fine particles are effectively incorporated into the meal matrix.

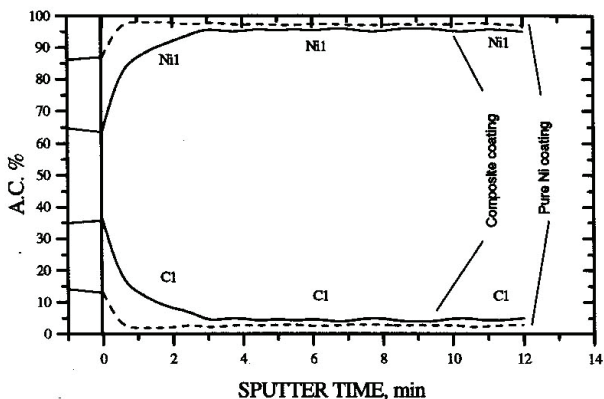


Fig. 3. AES sputter-etch elemental profiles of pure and composite with nanodiamond Ni coatings.

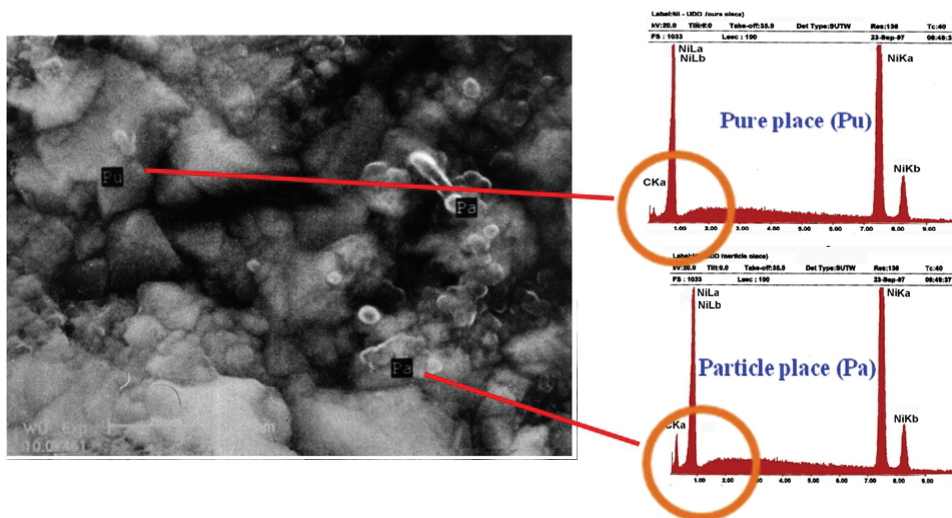


Fig. 4. SEM image and local X-ray analysis of composite Ni-nanodiamond coating.

Based on the experimental data (Timoshkov et al. 1999), the qualitative codeposition model of the composite coatings with the ultra-fine particles was suggested. The peculiarities of the ultra-fine particles behaviour are considered in the model. The model worked out is based on the assumption the codeposition of ultra-fine particles proceeds through the following stages (Fig.5):

- coagulation of ultra-fine particles in plating solution,

- formation of quasi-stable aggregates and therefore change of system dispersion constitution,
- transport of the aggregates to the cathode surface by convection, migration and diffusion,
- disintegration of the aggregates in the near-cathode surface,
- weak adsorption of ultra-fine particles and aggregate fragments onto the cathode surface,
- strong adsorption of dispersion fraction (embedding).

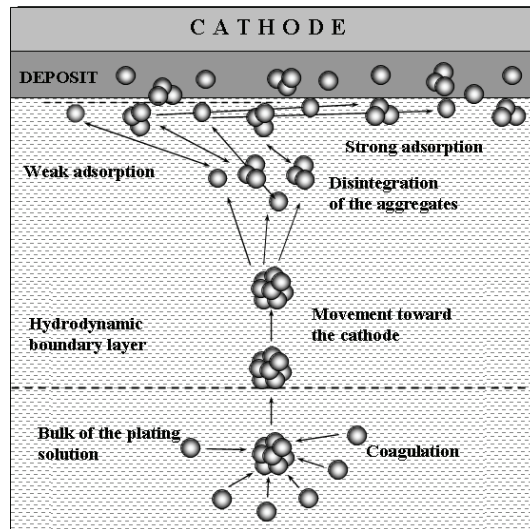


Fig. 5. Model of nanoparticles codeposition process.

Hydrophobic colloidal systems are thermodynamically unstable due to the surplus of the surface energy. They exist owing to stabilization by protective ionic and molecular layers. In general, in the bulk of suspension the particles encounter one another because the Brownian movement, gravity and convection. The forces between them determine whether the encounters result in sticking the particles or the particles remain free.

Behaviour of dispersed systems is described by DLVO theory. Stability or coagulation rate of suspensions depends on sign and magnitude of overall potential energy of interaction between the particles. Positive electrostatic repulsion energy $U_r(h)$ decreases by exponential law, whereas negative molecular attraction energy $U_a(h)$ is inversely proportional to squared distance. As a result, at small distances ($h \rightarrow 0$, $U_r(h) \rightarrow \text{const}$, $U_a(h) \rightarrow -\infty$) and large distances (exponent diminishes much rapidly than power function), the attraction energy between the particles prevails. The electrostatic repulsion energy prevails at intermediate distances. The primary minimum 1 corresponds to direct sticking of particle. In this case, the particles are irreversibly stuck (coalescence). The secondary minimum 2 corresponds to attraction through interlayer of environment. In this case, the aggregates may be counteracted relatively easily. The maximum corresponding to intermediate distances characterizes the potential barrier, which prevents sticking the particles. Forces of interaction are extended for hundreds of nanometers.

In the consideration of interaction between the particles, the following conclusions from DLVO theory should be mentioned as well. The height of the energy maximum and the depth of the primary and secondary maximum depend on the parameters of the systems, namely the zeta potential, particle size, electrolyte concentration (and valence) and the Hamaker constant. At low electrolyte concentration, the energy maximum may reach high values and this prevents particle aggregation. At increase of the electrolyte concentration, the height of the energy maximum decreases and disappears at a critical concentration (which depends on valence of electrolyte). The coagulation becomes more rapid. Thus, to enhance the suspension stability, one needs to reduce the electrolyte concentration and increase the zeta potential.

The transport of the particles toward the cathode surface occurs by convection, migration, diffusion, and Brownian movement.

Migration is the movement of cations, anions or charged particles through the solution under influence of applied potential between the electrodes in that solution. *Diffusion*. Electrode reaction deplete the concentration of oxidant or reluctant at an electrode surface and produces a concentration gradient there. This gives the rise to the movement species from the higher to the lower concentration. Unlike migration, which only occurs for charged particles, diffusion occurs for both charged and uncharged particles. *Convection* includes thermal and stirring effects, which can arise extraneously through vibration, shock and other types of stirring and temperature gradients. *Brownian movement*. It is known, the Brownian movement is affected strongly by the particle size, and may be neglected in the case of the particles size is above 1 μm .

Stirring mode is required to be the transition mode between the turbulent flow and the laminar flow in the bulk of plating bath. Such a mode is of most practical significance. It is because the laminar flow does not provide the sufficient stirring of the electrolyte-suspension. Alternatively, at the stirring rate corresponding to the turbulent mode, the conditions preventing totally the particles embedment appear.

In the near-cathode region, the aggregate is influenced by the forces of different nature and direction. Motion of the aggregate is determined by resultant force, and integrity of aggregate – by sum of forces values as well. For the investigated system, the following forces are considered:

- mechanical forces, associated with interaction with the fluid flow and other particles, gravity and buoyancy;
- electrical forces, connected with the electric field that presents in the plating solution during electrodeposition process;
- molecular forces acting on the particle in the vicinity of the cathode surface.

Mechanical forces. At the laminar liquid flow in the boundary hydrodynamic layer the law of viscous friction is followed in this region, and the boundary conditions are following: $V=0$ at $y=0$ and $V=V_0$ at $y=\infty$.

If the particle moves in the flow having transverse velocity gradient of liquid movement the rotation motion can be imparted to the particle because the different velocities of flow past a particle from the top and from the bottom. The transverse particle migration appears as the result of the rotational motion. The transverse particle migration results from pressure drop on the side where the sum of the tangential velocity components of flowing past and rotating the particle reaches the maximum. The transverse particle migration is directed always toward this maximum. In the case being considered particle moves away from the

cathode surface. When the particle is trapped by cathode, the longitudinal force by flow of the plating solution affects the particle. If this force exceeds the friction force keeping the particle onto the cathode surface, the particle is detached from the growing deposit.

Besides the forces connected to interaction between the particle and hydrodynamic flow, the gravity and buoyancy contribute to particle motion. The sum of forces by gravity and buoyancy results in the sedimentation force.

Collisions between the particles in the near-cathode region may change the particle trajectory promoting or preventing the particle movement to the cathode. Moreover, the particle in the electrolyte may collide with the particle trapped by the cathode and prevent embedment.

Electric forces. The ions in the double layer around the particle interact with the electric field in the plating solution. This results in the particle motion along the lines of electric field. The motion is affected by the fluid permittivity, particle size, intensity of electric field in the particle place, and zeta potential. Sign and value of zeta potential is determined by both the particle nature and the electrolyte constitution and can be changed by addition of surfactants into the plating solution. In the near-cathode region, the cathode itself affects ambiguously the electrophoretic particle motion. On the one hand, modification of the electric field lines in the near-cathode region slows down the particle movement, and on the other hand, the cathode surface itself increases the intensity of the electrophoretic movement. It should be emphasized that it is not possible measurement of zeta potential in the near-cathode region because it depends on many factors and can change not only its value but the sign as well. Therefore, it is difficult task to evaluate the contribution of electrophoretic particle motion into the codeposition process.

In the near-cathode region, the osmotic pressure of the electrolyte affects the particle motion. The electroosmotic motion is the phenomenon of liquid movement through porous body under application of electric field. Assuming the particles in the near-cathode region as a porous bodies, the ionic species move through this "body" due to electric field in the plating solution. In its turn, the ion flow exerts the pressure upon the particles and assists the particle movement toward the cathode surface. It should be mentioned that the electroosmotic motion of particle is influenced by those parameters as for electrophoretic motion (see above).

Molecular forces. At the immediate vicinity of a cathode surface the van der Waals attraction force appears. It occurs with all types atoms or molecules. It arises from the charge fluctuations within an atom or molecule that is associated with the motion of its electrons. A strong repulsive force appears at short distances, when the electrolyte concentration exceeds a certain value. This force is called the structural or hydration force. It originates from the fact that the thin solvent layer presents near the interfaces. This solvent layer is ordered by hydration of cations adsorbed onto surfaces as the interfaces approaches each other. The hydration force results from change in the structure of solvent between the interfaces and prevents the interfaces from close approach.

As particles aggregate approaches the near-cathode region, the force field increases. If these forces exceed a certain critical value, which keeps the particles in the aggregated state, the aggregates are disintegrated. Further, the solitary particles and the aggregate chips interact with the cathode and can be adsorbed weakly onto the cathode. The weak adsorption step assumes the interaction between the particle and cathode surface through adsorbed layers of ions and solvent molecules. Further, the electric field helps to uncover the particle. The thin

interlayer between the cathode surface and particle disappears. It leads to strong field-assisted adsorption and the particle is overgrown with deposit.

A structural investigations confirm proposed model of heterogeneous nanocomposite coating formation. Fig.6 shows that pure Ni coatings contain twins, dislocation aggregates inside the grains, and a concentration of solitary dislocations and dislocation walls of 20 nm thick along the grain boundaries. The average grain size is about 500 nm. As for nanocomposite coatings the grain size reduces up to 30-100 nm. An accumulation of ball-type dislocations along the grain boundaries takes place. Thus, for the first time it was determined that during codeposition of matrix and nanodiamond particles, nanocrystalline Ni electrodeposits were formed.

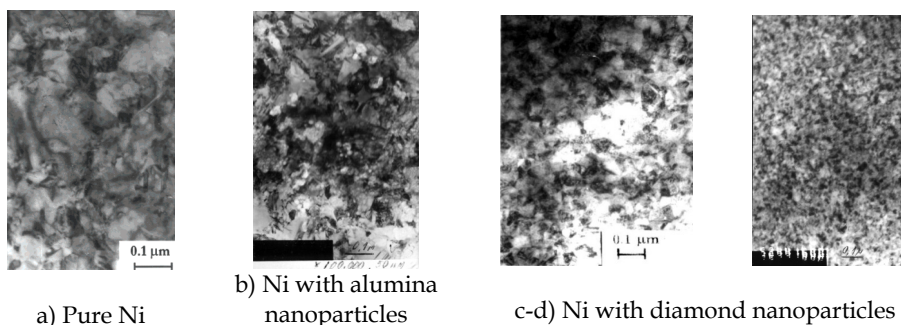


Fig. 6. TEM micrographs of pure Ni and nanocomposite coatings

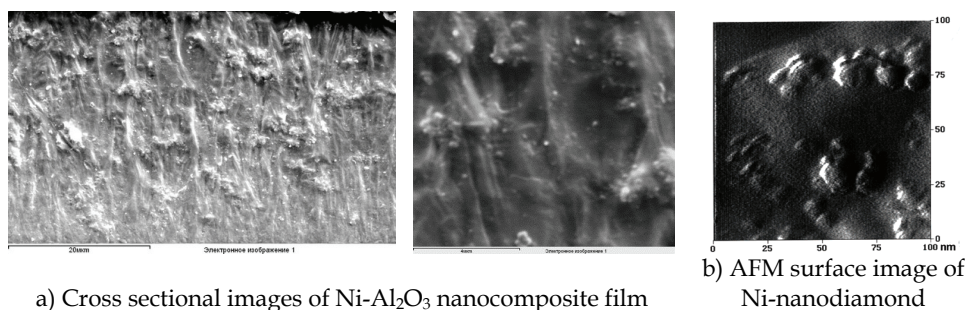


Fig. 7. SEM and AFM images of nanocomposite materials

Cross-sections show that ultra-fine particles are effectively incorporated into the metal matrix (Fig.7). These nanoparticles are distributed in the matrix volume uniformly. Small fragments of aggregates and separate nanoparticles form heterogeneous structure of nanocomposite.

4. MEMS based nanocomposite elements

Micro and nanosystems are the completed devices that combine into one sensor, electronic, and mechanical parts. Mechanical interaction between nano-, micro-, and macro world is the limiting factor for such a complex system. Three dimensional moveable structures should be

integrated in micro and nanosystems from design and technology perspective. Moreover, in general reliability of the systems is determined by the reliability of the mechanical part. Fig. 8 shows that as MEMS become more complicated and for the implemented tasks of higher level, increasing the capability to data processing, improving the sensitivity and possibility to generate mechanical response to some action, the number of the elements should be increased and reaches 10^9 for both electronic and mechanical elements.

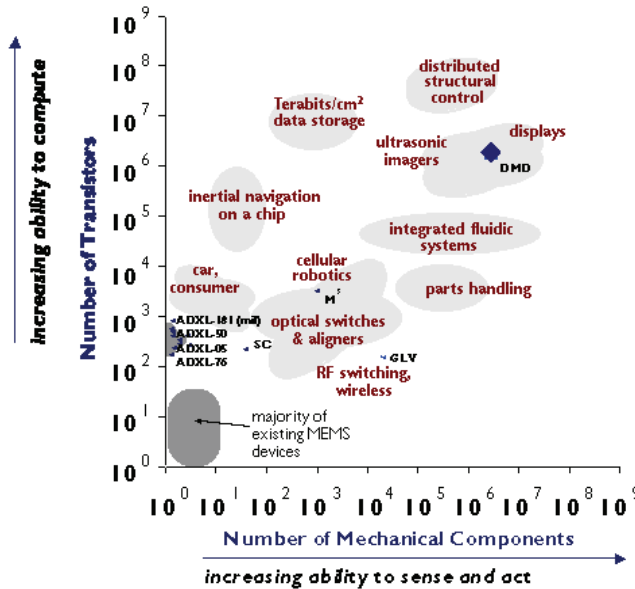


Fig. 8. Progress trend and interdependence of electronic and mechanical parts of MEMS (Pan, 1999).

Technologies of microelectronics have developed and improved for ten years, and at present they achieve perfection. On the other hand, mechanical elements of MEMS require the special design and technology methods to be developed. It is necessary to point out, that upon the movement from pure scientific investigation to practical use of the systems, the reliability are of the great importance. For present stage of MEMS/NEMS development mechanical elements possess significantly lower reliability in comparison with electronic ones and, consequently, reliability of the systems is determined by the reliability of the mechanical part namely.

LIGA (Lithografie, Galvanoformung, and Abforming) technology is the well-known classical process to produce mechanical microelements for MEMS (Fig.9). The main stages of the LIGA process are: obtaining 3D mould of the element with high aspect ratio; metal (alloy) deposition into the form by plating methods; removing the mould to release the elements.

In terms of functionality, the most important properties of the micromechanical elements are friction and wear resistance. Codeposition process instead pure metal (alloy) plating allows increasing reliability of the elements and MEMS in general significantly. For nanocomposite systems, the mechanical properties are determined by the phase composition of the

materials, i.e. by the matrix-to-particle content ratio. Increase of particles concentration in electrolyte influences on increase of foil microhardness slightly. Fragility increases significantly. It deteriorates reliability during exploitation.

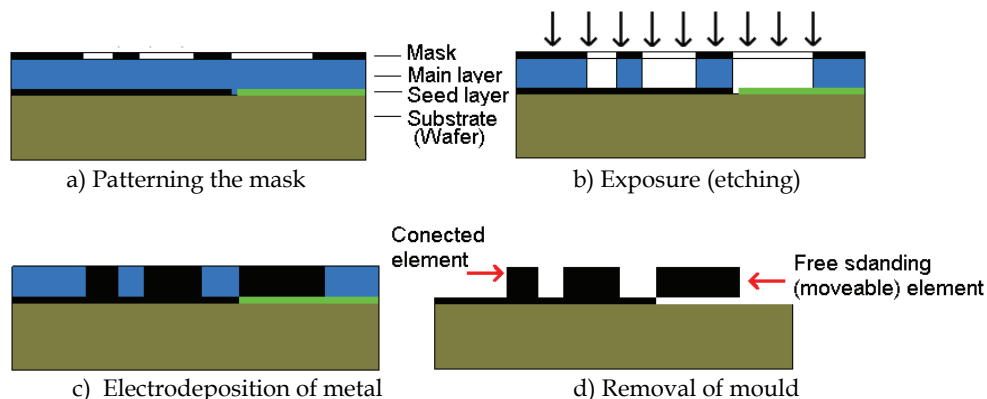


Fig. 9. Process flow of LIGA technology.

One of the main characteristics of nickel deposits is internal stress. Big stress can be reason of crack formation at deposition process or operation. Strain and compressing stress is typical for nickel deposits. Sign of stress to a great extent depends on dopes in electrolyte. Its value is up to nature of electrolyte. Deposits from sulphate electrolyte has high internal stress, while from sulphamate electrolyte - small stress [9]. Internal stress in nickel deposits depends on concentration of basic components in electrolyte. It's determined that tendency to decrease internal stress to zero with following transfer to compressing tensions is observed in sulphamate electrolyte with concentration change of nickel salt from 100 till 800 g/l. Significant change was in concentration range 350-650 g/l. Boric acid don't influence almost on properties of nickel deposits. Variation of pH in solution has big influence on value of internal stress. Minimum of stress displaces to range of higher pH with lowering of nickel amidosulfate concentration. Internal stress of deposits decreases with increase of electrolyte temperature. There is small stress at deposition temperature 60°C. It can be explained by crystal enlargement at high temperature.

Hardness of nickel deposit depends on nickel amidosulfate concentration slightly. But it changes noticeably with increase current density and pH of electrolyte. It can be explained by structural changes of deposit. Structure refinement is observed at increase of pH. It goes with increase of hardness. Hardness decreases sharply at high current density. It increases insignificantly at current density 1-5 A/dm². Hardness of nickel deposits reduces on 15-20 per cent with increase of electrolyte temperature from 20 till 60 °C as a result of enlargement of its structure. Hardness increases at addition in electrolyte organic additives, which promote to refinement of structure. These additives are saccharin, benzenesulphide, propargyl alcohol. Hardness can be increased till 600-700 kg/mm² by codeposition nickel with ultradispersed particles..

Among the coatings tested, composite nickel coatings containing ultra fine diamond particles show a lower coefficient of friction. The amount of particles in the coatings affects the wear rate (Fig.10). The wear volume for pure Ni and composite coatings is shown for fretting tests performed with 100,000 cycles (Fig. 11).

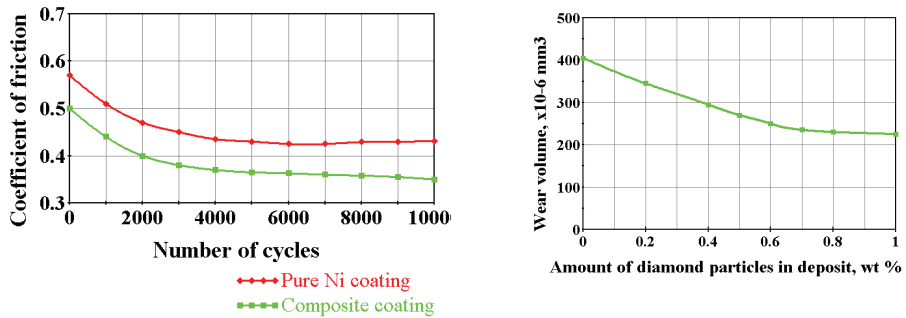


Fig. 10. Coefficient of friction and wear volume for pure and nanocomposite Ni.

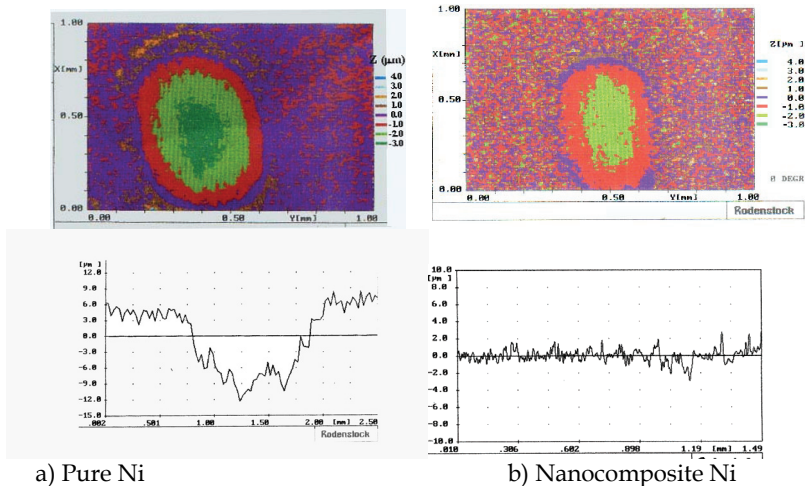


Fig. 11. Light profilometry and position-depth profiles of fretting scars after 100,000 cycles.

The amount of particles in the coatings affects the wear rate. The friction behaviour of multiphase materials has been described in the literature (Mezlini and et al., 2009). The main problem with these approaches is that they are static ones and applied to ideal surfaces because during wear of a multiphase material the topography changes in practice continuously. Localised wear of the matrix takes place in the first phase. After that, the particles become more loaded. This dynamic process may lead to an increased wear resistance of composite materials. Of course, the fretting wear properties of composite coatings are also influenced by the size, shape and distribution of the reinforcing phase. Some MEMS nanocomposite LIGA elements for different types of micromotors were produced and tested (Fig.12).

Friction, wear and corrosion are the key problems for MEMS with real mechanically moveable elements. Codeposition processes allow getting nanocomposite elements with high operate reliability: wear resistance increased in 2-2.5 times, microhardness increased in 2 times, coefficient of friction and corrosion current were reduced factor 1.5 and 1.6 respectively. Developed technologies were tested on prototypes of the electromagnetic and pneumatic micromotors.

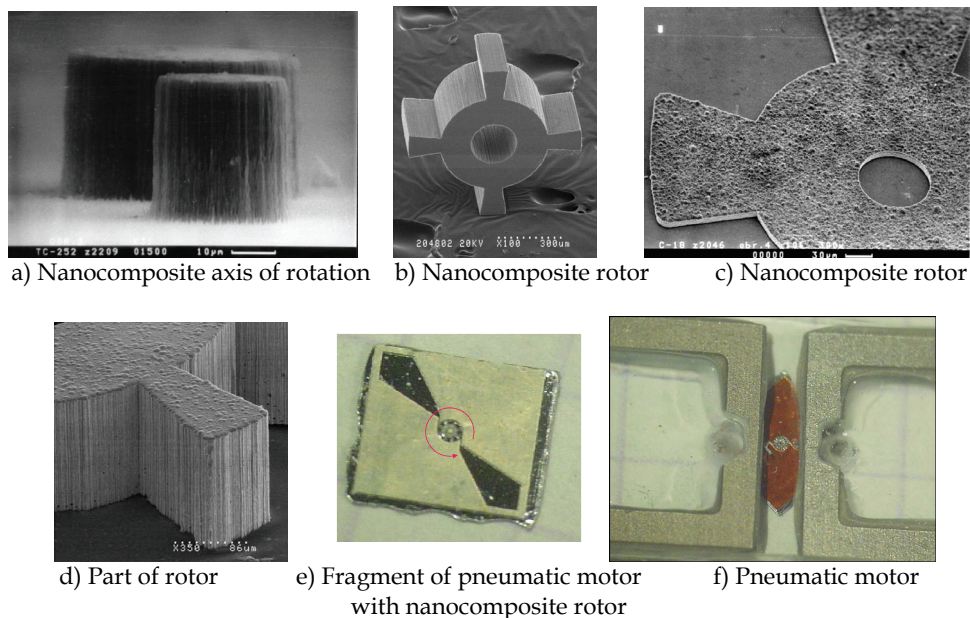


Fig. 12. Nanocomposite MEMS elements.

5. Nanocomposite materials for roll-to-roll and nanoimprint technologies

Gordon Moore projected that the number of components per chip would reach a doubling every two years (Moore, 1975). And the prediction is not going to stop soon. Modern semiconductor industry is following this trend for more than 45 years. And according to International Technology Roadmap for Semiconductors (ITRS) in 2011 28nm halfpitch node is going to be introduced for high volume manufacturing (HVM) in flash memory as main driver for technology shrinkage (<http://www.itrs.net>).

Modern lithography supports a Moore’s law to enable further shrinkage of feature size. As habitual immersion 193nm lithography is approaching its resolution limit, lithography R&D needs new techniques to step into 1x technology node. Candidates for future nanopatterning technologies are extended Double Patterning (DP) (Noelscher et al., 2009) with ArF immersion lithography, extreme ultraviolet (EUV) lithography, multi electron beam lithography (EBL) and nanoimprint lithography (NIL). Each approach has own advantages and disadvantages. At 1x node DP, EUV and EBL would have low throughput with high cost per layer. NIL in comparison with competitors offers sub-10 nm resolution, high-throughput and low-cost patterning, and has a chance to be next generation lithography in future HVM.

Nanoimprint lithography was invented in 1995 by Prof. Stephen Y. Chou (Chou et al., 1995). Schematic NIL process is presented on Fig.13. In that faraway time he demonstrated a feasibility of printing 25nm contact holes, vertical and smooth sidewalls, and nearly 90° corners. Similar technology requirements are going to be used in production soon.

As it is shown on fig.13 a mould is pressed into a thin thermoplastic polymer film that is heated above its glass transition temperature. At this temperature the polymer behaves as a

viscous liquid. It can flow under a pressure and fully repeat the mould. After cooling down resist is hardened and the mould is removed from the substrate. Pattern could be transferred into underlayer by etching process. Quite simple principle of operation makes NIL tools cheap, fast and reliable.

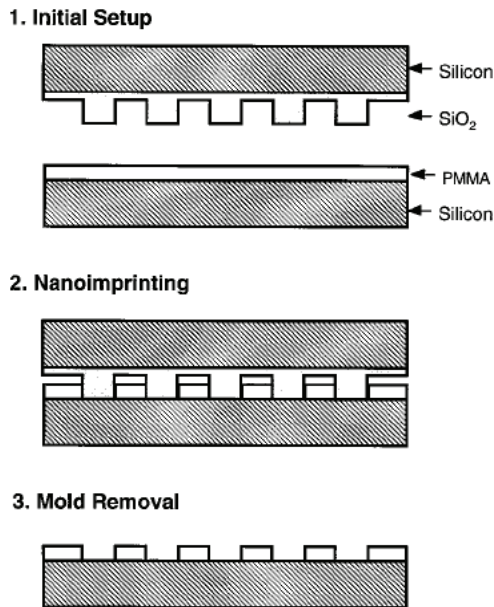


Fig. 13. Schematic of nanoimprint lithography process.

There are many different types of NIL processes, but three schemes are important: soft-lithography, thermoplastic nanoimprint process and resist-dispense photo nanoimprint process (Choi, 2010).

The template for soft lithography is made with a very flexible material (Xia et al., 1998). For example, in micro-contact printing (μCP) 'ink' adhered to features on a template is transferred to a substrate using contact of the inked template and the substrate. This layer acts as an etch mask for subsequent etch processes.

In photo nanoimprint lithography a low-pressure of template and room temperature process is achieved due to the use of a low-viscosity UV-curable resist. The resist is dispensed in picoliter drops over the printing area. With low pressure the template is placed on the substrate, and subsequent UV curing induces cross-linking in the resist material. The transparency to UV light is required from template material, what significantly reduce the list of possible materials.

Thermoplastic nanoimprint lithography possesses sub-10 nm replication resolution and has the most attractive cost per layer. Principle of thermoplastic nanoimprint lithography mentioned above, where the template is in contact with a high viscosity spin-coated resist. There is no material restriction for templates, so wide range of materials can be used: metals, dielectrics or semiconductors. Application of nanocomposite materials could improve reliability of this process.

Also some other types of NIL are in the interest of research groups, such as nanoimprint with incorporation of carbon nanotubes (CNT) (Choi et al., 2008), electrochemical nanoimprint (Hsu et al., 2007) and laser assisted direct imprint (Chou et al., 2002).

Manufacturing requires a high throughput to production equipment. To obtain very high throughput with modest resolution an alternative approach to flat NIL - roller nanoimprint lithography (R-NIL) has been proposed (Tan et al., 1998). Compared with basic flat thermoplastic NIL, R-NIL has the advantage of better uniformity, less force, and the ability to repeat a mask continuously on a large substrate. Two methods of roller nanoimprint were presented: imprint using a cylinder mold by mounting a master mold of cylinder shape around the roller, and imprint using a flat mold by putting the mold directly on the substrate and rotating the roller on top of the mold. Roller nanoimprint tool was developed by Hitachi Ltd. (Fig.14) (<http://www.hitachi.com>).

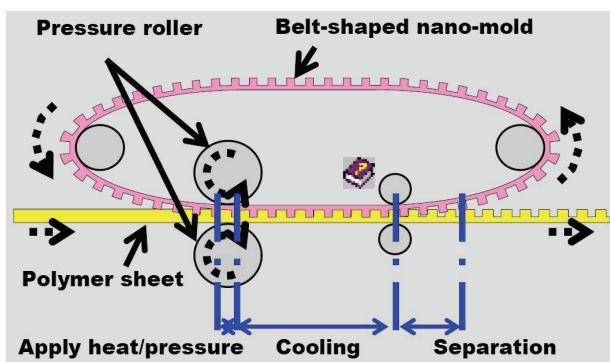


Fig. 14. Schematic diagram of roller nanoimprint tool presented by Hitachi in 2006.

The key concerns for nanoimprint lithography are template patterning, overlay, defects and template wear. Mask patterning requires 1x scale to printed pattern and could be made by means of e-beam and ion-beam lithography. But that's making mask writing at high resolution quite expensive. Due to heat-cool cycles of the template and high pressure compression into resist, it is very difficult using thermoplastic NIL to effect nanoscale alignment and overlay of printed structures as needed in semiconductor device manufacturing.

But the main problem of NIL is low robustness of template due to high pressure of pressing, and it leads to high defectivity level. However, the use of amorphous metals (metallic glasses) (Kumar et al., 2009) and nanocrystalline composite metals and alloys allows to pattern the template on sub-100 nm scale, what can significantly reduce the template cost and improve robustness.

Other issues of NIL, and especially in roller NIL, are resist pattern deformation and fracture during separation process of mask from substrate due to adhesion and friction forces (Wu et al., 2009; Kim et al., 2010).

Usage of bulk nanocomposite templates can improve reliability of NIL processing. Such materials have advantages in comparison with conventional crystalline templates such as good wear resistance, high microhardness, low adhesion, 3D repeatability of mold and low cost of production. The properties of nanocomposite materials are described above in this chapter. Reliability of the conventional templates could be improved by deposition of

antisticking layers, such as diamond-like carbon (DLC) layers, composite chrome coating with nanodiamond particles presented further.

Nanocrystalline structure of composite metal coating allows to resolve sub-100nm features on nanoimprint templates due to its reduced grain size up to 30-100 nm. Test mold structures of 1 μ m wide (Fig.15) are filled with nanocomposite metal material using developed LIGA-like technology. Deposited metal repeats the mold shape.

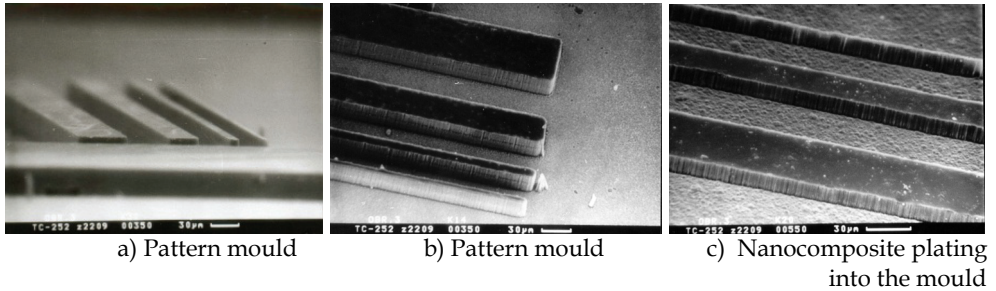


Fig. 15. Test polyimide patterns with minimum feature size of 1 μ m for following plating of nanocomposite metal.

As feasibility of 1 μ m feature transfer from the mold to composite metal template is shown, future activities will be directed to produce sub-100nm metal features. Advantage of the use of nanocomposite materials for roller NIL is proved on example of its application in roll-2-roll technology presented below.

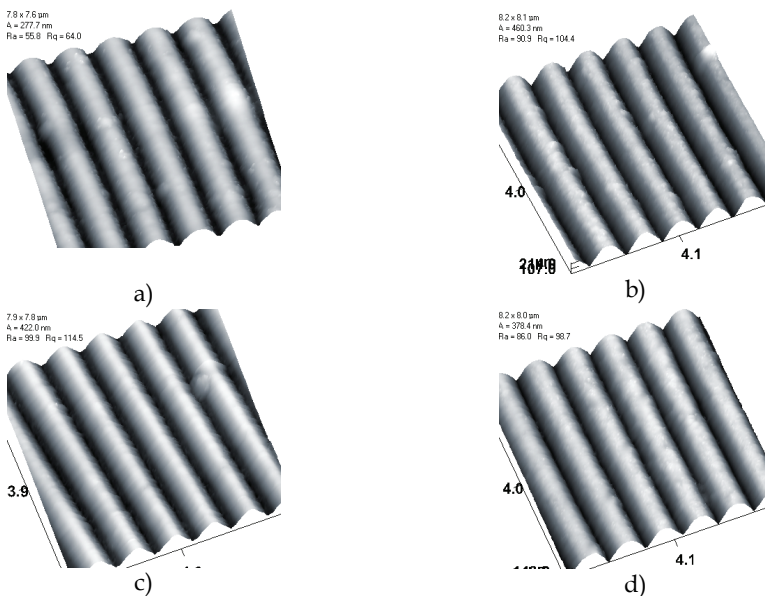


Fig. 16. AFM images of test nanocomposite samples of copies: a – pure Ni, b – Ni with Al_2O_3 , c – Ni with diamond particles, d – Ni with aluminum monohydrate.

Also, high precision galvanoplastic technology is used in holographic industry to produce optical diffraction gratings and images. Roll-to-roll technology is the basis for replication by mechanical pressing of metal matrix into multilayer polymer basis. Working nanocomposite nickel matrix was developed, as well as composite chromium protective coating deposited with nanodiamond particles on top of pure nickel matrix.

Nickel foils are deposited from bath: nickel sulfamic-acid water - 400-420 g/l, boric acid - 35-40 g/l, saccharin sodium salt - 0,5-1 g/l, surfactant - 0,2-2 g/l, ultra-dispersed particles - 2-10 g/l, temperature - 38-42 °C, current density - 2,2-2,5 A/dm², pH - 4,0-4,2. Deposition rate is 30 μm/h. Optimal concentration of ultra-dispersed particles is defined experimentally: Al₂O₃ - 4,0 g/l; UDD - 2,0 g/l, AlOOH - 5,0 g/l. Increase of particles concentration in electrolyte influences on increase of foil microhardness slightly. Fragility increases significantly. It deteriorates reliability during exploitation.

Patterned grating copies and gratings before and after test are shown on Fig. 16 and 17 respectively. They have been tested by stamping method on 2000 m aluminized lamsan tape. Test results show the increase of holographic matrixes runability on 60-400% with improved printed image quality.

Application of composite materials in NIL and roll-2-roll process is the right way to solve issues and improve reliability of templates and whole technology at all. It helps to bring NIL into HVM, and especially for roller NIL to get even higher throughput than step-and-print nanoimprint lithography.

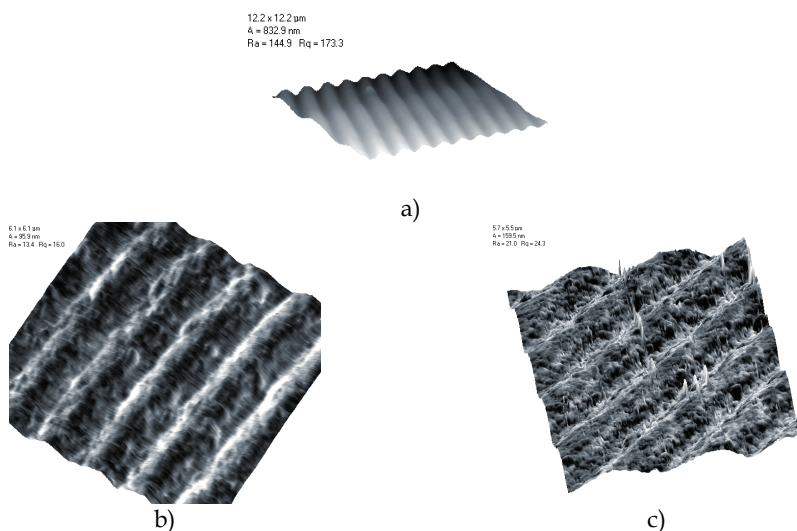


Fig. 17. Reliefs of grating copies before (a) and after test (b,c).

6. Conclusion

This chapter describes positive consequences of introduction of the nanocomposites in the advanced technologies. Application of nanocomposites in MEMS, NEMS, NIL and roll-2-roll technologies makes it possible to improve quality and reliability of these processes and end products.

Nanocomposite technology may be integrated in the systems technology by replacement of homogeneous pure materials by heterogeneous nanocomposites. This allows to improve set of physical mechanical properties, such as wear resistance, microhardness, corrosion resistance and friction coefficient. Nanocrystalline structure of nanocomposites enables to resolve sub-100nm features in NEMS and NIL applications.

Application of such nanocomposite materials is the only way of industrial development for advanced systems and technologies such as moveable MEMS elements, working matrix in roll-to roll and nanoimprint technologies.

7. References

- Choi, J.; Jung, S.; Choi, D.; Jeong, J. and Lee, E. (2008). *Direct soft UV-NIL with resist incorporating carbon nanotubes*, Microelectronic Engineering, Vol. 85, pp. 195-201
- Choi, J. (2010). *Status of UV Imprint Lithography for Nanoscale Manufacturing*, In G. Wiederrecht, Handbook of Nanofabrication. pp. 149-181. Amsterdam: Elsevier B.V.
- Chou, S.Y.; Krauss, P.R. and Renstrom, P.J. (1995). *Imprint of Sub-25 Nm Vias and Trenches in Polymers*. Applied Physics Letters, №67(21), pp. 3114-3116
- Chou, S.Y.; Keimel, C.; Gu, J. (2002). *Ultrafast and Direct Imprint of Nanostructures in Silicon*, Nature № 417 (6891): pp.835-837.
- Fransaer, J.; Celis, J-P. and Roos, J.R. (1992). *Analysis of the electrolytic codeposition of non-Brownian particles with metals*, Journal of The Electrochemical Society, 139 (2) (1992), pp. 413 -425.
- Hsu, Keng H.; Schultz, Peter L.; Ferreira, Placid M. and Fang, Nicholas X. (2007). *Electrochemical Nanoimprinting with Solid-State Superionic Stamps*, Nanoletters Vol. 7, No. 2 pp. 446-451
- Kim, Kwang-Seop; Kim, Jae-Hyun; Lee, Hak-Joo and Lee, Sang-Rok (2010). *Tribology issues in nanoimprint lithography*, Journal of Mechanical Science and Technology № 24 pp. 5-12
- Kumar; Tang, Hong X. and Schroers, Jan (2009). *Nanomoulding with amorphous metals*, Golden, Nature №457, pp. 868-872
- S. Mezlini, S; and others (2009). *Correlation Between Tribological Parameters and Wear Mechanisms of Homogeneous and Heterogeneous Material*. Tribology Letters Volume 33, Number 2, pp.153-159.
- Moore, G. (1975). *Progress in Digital Integrated Electronics*, IEEE, IEDM Tech Digest pp.11-13
- Noelscher, C.; Timoshkov, V. and others (2009). *Double patterning down to $k1=0.15$ with litho trim*. J. Micro/Nanolith. MEMS MOEMS 8(1), 011005(Jan-Mar 2009)
- Pan, J. (1999). *MEMS and Reliability*. Dependable Embedded Systems, Carnegie Mellon University
- Tan H, et al. (1998). *Roller nanoimprint lithography*. Journal of Vacuum Science and Technology № 16(6), pp. 3926-3928
- Timoshkov, Yu.; Gubarevich, T.; Orekhovskaya, T.; Molchan, I. and Kurmashev V. (1999). *Properties of Ni-composite coating with different type of ultra-dispersed diamond particles*, Galvanotechnique and surface technologies, v.7, 2, pp.20-26, Russia
- Wu, Cheng-Da; Lin, Jen-Fin and Fang, Te-Hua (2009). *Molecular Dynamics Simulations of the Roller Nanoimprint Process: Adhesion and Other Mechanical Characteristics*, Nanoscale Res Lett № 4, pp. 913-920
- Xia, Y. and Whitesides, G. M. (1998). *Soft Lithography*, Angewandte Chemie - International Edition in English № 27, pp. 550-575

Nanocomposite Thin Films Resulting from Au Nanoclusters Dispersed in a Titanium Oxide Dielectric Matrix: the Surface Plasmon Resonance Effect

M. Torrell¹, L. Cunha¹, M.I. Vasilevskiy¹, E. Alves²,
N.P. Barradas², A. Cavaleiro³ and F. Vaz¹

¹*Universidade do Minho, Centro de Física, Braga,*

²*Instituto Tecnológico e Nuclear and CFN da Universidade de Lisboa, Sacavém,*

³*SEC-CEMUC – Universidade de Coimbra, Dept. Eng. Mecânica, Pólo II, Coimbra, Portugal*

1. Introduction

The increasing interest of the scientific community in the nanocomposite thin films containing noble metal nanoparticles (MNP) embedded in dielectric matrices is related to a relatively wide range of possible applications. Although it may sound strange, the awareness of the properties and applications of this kind of nanocomposites already existed many centuries ago. To begin with, MNP provided different colours in Roman glasses, as the well-known Lycurgus Cup from the third century, which nowadays can be visited in the British Museum of London. Another remarkable example of this ancient use of this kind of nanocomposite system is the on the fabrication of medieval cathedrals' windows that were decorated with noble metal powders (commonly from Au). For certain powder conditions, the addition would give rise to astonishing effects on the cathedral windows, namely in certain tones of blue and red that could be obtained. This was done during centuries. More recently, the use of these films on high value consumer goods is gaining increasing interest, namely for decorative applications, jewellery and some domestic technological devices and furniture.

The rapid development of different preparation approaches and the increasing knowledge that is becoming available from the study of the scientific content that is involved in these nanocomposites, together with a detailed characterisation of their main properties, is bringing an increasing amount of new and modern applications, beyond those of purely decorative purposes. Among the new possibilities, it worth mention those related with the fabrication of colour filters (Takele et al, 2006) bio- and optical sensors (Hutter & Fendler, 2004; Walters & Parkin, 2008; Torrell et al., 2010a), absorption elements of solar cells (Walters & Parkin 2008), enhancement of electrical/thermal conductivity of coatings, photocatalytic antibacterials (Wang et al., 2006a), pollutant-degradation materials (Pacholski et al., 2004; Wu & Tseng, 2006; Li et al., 2009), gas sensors (Atashbar et al., 1998; Walton et al., 1998), nonlinear optical devices (Walters & Parkin, 2008; Cho et al., 2000;

Hache et al., 1988) and the recent Surface Enhanced Raman Scattering effect (SERS) (Kim et al., 2010). Most of these applications rely on the tailoring of the so-called Surface Plasmon Resonance (SPR) absorption, which is highly dependent of the type of the noble metal that is selected (typically silver and gold), the possibility of the metallic atoms to form a network of clusters (at the nanometric scale), their correspondent morphology (size, shape and distribution behaviour), but also on the dielectric properties of the medium where the metallic nanoparticles (nanoclusters) are dispersed (Dalacu & Martinu, 1999; Cho et al., 2000; Dalacu & Martinu, 2000; Bohren & Huffman, 1998; Deng et al., 2008; Matsuoka et al., 1997; Liao et al. 1997; Mandal et al., 2002; Sella et al., 2009; Zhou et al., 2004).

The Surface Plasmon effect is defined as the collective oscillation of the free or conduction electrons, induced by an external electromagnetic field. As already mentioned above, this oscillation effect can be tuned by the changes on the nanocomposite morphology, especially in what concerns to the particular clustering size (at the nanometric scale), shape (spherical, elongated or even other more complicated forms) and distribution (either uniform or localized) (Dalacu & Martinu, 1999; Cho et al., 2000; Dalacu & Martinu, 2000). Other important factors are the distances of the metallic particles in the dielectric medium, which can be changed by changing their matrix populations, and the crystallographic structure of the dielectric oxide matrix (Mandal et al., 2002; Cho et al. 2004). A strong local field effect arises from the dielectric confinement and shows a maximum at the so-called SPR frequency, where the quantized collective motion of the confined free electrons is resonantly-coupled to the incident electromagnetic field, yielding characteristic absorption bands. This is exactly the basis for most of the upper referred application possibilities and examples. However, only metals with free electrons, and in particular those from the eleventh group elements of the periodic table (e.g. Au, Ag and Cu), possess Plasmon Resonances in the visible spectrum (Liz-Marzan, 2004), and thus restricting the available possibilities. This group of metals offer a quasi-free-electron behaviour on the UV-visible range, resulting, for example, in intense and attractive colourations.

The methods to fabricate these nanocomposite thin films, where metallic nanoparticles are dispersed in non-aqueous dielectric media (latex, polystyrene, TiO₂, SiO₂, among others), using for example Physical Vapour Deposition methods (PVD) or Chemical Vapour Deposition methods (CVD), is actually becoming one of the most important fields in specific areas of materials science, integrating a new aim for the use of nanoscience and nanotechnology (Walters & Parkin, 2008; Wang et al., 2006b; Armelao et al., 2006). PVD-based methods, such as reactive magnetron sputtering, have become established in the actual market as an important competitor to classic electrochemical processes (Navinsek et al., 1999; Fenker et al., 2004). The great advantage is that they allow overcoming the highly restrictive normative, namely the environmental ones, that are being applied on the decorative and protector electrochemical films industry.

Taking all the above considerations into account, this chapter intends to give a small contribute to the basic knowledge on the preparation, characterization and performance of nanocomposites coatings, consisting of gold nanoclusters dispersed in a titanium oxide dielectric matrix. Due to the high degree of flexibility on the basic preparation parameters, associated to an easy up scaling of the laboratory-based work to industrial environment, the reactive magnetron sputtering (DC) method was selected for the preparation of the nanocomposites, in the form of thin solid films. The tailoring of the SPR effect (the change on the size, shape and distribution of the noble metal – gold, clusters) was carried out by the application of an after deposition thin film annealing protocol.

2. Theoretical background

Surface Plasmon Resonance, SPR, in Metallic NanoParticles, MNP, is the result of the collective oscillations of the free electrons, induced by an external electromagnetic radiation. Its spectral characteristics depend on both MNP and host matrix properties. Let us recall the essential SPR features in a single metallic particle embedded in a dielectric matrix by considering a perfectly spherical particle and the dipole approximation of the Mie theory (Mie, 1908). This approximation is valid particles with a radius significantly smaller than the wavelength of the incident electromagnetic radiation. The Surface Plasmon Resonance condition is then given by:

$$\varepsilon_s + 2\varepsilon_h = 0 \quad (1)$$

where $\varepsilon_h = n_h^2$ is the dielectric constant of the host matrix and ε_s denotes the dielectric function of the metal. In the simple Drude model,

$$\varepsilon_s(\omega) = \varepsilon_\infty \left[1 - \frac{\omega_p^2}{\omega(\omega + i\Gamma_p)} \right] \quad (2)$$

where ε_∞ is a positive constant, and Γ_p is a Plasmon damping parameter (proportional to the electron scattering rate). This parameter depends on the nanoparticles size and has a direct and important effect on the width of a single SPR peak. For spherical Au nanoparticles, the following expression has been proposed (Mie, 1908):

$$\hbar\Gamma_p(R) = \hbar\Gamma_p(\text{bulk}) + g_s v_F / R = 0.0244 + 0.922g_s / R \quad [\text{eV}] \quad (3)$$

where v_F is the Fermi velocity, g_s is a geometrical factor of the order of unity, and R the nanoparticle radius (in nanometers). For the geometrical factor, a value of $g_s \approx 0.7$ has been suggested (Baida et al., 2009). The intensity of the resonance is inversely proportional to Γ_p and directly proportional to the particle volume (R^3).

$$\omega_p = \sqrt{4\pi n e^2 / (\varepsilon_\infty m^*)} \quad (4)$$

is the plasma frequency, where n corresponds to the free electron concentration and m^* denotes the effective mass. Assuming that $\Gamma_p \ll \omega_p$, Eqs. (1) and (2) enables to characterize the SPR frequency for a spherical nanoparticles, on the following form:

$$\omega_{\text{SPR}} = \frac{\omega_p}{\sqrt{1 + 2\varepsilon_h / \varepsilon_\infty}} \quad (5)$$

Equation (5) shows that the SPR spectral position is, in fact, independent of the nanoparticles size, but depending much on the dielectric constant of the host matrix. In order to achieve a SPR effect in the visible range, one is practically limited to the noble metals and still has to use host materials with sufficiently high dielectric constant. The width of the resonance is proportional to Γ_p , which increase for smaller particles due to an additional scattering mechanism, called surface scattering, becomes more important as R decreases. The intensity of the SPR peak is proportional to the particle volume.

The SPR characteristics are affected by the shape and orientation of the particles in the matrix if they are not spherical (Rodriguez-Fernandez et al. 2009). For example, axial-symmetric nanorods are supposed to produce two SPRs, with the characteristic frequencies given by:

$$\omega'_{SPR} = \frac{\omega_p}{\sqrt{1 + (\eta_{||}^{-1} - 1)\epsilon_h/\epsilon_\infty}} \quad \text{and} \quad \omega''_{SPR} = \frac{\omega_p}{\sqrt{1 + (\eta_{\perp}^{-1} - 1)\epsilon_h/\epsilon_\infty}} \quad (6)$$

where $\eta_{||}$ and η_{\perp} are geometrical factors, commonly known as depolarization coefficients (Landau & Lifshitz, 1984), which correspond to some non-negative numbers obeying the relation:

$$\eta_{||} + 2\eta_{\perp} = 1 \quad (7)$$

The first resonance takes place for electromagnetic waves polarized along the nanorod axis, while the second corresponds to the perpendicular polarisation. If nanorods are embedded in a matrix in a random-orientation fashion, then one would expect to observe both SPRs. If matrix, in a random-orientation fashion, then one should expect we approximate nanorods by elongated (prolate) spheroids with eccentricity e , the depolarization coefficients are given by:

$$\eta_{||} = \frac{1 - e^2}{e^3} \left(\frac{1}{2} \log \frac{1 + e}{1 - e} - e \right) \leq \frac{1}{3} \quad (8)$$

$$\eta_{\perp} = \frac{1 - \eta_{||}}{2} \geq \frac{1}{3} \quad (9)$$

Using these relations one can see that $\omega'_{SPR} < \omega_{SPR} < \omega''_{SPR}$. The two resonances corresponding to Eq. (6) merge into a single one determined by Eq. (5), when $\eta_{||} = \eta_{\perp} = 1/3$ (spherical nanoparticles).

Inter-particle spacing (i.e., the particle concentration) can also have an effect on the SPR intensity, peak position and width. It is related to an electromagnetic dipole-dipole interaction between the nanoparticles. These effects become considerable when the volume fraction of the particles is above $\approx 10\%$. The theoretical predictions (Landau & Lifshitz, 1984; Ung et al., 2001) indicate that increased volume fraction of gold MNP raises the SPR intensity and leads to a red shift of the position of the resonance. A typical effect of the SPR effect is the red shift of the absorption band, which is related to a change in the phase composition of the matrix: the transition temperature of the anatase to rutile TiO_2 . The two phases have different values of the refractive index, reported as $n_{\text{anatase}} = 2.5$ and $n_{\text{rutile}} = 2.9$ at $\lambda = 550 \text{ nm}$ (Song et al., 2005).

A model of the optical properties of the Au: TiO_2 composite films was performed in order to quantify the previous arguments.

3. Optical spectra modelling

To describe the correlation between the morphological/structural changes of the films (promoted by an external input such as an annealing treatment) with the optical spectra of the nanocomposite films, theoretical models of the effective dielectric function using the

approaches known in the optics of composite and layered media the optical behaviour can be developed.

Considering that the wavelength of the electromagnetic radiation is much larger than both the particle size and the inter-particle distance, the composite medium can be described by an effective dielectric function (EDF). There are two well-known mean-field theories for the EDF calculation, proposed, respectively, by Maxwell-Garnett and Bruggemann (Genzel & Kreibig, 1980; Shalaev, 2000). The first one is valid in the low-concentration limit (volume fraction of the particles $f \ll 1$), while the second can be applied when both f and $(1-f)$ are not too small. Some further studies are published in the scientific bibliography (Genzel & Kreibig, 1980; Shalaev, 2000). For most of the nanocomposites usually studied, one has $f \approx 0.1$, and none of these classical approximations is suitable. The Maxwell-Garnett (MG) approximation (assuming independent polarisable particles) can be improved and, consequently, extended to higher f by taking into account the dipole-dipole interactions between the particles (Vasilevskiy & Anda, 1996; Vasilevskiy 2000). This formalism will be hereafter referred to as renormalized Maxwell-Garnett (RMG) approximation, since it considers a polarizability of the particles renormalized by their interactions (M. Torrell et al., 2010b). It is conceptually equivalent to the average T-matrix approximation known in the theory of disordered media (Shalaev, 2000). The RMG approach has been generalized to non-spherical particles in Ref. (Vasilevskiy & Anda, 1996).

An individual particle, polarized by the external electromagnetic field but not interacting with other particles, is described by a bare polarizability tensor with the principal components given by:

$$\alpha_i = \frac{\varepsilon_s/\varepsilon_h - 1}{(\varepsilon_s/\varepsilon_h - 1)\eta_i + 1} \left(\frac{V}{4\pi} \right) \quad i = 1, 2, 3. \quad (10)$$

Here V is the particle volume and η_i are the depolarization coefficients mentioned in the Introduction (two of them coincide if the particle possesses axial symmetry). For a spheroid with (small) eccentricity e , they are given by (Landau & Lifshitz, 1984):

$$\eta_{\perp} = \frac{1}{3} \mp \frac{1}{15} e^2, \quad i = 1, 2; \quad \eta_{\parallel} = \frac{1}{3} \pm \frac{2}{15} e^2, \quad i = 3, \quad (11)$$

where the two signs correspond to the prolate (elongated) and oblate shape, respectively.

Within the classical MG approximation, the effective dielectric function, ε^* , of the composite medium containing a small fraction of separate inclusions is obtained from the relation:

$$\frac{\varepsilon^* - \varepsilon_h}{\varepsilon^* + 2\varepsilon_h} = \frac{4\pi}{3} N \bar{\alpha}, \quad (12)$$

where $N = f/V$ is the particle's concentration and $\bar{\alpha} = \sum_i \alpha_i / 3$.

The dipole-dipole interaction between the particles renormalizes their average polarizability, which becomes:

$$\alpha^* = \frac{2\bar{\alpha}}{\gamma} \left\{ 1 - \frac{\sqrt{1-\gamma(1-\delta)}}{2} \left[\sqrt{1-\nu^2} + \frac{\arcsin(\nu)}{\nu} \right] \right\}, \quad (13)$$

$$\text{where } \nu^2 = \frac{3\gamma\delta}{1-\gamma(1-\delta)}, \quad \gamma = f\left(\frac{4\pi\bar{\alpha}}{3V}\right)^2 \quad \text{and} \quad \delta = \pm\left(\frac{e^2}{15}\right)\frac{\epsilon_s/\epsilon_h - 1}{\epsilon_s/\epsilon_h + 2}$$

Note that $\alpha^* \rightarrow \bar{\alpha}$ when $f \rightarrow 0$, Eq. (13) is valid for uniform size particles and the more sophisticated formulae, taking into account the nanoparticles size dispersion, can be found in Ref. (Vasilevskiy & Anda, 1996). The effective dielectric function within the RMG approach is calculated by Eq. (12) with α^* replacing $\bar{\alpha}$. Once the dielectric function $\epsilon^*(\omega)$ is described it is possible to calculate the optical properties of the thin film nanocomposites. For thin films the eventual multiple reflections at the interface(s) have to be taken into account, causing the interference effect also detected in these materials for low concentrations of nanoparticles or very small sizes. When the dielectric functions of the film and the substrate are known, the most convenient method is to use the transfer matrix formalism to calculate the transmission and reflection spectra.

Calculated absorption spectra are presented in figures 1 through 3. As one can see from figure 1, the dipole-dipole interaction (taken into account within the RMG approach) becomes increasingly important as the volume fraction of Au nanoparticles increases. All the other results shown were obtained using the RMG approximation.

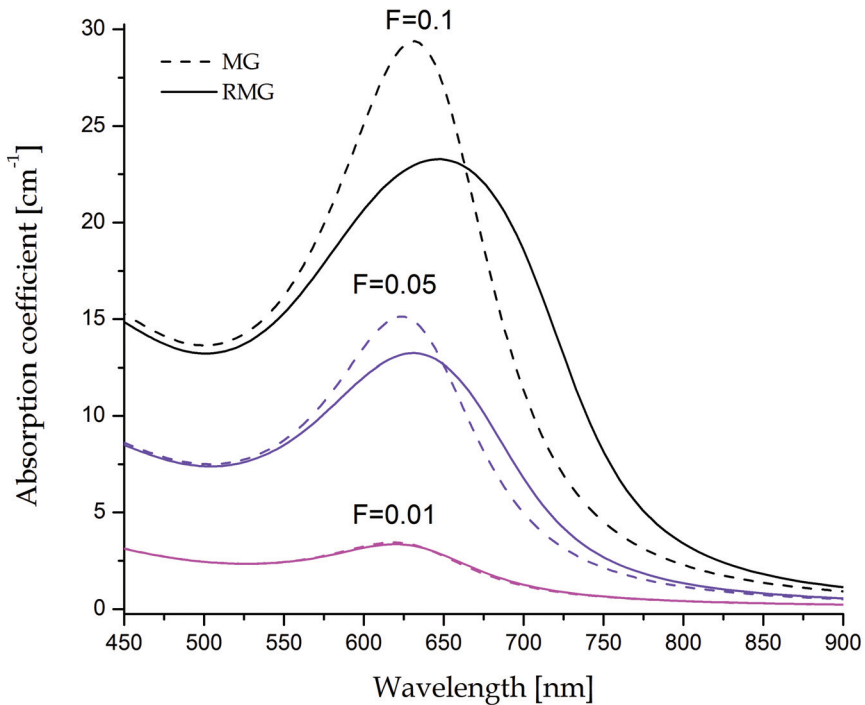


Fig. 1. Simulation of the absorption spectra of Au:TiO₂ nanocomposites with different volume fraction of Au considering spherical clusters of 10 nm, calculated using the standard MG and RMG approximations.

Figure 2 shows that a decrease of the mean nanoparticles radius, $\langle R \rangle$, results in a broader absorption spectrum while the peak position remains practically unshifted. Contrary to what one might expect, size dispersion does not produce an additional inhomogeneous broadening of the absorption band (as it is typical of semiconductor nanoparticles). On the contrary, the absorption peak becomes slightly narrower and higher. For the same $\langle R \rangle$, a broader size distribution increases the number of large nanoparticles, which absorb more strongly (notice that $\bar{\alpha}$ is proportional to the volume) and are characterized by a smaller homogeneous broadening.

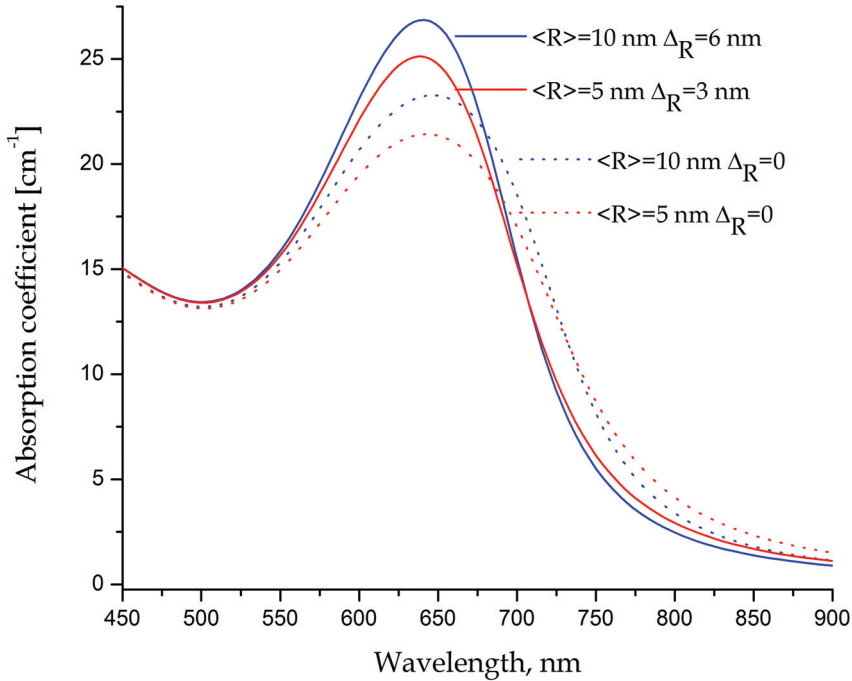


Fig. 2. Simulation of absorption spectra of nanocomposites containing Au spherical nanoparticles of different mean radius and size dispersion.

Figure 3 demonstrates the effect of nanoparticles shape on the SPR. It is clearly seen that there are two separate resonances already for moderately elongated nanoparticles ($e = 0.75$ corresponds to an aspect ratio of just 1.25). For nanorods $\eta_{||} \rightarrow 0$ and the low-frequency SPR should be strongly red-shifted with respect to ω_{SPR} characteristic of spherical nanoparticles.

4. Nanocomposite films production and characterization techniques

It has been demonstrated that one of the easiest methods to produce nanocomposites thin films of noble metal nanoparticles embedded in dielectric matrix is the magnetron sputtering technology. In this chapter, a one-step deposition has been used to produce the host dielectric matrix (TiO₂) and the gold nanoparticles.

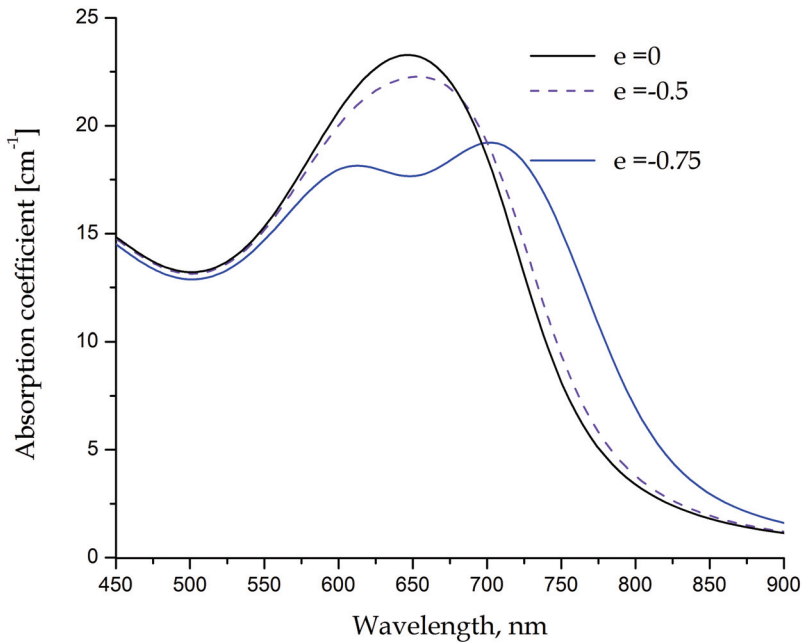


Fig. 3. Simulation of the absorption spectra of nanocomposites containing Au nanoparticles of spherical shape with different eccentricity.

To deposit a batch of Au:TiO₂ thin films onto silicon (100) and quartz substrates, a laboratory-sized magnetron PVD deposition apparatus was used. The rectangular magnetrons were disposed vertically in a closed field configuration in the deposition chamber. Only one electrode was powered, composed of a titanium target (99.6 % purity), with different amounts of Au pellets (with a 40 mm² surface area and approximately 2 mm thickness), symmetrically incrustated in its preferential erosion zone. A constant dc current density of 100 A m⁻² was applied. A mixture of argon and oxygen was injected with constant fluxes of 60 sccm and 10 sccm, corresponding to partial pressures of 0.3 Pa and 0.08 Pa, respectively. The final working pressure (\approx 0.38 Pa) and deposition temperature (about 150 °C) were kept approximately constant during the entire coating deposition process. The temperature of the coated substrates was monitored with a thermocouple placed close to the surface of the substrate holder.

Samples were placed in a rotating substrate holder in grounded condition. All samples were heat treated through annealing experiments in vacuum, after film deposition. Annealing treatments were carried out in a secondary vacuum furnace, after its evacuation to about 10⁻⁴ Pa. The selected temperature range varied from 200 to 800 °C, and the isothermal period was fixed to 60 min, after a heating ramp of 5 °C/min. The samples cooled down freely in vacuum before their removal to room conditions. The chemical uniformity and the atomic composition of the as-deposited samples were measured by Rutherford Backscattering Spectroscopy (RBS) using either a 1.4 or 1.75 MeV proton beam and a 2 MeV ⁴He. The scattering angles were 140° (standard detector, IBM geometry) and 180° (annular detector), and the incidence angle was varied between 0 and 30°. Composition profiles for the as-

deposited samples were generated using software code NDF (Barradas et al., 1997). For the ^{16}O data, the cross-sections given by Gurbich (Gurbich, 1997) were used. The analyzed area was about $0.5 \times 0.5 \text{ mm}^2$. In addition, for some samples, Particle Induced X-ray Emission (PIXE) measurements were performed to check for impurities.

All coatings were characterized by X-ray diffraction (XRD), using a Philips PW 1710 diffractometer (Cu-K α radiation), operating in a Bragg-Brentano configuration. XRD patterns were deconvoluted assuming to be Voigt functions to yield the peak position, integrated intensity and integrated width (IntW). The average nanoparticles size was determined by three different methods (Integral Breath, Fourier analysis, and Scherrer formula), using the Au-fcc (111) peak parameters obtained from the XRD patterns. The thickness and morphology of the films were studied by NanoSEM FEI Nova 200 scanning microscopy and transmission electron microscopy (TEM) using a Hitachi 800H apparatus. TEM microscopy has been used also to characterize the shape, size and distribution of Au nanoparticles with respect to the annealing temperature. Optical properties (Transmittance-absorbance) were characterized using a UV-Vis-NIR Spectrophotometer (Shimadzu UV 3101 PC) in the spectral range from 200 nm to 900 nm. SEM images of the coatings have been obtained by a NanoSEM FEI Nova 200 scanning microscopy.

5. Experimental results and discussion

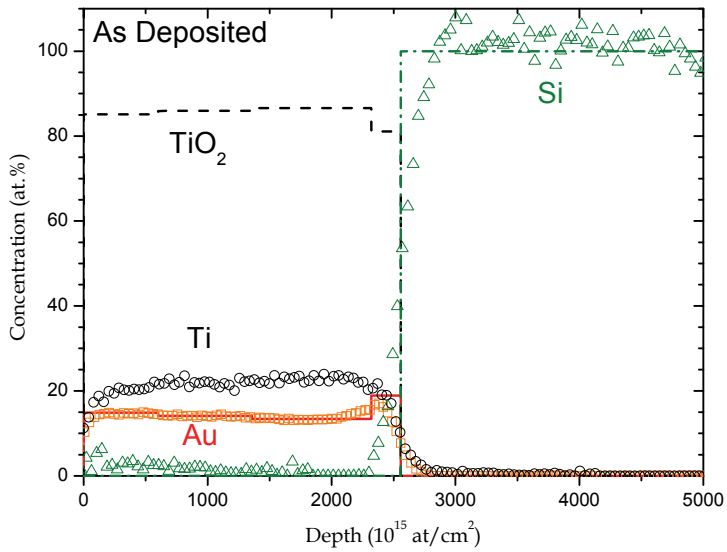
5.1 Composition and structure

The Au concentration in the samples, studied by RBS, was found to be close to 12 at. %. The elemental concentration analysis also revealed that the ratio O/Ti was always very close to 2, which suggests the presence of a stoichiometric-like TiO_2 matrix, with no apparent variation during the annealing experiments (as far as it concerns the resolution of the measurement techniques). The optimum Au nanoparticles concentration that was placed in the films has been previously studied and published. The Au volume fraction, f_{Au} , was determined as being close to 0.18 (considering $\rho(\text{Au}) = 19.3 \text{ g/cm}^3$ and $\rho(\text{TiO}_2) = 4 \text{ g/cm}^3$). It was already known, that for this type of nanocomposites, the range between 10 and 20 at. % Au conducted to the highest and most evident SPR activity on the optical properties (Armelaio et al., 2006).

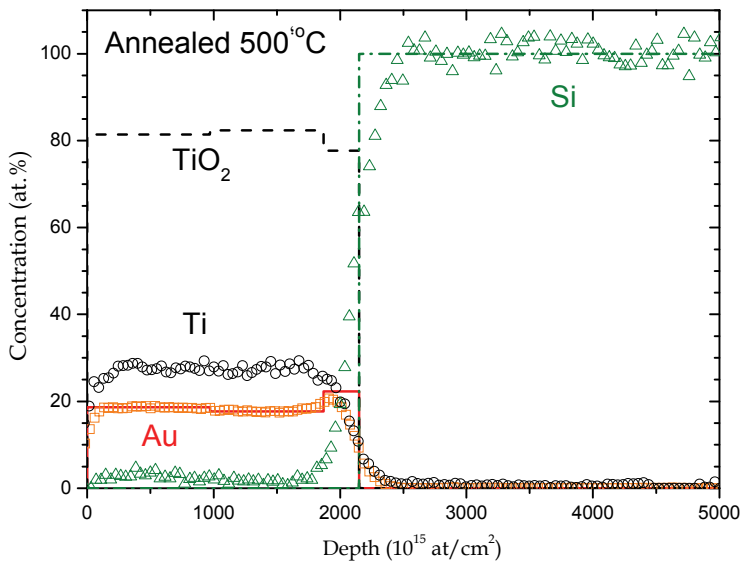
Beyond the annealing treatment, onset of a composition gradient could be expected due to enhanced Au diffusion into the substrate (Alves et al., 2011). However, it is not seen until the 800 °C annealing temperature as revealed by the RBS analysis (Figure 4). For temperatures up to 700 °C, the composition profile analysis indicates that the samples are practically homogeneous across the film thickness. These results can have an influence on the optical properties of the films.

Measurements of the coatings thickness were carried out by scanning electron microscopy observation (cross-section view, figure 5). The cross section confirms that the films have approximately 300 nm. The cross-section micrograph shown in Fig. 5 reveals that the film grows in a compact and dense featureless structure, without any special growing characteristics (featureless growth).

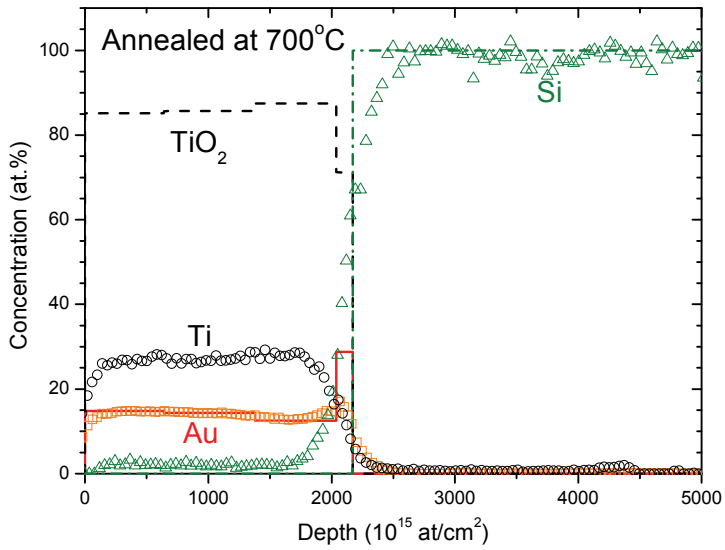
In spite of the small round features observed in SEM micrographs, the use of backscattering electron images undoubtedly showed that no signs of Au agglomerations were detected (in the as-deposited films), at least within the 2 nm maximum lateral resolution of the used SEM instrument. From SEM micrographs, one cannot take any conclusive results from the annealed samples, which show very similar results, without any clear evidences in the



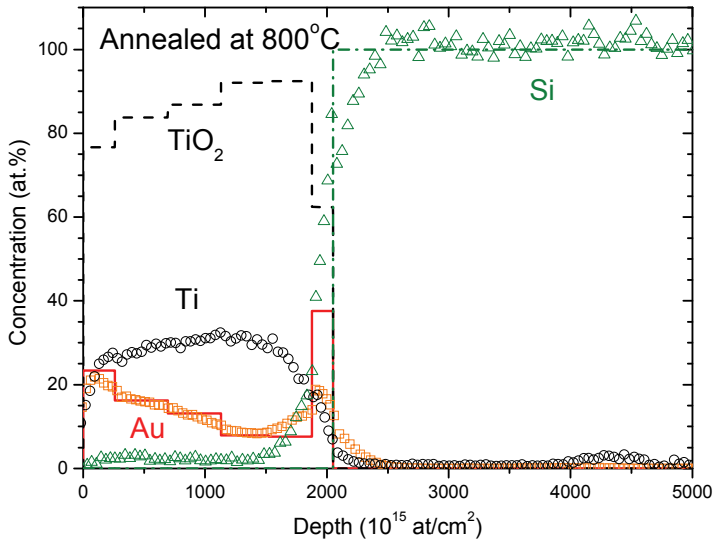
a)



b)



d)



e)

Fig. 4. Concentration profile of the nanocomposite annealed at: a) As Deposited b) 500°C c) 700 °C and e) 800 °C.

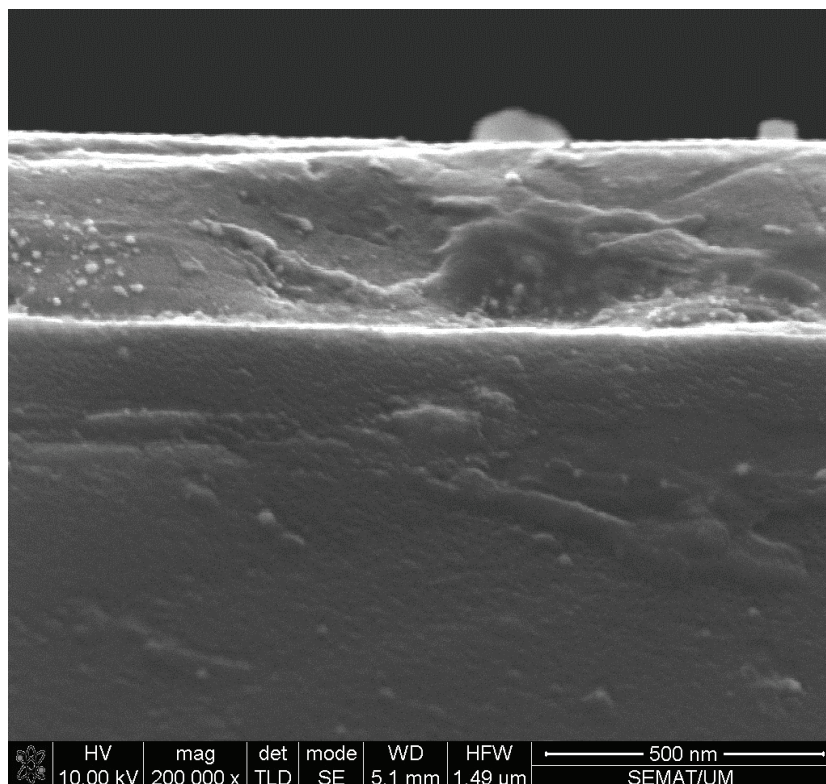


Fig. 5. Cross-section of the $\text{TiO}_2\text{:Au}$ nanocomposite obtained by SEM.

morphological variations that may have occurred as a result of the annealing process. In order to check for clear evidences of any (micro) structural changes, which could then be used to correlate with the overall coatings behaviour, a set of XRD experiments were carried out. Diffraction profiles of all the samples, from as-deposited and annealed samples were then characterized in detail. Figure 6 shows the diffractograms obtained for the samples prepared as a function of the annealing temperature.

The set of results from the whole series of samples evidences one of the main information of this research: a clear change on the crystallographic structure of the matrix (TiO_2) and on the Au nanoparticles. The as-deposited films show an amorphous structure, without any visible traces of crystalline Au or any of the known crystalline phases of titanium oxides. However, the annealing process lead to the crystallization of the amorphous films, firstly by the detection of crystalline Au, followed by some crystallization of the TiO_2 matrix, but with this last occurring only for temperatures above 300 °C. The presence of Au, with a face centered cubic-like structure [ICDD card N° 04-0787], is evidenced for annealing temperatures above 200 °C, as evidenced by the presence of the (111) peak, localized at $2\theta \approx 38.2^\circ$, as well as the (200) peak, at $2\theta \approx 44.4^\circ$, with this last one appearing for annealing temperatures above 400 °C, exactly at the temperature where the first signs of TiO_2 crystallization have also appeared.

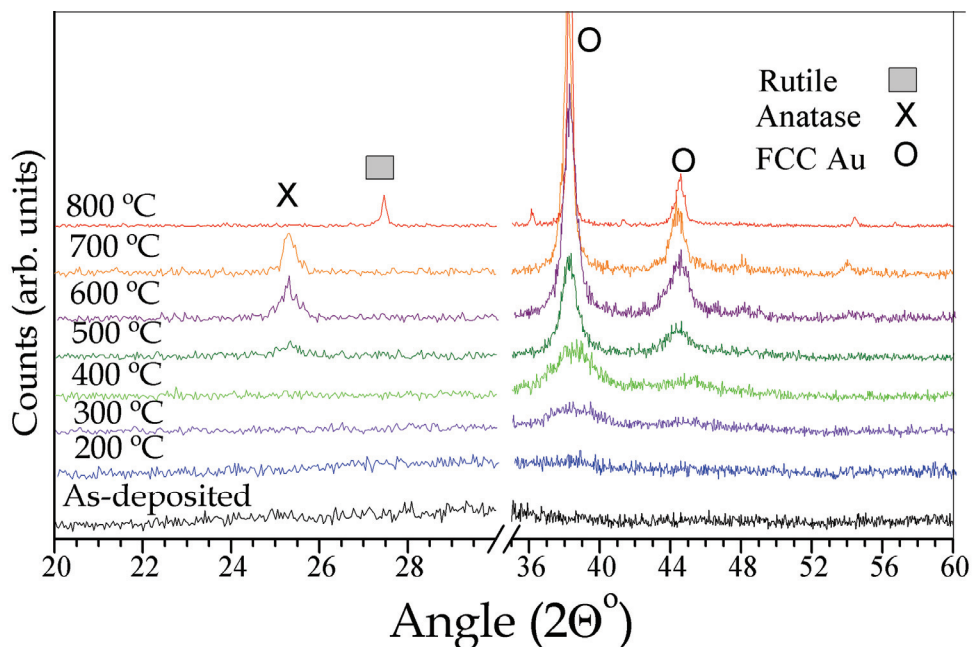


Fig. 6. X-Ray diffractogram of the nanocomposites annealing at different temperatures.

If the results of the XRD patterns are carefully looked, it can be also concluded that the initial broad Au (111) peak, which starts to be detected at an annealing temperature of 300 °C, becomes sharper. This increase of the intensity of the peaks, that also become narrower, is led by the growth of the nanoparticles, as a result of the diffusion and coalition of Au atoms. The Au clusters grow in size as the annealing temperature increases, followed by some crystallization of the amorphous oxide dielectric matrix that occurs at an annealing temperature above 400 °C. The diffraction patterns seem to indicate that the amorphous TiO₂ matrix crystallizes in the anatase form [ICDD 21-1272], as in fact suggested in similar studies where annealing of TiO₂-based films is involved (Manera et al., 2008). These results suggest that, at 500 °C, a nanocomposite film consisting of a crystalline dielectric TiO₂ matrix embedded with Au clusters was formed. At annealing temperatures above 700 °C, the TiO₂ phase changes from the anatase to the rutile [ICDD 21-1276] structure. This is in accordance with results available in the literature (Hasan et al., 2009; Martin et al., 1997). The access of this nanocomposite structure up to 500 °C should be responsible for the appearance of SPR activity, which can be used to tune some of the film properties, namely the optical ones.

The role of the changes in the dielectric matrix have also been studied, and found to affect the position of the absorbance peak of the SPR. It is known that the effective dielectric function of the matrix has a direct dependence on the refractive index. A crystallization of TiO₂ structure promotes an increase in the refractive index. This change brings an increase on the dielectric function values leading a red shift of the absorbance peak. The XRD shows that the TiO₂ transforms from an amorphous phase, with a refractive index $n = 2.2$, to anatase, with a refractive index $n = 2.6$, and finally transforms to rutile that has a refractive index $n = 2.9$.

The overall set of results that were obtained in the frame of the presented work seems to indicate that the structural changes of the Au clusters may have significant importance for the SPR activity. As it is further detailed on the following sections, the first evidences of the Au crystallization (300 °C) are found to correspond to the main changes on the optical properties (reflectivity, colour and absorbance), as well.

Figure 7 shows the results of the average size (diameter) of the gold particles in the nanocomposite films, based on three different calculations, integral-Breadth, Fourier analysis and Scherrer experimental formula, applied to the XRD patterns. The values of gold particles (clusters) size range from about 2 nm at 300 °C to approximately 30 nm at 800 °C. In accordance to the results plotted in figure 7, the Au particles are confined on the nanometrical scale, which growth led by the diffusion of the Au atoms, promoted by the annealing treatments. The SPR activity and the related changes on the optical properties are directly affected by this growth. Figure 7 clearly illustrates a continuous increase of the Au particles size in this temperature range. The main SPR activity has been reported between 400 °C and 600 °C, where the average grain size is within 3 nm to 15 nm (M.Torrell et al., 2010a) At temperatures below 300 °C the size of Au clusters is too small to be considered as a crystalline structure phase dispersed on the dielectric matrix.

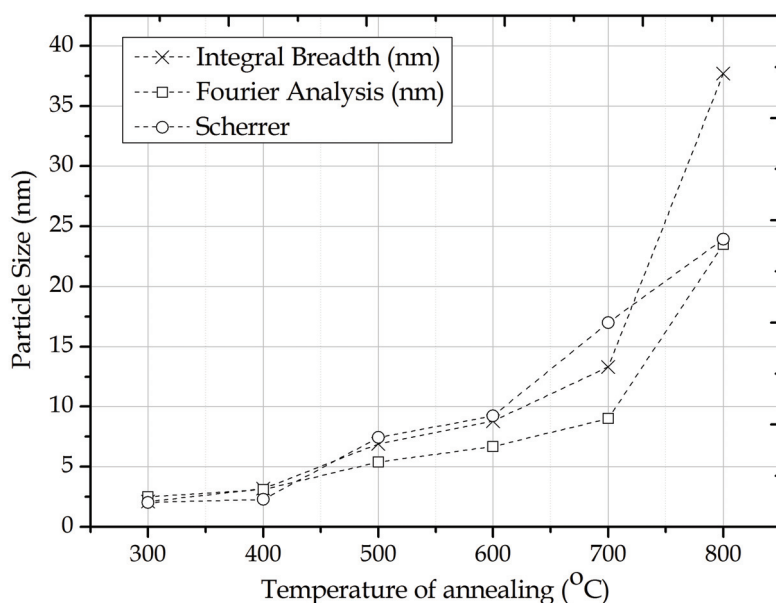
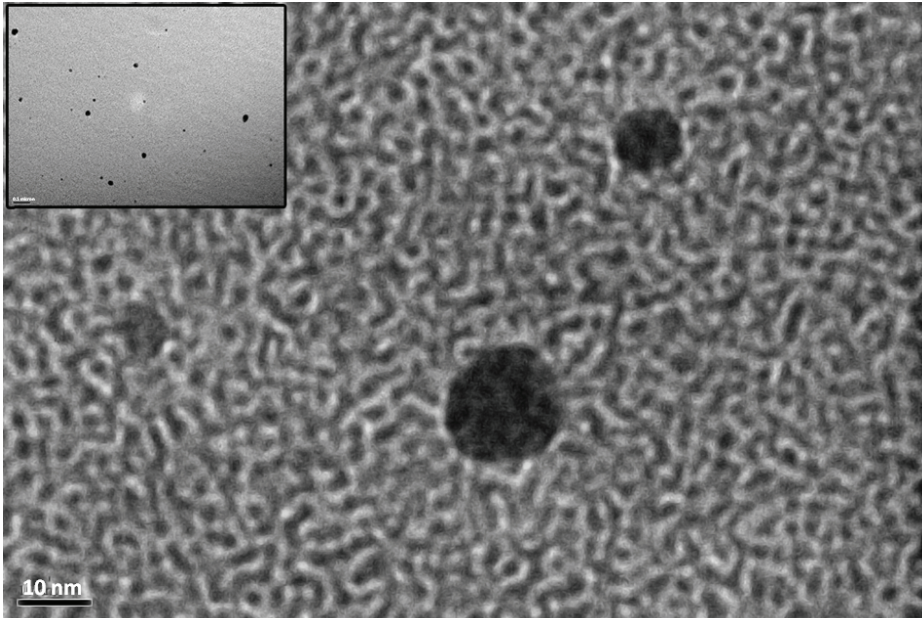
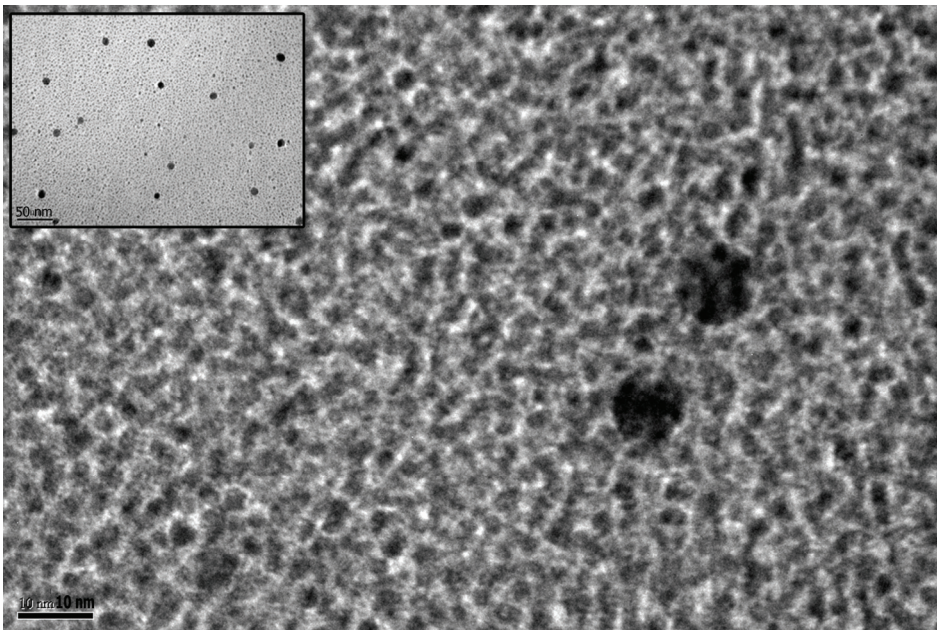


Fig. 7. Size of the Au clusters determined from the XRD Au-fcc (111) peak.

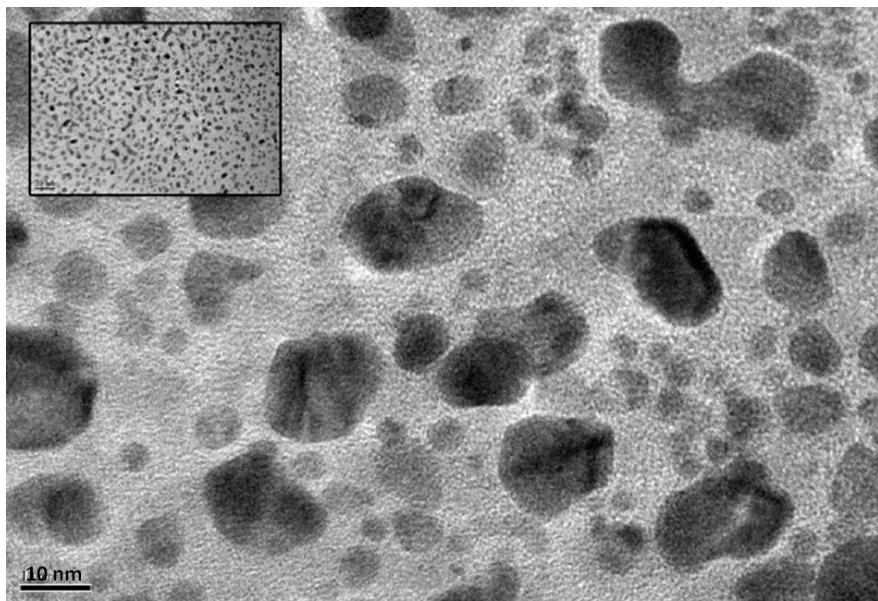
The nanoparticles growth and the matrix crystallization studied by XRD have been confirmed by transmission electron microscopy (TEM). The micrographies obtained by TEM of the samples annealed at different temperatures confirm this nanoparticles growth process that starts to be a fine atomic dispersion, and start to coalesce with the annealing treatments. Figure 8a) shows the TEM micrographs of the as-deposited sample. The Au nanoparticles are present just as an atomic dispersion of small nanoparticles in an amorphous matrix.



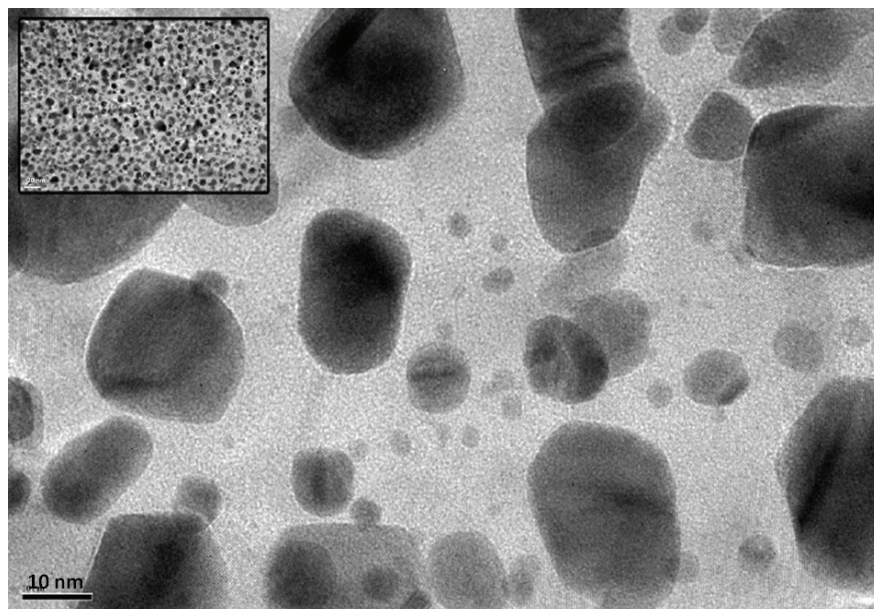
a)



b)



c)



d)

Fig. 8. TEM micrographs of the a) as-deposited sample; b) 300 °C annealed sample; c) 500 °C annealed sample and d) TEM micrographs of the 700 °C annealed sample.

Figure 8b) shows the sample annealed at 300 °C, where the Au nanoclusters start to have sizes larger than 2-3 nm, allowing their detection by XRD analysis. After annealing for 1 hour at 500 °C, the Au nanoclusters achieve average sizes around 10-12 nm. They show a homogenous dispersion on the matrix and quite symmetric spherical shape as can be observed in figure 8c). In this figure, and as it is confirmed by the electron diffraction results, the matrix starts to crystallize. The sample analysed by TEM, shown in figure 8d), was annealed at 700 °C. The nanoclusters shows sizes around 15-20 nm and a decrease on their spherical symmetry. At this annealing temperature, the XRD analysis evidences a higher degree of crystallization of the TiO₂ matrix. Analyzing the nanoclusters size by the TEM micrographs, one can start to define three different groups of samples (or different groups of annealing temperatures) that that may be correlated with their optical properties. The first group of samples (group I) may include the as-deposited sample and the one that was annealed at 300 °C, where the Au is still dispersed with very small cluster sizes in the limit of what can be considered and detected as a crystal (group I). In this first group, the TiO₂ matrix is completely amorphous. The second group (group II) includes the samples annealed from 400 to 600 °C, represented in figure 8c) by the sample annealed at 500 °C. The Au nanoclusters are homogeneously dispersed on the matrix, forming small nanocrystals with quite spherical shape. The matrix starts to crystallize as anatase. The last group (group III) includes the samples annealed at higher temperatures (700 and 800 °C). In these samples, it is detected diffusion of the clusters to the inner and outer interfaces (Figure 4). It is noticed the tendency to lose the spherical symmetry of the nanoclusters that present sizes above 20nm. The TiO₂ matrix is mostly crystallized and the anatase phase transforms to rutile.

5.2 Optical properties

The SPR effect is mainly detected by the changes on the optical properties of the nanocomposite films. The influence of the size and shape of the Au clusters embedded into the dielectric matrix can be accessed by reflectivity, absorbance and colour measurements. All these properties have been characterized and are discussed in this chapter, and correlated with the different morphologies of the films described in the previous section. Important changes of the reflectivity behaviours were found in the annealed samples, when compared to the as-deposited ones.

The interferometric optical behaviour disappears at 300 °C as can be observed in figure 9, which correlates with the change from group I samples to those from group II, as stated in the previous section. The reflectance spectra show a clear change from interference-like to intrinsic metallic like behaviour, similar to the one obtained for pure Au (Wang et al., 2006c), with the increase of the annealing temperature. The samples of groups II and III show a minimum of reflection close to 500 nm, followed by a progressive increase of the reflection intensity in the highest wavelength of the visible region of the electromagnetic spectrum.

The minimum in the reflectivity intensity has been detected at similar values of the wavelength (500 - 515 nm) with a slight blue shift with increasing annealing temperatures. Furthermore, a clear tendency for having steeper positive slope of the reflection at higher wavelengths than the minimum of the reflectance is detected. This becomes more evident with the increase of the temperature.

A clear correlation between the changes of the reflectivity and of the other optical properties with the XRD results is found. In fact, the disappearance of the interferometric features in the reflectance spectra occurs at the same annealing temperature where the Au

crystallization starts to be detected. The relatively low values of the reflectivity at shorter wavelengths are characteristic of high free electron density systems (Yate et al., 2009).

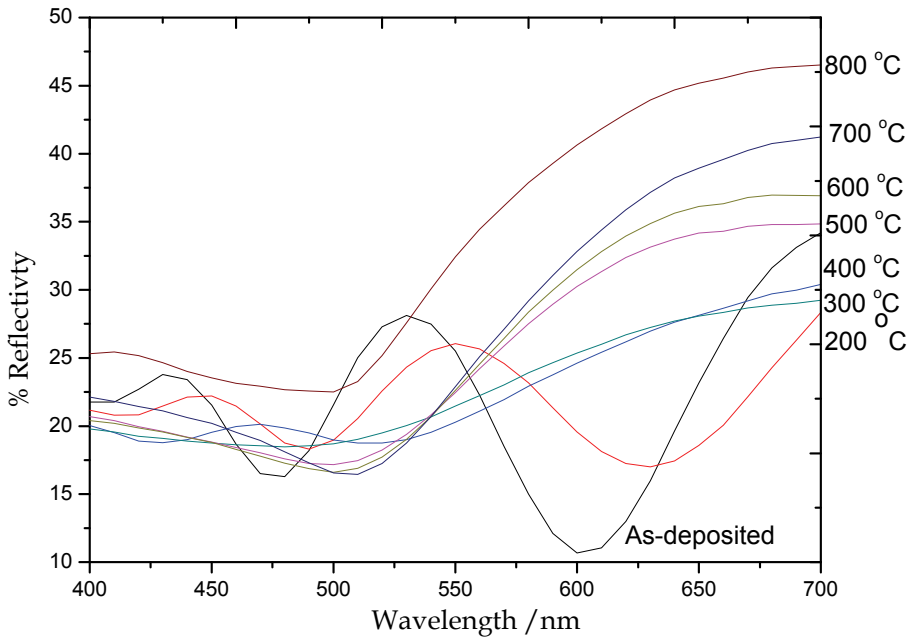


Fig. 9. Reflectivity spectra of the nanocomposites samples annealed at different temperature.

Increasing the annealing temperature, the films of group II and group III change their behaviour in comparison with the as deposited sample, from interference-like to intrinsic-like, as revealed by the surface colour tones that tend to a red-brownish colour, in comparison to the interferometric tones of the as-deposited and 200 °C annealed samples (group I), figure 10. As evidenced in figure 6, associated with the first change on the reflectivity trend, a broad peak positioned at $2\theta \approx 38.1^\circ$ was detected in the XRD pattern, which was indexed as Au (111) planes. At higher temperatures, the Au (111) XRD peaks become narrower and more intense, indicating higher crystal sizes (Figure 7), which is followed by the increase of the reflectivity and the complete vanishing of the interference bands (Figure 9).

The detailed analysis of the colour changes due to the SPR effect was studied by the CIELab colour space. The evolution of the colour parameters is shown in figure 10. The change from the interference tones towards the intrinsic red-brownish, is followed by a significant increase of the a^* parameter (redness) and a slight increase of the b^* parameter (yellowness) of the CIELab scale. The most abrupt change in the a^* parameter is detected in the 300 °C annealed sample, again coincident with the detection of Au precipitation and the transition from interference to intrinsic behaviour shown in the reflectivity curves (transition to group II samples). The magnitude of the change of the colour parameters is directly correlated with the magnitude of the change of the reflectivity values reported on figure 9.

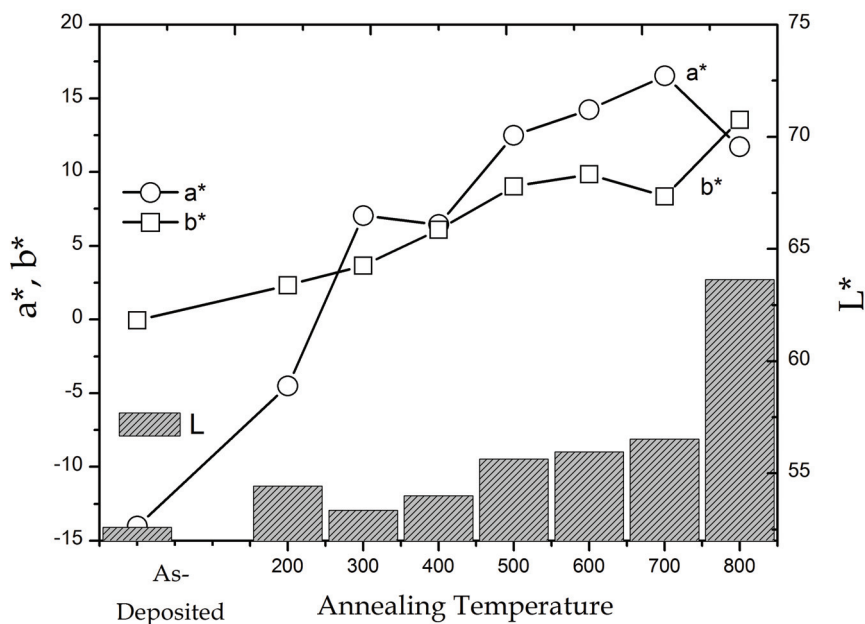


Fig. 10. Cielab colour space parameters of the as deposited and annealed samples.

In order to characterise the Surface Plasmon Resonance (SPR) activity, and correlate it with the changes in the morphology described above, the absorbance measurements ($A = \ln 1/T$) are presented in the figure 11. SPR is manifested as a distinct peak in the absorbance spectrum (Lee et al., 1999, Torrell et al., 2010c), and has been reported in several nanocomposite materials through the localization of an absorbance band on the visible wavelength range (Takele et al., 2006; Dalacu & Martinu 1999; Lee et al., 1999, Manera et al., 2008; Zakrzewska et al., 2003; J. Vosburgh & Doremus 2004.). Figure 11 shows the absorbance behaviour of the films analysed.

At the same wavelength, for the same annealed sample, higher reflectivity is linked to lower absorbance intensity. The changes in the absorbance spectra can be detected already at 300 °C, also confirming the first crystallization evidences through the precipitation of the Au clusters.

It is important to highlight that the Surface Plasmon Resonance activity or effect starts to be evident for higher annealing treatments. At temperatures of 500 °C the transmittance of the sample is close to 0 for a wide range of wavelength values, so the absorbance cannot be measured accurately. When the annealing temperature is increased, the optical density increases, but a slight red shift is also detected, together with an enhancement of the absorbance peak intensity. The absorbance peak is shifted from 587 nm to 610 nm. The peak red shift of the Au:TiO₂ samples has to be ascribed to different factors. The first is the growth of the nanoparticles, that is also related, at temperatures above 600°C to a drop on the spherical symmetry, and the variance in the dielectric constant of titanium oxide matrix that exist as different ratios of amorphous/anatase phases due to the different annealing treatments (Lee et al., 1999; Wang et al. 2005) are some of these factors. So the matrix

presents a different dielectric constant for each annealing temperature modifying the energy of the SPR absorption, located at larger wavelengths for more crystalline matrixes (higher annealing temperatures).

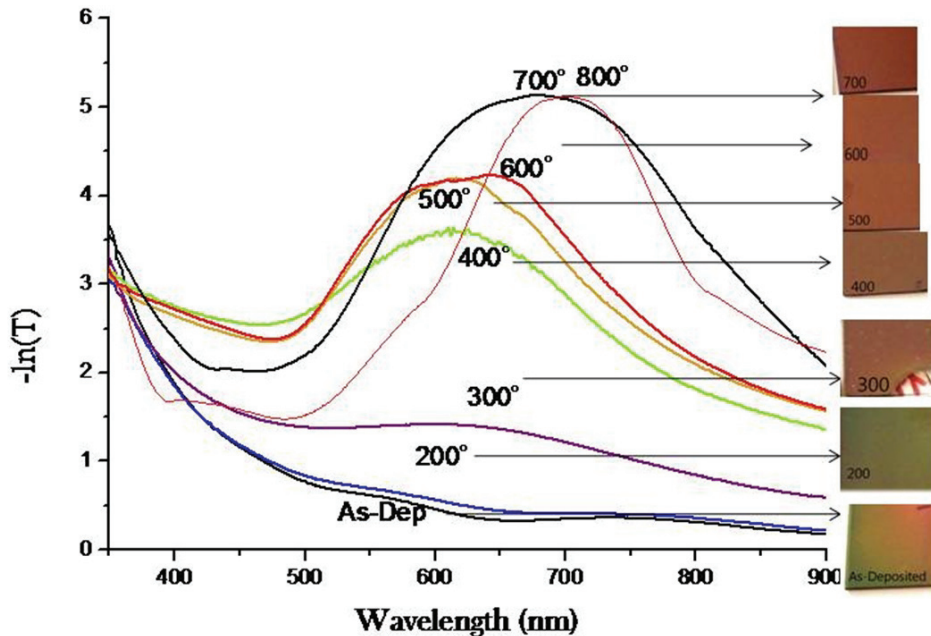


Fig. 11. Absorption spectra of the as deposited and annealed samples.

In general, the absorption peaks are relatively broad, especially those of samples annealed at low temperatures. It is well known that SPR activity depends strongly upon the morphology of the nanoparticles, namely the size and shape of the metal clusters (Lee et al., 1999; Manera et al., 2008; Dalacu & Martinu 1999). Considering a global analysis, the same three groups of samples are clearly defined in the morphological and optical results. The first group of samples (as-deposited and 200 °C annealed sample) reveal interference-like behaviour (both in reflectance and absorbance), with a surface tone characteristic of interference coloured materials (rainbow-like aspect). The samples from the second group (300, 400 500, 600 °C annealed samples) show low absorbance results and the colour tones change clearly to intrinsic-like ones, which can be characterized as light red brownish. Finally, there is a group of samples with higher SPR behaviour (samples annealed at 700 °C and higher temperatures). At these temperatures the spherical symmetry of the particles starts is lost and the cluster size is significantly larger. This higher effect of the SPR on the samples annealed at temperatures at 500° C or higher, can be clearly seen on the reflectance (Figure 9), colour coordinates (Figure 10) and absorbance (Figure 11) results. It is important to highlight that TiO₂ films do not show any of these optical changes under the same heat treatment (Dakka et al. 2000).

Once all the experimental results and the theoretical models are exposed, the reasons of the changes in the optical properties are clarified. The models indicate that the red shift of the

absorption band is produced by the change of the dielectric constant of the host material. The matrix crystallization from amorphous to the anatase and rutile phases increase the refractive index producing a change on the dielectric function that leads to the red shift, while the band broadening is caused by the break of the spherical symmetry of the nanoparticles leading to the splitting of the SPR frequency ($\omega'_{SPR} < \omega_{SPR} < \omega''_{SPR}$). The growth of elongated nanoparticles is characteristic of samples annealed at 700 - 800 °C (zone III) and it is probably related to the coalescence of smaller nanoparticles. It is important to highlight that an increase on the size of the nanoparticles leads to the growth of the SPR intensity but does not affect its position, as long as the characteristic wavelengths are much larger than $\langle R \rangle$ and the typical inter-particle distance.

In order to summarise and correlate the experimental results obtained on the morphology and optical properties of the nanocomposites, figure 12 shows the SPR absorption peak position and the Au clusters size. It's clear the correlation between the cluster grow, that it is also a parameter that is correlated with the crystallinity of the samples, and after 500°C annealed a drop on the Au particle symmetry, and the red shift of the absorption peak position.

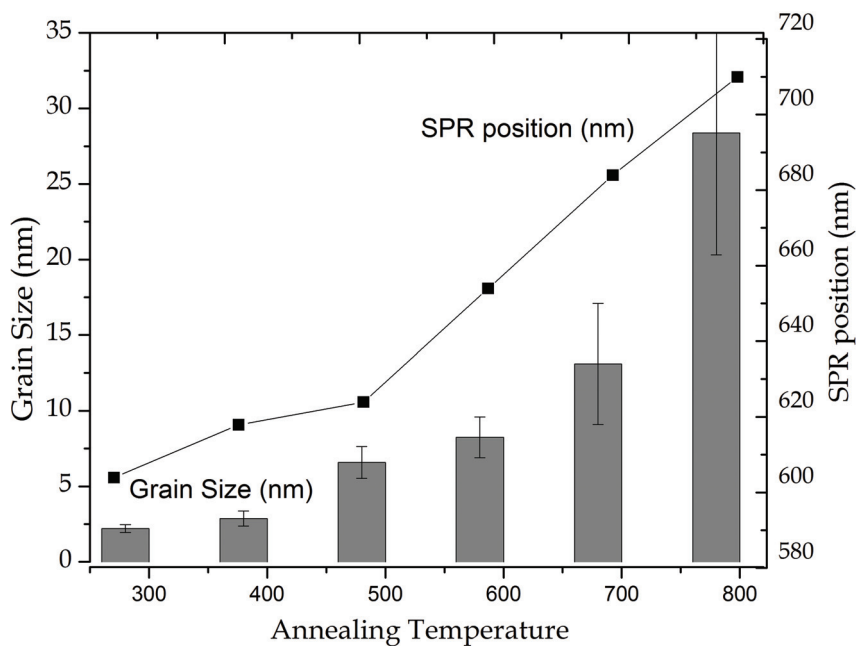


Fig. 12. SPR absorption peak red shift correlated with the Au cluster growth.

6. Conclusions

Comparing globally the overall set of results obtained for different annealing temperatures, we can conclude that the as-grown and low-temperature (zone I) annealed TiO₂/Au

composite films do not reveal a SPR absorption because there are just clusters of few Au atoms (< 1 nm, not detectable by XRD) present in these samples. Higher annealing temperatures (corresponding to zones II and III) are required to produce gold NPs and, consequently, the SPR effect on the optical spectra. Such annealing treatments affect both the TiO₂ matrix, in what concerns its crystalline/amorphous structure and phase composition, and the metallic phase, not only changing the nanoparticles size but also the shape. The morphological modifications are evidenced by the TEM images, XRD data and the optical parameters. The experimental data are supported by the theoretical models. The red shift of the SPR band is mainly produced by the change of the dielectric constant of the host material due to its crystallization while the band broadening is caused by the break of the spherical symmetry of the nanoparticles leading to the splitting of the SPR frequency. The growth of elongated nanoparticles is characteristic of samples annealed at 700 - 800 °C (group III) and probably is related to the coalescence of smaller nanoparticles. Presented results show that the characteristics of the SPR resonance can be tuned by choosing the appropriate annealing temperature, namely, it is possible to change the SPR position in the range of approximately 610-710 nm and also the width of the absorption band. The "one step" co-sputtering of a Ti-Au target, followed by an appropriate thermal treatment, is a useful way to produce composite TiO₂/Au films with adjustable nanostructure and, consequently, controllable SPR-related optical properties and colour.

7. Acknowledgements

The authors acknowledge the Portuguese Foundation for Science and Technology (FCT) for the financial support through project PTDC/CTM/70037/2006 funded under the program "Programa Operacional Factores de competitividade (COMPETE)" from "Quadro de Referência Estratégico Nacional (QREN)" co-participated by FEDER.

8. References

- Takele H., Greve H., Pochstein C., Zaporojtchenko V., Faupel F., (2006) Plasmonic properties of Ag nanoclusters in various polymer matrices. *Nanotechnology*, 17, 14 (Jul 2006) 3499-3505.
- Hutter E., Fendler J. H., (2004) Exploitation of Localized Surface Plasmon Resonance. *Advanced Materials*, 16(19), (Oct. 2004) 1685-1706.
- Walters G., Parkin I. P., (2008) The incorporation of noble metal nanoparticles into host matrix thin films: synthesis, characterisation and applications. *Journal of Materials Chemistry*, 19, 5 (Aug 2008) 574-590.
- Torrell M., Machado P., Cunha L., Figueiredo N.M., Oliveira J.C., Louro C., Vaz F., (2010) Development of new decorative coatings based on gold nanoparticles dispersed in an amorphous TiO₂ dielectric matrix *Surface and Coatings Technology*, 9-10, 204, (Jan 2010) 1569-1575.
- Wang C. M., Lian J., Ewing R.C. & Boatner L.A., (2006) Ion-beam implantation and cross-sectional TEM characterization of Gd₂Ti₂O₇ pyrochlore. *Nuclear Instruments and Methods*, 242 (Jan 2006) 448-451.
- Pacholski C., Kornowski A., & Weller H., (2004), *Angewandte Chemie International Edition* 43, 36, (Sept 2004) 4774-4777.

- Wu J. & Tseng C.,(2006) Photocatalytic properties of Au/ZnO nanorod composites. *Applied Catalysis B: Environment*, 66,(June 2006) 51-57.
- Li Y., Hu Y., Peng S., Lu G.& Li S., (2009) *Journal Physical Chemistry. C*. 113,21, (2009) 9352-9358.
- Atashbar M. Z., Sun H. T., Gong B., Wlodarski W., & Lamb R. (1998), XPS study of Nb-doped oxygen sensing TiO₂ thin films prepared by sol-gel method. *Thin Solid Films*. 326, (Aug. 1998) 238-244.
- Walton R. M., Dwyer D. J., Schwank J. W., & Gland J. L., (1998) Gas sensing based on surface oxidation/reduction of platinum-titania thin films I. Sensing film activation and characterization. *Applied Surface Science* 125, (Feb 1998) 187-198.
- Cho S., Lee S., Oh S., Park S. J., Kim W. M., Cheong B., Chung M., Song K. B., Lee T. S., Kim S. G. (2000) Optical properties of Au nanocluster embedded dielectric films. *Thin Solid Films*, 377-378,(Dec 2000) 97-102.
- F. Hache, D. Richard, C. Flytzanis, and K. Kreibig, The Optical Kerr Effect in Small Metal Particles and Metal Colloids - the Case of Gold. *Applied Physics A: Materials Science & Processing* 47, 4 (Jul 1988) 347-357.
- Kim K., Lee H. B., Yoon J. K., Shin D. & Shin K. S. (2010), Surface-Enhanced Raman Scattering on Aggregates of Platinum Nanoparticles with Definite Size. *Journal Physical Chemistry C* 114, (Oct 2010) 13589-13595.
- Dalacu D., Martinu L., (1999) Spectroellipsometric characterization of plasma-deposited Au/fluoropolymer nanocomposite films, *Journal of Vacuum Science Technology A* 17(3), (Feb. 1999) 877-883.
- Dalacu D., Martinu L., (2000) Spectroellipsometric characterization of plasma-deposited Au/SiO₂ nanocomposite films, *Journal of Applied. Physics* 87(1), (Aug. 2000) 228- 236.
- Bohren C. F. & Huffman D. R., Absorption and Scattering of Light by Small Particles, Wiley Professional Paperback Edition, New York, (1998).
- Deng H., Yang D., Chen B. & Lin C. W., (2008) Simulation of surface plasmon resonance of Au-WO_{3-x} and Ag-WO_{3-x} nanocomposite films. *Sensors and Actuators B: Chemical* 134, (Apr. 2008) 502-509.
- Matsuoka J., Yoshida H., Nasu H. & Kamiy K., Preparation of gold microcrystal-doped TiO₂, ZrO₂ and Al₂O₃ films through sol-gel process. *Journal of Sol-Gel Science and Technology* 9,2, (1997) 145-155.
- Liao H. B., Xiao R. F., Fu J. S. & Wong G. K. L, (1997) Large third-order nonlinear optical susceptibility of Au-Al₂O₃ composite films near the resonant frequency. *Applied Physics B: Lasers and Optics* 65, (1997) 673-676.
- Mandal S. K., Roy R. K. & Pal A. K., (2002) Surface plasmon resonance in nanocrystalline silver particles embedded in SiO₂ matrix. *Journal of Physics D: Applied Physics* 35, (Sept. 2002) 2198-2205.
- Sella C., Chenot S., Reillon V. & Berthier S., (2009) Influence of the deposition conditions on the optical absorption of Ag-SiO₂ nanocermet thin films. *Thin solid films* 517,(Aug. 2008) 5848-5854.
- P. Zhou, H. Y. You, J. H. Jia, J. Li, T. Han, S. Y. Wang, R. J. Zhang, Y. X. Zheng and L. Y. Chen, (2004) Concentration and size dependence of optical properties of Ag:Bi₂O₃

- composite films by using the co-sputtering method. *Thin solid films* 455-456, (Aug. 2005) 605-608.
- Cho S.H., Lee S., Ku D. Y., Lee T. S., Cheong B., Kim W.M., Lee K.S., (2004) Growth behavior and optical properties of metal-nanoparticle dispersed dielectric thin films formed by alternating sputtering, *Thin solid films* 447-448 (Jan. 2004) 68-73.
- Liz-Marzán L.M., (2004) Nanometals: Formation and Color, *Materials Today* 7,2 (Dec. 2004) 26-31.
- Wang C.M., Shutthanandan V., Zhang Y., Thevuthasan S., Thomas L. E., W(2009) eber W. J., Duscher G. (2006) Atomic level imaging of Au nanocluster dispersed in TiO₂ and SrTiO₃, *Nuclear Instruments and Methods Physical Research Section B*, 242 (Jan. 2006) 448-450.
- Armelaio L., Barreca D., Bottaro G., Gasparotto A., Gross S., Maragno C., Tondello E., (2006) Recent trends on nanocomposites based on Cu, Ag and Au clusters: A closer look, *Coordination Chemical Review* 250,11-12 (2006) 1294-1314.
- Navinsek B., Panjan P., Milosev I., (1999) PVD coatings as an environmentally clean alternative to electroplating and electroless processes, *Surface and Coating Technology*. 116-119 (Sept. 1999) 476-487
- Fenker M., Jackson N., Spolding M., Nicole P., Schönhute K., Gregory G., Hovsepian P.E., Munz W.D., (2004) Corrosion performance of PVD-coated and anodised materials for the decorative market, *Surface and Coatings Technology* 188-189 (2004) 466- 472.
- Mie. G. (1908) Beiträge zur Optik Trüber Medien, speziell Kolloidaler Metallösungen. *Ann. Phys.* 25 (1908) 377-452.
- H. Baida, P. Billaud, S. Marhaba, D. Christofilos, E. Cottancin, Crut A., Lermé J., Maioli P., Pellarin M., Broyer M., Del Fatti N., Vallée F., Sánchez-Iglesias A., Pastoriza-Santos I. & Liz-Marzán L. M., (2009) Quantitative Determination of the Size Dependence of Surface Plasmon Resonance Damping in Single Ag@SiO₂ Nanoparticles. *Nanoletters* 9 (2009) 3463-3469.
- Rodríguez-Fernández J., Novo C., Myroshnychenko V., Funston A. M., Sánchez-Iglesias A., Pastoriza-Santos I., Pérez-Juste J., García de Abajo F. J., Liz-Marzán L. M., & Mulvaney P., (2009) Spectroscopy, Imaging, and Modeling of Individual Gold Decahedra. *Journal of Physical Chemistry C*. 113, (Oct. 2009) 18623-18631.
- Landau L. D. & Lifshitz E. M., *Electrodynamics of Continuous Media*, Pergamon, Oxford (1984).
- Ung T., Liz-Marzan L. M., & Mulvaney P., (2001) Optical Properties of Thin Films of Au@SiO₂ Particles. *Journal of Physical Chemistry. B*, 105, (Apr. 2001) 3441-3452.
- Song G. B., Liang J. K., Liu F. S., Peng T. J., & Rao G. H.. (2005) Preparation and phase transformation of anatase-rutile crystals in metal doped TiO₂/muscovite nanocomposites. *Thin Solid Films*. 491 (2005) 110-116.
- Genzel L., Kreibig U., *Zeitschrift Für Physik B Condensed Matter* 37, (1980) 93-101.
- Shalaev V. M., *Non-linear Optics of Random Media*, Springer, Berlin, (2000).
- Vasilevskiy M. I. & Anda E. V. (1996), Effective dielectric response of semiconductor composites, *Physical Review. B*. 54, (Aug. 1996) 5844-5851.
- Vasilevskiy M. I., (2000), Effective Dielectric response of composites containing uniaxial inclusions, *Physical Status Solidi B*, 219, (May 2000) 197-204.

- Torrell M., Cunha L., Kabir Md. R., Cavaleiro A., Vasilevskiy M.I., Vaz F. Nanoscale color control of TiO₂ films with embedded Au nanoparticules, *Material Letters*. 64, 23 15, (2010) 2624-2626.
- Barradas N.P., Jeynes C., Webb R.P., (1997) Simulated annealing analysis of Rutherford backscattering data, *Applied Physics Letter* 71, (May 1997) 291-293.
- Gurbich A.F. (1997) Evaluation of non-Rutherford proton elastic scattering cross section for oxygen. *Nuclear Instruments and Methods in Physics Research Section B*. 129 (Apr. 1997) 311-316.
- Alves E., Franco N., Barradas N. P., Nunes B., Lopes J., Cavaleiro A., Torrell M., Cunha L., & Vaz F. (2011). Structural and optical studies of Au doped titanium oxide films. *Nuclear Instruments and Methods in Physics Research Section B: Beam Interactions with Materials and Atoms*. In Press (2011). Accepted Manuscript.
- Armelaio L., Barreca D., Bottaro G., Gasparotto A., Gross S., Maragno C., Tondello E., (2006) Recent trends on nanocomposites based on Cu, Ag and Au clusters: A closer look, *Coord. Chem. Rev.* 250(11-12) (2006) 1294-1314
- Manera M.G., Spadavecchia J., Buso D., de Julian Fernandez C., Mattei G., Martucci A., Mulvaney P., Pérez-Juste J., Rella R., Vasanelli L., Mazzoldi P., (2008) Thin films of TiO₂ nanocrystals with controlled shape and surface coating for surface plasmon resonance alcohol vapour sensing, *Sensors and Actuators, B* 132(1) (2008) 107-115.
- Hasan M., Haseeb A., Saidur R., Masjuki H., Hamdi M., (2009) Influence of substrate and annealing temperatures on optical properties of RF-sputtered TiO₂ thin films, *Opt. Mater.* (2009) In Press. doi:10.1016/j.optmat.2009.07.011.
- Martin N., Rousselot C., Rondot D., Palmino F., Mercier R., (1997) Microstructure modification of amorphous titanium oxide thin films during annealing treatment, *Thin solid films*. 300 (1-2) 113-121.
- Wang C.M., Shutthanandan V., Zhang Y., Thevuthasan S., Thomas L. E., Weber W. J., Duscher G., (2006) Atomic level imaging of Au nanocluster dispersed in TiO₂ and SrTiO₃, *Nuclear Instruments and Methods in Physics Research Section B*. 242 (2006) 448-450.
- Yate L., Martínez-de-Olcoz L., Esteve J., Lousa A., (2009) Control of the bias voltage in d.c. PVD processes on insulator substrates, *Vacuum*. 83(10) (2009) 1287-1290.
- Lee M., Chae L., Lee K.C., (1999) Microstructure and surface plasmon absorption of sol-gel-prepared Au nanocluster in TiO₂ thin film, *Nanostructured Materials* 11(2) (1999) 195-201.
- M. Torrell, L. Cunha, A. Cavaleiro, E. Alves, N. P. Barradas, and F. Vaz, (2010) "Functional and optical properties of Au:TiO₂ nanocomposite films: The influence of thermal annealing," *Applied Surface Science* 256,22, (2010) 6536-6542
- Zakrzewska K., Radecka M., Kruk A., Osuch W., (2003) Noble metal/titanium dioxide nanocermet for photoelectrochemical applications, *Solid State Ionic* 157(1-4) (2003) 349-56.
- Vosburgh J., Doremus R.H., Optical absorption spectra of gold nano-clusters in potassium borosilicate glass, *J. Non-Cryst. Solids* 349 (2004) 309-314.

- Wang J., Lau W.M., Li Q., (2005) Effects of particle size and spacing on the optical properties of gold nanocrystals in alumina, *Journal of Applied Physics* 97(11) (2005) 114303-114308.
- Dakka A., Lafait J., Abd-Lefdil M., Sella C., Maaza M., (2000) *Eur. Phys. Journal of Applied Physics* 9 (2000) 105-114.

Comparative Study of Membranes Obtained from PA6 and PA66/National Clay Nanocomposites

Amanda M. D. Leite, Edcleide M. Araújo, Vanessa da N. Medeiros,
Rene A. da Paz and Hélio de L. Lira
Federal University of Campina Grande (CCT/UAEMa/Bloco CL)
Brazil

1. Introduction

Polyamide is an important group of the thermoplastic excellent solvent resistance and good processability. However, polyamide exhibits a relatively rapid crystallization rate, which makes it to have some drawbacks such as high mold shrinkage and dimensional instability. In order to control the crystallization rate and the crystallinity, then achieve the desired morphology and properties, a great deal of efforts has been made on studying the crystallization kinetics corresponding to the change of the performed properties (Liu & Yang, 2009; Lu et al., 2001; Run et al., 2005).

Composite materials are widely used in various fields, such as the automotive industry, aeronautics, and communications. Depending on the composite nature and structure, many properties can be improved: hardness, tenacity, deformation temperature, price, and so forth. Nanocomposites refer to composites in which one of the components has at least one dimension of about a few nanometers. They are a relatively new class of material. The nanoscale dispersion gives better mechanical properties. A few articles focus on the advantages of using nanocomposites (Varlot et al., 2001).

Polymer nanocomposites are an area of substantial scientific interest and of emerging industrial practice. Hybrid combinations of natural fillers and polymers were presented to the public for the first time in 90s (Pfaendner, 2010). In recent years, the dispersion of low loadings (ca. 5%) of inorganic particles in the nanosize scale in organic polymers is a challenge for the preparation of new composite materials with enhanced mechanical, gas barrier and flame retardant properties, when compared to those of composites prepared with micron size particles. A homogenous dispersion of nanoparticles is believed to contribute better to the property improvement (Herrero et al., 2010; Dubois, 2000).

Although fillers like alumina, silica, etc., can be added, layered inorganic compounds possess unique properties to be active as fillers in polymeric nanocomposites. They can be, in fact, exfoliated into single layers, each of them having a thickness of the order of nanometers (from ca. 0.7 to 2.5 nm) and by ion exchange or grafting reactions the surface of the layers may be functionalized with organic groups that increase the compatibility with the polymers (Herrero et al., 2010). In addition, layered solids may intercalate polymeric chains in their interlayer regions. Until now, however, the clay materials involved in this

field have been mostly focused on montmorillonite-type layered silicates whose layers have a relatively low charge density and from which exfoliated montmorillonite-type layered silicate/polymer nanocomposites can be easily obtained (LeBaron et al., 1999; Lagaly, 1999). Montmorillonite is one of the most commonly used clay minerals in polymer nanocomposites, due to its high cation exchange capacity, excellent swelling ability, high aspect ratio and ease for modification (Xi et al., 2005). However, it is very difficult for the hydrophilic montmorillonite to be exfoliated and well-dispersed in a hydrophobic polymer matrix. Therefore, two main objectives for modification are: to expand the interlayer space of the clay, allowing large polymer molecules to enter into the interlayer space, and to improve the miscibility of clay with the polymer, thereby achieving a good dispersion of clays in the polymer matrix (Zhao et al., 2010).

Several methods have been developed to produce clay/ polymer nanocomposites (Dubois, 2000). Three methods were developed in the early stages of this field and have been applied widely. These are: in situ polymerization (Wang et al., 2005), solution induced intercalation (Qiu et al., 2006), and melt processing (Lee et al., 2006).

A membrane is an interphase between two adjacent phases acting as a selective barrier, regulating the transport of substances between the two compartments. The main advantages of membrane technology as compared with other unit operations in (bio)chemical engineering are related to this unique separation principle, i.e. the transport selectivity of the membrane. Separations with membranes do not require additives, and they can be performed isothermally at low temperatures and—compared to other thermal separation processes—at low energy consumption (Ulbricht, 2006). The primordial function of a membrane is to act as a selective barrier, allowing the passage of certain components and the retention of others from a determined mixture, implying the concentration of one or more components both in the permeate and in the retentate. Its selectivity is related to the dimensions of the molecule or particle of interest for separation and the pore size, as also the solute diffusivity in the matrix and the associated electric charges (Coutinho et al., 2009).

The separation performance of a membrane is influenced by its chemical composition, temperature, pressure, feed flow and interactions between components in the feed flow and the membrane surface (Lin, et al., 1997).

The membranes can be classified as symmetrical or asymmetrical. This asymmetry is considered with respect to the internal structure of the membranes. Symmetrical membranes show uniform pore sizes in their cross-section whereas the pores of asymmetric membranes are usually larger the further they are from the filter surface. In general the most important characteristics of membranes are: thickness, pore diameter, solvent permeability and porosity. Other important parameters are: permeate flow rate, heat, chemical and mechanical resistance (Coutinho et al., 2009). From the morphological point of view, membranes can be divided into two large categories: dense and porous. Membranes are considered to be dense when transport of the components involves a stage of dissolution and diffusion across the material constituting the membrane. On the other hand a membrane is denominated as porous when permeate transport occurs preferentially in the continuous fluid phase which fills the membrane pores (Habert, Borges, & Nobrega, 2006).

Several industrial separation processes make use of polymeric membranes. When porous polymeric membranes are needed, phase separation of polymer solutions is the fabrication method of choice. First, a polymer solution is cast on a support. Then, the phase separation can be induced by means of contacting the polymer solution with a suitable non-solvent in

the liquid or vapor phase (liquid induced phase separation or vapor induced phase separation). Diffusional exchange of solvent and non-solvent induces a thermodynamic instability in the polymer solution causing phase separation to occur into a polymer-rich phase and a polymer-lean phase. The polymer-rich phase forms the body of the membrane, whereas the polymer-lean phase will form the porosity inside the membrane. The morphology of the membrane depends strongly on the conditions under which the phase separation is carried out (Boom et al., 1992; Witte et al., 1996; Bulte et al., 1996).

Adding the inorganic nanoparticles into polymeric materials to improve the filtration membrane properties has attracted broad attentions in the development of membrane science and technique. Many literatures (Yang et al., 2007; Uragami et al., 2005; Nagarale et al., 2005) indicated that adding proper inorganic nanoparticles in polymeric casting solution could suppress the formation and growth of macrovoids, to increase the number of small pores and run-through pores, to improve the porosity, hydrophilicity and permeability with almost unchanged retention, and to enhance the mechanical and thermal stabilities and the anti-fouling performance.

Therefore, the aim of this work was to evaluate the thermal behavior of microporous membranes obtained from nanocomposites of PA6 and PA66/national clay.

2. Experiment

2.1 Materials

Bentonite clay Brasgel PA (sodium), with CEC (cation exchange capacity) = 90 meq/100 (method of adsorption of methylene blue) passed through ABNT sieve no. 200 ($D = 74\mu\text{m}$), cream colored, supplied by Bentonit União Nordeste (BUN) located in Campina Grande-PB. The polymer matrix used was a polyamide 6 (Technyl C216) and polyamide 66 (Technyl A216) provided by Rhodia/ SP, in the form of white pelets. It was used the Genamin (hexadecyltrimethylammonium chloride) quaternary ammonium salt, produced by Clariant/PE. For the preparation of membranes, it was used the formic acid solvent at 99% by Vetec/SP.

2.2 Methodology

To make the clay compatible with the polymer matrix, the sodium ions present between the layers of clay were exchanged for ions of the quaternary ammonium salt (Genamin) to produce the organoclay, called OMMT. To obtain the organoclay (OMMT) a suitable treatment was suitable for the salt, based on the CEC of clay, according to procedure reported in previous studies (Leite et al., 2009; Araujo et al., 2007).

To obtain the nanocomposites of polyamide/clay there has been a preparation of concentrates (1:1) in an internal mixer coupled to a torque rheometer from Haake System 90-Büchler, operating at 240°C for polyamide 6 and 260°C for polyamide 66, at 60 rpm for 10 minutes. The concentrates obtained were granulated and added to the polymer matrix in quantities necessary to obtain nominal concentrations of 3 wt% clay. The mixtures were processed in a counterrotating twin screw extruder coupled to a torque rheometer System 90 from Haake-Büchler at a temperature of 240°C for polyamide 6 and 260°C for the polyamide 66 in all heating zones and speed of the screws at 60 rpm. Before any processing step, the polyamide materials were dried at $80 \pm 5^\circ\text{C}$ for 24 hours in the vacuum oven before being processed for removal of moisture (Leite et al., 2009).

The method of phase inversion by immersion-precipitation technique was used in the preparation of membranes. Polyamide 6 and Polyamide 66 and the nanocomposites (dried

at 80°C under vacuum for a period of 24 hours) were dissolved in a quantity in weight of 20% polymer and 80% formic acid at a temperature of 40°C, until complete dissolution of the polymer. When dissolved in formic acid, polyamide forms a clear and homogeneous solution whereas nanocomposites form a turbid one. After being prepared, the solution was spread on a glass plate and then quickly immersed in a bath of distilled water, a non-solvent element. After completion of the precipitation, the membrane was removed and washed with distilled water then dried in an oven at 50°C for 2 hours.

2.3 Characterization

2.3.1 X-ray Diffraction (XRD)

The spacing basal of the samples was observed by X-ray diffraction (XRD) at room temperature by XRD-6000 Shimadzu diffractometer (40 kV, 30 mA) using CuK α radiation ($\lambda = 0.154$ nm) at the rate of 2° min⁻¹ in the range of 2.0–30°.

2.3.2 Transmission Electron Microscope (TEM)

The phase morphologies of the nanocomposites were observed by transmission electron microscope (TEM), Philips CM 120, operating at an acceleration voltage of 120 kV. Samples were cryogenically microtomed (–80 °C) into ultrathin sections (~30 nm thick) from films with a diamond knife using a RMC MT-7000.

2.3.3 Scanning Electron Microscopy (SEM)

The structures of the membranes were characterized by SEM SSX 550 Superscan—Shimadzu, operating with 15 kV. All samples were gold sputtered.

2.3.4 Water flux

For the testing of water permeability, we used a perpendicular Amicon filtration cell (effective area = 28.7 cm²), coupled to a filtration system (Figure 1). The membranes were tested for permeability at different pressures: 0.5 and 1.0 bar. The collections of permeated water was measured in an interval of 3 minutes, and each collection was made for a period of 1 minute

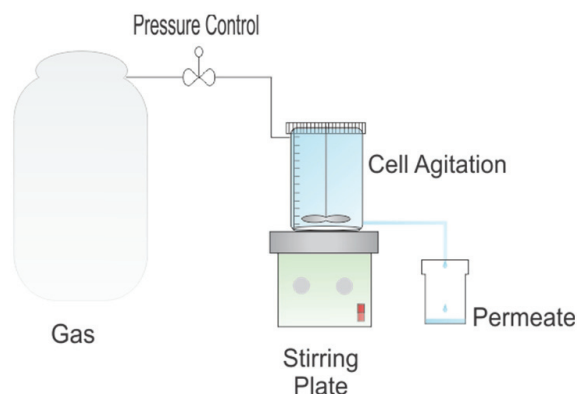


Fig. 1. Schematic representation of the used filtering system.

3. Results and discussion

3.1 X- Ray Diffraction of clay and nanocomposites (XRD)

The XRD patterns were made to the clay without treatment (MMT) and clay treated with Genamin. Figure 2 shows that there was a shift of the 2θ angle of 6.97° (MMT, $d_{001} = 12.74 \text{ \AA}$) to 4.01° (OMMT, $d_{001} = 22.34 \text{ \AA}$). The shift to smaller angles and, consequently, increasing the basal spacing, it indicates that the intercalation of molecules in the salt between the layers of clay. showing an expansion of the basal interplanar distance, indicating the intercalation of the salt in the clay. The interlayer distance is determined by the diffraction peak in the X-ray method, using the Bragg equation. The results indicated that the quaternary ammonium salt Genamin was intercalated between two basal planes of MMT, leading to an expansion of the interlayer spacing, conform reported too in others works (Fornes et al., 2001; Araujo et al., 2007) that used this quaternary ammonium salt in the organophilization of bentonite clays of same precedence.

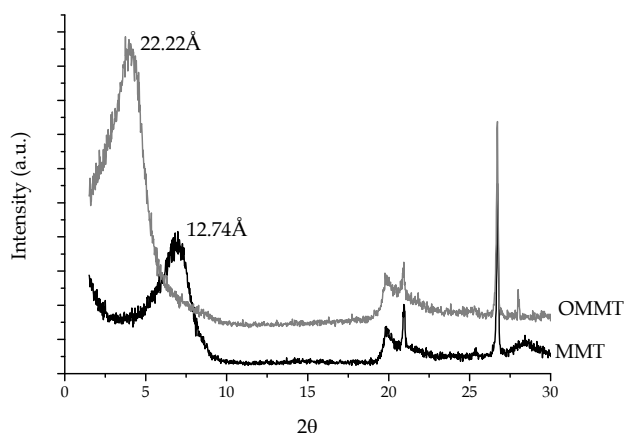


Fig. 2. XRD patterns of MMT and OMMT clays

Figure 3 (a and b) shows the X-ray diffraction patterns of clay without treatment (MMT), treated (OMMT), and the nanocomposites of polyamide 6 and 66. It is observed that the clay without treatment presents an interplanar basal distance of about 12.74 \AA , a characteristic of the clay minerals in smectite group. Concerning treated clay there was a peak shift to lower angles in the order of 22.22 \AA , showing an expansion of the basal interplanar distance, indicating the intercalation of the salt in the clay.

Regarding the nanocomposites of polyamide/clay that were analyzed through films, it can be observed that the characteristic peak of the treated clay no longer appears. This result shows that apparently the nanocomposites obtained present an exfoliated or partially exfoliated structure. This will then be confirmed by transmission electron microscopy.

3.2 Transmission Electron Microscopy (TEM)

The photomicrographs of Figure 4 (a and b) show the PA 6/MMT and PA 66/MMT systems. For the PA system 6/MMT presents a partially exfoliated morphology, composed of layers of clay and some clusters dispersed in the polymer matrix, since for

photomicrography 66/MMT PA system, there is a morphology composed predominantly of small and large clusters of lamellae of clay, ie a structure with partial intercalation, also called a microcomposite.

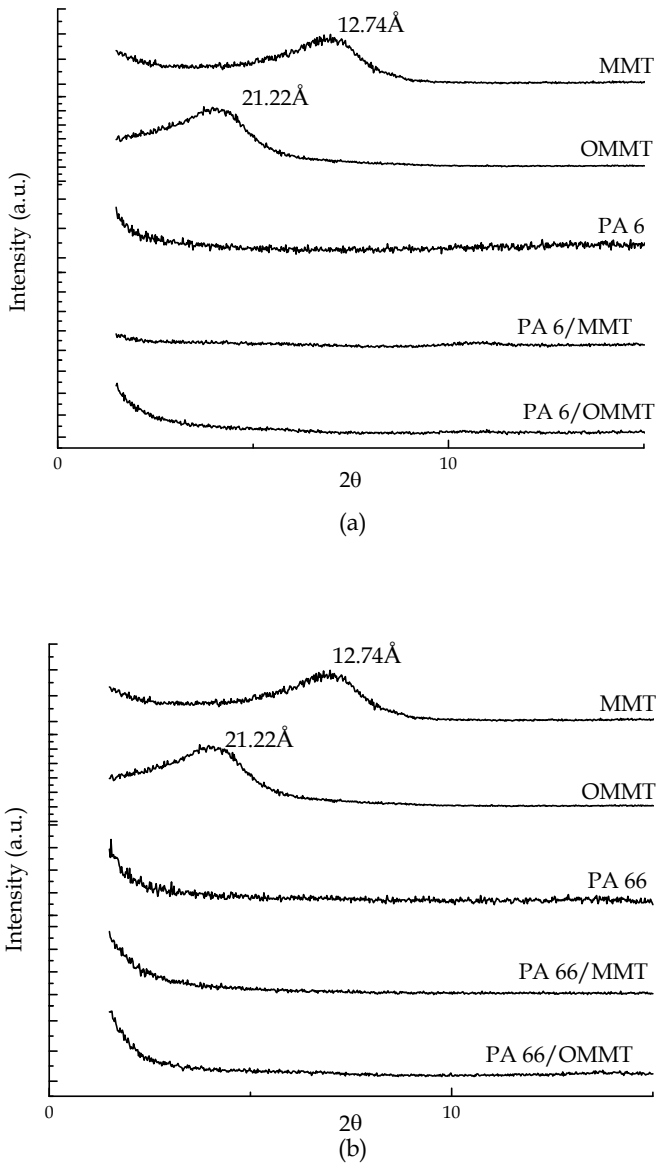


Fig. 3. XRD patterns of MMT and OMMT clays and nanocomposites of (a) PA 6 and (b) PA 66

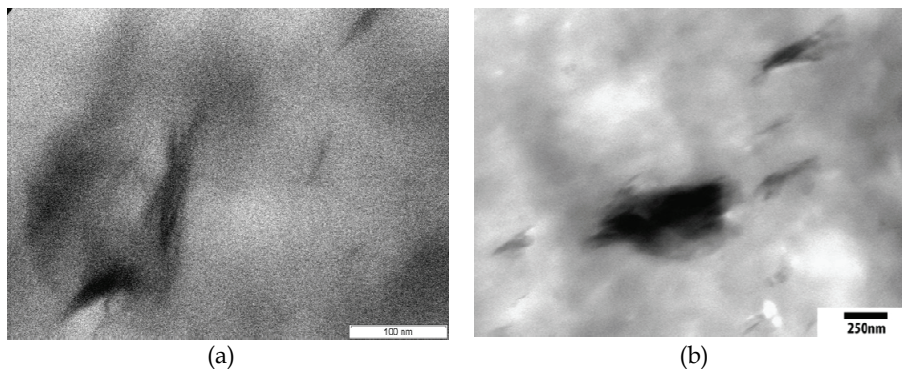


Fig. 4. TEM photomicrographs of the nanocomposites films of (a) PA 6/MMT and (b) PA 66/MMT.

Figures 5a and b respectively show photomicrographs of nanocomposites of polyamide 6 and polyamide 66 with treated clay. Figure 5a makes it possible to observe a partially exfoliated morphology, composed of layers of clay and some clusters dispersed in the polymer matrix. Figure 5b presents a similar morphology however showing an absence of clusters. It apparently presents a more exfoliated morphology compared to nanocomposite polyamide 6/OMMT. In a general way, the quaternary ammonium salt studied favored the production of nanocomposites with a predominantly exfoliated structure, thus confirming the results of X-ray diffraction previously obtained and displayed.

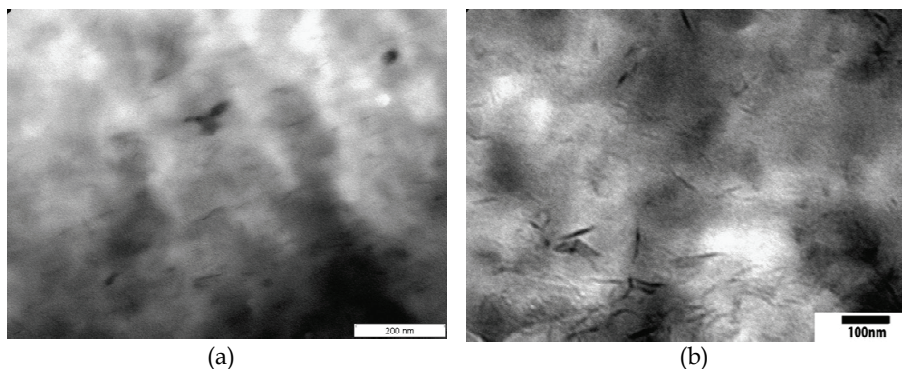
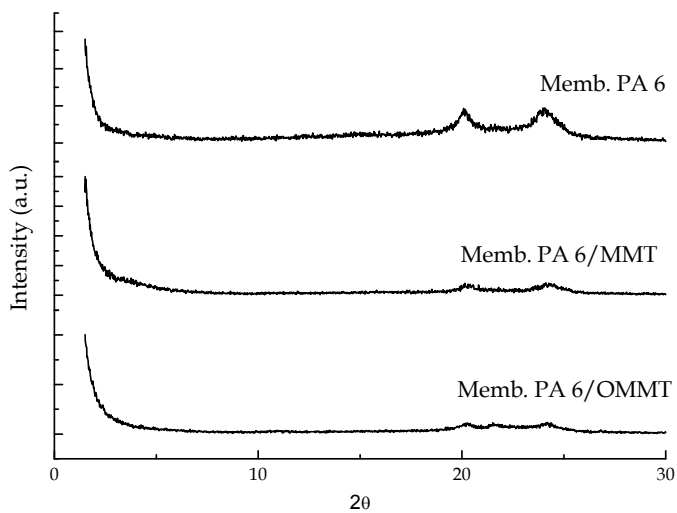


Fig. 5. TEM photomicrographs of the nanocomposites films of (a) PA 6/OMMT and (b) PA 66/OMMT.

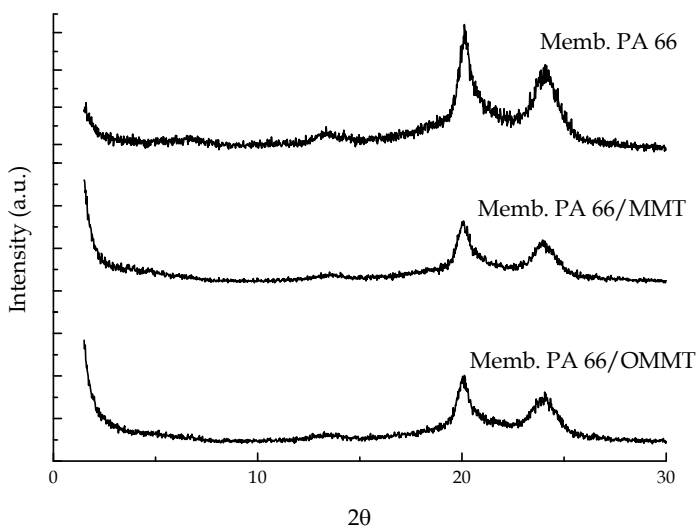
3.3 X- Ray Diffraction (XRD) of membranes

Figure 6 (b) shows the XRD diffractograms of the membranes prepared from polyamide 6 and 66 and its nanocomposites. According to what has been mentioned for the XRD diffractograms of the films obtained from the granules of nanocomposites, Figure 3, we can also emphasize here the disappearance of the characteristic peak of clay, confirming the exfoliation of the membranes produced from the nanocomposite, ie, behavior similar to that previously studied. Through these diffractograms, one can see the presence of two peaks at

2θ of about 20° and 24° for all compositions of the membranes. The appearance of both peaks may be related to the formation of a crystalline polyamide phase, called phase α (alpha) (Kohan, 1995).



(a)



(b)

Fig. 6. XRD patterns of membranes obtained of (a) PA 6 and (b) PA 66

According to Khanna and Kuhn (1997), polyamide can take two crystallographic forms, α monoclinic and monoclinic or γ pseudo-hexagonal. In the α form, the hydrogen bonds are formed between antiparallel chains, and γ form between parallel chains by hydrogen bonds, causing the twist of the molecular chains in zig-zag planes. As a result of this phenomenon, the crystal density and heat of fusion of γ form, where interactions between the chains are weaker, are less than α form. The α way can be identified in XRD pattern of X-ray diffraction peak at 2θ approximately 24° , the crystalline γ form is shown in diffractogram as a peak between 21 and 22. As seen, the introduction of clay and formic acid changes the shape of these peaks, probably by changing the crystallinity of PA.

3.4 Scanning Electron Microscopy (SEM)

3.4.1 Top surface

In Figure 7 (b) are shown photomicrographs of the top of the membranes of pure polyamide 6 and 66. For the membrane of polyamide 6, this surface is virtually skinless, composed of 'sheaf-like' crystallites, as in the membrane interior. The sizes of the crystallites are considerably smaller than those in Fig. 7(a), suggesting that there is a much higher nucleation density during precipitation in this top surface. Already the polyamide 66 membranes, presents a continuous skin composed of intersecting polygonal plates with approximately linearly boundaries. These crystalline plates resemble the two-dimensional spherulites commonly observed in melt-crystallized films.

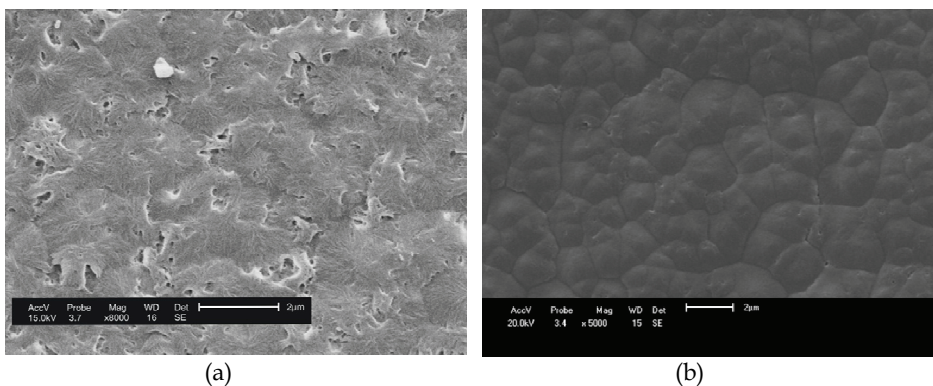


Fig. 7. SEM images of the top surface of (a) PA 6 (b) PA 66

Figures 8 and 9 shows the photomicrographs of the top of the membranes obtained from nanocomposites of PA6 and PA66. Analyzing the images, it can be seen that the membranes obtained from the nanocomposites show a higher amount of pores and their distribution more uniformly compared to the membrane of PA 6. Moreover, it is observed that the presence of clay treated decreases pore size. As for the PA 66 membrane there is a behavior similar to the membrane of pure PA 66. It appears that for the membranes obtained from PA6 It shows the presence of particles to the membrane obtained from the pure polymer can be attributed to the presence of such a differential precipitation on the membrane surface or to an incomplete dissolution of the polymer during the preparation of the solution to obtain the membranes. The membranes with the presence of clay can be attributed to an incomplete homogenization of the clay with the polymer during preparation of the solution.

The agglomeration of the layers of clay, because of possible interactions of molecules present in the clay of the salt with formic acid. These clusters are seen macroscopically in the membrane where it was used nanocomposite with treated clay.

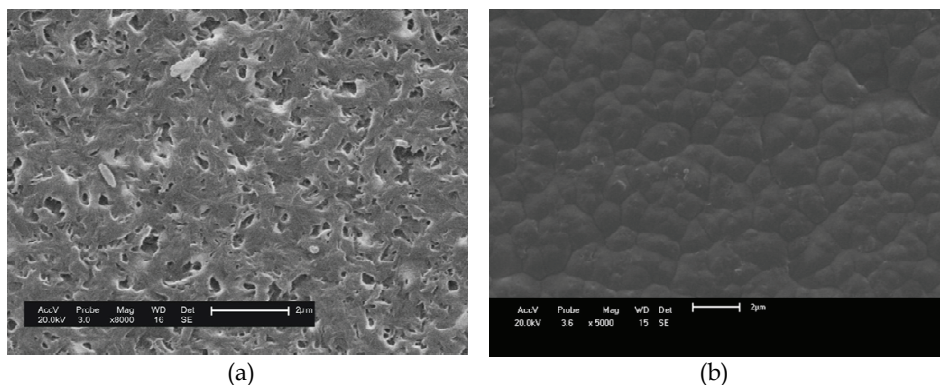


Fig. 8. SEM images of the top surface of (a) PA 6/MMT (b) PA 66/MMT

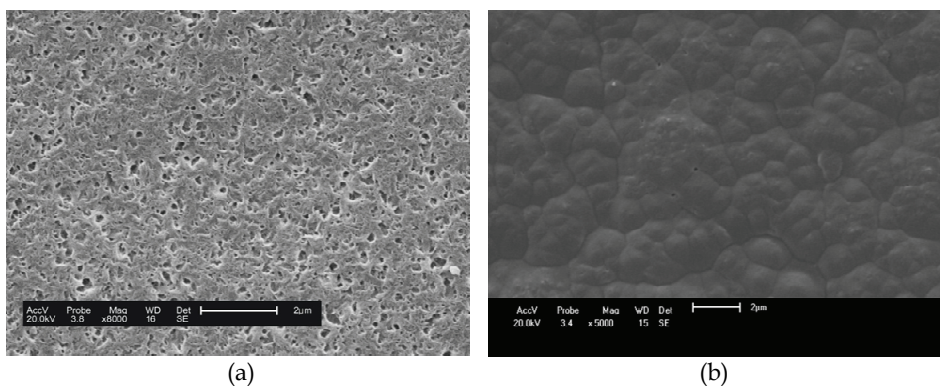


Fig. 9. SEM images of the top surface of (a) PA 6/OMMT (b) PA 66/OMMT

3.4.2 Cross section

In the cross section of membranes obtained is possible to observe a variation in pore size along its thickness. For all membranes, we visualized a layer of skin and filter just below the skin to the porous layer with pores distributed uniformly spherical (Figures 10 to 12). These figures show that the skin pores filter has very small or even nonexistent, and that the porous layer has interconnected pores and well distributed. This difference in morphology in cross section that arises or is defined (also) the selectivity of the membrane, which will be investigated by measuring the flow. For all cross sections analyzed was possible to observe the formation of macrovoids and the presence of a dense skin, this probably occurred because of a delay precipitation in obtaining membrane. Generally, membranes PA 66 have a porous layer with pores much smaller when compared membranes obtained by the PA 6. The membranes of polyamide 66 and their nanocomposites present a thicker filter skin and

lower pores in the porous layer when compared to membranes made of polyamide 6. This increased thickness directly implies on the permeate flux.

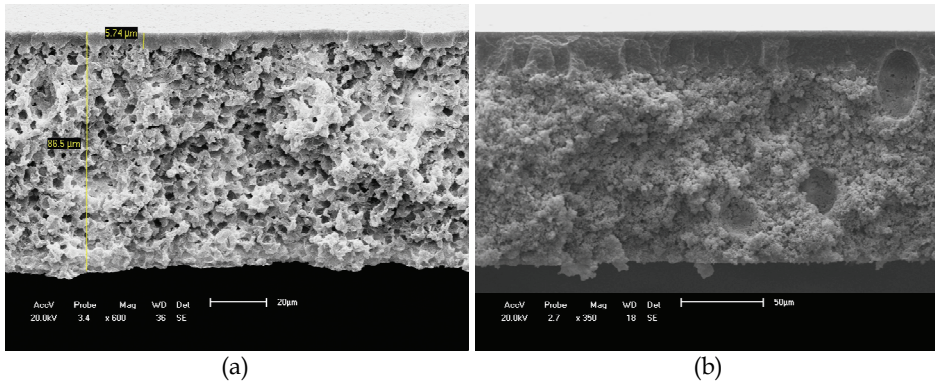


Fig. 10. SEM images of the cross section of (a) PA 6 (b) PA 66

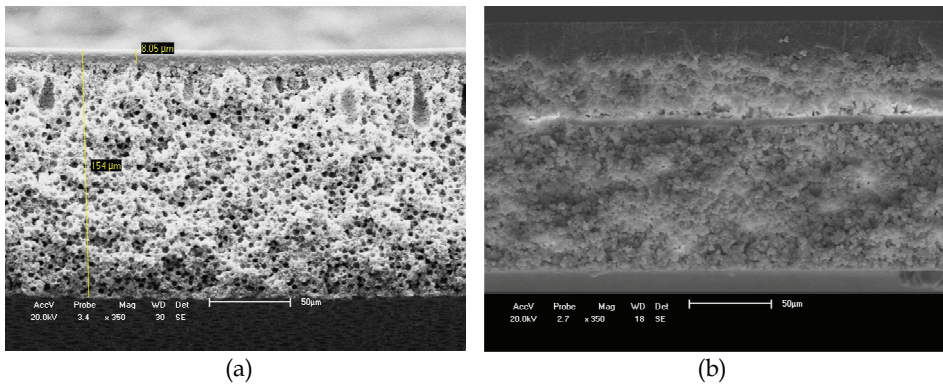


Fig. 11. SEM images of the cross section of (a) PA 6/MMT (b) PA 66/MMT

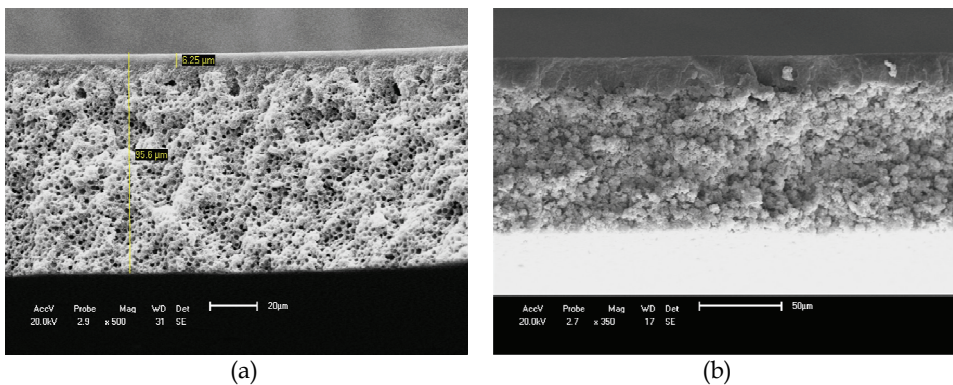
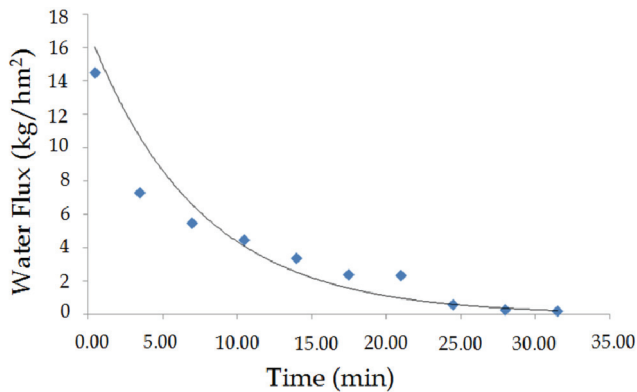


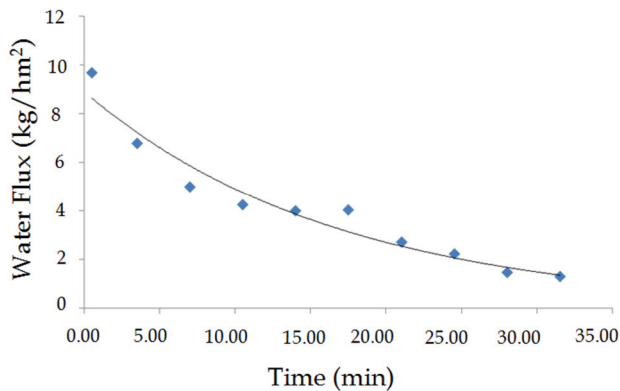
Fig. 12. SEM images of the cross section of (a) PA 6/OMMT (b) PA 66/OMMT

3.5 Water flux

Figures 13 and 14 (b) show the curves of flux measurements made with distilled water in a cell filtration membranes for PA 6 and PA 66 at pressures of 0.5 and 1.0 bar respectively. For membranes of PA 6 and PA 66, the curves behave similarly, with a tendency to stay constant at low values of flow after 30 minutes. This trend can be attributed to the fact that a swelling of the matrix when in contact with water and gradually decreasing the pores, thereby precluding the permeability of water. Swelling occurred may have been caused by the hygroscopicity of the polymer used. Polyamide 6 and polyamide 66 in the form of granules showed a percentage of 1.7% absorption of water in an immersion in period of 24 hours (Wiebeck 2005).

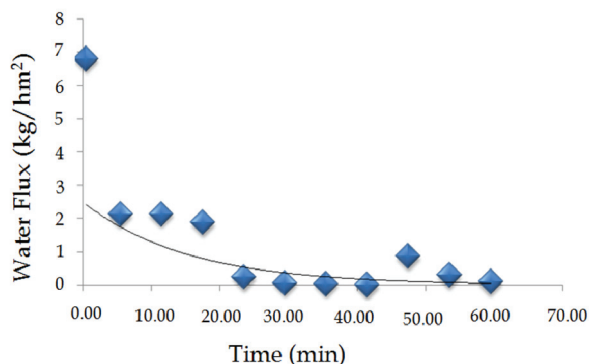


(a)

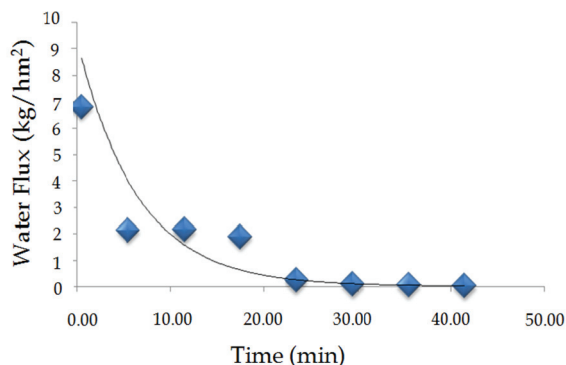


(b)

Fig. 13. Curves of water flow to the membrane of PA 6 obtained for pressures of (a) 0.5 bar and (b) 1.0 bar.



(a)



(b)

Fig. 14. Curves of water flow to the membrane of PA 66 obtained for pressures of (a) 0.5 bar and (b) 1.0 bar.

However, the membrane of PA 6 and PA 66 having a porous structure, a period of just five minutes immersed in water, swells and almost blocking the passage of water through the pores. A membrane with pores smaller and capable of swelling further reduces their pores and, consequently, the permeate flux is practically annulled. Even with the application of higher pressure, the performance remained the same, although the initial flow obtained with the membranes at a higher pressure was lower, perhaps caused by a compression of the membrane, is characteristic of the technique used in the preparation of membranes (reversed phase).

The membranes obtained from the nanocomposites, ie, where there was the presence of clay and generally larger pores compared to the membranes of PA 6 and PA 66, they were impossible to perform, even under the effect of swelling. It was hoped that the presence of clay which change the morphology of the membrane pores, favoring a better distribution and larger sizes of these, alter membrane permeability.

3. Conclusion

Based on the results obtained and presented in this study, we conclude that the presence of molecules of salt in the clay was checked by increasing interplanar basal evidenced in the XRD diffractograms, and that nanocomposites showed exfoliated and/or partially exfoliated structures, also evidenced by XRD and confirmed by the TEM photomicrographs, which showed some lamellae of clay agglomerates dispersed in polymer matrix. XRD diffractograms of the membranes confirmed the obtaining exfoliated and/or partially exfoliated structure.

SEM photomicrographs of the membranes obtained from nanocomposites present a higher amount of pores and a more uniform distribution when compared to pure polyamide membrane. Membranes of polyamide 66 present thicker skin filter. The membranes showed a low flow of distilled water and this was practically stopped in time, thus showing a swelling in the membrane structure and with increasing pressure, the initial flow was even lower, indicating it may have caused a compression of the membrane during the test. In general, asymmetric microporous membranes of PA 6, PA 66 and their nanocomposites were successfully obtained, where the presence of clay provided a considerable structural change.

4. Acknowledgment

The authors thank Rhodia/SP, Bentonit Uniao Nordeste (BUN), Clariant/PE, DEMa/UFCG, CAPES/Pro-Engenharia, CAPES/PROCAD/NF, MCT/CNPq, ANP/PRH-25 and RENAMI, for financial support.

5. References

- Araujo, E. M.; Barbosa, R.; Oliveira, A. D.; Morais, C. R. S.; Melo, T. J. A.; Souza, G. A. (2007). Thermal and Mechanical Properties of PE/Organoclay nanocomposites. *J. Therm Anal Calorim.* Vol.87, pp.811-814.
- Boom, R. M.; Wienk, I. M.; Boomgaard, T. V. D.; Smolders, C. A. (1992). Microstructures in phase inversion membranes. Part 2. The role of a polymeric additive. *J. Membr. Sci.* Vol. 2-3, pp. 277-292.
- Bulte, A. M. W.; Mulder, M.H.V.; Smolders, C. A.; Strathmann, H. (1996). Diffusion induced phase separation with crystallizable nylons, I. Mass transfer processes for nylon 4,6. *J. Membr. Sci.* Vol.1, pp. 37-49.
- Coutinho, C. M.; Chiu, M. C.; Basso, R. C.; Ribeiro, A. P. B.; Gonçalves, L. A. G.; Viotto, L. A. (2009). State of art of the application of membrane technology to vegetable oils: A review. *Food. Res.* Vol.42, pp.536-550.
- Dubois, A. L. (2000). Polymer-layered silicate nanocomposites: preparation, properties and uses of a new class of materials. *Mat. Sci. Eng.* Vol.28, pp.1-63.
- Fornes, T. D.; Yoon, P. J.; Keskkula, H.; Paul, D. R. (2001). Nylon 6 nanocomposites: the effect of matrix molecular weight. *Polymer.* Vol.42, No.25, pp.9929-9940.
- Habert, A. C.; Borges, C. P.; Nobrega, R. (2006). Processos de separação por membranas. Rio de Janeiro: E-papers.

- Herrero, M. ; Benito, P. ; Labajos, F. M. ; Rives, V. ; Zhu, Y. D. ; Allen, G. C. ; Adams, J. M. (2010). Structural characterization and thermal properties of polyamide 6.6/Mg,Al/adipate-LDH nanocomposites obtained by solid state polymerization. *J. Sol. Stat. Chem.* Vol. 183, pp1645-1651.
- Khanna, Y.P.; Khun, W.P. (1997). Measurement of crystalline index in nylons by DSC: Complexities and recommendations. *J. Polym. Sci.* Vol. 35, pp.2219-2231.
- Kohan, I. M. (1995). *Nylon Plastics Handbook*. Hanser Publishers, Munich Vienna, New York.
- Lagaly, G. (1999). Introduction: from clay mineral-polymer interactions to clay mineral-polymer nanocomposites. *Polymer*. Vol.15. No.1-2, pp,1-9.
- LeBaron, P. C. ; Wang, Z. ; Pinnavaia, T. J. (1999). Polymer-layered silicate nanocomposites: an overview. *Polymer*, Vol.15. No.1-2, pp,11-29.
- Lee, W. D.; Im, S. S.; Lim, H. M.; Kim, K. J. (2006). Preparation and properties of layered double hydroxide/poly(ethylene terephthalate) nanocomposites by direct melt compounding. *Polymer*. Vol 47, No. 4, pp. 1364-1371.
- Leite, A. M. D.; Maia, L. F.; Paz, R. A.; Araujo, E. M.; Lira, H. L. (2009). Thermal properties from membrane of polyamide 6/ montmorillonite clay nanocomposites obtained by immersion precipitation method. *J. Therm Anal Calorim.* Vol.97, pp.577-580.
- Lin, L.; Rhee, K. C.; Koseoglu, S. S. (1997). Bench-scale membrane degumming of crude vegetable oil: Process optimization. *J. Membr. Sci.* Vol. 134, pp.101-108.
- Liu, Y; Yang, G. (2009). Non-isothermal crystallization kinetics of polyamide-6/graphite oxide nanocomposites. *Thermochim. Acta*, Vol.500, pp. 13-20.
- Lu, X. F.; Hay, J. N. (2001). Isothermal crystallization kinetics and melting behaviour of poly(ethylene terephthalate). *Polymer*, Vol. 42 No. 23, pp.9423-9431.
- Nagarale, R. K.; Shashi, V. K.; Rangarajan, R. (2005). Preparation of polyvinyl alcohol-silica hybrid heterogeneous anion-exchange membranes by sol-gel method and their characterization. *J. Membr. Sci.* Vol.248, pp. 37-44.
- Pfaendner, R. (2010). Nanocomposites : Industrial opportunity or challenge ?. *Polym. Degrad. Stab.* Vol.95, pp.369-373.
- Qiu, L.; Chen, W.; Qu, B. (2006). Morphology and thermal stabilization mechanism of LLDPE/MMT and LLDPE/LDH nanocomposites. *Polymer*. Vol.47, No. 14, pp. 922-930.
- Run, M.T. ; Wu, S. Z. ; Zhang, D.Y. ; Wu, G. (2005). Melting behaviors and isothermal crystallization kinetics of poly(ethylene terephthalate)/mesoporous molecular sieve composite. *Polymer*, Vol. 46. No. 14, pp.5308-5316.
- Ulbricht, M. (2006). Advanced functional polymer membranes. *Polymer*. Vol. 47, No.7, pp.2217-2262.
- Uragami, T.; Matsugi, H.; Miyata, T. (2005). Pervaporation characteristics of organic-inorganic hybrid membranes composed of poly(vinyl alcohol-co-acrylic acid) and tetraethoxysilane for water/ethanol separation. *Macromolecules*. Vol. 38, pp.8440-8446.
- Varlot, K.; Reynaud, E.; Kloppfer, M. H. ; Vigier, G. ; Varlet, J. (2001). Clay-Reinforced Polyamide : Preferential Orientation of the Montmorillonite Sheets and the Polyamide Crystalline Lamellae. *Pol. Sci.B.* Vol.39, pp.1360-1370.

- Wang, G. A.; Wang, C. C.; Chen, C. Y. (2005). The disorderly exfoliated LDHs/PMMA nanocomposite synthesized by in situ bulk polymerization. *Polymer*. Vol. 46, No.14, pp.5065-5074.
- Wiebeck, H.; Harada, J. (2005). *Plásticos de engenharia: Tecnologia e aplicações*. 1a ed., Artliber Editora Ltda, Brazil.
- Witte, P. V.; Dijkstra, P. J.; Van Den Berg, J. W. A.; Feijen, J. (1996). Phase separation processes in polymer solutions in relation to membrane formation. *J. Membr. Sci.* Vol. 1-2, pp. 1-31.
- Xi, Y.; Frost, R.L.; He, H.; Klopogge, T.; Bostrom, T. (2005). Modification of Wyoming montmorillonite surfaces using a cationic surfactant. *Langmuir*, Vol. 21, pp.-8675-8680.
- Yang, Y.; Zhang, H.; Wag, P.; Zheng, Q.; Li, J. (2007). The influence of nano-sized TiO₂ fillers on the morphologies and properties of PSF UF membranes. *J. Membr. Sci.* Vol.288, pp. 231-238.
- Zhao, F.; Bao, X.; McLauchilin, A. R.; Gu, J.; Wan, C.; Kandasubramanian, B. (2010). Effect of POSS on morphology and mechanical properties of polyamide 12/montmorillonite nanocompósitos. *Appl.Clay*. Vol 47, pp.249-256.

Part 2

Material Nanocomposites

Clay-Containing Polysulfone Nanocomposites

Priscila Anadão
Polytechnic School, University of São Paulo
Brazil

1. Introduction

Although there are several definitions of composite materials (Callister, 1994; Chawla, 1987; Hull, 1981; Padilha, 1997; Van Vlack, 1984), composites are artificial multiphase materials in which their constituents are chemically distinct and separated by an easily distinct interface (Moffatt et al., 1964).

Some familiar materials are examples of composites: the concrete used in buildings, car tires, the asphalt of our streets. The distinction of artificial materials is necessary due to materials that could be included in this definition, but which occur in a natural way, as, for example, wood (lignine + cellulose fibers), bones (collagen + apathite) in which the combination of different phases results in an enhanced material as compared to the individual phases.

Polymer/ clay nanocomposites are a new class of composites with polymer matrixes in which the dispersed phase is the silicate constituted by particles that have at least one of the dimensions in nanometer level. One of the components is the matrix, in which the particles of the second material are dispersed. The most used mineral particles in these nanocomposites are smectitic clays (montmorillonite, saponite and hectorite), having their particles lamellae morphology with sides in micrometer level and thickness around one nanometer (Alexandre & Dubois, 2000; Esteves et al., 2004).

The montmorillonite particles are extremely small and, therefore, their structure can only be studied by X-ray diffraction. The unitary layer of the montmorillonite consists in three sheets: one octahedral sheet composed of hydrargilite-brucite included between two tetrahedral sheets composed of silicon and oxygen. These sheets are combined in such a way that the tetrahedral edges of each silica layer form a common layer with one of the hydroxyl layers of the octahedral sheet, with oxygen atoms instead of hydroxyl groups (Papin, 1993). The layers are continuous in the a and b directions and are stacked in the c direction (Fig. 1). Water and other polar molecules can enter the unitary layers causing an expansion in the c direction. The dimension of the c axis of the montmorillonite varies from 9.6 Å, when any polar molecule is between the unitary layers, until complete separation in some cases (Brigatti et al., 2006).

The interest in the production of polymer nanocomposites comes from the large range of possible applications which involves this type of material. Features such as higher resistances towards high temperatures, UV radiation, high gas impermeability, low expansibility and processing flexibility can be achieved by the production of this type of nanocomposite. Moreover, polymers have a great well-established variety of types of processing as, for example, blending, compression, fusion, mixture and polymerization,

among others, satisfying premises for the production of the most different types of products, such as films, membranes, automotive parts, electronics, packaging materials, etc (Ke & Strove, 2005).

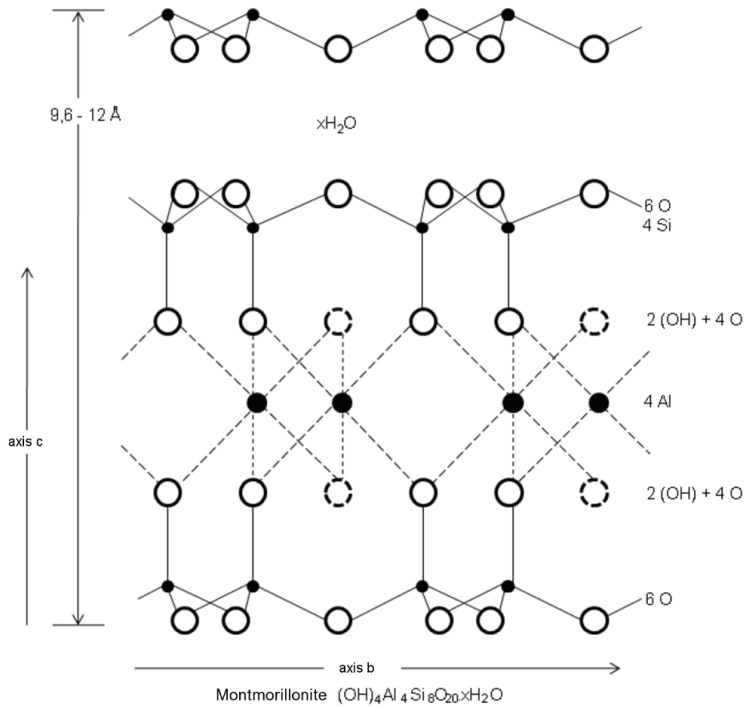


Fig. 1. Schematical representation of the montmorillonite structure (Papin, 1993).

One example of a polymer that has a wide versatility is polysulfone. Its importance is due to its mechanical, thermal and chemical stability as well as its excellent processability. A field which largely uses polysulfone is the membrane area in applications such as microfiltration, ultrafiltration, reverse osmosis and gas separation (Summers et al., 2003). However, the further enhancement in its physical property of polymer substrate is desirable for specific and enhanced applications.

Several reviews about polymer-clay nanocomposites were carried out in the last years (Choudalakis & Gotsis, 2009; Mittal, 2009; Pavlidou & Papaspyrides, 2008; Ray & Okamoto, 2003; Schmidt et al., 2002; Yeh & Chang, 2008). Considering the great attention that has been paid to polymer-clay nanocomposites and to polysulfone, presenting researches which involve polysulfone-clay nanocomposites is opportune. In this chapter, a brief history of thermoplastic nanocomposites, nanocomposite morphologies, types of polymer-clay nanocomposite production, modifications in polymer and clay structures which allow them to be used in nanocomposite preparation will be presented. Hence, having these concepts developed, works related to the preparation and characterization of clay-containing polysulfone nanocomposites, giving priority to papers and patents which describe this material, will be detailed.

2. The history of thermoplastic nanocomposites

Until the early 1970s, minerals were used in polymers only as fillers, aiming to reduce costs, since these fillers are generally heavier and cheaper than the polymer to which they are added.

During the 1970s, some changes occurred in the international scenario, as, for example, the vertiginous increase in the petroleum price during and after the 1973 and 1979 crisis (Rabello, 2000). These facts, together with the introduction of polypropylene in commercial scale, besides the development of materials with mica, glass spheres and fibers, talc and calcium carbonate, led to an expansion of the ceramic raw material market as fillers and to the beginning of the research into the interactions between polymers and fillers.

During the 1980s and 90s, these investigations advanced, leading to a higher understanding of the mechanisms of interactions with different types of polymers. All these researches raised mineral from the simple filler condition to the functional filler condition.

Although polymer-clay nanocomposites appeared before the 1980s (Carter et al., 1950), only at the end of this decade, works which guided to the development of thermoplastic nanocomposites began to appear in the literature, which were developed by Toyota by using polyamide 6 and organophilic clays specially prepared for this nanocomposite (Kawasumi, 1989; Okada et al., 1988).

These works guided to the first commercial applications of these nanocomposites in timing belt covers of Toyota vehicles, in collaboration with UBE company, a Japanese polyamide 6 industry. This material had only 5 wt.% special clay which sensibly improved the features of this material as compared to that of pure polyamide 6. According to Toyota, the nanocomposite formation provided an increase of 40% in the rupture tension, 60% of the tensile modulus and 126% in the flexion modulus, together with the increase in the thermal distortion temperature from 65 to 152°C in comparison with pure polymer.

From then on, several other companies have presented thermoplastic nanocomposites, the great majority of them with polyamide and polypropylene for automotive applications. The choice for the automotive sector is justified by the need of obtaining sufficient volume of this material, which is a great problem nowadays. Still, General Motors, the industry that uses the most nanocomposites in the world, used only 245 tons of these materials in 2003 (Cox et al., 2004; Patterson, 2004).

Another application that has gained attention is the gas barrier, using polyamide and polyester as the matrix (Conway, 2004; Goldman & Copsey, 2004). However, a large-scale commercial application of these materials is still necessary, since, although their performance is better, the competition with other materials is harmed when the cost-benefit ratio is analyzed.

3. Polymer-clay nanocomposite morphologies

Depending on the interfacial interactions forces between polymer matrix and silicate, three different types of nanocomposites are thermodynamically accepted (Fig. 2):

- intercalated nanocomposites: in the intercalated nanocomposites, the insertion of polymer matrix in the silicate structure occurs in a regular way, crystallographically, by alternating polymer chains and silicate layer, whose distance between each other varies from 1 to 4 nm, distance in the range of the polymer chain length;

- flocculated nanocomposites: they are the same as intercalated nanocomposites, except for the fact that some silicate layers are, sometimes, flocculated due to the interactions between hydroxyl groups of the silicate;
- exfoliated nanocomposites: in the exfoliated nanocomposites, the individual clay mineral layers are randomly separated in a continuous polymer matrix by an average distance which depends on the clay charge. Generally, the clay content in an exfoliated nanocomposite is much lower than in an intercalated nanocomposite (Ke & Stroeve, 2005; Ray & Okamoto, 2003).

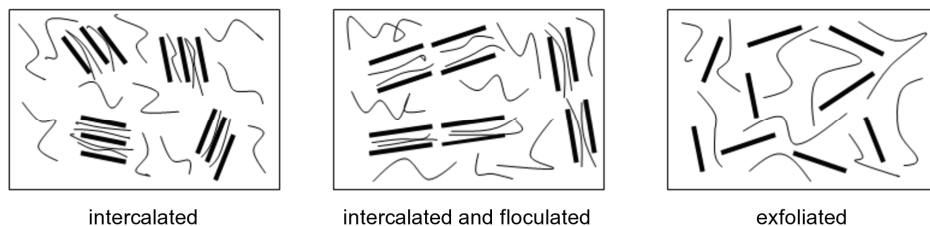


Fig. 2. Illustration of the three types of thermodynamically accepted nanocomposites (Anadão et al., 2011)

4. Nanocomposite production methods

Four methods are used in nanocomposite preparation. In situ polymerization was the first method developed. In this technique, a monomer is used as a medium for the clay dispersion and favorable conditions are performed in order to carry out the polymerization between the clay mineral layers. Polymerization can be initiated by heat or radiation, by the diffusion of an adequate initiator or a fixed catalyzer inside the layers before the filling step by the monomer.

There are cases in which complete exfoliation occurs, since the driving force for complete exfoliation is polymerization. Due to the fact that the clay mineral has high surface energy, the clay mineral layers exert attraction on the monomer units towards the inside of the galleries until equilibrium is reached. The polymerization reactions occur between the layers with lower polarities and displace the equilibrium, aiming at the diffusion of new polar specimens between the layers to progressively exfoliate the clay mineral.

The second method is the solution dispersion in which the silicate is exfoliated in single layers by using a solvent in which the polymer (or pre-polymer in the case of insoluble polymers such as polyimide) is soluble. Such silicate layers, counting on weak forces that maintain the layers united can be easily dispersed in an adequate solvent by the entropy increase caused by the disorganization of the layers which exceeds the organizational entropy of the lamellas.

Polymer is, then, adsorbed in the delaminated layers, and when the solvent is evaporated (or the mixture is precipitated), layers are reunited, filled with polymer to form, in the best case, an ordered multilayer structure, that is, an intercalated morphology.

Moreover, there is melt intercalation. In this method, silicate is mixed with the thermoplastic polymer matrix in its melt state. Under these conditions and if the layer surface is

sufficiently compatible with the chosen polymer, polymer chains can be dragged to the interlamellar space and form an intercalated or exfoliated nanocomposite.

The driving force in the melt intercalation process is the enthalpic contribution of the interactions between polymer and clay. The advantage of this technique is the non-use of solvent (Ke & Stroeve, 2005; Souza et al., 2006).

Finally, a less common method is also employed, in which a clay slurry is directly mixed with the polymer. The idea of this technique consists in increasing the basal spacing of the clay in the first stage of the process, by the polymerization of the monomers or clay suspension in water/solvents and hence, the polymer matrix is intercalated in the increased basal spacing (Kaneko et al., 2007).

5. Clay and polymer modifications for nanocomposite formation

In some cases, polymer or clay is not chemically compatible and there is thus the need of chemical modification of these materials for nanocomposite formation. Two commonly used techniques are: the use of a compatibilizer agent and clay organophilization.

Frequently, a compatibilizer agent can be a polymer which has chemical compatible nature with the polymer and the clay, by a treatment, such as the grafting of a chemical element containing reactive groups or copolymerization with another polymer also containing reactive groups, compatibility is provided between the materials that will form the nanocomposite (Ke & Stroeve, 2005).

Clay organophilization aims at a better interaction of the clay with the polymer, consisting of the exchange of interlamellar cations (generally sodium and calcium ions) by organic molecules with positive charges that neutralize the negative charges of the silicate layers, aiming to produce an organophilic clay. Generally, amino acids (Usuki et al., 1993), alkylammonium and other salts of this family are used and improve clay wettability by the polymer matrix, facilitating the penetration of the organic molecules between their platelets (De Paiva et al., 2008; Leite et al., 2010).

6. Clay-containing polysulfone nanocomposites

Researches into clay-containing polysulfone nanocomposites began to appear in the literature in 2001. After that, an expressive number of papers and patents have been published in several specialized journals. Next, examples of the scientific advances related to these materials will be presented, according to the following division: polysulfone (PSf), poly(ether sulfone) (PES) and derivatives of polysulfone.

6.1 Polysulfone-clay nanocomposites

In the literature, some papers about PSf-clay nanocomposites are presented. The first one, published in 2001, is about the preparation of a polysulfone nanocomposite with montmorillonite organically modified with dodecylammonium bromide by solution dispersion in dimethylacetamide. Exfoliated nanocomposites were produced and had an improved thermal stability and mechanical properties, although, according to the authors, these two properties were not considerably improved since polysulfone is a high performance polymer with very good properties and it is harder to improve them. Moreover, authors proposed to perform other tests in the future in order to evaluate

different properties, such as, for example, corrosion and diffusion properties (Sur et al., 2001).

Therefore, another study which used solution dispersion, investigated the corrosion properties of a polysulfone nanocomposite membranes prepared with Kunipia-F montmorillonite organomodified with dodecylamine. Low clay contents (as 1 wt.%) produced nanocomposites with superior anticorrosion and barrier properties as a result of the dispersed silicate layers which hinder the diffusion path of oxygen and water (Yeh et al., 2004).

A patent also showed the possibility of preparing polysulfone nanocomposites with smectite clay organomodified with quaternary ammonium ions by two types of organophilization: clay dispersion in water or extrusion of the dry clay with the organomodifier. Nanocomposite preparation was performed by melt intercalation in several types of machines such as extruders, rolls mills, Banbury® type mixers and Banbury® continuous mixers. Features such as improved tensile modulus, tensile strength, gas barrier and heat distortion temperatures could be obtained by creating intercalated or exfoliated mixtures (Ross & Kaizerman, 2003).

A blend composed of PSf, cyanate ester and organophilic MMT was prepared by melt intercalation. Although the flexural modulus was not significantly modified, thermal stability fracture toughness and fracture energy were improved in comparison with the two matrixes due to the good adhesion level of PSf particles to the matrix as well as the homogenous dispersion of the clay mineral platelets into the system (Mondragón et al., 2006).

In 2006, polysulfone nanocomposite membranes were again prepared by solution dispersion in NMP by using an unmodified (Cloisite Na) and organically modified (Cloisite 30B and 93) clays. Only the use of Cloisite 30 B promoted the nanocomposite formation, with an exfoliated/ intercalated morphology. This structure led to enhanced mechanical properties and wettability, while this structure also allowed its use in ultrafiltration operations (Monticelli et al. 2006).

Another nanocomposite, composed of polysulfone and epoxy, with a montmorillonite organomodified with cetyltrimethylammonium bromide was produced by solution dispersion. Homogeneous exfoliated nanocomposites with very improved mechanical properties were obtained (Rajasekaran et al., 2008).

Polysulfone nanocomposites were prepared by contacting a polymeric antimicrobial agent with clay (e.g. Cloisite Na⁺) and a posterior dispersion of the clay platelets in the polysulfone matrix for many applications (Gao et al., 2008).

Sulfonated polysulfone, produced by sulfonation with chlorosulfonic acid, was used with laponite in the preparation of a nanocomposite proton exchange membrane by solution dispersion. It was found that proton conductivity, an important feature in proton exchange membrane, was increased by 25% without affecting water retention, allowing its use as a fuel cell (Lixon-Buquet et al., 2008; Lixon-Buquet et al., 2010).

In 2005, the preparation of polysulfone-clay nanocomposite membranes for filtration area was initiated at the University of São Paulo, Brazil. Since membrane technology has an important role in separation techniques, such as water and wastewater treatment, chemical, metallurgical and petrochemical-related industries, food industries and bioseparation area, special attention should be given to the preparation of membranes, especially the polymer membranes which are largely used in these separation processes. After researches with the

preparation of polysulfone membranes, performed in the beginning of 2000, it was found that the hydrophilicity of the membranes was low and could cause a reduction in water flux and the formation of fouling onto membrane surface. Therefore, an alternative should be found to improve this property.

Techniques such as the use of plasma and sulfonation reactions are used to improve this feature. However, besides enhancing hydrophilicity, mechanical and thermal properties are harmed by using these approaches. Therefore, it was necessary to investigate a technique that could improve membrane wettability without harming other material properties.

Once nanocomposite technology is known to be effective in the improvement of several properties, it was chosen for the preparation of a more hydrophilic membrane. Since sodium montmorillonite from Wyoming is a hydrophilic clay, this clay was then used in the preparation of polysulfone nanocomposite membrane.

The wet-phase inversion method, firstly developed by Loeb and Sourirajan (Loeb & Sourirajan, 1962), is extensively used in the preparation of polymer membranes and consists of the dissolution of the polymer in an appropriate solvent, followed by casting onto a glass plate and immersion of this apparatus-containing the polymer film in a non-solvent bath, where an exchange between solvent and non-solvent will take place, producing membrane coagulation and formation. A combination of solution dispersion, from nanocomposite technology, with the last step of the wet-phase inversion method, that is, the immersion in a non-solvent bath, was used to produce the polysulfone-montmorillonite membranes.

The chosen polymer was polysulfone Udel® P-1700, kindly supplied by Solvay Advanced Polymers; the solvent was N-methyl-2-pyrrolidone and the non-solvent was distilled water at room temperature. Sodium montmorillonite from Wyoming (Sigma commercial name), with cation exchange capacity equal to 95 meq/ 100g, was used without any organophilization.

Different clay contents were studied in this research, which were 0.0, 0.5 and 3.0 wt.% and dispersions consisting of these montmorillonite contents and 25 wt.% PSf were prepared under vigorous mechanical stirring. These dispersions were cast onto a glass support and were immersed in distilled water bath. After 1 minute, membranes were completely detached from the glass surface.

Small-angle X-ray diffraction (SAXRD) [40 kV-30 mA; CuK α radiation ($\lambda = 0.154$ nm); at the rate of 0.6°/ min in the range of 1.5 - 25° (2θ)], transmission and scanning electron microscopies (TEM and SEM, respectively) were used in order to investigate membrane and nanocomposite morphologies.

Thermal properties were evaluated by thermogravimetry (TGA) (25-900°C, air flow of 50 mL/min; heating rate of 10°C/min and sample mass of 5 mg) and mechanical properties were determined by tensile tests, according to standard ASTM D882-02. Water contact angle measurements were performed to quantify membrane hydrophilicity from free energy of hydration given by Young-Dupré equation (Eq. 1):

$$(1 + \cos\theta) \gamma_w^{\text{TOT}} = - \Delta G_{\text{SW}} \quad (1)$$

Where γ_w^{TOT} is the total surface tension of the water, equal to 73 mJ. m⁻² (Lapointe et al., 2005).

From SAXRD results (Table 1), it was possible to note that, since MMT presented a basal spacing of 14.8 Å and both diffractograms showed a basal spacing of 13 Å, there was the formation of intercalated nanocomposites. In order to prove the intercalation of the

polysulfone chains between the silicate layers, membranes were calcinated until 300°C and SAXRD were again performed. Again, the basal spacings of 13 Å were detected, showing that polymer chains were intercalated in these materials and no water molecules, in this last case, the basal spacing would be reduced to 10 Å, which would mean the collapse of the clay mineral layers due to the absence of polymer chains between them (Grim & Güven, 1978) Aiming to support SAXRD results, TEM images were obtained. In the membrane prepared with 3.0 wt.% clay, besides PSf intercalation, individual clay mineral platelets could be seen, therefore, showing a complex morphology with partial intercalation/ exfoliation structure (Fig. 3).

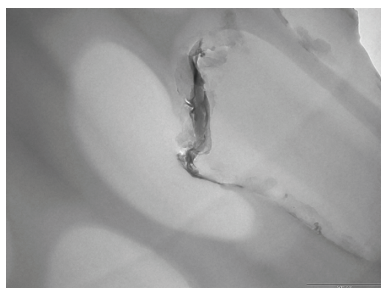


Fig. 3. TEM image of the membrane prepared from the dispersion containing 3 wt.% clay.

The dispersion of the clay particles in the PSf matrix was also evaluated by SEM micrographs (Fig. 4). Clay mineral particles could not be seen in the SEM cross-section micrographs of any of the membranes, which means that there was a good dispersion in the polymer matrix. Moreover, the addition of clay did not promote a change in the cell-like cross-section morphology. Therefore, nanocomposite membranes could be used in the same applications to which PSf membranes were designated.

Clay addition did not change the profile of the TGA curves, either, in comparison with PSf properties (Lisa et al., 2003). Polysulfone nanocomposites presented a two-stage mass loss event around 450°C ascribed to PSf decomposition. From Table 1, it is possible to observe an increase in the onset temperature of decomposition by 3 and 29°C, respectively. This improvement in thermal stability can be explained by the barrier properties conferred by the clay mineral layers which hamper oxygen diffusion into the material and by the labyrinth effect, which is related to the tortuous path the oxygen molecules have to go through. Then, these two combined effects delay volatilization (Lu et al., 2006).

Clay content (wt.%)	d_{001} of the non-calcinated membranes (Å)	d_{001} of the calcinated membranes (Å)	Onset temperature of decomposition (°C)	Elongation at break (%)	Tensile strength (MPa)	ΔG_{SW} (mJ m ⁻²)
0.0	0	0	449	31.7±0.7	7.8±0.5	-92.4
0.5	13	13	452	33.8±0.6	8.3±0.6	-95.3
3.0	13	13	478	36.4±0.8	9.8±1.1	-96.1

Table 1. Basal spacing (d_{001}) of the non-calcinated and calcinated membranes, onset temperature of decomposition, elongation at break, tensile strength and free energy of hydration (ΔG_{SW}) of the membranes according to clay content.

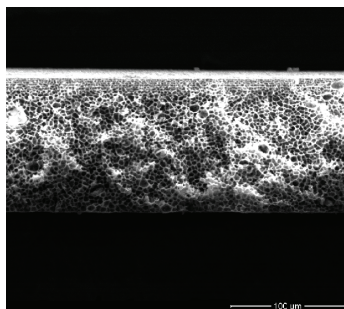


Fig. 4. SEM image of the membrane prepared from the dispersion containing 3 wt.% clay.

An improvement of the mechanical properties could also be observed by the nanocomposite formation, as can be seen in Table 1. Although montmorillonite addition is known to reduce elongation at break (Nigam et al. 2004), this feature was improved in the nanocomposite membranes probably due to a rearrangement of the clay mineral layers in the direction of deformation (Yeh et al., 2004).

Lastly, hydrophilicity was increased with the increase of the clay content and the free energy of hydration values of the nanocomposite membranes were closer to the value of true hydrophilic materials, $\Delta G_{SW} \leq -113 \text{ mJ m}^{-2}$ (van Oss, 1994).

Therefore, a polysulfone nanocomposite membrane, able to be used in filtration operations, with higher hydrophilicity and improved thermal and mechanical properties was obtained by the use of a hydrophilic clay by combining solution dispersion and wet-phase inversion techniques (Anadão et al., 2010).

6.2 Poly(ether sulfone)-clay nanocomposites

Some studies about poly(ether sulfone)-clay nanocomposites can also be found in the literature. The first one was published in 2006 and was related to the investigation of barrier properties of plasma-modified poly(ether sulfone)/ organomodified montmorillonite nanocomposites. Remarkable enhancements in the storage modulus and water/ oxygen permeability were observed in comparison to the pure PES (Wu & Yang, 2006).

The use of attapulgites in the preparation of a nanocomposite with epoxy/ poly(ether sulfone) blends was also studied. The arrangement of attapulgite particles increased the interaction between the epoxy and the poly(ether sulfone) phases and improved the modulus of the material (Zhao et al., 2008).

In 2010, a research was performed concerning a sulfonated poly(ether sulfone) -organophilic montmorillonite nanocomposite proton exchange membrane prepared by solution dispersion with different clay contents. The membrane produced with 3.0 wt.% clay showed the maximum selectivity, $520,000 \text{ S s cm}^{-1}$; besides, all membranes showed a better direct methanol fuel cell performance in comparison with a Nafion® 117 membrane. Other features, such as low cost, convenient processability, reduced methanol permeability, among others, demonstrated the potential of this nanocomposite material to be applied in direct methanol fuel cell applications (Hasani-Sadrabadi et al. 2010).

An epoxy- poly(ether sulfone)-Cloisite 30 B nanocomposite was prepared and characterized by a group from India. The use of two different preparation techniques, ultrasonication and planetary ball milling, led to the formation of distinct morphologies: intercalated and

exfoliated, respectively. Although the addition of clay promoted an improvement in all studied mechanical properties, especially in those with exfoliated morphology, an accentuated decrease in tensile and flexural strength with higher clay contents. Barrier properties were also enhanced and optical transparency was retained until 5 wt.% clay (Asif et al., 2010).

6.3 Derivatives of polysulfone-clay membranes

As far as the author knows, there is only one study about a derivative of polysulfone, poly(arylene ether sulfone), so far. An exfoliated nanocomposite was produced by solution dispersion technique. A higher value of proton conductivity and methanol permeability were obtained in comparison to Nafion® 115, a material widely used in fuel cell membrane. Mechanical properties were also improved in relation to pure polymer. These features showed that these nanocomposites can be used in direct methanol fuel cell operations (Choi et al., 2008).

7. Conclusion

As remarked by the author of the first published paper about polysulfone nanocomposites, as polysulfone plastics are considered high-performance polymers, features such as mechanical and thermal properties are not significantly improved by nanocomposite formation. However, other properties, such as barrier, corrosion and hydrophilicity properties could be improved by the use of the clay nanocomposite technology.

Except for my research, which used sodium montmorillonite, other works showed the extensive use of organoclays in the preparation of these nanocomposites. The most used preparation method was the solution dispersion; therefore, melt intercalation can also be a possibility to produce polysulfone-clay nanocomposite membranes and it could be further investigated in the future. As polysulfone-clay nanocomposites were mainly produced by this technique, which can be used together with the wet-phase inversion method, widely used in membrane preparation, as shown in this author's results, the applications of the nanocomposites presented in the literature is extremely focused on the membrane area, especially in filtration and fuel cell areas. The studies regarding the use of blends composed of polysulfone and other polymer showed that these nanocomposites could be used in the aerospace area.

Finally, having a knowledge developed in these areas, specific improved features can be obtained in the future by using clay nanocomposite technology with different types of clays. Moreover, as mentioned before, the investigation into the use of different techniques to prepare polysulfone can be interesting in order to produce nanocomposites with different properties.

8. Acknowledgment

Solvay is acknowledged for providing polysulfone Udel®.

9. References

- Alexandre, M. & Dubois, P. (2000) Polymer-layered silicate nanocomposites: preparation, properties and uses of a new class of materials. *Materials Science & Engineering R*, Vol. 28, pp. 1-63.

- Anadão, P., Sato, L.F., Wiebeck, H. & Diaz, F.R.V. (2010) Montmorillonite as a component of polysulfone nanocomposite membranes. *Applied Clay Science*, Vol. 48, pp. 127-132.
- Anadão, P.; Wiebeck, H. & Díaz, F.R.V. (2011). Panorama da pesquisa acadêmica brasileira em nanocompósitos polímero/ argila e tendências para o futuro. *Polímeros: Ciência e Tecnologia*, in press.
- Asif, A.A., John, B., Rao, V.L. & Ninan, K.N. (2010) Surface morphology, thermomechanical and barrier properties of poly(ether sulfone)-toughened epoxy clay ternary nanocomposites. *Polymer International*, Vol. 59, pp. 986-997.
- Brigatti, M.F., Galan, E. & Theng, B.K.G. (2006) Structures and mineralogy of clay minerals. In: *Handbook of Clay Science*, Bergaya, F., Theng, B.K.G. & Lagaly, G., pp.19-86, Elsevier: Amsterdam.
- Callister, W.D. (1994) *Materials Science and Engineering: an introduction*. John Wiley & Sons, New York.
- Carter, L.W., Hendricks, J. G. & Bolley, D. S. (1950). *Elastomer Reinforced With A Modified Clay*. National Lead Co. US Patent 2531396.
- Chawla, K.K. (1987) *Composite Materials: Science and Technology*. Springer Verlag, New York.
- Choi, Y.S., Kim, T.K., Kim, E.A., Joo, S.H., Pak, C., Lee, Y.H., Chang, H. & Seung, D. (2008) Exfoliated sulfonated poly(arylene ether sulfone)-clay nanocomposites. *Advanced Materials*, Vol. 20, pp. 2341-2344.
- Choudalakis, G. & Gotsis, A.D. (2009) Permeability of polymer/ clay nanocomposites: A review. *European Polymer Journal*, Vol. 45, pp. 967-984.
- Conway, R. (2004) Using nanotechnology to provide active and passive barriers in beverage packaging application. *Proceedings of 4th World Congress in Nanocomposites*, San Francisco, Sep. 2004.
- Cox, H., Dearlove, T., Rodges, W., Verbrugge, M. & Wang, C. S (2004) Nanocomposite systems for automotive applications. *Proceedings of 4th World Congress in Nanocomposites*, San Francisco, Sep. 2004.
- Esteves, A.C.C., Barros-Timmons, A. & Trindade, T. (2004) Nanocompósitos de matriz. polimérica: estratégias de síntese de matérias híbrid. *Química Nova*, Vol. 27, pp. 798-806.
- De Paiva, L., Morales, A. & Díaz, F.R.V. (2008) Organoclays: Properties, preparation and applications. *Applied Clay Science*, Vol. 42, pp. 8-24.
- Gao, F. & Nigmatullin, R. (2008) *Method of preparing an antimicrobial polymer nanocomposites*. Nottingham Trent University. UK Patent 2450475.
- Goldman, A.Y. & Copey, C.J. (2004) Multilayer barrier liner material with nanocomposites for packaging applications. *Proceedings of 4th World Congress in Nanocomposites*, San Francisco, Sep. 2004.
- Grim, R.E., Güven, W., (1978) *Developments in sedimentology - Bentonites - geology, mineralogy, properties and uses*. Elsevier, New York.
- Hasani-Sadrabadi, M.M., Dashtimogradam, E., Ghaffarian, S.R., Hasani-Sadrabadi, M.H., Heidari, M. & Moaddel, H. (2010) Novel high-performance nanocomposite proton exchange membranes based on poly(ether sulfone). *Renewable Energy*, Vol. 35, pp. 226-231.

- Hull, D. (1981) *An Introduction to Composite Materials*. Cambridge University Press, Cambridge.
- Kaneko, M.L.Q.A., Torriani, I. & Yoshida, I.V.P. (2007) Morphological evaluation of silicone/clay slurries by small-angle/wide-angle X-ray scattering. *Journal of Brazilian Chemistry Society*, Vol. 18, pp. 765-773.
- Kaneko, M.L.Q.A., Torriani, I. & Yoshida, I.V.P. (2007) Morphological evaluation of silicone/clay slurries by small-angle/wide-angle X-ray scattering. *Journal of Brazilian Chemistry Society*, Vol. 18, pp. 765-773.
- Kawasumi, M. (1989) *Process for producing composite material*. Kabushiki Kaisha Toyota Chuo Kenkyusho. US Patent 4810734.
- Ke, Y.C. & Stroeve, P. (2005). *Polymer-Layered Silicate and Silica Nanocomposites*. Elsevier. Amsterdam.
- Lapointe, J.-F., Gauthier, S.F., Puliot, Y. & Bouchard, C. (2005) Characterization of interactions between β -lactoglobulin tryptic peptides and a nanofiltration membrane: Impact on the surface membrane properties as determined by contact angle measurements. *Journal of Membrane Science*, Vol. 261, pp. 36-48.
- Leite, I.F., Soares, A.P.S., Carvalho, L.H., Raposo, C.M.O. & Malta, O.M.L. (2010) Characterization of pristine and purified organobentonites. *Journal of Thermal Analysis and Calorimetry*, Vol. 100, pp. 563-569.
- Lisa, G., Avram, E., Paduraru, G., Irimia, M., Hurduc, N. & Aelenei, N. (2003) Thermal behaviour of polystyrene, polysulfone and their substituted derivatives. *Polymer Degradation Stability*, Vol. 82, pp.73-79.
- Lixon-Buquet, C., Dargent, E., Langevin, D., Marais, S. & Nguyen, Q.T. (2008) Synthesis and characterization of a new sulfonated polysulfone/clay-SO₃H as proton exchange membrane for fuel cell application. *Proceedings of Fundamental and Developments of Fuel Cell Conference*, Nancy, Dec. 2008.
- Lixon-Buquet, C., Fatyeyeva, K., Poncin-Epaillard, F., Schaetzel, Dargent, E., Langevin, D., Nguyen, Q.T. & Marais, S. (2010) New hybrid membranes for fuel cells: Plasma treated laponite based sulfonated polysulfone. *Journal of Membrane Science*, Vol. 351, pp. 1-10.
- Loeb, S. & Sourirajan, S. (1962) High-flow semipermeable membranes for separation of water from saline solutions. *Advances in Chemistry Series*, Vol. 38, pp. 117-132.
- Lu, H., Hu, Y., Ling, M., Chen, Z. & Fan, W. (2006) Structure characteristics and thermal properties of silane-grafted-polyethylene/clay nanocomposite prepared by reactive extrusion. *Composite Science and Technology*, Vol. 66, pp. 3035-3039.
- Mittal, V. (2009) Polymer layered silicate nanocomposites: A Review. *Materials*, Vol. 2, pp. 992- 1057.
- Mofatt, W.G., Persall, G.W. & Wulff, J. (1964) *The Structure and Properties of Materials. Vol. 1: Structure*. John Wiley & Sons, New York.
- Mondragón, I., Solar, L., Nohales, A., Vallo, C.I. & Gómez, C.M. (2006) Properties and structure of cyanate ester/ polysulfone/ organoclay nanocomposites. *Polymer*, Vol. 47, pp. 3401-3409.

- Monticelli, O., Bottino, A., Scandale, I., Capannelli, G. & Russo, S. (2007) Preparation and properties of polysulfone-clay composite membranes. *Journal of Applied Polymer Science*, Vol. 103, pp. 3637-2644.
- Nigam, V., Setua, D.K., Mathur, G.N. & Kar, K.K. (2004) Epoxy-montmorillonite clay nanocomposites: Synthesis and characterization. *Journal of Applied Polymer Science* Vol. 93, pp. 2201-2210.
- Okada, A., Fukushima, Y., Kawasumi, M., Inagaki, S., Usuki, A., Sugiyama, S., Kurauchi, T. & Kamigaito, O. (1988) *Composite material and process for manufacturing same*. Kabushiki Kaisha Toyota Chou Kenkyusho. US Patent 4739007.
- Padilha, A.F. (1997) *Materiais de Engenharia - microestrutura e propriedades*. Hemus Editora, São Paulo.
- Papin, R. (1993) Bentonite. In: *Kirk-Othmer Encyclopedia of Chemical Technology*, Kirk Othmer, Vol. 3, pp. 339-360, John Wiley & Sons: New York.
- Patterson, T. (2004) Nanocomposites- our revolutionary breakthrough. *Proceedings of 4th World Congress in Nanocomposites*, San Francisco, Sep. 2004.
- Pavlidou, S. & Papispyrides, C.D. (2008) A review on polymer-layered silicate nanocomposites. *Progress in Polymer Science*, v. 33, pp. 1119-1198.
- Rabello, M.S. (2000) *Aditivação de Polímeros*. Artliber Editora, São Paulo.
- Rajasekaran, R., Karikalchozhan, C. & Alagar, M. (2008) Synthesis, characterization and properties of organoclay-modified polysulfone/ epoxy interpenetrating polymer network nanocomposites. *Chinese Journal of Polymer Science*, Vol. 26, pp. 669-678.
- Ray, S. S. & Okamoto, M. (2003) Polymer/layered silicate nanocomposites: a review from preparation to processing. *Progress in Polymer Science*, Vol. 28, pp. 1539-1641.
- Ross, M. & Kaizerman, J. (2003) *Smectite clay/ organic chemical/ polymer compositions useful as nanocomposites*. Elementis Specialties Inc., US Patent 6521690.
- Schmidt, D., Shah, D. & Giannelis, E.P. (2002) New advances in polymer/layered silicate nanocomposites. *Current Opinion in Solid State and Materials Science*, Vol. 6, pp. 205-212.
- Souza, M.A., Pessan, L.A. & Rodolfo Jr., A. (2006) Nanocompósitos de poli(cloreto de vinila) (PVC)/ argilas organofílicas. *Polímeros: Ciência e Tecnologia*, Vol. 16, pp. 257-262.
- Summers, G.J., Ndawuni, M.P. & Summers, C.A. (2003) Dipyriddy functionalized polysulfones for membrane production. *Journal of Membrane Science*, Vol. 226, pp. 21-33.
- Sur, G.S., Sun, H.L., Lyu, S.G. & Mark, J.E. (2001) Synthesis, structure, mechanical properties, and thermal stability of some polysulfone/organoclay nanocomposites. *Polymer*, Vol. 42, pp. 9783-9789.
- Usuki, A., Kawasumi, M., Kojima, Y., Okada, A., Kurauchi, T. & Kamigaito, O. (1993) Swelling behavior of montmorillonite cation exchanged for o-aminoacids by ϵ -caprolactam. *Journal of Materials Research*, Vol. 8, pp. 1174-1178.
- Van Oss, C.J. (1994) *Interfacial forces in aqueous media*. Marcel Dekker, New York.
- Van Vlack, L.H. (1984) *Princípios de Ciência e Tecnologia dos Materiais*. Campus, Rio de Janeiro.
- Wu, T.-M. & Yang, S.-H. (2006) Surface characterization and barrier properties of plasma-modified polyethersulfone/ layered silicate nanocomposites. *Journal of Polymer Science: Part B Polymer Physics*, Vol. 44, pp. 3185-3194.

- Yeh, J.-M., Chen, C.-LL., Chen, Y.-C., Ma, C.-Y., Huang, H.S. & Yu, Y.-H. (2004) Enhanced corrosion prevention effect of polysulfone-clay nanocomposite materials prepared by solution dispersion. *Journal of Applied Polymer Science*, Vol. 92, pp. 631-637.
- Yeh, J.-M. & Chang, K.-C. (2008) Polymer/layered silicate nanocomposite anticorrosive coatings. *Journal of Industrial and Engineering Chemistry*, Vol. 14, pp. 275-291.
- Zhao, L., Zhan, G., Yu, Y., Tang, X. & Li, S. (2008) Influence of attapulgites on cure-reaction-induced phase separation in epoxy/poly(ether sulfone) blends. *Journal of Applied Polymer Science*, Vol. 108, pp. 953-959.

Processing and Characterization of Alumina / Chromium Carbide Ceramic Nanocomposite

Jow-Lay Huang and Pramoda K. Nayak
*National Cheng Kung University
Taiwan*

1. Introduction

Materials with nano-scale components as reinforcement phase are adding new dimensions to composite materials, thereby facilitating major improvement in functional and structural properties. Ceramic nanocomposites are the blends of different ceramic matrices with nanometer sized functional particles. The advantages of these nanocomposites include: improved mechanical properties, surface properties, decreased permeability to gases, water and hydrocarbons, higher thermal stability and heat distortion temperature, higher chemical resistance, smoother surface appearance and higher thermal conductivity. The incorporation of only a few percent of nano-sized particles makes great property changes and formerly unachievable property combinations possible.

The ceramic nanocomposites can be divided into three types; intragranular composite, intergranular composite and nano/nano composite (Niihara, 1991) according to their microstructures. In intra and intergranular nano-composite, the nano-sized particles are dispersed mainly within the matrix grains or at the grain boundaries of the matrix, respectively. The aim of these composites is to improve the mechanical properties such as hardness, fracture strength, toughness and also high temperature mechanical properties such as hardness, strength, creep and fatigue fracture resistances. On the other hand, nano/nano composites are composed of the dispersoids and matrix grains within the nanometer size. The primary purpose of this type of nano-composite is to add new functions such as machinability and super plasticity like metals to ceramics.

1.1 Synthesis of ceramic nanocomposite

Chemical Vapor Deposition (CVD) is a very preferable method to disperse the nano-sized second phases into the matrix grains or at the grain boundaries (Niihara & Hirai, 1986). $\text{Si}_3\text{N}_4/\text{TiN}$ was the first system prepared by CVD. However, the CVD process is not applicable to fabricate the large and complex shaped component for the mass production and also it is very expensive. Processing route is another technique to prepare ceramic nanocomposites. Following the initial work of (Niihara & Nakahira, 1988), several research groups have tried to synthesize the nanocomposites using processing route. There are several methods involve in processing route such as conventional powder processing (Borsa et al., 1999; Carroll et al., 1996; Niihara et al., 1989; Shapiro et al., 2009), sol-gel processing (Liu et al., 2006; Xu et al., 1994) and polymer processing (Borsa & Brook, 1995; Galusek et al.,

2007). The ceramic nanocomposites can be synthesized using microwave plasma (Vollath et al., 1997; Vollath & Szabó, 2006). In this process, the matrix material is coated with a layer of second phase material. The main advantage of this technique is that the reaction product does not form hard agglomerates because of the specific conditions during synthesis. Oxide and nitride based ceramic nanocomposites have been synthesized using microwave plasma technique (Vollath & Sickafus, 1993; Vollath & Sickafus, 1992). Recently developed spark plasma synthesis (SPS) is an advanced technique for the synthesis of ceramic nanocomposites. The technique has a great advantage over conventional sintering technique, since the whole process can be complete in a few minutes, thus allowing nanosized grains of the sintering powder, and its crystal structure as well, to be retained in the sintered body. Various ceramic nanocomposites have been synthesized using SPS in literature (Dusza et al., 2009; Kumari et al., 2009; Trombini et al., 2009).

Furthermore, using all the above synthesis techniques for preparing ceramic nanocomposite, the nanoscaled reinforced particles are difficult to disperse uniformly on the micro-scale matrix particles. This problem is ascribed to the fact that nano-scale particles agglomerate easily due to the interaction between the particles. The agglomeration promote the generation of voids during the densification and microstructural inhomogeneity. Kunii & Levenspiel, 1977 have recognized that a fluidized bed reactor can supply an environment with a uniform temperature and concentration of the coating precursor, which can provide the possibility of a good dispersion of reinforcing nano-particles in a matrix. A precursor vaporized at a low temperature is the major characteristic of the metal-organic chemical vapor deposition (MOCVD) process. The combination of conventional fluidized bed technology with standard chemical vapor deposition has been proven to be an effective method to deposit particles (Chen & Wei, 2002; Tsugeki et al., 1993).

1.2 Characteristics of ceramic nanocomposite

Microstructure and mechanical properties such as micro hardness, fracture strength, and fracture toughness are the main characteristics of ceramic nanocomposite materials. Apart from this, the nanocomposites also exhibit electro conductive, wear resistance, creep resistance and high temperature performance. One of the major characteristics and the greatest disadvantages of ceramics is their brittleness. Researchers have tried to compensate these disadvantages and to improve the strength of the nanocomposite. It has been observed that the fracture strength of the brittle materials can only be improved by the increase in fracture toughness or by reduction in critical flaw size (Davidge, 1979). Therefore, much effort has been invested in advanced processing technology to reduce the size and density of processing flaws (Lange, 1989). However, the design of tougher, flaw-tolerant ceramics is a more interesting approach for wider industrial applications. The fracture toughness can be increased by incorporating various energy-dissipating components such as whiskers, platelets or particles into the ceramic microstructure (Becher, 1991; Lange, 1973). The reinforcements serve to deflect the crack or to provide bridging elements hindering further opening of the crack. Another concept is to incorporate metallic ligaments into the ceramic matrix (Sigl et al., 1988) to form crack bridging elements that absorb energy by plastic deformation.

1.3 Mechanisms of ceramic nanocomposite

In 1997, Sternitzke reviewed the modeling (strengthening and toughening mechanisms) of nanocomposites and divided the mechanisms into three groups; c-mechanism, K-

mechanism and grain boundary strengthening mechanism. The c-mechanism is based on the fact that the matrix becomes refined following the adding of nano-sized silicon carbide. A refinement of the grain size leads to smaller critical flaw size and higher strength. K-mechanism relates to R-curve behavior, crack deflection, and crack bowing during a crack extension. Ohji et al., 1998 proposed a particle-bridge mechanism, where there exists crackface shielding when nano-size particles bridge the crack surfaces. Crack deflection and crack bowing are related to the interactions of a crack front with second-phase inclusions which depend on the differences in the thermoelastic properties of the matrix and inclusions. Levin et al., 1995 and Sekino et al., 1997 explained that the strengthening mechanism of nanocomposites results from residual stresses around the second-phase particles, and matrix weakening and grain boundary strengthening produce the change of the fracture mode. Only nano-sized dispersed particles can improve the strength and the fracture toughness.

2. Alumina/chromium carbide nanocomposite

Alumina is one of the important materials in structural ceramic application because of its excellent mechanical properties, good chemical stability and high temperature characteristics (Ghate et al., 1975; Wang & Hsu, 1996). Its intrinsic brittleness and relatively poor reliability however, made the toughening of alumina ceramics an important and challenging area of research now days. The incorporation of secondary ceramic reinforcement phases (e.g. particulates, fibers, or platelets) has been proven to be an easy, safe and economically toughening technique for alumina ceramics (Chou & Green, 1992; Lio et al., 1989). There are several approaches by the researchers to toughen the alumina matrix with addition of different secondary phases. Among all the approaches, SiC reinforcement particles on Al_2O_3 composites mostly improve the mechanical properties (Anyu, 1999; Sternitzke, 1997). But the toughness enhancement is not significant for these composites. On the other hand, incorporating chromium carbide particles into Al_2O_3 matrix has been successfully achieved for toughening purposes (Fu et al., 1994; Huang et al., 2000; Lii et al., 1999). These aluminum oxide/chromium carbide composites demonstrate superior mechanical properties to those of matrix phase due to the high Young's modulus of chromium carbide and its outstanding ability to resist high temperature erosion at temperatures up to 1000° C. In addition, the good electrical conductivity of chromium carbide makes electrical discharge machining possible.

Besides second phase particles, solid solution strengthening is another mechanism for the Al_2O_3 matrix. Chromia (Cr_2O_3) has been used to improve the physical properties of Al_2O_3 (Bradt, 1967). As Cr_2O_3 has the same corundum crystal structure similar to Al_2O_3 , Al_2O_3 - Cr_2O_3 can form substitutional solid solution in all ranges at high temperature. The addition of Cr_2O_3 was found to increase the hardness, tensile strength, and thermal shock resistance of Al_2O_3 .

This chapter will emphasize on the processing of Alumina/Chromium carbide ceramic matrix composite by metal oxide chemical vapor deposition (MOCVD) in fluidized bed and analysis of these composites using various characterization techniques. The synthesis parameters, microstructure and mechanical properties of the alumina/chromium carbide prepared by three different processes such as (i) Hot press sintering, (ii) Carbothermal reduction, and (iii) Spark plasma sintering, have been investigated and summarized in details in the following sections.

2.1 Experimental details

This section describes the raw powders, different types of synthesis procedures such as MOCVD, Hot press sintering (HP), Carbothermal reduction, Spark plasma sintering (SPS), and various characterization techniques such as X-ray diffraction (XRD), scanning electron microscopy (SEM), transmission electron microscopy (TEM), and energy dispersive spectroscopy (EDS), X-ray photoelectron spectroscopy (XPS) and electron energy loss spectroscopy (EELS) used in the current work. The flow chart showing the detailed experimental procedure is given in Fig.1.

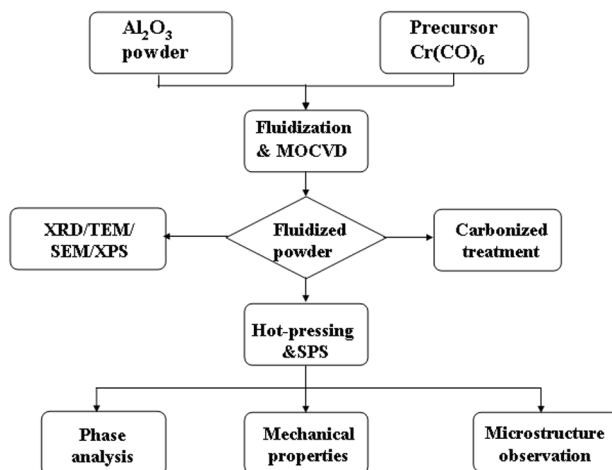


Fig. 1. Flow chart of the experimental procedure adopted in the current work.

2.1.1 Powder and sample preparation

Chromium hexacarbonyl ($\text{Cr}(\text{CO})_6$, 99%, Strem Chemicals Co., USA) was used as the precursor of chromium oxide in the MOCVD process. Aluminum oxide powder with the average particle size of about 0.2–0.4 μm (A16-SG, Alcoa, USA) was used as the matrix powder. A vaporized precursor carried by He gas (99.9% pure) was introduced into the fluidized bed reactor for the MOCVD process. Based on the results of Lander & Germer, 1947, the precursor container was kept at 75°C in a vacuum (10 torr) in the present experiment. To investigate the influence of the temperature on the product deposited on the fluidizing Al_2O_3 particles, the $\text{Cr}(\text{CO})_6$ vapor was decomposed in the fluidized chamber at 300 and 400 °C, respectively. The apparatus consisted of six main components: gas supply, MOCVD precursor, fluidized bed reactor, power supply, temperature controller, cold trap and vacuum system, as shown schematically in Fig. 2. (Lin et al., 2006a). The pressure in the chamber was measured with a pressure meter. A rotary vacuum pump was set up with a cold trapping system. The temperature controllers (TC) were connected to a heating system that controlled the temperature of the fluidized reactor and precursor container.

2.1.2 Characterization of the fluidized powder

The fluidized powders were analyzed by x-ray diffraction (XRD; Rigaku D/MaxII, Japan), and transmission electron microscopy (TEM; Hitachi FE-2000, Japan) equipped with energy

dispersive x-ray spectroscopy (EDS; UK). X-ray photoelectron spectroscopy (XPS; VG Scientific 210, UK) was used to determine the coating phases by binding energy. A Brunauer-Emmett-Teller (BET) instrument Micromeritics Gemini 2360, USA) was used to measure the specific surface area by nitrogen adsorption, and C/O analyzer (LECO CS-244, USA) was used to measure the carbon content of coated powder by a combustion method. Fig. 3 shows the XRD patterns of decomposed $\text{Cr}(\text{CO})_6$ prepared in fluidized bed at 300°C and 400°C . It is observed that at 300°C , the powder is completely amorphous in nature, whereas at 400°C , the powder consists of Cr_2O_3 along with CrC_{1-x} phase (Lin et al., 2006b).

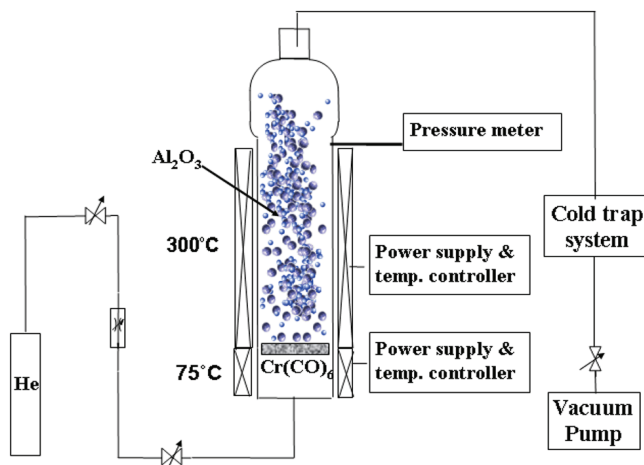


Fig. 2. Schematic diagram of MOCVD and fluidized bed.

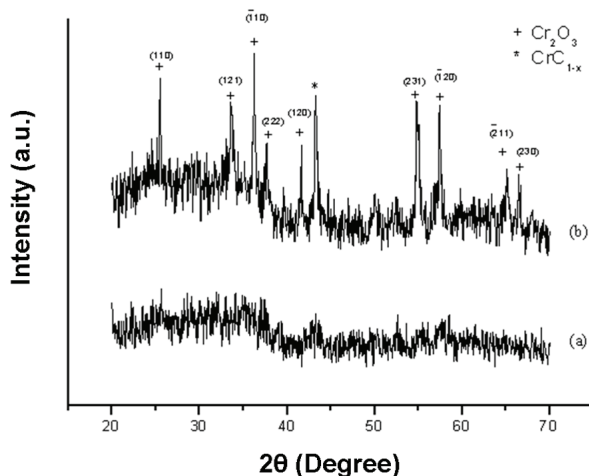


Fig. 3. XRD pattern of decomposed $\text{Cr}(\text{CO})_6$ prepared in fluidized bed at (a) 300°C (b) 400°C .

The pyrolysis of precursor $\text{Cr}(\text{CO})_6$ at 300°C results the formation of Cr_2O_3 , C-Cr and C-C bonds observed from XPS spectra (Fig. 4). This figure displays the XPS spectra of the Cr $2p$ and C $1s$ regions of the as-deposited powder prepared at 300°C . Fig. 4a shows two peaks corresponding to the spin-orbit splitting $2p_{1/2}$ (right) and $2p_{3/2}$ (left) of Cr with bonding energies of 586.3 and 576.6 eV, respectively. The band shift of these two peaks is 9.7 eV, which is in good agreement with previously reported data (Wagner et al., 1979) and confirms the existence of Cr_2O_3 particles in the as-deposited powder. The XPS spectra of the C $1s$ regions in Fig. 4b provide the evidence for which at least two forms of carbon in the as-deposited powder exist. One is free carbon (C-C) at 284.6 eV, and the other carbon bonded to chromium atoms (C-Cr) at 283.5 eV.

The decomposed precursor deposits uniformly over Al_2O_3 and the deposited nano particles ($\sim 30\text{ nm}$) are shown in the TEM micrograph (Fig. 5a). The insert shows the TEM pattern of the deposited nano particles, which is amorphous in nature. From the EDS spectrum shown in Fig. 5b, it is confirmed that the nanoparticles consist of mostly Cr and O along with small amount of C. The presence of Cu is the contribution from Cu grid.

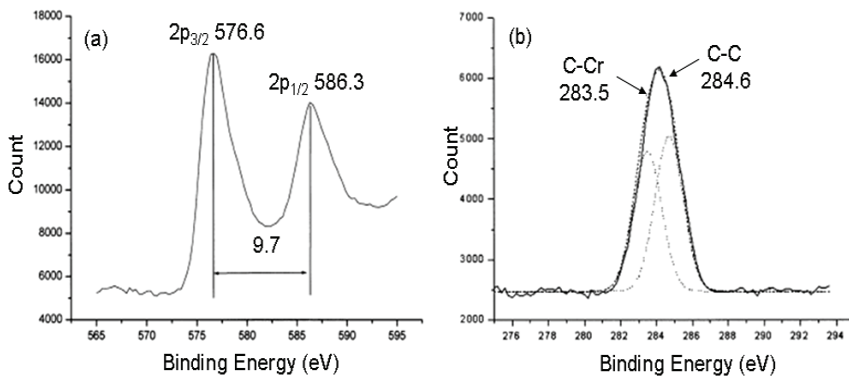


Fig. 4. X-ray photoelectron spectra of the (a) Cr $2p$ regions and (b) C $1s$ regions of as deposited composite powders prepared at 300°C in fluidized bed.

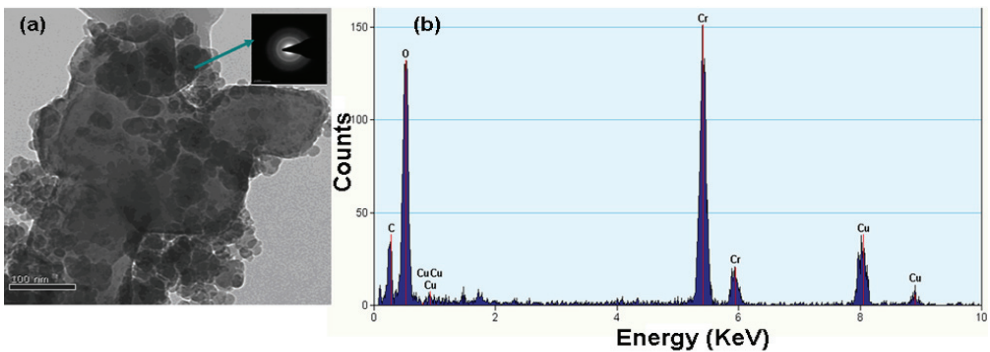


Fig. 5. TEM micrographs of (a) nanoparticles deposited on alumina particle (b) EDS spectrum of the coating particle.

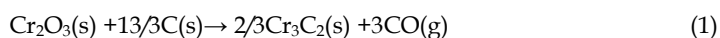
Table 1 shows the carbon content of the samples prepared at different fluidized temperature. The carbon content is 0.75 and 0.23% for the samples fluidized at 300 and 400°C, respectively. It indicates that the as-deposited amorphous powder prepared at 300 °C has more carbon content than the crystalline powders prepared at 400°C. This was probably because of the amorphous powder has specific surface area (25.5m²/g) larger than the crystalline powder (11.2 m²/g).

Specimen	Fabricated in Fluidized reactor	Carbon content (%)	BET surface area (m ² /g)
1	300° C, 2h	0.75	25.5
2	400° C, 2h	0.23	11.2

Table 1. Specific surface area and carbon content of specimens

3. Carbothermal treatment of Cr₂O₃ particles dispersed on Al₂O₃ particles

The carbothermal treatment of the prepared Cr₂O₃/Al₂O₃ powders was first performed in a graphite furnace at a variety of temperatures from 700 to 1150 °C in a vacuum condition (10⁻³ Torr) for 2h. Fig. 6. shows the XRD patterns of the fluidizing powders treated from 700 to 1150 °C in the graphite furnace for 2 h. The Cr₂O₃ peaks seen in the XRD patterns clearly indicate that the amorphous Cr₂O₃ has crystallized, but does not carbonize at temperatures under 1000 °C. As reported by Bouzy et al., 1993 and Bewilogua et al., 1988, an annealing treatment causes a transformation of the metastable carbide CrC_{1-x} into the stable carbide phase Cr₃C₂. Here, Cr₃C₂ peaks are not observed in the XRD patterns shown in Fig. 6a-6d, consequently, suggesting that the CrC_{1-x} content of the decomposed Cr (CO)₆ is too little to be found in XRD patterns. According to the XRD pattern shown in Fig. 6e, Cr₂O₃ reacts with carbon and transforms into Cr₃C₂ when the treatment temperature is 1150 °C. This carbothermal reaction process (Storms, 1967) can be shown as the following equation:



3.1 The formations of Cr-carbide/Al₂O₃ nanocomposite and Cr₂O₃/Al₂O₃ solid solution

After carbothermal treatment, the fluidized powders undergone hot pressed sintering at 1400° C. For this process, the 200 mesh fluidized powder was first die-pressed, and then put into a BN-coated graphite die and hot-pressed at a pressure of 25MPa in a HP furnace (High-multi 5000, Fujidempa Kogyo Co., Ltd., Japan) at 1400°C under vacuum (5×10⁻⁴ torr). The detailed sintering conditions of the different samples are listed in Table 2.

Samples	Sintering powders	Sintering conditions
ALO	Pure alumina powder	1400°C/1h, pressure 25 MPa
Sample 1	Composite powders fluidized at 300° C for 1 h	1000°C/1h, 1400°C/1h, 25 MPa
Sample 2	-do-	1150°C/1h, 1400°C/1h, 25 MPa
Sample 3	-do-	1400°C/1h, pressure 25 MPa

Table 2. Sintering conditions of hot pressed samples

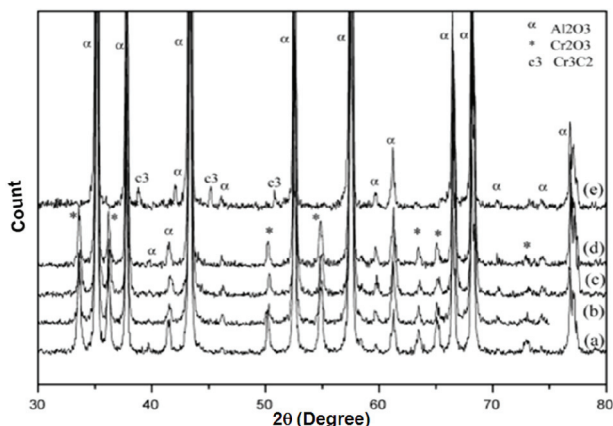


Fig. 6. XRD patterns of the powder thermally treated at a variety of temperatures: (a) 700 °C, (b) 800 °C, (c) 900 °C, (d) 1000 °C, and (e) 1150 °C in a vacuum in a graphite furnace for 2 h for the fluidized powders prepared in the fluidized bed.

Fig. 7 shows the XRD patterns of the samples thermally treated under different conditions. The Si peaks shown in the XRD pattern were used for calibration. First, Fig. 7a and 7b indicate that the Al_2O_3 peaks for sample 1 shifted to lower angles than those for Al_2O_3 . For pure Al_2O_3 , the pure alumina powder was hot pressed at 1400 °C, while for sample 1, the fluidized powder was pre-sintered at 1000 °C before the hot pressing at 1400 °C. During the pre-sintering at 1000 °C, most of the Cr_2O_3 reacted with Al_2O_3 to form an $\text{Al}_2\text{O}_3\text{-Cr}_2\text{O}_3$ solid solution and thus the Al_2O_3 peaks shifted to lower angles in the XRD pattern. Furthermore, the color of the pieces is dark red (Nassau, 1983) as observed in sample 1, due to the $(\text{Al}, \text{Cr})_2\text{O}_3$ solid solution reaction product. Secondly, a comparison with the peaks of Al_2O_3 reveals that the Al_2O_3 diffraction peaks of sample 2, as shown in Fig. 7c, shift to lower angles, occurring simultaneously with the peaks of Cr_3C_2 . Consequently, besides forming a solid solution, some of the Cr_2O_3 reacts with carbon as equation (1) to form chromium carbide Cr_3C_2 when the powders have been pre-sintered at 1150 °C (Lin et al., 2007). Finally, Fig. 7d shows the XRD patterns of sample 3, which is similar to the results of sample 2. In addition to forming a solid solution, some of the Cr_2O_3 was also carbonized. However, it transformed into mixed phases of Cr_3C_2 and Cr_7C_3 when the fluidized powders were hot pressed at 1400 °C. Berger et al., 2001 reports that Cr_7C_3 is formed at an elevated temperature (>1150 °C). Moreover, the TG/DTA results of our paper (Lin et al., 2005) also indicate that the generation temperature of Cr_7C_3 is about 1170 °C. This carbothermal reaction process (Bradt, 1967) can be shown as reaction (2). Consequently, not only Cr_3C_2 , but also Cr_7C_3 is formed in sample 3, hot pressed at 1400 °C.

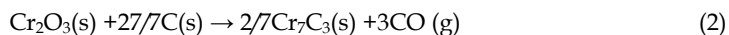


Fig. 8a shows the SEM micrograph of pure Al_2O_3 and 8b is the High Angle Annular Dark Field scanning transmission electron microscopy (HAADF STEM) image of sample 1, showing almost all the Cr^{3+} replaced the Al^{3+} and formed an $\text{Al}_2\text{O}_3\text{-Cr}_2\text{O}_3$ solid solution. According to Bondioli et al., 2000, at temperatures of over 1000 °C the complete ranges of substitutional solid solutions are obtained. Fig. 8c and 8d are the HAADF STEM images of samples 2 and 3, respectively, showing that in addition to forming a solid solution,

nanosized chromium carbide particles also disperse uniformly in the alumina matrix. Comparing the HAADF STEM images of samples, sample 2 has smaller alumina grain size ($0.7\mu\text{m}$) than others (sample 1: $1.5\mu\text{m}$, sample 3: $0.9\mu\text{m}$.) This is because it has much nanosized particles on the Al_2O_3 grain boundaries, which effectively inhibit the grain growth. The volume percentages of the reinforced particles showing in Fig. 8c and 8d are 4.5 and 1.5 vol%, respectively. Conversely, the Al_2O_3 grains of sample 1 have a larger growth size as a result of the diffusion of Cr atoms inducing grain boundary migration (DIGM) (Han et al., 1995). The drive force for the migration is believed to rise from the coherency strain in the Cr_2O_3 diffusion zone in front of the migrating grain boundaries.

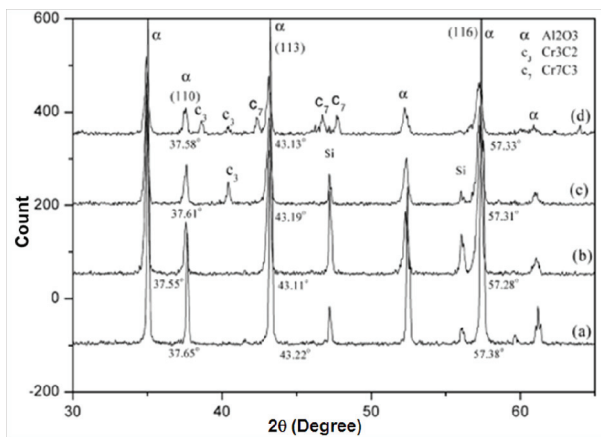


Fig. 7. XRD patterns of hot pressed samples: (a) Al_2O_3 , (b) sample 1, (c) sample 2, and (d) sample 3.

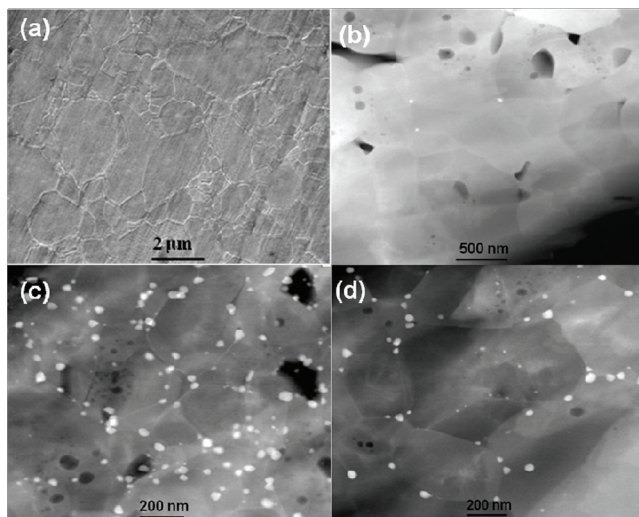


Fig. 8. SEM micrograph of (a) pure Al_2O_3 ; HAADF STEM micrographs of samples: (b) sample 1: $\text{Al}_2\text{O}_3\text{-Cr}_2\text{O}_3$, (c) sample 2: $\text{Al}_2\text{O}_3\text{-Cr}_3\text{C}_2$ and (d) sample 3: $\text{Al}_2\text{O}_3\text{-Cr}_7\text{C}_3$.

There are two HRTEM micrographs of interfaces shown in Fig. 9. One is the interface between the Cr_3C_2 and Al_2O_3 and the other is the interface between Cr_7C_3 and Al_2O_3 . The interface between Al_2O_3 and Cr_3C_2 is non-coherent, as shown in Fig. 9a. The smaller illustrations in Fig. 9a show Al_2O_3 with hexagonal and Cr_3C_2 with orthorhombic structure. The lattice spacing of the Al_2O_3 ($\bar{1} 0 1 4$) is 0.255 nm and that of the Cr_3C_2 (0 0 2) is 0.115 nm. The spacing difference between these two planes is large. However, the interface between Al_2O_3 and Cr_7C_3 is semi-coherent, as shown in Fig. 9b. Structures of both Al_2O_3 and Cr_7C_3 are hexagonal. The lattice spacing of the Al_2O_3 plane ($\bar{1} 1 0 2$) and Cr_7C_3 plane ($2 \bar{2} 0 1$) are 0.349 and 0.360 nm, respectively. There is little difference between the lattice spacing of these two hexagonal planes.

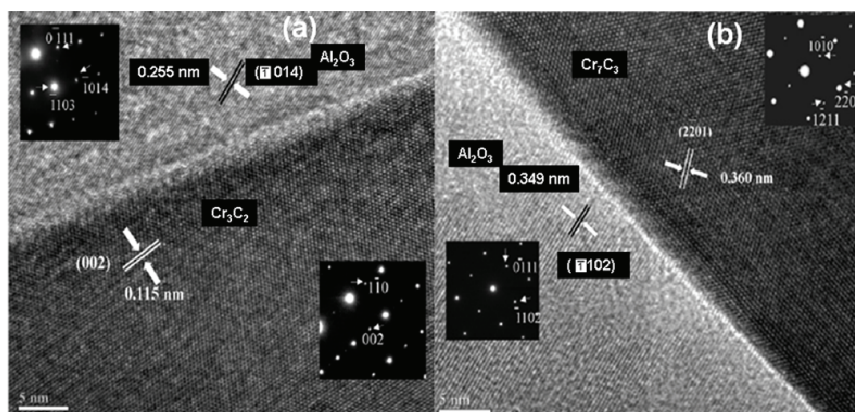


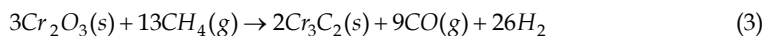
Fig. 9. Lattice images of the interfaces (a) between Cr_3C_2 and Al_2O_3 , and (b) between Cr_7C_3 and Al_2O_3 .

3.2 Carbothermal reduction of Cr_2O_3 using methane as carbonization source

The conventional route for Cr_3C_2 composite synthesis mainly involves the reduction of chromium oxide by methane gas (Anacleto & Ostrovski, 2004). However, besides the three stable chromium carbides, Cr_3C_2 , Cr_7C_3 , and Cr_{23}C_6 , several metastable carbides such as Cr_3C , CrC_{1-y} , Cr_5C_2 and $\text{Cr}_3\text{C}_{2-x}$ also have been reported, which emanate during different preparation methods and for different Cr/C contents (Bewilogua et al., 1988; Bouzy et al., 1993; Inoue & Masumoto, 1979). Lerch & Rousset, 1994 indicated that the $\text{CrO}_{1.9}$ with high surface area (200–350 m^2/g) reduced at 700 °C in an atmosphere of methane and hydrogen mixture leading to the formation of stable Cr_3C_2 and metastable $\text{Cr}_3\text{C}_{2-x}$. The metastable $\text{Cr}_3\text{C}_{2-x}$ powder was also prepared by Loubière et al., 1995 & 1996 using $\text{CH}_4\text{-H}_2$ atmosphere from the carburization of metastable chromium oxide. The metastable $\text{Cr}_3\text{C}_{2-x}$ is a Re_3B -type structure, readily formed by carburization of high specific surface area chromium oxide and usually co-existent with Cr_2O_3 , Cr_3C_2 and free carbon.

In the previous sections, we have discussed the synthesis of $\text{Cr}_2\text{O}_3/\text{Al}_2\text{O}_3$ composite powders by the decomposition of chromium hexacarbonyl in a fluidized bed. This was followed by the hot-pressing of the composite powders in a graphite mode eventually leading to its transformation into a $\text{Cr}_3\text{C}_2/\text{Al}_2\text{O}_3$ nanocomposite. One of the major drawbacks in this synthesis process was the formation of undesirable $\text{Al}_2\text{O}_3\text{-Cr}_2\text{O}_3$ solid

solution at a high temperature, which leads to abnormal grain growth of the Al_2O_3 matrix and eventually decreased the desired Cr_3C_2 contents in the composite. In order to carburize the chromium oxide completely, a new approach is reported by using the carburization process of nanosized chromium oxide formed from a metal-organic chromium hexacarbonyl precursor in a carburizing mixture of CH_4/H_2 gas. For this process, the as received powder after fluidization was carburized in an alumina tube furnace in the presence of a methane-hydrogen mixture (1:9) at 700–850 °C for 5 h. The H_2 restrain the CH_4 to decompose fast and using CH_4 as carbon source, the carbothermal reduction reaction becomes



Where, $\Delta G = 262564.44 - 236.79T$ (Cal) and ($T > 841^\circ \text{C}$)

Fig. 10 shows the XRD patterns of the decomposed powder carburized at 700–850 °C for 5 h in $\text{CH}_4\text{-H}_2$ gas. At the carburization temperature of 700 °C, the pattern displays sharp peaks that index with the Cr_2O_3 phase. At the increased carburization temperature of 750 °C, the intensity of Cr_2O_3 peaks decreases significantly accompanied by some incipient low intensity peaks which could be indexed with metastable $\text{Cr}_3\text{C}_{2-x}$. When the temperature reaches to 800 °C, the Cr_2O_3 phase disappears, concomitant with a complete transformation to the $\text{Cr}_3\text{C}_{2-x}$ phase. Further increase of the carburization temperature to 850 °C, leads to the formation of the stable Cr_3C_2 phase along with a small amount of $\text{Cr}_3\text{C}_{2-x}$ metastable phase (Wang et al., 2010).

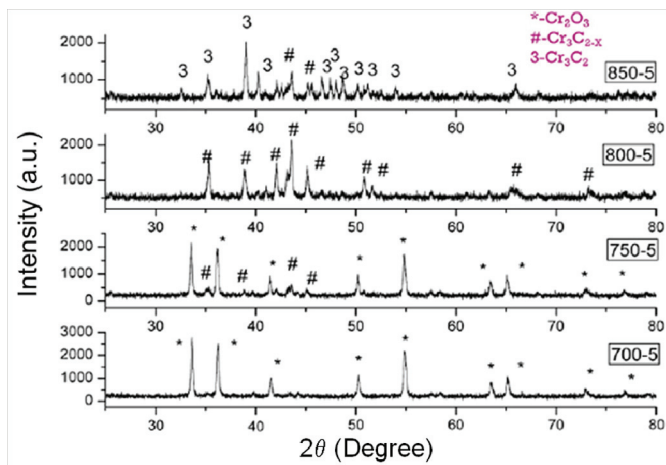


Fig. 10. XRD patterns of the decomposed precursor at different temperature.

For further validation of carburization process, the powders for different carburization temperature were characterized by TEM. Fig. 11a shows the TEM micrograph of the powder treated at 700 °C, where the particle size is found to be around 40 nm. The diffraction pattern verifies its phase for the chromium oxide Cr_2O_3 , (rhombohedral structure). The high resolution image shows a clear atomic image inside the powder. A thin amorphous layer is visible in a different contrast outside the boundary surface. This can be attributed to the adsorption of carbon deposit on the powder surface. Fig. 11b shows the TEM and HRTEM

of powdered samples carburized at 800 °C for 5 h. The spherical shape has transformed to faceted irregular grain. The diffraction pattern confirms that the phase is attributed to metastable $\text{Cr}_3\text{C}_{2-x}$, which is in accordance with the XRD result. The HRTEM image shows that there are several carbon nanofilms formed around the surface of the powder surface. The Fast Fourier transform (FFT) pattern of these layers, shows two obvious halo spots that are attributed to the graphene structure of carbon nanofilms. The TEM micrographs of the powders, carburized at 850 °C, show that the powder is encapsulated by layers of graphene, as shown in Fig. 11c. The diffraction pattern verifies that the powder comprises the stable Cr_3C_2 phase.

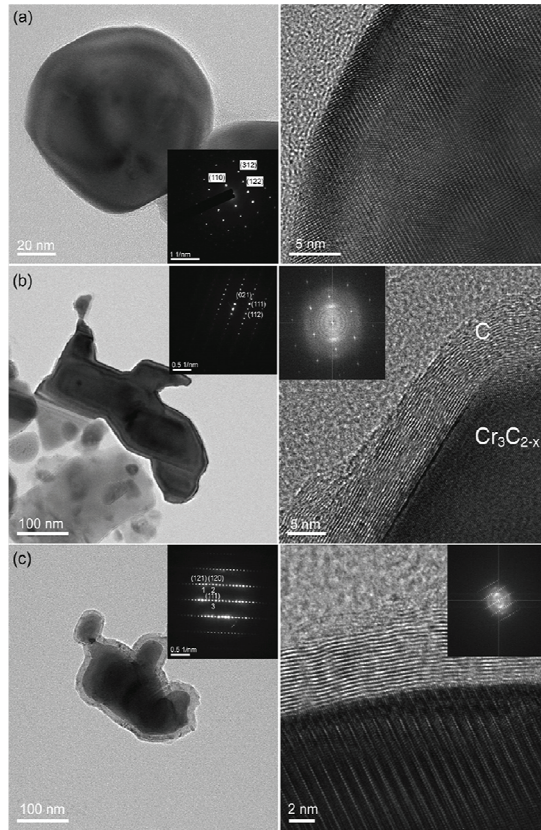


Fig. 11. TEM image of decomposed powder after the carbonized treatment (a) 700 °C/5 h; (b) 800 °C/5 h; (c) 850 °C/5 h.

The phase transformation from Cr_2O_3 to Cr_3C_2 via an intermediate state $\text{Cr}_3\text{C}_{2-x}$ has been identified using electron-energy loss spectroscopy (EELS). The EELS of prepared samples were characterized by field emission gun scanning transmission electron microscopy (FEG-STEM) equipped with energy dispersive X-ray detector (EDS) and energy filter (Gatan). Fig.12 shows the EELS spectra of Cr L edge for the sample of the decomposed precursor and the samples carbonized at 800°C and 850°C. The chromium L edges have features comprising

two sharp L_2 and L_3 , known as “white lines” (Lozzi et al., 1991) and a continuum background following the edge. The sharp double peaks are due to transitions from the $2p^{1/2}$ and $2p^{3/2}$ core levels towards $3d$ states above E_f . The sharp peaks of L_2 and L_3 at threshold are due to the transitions from the $2p^{1/2}$ core levels to $3d^{3/2}$ states and the $2p^{3/2}$ core levels to $3d^{3/2} 3d^{5/2}$, respectively. The L_3/L_2 white line ratio is correlated to the electron occupancy and spin pairing in $3d$ band. The variations of the ratio are due to the interaction between chromium and surrounding atoms. A change of the L_2 , L_3 edge intensities in the samples indicates a variation of the d holes because the edge intensity is proportional to the number of the empty final states available. The ratio of L_3/L_2 of sample shown in Fig. 12a is higher than that of carbonized samples. According to the results of Arévalo-López & Alario-Franco, 2009, the ratio of L_3/L_2 for the Cr_2O_3 is about 1.6 and from the report of Fan et al., 1999, the ratio of L_3/L_2 for the Chromium carbide is about 1. A comparison between Fig.12b and 12c shows L_3 edge of the sample carbonized at $850^\circ C$ is $577.72 eV$, while that of sample carbonized at $800^\circ C$ is $575.42 eV$. The shift in energy ($2.3 eV$) is called the chemical shift. This result is due to the transformation from the metastable carbide to stable carbide, because the EELS represent the difference in energy between a core-level initial state and the lowest energy final state of an excited electron. But the energy loss close to $577.72 eV$ for the decomposed precursor (Daulton et al., 2002), which consists of Cr_2O_3 is same as the sample carbonized at $850^\circ C$. It is observed that there is no chemical shift between this two species because Cr_2O_3 and Cr_3C_2 are both chemically stable compounds.

The π electron formed sp^2 bonding observed from the EELS spectra of C K edges as shown in Fig. 12. The peak of sp^2 bonding is sharper when the carbonized temperature increases from $800^\circ C$ to $850^\circ C$. The sharpening of sp^2 peak is attributed to the formation of graphite like carbon according to Fan et al., 1999. In Cr_3C_2 , C is graphite like rather than diamond like, which comprising of sp^3 bonded carbon atoms. For the as decomposed precursor, the content of carbon was little and formed amorphous phase. More carbon produced from the pyrolysis of methane coated on the Cr_2O_3 surface and then formed graphite phase and metastable carbide of Cr_3C_{2-x} when the sample was treated at $800^\circ C$ for 5 hours. The increase of treated temperature to $850^\circ C$, enhanced the process of carbonizing reaction leading to more graphite formation followed by transformation of metastable Cr_3C_{2-x} to stable carbide of Cr_3C_2 (Lin et al., 2011).

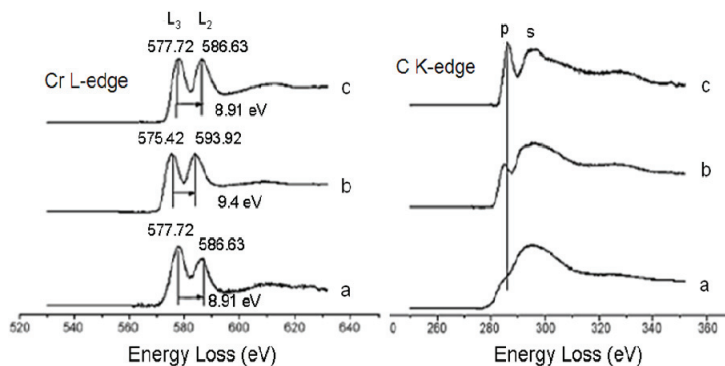


Fig. 12. EELS of Cr L edges & C K edges : (a) decomposed precursor, (b) carbonized at $800^\circ C/5 h$ (Cr_3C_{2-x}), and (c) carbonized at $850^\circ C/5 h$ (Cr_3C_2).

Based on these above results, one could hypothesize the following phase transformation steps: In the first step, the methane decomposes to elemental carbon and hydrogen (Muradov, 1998 & 2001). The carbon reacts with the Cr_2O_3 at temperatures higher than 800°C , and produce partial Cr_3C_2 phase and $\text{CO}_{(g)}$. The $\text{CO}_{(g)}$ can also carburize the Cr_2O_3 further. There are three kinds of carbon sources in the system viz. free carbon from the decomposition of methane, CO from above reaction and C-C bonding from the precursor. Finally, the unreacted redundant carbon sources would deposit on the surface of the powder as the lamellar graphene. The graphene deposited during the carburization has an important role for the formation of meta-stable $\text{Cr}_3\text{C}_{2-x}$ and stable Cr_3C_2 . Initially, carbon gets absorb on the surface of chromium oxide at low temperature. As the temperature rises, substantial amount of carbon is available, leading to metastable chromium carbide. Finally, as the temperature increases further, the redundant carbon forms the graphene layers. Further thickening of the graphene films, generates a mechanical stress (Loubière et al., 1996) which assists the transformation of meta-stable $\text{Cr}_3\text{C}_{2-x}$ state to stable Cr_3C_2 phase.

3.3 Microstructure and mechanical properties of $\text{Cr}_3\text{C}_2/\text{Al}_2\text{O}_3$ nanocomposites

As discussed in the previous sections, the carbonization treatment of initial powders without using methane as the carbon source leads to the formation of $(\text{Cr}_3\text{C}_2, \text{Cr}_7\text{C}_3)/\text{Al}_2\text{O}_3$ nanocomposites, where as carbonization using methane as carbon source leads to $\text{Cr}_3\text{C}_2/\text{Al}_2\text{O}_3$ nanocomposites, which is the desired material. In order to improve the mechanical properties of these $\text{Cr}_3\text{C}_2/\text{Al}_2\text{O}_3$ nanocomposites, the carbonized powders were undergone hot-press sintering at 1400°C for 1 hr in vacuum.

Fig. 13 shows the SEM micrographs of monolithic Al_2O_3 and $\text{Cr}_3\text{C}_2/\text{Al}_2\text{O}_3$ nanocomposites carbonized at different temperatures for 5 hours and hot-pressed at 1400°C for 1 hr in vacuum. One can see that there is abnormal grain growth of Al_2O_3 shown in Fig. 13a. In case of $\text{Cr}_3\text{C}_2/\text{Al}_2\text{O}_3$ nanocomposite, the dispersion secondary phase, Cr_3C_2 is uniform (Fig. 13b) and the abnormal grain growth has been inhibited. The grain size distribution of monolithic Al_2O_3 and $\text{Cr}_3\text{C}_2/\text{Al}_2\text{O}_3$ nanocomposites has been shown in Fig. 14. The nanocomposite exhibits low grain size than that of pure alumina. It implies that addition of Cr_3C_2 decreases the grain size and inhibits the growth of alumina matrix.

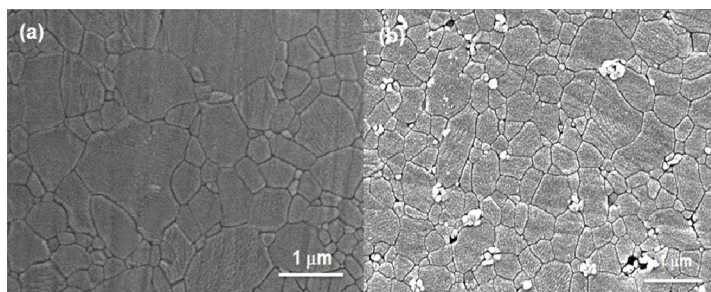


Fig. 13. SEM micrographs of (a) monolithic Al_2O_3 and (b) $\text{Cr}_3\text{C}_2/\text{Al}_2\text{O}_3$ nanocomposites by carbonized at different temperatures for 5 hours and hot-pressed at 1400°C for 1 hr in vacuum.

The TEM micrograph of $\text{Cr}_3\text{C}_2/\text{Al}_2\text{O}_3$ nanocomposites shown in Fig.15 illustrates two types of inclusion of Cr_3C_2 onto the Al_2O_3 matrix i.e. inter-type inclusion (Fig.15a) and intra-type inclusion (Fig. 15b). Fig. 16 shows the SEM micrographs of the fracture surface of monolithic

Al_2O_3 and $\text{Cr}_3\text{C}_2/\text{Al}_2\text{O}_3$ nanocomposites under the same carbonization condition. The fracture surface of pure alumina is intergranular in nature, where as transgranular fracture surface is observed in $\text{Cr}_3\text{C}_2/\text{Al}_2\text{O}_3$ nanocomposites.

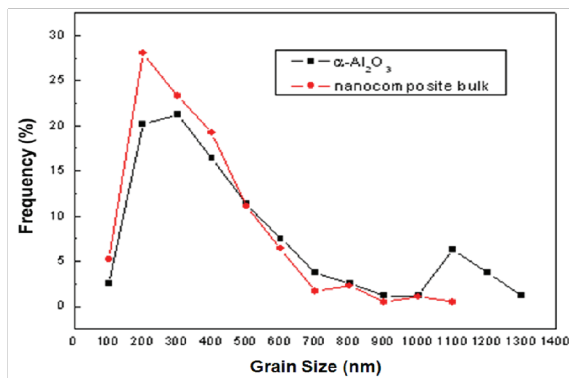


Fig. 14. Grain size distribution of (a) monolithic Al_2O_3 and (b) $\text{Cr}_3\text{C}_2/\text{Al}_2\text{O}_3$ nanocomposites prepared by carbonization at different temperatures for 5 hours followed by hot-press sintering at 1400°C for 1 hr in vacuum.

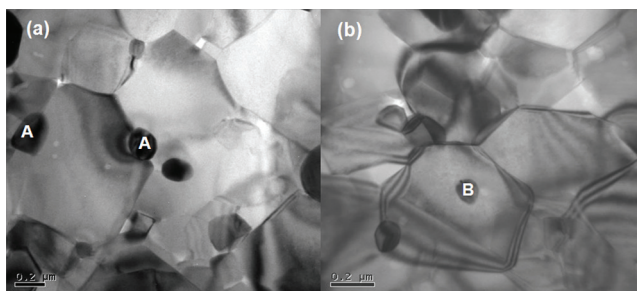


Fig. 15. TEM micrographs of $\text{Cr}_3\text{C}_2/\text{Al}_2\text{O}_3$ nanocomposites (a) inter-type inclusion in A (b) intra-type inclusion in B.

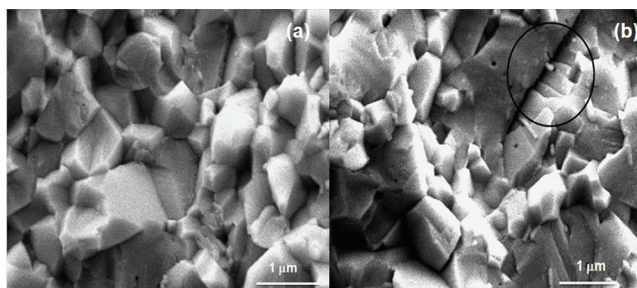


Fig. 16. SEM micrographs of the fracture surface (a) monolithic Al_2O_3 and (b) $\text{Cr}_3\text{C}_2/\text{Al}_2\text{O}_3$ nanocomposites prepared by carbonized at different temperatures for 5 hours hot-pressed at 1400°C for 1 hr in vacuum.

The basic mechanical properties such as hardness, fracture strength and toughness of pure alumina as well as of this nanocomposite have been analyzed and mentioned in table 3. The fracture strength was determined by 4-point bending (Shimadzu AG-IS 100KN, Japan). The toughness was measured by Single-Edge-Pre-cracked Beam (SEPB). A precrack with depth of 0.254mm was conducted in the center of sample by a diamond cutter with a thickness of 0.15mm. It is observed that the nanocomposite exhibits improved hardness, fracture strength and fracture toughness in comparison to monolithic alumina. The relationship between the microstructure and improved mechanical property has been investigated and described below.

Specimen	Hardness	Strength (4 pt-bending)	Toughness (Indentation Fracture method)
Al ₂ O ₃	18.4 GPa	375 MPa	4.0 MPa.m ^{1/2}
Cr ₃ C ₂ /Al ₂ O ₃	19.8 GPa	520 MPa	5.5 MPa.m ^{1/2}

Table 3. Mechanical property measurements on monolithic Al₂O₃ and Cr₃C₂/Al₂O₃ nanocomposites

The nanocomposites consisting of Cr₃C₂ particles dispersed within Al₂O₃ matrix grains, result in the generation of thermally induced residual stresses after hot-pressed sintering at 1400°C. The mismatch in thermal expansion co-efficient between the matrix (α -Al₂O₃= 8.4*10⁻⁶/ °C), and the dispersed particles (Cr₃C₂=11.2*10⁻⁶/ °C) yields highly localized residual stresses around the particles. These stresses reduce quickly as distance from the boundary increases because of the nano-sized particles, which can generate only small defects such as dislocations shown in Fig. 17a in close vicinity to the particles (Awaji et al., 2002; Choi & Awaji, 2005). In the monolithic alumina, crack propagates along with the grain boundaries due to the existence of defects and the compress residual stresses resulting from anisotropic thermal expansion, Young's modulus along the crystal axes, and crystallographic misorientation across the grain boundaries. The fracture toughness of grain boundaries is usually lower than that within the grains. However, in nanocomposites, the dislocations around the Cr₃C₂ particles release residual stresses in the Al₂O₃ matrix. Consequently, the defect size along the grain boundaries is reduced. Also, the dislocations serve as origins of small stress concentrations, and create nano-cracks around the propagating crack tip. These nano-cracks slightly reduce the strength of the alumina matrix, while reduction of both the residual stresses along the grain boundaries and the strength in the matrix lead to a change in the fracture mode from that of the intergranular fracture in monolithic alumina to that of transgranular fracture in nanocomposites, as shown in Fig. 16b. In addition, due to the effect of nano-cracking, the step-wise fracture surface rather than a planar cleavage plane is observed in the nanocomposites (Choi et al., 2004), as shown in Fig. 17b. The reinforcement of the Cr₃C₂ particles, small grain size of Al₂O₃ matrix and reduction of both the defect size along the grain boundaries and the tensile residual stresses in the matrix grains by dislocations result in improvement of the strength of nanocomposites.

In the case of Cr₃C₂-Al₂O₃ solid solution described in the previous section, the Cr³⁺ ions increase the growth rate of Al₂O₃ grain because of the coherency strain energy at grain boundary (Harabi & Davies, 1995; Paek et al., 1996; Riu et al., 2000). However, this

phenomenon is not found in the nanocomposites. It is attributed that the secondary particles of Cr_3C_2 inhibits the growth of alumina matrix. The fracture strength is increased by the grain-boundary modification caused the compressive stress generated by the substitution of bigger Cr^{3+} ion (0.076 nm) in place of smaller Al^{3+} ion (0.068nm). The localized compressive stress helps in strengthening the grain boundary, and then the fracture strength increases by this effect (Lii et al., 1999). The higher toughness of the nanocomposites relative to monolithic alumina may be connected with the stepped transgranular cleavage. The direction of crack propagation within the matrix grains is affected by these dislocations.

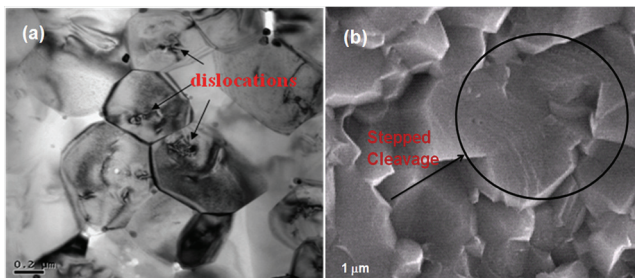


Fig. 17. (a) dislocations and (b) stepped cleavage observed in $\text{Cr}_3\text{C}_2/\text{Al}_2\text{O}_3$ nanocomposites.

4. Densification behavior of $\text{Al}_2\text{O}_3\text{-Cr}_2\text{O}_3/\text{Cr}_3\text{C}_2$ nanocomposites prepared by Spark Plasma Sintering

Compared with conventional hot pressed sintering, spark plasma sintering (SPS) has recently attracted increasing interest due to its ability of rapidly heating the powder compact to high temperatures and consolidating it to high densities within very short time. SPS utilizes applied pressure along with temperature and a pulsed direct current to densify materials. SPS is heralded for its promise in retaining nanostructure features, producing grain boundaries devoid of impurities as well as many other benefits (Kim et al., 2007; Munir et al., 2006; Shen et al., 2002).

As described earlier, the initial powders used for this sintering process were $\text{Al}_2\text{O}_3\text{-Cr}_2\text{O}_3$, which were prepared by metal organic chemical vapor deposition (MOCVD) in a fluidized bed. The nanosized composite powders fabricated in the fluidized bed for 30 and 60 minutes were named as S-30 and S-60, respectively. The pressure of reaction chamber was controlled at 10 torr, and the reaction temperature was kept at 300 °C. The fluidized powders were densified by a SPS process (SPS-515S, Shumitomo, Japan). The 1.5gram of powder (pure Al_2O_3 , S-30, S-60) was put into a graphite mold of 15.5mm diameter. The uniaxial pressure of 50Mpa was imposed on the powder and the vacuum level was less than 6 Pa. The heating rate from room temperature to 600°C and from 600°C to sintering temperature was 200°C/min and 100°C/min, respectively with a holding time of 10 minutes. There were four different sintering temperature conditions of 1200°C, 1250°C, 1300°C and 1350°C conducted in this study.

4.1 Effect of SPS sintering temperature on the color changes of compacts

The color of compacts prepared under different SPS conditions is shown in Fig.18. It is observed that the color of compacts sintered at 1200°C is green; the color of 1250°C compact

is purple; while that of 1300°C and 1350°C are black. Fig. 19 indicates the XRD patterns of the compacts processed by various SPS temperatures. Besides Al_2O_3 peaks, the Cr_2O_3 peaks are found in the compact sintered at 1200°C. Compared with the peak of pure- Al_2O_3 , the Al_2O_3 peaks of compact sintered at higher temperature have slight shifted to lower angles. It means only a little solid-solution of $\text{Al}_2\text{O}_3\text{-Cr}_2\text{O}_3$ has formed in this compact. This result is special to the compacts fabricated by conventional densification methods in which significant pink solid-solution of $\text{Al}_2\text{O}_3\text{-Cr}_2\text{O}_3$ was formed. According to Bondioli et al.,2000, the complete ranges of $\text{Al}_2\text{O}_3\text{-Cr}_2\text{O}_3$ solid solution can be obtained for the reaction temperature higher than 1000°C.

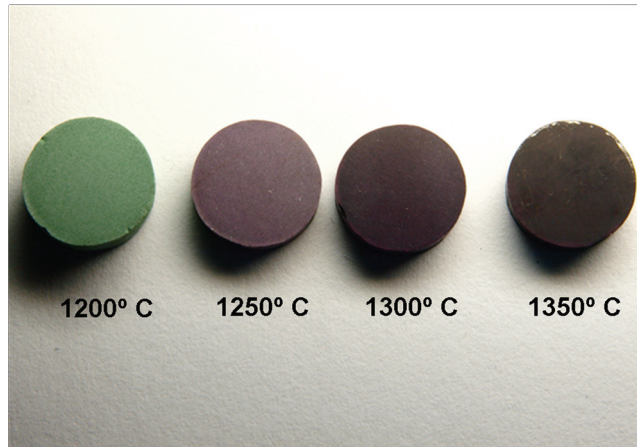


Fig. 18. Optical micrograph of compacts prepared by different SPS temperatures from 1200°C to 1350°C.

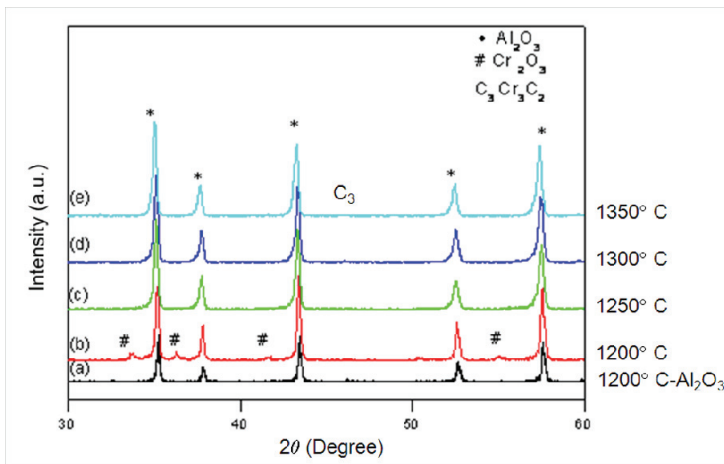
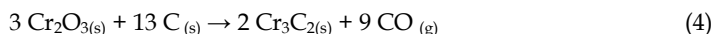


Fig. 19. XRD patterns of (a) pure Al_2O_3 sintered at 1200°C, and the compact at (b) 1200°C, (c) 1250°C, (d) 1300°C and (e) 1350°C for 10 min by SPS.

It is suggested that due to the higher heating rate and short holding time, the most of Cr^{3+} doesn't have enough time to diffuse into Al_2O_3 matrix and remains as Cr_2O_3 phase after the SPS process. The color of pure Cr_2O_3 is green, and so the composite is with green appearance. For the compact sintered at 1250°C , the Cr_2O_3 peaks are disappeared in the XRD pattern because more Cr_2O_3 react with Al_2O_3 matrix to form pinker solid solution in this higher sintering temperature. According to Equation 4 given in (Kubaschewski et al. 1979), chromium carbide would form probably when the temperature is higher than 1150°C . It is believed that there is little black carbide formed when sintered at 1250°C , so the compact exhibits purple color. It is reasonable that the more Cr^{3+} diffuse into Al_2O_3 matrix with the increase in sintering temperature. In comparison to other compacts, more Al_2O_3 peaks of the compact sintered 1350°C have shifted to lower angles observed from XRD patterns. It indicates that more solid solution is formed at a higher temperature. The amount of the solid solution of $\text{Al}_2\text{O}_3\text{-Cr}_2\text{O}_3$ and Cr_3C_2 increases with the increase of sintering temperature.



$$\text{Where, } \Delta G = 261313.95 - 188.5 T \text{ (cal)}$$

The black color of the compact prepared at 1350°C is relevant to the formation of chromium carbide. More Cr_3C_2 is formed as the temperature is over than 1150°C . Cr_3C_2 nanoparticle is observed for the compacts prepared at 1300°C and 1350°C . The TEM diffraction pattern shows the particle with Cr_3C_2 phase as shown in Fig. 20. Although the peak of Cr_3C_2 peaks are not obvious in the XRD patterns in Fig. 19., but based on the Equation 1, sintering at a higher temperature is beneficial to form Cr_3C_2 . In our previous study (Lin et al., 2007), Cr_3C_2 peaks are easy to be found in the XRD patterns as compacts prepared by HP densification in which the vacuum maintained at about 10^{-5} torr, however in this SPS process that is about 6 pa ($\sim 10^{-2}$ torr). According to the report of Chu & Rahmel, 1981, carbon would be consumed by oxygen in a higher oxygen pressure in SPS process and inhibits the formation of Cr_3C_2 .

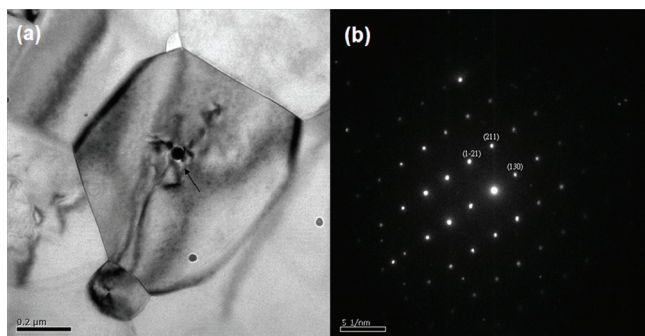


Fig. 20. TEM micrographs of nanocomposites sintered at 1350°C (a) bright field image; (b) SADP of particle in (a).

4.2 Effect of SPS sintering temperature on shrinkage behavior

Fig. 21 shows the sintering shrinkage curves of the pure Al_2O_3 , nanocomposite powders of S-30 and S-60 during the SPS densification in the temperature range $1200^\circ\text{C} \sim 1350^\circ\text{C}$ with holding time of 10 minutes. The y-axis $\Delta L/L_0$ (%) represents the shrinkage profile directly

during densification of the powders in real-time. The trend of Al_2O_3 curve becomes flat at 1200°C , but the curves of S-30 and S-60 still trended up. This means the shrinkage Al_2O_3 has already stopped, but S-30 and S-60 continue shrinking during the period of holding time.

This result is consistent with the apparent density shown in Fig. 22. It shows that pure Al_2O_3 exhibits a higher density than S-30 and S-60, for the sintering temperature at 1200°C and 1250°C . The amount of shrinkage of S-30 is more significant than S-60. The temperature at which the shrinkage vanishes for S-30 and S-60 is 1300°C and 1350°C , respectively as shown in Fig. 21c and 21d. The curves of pure Al_2O_3 , S-30 and S-60 are trended down for the holding temperature at 1350°C . This signifies that all the powder compacts undergone thermal expansion after completion of the sintering shrinkage. The densities of S-30 and S-60 are increased significantly when the temperature rises to 1300°C and 1350°C .

Fig. 21d illustrates that the pure Al_2O_3 starts to densify at about 950°C and finishes at about 1300°C . For S-60 and S-30, the densification temperature starts at about 1050°C and 1100°C , separately, and finishes at 1350°C for both. Actually S-60 finishes its densification after holding about 50 seconds. The second phase particles decrease the diffusivity of grain boundary and lattice, and result in the retardation of densification (Chae et al., 2006). According to XRD spectrum shown in Fig. 19, the delay on the densification process for the nanocomposites is due to the Cr_2O_3 particles coated on Al_2O_3 as sintered at 1200°C . Cr_2O_3 plays as a second phase to inhibit the grain growth during densification. While some of Cr_2O_3 changes to Cr_3C_2 to be the second phase as temperature increases to 1300°C and 1350°C (Lin et al., 2011).

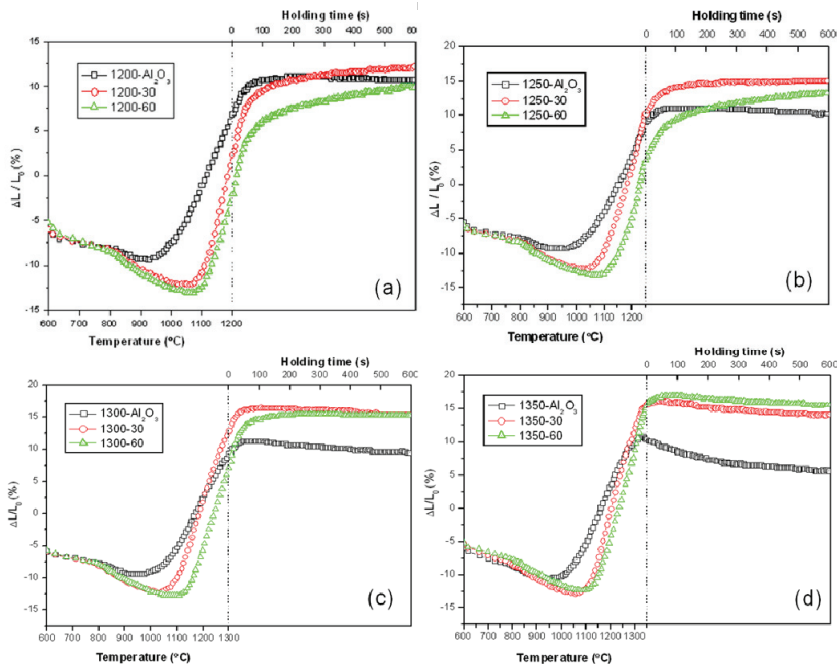


Fig. 21. Sintering shrinkage curves of Al_2O_3 , S-30 and S-60 sintered at (a) 1200°C , (b) 1250°C (c) 1300°C (d) 1350°C for 10min by SPS.

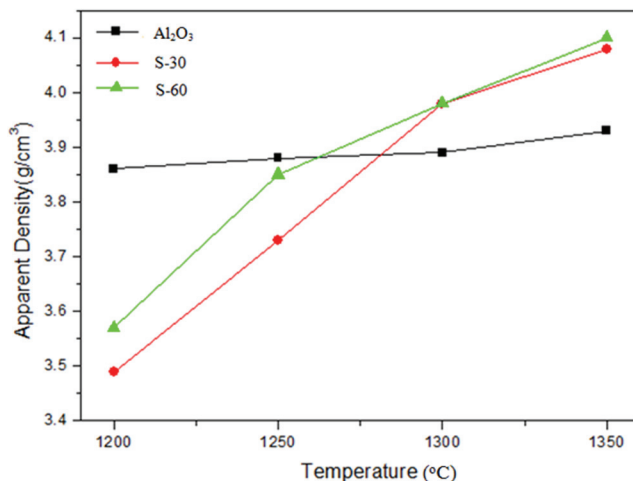


Fig. 22. The apparent density of the specimen of Al₂O₃, S-30, and S-60 prepared at a different SPS sintering temperature from 1200°C to 1350°C.

4.3 Effect of SPS sintering temperature on microstructures and mechanical properties

The fine grains of Al₂O₃-Cr₂O₃/Cr-carbide nanocomposites were prepared by employing spark plasma sintering (SPS) technique. The basic mechanical properties like hardness, fracture strength and toughness were analyzed. The fracture surfaces of the nanocomposites are shown in Fig. 23. It indicates that the pure alumina has larger grain size than that of S-30 and S-60 densification samples. The nanosized reinforced particles (Cr₃C₂) are found in the alumina matrix. S-60 densification sample has smallest grain size due the more amounts of secondary phase particles to inhibit its grain growth. The hardness, fracture strength and toughness of the S-30 and S-60 nanocomposites are present in Fig. 24. The S-60 nanocomposite exhibits highest fracture strength and toughness. The increase in hardness, fracture strength and toughness of nanocomposites over monolithic alumina is due to the strengthening of secondary phase of Cr₃C₂ particles and solid solution of Al₂O₃-Cr₂O₃. The co-relation between the microstructure and mechanical properties is similar to that of nanocomposites prepared using hot press sintering described in section 3.3.

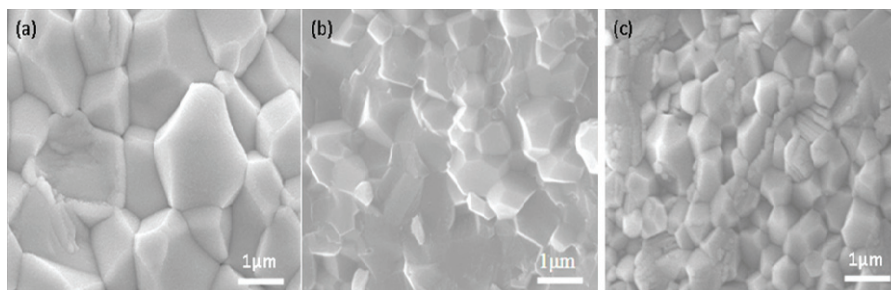


Fig. 23. SEM micrographs of fracture surface of 1350°C fully dense SPS specimen of (a) Al₂O₃, (b) S-30, (c) S-60.

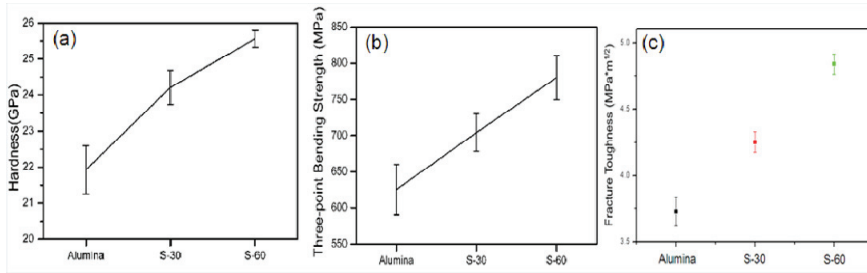


Fig. 24. (a) Hardness, (b) Fracture Strength and (c) Toughness of Chromium Carbide/Alumina nanocomposites sintered at 1350 °C for 10min by SPS.

5. Conclusion

Nanoscaled Cr_2O_3 powder with an average particle size of 20–40 nm, coated on alumina particles, has been produced by means of chemical vapor deposition in a fluidized chamber, using the pyrolysis of $\text{Cr}(\text{CO})_6$ precursor. The pyrolysis of $\text{Cr}(\text{CO})_6$ at 300 and 400 °C produces amorphous and crystalline Cr_2O_3 particles, respectively. The decomposed precursor consists of Cr_2O_3 , CrC_{1-x} and C. To prepare nanoscaled chromium carbide powder from the nanometer-sized Cr_2O_3 , carbonizing behavior of the Cr_2O_3 particles was investigated using a graphite furnace at 1150 °C. It was found that, when amorphous Cr_2O_3 powders were carbonized at 1150 °C, the powder was transformed into Cr_3C_2 , while the crystalline Cr_2O_3 was transformed into a mixture of Cr_7C_3 and Cr_3C_2 . These transformations were confirmed by X-ray diffraction (XRD), transmission electron microscopy (TEM), and energy dispersive spectroscopy (EDS). A solid solution of $\text{Al}_2\text{O}_3\text{-Cr}_2\text{O}_3$ and an $\text{Al}_2\text{O}_3\text{-Cr}_2\text{O}_3/\text{Cr}_3\text{C}_2$ nanocomposite were formed when these fluidized powders were pre-sintered at 1000 and 1150 °C, respectively before hot-pressing at 1400 °C. In addition, an $\text{Al}_2\text{O}_3\text{-Cr}_2\text{O}_3/\text{Cr}$ -carbide (Cr_3C_2 and Cr_7C_3) nanocomposite was formed when the particles were directly hot pressed at 1400 °C.

The undesirable solid solution leads to abnormal grain growth of the Al_2O_3 matrix and decreases the desired Cr_3C_2 contents in the composite. In order to avoid this drawback, carbothermal reduction process was adopted using methane as the carbonization source. The carbonization process involved the sequential deposition of carbon on the outer surface of the Cr_2O_3 powder followed by carbon diffusion into the powder, leading to the formation of metastable $\text{Cr}_3\text{C}_{2-x}$ phase and stable Cr_3C_2 in the temperature range 700–850 °C. The phase transformation from Cr_2O_3 to Cr_3C_2 has been characterized by XRD, X-ray photoelectron spectroscopy (XPS) and electron energy loss spectroscopy (EELS). It is observed that the formation of carbon nanofilms surrounding the carbide crystallites provides the stress and assists the phase transformation from metastable $\text{Cr}_3\text{C}_{2-x}$ to stable Cr_3C_2 .

The densification behavior of $\text{Al}_2\text{O}_3\text{-Cr}_2\text{O}_3/\text{Cr}_3\text{C}_2$ nanocomposites has been studied using the recently developed SPS technique. Different colors of the compacts such as green, purple and black were observed during densification process at different SPS temperatures from 1200 °C to 1350 °C. These changes in color were relevant to the existence of secondary phase of green Cr_2O_3 , pink solid solution of $\text{Al}_2\text{O}_3\text{-Cr}_2\text{O}_3$ and black Cr_3C_2 at different SPS temperature. This SPS process reduces the abnormal grain growth of Al_2O_3 , which appears

during hot press sintering and $\text{Al}_2\text{O}_3\text{-Cr}_2\text{O}_3/\text{Cr}_3\text{C}_2$ nanocomposites exhibit small grain size in this process. The microstructure and basic mechanical properties such as hardness, fracture strength and toughness of pure alumina as well as this nanocomposite have been analyzed. The microstructure of dislocation, transgranular and step-wise fracture surface were observed in the nanocomposites. The nanocomposites show fracture strength (780MPa) and fracture toughness ($4.8 \text{ Mpa}\cdot\text{m}^{1/2}$), which is higher than monolithic alumina. In comparison with monolithic alumina, the $\text{Al}_2\text{O}_3\text{-Cr}_2\text{O}_3/\text{Cr}_3\text{C}_2$ nanocomposites exhibit higher hardness, fracture strength and toughness due to the strengthening of secondary phase of Cr_3C_2 particles and solid solution of $\text{Al}_2\text{O}_3\text{-Cr}_2\text{O}_3$.

6. Acknowledgment

Authors are thankful to National Science Council of Taiwan for its financial support under the contract No: 99-2923-E-006- 002-MY3 to carryout the present work.

7. References

- Anya, C. C. (1999). Microstructural nature of strengthening and toughening in $\text{Al}_2\text{O}_3\text{-SiC}(p)$ nanocomposites. *Journal of Materials Science*, Vol. 34, No. 22, pp. 5557-5567, ISSN 0022-2461
- Awaji, H.; Choi, S.-M. & Yagi, E. (2002). Mechanisms of toughening and strengthening in ceramic-based nanocomposites, *Mechanics of Materials*, Vol. 34, pp. 411–422, ISSN 0167-6636
- Anacleto, N. & Ostrovski, O. (2004). Solid-state reduction of chromium oxide by methane-containing gas. *Metallurgical and Materials Transactions B*, Vol. 35, No. 4, pp. 609-615, ISSN 1073-5615
- Arévalo-López, A. M. & Alario-Franco, M. A. (2009). Reliable method for determining the oxidation state in chromium oxides. *Inorganic Chemistry*, Vol. 48, pp. 11843–11846, ISSN 0020-1669
- Bradt, R. C. (1967). Cr_2O_3 solid solution hardening of Al_2O_3 . *Journal of the American Ceramic Society*, Vol. 50, No. 1, (January 1967), pp. 54–55, ISSN 1551-2916
- Bewilogua, K.; Heinitz, H.-J., Rau, B. & Schulze, S. (1988). A chromium carbide phase with B1 structure in thin film prepared by ion plating. *Thin Solid Films*, Vol. 167, No. 1-2, (December 1988), pp. 233–243, ISSN 0040-6090
- Becher, P. F. (1991). Microstructural design of toughened ceramics. *Journal of the American Ceramic Society*, Vol. 74, No. 2, (February 1991), pp. 255-269, ISSN 1551-2916
- Bouzy, E.; Bauer-Grosse, E. & Le Caër, G. (1993). NaCl and filled Re_3B -type structures for two metastable chromium carbides. *Philosophical Magazine B*, Vol. 68, No. 5, pp. 619–638, ISSN 0958-6644
- Borsa, C. E. & Brook, R. J. (1995). Fabrication of $\text{Al}_2\text{O}_3/\text{SiC}$ nanocomposites using a polymeric precursor for SiC. In *Ceramic Transactions* Vol. 51, *Ceramic Processing and Science*, The American Ceramic Society, H. Hausner, G. L. Messing and S.-I. Hirano, (Ed.), 653-657, Westerville, OH
- Borsa, C. E.; Ferreira, H. S. & Kiminami, R. H. G. A. (1999). Liquid Phase Sintering of $\text{Al}_2\text{O}_3/\text{SiC}$ Nanocomposites. *Journal of the European Ceramic Society*, Vol. 19, No. 5, (May 1999), pp. 615-621, ISSN 0955-2219

- Bondioli, F.; Ferrari, A. M., Leonelli, C. & Manfredini, T. J. (2000). Reaction mechanism in alumina/chromia($\text{Al}_2\text{O}_3\text{-Cr}_2\text{O}_3$) solid solutions obtained by coprecipitation. *Journal of the American Ceramic Society*, Vol. 83, No.8, (August 2000) pp. 2036–2040, ISSN 1551-2916
- Berger, L.-M.; Stole, S. Gruner, W. & Wetzig, K. (2001). Investigation of the carbothermal reduction process of chromium oxide by micro- and lab-scale methods. *International Journal of Refractory Metals and Hard Materials*, Vol. 19, No. 2, (March 2001), pp. 109–121, ISSN 0263-4368
- Chu, W. F. & Rahmel, A. (1981). The Conversion of Chromium Oxide to Chromium Carbide. *Oxidation of Metals*, Vol. 15, pp. 331-337, ISSN 1573-4889
- Chou, Y. S. & Green D. J. (1992). Silicon carbide platelet/alumina composites: I, Effect of forming technique on platelet orientation. *Journal of the American Ceramic Society*, Vol. 75, No. 12, (December 1992), pp. 3346-3352, ISSN 1551-2916
- Carroll, L.; Sternitzke, M. & Derby, B. (1996). Silicon carbide particle size effects in alumina based nanocomposites. *Acta Materialia*, Vol. 44, No. 11, (November 1996), pp. 4543-4552, ISSN 1359-6454
- Chen, C. L. & Wei, W. C. J. (2002). Sintering behavior and mechanical properties of nano-sized $\text{Cr}_3\text{C}_2/\text{Al}_2\text{O}_3$ composites prepared by MOCVI process. *Journal of the European Ceramic Society*, Vol. 22, No.16, (December 2002), pp. 2883-2892, ISSN 0955-2219
- Choi, S. M.; Honda, S., Nishikawa, T., Awaji, H., Gnanam, F. D., Vishista, K. & Kuroyama, T. (2004). Design concept of strengthening and toughening mechanisms in nanocomposites – ceramic metal nanocomposites. *Journal of the Ceramic Society of Japan*, Vol. 112, pp. S912-S915, ISSN 0914-5400
- Choi, S. M. & Awaji, H. (2005). Nanocomposites-a new material design concept. *Science and Technology of Advanced Materials*, Vol. 6, pp. 2-10, ISSN 1468-6996
- Chae, J. H.; Kim, K. H. Choa, Y. H. Matsushita, J. I. Yoon, J. W. & Shim, K. B. (2006). Microstructural Evolution of $\text{Al}_2\text{O}_3\text{-SiC}$ Nanocomposites During Spark Plasma Sintering. *Journal of Alloys and Compounds*, Vol. 413, pp. 259-264, ISSN 0925-8388
- Davidge, R. W. (1979). *Mechanical behaviour of ceramics*, Cambridge Solid State Science Series, ISBN : 978-0521293099, Cambridge University Press
- Daulton, T. L.; Little, B. J. Lowe, K. & Jones-Meehan, J. (2002). Electron energy loss spectroscopy techniques for the study of microbial chromium(VI) reduction. *Journal of Microbiological Methods*, Vol. 50, pp.39-54, ISSN 0167-7012
- Dusza, J.; Blugan, G., Morgiel, J., Kuebler, J., Inam, F., Peijs, T., Reece, M. J. & Puchy V. (2009). Hot pressed and spark plasma sintered zirconia/carbon nanofiber composites, *Journal of the European Ceramic Society*, Vol. 29, No. 15, (December 2009), pp. 3177–3184, ISSN 0955-2219
- Fu, C. T.; Wu, J. M. & Li, A. K. (1994). Microstructure and mechanical properties of Cr_3C_2 particulate reinforced Al_2O_3 matrix composites. *Journal of Materials Science*, Vol. 29, No.10, pp. 2671-2677, ISSN 0022-2461
- Fan, X.; Dickey, E. C., Pennycook, S. J. & Sunkara, M. K. (1999). Z-contrast imaging and electron energy-loss spectroscopy analysis of chromium-doped diamond-like carbon films. *Applied physics letters*, Vol. 75, pp. 2740-2742, ISSN 0003-6951
- Ghate, B. B.; Smith, W. C., Kim, C., Hasselman, D. P. H. & Kane, G. E. (1975). Effect of chromia alloying on machining performance of alumina ceramic cutting tools.

- American Ceramic Society Bulletin, Vol. 54, No.2, (February 1975), pp. 210-215, ISSN 0002-7812
- Galusek, D.; Sedl' a'cek, J., Švan'c'arek, P., Riedel, R., Satet, R. & Hoffmann, M. (2007). The influence of post-sintering HIP on the microstructure, hardness, and indentation fracture toughness of polymer-derived Al₂O₃-SiC nanocomposites. *Journal of the European Ceramic Society*, Vol. 27, No. 2-3, pp. 1237-1245, ISSN 0955-2219
- Harabi, A. & Davies, T. J. (1995). Densification and grain growth in sintered alumina-chromia powder mixtures. *British Ceramic Transactions*, Vol. 94, pp. 97-102, ISSN 0967-9782
- Han, S. C.; Yoon, D. Y. & Brun, M. K. (1995). Migration of grain boundaries in alumina induced by chromia addition. *Acta Metallurgica et Materialia*, Vol. 43, No.3, (March 1995), pp. 977-984, ISSN 1359-6454
- Huang, J. L.; Lin, H. D. Jeng, C. A. & Lii, D. F. (2000). Crack growth resistance of Cr₃C₂/Al₂O₃ composites. *Material science and Engineering A*, Vol. 279, No. 1-2, (February 2000), pp. 81-86, ISSN 0921-5093
- Inoue, A. & Masumoto, T. (1979). Formation of Nonequilibrium Cr₃C Carbide in Cr-C Binary Alloys Quenched Rapidly From the Melt. *Scr. Metall.*, Vol. 13, pp. 711-715, ISSN 1359-6462
- Kunii, D. & Levenspiel, O. (1977). *Fluidization Engineering*, pp. 195-223, ISBN 10:0-409-90233-0, Huntington, NY, ISBN 10: 0-409-90233-0
- Kubaschewski, O. & Alcock, C. B. (1979). *Metallurgical thermochemistry, 5th ed.* ISBN 9780080208978, Netherlands
- Kim, B. N.; Hirga, K. Morita, K. & Yoshida, H. (2007). Spark Plasma Sintering of Transparent Alumina, *Scripta Materialia*, Vol. 57, pp. 607-610, ISSN 1359-6462
- Kumari, L.; Zhang, T., Du, G. H., Li, W. Z., Wang, Q. W., Datye, A. & Wu, K. H. (2009). Synthesis, microstructure and electrical conductivity of carbon nanotube-alumina nanocomposites. *Ceramics International*, Vol. 35, No. 5, (July 2009), pp. 1775-1781, ISSN 0272-8842
- Lander, J. J. & Germer, L. H. (1947). Plating molybdenum, tungsten, and chromium by thermal decomposition of their carbonyls. *Am. Inst. Min. Metal. Eng. Tech.*, Vol. 14, No. 6, pp. 1-42
- Lange, F. F. (1973). Effect of microstructure on strength of Si₃N₄-SiC composite system. *Journal of the American Ceramic Society*, Vol. 56, No. 9, (September 1973), pp. 445-450, ISSN 1551-2916
- Lange, F. F. (1989). Powder processing science and technology for increased reliability. *Journal of the American Ceramic Society*, Vol. 72, No.1, (January 1989), pp. 3-15, ISSN 1551-2916
- Lio, S.; Watanabe, M., Matsubara, M. & Matsuo, Y. (1989). Mechanical properties of alumina/silicon carbide whisker composites. *Journal of the American Ceramic Society*, Vol. 72, No. 10, (October 1989), pp. 1880-1884, ISSN 1551-2916
- Lozzi, L.; Passacantando, M. Picozzi, P. Santucci, S. & Crescenzi, M. D. (1991). Electronic structure of Cr clusters on graphite. *Atoms, Molecules and Cluster*, Vol. 20, pp. 387-390.
- Lerch, A. & Rousset, A. (1994). Influence of morphology on textural properties and on the reactivity of chromium oxides obtained by decomposition of oxalate precursors

- (NH₄)₃[Cr(C₂O₄)₃]. *Thermochimica Acta*, Vol. 232, No. 2, (February 1994), pp. 233-242, ISSN 0040-6031
- Levin, I.; Kaplan, W. D. Brandon, D. G. & Layous, A. (1995). Effect of SiC Submicrometer Particle Size Content on Fracture Toughness of Alumina-SiC " Nanocomposites". *Journal of the American Ceramic Society*, Vol.78, No. 1, pp. 254-256, ISSN 1551-2916
- Loubière, S.; Laurent, Ch., Bonino, J. P.& Rousset, A.(1995). Elaboration, Microstructure and Reactivity of Cr₃C₂ powders of different morphology. *Materials Research Bulletin*, Vol. 30, pp. 1535-1546, ISSN 0025-5408
- Loubière, S.; Laurent, Ch., Bonino, J. P.& Rousset, A. (1996). A metastable chromium carbide powder obtained by carburization of a metastable chromium oxide. *Journal of Alloys and Compounds*, Vol. 243, pp. 59-66, ISSN 0925-8388
- Lii, D. F.; Huang, J. L. Huang, J. J. & Lu, H. H. (1999). The interfacial reaction in Cr₃C₂/Al₂O₃ composites. *Journal of Materials Research*, Vol. 14, No.3, (March 1999), pp. 817-823, ISSN 0884-2914
- Lii, C. L.; Riu, D. H., Sekino, T. & Niihara, K. (1999). Fabrication and Mechanical Properties of Al₂O₃ Solid Solution with low addition of Cr₂O₃. *Key Engineering Materials*, Vols. 161-163, pp. 161-164, ISSN 1662-9795
- Liu, X. K.; Zhu, D. M. & Hou, W. C. (2006). Microwave permittivity of SiC-Al₂O₃ composite powder prepared by sol-gel and carbothermal reduction. *Transactions of Nonferrous Metals Society of China*, Vol. 16, pp. s494-s497, ISSN 1003-6326
- Lin, H. T.; Huang, J. L., Lo, W. T. & Wei, W. C. J. (2005). Investigation on carbonizing behaviors of nanometer-sized Cr₂O₃ particles dispersed on alumina particles by MOCVD in fluidized bed. *Journal of Material Research*, Vol. 20, No. 8, (August 2005), pp. 2154-2160, ISSN 0884-2914
- Lin, H. T.; Huang, W. S. Wang, S. C. Lu, H. H. Wei, W. C. J. & Huang, J. L. (2006). Investigation of chromium carbide/alumina nano-composite prepared via MOCVD in fluidized bed and densification process. *Materials Science and Engineering B*, Vol. 127, No. 1, (February 2006), pp. 22-28, ISSN 0921-5107
- Lin, H. T.; Huang, J. L. Wang, S. C. & Lin, C. F. (2006). Preparation of nano-scale Cr₃C₂ particles dispersed on alumina particles by MOCVD in fluidized reactor and carbothermal treatment. *Journal of Alloys and Compounds*, Vol. 417, No. 1-2, (June 2006), pp. 214-219, ISSN 0925-8388
- Lin, H. T.; Huang, J. L. & Wang, S. C. (2007). Investigation of Hot-Pressed Al₂O₃-Cr₂O₃/Cr₃C₂ Nanocomposite, *Key Engineering Materials*, Vol. 351, pp. 93-97, ISSN 1662-9795
- Lin, H. T.; Wang, S. C., Huang, J. L. & Chang, S. Y.(2007).Processing of Hot Pressed Al₂O₃-Cr₂O₃/Cr-carbide Nanocomposite Prepared by MOCVD in a Fluidized Bed. *Journal of the European Ceramic Society*, Vol. 27, pp. 4759-4765, ISSN 0955-2219
- Lin, H. T.; Nayak, P. K. Wang, S. C. Chang, S.Y. & Huang, J. L. (2011) Electron-energy loss spectroscopy and Raman studies of nanosized chromium carbide synthesized during carbothermal reduction process from precursor Cr(CO)₆. *Journal of the European Ceramic Society*, Article in Press, ISSN 0955-2219
- Lin, H. T.; Liu, B. Z. Shio, C. W. & Huang, J. L. (2011). Study of color change in Al₂O₃-Cr₂O₃/Cr₃C₂ Nanocomposites prepared by Spark Plasma Sintering, *Ceramics Internationals*, In Press, ISSN 0272-8842

- Muradov, N. Z. (1998). CO₂-Free Production of Hydrogen by Catalytic Pyrolysis of Hydrocarbon Fuel. *Energy & Fuels*, Vol. 12, pp. 41-48, ISSN 0887-0624
- Muradov, N. Z. (2001). Hydrogen via methane decomposition: an application for decarbonization of fossil fuels, *International Journal of Hydrogen Energy*, Vol. 26, pp. 1165-1175, ISSN 0360-3199
- Munir, Z. A.; Anselmi-Tamburini, U. & Ohyanagi, M.(2006).The Effect of Electric Field and Pressure on the Synthesis and Consolidation of Materials: A Review of the Spark Plasma Sintering Method. *Journal of Materials Science*, Vol. 41,pp. 763-777, ISSN 0022-2461
- Nassau, K.(1983). *The Physics and Chemistry of Color*. Wiley, New York, pp. 77-106
- Niihara, K. & Hirai, T. (1986). Super-Fine Microstructure and Toughness of Ceramics. *Bull. Cerum. Soc. Jpn.*, Vol. 21, No. 7, pp.598-604
- Niihara, K & Nakahira, A. (1988). Strengthening of oxide ceramics by SiC and Si₃N₄ dispersions. In: *Proceedings of the Third International Symposium on Ceramic Materials and Components for Engines*, The American Ceramic Society, V. J. Tennery, (Ed.), 919-926, Westerville, Ohio
- Niihara, K.; Nakahira, A., Sasaki, G. & Hirabayashi, M. (1989). Development of strong Al₂O₃/SiC composites, *Proceedings of the First MRS International Meeting on Advanced Materials*, ISBN 1558990305, Sunshine City, Ikebukuro, Tokyo, Japan, May-June, 1988, Vol. 4, pp. 129-134, ISBN 1558990305
- Niihara, K. (1991). New design concept for structural ceramics-Ceamic nanocomposites. *The Centennial Memorial Issue of The Ceramic Society of Japan*, Vol. 99, No. 10, pp. 974-982, ISSN 0914-5400
- Ohji, T.; Jeong, Y-K., Choa, Y-H. & Niihara, K. (1998). Strengthening and toughening mechanisms of ceramic nanocomposites, *Journal of the European Ceramic Society*, Vol. 81, No. 6, (June 1988), pp.1453-1460, ISSN 0955-2219
- Paek, Y. K.; Lee, H. Y. & Kang, S. -J. L. (1996). Direction of liquid film migration induced by chromic oxide in alumina-anorthite. *Journal of the American Ceramic Society*, Vol. 79, pp. 3029-3032, ISSN 1551-2916
- Riu, D. H.; Kong, Y. M., & Kim, H. E. (2000). Effect of Cr₂O₃ addition on microstructural evolution and mechanical properties of Al₂O₃. *Journal of the European Ceramic Society*, Vol. 20, pp.1475-1481, ISSN 0955-2219
- Storms, Edmund K.(1967). *The Refractory Carbides*. Refractory Materials, Vol. 2, New York, Academic Press, pp. 247-268
- Sigl, L. S.; Mataga, P. A., Dalglish, B. J., McMeeking, R. M. & Evans, A. G.(1988). On the toughness of brittle materials reinforced with a ductile phase. *Acta Metallurgica*, Vol. 36, No. 4, (April 1988), pp. 945-953, ISSN 1359-6454
- Sekino, T. & Niihara, K. (1997). Fabrication and mechanical properties of fine-tungsten-dispersed alumina-based composites, *Journal of Materials Science*, Vol. 32, No. 15, (November 1997), pp. 3943-3949, ISSN 0022-2461
- Sternitzke, M. (1997). Review: structural ceramic nanocomposites, *Journal of the European Ceramic Society*, Vol. 17, No.9, pp. 1061-1082, ISSN 0955-2219
- Shen, Z.; Johnsson, M. Zhao, Z. & Nygren, M. (2002). Spark Plasma Sintering of Alumina. *Journal of the American Ceramic Society*, Vol. 85, pp. 1921-1927, ISSN 1551-2916
- Shapiro, I. P.; Todd, R. I., Titchmarsh, J. M. & Roberts, S.G.(2009). Effects of Y₂O₃ additives and powder purity on the densification and grain boundary composition of

- Al₂O₃/SiC nanocomposites. *Journal of the European Ceramic Society*, Vol. 29, N0. 9, (June 2009), pp. 1613–1624, ISSN 0955-2219
- Tsugeki, K.; Kato, T., Koyanagi, Y., Kusakabe, K. & Morooka, S. (1993). Electro conductivity of sintered bodies of α -Al₂O₃-TiN composite prepared by CVD reaction in a fluidized bed. *Journal of Materials Science*, Vol. 28, No. 12, pp. 3168-3172, ISSN 0022-2461
- Trombini, V.; Pallone, E. M. J. A., Tamburini, U. A., Munir, Z. A. & Tomasi, R.(2009). Characterization of alumina matrix nanocomposite with ZrO₂ inclusions densified by spark plasma sintering, *Materials Science and Engineering: A*, Vol. 501, No. 1-2, (February 2009), pp. 26–29, ISSN 0921-5093
- Vollath, D. & Sickafus K. E. (1992). Synthesis of nanosized ceramic oxide powders by microwave plasma reactions. *Nanostructured Materials*, Vol. 1, No.5, (September-October 1992), pp. 427-437
- Vollath, D. & Sickafus, K. E. (1993). Synthesis of nanosized ceramic nitride powders by microwave supported plasma reactions. *Nanostructured Materials*, Vol. 2, No. 5, (September-October 1993), pp. 451-456
- Vollath, D.; Szabó D. V. & HauBelt, J. (1997). Synthesis and Properties of Ceramic Nanoparticles and Nanocomposites, *Journal of the European Ceramic Society*, Vol. 17, No. 11, pp. 1317-1324, ISSN 0955-2219
- Vollath, D. & Szabó, D. V. (2006). Microwave Plasma Synthesis of Ceramic Powders, In: *Advances in Microwave and Radio Frequency Processing*, Part-IX, pp. 619-626, Springer
- Wagner, C. D.; Riggs, W. M., Davis, L. E., Moulder, J. F. & Muilenberg, G. E.(1979). *Handbook of X-ray Photoelectron Spectroscopy*, Perkin-Elmer Corp., Minnesota, USA
- Wang, Y. & Hsu, S. M. (1996). The effects of operating parameters and environment on the wear and wear transition of alumina. *Wear*, Vol. 195, No. 1-2, (July 1996), pp. 90-99, ISSN 0043-1648
- Wang, S. C.; Lin, H. T. Nayak, P. K. Chang, S. Y. & Huang, J. L. (2010). Carbothermal reduction process for synthesis of nanosized chromium carbide via metal-organic vapor deposition. *Thin Solid Films*, Vol. 518, pp. 7360–7365, ISSN 0040-6090
- Xu, Y.; Nakahira, A. & Niihara, K. (1994). Characteristics of Al₂O₃-SiC nanocomposite prepared by sol-gel processing. *Journal of the Ceramic Society of Japan*, Vol. 102, No. 3, pp. 312-315, ISSN 0914-5400

Environmentally-Safe Polymer-Metal Nanocomposites with Most Favorable Distribution of Catalytically Active and Biocide Nanoparticles

A. Alonso¹, J. Macanás², G.L. Davies³, Y.K. Gun'ko³,
M. Muñoz¹ and D.N. Muraviev¹

¹*Universitat Autònoma de Barcelona*

²*Universitat Politècnica de Catalunya*

³*Trinity College Dublin*

^{1,2}*Spain*

³*Ireland*

1. Introduction

As rule of thumb, nanomaterials (NMs) possess different properties compared to the same material in its coarser or bulk form (Schulenburg, 2008). Once a material is reduced below 100 nm in size, its components begin demonstrating unusual features based on quantum mechanics, rather than macroscopic Newtonian mechanics, which influence a variety of material properties such as conductivity, heat transfer, melting temperature, optical properties, magnetization, etc. (Bhushan, 2007). Taking advantage of these singular properties in order to develop new products (and also new synthetic procedures) is the main purpose of Nanotechnology, and that is why it is frequently regarded as “the next industrial revolution” (Lane, 2002; Miley et al., 2005). Although Nanoscience and Nanotechnology are quite recent disciplines, there have already been a high number of publications which discuss these topics (Ajayan et al., 2005; Blackman, 2008; Campelo et al., 2009; Giannazzo et al., 2011; Hassan, 2005; Joo, 2006; Klabunde, 2005; Li et al., 2008; Macanás et al., 2011; Nicolais & Carotenuto, 2005; Rozenberg & Tenne, 2008; Schmid, 2010; Vatta et al., 2006; Zeng, 2004). However, some important concepts are still under debate. The safety of nanomaterials is of high priority, but more fundamental ideas are also quite unclear nowadays. NMs are commonly defined as discrete objects whose size is less than 100 nm in at least one dimension (Haverkamp, 2010). Nanocomposites are known as materials which include in their composition one or more functional materials. Nanotechnology is a multidisciplinary field, as it combines the knowledge from different disciplines: chemistry, physics and biology amongst others (Klabunde, 2005; Schmid, 2006, 2010). Surface chemistry is also of great importance to the properties of NMs and nanoparticles (NPs) in particular. This is thanks to decreasing NPs size which causes their surface effects to become more significant, due to an increase in the volume fraction of surface atoms, which determines in some instances their special properties (Bowker, 2009). NPs have always been present in the

environment and have been used by humans in coincidental way, for example in decorative glasses and ceramics (Macanás et al., 2011; Walter et al., 2006). Some examples are carbon black, lustre pottery, or some catalysts, which were often used without knowing their nanoscale nature (Haverkamp, 2010). More recently, an important source of NPs are diesel engine emissions or dust from road fragmentation (Gramotnev, D. K. & Gramotnev, G. 2005; Haverkamp, 2010; Ristovski, 2006). In any case, engineered NPs are of the most economic importance at present (Hillie & Hlophe, 2007; Ju-Nam & Lead, 2008; Maynard, 2007; Narayan, 2010; Schulenburg, 2008; Schmid, 2010; Theron et al., 2008). Indeed, NPs are already applied in paints, where they serve to break down odour substances, on surgical instruments in order to keep them sterile, in highly effective sun creams, in slow release pharmaceuticals and many others (Schulenburg, 2008).

The development of uniform nanometer sized particles has been intensively pursued and within this broad field, metal NPs (MNPs) have attracted particular interest (Blackman, 2008; Campelo et al., 2009; Hyeon, 2003; Klabunde, 2005; Macanás et al., 2011; Park & Cheon, 2001; Schmid, 2010). The synthesis of MNPs may be carried out through various synthetic routes based either in bottom-up or top-down approaches, which have been summarized in recent publications (Ajayan et al., 2005; Bhushan, 2007; Campelo et al., 2009; Klabunde, 2005; Macanás et al., 2011; Schmid, 2010). One of the most frequently used procedures involves the use of capping stabilizing agents or surfactants, which help to prevent NPs aggregation and Ostwald ripening (Houk, et al., 2009; Imre et al., 2000). In such cases, stabilizers not only preserve NPs size but they also play a crucial role in controlling the shape of the NPs (Haverkamp, 2010; Kidambi & Bruening, 2005; Zeng et al., 2007). More exotic procedures have also been used for NPs synthesis including the use of ultrasound irradiation in the presence of aliphatic alcohols, docecyl sulfate or polyvinyl-2-pyrrolidone (Haverkamp, 2010; Vinodgopal et al., 2006). UV light, thermal treatments, cryochemical methods, pyrolysis or laser ablation have also been used, for instance, for silver or silver-gold NPs synthesis producing either simple or core@shell structures (Haverkamp, 2010; Nicolais & Carotenuto, 2005; Rao et al, 2004).

1.1 Drawbacks of nanoparticles

The main limitation in the wide application of MNPs is their insufficient stability arising from their tendency to self-aggregate (Houk et al., 2009; Imre et al., 2000; Macanás et al., 2011). In many instances, NPs are dispersed after synthesis in a liquid or solid medium by using different mechanochemical approaches (*transfer*) but the success of such approaches for dispersing the NPs is limited by their re-aggregation. This problem is common for many NPs obtained by using *ex-situ* fabrication techniques, i.e. NPs synthesized in a phase different from that of their final application (Campelo et al., 2009; Nicolais & Carotenuto, 2005). A completely opposite strategy that avoids NPs transfer stage is *in-situ* fabrication (Figure 1). In this case, NPs can be grown inside a matrix using different techniques, yielding a material that can be directly used for a foreseen purpose.

Another critical issue concerning NPs is their environmental and health safety risks, sometimes referred as nanotoxicity (Bernard et al., 1990; Borm & Berube, 2008; Chen & Fayerweather, 1988; Li et al., 2008).

NMs safety doubts have been underlined and their use has come under some scrutiny by both private and public institutions, regarding in particular the possible hazards associated with NPs either deliberately or inadvertently produced (Abbott & Maynard, 2010; Hassan, 2005; Ju-Nam & Lead, 2008; Klabunde, 2005;; Maynard, 2007; Theron et al., 2008).

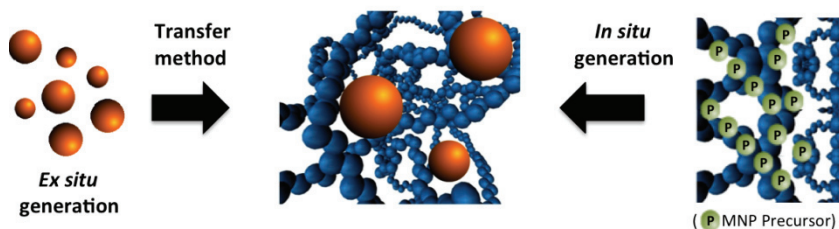


Fig. 1. Schematic comparison of *ex-situ* and *in-situ* nanoparticle generation methods.

Nowadays, there is a claim for more restrictive legislation that could allow a better protection for both human beings (workers and customers) and the global environment. A massive industrial production of NMs in the near future may result in the appearance of both NPs and the waste generated during their production in various environments, yielding the possibility that humans could be exposed to these NPs through inhalation, dermal contact or ingestion and absorption through the digestive tract.

When considering the environmental risks of NMs, a paradox arises when one understands that potentially dangerous NMs also have the potential to produce more environmentally friendly processes, so-called 'green chemistry', and can be used to deal with environmental contaminants (Albrecht et al., 2006; Bell et al., 2006; Bottero et al., 2006; Haverkamp, 2010; Joo, 2006; Schmid, 2010; Schulenburg, 2008; Yuan, 2004).

An example of that is the use of engineered NPs for water treatment and groundwater remediation, which has been proved to be efficient but has also raised concerns for human exposure to NPs contained in the treated water. In order to guarantee the safe use of NMs, some aspects must be taken into account: knowledge, detection and prevention.

A comprehensive knowledge of properties of these materials (both physical and chemical) is important to find standards and control materials to work with as reference models (British Standards Institute: BSI PAS 130 [BSI], 2007; International Standards Organisation: ISO/TS 27687:2000 [ISO], 2000; Maynard, & Howard, 1999). Up to now, some environmental and health aspects of NPs have already been investigated (Abbott & Maynard, 2010; Li et al., 2008). An investigation into whether a substance is dangerous or not involves a determination of the material's inherent toxicity, the manner of its interaction with living cells and the effect of exposure time (Bottero et al., 2006). It should be noted that the doses or exposure concentrations used in *in vitro* and *in vivo* toxicological studies are most often extraordinarily high in comparison with possible accidental human exposure (Borm & Berube, 2008; Abbott & Maynard, 2010). Consequently, more research is needed before generalized statements can be made regarding NPs ecotoxicology. Few initiatives in this direction have been started so far. However, the German Federal Ministry for Education and Research, together with industry, has established the research programme NanoCare. This programme has a budget of €7.6 million and aims to assess and communicate new scientific knowledge of the effects of NPs on health and the environment (Schulenburg, 2008). Scientists and technologists in this area have to deal with NPs presence in the environment but do not have the appropriate tools and analytical methods for NPs detection and quantification to guarantee a satisfactory detection (Giannazzo et al., 2011). It is vital that efforts are dedicated towards this direction, as we have not yet invented a so-called "Geiger counter for NPs".

Currently, prevention of the escape of NPs to the environment is the best approach under consideration. If NPs do not reach the environment, we can confidently eliminate the danger for living beings (Zeng, 2004). In this sense, the embedding of NPs into organic or inorganic matrices reduces their mobility and prevents their appearance in the environment (Ajayan et al., 2005; Macanás et al., 2011). The use of nanocomposites such as these might be the simplest way to increase the safety of NMs. A complimentary approach to ensure the safety of NMs is to use magnetic NPs in their design (Vatta et al., 2006). Magnetic NPs are of great interest for researchers from a wide range of disciplines due to their useful properties and reaction to a magnetic field (Belotelov et al., 2005; Hayashi, 2007). In fact, polymeric materials containing magnetic NPs with certain functionalities (e.g., catalytically-active or bactericide) can find numerous technological applications. Their popularity lies in the fact that magnetic NPs can be easily recovered if leakage from the nanocomposite occurs by using simple magnetic traps (Hyeon, 2003; Qiao et al., 2007).

At the same time, immobilization of NPs within a solid matrix may cause potential problems. For example, during a catalytic reaction, if the support has a dense structure, diffusion of reactants to the nanocatalysts may cause diffusion resistance. Therefore, it is necessary to tune the structural properties of nanocomposites to make such functional NPs maximally accessible by the substrates of interest (chemical reagents to be catalyzed or bacteria to be eliminated) and active (Xu & Bhattacharyya, 2005).

1.2 Nanocomposites

The engineering of nanocomposites for different applications has been extensively tackled in the last decade, as demonstrated in the literature analysis depicted in Figure 2. In the words of Ajayan, “the promise of nanocomposites lies in their multifunctionality, the possibility of realizing unique combinations of properties unachievable with traditional materials” (Ajayan et al., 2005).

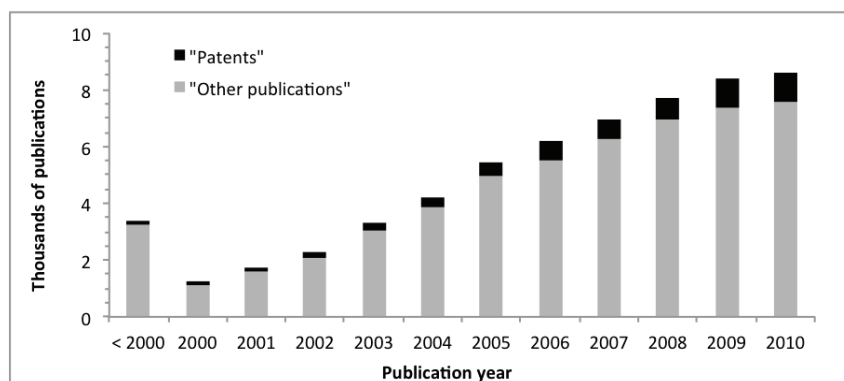


Fig. 2. Bibliographic analysis for the term “nanocomposite” in Scifinder Scholar.

Depending on the nature of the nanophase and the matrix, a wide variety of nanocomposites can be prepared (Kim & Van der Bruggen, 2010). These composite materials can assume a mixture of the beneficial properties of their parent compounds, leading to materials with improved physical properties and unprecedented flexibility (Figure 3). Among them, we will focus our attention on polymer-metal composites.

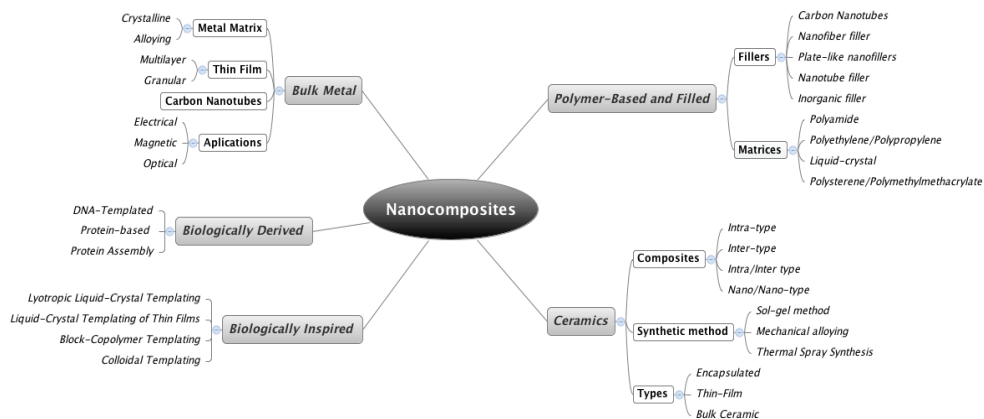


Fig. 3. General overview of nanocomposites.

2. Polymer-metal nanocomposites

The idea of using polymer-metal nanocomposites can be advantageous from two different points of view. Firstly, the development of polymer-stabilized metal NPs is considered to be one of the most promising solutions to the issue of NPs stability, by preventing their self-aggregation. Secondly, the use of immobilized NPs reduces the chances of their appearance in the environment (Klabunde, 2005; Nicolais & Carotenuto, 2005; Pomogailo & Kestelman, 2005; Rozenberg & Tenne, 2008). In addition, the incorporation of MNPs into polymeric matrices can endow the polymer with distinctive properties (Corain & Kralik, 2000; Jin et al., 2007; Pomogailo, 2000; Pomogailo et al. 2003; Muraviev 2005). A non exhaustive list of these advantages include: high permanent selectivity, low electrical resistance, good mechanical stability, high chemical stability, decreased permeability to gases, water and hydrocarbons, thermal stability, surface appearance and electrical conductivity (Nicolais & Carotenuto, 2005). In any case, the properties will highly depend on the type of nanocomposites and the procedures used for their preparation (see Figure 4 below).

The polymer-embedded nanostructures are potentially useful for a number of technological applications, especially as advanced functional materials (e.g., high-energy radiation shielding materials, microwave absorbers, optical limiters, polarisers, sensors, hydrogen storage systems, etc.) (Belotelov et al., 2005; Nicolais & Carotenuto, 2005). This chapter, apart from environmentally friendly nanocomposites materials and their advantages, is also focused on two kinds of applications: catalysis and biocide activity.

Polymer-metal nanocomposites can be prepared by two different approaches, namely, *in situ* and *ex situ* techniques. In the first case MNPs can be generated inside a polymer matrix by decomposition (e.g., thermolysis, photolysis, radiolysis, etc.) or by the chemical reduction of a metallic precursor inside the polymer. In the *ex situ* approach, NPs are first produced by soft-chemistry routes and then dispersed into polymeric matrices (Nicolais & Carotenuto, 2005). Within these categories of technologies, many different methods are used to produce inorganic NPs-based nanocomposites (Pomogailo & Kestelman, 2005). Both chemical and physical techniques can be used for this purpose but chemical processes have several advantages because of their relative simplicity. Inside this group of techniques there are two general types of procedures based on in-situ and ex-situ techniques (Figure 4).

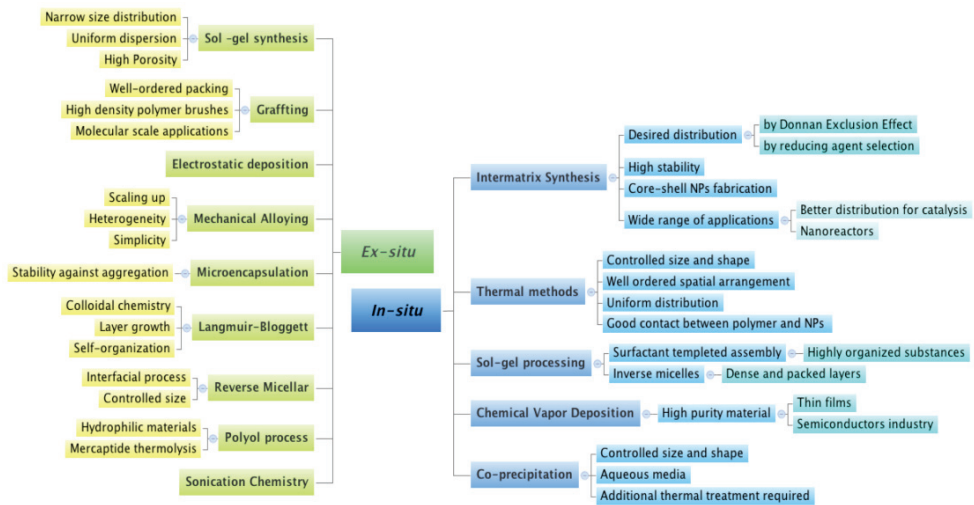


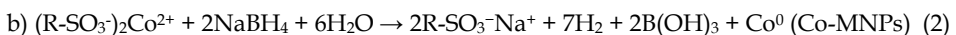
Fig. 4. *Ex situ* and *in situ* methods for polymer-metal nanocomposites synthesis.

Due to their technological advantages, *in situ* approaches are currently the focus of much attention and applications (Christy, 2003). Such approaches allow the preparation of a variety of metal-polymer nanocomposites with highly controllable particle size, material morphology and other properties. One of the most promising routes to produce the Polymer Stabilized/Supported MNPs (PSMNPs) and nanocomposites base on these is Intermatrix Synthesis (IMS), which consists of sequential loading of the functional groups of the polymer with desired metal ions (MNP precursors), followed by their chemical reduction (Alonso, 2010; Muraviev, 2005). The main advantages of this method are explained in detail in the following section.

3. Intermatrix synthesis of polymer-metal nanocomposites

3.1 Advantages

Figure 5 shows the main variables, which can be chosen as working parameters to carry out IMS of MNPs with desired composition and structure via an *in-situ* approach. The synthetic procedure and, consequently, the properties of the final nanocomposite will be determined by the following parameters (see Table 1): polymer matrix type and porosity, type of the functional groups, metal reduction conditions and some others. For example, the functional groups of the polymer, which may be cationic or anionic, determine the type of MNPs precursor and the sequence of IMS stages. PSMNP formation involves two simple consecutive stages: a) the loading of the functional groups of the polymer with metal ions (e.g., Co^{2+}) followed by b) their reduction inside the matrix resulting in the formation of monometallic MNPs. Reduction can be carried out by using NaBH_4 or other reducing agents. These two stages may be described by the following equations:



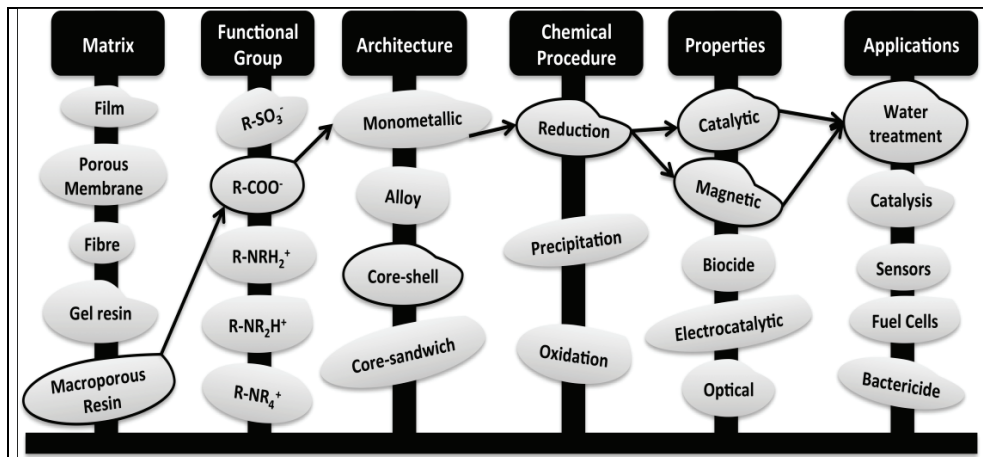


Fig. 5. Synthetic possibilities of IMS of MNPs.

As can be seen from equation (2), the functional groups of the polymer ($R-SO_3^-$) appear completely regenerated after the second IMS stage (metal reduction), i.e. they are converted back into their initial ionic form. This means that the metal-loading-reduction cycle can be repeated. In other words, the IMS method allows for multiple sequential metal-loading-reduction cycles. For example, this allows the production of core@shell MNPs by coating the monometallic MNPs obtained after the first cycle with a secondary functional metal shell. The properties of the metal shell (e.g. catalytic or bactericide) will determine the properties of the final nanocomposite.

Since the PSMNPs are strongly captured inside the polymer matrix, the hosting polymer prevents MNPs escape into the medium under treatment, providing the first level of the nanocomposite safety. In addition, IMS of bimetallic core@shell MNPs consisting of magnetic (specifically superparamagnetic) cores coated with a functional shell is of particular interest as it can also increase the nanocomposite safety. Indeed, the superparamagnetic nature of MNPs provides an additional level of the material safety as any MNPs leached from the polymer matrix can be easily captured by magnetic traps. This permits either complete prevention of any post-contamination of the treated medium or recycling of MNPs, a particularly important consideration when they contain precious metals. This novel strategy for the synthesis of new nanocomposite materials is based on 1) IMS of a low-cost metal core (e.g. Co, Fe or their oxides) with super-paramagnetic properties and 2) coating of the core with functional metal shell of desired thickness with catalytic or bactericide properties (e.g., Pd, Pt or Ag). Different kinds of functional polymers can be used for this purpose (see Table 1). The use of different polymeric materials for the synthesis of core@shell PSMNPs permits the final polymer-metal nanocomposites in different applications, such as catalysis or water disinfection filters, with the maximum efficiency.

Moreover, it has been shown that IMS of MNPs inside a polymer matrix results in the appearance of additional nanoporosity of the polymer, enhancing the mass transfer characteristics of the nanocomposite in comparison with those of the unmodified polymer.

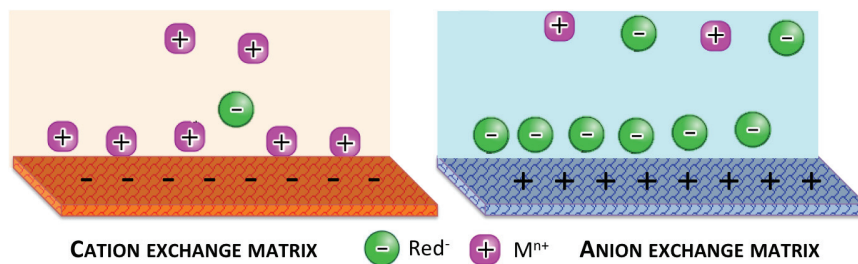


Fig. 6. Donnan exclusion effect.

3.2 Donnan-exclusion-effect as powerful tool for tuning structural properties of polymer-metal nanocomposites

An important property of nanocomposite materials is the accessibility of substrates of interest (chemical reagents or bacteria) to the functional MNPs. In this regard the distribution of MNPs on the surface of polymeric matrices appears to be the most favourable for their practical applications. The Donnan exclusion effect (Figure 6) is based on the exclusion (inability to deeply penetrate inside the polymer) of co-ions when the sign of their charge coincides with that of the polymer functional. This effect is observed, for instance, in IMS of MNPs in polymers with negatively charged functional groups when reducing metal ions with borohydride anions to zero-oxidation state. The polymer matrix bears negative charges due to the presence of well dissociated functional groups (see above equation 2). This means that the borohydride anions cannot deeply penetrate inside the matrix due to the action of electrostatic repulsion. The action of this driving force results in the formation of MNPs mainly near the surface of the polymer. Therefore, the desired distribution of MNPs inside stabilizing polymer can be achieved by using the Donnan exclusion driven IMS of MNPs in the functional polymers (e.g., ion-exchangers materials). The use of IMS coupled with Donnan exclusion effect allows the most favourable distribution of MNPs inside respective nanocomposites making them maximally accessible for the bacteria to be eliminated or reactants to be catalyzed (Alonso et al., 2010; Medyak, 2001; Yegiazarov, 2000).

Borohydride is one of the most often selected reducing agents for the synthesis of various MNPs, however in certain cases, e.g. in the case of iron and some other metals, the metal reduction can be accompanied by the appearance of boride impurities in the final material. At the same time, the high rate of the reduction process and some other advantages make it one of the most popular reducing agents. An alternative can be hydrazine hydrate, which has the some advantages such as, its strong reducing capability and low cost amongst others, and which has been used for the synthesis of a variety of metals (Xiaomin et al., 2005). However, its non-ionic nature limits the conditions of its application in the Donnan exclusion driven IMS of MNPs by low pH interval.

The reduction process can also affect the main MNPs parameters such as their shape and size, possible aggregation rate and structure as well as their distribution inside the supporting polymer (Sarkar, 2010). For instance, the use of mild reducing agents like N_2H_4 leads to much larger MNPs than a stronger reducing agent (such as $NaBH_4$) does. The SEM images shown in Figure 7 demonstrate the difference in MNPs distribution as the result of varying of the strength of the reducing agent.

As can be seen in Figure 7, the quantity of reduced metal (see the thickness of white peripheral layer) varies significantly with the strength of reducing agents ($\text{NaBH}_4 \gg \text{Na}_2\text{S}_2\text{O}_4$). At the same time, their anionic nature provides the desired surface distribution of MNPs due to the action of Donnan exclusion effect.

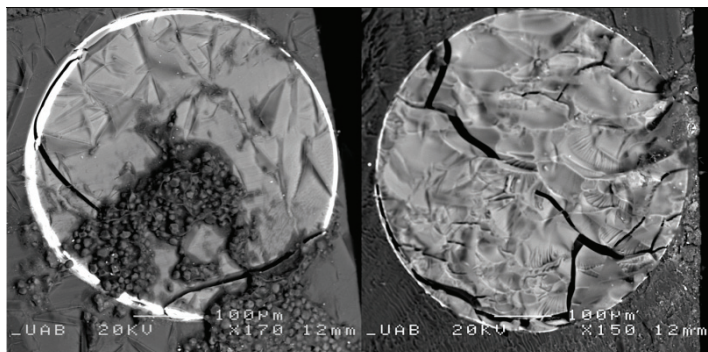


Fig. 7. SEM images of Pd-PSMNPs modified gel-type sulfonic resin reduced by 0.5M solutions of a) NaBH_4 and b) $\text{Na}_2\text{S}_2\text{O}_4$.

3.3 Non-crosslinked and crosslinked polymeric matrices

Ion-exchange materials are also known as ion exchange resins, whose matrices bear either cationic or anionic functional groups. The properties of ion exchange resins are determined by the degree of cross-linking of their matrices and the specific amount and type of ion exchange groups (functional groups). The polymer structure and the cross-linking degree determine the main chemical, physical and mechanical properties of these materials such as their swelling ability and the mobility of exchanging ions inside the matrix (the intermatrix diffusivity), which are also very important for IMS of MNPs. Non-crosslinked gel polyelectrolytes can also be used for this purpose as they have some advantages, such as solubility in some organic solvents. This can be used for preparation of MNPs solutions (or inks), which can be applied for the purposeful modification of the surfaces of some devices, such as, electrochemical sensors (Macanás et al, 2011; Muraviev 2005). Some examples of polymeric matrices, which have been used for IMS of Pd@Co MNPs are listed in Table 1).

The membranes made of non-cross-linked sulfonated polyetherether ketone (SPEEK) have been used as a model polymeric matrix for IMS of various MNPs to optimize the synthetic conditions and to study the structural characteristics of both MNPs and respective nanocomposites. The practical applications of functional MNPs-based nanocomposites (in catalysis or water treatment) require the use of cross-linked polymers in the form of granulated resins or fibers of both gel and macroporous types.

The matrices of macroporous polymers, being highly crosslinked, are generally tougher than their gel analogs and are more resistant to mechanical stresses, osmotic pressure, and chemical degradation due to the action of oxidizing agents. On this basis, the nanocomposites are optimally applicable to catalytic processes (Qiao, 2007).

In summary, the main properties of ion exchange materials which must be taken into account before IMS of MNPs can be carried out are the following: 1) uniform or controlled bead or fiber size, 2) chemical and physical resistance, 3) sufficiently high ion-exchange capacity, 4) fast ion-exchange kinetics and some others.

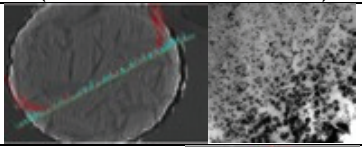
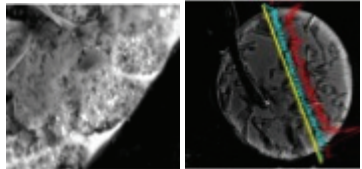
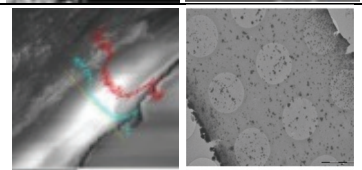
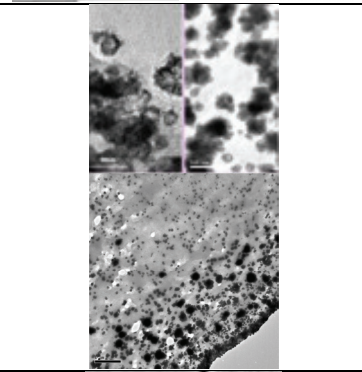
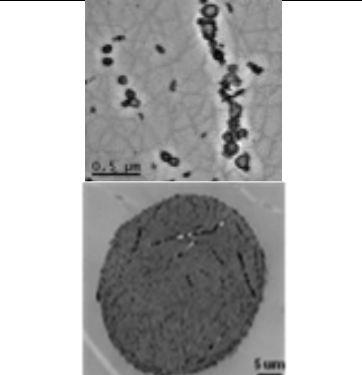
Functional group	Form	Polymeric matrix	SEM, TEM images and EDS spectra of resulting nanocomposites (Pd-red, and Co-blue Line)
R-SO ₃ ⁻	Granulated gel resin	PE-PVB	
R-COO ⁻	Granulated macroporous resin	Acrylic	
R-SO ₃ ⁻	Membrane (dense)	SPEEK	
R-SO ₃ ⁻	Fiber (non-woven)	PP fiber with graft copolymer of styrene and divinylbenzene	
R-COO ⁻	Fiber (non-woven)	PP fiber with graft copolymer of acrylic acid on polypropylene	

Table 1. Examples of polymeric matrices applicable for IMS of MNPs.

4. Magnetic nanoparticles

Magnetic NPs are of great interest for researchers from a wide range of disciplines, including catalysis, biotechnology/biomedicine and environmental science and technology (Hyeon, 2003; Lu et al., 2007; Pankhurst et al., 2003; Vatta et al., 2006). For many practical applications, it is necessary to develop some strategies to chemically stabilize the magnetic NPs against degradation (e.g., oxidation) during (or after) their synthesis and, especially, during their use. Therefore, many efforts have been dedicated to the synthesis of polymeric materials containing magnetic NPs, making them ideal candidates for many technological applications (Qiao, 2007; Suchorski et al., 2008). Systems based on these kinds of nanocomposites are employed in magnetic recording devices, ferrofluids, medical diagnosis, drug delivery, pigments for paintings and ceramics (Bastida et al., 2006).

For example, a new family of potential contrast agents has been recently synthesized based on magnetic nanoparticles stabilized using commercially available polyelectrolytes (such as poly(sodium-4-styrene) sulfonate) that act as both nanocomposite assembly directors and water-stable surfactants, instead of the classical biopolyelectrolyte DNA (Corr et al., 2008; Davies et al., 2011). Hence, using straight-forward one-step procedures, magnetic fluids can be prepared. Similar approaches have also been developed for non-magnetic nanoparticle suspensions (Alonso et al., 2010; Kidambi & Bruening, 2005).

It is also important to note that quite different metals or their compounds show similar magnetic properties. Therefore, a wide variety of magnetic NMs and nanocomposites based on these can be prepared. These NMs can be iron oxides, such as Fe_3O_4 , pure metals, such as Fe and Co, spinel-type ferromagnets, such as MgFe_2O_4 , MnFe_2O_4 , and CoFe_2O_4 and some others (Davies et al., 2011). The main advantages and drawbacks of magnetic NMs are summarized in Figure 8. For instance, regarding the materials safety, it is important to notice that due to their low level of toxicity and their good magnetic properties, the use of ferrites is very convenient for biological applications (Laurent et al., 2008).

However, magnetic NPs do not usually have the desired properties required for their immediate application in catalysis or water disinfection. Therefore, they can serve as a magnetic core in core@shell MNPs, in which the shell consists of the metal with the desired activity (catalytic or bactericide). Core@shell MNPs of this type can be easily prepared by using IMS technique (Macanás et al., 2011) and the resulting nanocomposites can be applied in catalysis or water treatment (Medyak, 2001). In catalysis, for instance, due to the magnetic properties of MNPs, the nanocomposites can be easily recovered and reused in sequential catalytic cycles, which is particularly important for MNPs containing platinum group metals.

In fact, the synthesis of new nanocomposite materials based on the synthesis of polymer-immobilized bi- and poly-metallic NPs with core@shell architecture consisting of a low-cost magnetic (ferromagnetic or super-paramagnetic) core coated with a functional shell (having, for example, catalytic or bactericidal properties) is of particular interest for many advanced applications (Corain & Kralik, 2000; Medyak, 2001; Muraviev et al., 2008a).

It is also important to emphasize that in some cases the performance of such nanocomposite materials in their practical application can be comparable to (or often even better than) that of their monometallic analogs (containing shell-metal NPs). At the same time, the cost of nanocomposites containing core@shell MNPs is far lower due to significantly lower loading with precious metals (e.g., Pt, Pd or Ag). These considerations represent an additional advantage of these NMs.

As it has been previously reported (Muraviev et al., 2006, 2008b) that the IMS technique makes it possible to prepare both mono-component and bi-component NPs (metal- or metal oxide-based) in different cation exchange matrices (Table 1, Figure 9). In all cases, the polymer-metal nanocomposites demonstrate quite strong magnetic properties and are easily attracted by permanent magnets. Some parameters such as NPs size and spatial distribution were studied by examining sample cross-sections by Scanning Electron Microscopy (SEM) (see Figure 9). Similar results were obtained for Ag@Co and Ag@ferrite (such as Fe_3O_4 and MnFe_2O_4) PSMNPs synthesized in different types of polymer matrices (sulfonic and carboxylic resins) following modified literature procedures (Corr et al., 2008, Alonso, 2011).

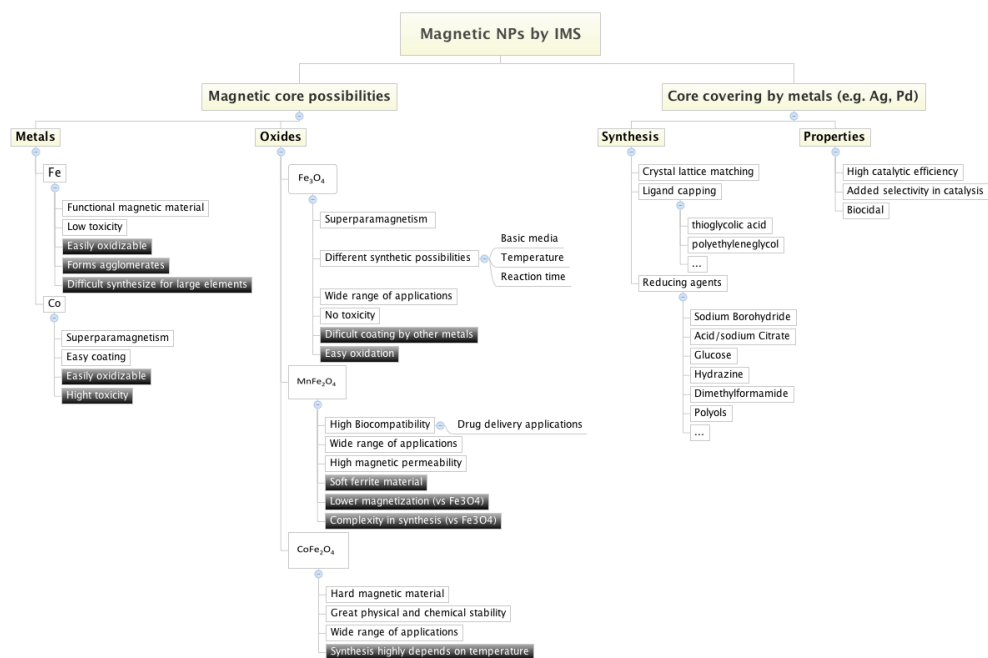


Fig. 8. General overview of preparation of magnetic nanocomposites by IMS technique. Advantages and drawbacks are given in white and black, respectively.

In all cases, NPs were distributed heterogeneously inside polymer matrices and with far higher concentrations on the surfaces of the nanocomposites. This distribution is favorable for both catalytic and water disinfection applications.

The magnetic properties of both bimetallic (Pd@Co and Ag@Co) and metal-metal oxide (Ag@ Fe_3O_4) core@shell NPs within the different polymer resins were found to be superparamagnetic at room temperature (Figure 10). Magnetic measurements were carried out using SQUID magnetometer and Vibrating Sample Magnetometer.

The magnetization of polymer-Pd@Co nanocomposites can be seen in Figure 10 (see left hand side), and is higher for the sulfonic resin than for the carboxylic one. This difference can be attributed to a higher Co concentration in the first resin in comparison with the second one (due to the conditions of IMS procedure). The magnetization of the NPs magnetite does not decrease after their coating with silver shell, as shown in Figure 10b.

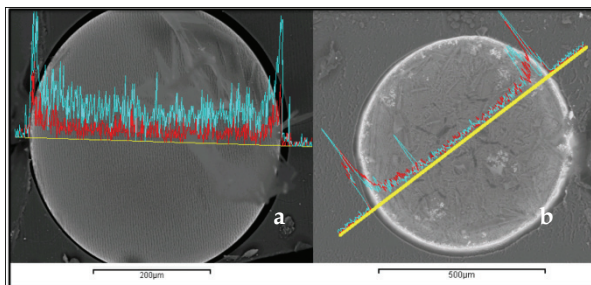


Fig. 9. SEM images of ferric oxide NPs in sulfonic ion exchange polymers: a) MnFe_2O_4 gel-type resin where the blue line represents Mn and the red line represents Fe, and b) $\text{Ag@Fe}_3\text{O}_4$ gel-type resin where blue line represents Ag and the red line represents Fe.

Moreover, as it can be seen the bimetallic $\text{Ag@Fe}_3\text{O}_4$ NPs demonstrate a sort of a synergistic effect towards magnetization similar to that reported for Pt@Co alloys (Lee et al., 2005) and Pd@Co core@shell MNPs (Durand et al., 2008) however, this point requires further investigation.

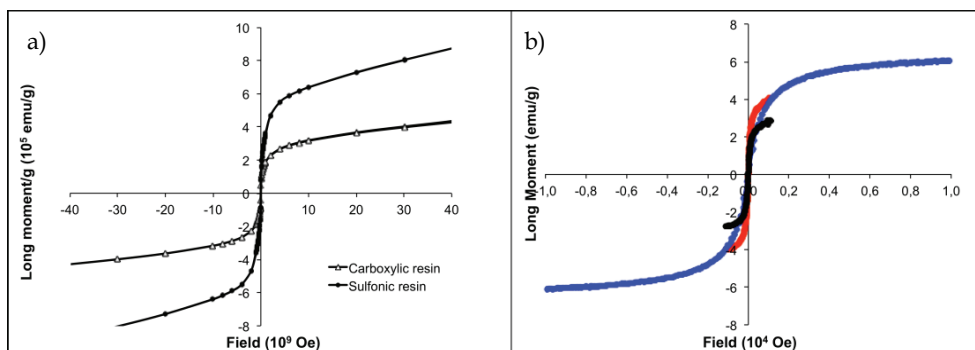


Fig. 10. a) SQUID hysteresis curves of Pd@Co NPs in carboxylic and sulfonic resins and, b) SQUID hysteresis curve of ferrite core NPs synthesized in sulfonic resin: blue) $\text{Ag@Fe}_3\text{O}_4$, red) Fe_3O_4 , black) $\text{Ag@Fe}_3\text{O}_4$ half concentration compared with blue).

5. Applications of polymer-metal nanocomposites

5.1 Catalysis

As previously mentioned, catalysis is one of the largest areas of MNPs application (Campelo et al., 2009; Zeng, 2004). Platinum Group Metal (PGM) NPs are very well-known as highly selective catalysts and are widely used in organic synthesis, chemical industry and other areas (Durand et al., 2008). Heterogeneous catalytic reactions are known to proceed on the surface of the catalyst. This means that in the case of monometallic MNPs, the central part of the catalyst particle does not take part in the catalytic process and can be substituted by another metal. The synthesis of core@shell catalyst MNPs composed of a low-cost metal core coated with a thin PGM-shell can substantially lower the total cost of the catalyst in comparison with monometallic PGM-MNPs. Incorporating a core metal with magnetic

functionality provides an additional advantage to these nanocatalysts, allowing them to be easily recovered from the reaction mixture and recycled.

Pd@Co MNPs synthesized in different polymeric matrices have been tested as catalysts for various cross-coupling reactions (Table 1, Figure 11) (Son et al, 2004), although they can also be applied as catalysts in other processes like dehalogenation, hydrodechlorination, carbonylation or oxidation (Wilson et al., 2006; Umpierre et al., 2005).

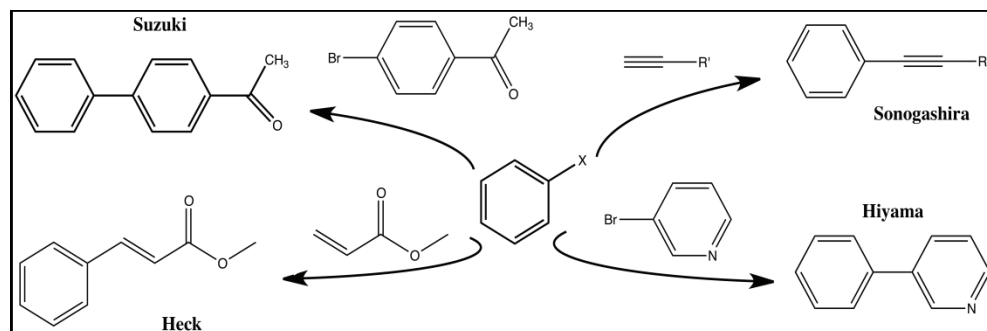


Fig. 11. Typical cross-coupling reactions tested with Pd@Co NPs as catalyst.

Non-supported monometallic palladium MNPs have been efficiently used to study NP effects in catalysis. Supported Pd-MNPs embedded in polyelectrolyte films, beads or fibers can be easily prepared by employing the IMS technique (Alonso et al., 2010; Ouyang et al., 2010). Certain types of Pd-PSMNPs synthesized by IMS have been tested as catalysts for the Suzuki reaction (Medyak, 2001), which is a cross coupling reaction between arylboronic acids and aryl halides leading to the formation of biphenyls (Niembro et al., 2008). However, bimetallic catalysts such as alloy MNPs or core@shell MNPs are of particular interest for several reasons: i) the combination of two metals may provide control over catalytic activity, selectivity and stability, and ii) by controlling the thickness of a catalytically-active shell, one can improve the “catalytic atom economy” (Baranchikov, 2007).

The catalytic activity of various nanocomposite materials in the form of a membrane, fiber or granulated resin (bearing either carboxylic or sulfonic groups, Table 1) with core@shell Pd@Co PSMNPs distributed mainly on the surface part of the polymeric matrix was tested in Suzuki cross-coupling reaction (Figure 12).

As shown in Figure 12, the catalytic activity of fibrous nanocomposites does not depend on the type of fiber functionality and both carboxylic and sulfonic fibers achieve a 100% reaction yield. Due to the higher stability of the carboxylic matrix it was possible to successfully use it in the successive catalytic cycles (up to 3). The insufficient chemical stability of the sulfonic fibers did not allow their complete separation and recovery from the final reaction solution mixture, despite the magnetic properties of the material. When using a sulfonated polyetheretherketone (SPEEK) nanocomposite membrane, the reaction yield in the second catalytic cycle was dramatically reduced due to the partial dissolution of this non-crosslinked polymer in the solvent mixture (DMF:water) under the reaction conditions and substantial loss of the catalyst PSMNPs. The results obtained with granulated ion exchange resin nanocomposites show that their catalytic efficiency is lower than that observed for the fibers what can be attributed to the higher surface area of fibers providing

increased contact between the reagents and catalyst MNPs. Although no dramatic differences have been observed between carboxylic or sulfonic resins, the macroporous structure of the later is known to be more applicable for catalytic reactions (Biffis et al., 2000; D'Archivio et al., 2000; Zagorodni, 2007).

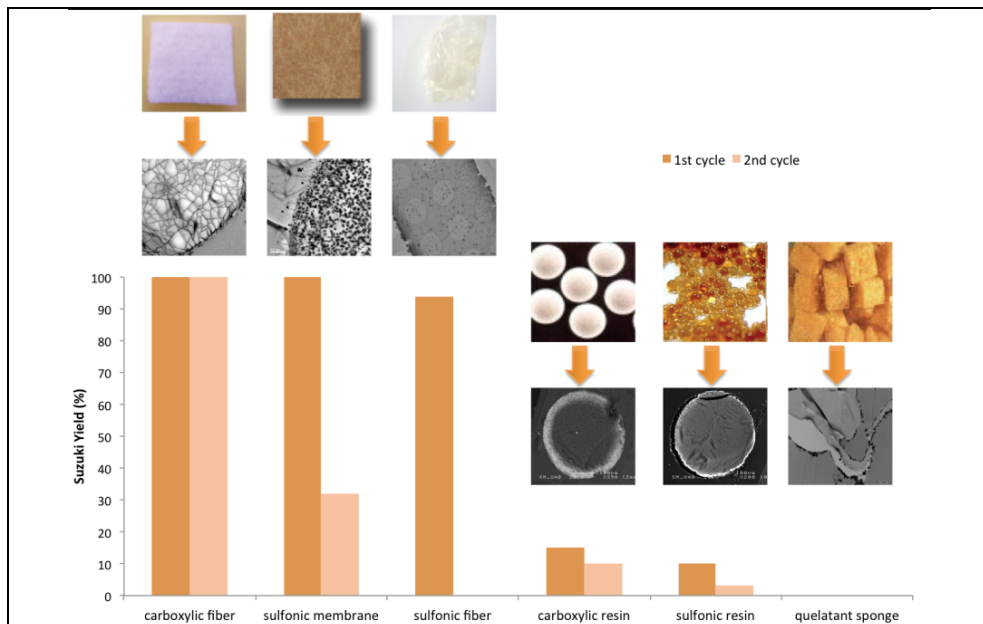


Fig. 12. Comparison of catalytic activity for different kinds of catalytic nanocomposites.

Finally, the nanocomposite sponge demonstrated essentially zero catalytic activity due to difficulties associated with the accessibility of reactants to the catalyst MNPs located mainly in the internal part of the sponge.

Therefore, the properties of the polymeric matrices themselves (distinct from those of MNPs) represent another important parameter, which determines the applicability of the catalytically-active nanocomposite under certain reaction conditions. The chemical stability, the specific surface area and the penetrability of the nanocomposite matrix towards chemical reagents are also important parameters, which has to be taken into account when choosing the polymeric supports for IMS of catalytically-active MNPs.

5.2 Biocide and antibiofouling applications

The presence of microorganisms in water makes disinfection treatment before consumption a necessity. In the majority of cases, the potable water is currently disinfected by using various chemicals such as ozone, chlorine and some of its compounds and others having bactericide properties. The Chemical-free disinfection is considered to be an attractive alternative and it is usually associated with silver metal. While silver has been known to be a bactericide element for at least 1200 years, colloidal silver or silver MNPs have recently been recognized and tested in various applications as excellent antimicrobial agents because of their high biocide activity (Kong & Jang, 2008; Law, 2008; Pal et al., 2007). The

antibacterial action of silver MNPs is still under debate but it has been reported to be similar to that of silver ions, which bind to DNA, block transcription, and therefore interrupt the bacterial respiration and the adenosine triphosphate synthesis. In *in vivo* assays, the majority of Ag-MNPs are often located in the membranes of treated *E. coli* cells and only a few of them penetrate inside the cells. However, the exact biochemical and molecular aspects of the actions of this distinct silver species have never been directly addressed (Sondi & Salopek-Sondi, 2004).

Ag-MNPs purportedly present high antibacterial activity, relatively low toxicity, chemical and thermal stability, and a long-lasting action period (Cubillo et al., 2006). The stabilization and immobilization of Ag-MNPs in different matrices has recently gained great attention from scientists and technologists for two main reasons: i) immobilization in the matrix can improve the safety of the material (due to the reasonable doubt of their human toxicity) and ii) the immobilization improves the handling of MNPs and simplifies their final application. The use of Ag-MNPs containing nanocomposites can also help to solve another important technological problem associated with water treatment, known as biofouling. The Biofouling (or biological fouling) is the undesirable accumulation of microorganisms on the surface of water treatment devices and materials such as, reverse osmosis membranes, cooling water cycles, ion exchange resins, etc. (Kim & Van der Bruggen, 2010).

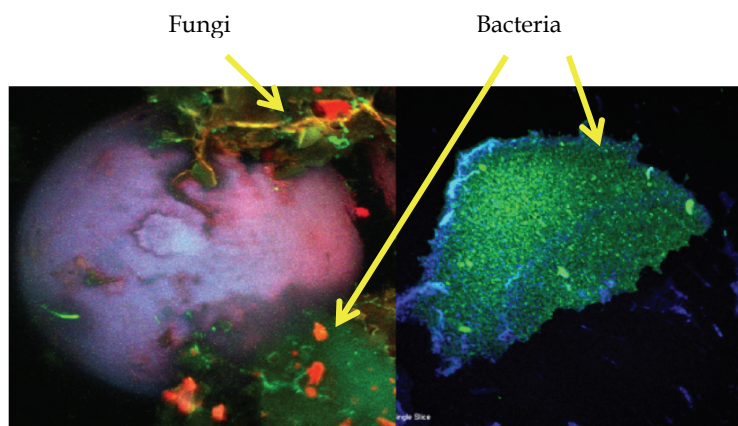


Fig. 13. Confocal microscope image of surface of carboxylic ion exchange resin after being used for the domestic water treatment.

As an example, Figure 13 shows confocal microscope images of the biofouling of ion exchange resin beads taken after their use in a conventional domestic tap water treatment filter usually used for the removal of undesired metal ions (hardness ions, iron, heavy metal ions, etc.). As shown, the surface of the resin beads appears to be strongly contaminated by the accumulated fungi and bacteria. The use of ion exchange resins modified with Ag@Co MNPs for conventional domestic water treatment helps to solve this problem. The surface of the nanocomposite resin beads appears to be far less biocontaminated after the treatment of the same water volume. A similar solution can be used for prevention of biofouling of the membranes used at reverse osmosis water treatment plants (Taurozz, 2008). The surface modification of ion exchange materials used for traditional water treatment (ion exchange resins, membranes, etc.) with ecologically safe MNPs, which have high biocide activity (e.g.,

Ag@Co or Ag@Fe₃O₄) can successfully solve the problems associated with biofouling of their surfaces in the course of water treatment processes.

The authors of this chapter (A. Alonso, M. Muñoz and D.N. Muraviev) have recently developed and patented (Muraviev et al., PCT/ES2010/000323, 23th of July, 2010) a methodology for the surface modification of commercially available ion exchange materials with core@shell MNPs containing silver shell and a magnetic core (Savage & Diallo, 2005). These materials represent the environmentally friendly bactericide nanocomposites suitable for conventional water treatment coupled with reagent-free disinfection. The main advantages of such materials are:

- First, MNPs are strongly captured inside the polymer matrix that prevents their escape into the medium under treatment.
- Second, the surface distribution of MNPs within the material provides their contact with the bacteria to be eliminated and fast water disinfection.
- Third, the super-paramagnetic nature of MNPs provides an additional level of the material safety as the use of a simple magnetic trap prevents any post-contamination of treated water with MNPs leached from the polymer matrix.
- Fourth, the surface location of MNPs does not essentially influence the main characteristics of the ion exchange material such as, the ion exchange capacity and some others, which permits the use of these nanocomposites for complex water treatment, including removal of undesired ionic contaminants and reagent-free disinfection.

The bactericide properties of the nanocomposites were evaluated by using antibacterial kinetics tests, by the determination of the minimum inhibitory concentration, and by the modified Kirby-Bauer test. The antibacterial activity of Ag@Co-PSMNPs towards several types of microorganisms such as *Escherichia coli*, *Staphylococcus aureus* (Gram-positive bacteria), *Salmonella*, *Klebsiella*, *Pseudomonas aeruginosa*, *Enterobacter* (all Gram-negative bacteria) was tested and confirmed high bactericide activity of the nanocomposites (Alonso et al., Unpublished results).

The antibiofouling activity of nanocomposite materials was evaluated by carrying out the following tests: water with a constant concentration of *Pseudomonas Putida* (10³cfu/ml) was passed through the columns loaded with non-modified ion-exchange resin and with the same resin modified with Ag-MNPs. The samples of treated water were collected periodically, seeded, incubated and subjected to Petri dish recounts. Figure 14 shows that the colonies of *Pseudomonas* were formed on the surface of polymer without Ag-MNPs whereas the surface of Ag-MNPs modified resins appeared to be essentially free from biofouling.

The results presented in this section represent an integration of Nanotechnology and Bacteriology, which may lead to possible important advances in the formulation of new types of bactericides. Moreover, additional studies of the biocide activity of these nanomaterials towards Gram-positive and Gram-negative bacteria of other types have also been carried out in order to fully evaluate their potential use as a new bactericidal material.

5.3 Complex water treatment

In many countries the microbial contamination of potable water sources poses a major threat to public health and the emergence of microorganisms resistant to multiple antimicrobial agents increases the demand for improved disinfection methods (Ruparelia, 2008). The importance of potable water for the people in some countries dictates the need for the development of innovative technologies and materials for the production of safe potable water.

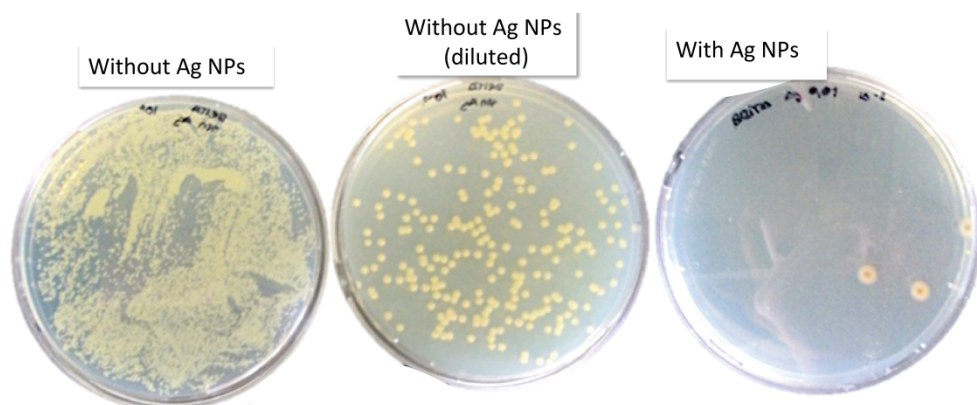


Fig. 14. Petri dishes with cultures from treated and untreated water.

Nowadays the different strategies for water disinfection include (Das, 2005): chemical agents (e.g. chlorine and its compounds, ozone, hydrogen peroxide and some others), physical treatment (e.g. heat, UV-irradiation, etc.) and mechanical means (e.g., ultrafiltration). All these strategies differ from each other by their efficiency, water treatment cost and potential usability. For instance, heat is commonly used in the beverage and dairy industry, but it is not a feasible means of disinfecting large quantities of wastewater because of the high cost. The use of oxidizing chemical substances can cause corrosion in the water treatment and supplying facilities.

Thus, new approaches for the complex water treatment are continually being examined. However, it appears to be quite difficult to fulfill all the necessary requirements such as, lower overall treatment cost, durability and high efficiency, higher than current options for the removal of contaminants from water. Nanotechnology has been identified as a technology that could play an important role in resolving many of the problems involving water purification and quality (Bottero et al, 2006; Savage & Diallo, 2005; Theron et al., 2008; Weber et al., 2003). As such, the application of MNPs has been extensively studied for reductive dechlorination of halogenated organic compounds in ground water (Xu & Bhattacharyya, 2005). One of the most efficient elements is iron nanoparticles as pure monometallic entities or in combination with platinum (bimetallic particles). However, the long-term stability of these nanoparticles can be enhanced by immobilization in a solid support (Ponder et al., 2000). A variety of nanomaterials are in various stages of research and development, each possessing unique functionalities that are potentially applicable to the remediation of industrial effluents, groundwater, surface water and drinking water.

It is worthy to note that ion exchange materials are widely used for various water treatment processes, mainly to eliminate undesired or toxic ionic impurities such as hardness ions, iron, heavy metals, and others. The modification of such supports with bactericide MNPs enables the combination of traditional water treatment with disinfection to eliminate microbiological contaminants. Using this approach, two complementary water treatment steps could be performed with a single material. Nonetheless, the following important

points have to be taken into account when using silver MNPs as a bactericide agent (Savage& Diallo, 2005):

1. The size of microorganisms to be eliminated from water in the course of its disinfection with polymer-metal nanocomposite does not allow them to deeply penetrate inside solid biocide materials. For this reason, Ag-MNPs have to be located near the surface of the immobilizing matrix to make them maximally accessible to bacteria.
2. Since, free Ag-MNPs have been reported to be far more toxic than bulk silver metal polymer-stabilized silver MNPs and the nanocomposites based on these represent one of the most attractive solutions to this problem since these materials guarantee at least the first level of safety due to the strong retention of MNPs by polymer matrix.
3. Even if the immobilization of Ag-MNPs in the polymer might prevent post-contamination of treated water with MNPs, the surface location of Ag-NPs in the stabilizing polymer increases the probability of their uncontrollable escape from the matrix. This, in turn dictates the necessity providing the nanocomposite material with an additional safety level, which can be based on the use of ferromagnetic (or super-paramagnetic) polymer-stabilized-Ag-MNPs. In such cases, NPs which have escaped from the polymer into the treated water can be easily captured by a simple magnetic trap.

Finally we would like to emphasize that all of the above requirements are fulfilled by the materials developed by our group (Weber et al., 2003). A possible way to apply in complex water treatment is shown in **Figure 15**.

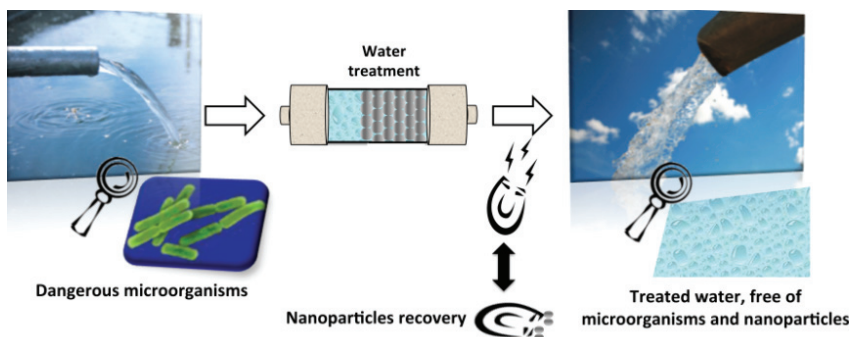


Fig. 15. Use of environmentally friendly nanocomposites for complex water treatment.

6. Conclusions

The following conclusions can be derived from the results summarized in this chapter:

1. The Intermatrix Synthesis (IMS) technique represents a promising technique that allows the production of a wide variety of polymer-metal nanocomposites of practical importance for different fields of modern science and technology. The attractiveness of this technique is determined not only by its relative simplicity but also by its flexibility and the possibility of tuning the specific properties of the final nanocomposites to meet

the requirements of their final applications. IMS technique gives a unique possibility of obtain monometallic, bimetallic or polymetallic MNPs with core@shell, core-sandwich and even more complex structures for the applications of interest.

2. The spectrum of polymers applicable for IMS of PSMNPs is quite wide and includes mainly functionalized polymers, i.e. those bearing functional groups, which are capable of binding to metal ions prior to their reduction inside the polymer matrix (IMS of PSMNPs). The dissociated ionogenic functional groups of the polymer bear certain charges, making it possible to couple the IMS technique with the Donnan exclusion effect when using ionic reducing agents bearing the charge of the same sign as that of the polymer at the metal reduction stage of IMS.
3. We have demonstrated that the nature of the agent used to reduce metal ions to MNPs plays an important part in IMS as it determines the conditions of MNPs formation inside the polymer matrix (metal reduction stage) and their distribution inside the matrix. Thus, the use of anionic reducing agents (e.g., borohydride) for IMS of PSMNPs in cation exchange matrices results in their formation mainly near the surface of the polymer. This type of MNP distribution is favorable for many practical applications of polymer-metal nanocomposites such as water disinfection, catalysis and some others.
4. The properties of metal-polymer nanocomposites are not determined only by the properties of the MNPs. The formation of MNPs within the polymer matrices may strongly modify the polymer morphology, for example due to the appearance of nanoporosity, which enhances the rate of mass transfer inside the nanocomposites as well as some other structural parameters which are of great importance in their practical applications.
5. The IMS of core shell PSMNPs consisting of super-paramagnetic cores coated with functional shells having for example, catalytic or bactericidal properties provides the polymer-metal nanocomposites with additional advantages. In the case of catalytic applications, the nanocomposites can be easily recovered from the reaction mixture and reused. In water treatment applications, the magnetic nature of MNPs permits prevention of their uncontrollable escape into the treated water by using simple magnetic traps.
6. Finally, the last and the most important conclusion, in our opinion, concerns the general strategy in the development of novel nanocomposite materials. This strategy has to be focused not only on the desired properties of the material, which is dictated by its further practical applications, but also on the material safety in both environmental and human health senses. The last point seems to be of particular importance for the further development of Nanoscience and Nanotechnology.

7. Acknowledgements

We are sincerely grateful to all our associates cited throughout the text for making this publication possible. Part of this work was supported by Research Grant MAT2006-03745, 2006-2009 from the Ministry of Science and Technology of Spain, which is also acknowledged for the financial support of Dmitri N. Muraviev.

We also thank ACCIÓ for VALTEC 09-02-0057 Grant within "Programa Operatiu de Catalunya" (FEDER). AGAUR is also acknowledged for the predoctoral grant supporting A.Alonso.

8. References

- Abbott, L.C. & Maynard, D.M. (2010). Exposure Assessment Approaches for Engineered Nanomaterials. *Risk Analysis*, vol. 30, 11, pp. 1634-1644
- Ajayan, P.M. et al. (2005). *Nanocomposite science and technology*. pp. 230
- Albrecht, M. A., C. W. Evans, & C. L. Raston. (2006). Green chemistry and the health implications of nanoparticles. *Green Chemistry*, 8, 5, pp. 417-432.
- Alonso, A. (2011). Unpublished results.
- Alonso, A., et al. (2010). Donnan-Exclusion-Driven distribution of catalytic ferromagnetic nanoparticles synthesized in polymeric fibers. *Dalton Transactions*, vol. 39, pp. 2579 - 2586
- Baranchikov, A.Y. (2007). Sonochemical synthesis of inorganic materials. *Russian Chemical Reviews*, vol. 76, 2, pp.133-151.
- Bastida, M.A. et al. (2006). Magnetic properties of Co/Ag core/shell nanoparticles prepared by successive reactions in microemulsions, *Journal of Magnetism and Magnetic Materials*, vol. 300, 1, pp. 185-191
- Bell, C. A. et al. (2006). Surface-functionalized polymer nanoparticles for selective sequestering of heavy metals. *Advanced Material*, vol. 18, 5, pp. 582-586.
- Belotelov, V.I., Perlo, P. & Zvezdin, A.K. (2005). Magnetooptics of granular materials and new optical methods of magnetic nanoparticles and nanostructures imaging. In: L. Nicolais and G. Carotenuto (Eds.). *Metal-Polymer nanocomposites*, John Wiley & Sons, pp. 201-240.
- Bernard, B.K. et al. (1990). Toxicology and carcinogenesis studies of dietary titanium dioxide-coated mica in male and female Fischer 344 rats. *Journal of Toxicology and Environmental Health*, 29, 4, pp. 417-429.
- Bhushan, B. (2007). Springer Handbook of nanotechnology (2nd Ed.). pp. 1916, ISBN: 354029855X
- Biffis et al. (2000). The Generation of Size-Controlled Palladium Nanoclusters Inside Gel-Type Functional Resins: Arguments and Preliminary Results. *Advanced Materials*, vol. 12, 24, pp. 1909-1912.
- Blackman, J.A. (2008). *Metallic nanoparticles*. pp. 385, ISBN: 9780444512406
- Borm, P. & Berube, D. (2008). A tale of opportunities, uncertainties, and risks. *NanoToday*, vol. 3, 1-2, pp. 56-59
- Bottero, J.Y., et al. (2006). Nanotechnologies: tools for sustainability in a new wave of water treatment processes. *Integrated Environmental Assessment and Management*, vol. 2, 4, pp. 391-395
- Bowker, M. (2009). A prospective: Surface science and catalysis at the nanoscale, *Surface Science*, vol. 603, 16, pp. 2359-2362
- British Standards Institute: BSI PAS 130. (2007). *Guidance on the labelling of manufactured nanoparticles and products containing manufactured nanoparticles*
- Campelo, J.M. et al. (2009). Sustainable Preparation of Supported Metal Nanoparticles and Their Applications in Catalysis. *ChemSusChem*, vol. 2,1, pp. 18-45
- Chen, J.L. & Fayerweather, W.E. (1988). Epidemiologic study of workers exposed to titanium dioxide. *Journal of Occupational Medicine and Toxicology*, 30, 12, pp. 937-942.

- Christy, R. (2003). Effects of Surface Coordination Chemistry on the Magnetic Properties of MnFe_2O_4 Spinel Ferrite Nanoparticles. *Journal of American Chemistry Society*, vol. 125, pp. 9828-9833
- Corain, B. & Kralik, M. (2000). *Journal of Molecular Catalysis A: Chemical*, vol.159, pp. 153.
- Corr, S. A. (2008). Linear Assemblies of Magnetic Nanoparticles as MRI Contrast Agents, *Journal of the American Chemical Society*, vol. 130, pp. 4214-4215
- Corr, S. A. (2007). *New Magnetic Nanocomposite materials*, Ph.D Thesis, pp.54, Chemistry from Trinity College Dublin
- Cubillo, A.E. et al. (2006). Antibacterial activity of copper monodispersed nanoparticles into sepiolite, *Journal of Materials Science*, vol. 41, 16, pp. 5208-5212.
- D'Archivio et al. (2000). Metal palladium dispersed inside macroporous ion-exchange resins: rotational and translational mobility inside the polymer network. *Journal of Molecular Catalysis A: Chemical*, vol. 157, 1-2, pp. 269-273
- Das. "Disinfection". In: Kirk-Othmer Encyclopedia of Chemical Technology. Kirk-Othmer Encyclopedia of Chemical Technology (2005) pp. 1-68
- Davies, G.-L., et al. (2011). NMR Relaxation of Water in Nanostructures: Analysis of Ferromagnetic Cobalt-Ferrite Polyelectrolyte Nanocomposites, *ChemPhysChem*, vol. 12, pp. 772-776.
- Durand, J. et al. (2008). An overview of palladium nanocatalysts: Surface and molecular reactivity. *European Journal of Inorganic Chemistry*, vol. 23, pp. 3577-3586
- Giannazzo, F. et al. (2011). Advanced materials nanocharacterization. *Nanoscale Research Letters*, vol. 6,1, pp. 107
- Gramotnev, D. K. & Gramotnev, G. (2005). A new mechanism of aerosol evolution near a busy road: Fragmentation of nanoparticles. *Journal of Aerosol Science*, 36, 3, pp. 323-340.
- Hassan, M. (2005). Small things and big changes in the developing world. *Science*, vol. 309, 5731, pp. 65-66
- Haverkamp, R.G. (2010). A Decade of Nanoparticle Research in Australia and New Zealand. *Particulate Science And Technology*, vol. 28, 1, pp. 1-40
- Hillie, T. & Hlophe, M. (2007). Nanotechnology and the challenge of clean water, *Nature Nanotechnology*, vol. 2, 11, pp. 663-664
- Houk, L.R., et al. (2009). The Definition of "Critical Radius" for a Collection of Nanoparticles Undergoing Ostwald Ripening. *Langmuir*, vol. 25, 19, pp. 11225-11227
- Hyeon, T. (2003). Chemical synthesis of magnetic nanoparticles. *Chemical Communications*, 8, pp. 927-934
- Imre, A., et al. (2000). Surface Ostwald ripening of Pd nanoparticles on the MgO (100) surface. *Applied Physics A*, vol. 71, pp. 19-22
- International Standards Organisation: ISO/TS 27687:2000. (2000). *Nanotechnologies - Terminology and definitions for nanoobjects - Nanoparticle, nanofiber and nanoplate*
- Joo, H. (2006). *Nanotechnology for environmental remediation*. pp. 165, ISBN: 0387288252
- Ju-Nam, Y. & Lead, J.R. (2008). Manufactured nanoparticles: An overview of their chemistry, interactions and potential environmental implications. *Science of the Total Environment*, vol. 400, 1-3, pp. 396-414

- Kidambi, S., & Bruening, M.L. (2005). Multilayered polyelectrolyte films containing palladium nanoparticles: Synthesis, characterization, and application in selective hydrogenation. *Chemistry of Materials*, 17, pp. 301-307
- Kim, J & Van der Bruggen, B. (2010). The use of nanoparticles in polymeric and ceramic membrane structures: Review of manufacturing procedures and performance improvement for water treatment. *Environmental Pollution*, vol. 158, 7, pp. 2335-2349
- Klabunde, k.J. (2005). Nanoscale Materials in Chemistry. *Wiley-VCH*, pp. 1-293
- Kong, H. & Jang, J. (2008). Antibacterial Properties of Novel Poly(methyl methacrylate) Nanofiber Containing Silver Nanoparticles. *Langmuir*, vol.24, 5, pp. 2051-2056
- Lane, N. (2002). Nanotechnologies meet market realities. *Chemical & Engineering News*, pp. 17
- Laurent, S. et al. (2008). Magnetic Iron Oxide Nanoparticles: Synthesis, Stabilization, Vectorization, Physicochemical Characterizations, and Biological Applications. *Chemical Reviews*, vol. 108, 6, pp. 2064-2110
- Law, N. (2008). Formation of Nanoscale Elemental Silver Particles via Enzymatic Reduction by *Geobacter sulfurreducens*. *Applied And Environmental Microbiology*, vol. 74, 22, pp. 7090-7093
- Lee, W.-R. et al. (2005). Redox-Transmetalation Process as a Generalized Synthetic Strategy for Core-Shell Magnetic Nanoparticles. *Journal of the American Chemical Society*, vol. 127, 46, pp. 16090-16097.
- Li et al. (2008). Antimicrobial nanomaterials for water disinfection and microbial control: Potential applications and implications. *Water Research*, vol. 42,18, pp. 4591-4602
- Lu, A-H. et al. (2007). Magnetic nanoparticles: synthesis, protection, functionalization, and application. *Angewandte Chemie International Edition*, vol.46, 8, pp. 1222 - 1244
- Macanás, J. et al. (2011). Ion-exchange assisted synthesis of polymer-stabilized metal nanoparticles. Solvent Extraction and Ion Exchange. *A series of Advances*, Taylor & Francis, vol.20, chapter 1.
- Maynard, A.D. (2007). Nanotechnology: The next big thing, or much ado about nothing?. *Annals of Occupational Hygiene*, vol. 51, 1, pp. 1-12
- Maynard, R. L. & Howard, C. V. (1999). Particulate Matter: Properties and Effects upon Health. *Bios Scientific Publishers*, Oxford UK.
- Medyak, G.V. (2001). *Russian Journal of Applied Chemistry*, vol. 74, 10, 16583.
- Miley et al. (2005). Nanotechnology. *Kirk-Othmer Encyclopedia of Chemical Technology*, pp. 1-29
- Muraviev, D.N. (2005). *Contribute to Science*, vol. 3, 1, pp. 17.
- Muraviev, D.N. et al. (2008). Novel strategies for preparation and characterization of functional polymer-metal nanocomposites for electrochemical applications. *Journal of Pure and Applied Chemistry*, vol. 80, 11, pp. 2425-2437.
- Muraviev, D.N. et al. (2008). Synthesis, stability and electrocatalytic activity of polymer-stabilized monometallic Pt and bimetallic Pt/Cu core-shell nanoparticles. *Physica Status Solidi A*, vol. 205, 6, pp. 1460-1464.

- Muraviev, D.N. et al. (2006). Novel routes for inter-matrix synthesis and characterization of polymer stabilized metal nanoparticles for molecular recognition devices. *Sensors and Actuators B: Chemical*, vol. B118, 1-2, pp. 408-417.
- Muraviev, D.N. et al. *Nanocomposite with bactericide activity*, PCT/ES2010/000323, (23th of July, 2010)
- Narayan, R. (2010). Use of nanomaterials in water purification. *Materials Today*, vol. 13, 6, pp. 44-46
- Nicolais, L. & Carotenuto, G. (2005). Metal-polymer nanocomposites. *Wiley-VCH*, pp. 300
- Niembro, S. et al. (2008). Phosphine-Free Perfluoro-Tagged Palladium Nanoparticles Supported on Fluorous Silica Gel: Application to the Heck Reaction. *Organic Letters*, vol. 10, pp. 3215.
- Ouyang, L. et al. (2010). Catalytic hollow fiber membranes prepared using layer-by-layer adsorption of polyelectrolytes and metal nanoparticles. *Catalysis Today*, vol. 156, 3-4, pp. 100-106
- Pal, S. et al. (2007). Does the Antibacterial Activity of Silver Nanoparticles Depend on the Shape of the Nanoparticle? A Study of the Gram-Negative Bacterium *Escherichia coli*. *Applied and Environmental Microbiology*, vol. 73, 6, pp. 1712-1720
- Pankhurst, Q.A. et al. (2003). Applications of magnetic nanoparticles in biomedicine. *Journal of Physics D: Applied Physics*, vol. 3,6, pp. 1-15
- Park, J. & Cheon, J. (2001). *Journal of American Chemical Society*, 123, pp. 5743-5746
- Pomogailo, A.D. & Kestelman, V.N. (2005). *Metallopolymer Nanocomposites*, Springer in Materials Science, pp. 553, ISSN: 0933033X
- Pomogailo, A.D. (2000). *Uspekh Khimii, Russian Chemical Reviews*, 69, p. 53.
- Pomogailo, A.D., et al. (2003). Polymer Sol-Gel Synthesis of Hybrid Nanocomposites. *Journal of Nanoparticle Research*, vol.5, pp. 497.
- Ponder, S.M. et al.(2000). Remediation of Cr(VI) and Pb(II) aqueous solutions using supported, nanoscale zero-valent iron. *Environmental Science Technology*, vol. 34, pp. 2564-2569.
- Qiao, R. (2007). Fabrication of Super-paramagnetic Cobalt Nanoparticles-Embedded Block Copolymer Microcapsules. *Journal of Physical Chemistry C*, vol. 111, pp. 2426-2429
- Qiao, R. et al. (2007). Fabrication of super-paramagnetic cobalt nanoparticles-embedded block copolymer microcapsules. *Journal of Physical Chemistry C*, vol. 111, pp. 2426-2429
- Rao, C.N.R. et al. (2004). *The Chemistry of Nanomaterials*. Wiley-VCH, pp. 1-762
- Ristovski, Z. D. (2006). Influence of diesel fuel sulfur on nanoparticle emissions from city buses. *Environmental Science Technology*, 40, 4, pp. 1314-1320.
- Rozenberg, B.A. & Tenne, R. (2008). Polymer-assisted fabrication of nanoparticles and nanocomposites. *Progress In Polymer Science*, vol. 33, 1, 40-112, ISSN: 00796700
- Ruparella, J.P. et al. (2008). Strain specificity in antimicrobial activity of silver and copper nanoparticles, *Acta Biomaterialia*, vol. 4, 3, pp. 707-716
- Sarkar, S., Sengupta, A.K. & Prakash, P. (2010). *Environmental Science Technology*, vol. 44, pp.1161-1166
- Savage, N. & Diallo, M. (2005). Nanomaterials and water purification: opportunities and challenges, *Journal of Nanoparticle Research*, vol. 7, pp. 331-342

- Schmid, G. (2010). *Nanoparticles: from theory to application* (2nd Ed.). pp. 533, ISBN: 978-3-527-32589-4
- Schmid, G. et al. (2006). *Nanotechnology: Assessment and Perspectives*. Gethmann Springer-Verlag, Berlin
- Schulenburg, M. (2008). *Nanoparticles – small things, big effects Opportunities and risks*. Federal Ministry of Education and Research, Berlin, Germany.
- Son, S.U et al. (2004). Designed Synthesis of Atom-Economical Pd/Ni Bimetallic Nanoparticle-Based Catalysts for Sonogashira Coupling Reactions, *Journal of American Chemistry Society*, vol. 126, 16, pp. 5026-5027
- Sondi, I. & Salopek-Sondi, B. (2004). Silver nanoparticles as antimicrobial agent: a case study on E. coli as a model, *Journal of Colloid and Interface Science*, vol. 275, 1, pp. 177-182.
- Suchorski, Y. et al. (2008). CO Oxidation on a CeO_x/Pt(111) Inverse Model Catalyst Surface: Catalytic Promotion and Tuning of Kinetic Phase Diagrams *Journal of Physical Chemistry C*, vol. 12, 50, pp. 20012-20017
- Taurozzi, J. S. (2008). Effect of filler incorporation route on the properties of polysulfone-silver nanocomposite membranes of different. *Journal of Membrane Science*, vol. 325, pp. 58-68
- Theron, J. et al. (2008). Nanotechnology and water treatment: Applications and emerging opportunities. *Critical Reviews In Microbiology*, vol. 34, 1, pp. 43-69
- Umpierre, A.P. et al. (2005). Selective Hydrogenation of 1, 3-Butadiene to 1-Butene by Pd(0) Nanoparticles Embedded in Imidazolium Ionic Liquids. *Advanced Synthesis and Catalysis*, vol. 347, pp. 1404-1412.
- Vatta, L.L. et al. (2006). Magnetic nanoparticles: Properties and potential applications. *Pure And Applied Chemistry*, vol. 78, 9, pp. 1793-1801
- Vinodgopal, K., Y. H. He, M. Ashokkumar & F. Grieser. (2006). Sonochemically prepared platinum-ruthenium bimetallic nanoparticles. *Journal of Physical Chemistry B*, vol. 110, 9, pp. 3849-3852
- Walter, P. et al. (2006). Early Use of PbS Nanotechnology for an Ancient Hair Dyeing Formula, *Nano Letters*, 6, pp. 2215-2219.
- Weber, A.P. et al. (2003). Size effects in the catalytic activity of unsupported metallic nanoparticles, *Journal of Nanoparticle Research*, vol. 5, pp. 293-298, 2003.
- Wen-Ji Jin et al. (2007), *Synthetic Metals*, 157, pp. 454-459
- Wilson, O.M. et al. (2006). The Effect of Pd Nanoparticle Size on the Catalytic Hydrogenation of Allyl Alcohol. *Journal of American Chemistry Society*, vol. 128, pp. 4510-4511.
- Xiaomin, N., et al. (2005). *Journal of Crystal Growth*, vol. 275, pp. 548-553
- Xu, J. & Bhattacharyya, D. (2005). Membrane-based bimetallic nanoparticles for environmental remediation: Synthesis and reactive properties. *Environmental Progress*, vol. 24, 4, pp. 358-366
- Yegiazarov, Yu.G. (2000). *Reactive and Functional Polymers*, vol. 44, pp. 145.
- Yuan, G. D. (2004). Natural and modified nanomaterials as sorbents of environmental contaminants. *Journal of Environmental Science Health Part A: Toxic Hazardous. Substances Environmental Engineering*, vol. 39, 10, pp. 2661-2670.

- Yujiro Hayashi. (2007). Diphenylprolinol Silyl Ether as a Catalyst in an Enantioselective, Catalytic, Tandem Michael/Henry Reaction for the Control of Four Stereocenters. *Angewandte Chemie International Edition*, vol. 46, pp. 1222 - 1244
- Zagorodni, A. (2007). *Ion exchange materials: properties and applications*. Elsevier, pp. 477, ISBN:9780080445526
- Zeng, H.C. (2004). *Nanostructured Catalytic Materials: Design and Synthesis*, Tailor & Francis, pp. 1-13
- Zeng, Q. H. et al. (2007). Growth mechanisms of silver nanoparticles: A molecular dynamics study. *Nanotechnology*, 18, 3, 035708.

Silicate Glass-Based Nanocomposite Scintillators

Martin Nikl¹, Daniel Nižňanský², Jakub Ruzicka²,
Carla Cannas³ and Takayuki Yanagida⁴

¹Institute of Physics, Academy of Sciences of the Czech Republic

²Faculty of Science, Charles University of Prague, Department of Inorganic Chemistry

³University of Cagliari, Chemistry department

⁴New Industry Creation Hatchery Center, Tohoku University

^{1,2}Czech Republic

³Italy

⁴Japan

1. Introduction

Scintillation materials are employed to detect X-ray and gamma-ray photons, neutrons or accelerated particles. Usually the wide band-gap insulator materials of a high degree of structural perfection are used in the form of artificially made single crystals. They accomplish fast and efficient transformation of incoming high energy photon/particle into a number of electron-hole pairs collected in the conduction and valence bands, respectively, and their radiative recombination at suitable luminescence centres in the material. Generated UV or visible light can be then detected with high sensitivity by conventional solid state semiconductor- or photomultiplier-based photodetectors, which are an indispensable part of scintillation detectors.

Development of scintillation materials was stimulated by the discoveries of X-rays in 1895 (Röntgen, 1896) and natural radioactivity of uranium and other elements soon after that (Becquerel, 1896; Curie, 1898). A simple photographic film was found rather inefficient for their detection. As a result, the search for materials able to convert $X(\gamma)$ rays to visible rays started immediately in order to couple them with sensitive photographic film-based detectors. CaWO_4 and ZnS -based powder phosphors were used for this purpose for a long time. But the development of true bulk single crystal scintillators started only at the end of 1940s when Tl -doped NaI and CsI and CdWO_4 crystals were reported to be applicable for scintillation detection (Weber, 2002).

As mentioned above, scintillation detectors were mainly based on single crystal materials. Despite their best figure-of-merit, by far not all intrinsically efficient compounds can be grown in the form of the bulk single crystals of the sufficient size and manufacturing costs acceptable for practical applications. Too high melting temperatures, the presence of phase transitions between the melting point and room temperature (RT), or stoichiometry problems arising from different volatility of binary constituents from the high temperature melt of complex compounds are just a few examples of problems potentially disabling a

single crystal preparation. In less demanding applications the suitably doped glasses are also used. However, their efficiency and stability in the radiation environment is usually much inferior to the single crystal systems. Modern technologies bring new material conceptions, e.g. the optical ceramics which found its use in the Computed Tomography medical imaging (Greskovich & Duclos, 1997; van Eijk, 2002).

Most recently, an innovative approach was reported consisting in preparation of composite materials composed of an inorganic scintillating phase embedded in an inert optical organic or inorganic material. However, the refractive index change between the two phases can result in scattering phenomena and transparency degradation. To diminish such a problem the active scintillator phase has to be scaled down to few tens of nanometers size, because then the visible light scattering is considerably reduced. Scaling down the crystalline phase to nano-metric size can change physical properties of the material itself and can offer a unique combination of optical, luminescence and scintillation characteristics which cannot be obtained in a bulk single phase material. While semiconductor nanocrystals have been a subject of study for more than thirty years, investigations of wide band-gap insulating nanocrystals begun only recently (Tissue, 1998; Meltzer et al., 1998). Nanocrystals of Y_2O_3 doped with europium or terbium were produced by condensation from gas phase (Bihari et al., 1997; Meltzer et al., 1999), sol-gel (Goldburt et al., 1997) or combustion (Muenchausen et al., 2007) methods. $Gd_2O_3:Eu$ was produced by sol-lyophilization (Louis et al., 2003; Mercier et al., 2004, 2006) and CBD (Cluster Beam Deposition) (Mercier et al, 2007) techniques. The band gap increase of a crystal due to exciton quantum confinement is a well known phenomenon in direct gap semiconductors like GaAs, GaN or CdSe. To a lesser extent, similar increase is observed also in insulating $Gd_2O_3:Eu$ nanocrystals (Mercier et al., 2007). In this material the reduced size can strongly influence the relative population of the dopant energy levels and the width of emission lines (Mercier et al., 2006); moreover, the presence of dopant ions on the nanocrystal surface can be evidenced by appearance of a specific emission band (Mercier et al., 2004). Luminescence efficiency can also be affected by quantum confinement; in fact, in $Y_2O_3:Tb$ an increase of Tb^{3+} luminescence efficiency is observed by reducing particle size probably because of the decrease of non-radiative recombination phenomena (Goldburt et al., 1997). Moreover, the fluorescence time decay is strongly affected by refractive index of the inert host material (Meltzer et al., 1999) and quenching phenomena are shifted towards higher concentrations with respect to the single crystal (Muenchausen et al., 2007).

Among reported attempts on preparation of such nanocomposite systems the fluoro-chloro-zirconate glass-ceramic can be mentioned: luminescence arises at Eu^{2+} -containing $BaCl_2$ nanocrystals with average size of 14 nm, thus, the material possesses good transparency (Johnson et al., 2006). CdTe nanoparticles show an efficient luminescence when embedded in $BaFBr:Eu$ (Chen et al., 2006). Nanoporous silica matrix impregnated by CdSe/ZnS luminescent nanoparticles or rhodamine dye shows also intense emission (Létant et al., 2006a, 2006b). Multiple quantum wells hybrid structures, where semiconducting PbI_4 layers are alternated with organic insulating ones, have shown superfast efficient luminescence (390 ps) due to excitonic superradiance and quantum confinement effect which might allow them to be used as ultra-fast scintillators (Shibuya et al., 2004).

Scintillation properties of the Ce-doped rare-earth orthosilicates were mentioned for the first time in early 1980s in the study dealing with the $Gd_2SiO_5:Ce$ (GSO) (Takagi et al., 1983). Following studies concerned mainly $Lu_2SiO_5:Ce$ (LSO) (Suzuki et al., 1992) and mixed Lu_2

$x\text{Y}_x\text{SiO}_5\text{:Ce}$ (LYSO) (Cooke et al., 2000) which became materials of choice for PET imaging in medicine. Single crystals of these orthosilicate materials were prepared by the Czochralski method using radio-frequency (RF) heating due to very high melting point of these compounds (between $\sim 1950\text{--}2150$ °C) (Melcher et al., 1993). The growth of single crystals of another stoichiometry in the $\text{SiO}_2\text{-RE}_2\text{O}_3$ system, namely $\text{RE}_2\text{Si}_2\text{O}_7$, was reported also in early 1980's and basic optical and luminescence characteristics were explored (Bretheau-Raynal et al., 1980; Vakhidov et al., 1981). However, scintillation characteristics of Ce-doped single crystals of $\text{Lu}_2\text{Si}_2\text{O}_7$ (LPS) started to be studied only in last decade (Pauwels et al., 2000). LPS:Ce has shown similar light yield and other scintillation characteristics as LSO:Ce, but no afterglow at RT was found due to the absence of TSL peaks close to RT which is a substantial advantage of this material (Pidol et al., 2007). Very recently also single crystal of YPS:Ce was grown and its scintillation properties were characterized (Feng et al., 2010). Several different methods were reported for the preparation of powder silicate phosphors which were considered for another applications like FED or cathodoluminescence screens (Holloway et al., 1999). Meijerink et al. (Meijerink et al., 1991) used the classic solid-state sintering to synthesize YSO:Ce. Kang et al. employed method of spray pyrolysis (Kang et al., 1999) which provides samples with better homogeneity. Combustion synthesis (Gonzalez-Ortega et al., 2005), hydrothermal (Cooke et al., 2006) and sol-gel (Marsh et al., 2002; Jiao et al., 2007) methods were also employed in order to reduce too high temperatures necessary for the preparation. Using pulsed laser deposition, YSO:Ce thin films were prepared and studied (Coetsee et al., 2007). Ce-doped lutetium pyrosilicate synthesis and photoluminescence characteristics were published recently (Sokolnicki et al., 2009). The sol-gel methods are well applicable to silicate-based synthesis due to stability of TEOS (tetraethoxysilane) which is used as an Si precursor. However, final results depend on many parameters like the temperature of gelation, type of solvent, use of the additives etc. The additives like formamide influence the surface tension in the pores (Brinker & Scherer, 1990) and help to prepare crack-free monolite samples. They participate in chemical reactions during the stages of hydrolysis and gelation (Niznansky & Rehspringer, 1995) and they also influence the phase evolution during heat treatment (Niznansky et al., 2001).

1.1 Phase diagram $\text{Y}_2\text{O}_3\text{-SiO}_2$

Yttrium and lutetium silicates have similar phase diagram which is shown in Fig. 1. It follows from Fig. 1 that two stoichiometric compounds, RE_2SiO_5 and $\text{RE}_2\text{Si}_2\text{O}_7$ (RE = Y, Lu), are stable at RT. Second important conclusion is the presence of the region with limited miscibility of SiO_2 and $\text{RE}_2\text{Si}_2\text{O}_7$ which is a condition favourable to preparation of $\text{RE}_2\text{Si}_2\text{O}_7$ nanocomposite in the silica matrix.

1.2 Structure of pyrosilicate

YPS crystallizes in several crystallographic forms. $\alpha\text{-Y}_2\text{Si}_2\text{O}_7$ crystallizes in the triclinic P-1 space group ($a=6.59$ Å, $b=6.64$ Å, $c=12.25$ Å, $\alpha=94^\circ$, $\beta=89^\circ$, $\gamma=93^\circ$) (Liddell & Thompson, 1986) at the temperature of 1100 °C. $\beta\text{-Y}_2\text{Si}_2\text{O}_7$ is isotypic with thortveitite, $\text{Sc}_2\text{Si}_2\text{O}_7$, and crystallizes in the $C2/m$ space group ($a=6.83$ Å, $b=8.97$ Å, $c=4.72$ Å, $\beta=101^\circ$) (Redhammer & Roth, 2003). Y^{3+} cation occupies a distorted octahedral site with Y-O bond lengths in the range 2.239 (2)–2.309 (2) Å. The SiO_4 tetrahedron is regular with Si-O bond lengths in the range 1.619 - 1.630 Å. Monoclinic $C2/m$ phase was obtained after heat treatment at 1300°C. $\gamma\text{-Y}_2\text{Si}_2\text{O}_7$ was found to crystallize in the monoclinic $P2_1/c$ space group (Leonyuk et al., 1999)

and its lattice parameters are $a=4.694 \text{ \AA}$, $b=10.856 \text{ \AA}$, $c=5.588 \text{ \AA}$, $\beta=96.01^\circ$. According to Dias et al. (Dias et al., 1990) the structure of high temperature phase $\delta\text{-Y}_2\text{Si}_2\text{O}_7$ has the orthorhombic space group $Pnam$ ($a=13.81 \text{ \AA}$, $b=5.02 \text{ \AA}$, $c=8.30 \text{ \AA}$).

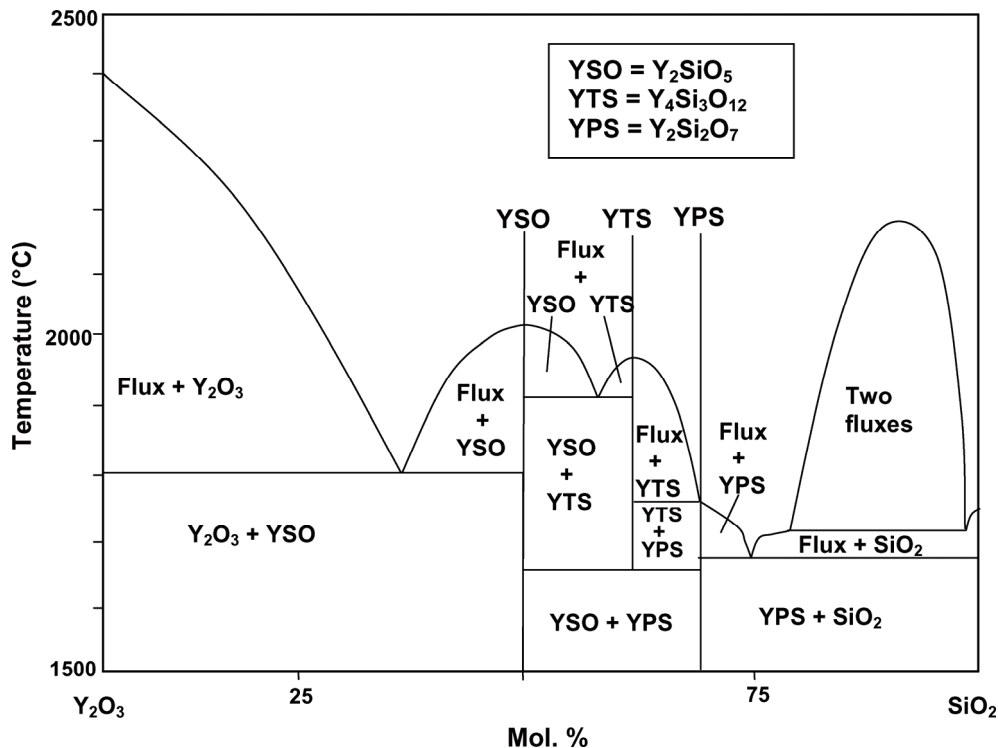


Fig. 1. Phase diagram of $\text{Y}_2\text{O}_3\text{-SiO}_2$ system

$\text{Lu}_2\text{Si}_2\text{O}_7$ has one stable crystallographic phase at RT representing the thorveitite structure with monoclinic symmetry, space group $C2/m$. It has a single crystallographic site for lutetium ions with six oxygen neighbours. It is a distorted octahedral site with $C2$ symmetry (Bretheau-Raynal et al., 1980; Soetebier et al., 2002).

This monoclinic structure can be briefly described as a stacking of alternating parallel layers of $[\text{LuO}_6]$ octahedral sharing edges and isolated $[\text{Si}_2\text{O}_7]$ groups. $[\text{Si}_2\text{O}_7]$ groups are formed by two $[\text{SiO}_4]$ tetrahedra sharing oxygen, Si-O-Si bond angle between tetrahedra is equal to 180° , see Fig. 2. The layers of $[\text{Si}_2\text{O}_7]$ groups are organized this way: Si atom of the $[\text{Si}_2\text{O}_7]$ group shares one oxygen atom from the $[\text{LuO}_6]$ layer above and two from the one below in the c -direction, the Si atom from the opposite side is in a reverse situation (Yan et al., 2006).

In this chapter, we describe the preparation of $\text{RE}_2\text{Si}_2\text{O}_7$ ($\text{RE} = \text{Y}$ (YPS), Lu (LPS)) compounds doped by Ce ions in powder form using the sol-gel method. XRD and SEM are employed to check the crystal structure, luminescence spectra and decays are measured to characterize Ce^{3+} ion emission in an LPS host. Furthermore, we prepare nanocomposites of Ce-doped $\text{RE}_2\text{Si}_2\text{O}_7$ in the silica matrix and use XRD, SEM, HRTEM and luminescence techniques for their characterization.

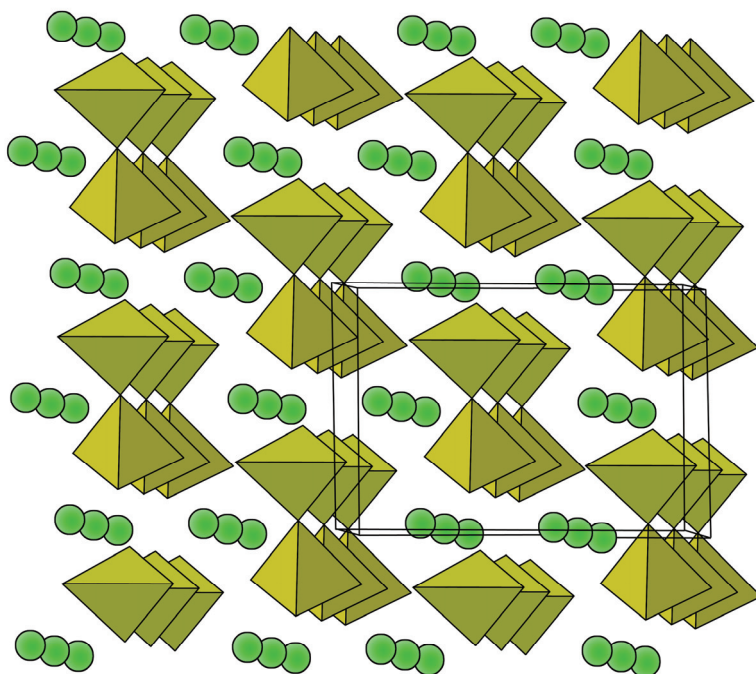


Fig. 2. Schematic diagram for the monoclinic structure of $\text{Lu}_2\text{Si}_2\text{O}_7$ crystal. Lu ions are green and $[\text{Si}_2\text{O}_7]$ groups are yellow. Reprinted from (Yan et al., 2006).

2. Experimental

2.1 Preparation of pyrosilicate powder phosphor

$\text{Y}(\text{NO}_3)_3 \cdot 6\text{H}_2\text{O}$ (in the case of YPS) or $\text{Lu}(\text{NO}_3)_3 \cdot 5\text{H}_2\text{O}$ (99.9%, Sigma-Aldrich), TEOS (98%, Sigma-Aldrich), 96% methanol and HNO_3 (0.03 M) were used as starting materials. First, $\text{RE}(\text{NO}_3)_3 \cdot n\text{H}_2\text{O}$ ($\text{RE} = \text{Y}, \text{Lu}$) was dissolved in methanol (CH_3OH) at RT and HNO_3 was added as catalyser for TEOS acid hydrolysis and condensation. Ce as doping element in the form of nitrate was then dissolved in methanol solution and the molar ratio Ce:RE was fixed onto the value of 1:199 (0,5 molar % of Ce). After dissolving had been completed, TEOS was added at the molar ratio TEOS : (RE+Ce) fixed at the values 1:1. The gelation time at 55°C was approximately 24 hours. The samples were left 2 days for ageing. Then, they were progressively dried at 50°C for 3 days in flowing N_2 -atmosphere. After drying they were successively annealed at 900°C , at 1100°C and 1300°C with heating rate of $1^\circ\text{C}/\text{min}$ under atmospheric pressure.

2.2 Preparation of YPS:Ce/SiO₂ a LPS:Ce/SiO₂ nanocomposites

The same starting materials were used for YPS(LPS):Ce/SiO₂ preparation like for pyrosilicate powder. The molar ratio of RE/Si was fixed onto 1/10. The final heating temperatures were chosen in the range of $1100 - 1300^\circ\text{C}$. The resulting samples were

transparent with yellowish colour due to presence of Ce doping cations. When the silica matrix had crystallized, samples became milky and non-transparent.

2.3 Characterization methods

Powder XRD spectra were measured at ambient temperature using Phillips X-pert diffractometer with Cu K α -radiation.

Thermal analysis (TG and DTA) measurements were carried out using SETARAM device and NETZSCH STA (QMS) 409/429-403 coupled to Mass Spectroscopy unit.

SEM was accomplished by Scanning Electron Microscope PHILIPS XL 30 CP and by Tescan Proxima SEM system equipped with SE, BSE and CL detectors.

Radio- and photoluminescence characterization was performed using model 5000M Spectrofluorometer, Horiba Jobin, Yvon equipped with single-grating monochromators and photon counting detectors. In case of radioluminescence and photoluminescence spectra the X-ray tube (40 kV, 15 mA) Seifert GmbH., and a D₂ continuous lamp were used as the excitation sources, respectively. In case of photoluminescence decays the hydrogen-filled nanosecond and microsecond pulse xenon flashlamps were used for the fast and slow decay kinetics measurements, respectively. Scintillation decay was measured using the ps X-ray pulse source excitation and streak camera detection, see the details in (Yanagida et al., 2010). SpectraSolve software package (Ames Photonics) was used to apply deconvolution procedures to extract true decay times. All measurements were performed at RT.

3. Results and discussion

3.1 Powder pyrosilicate materials

3.1.1 XRD measurements

Powder YPS prepared by sol-gel methods was heat-treated at three different temperatures (900, 1100 and 1300 °C) and characterized using XRD.

The samples heated at 900°C were amorphous. Triclinic P-1 phase was formed at 1100°C, while monoclinic C2/m phase was obtained after heat-treatment at 1300°C (Fig. 3)

We observe simpler situation in case of lutetium silicates (Lu₂Si₂O₇) because LPS have only one stable phase at RT. The samples annealed at 1100 °C show Lu₂Si₂O₇ pure phase pattern in agreement with PDF No. 35-0326, Fig. 4.

3.1.2 Electron microscopy

The TEM observations are consistent with the XRD results. Fig. 5 shows that the sample annealed at 900 °C has amorphous character, no regular crystalline shapes are observed.

The morphology of 1100 °C heat-treated samples (Fig. 6) is similar to the 900 °C heat-treated one. SEM image(left) show the particles of the size of few to several microns. Nevertheless, well developed crystals of the size of tens of nanometers are also observed (right part of the figure).

SEM and HR TEM of 1300 °C heat-treated YPS:Ce is shown at Fig. 7. The figure shows large crystallized particles of the size of microns. These particles no longer consist of submicron crystals (like in case of the 1100 °C heat-treated sample) but monolithic shape can be observed in TEM image (right side of Fig. 7).

The HRTEM observation of Lu₂Si₂O₇ (Fig. 8a) heat-treated powder shows characteristic non-agglomerate particles of the size of about 20 nm. At higher resolution (Fig. 8b), well ordered

structure of LPS crystal can be seen. In Fig. 8c, the selected area electron diffraction (SAED) pattern is shown.

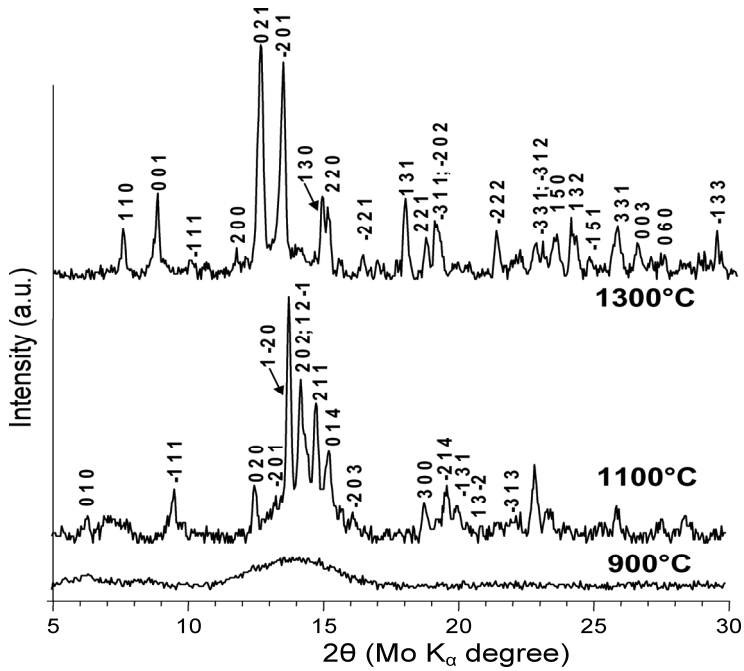


Fig. 3. X-ray diffraction pattern of the sample $Y_2Si_2O_7$, annealed at 900, 1100 and 1300 °C.

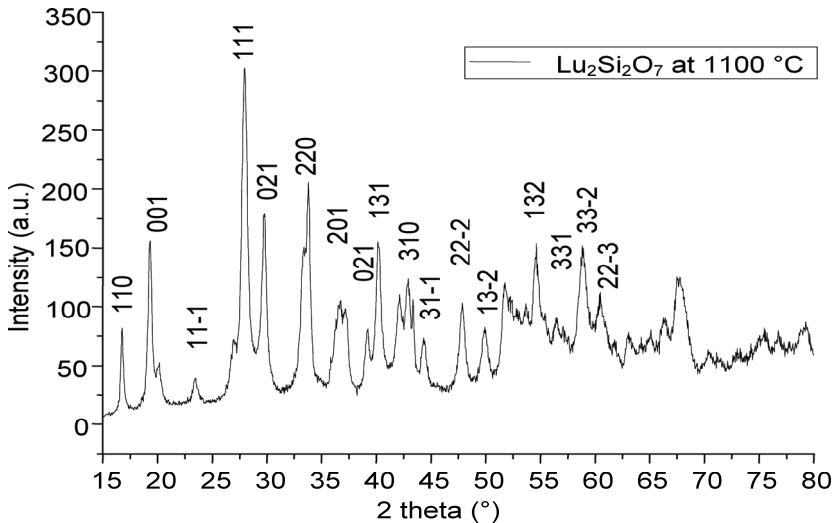


Fig. 4. X-ray diffraction pattern of the sample $Lu_2Si_2O_7$, annealed at 1100 °C

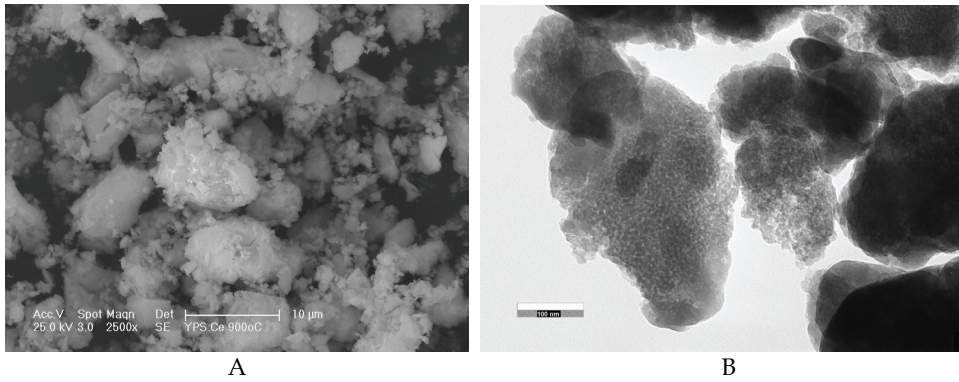


Fig. 5. SEM (A) and TEM (B) of YPS:Ce annealed at 900 °C.

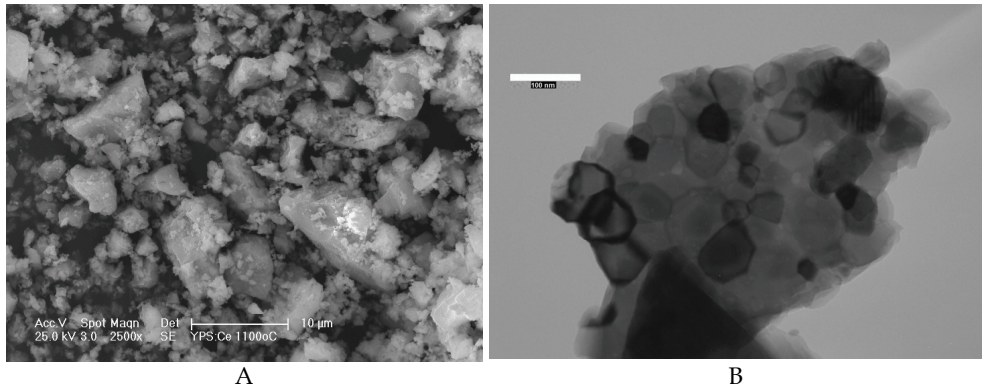


Fig. 6. SEM (A) and TEM (B) of YPS annealed at 1100 °C heat treated sample. Left image (SEM) shows the glassy aspect of sample while right image (TEM) shows the formation of nanometres-sized crystals.

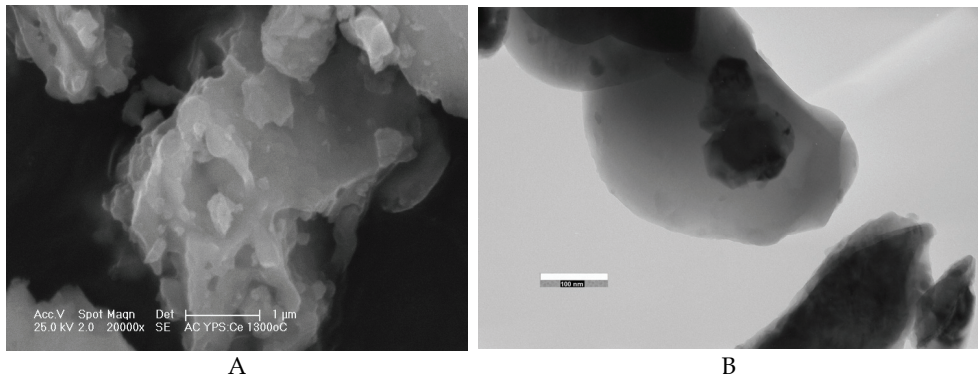


Fig. 7. SEM (A) and TEM (B) of 1300 °C heat treated YPS:Ce

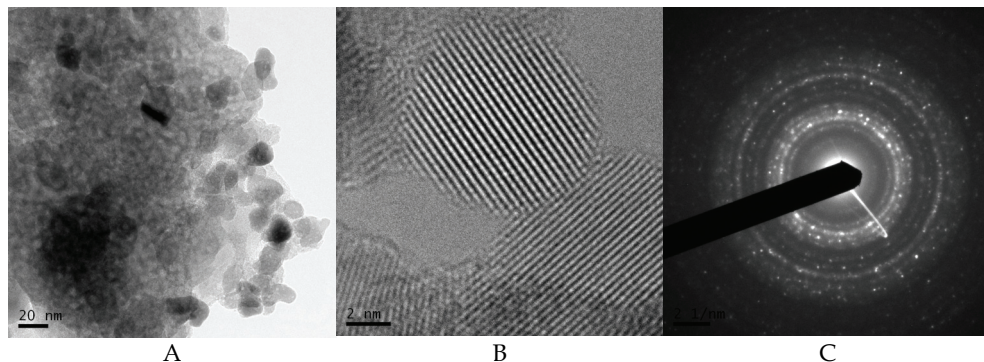


Fig. 8. (a, b, c) HRTEM measurement of $\text{Lu}_2\text{Si}_2\text{O}_7$

3.1.3 Luminescent properties

Radioluminescence spectra of the YPS:Ce samples were measured under X-ray excitation. The spectra are dominated by the $\text{Ce}^{3+} 5d_1-4f$ emission peaks at about 440 nm, Fig. 9. The intensity increased strongly with increasing temperature of the heat treatment. The maximum of the spectrum is noticeably long-wavelength shifted with respect to that of YPS:Ce single crystals (361+381 nm) (Feng et al., 2010). It points to a number of perturbation/defect-associated Ce sites in the YPS:Ce powder because such perturbations are known to shift Ce^{3+} emission to lower energy (Pedrini et al., 1992). In YPS:Ce with increasing annealing temperature the maximum of the spectrum shifts to shorter wavelength with approximately constant width (Fig. 10). Such intensity and shape evolution of the spectra can be caused by structural evolution with heat treatment temperature described before.

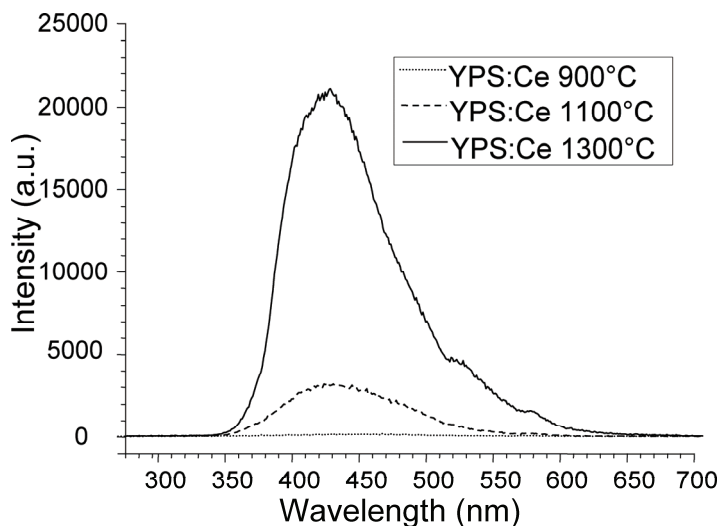


Fig. 9. Radioluminescence spectra dependence on the heat treatment temperature of the Ce-doped YPS (excitation by an X-ray tube, 40 kV) Spectra can be mutually compared in an absolute scale. Small dips around 510 nm and 565 nm are experimental artifacts

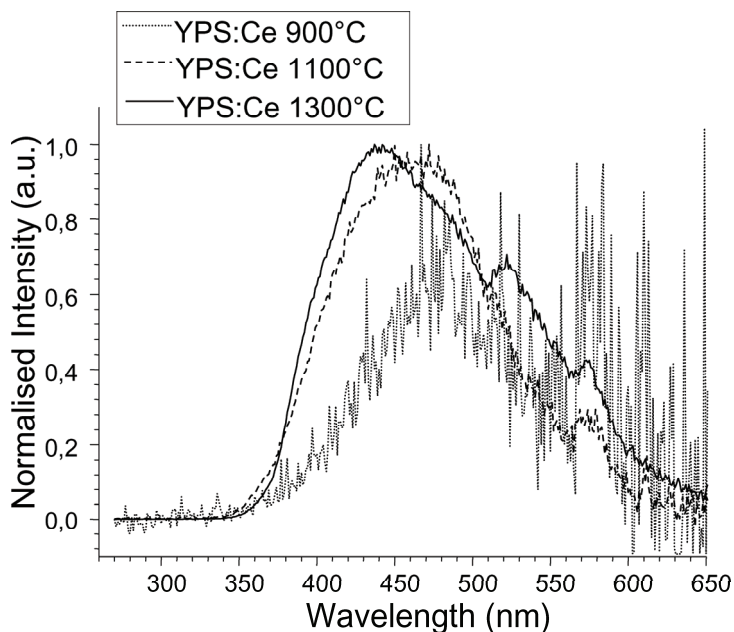


Fig. 10. Normalized radioluminescence spectra of YPS:Ce and their dependence on annealing temperature. Small dips around 510 nm and 565 nm are experimental artifacts.

Photoluminescence decays in Fig. 11 were measured for all the YPS:Ce samples. The decays are normalized for better comparison of the differences.

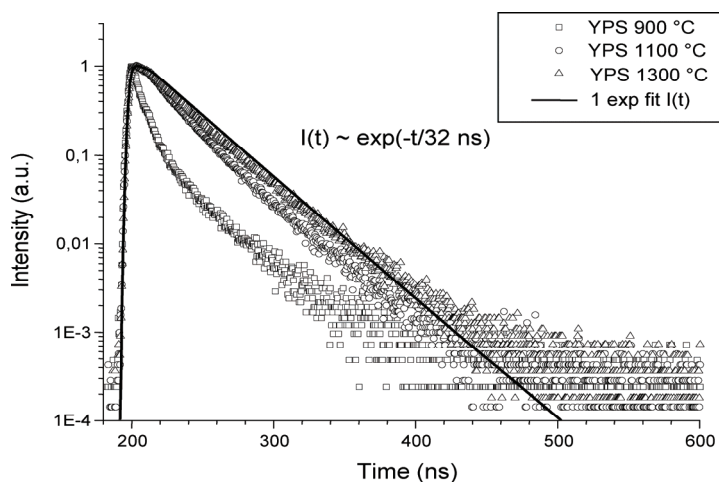


Fig. 11. Normalized photoluminescence decays of YPS:Ce heat-treated at different temperatures marked in the legend. Single exponential fit with decay time of 32 ns by a solid line is shown for 1300 °C treated samples to evaluate the decay time. exc = 345 nm, em = 440 nm.

There is a clear correlation between the decay shape and heat treatment temperature: in the sample treated at 1300 °C, the decay is close to a single exponential with the decay time of about 32 ns. The decay becomes faster and strongly deviated from a single exponential at lower heat treatment temperatures. The distortion of single exponential decay points to a nonradiative energy transfer (quenching) process which occurs from the Ce^{3+} relaxed $5d_1$ excited state towards a nearby lying defect level. The relative photoluminescence efficiency losses caused by this process were estimated from the integral of normalized decay curves. In the YPS host the Ce^{3+} photoluminescence quantum efficiency is diminished to 0.87 and 0.35 for 1100 °C and 900 °C heat-treated samples, respectively, relative to the 1300 °C heat-treated sample. In the 1300 °C heat-treated sample the non-decreasing temperature dependence of the Ce^{3+} decay time from 80 K up to the temperature well above RT (not shown here) evidences that the quantum efficiency of Ce^{3+} at RT is close to unity. The calculated photoluminescence efficiency losses related to the Ce^{3+} centre itself are much less significant with respect to the decrease of scintillation efficiency reflected in the radioluminescence intensity dependence on annealing temperature in Fig. 9. This means that the loss of scintillation efficiency in the samples heat-treated at lower temperatures occurs mainly in the transport stage, i.e. in the host material itself before reaching the Ce^{3+} luminescence centres.

In Fig. 12 the spectra are provided for the Ce-doped LPS. They correspond well with the earlier published data on LPS:Ce single crystals (Pidol et al., 2007; Feng et al., 2010), including Stokes shift value of 0.27 eV.

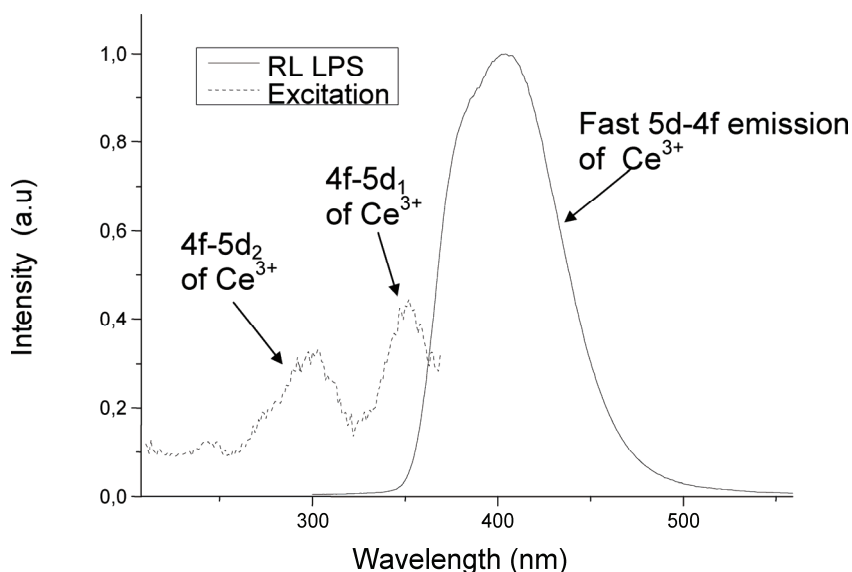


Fig. 12. Normalized PL excitation ($\text{em}=420$ nm) and RL (X-ray, 40 kV) spectra of Ce-doped LPS annealed at 1100 °C.

PL decay shows nanosecond decay time of 34 ns (Fig. 13), which is due to the allowed $5d-4f$ transition of Ce^{3+} and that is in very good agreement with that measured in LPS:Ce single crystals (Pidol et al., 2007; Feng et al., 2010). Decay acceleration in the initial part of the

decay curve might be due to an energy transfer from Ce^{3+} centres to some defects e.g. at grain surface layer.

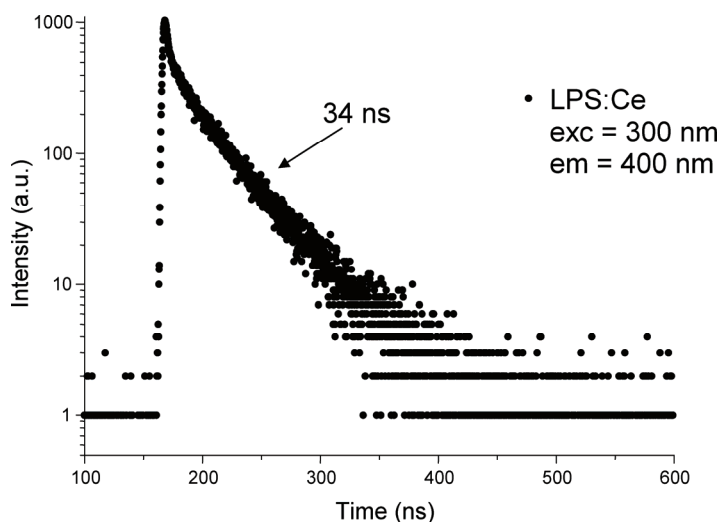


Fig. 13. Photoluminescence decays of the Ce-doped LPS (exc= 300nm, em=400 nm) annealed at 1100 °C. Decay time of 34 ns was evaluated in the tail of the decay.

3.2 Nanocomposite materials

The $\text{SiO}_2/\text{RE}_2\text{Si}_2\text{O}_7:\text{Ce}$ (RE = Y, Lu) nanocomposite samples were prepared using the same sol-gel method. The overstoichiometric ratio of RE/Si (1/10) was used for the material preparation.

The nanocomposites are transparent when silica matrix is amorphous, see Fig. 14, but during the heat treatment at the temperature of more than 1250 °C the crystallisation of amorphous silica matrix takes place and cristobalite structure is formed. Consequently, the sample breaks into small pieces of sub-millimetre size.

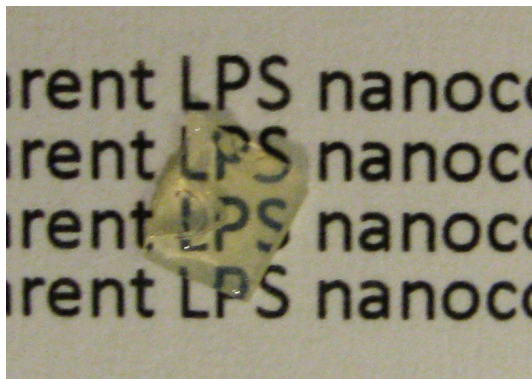


Fig. 14. Photo of the transparent $\text{SiO}_2/\text{Lu}_2\text{Si}_2\text{O}_7:\text{Ce}$ nanocomposite heat-treated at 1000 °C.

3.2.1 XRD measurements

$\text{SiO}_2/\text{Y}_2\text{Si}_2\text{O}_7$ system was prepared and heat-treated at different temperatures. The samples annealed at 1000°C are amorphous and transparent. Further increase of annealing temperature to 1100 - 1200°C leads to crystallisation of both silica matrix (into cristobalite) and of $\text{Y}_2\text{Si}_2\text{O}_7$ as shown in Fig. 15. Fig. 16 shows XRD spectra of the samples denoted as TK10 which are transparent. Annealing for 2h at 1000°C and 1100°C was carried out on the TK10 samples first and then a rapid thermal treatment (RTT) procedure was applied at 1250°C and 1300°C , consisting of increase of temperature from 1000°C or 1100°C to 1250°C - 1300°C in 2 minutes, 5 minutes at this temperature, cooling down in 5 minutes. The RTT temperature of 1300°C keeps sample transparent and amorphous but luminescent intensity improves. It is interesting to note that in case of non-transparent crystallized sample α -YPS phase is observed in XRD spectra, while in transparent ones rather β -YPS phase is found or sample remains purely amorphous.

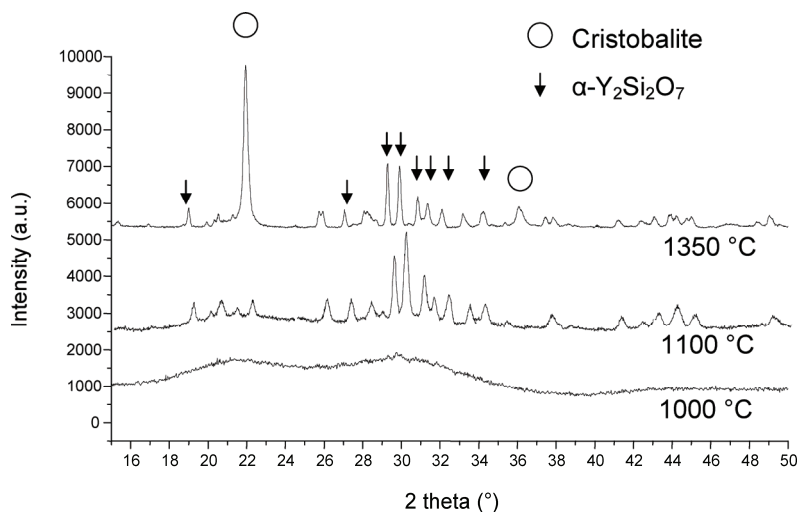


Fig. 15. XRD patterns of $\text{SiO}_2/\text{Y}_2\text{Si}_2\text{O}_7:\text{Ce}$ nanocomposites (denoted as A10) heat-treated at different temperatures.

The same XRD study was carried out for the lutetium analogs, see Fig. 17. The samples were progressively heat-treated at the temperatures from 1100°C to 1300°C (by 50°C , for 2 hours at a given temperature) and their XRD spectra were measured. The samples heat-treated up to 1200°C are mainly amorphous. Complete crystallization occurs at 1300°C , the XRD pattern of this sample consist of $\text{Lu}_2\text{Si}_2\text{O}_7$ and SiO_2 (cristobalite).

3.2.2 Electron microscopy

In Fig. 18 the SEM and HR TEM images of $\text{SiO}_2/\text{Y}_2\text{Si}_2\text{O}_7$ nanocomposites (Sample TK10 heat-treated at 1000°C and 1100°C) are shown.

SEM image with the lower resolution (Fig. 18a) shows the homogeneous glassy aspect of the sample. HRTEM images reveal the internal structure of this sample (Fig. 18b,c). Regular round $\text{Y}_2\text{Si}_2\text{O}_7$ particles of tens of nanometers size embedded in the silica matrix are clearly observed. The ideal round shape can be surprising because the crystals do not crystallize in

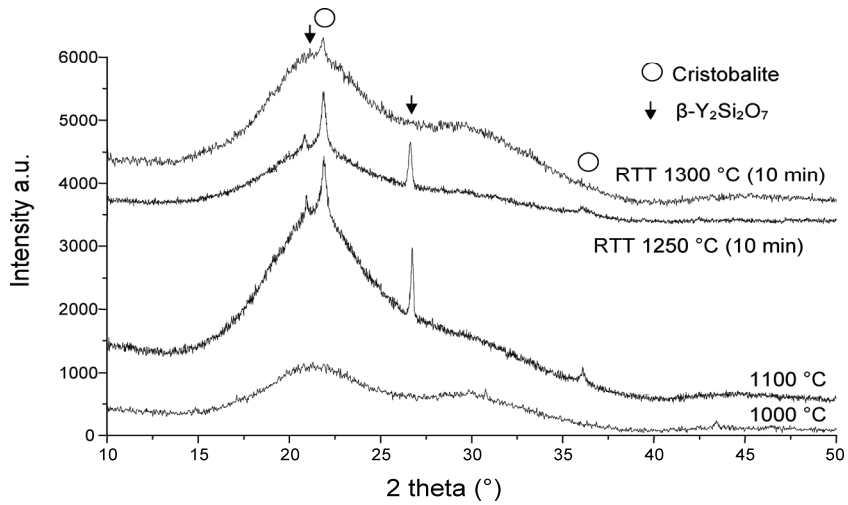


Fig. 16. TK samples annealed at 1000 °C, 1100 for 2 hours, RTT procedure then applied at 1250 °C and 1300 °C as described in the text before.

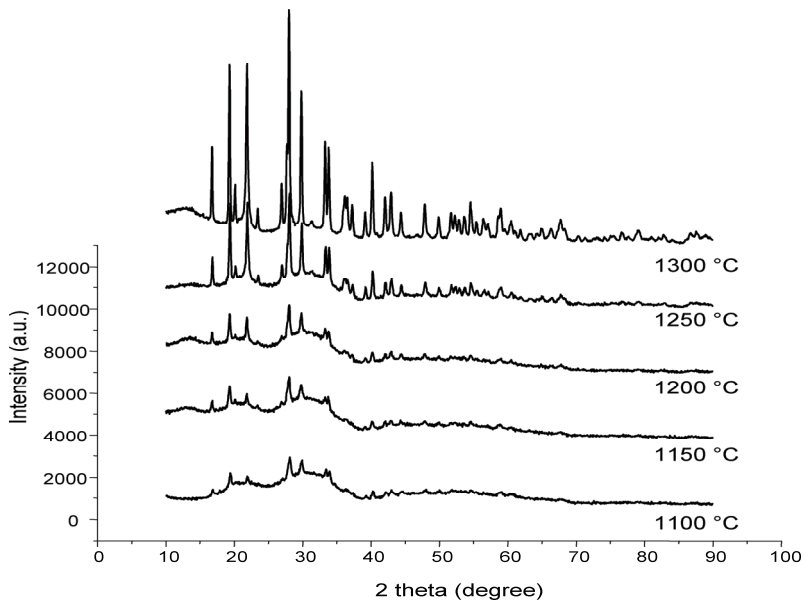


Fig. 17. XRD spectra of $SiO_2/Lu_2Si_2O_7$ composite after annealing at different, gradually increasing temperatures.

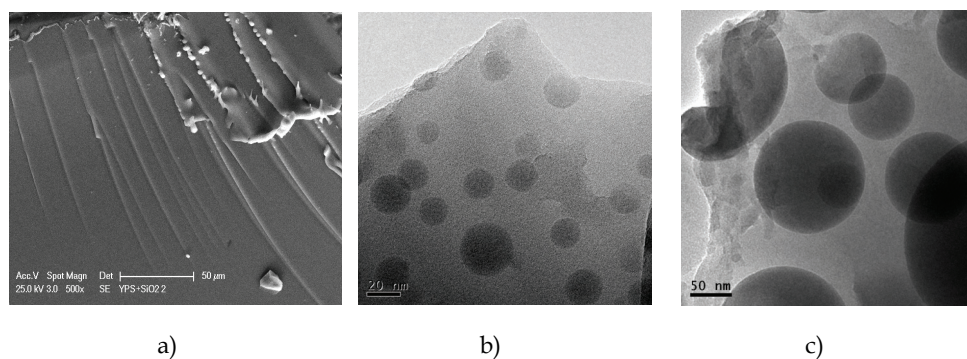


Fig. 18. SEM and HR TEM images of TK10 $\text{SiO}_2/\text{Y}_2\text{Si}_2\text{O}_7$ nanocomposite samples: a) corresponds to SEM of natural sample surface, annealed at 1000°C , b) HRTEM of sample annealed at 1000°C , c) HR TEM of sample annealed at 1100°C .

the shapes of spherical symmetry. The explanation is found in the Y_2O_3 phase diagram (Fig. 1). $\text{Y}_2\text{Si}_2\text{O}_7$ and SiO_2 are not miscible even in the liquid state. The surplus of SiO_2 leads to the phase separation of $\text{Y}_2\text{Si}_2\text{O}_7$ which forms spherical particles in order to minimize the surface energy (like the oil droplets in the water). The resulting nanocomposite is transparent if the particle size of these nanoparticles is smaller than $1/10$ of the wavelength of the used light, i.e. below 40-50 nm (Krell et al., 2009).

The nanocomposite $\text{Lu}_2\text{Si}_2\text{O}_7/\text{SiO}_2$ has the same tendency. The HRTEM images in Fig. 19 show the mean particle size increasing with the heat treatment temperature. Statistical evaluation of the particle size distribution from HRTEM image was performed and is shown in Fig. 20 for the sample heat-treated at 1100°C .

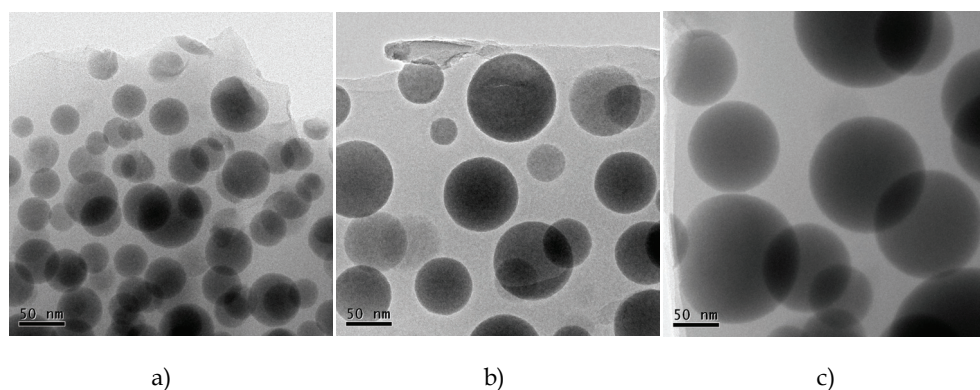


Fig. 19. HRTEM of $\text{SiO}_2/\text{Lu}_2\text{Si}_2\text{O}_7$ nanocomposite heat-treated at 1100°C (a), 1200°C (b) and 1300°C (c).

The average particle size of the 1100°C heat-treated sample is about 30 nm, the 1200°C heat-treated sample reaches the mean particle size of about 50 nm and the 1300°C heat-treated nanocomposite shows the particle size of about 100 nm.

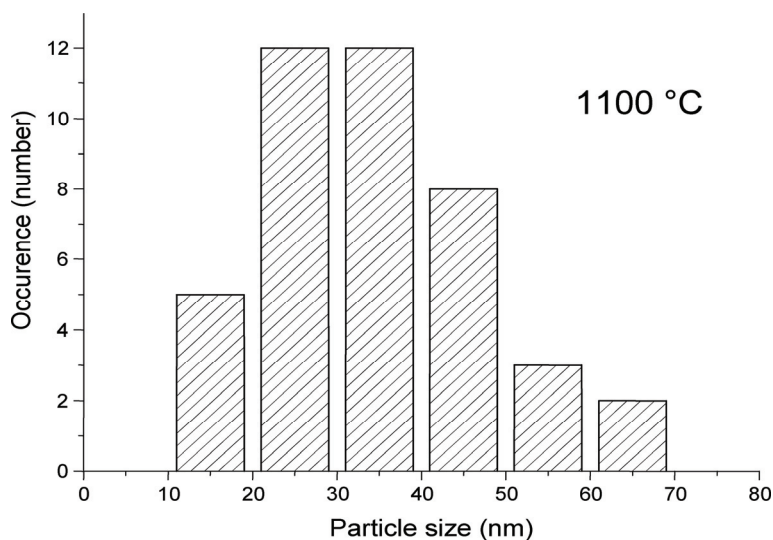


Fig. 20. Size distribution of LPS nanospheres for the sample heat-treated at 1100 °C evaluated from HRTEM images.

3.2.3 Thermal analysis

Thermal behaviour of the both Yttrium and lutetium nanocomposites was similar. Fig. 21 shows the TG and DTA analysis of $\text{SiO}_2/\text{Lu}_2\text{Si}_2\text{O}_7$ nanocomposite. First decrease of TG within the range of 200°C to 400°C corresponds to the elimination of organic species in the matrix and decomposition of the lutetium nitrate. The mass of $\text{SiO}_2/\text{Lu}_2\text{Si}_2\text{O}_7$ nanocomposite is constant above 800°C. DTA curve shows exo-effect at 300°C which corresponds to the oxidation of organic residue by nitrates. Second exo-effect situated near 1100°C probably corresponds to the crystallisation of both amorphous silica matrix and $\text{Lu}_2\text{Si}_2\text{O}_7$ as could be seen from XRD spectra. The crystallisation of both components took place simultaneously, therefore it was not possible to distinguish on process from the other. Moreover, the temperature of this transition varied significantly within the range of 1100 to 1250°C when some of the parameters (heating rate, air or inert atmosphere, different sample size) were changed in DTA measurement. It means that this crystallisation is kinetically very slow process, possibly hindered in big parts of the composite. This fact could be used for the RTT procedure when the crystallization of nanoparticles of $\text{Lu}_2\text{Si}_2\text{O}_7$ can be expected while silica matrix remains amorphous.

3.2.4 Luminescent properties

RL spectra of the bulk composite TK 10 YPS:Ce/ SiO_2 sample are shown in Fig. 22. Emission intensity of yet amorphous sample heat-treated at 1100 °C is smaller and its maximum is low energy shifted (455 nm) in comparison with the densely cracked one which was heat-treated at 1300 °C. The latter spectrum shows the subbands at about 360 nm and 382 nm which are very close to those in YPS:Ce single crystal (Feng et al., 2010). It can be interpreted that the Ce^{3+} centres are well embedded in regular YPS structure. Furthermore, comparison with standard BGO scintillator shows reasonable scintillation efficiency of the

nanocomposite YPS:Ce/SiO₂ system heat-treated at 1300 °C . In case of samples which were prepared in powder form from the very beginning the RL intensity shows even higher values compared to BGO, Fig. 23

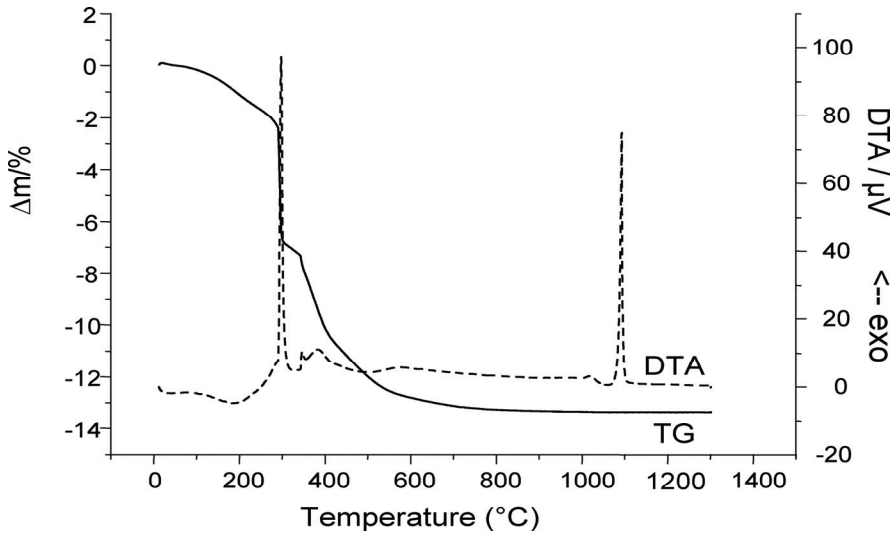


Fig. 21. TG and DTA analysis of SiO₂/LPS nanocomposite

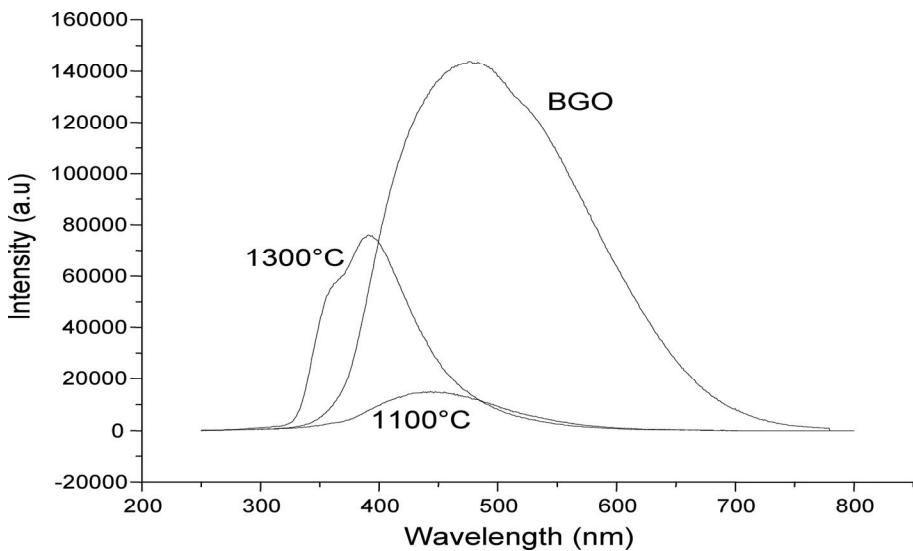


Fig. 22. RL spectra of the bulk TK 10 YPS:Ce/SiO₂ nanocomposite sample heat-treated at 1100 °C and 1300 °C and the spectrum of BGO standard scintillator sample.

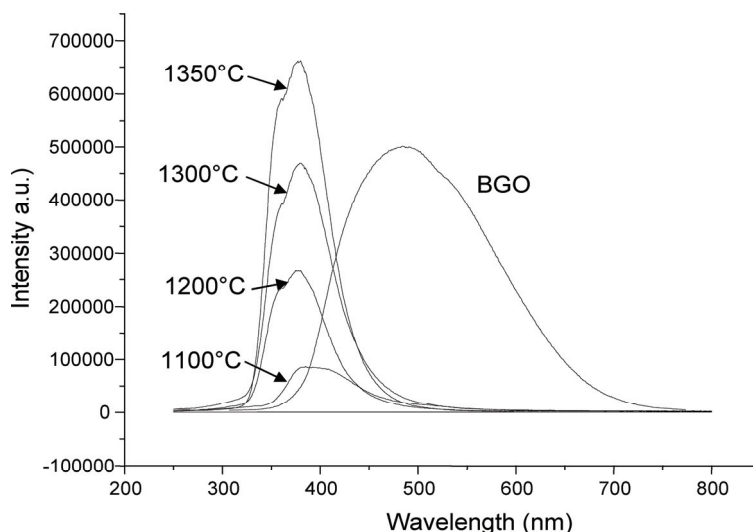


Fig. 23. RL spectra of A10 nanocomposite YPS:Ce/SiO₂ samples prepared in powder form. Annealing temperatures are shown in the figure, comparison with BGO standard scintillator sample is provided as well.

Fig. 24 shows the PL and PLE spectra of A10 powder nanocomposite sample. Very good correspondence of both emission and excitation subbands is found compared to the bands reported for YPS:Ce single crystal (Feng et al., 2010) which again points to embedding Ce³⁺ ions in well ordered YPS structure without excessive influence of any lattice flaws and perturbations.

Luminescence characteristics of LPS:Ce/SiO₂ nanocomposite samples were found to be quite analogous to those of yttrium-based system ones. RL intensity strongly increases with annealing temperature and comparatively higher intensities are obtained in comparison to the YPS:Ce/SiO₂ ones, see Fig. 25. Normalized spectra show high energy shift and smaller FWHM with increasing annealing temperature, see Fig. 26. Position of excitation and emission peaks for $T_{an}=1250-1300$ °C match reasonably well those of LPS:Ce single crystal (Pidol et al., 2007; Feng et al., 2010). RL spectrum for the highest annealing temperatures can be in fact perfectly decomposed in components belonging to undoped LPS, Ce³⁺ in SiO₂ and Ce³⁺ in LPS (Fig. 27)

PL decay of LPS:Ce/SiO₂ nanocomposite sample annealed at 1300 °C is given in Fig. 28. Leading decay time of 29 ns is slightly shorter compared to 32 ns found in LPS:Ce single crystal (Feng et al., 2010). It might be caused by the effect of small size of nanospheres of LPS:Ce and different refractive index of surrounding medium (Metzner et al., 1999). Slower decay tail of very low amplitude is of unclear origin. It could be related to Ce³⁺ ions close to LPS nanophase surface where e.g. tunneling from 5d₁ excited state of Ce³⁺ to a defect might exist. Scintillation decay of the same sample under the excitation by picosecond X-ray pulse is given in Fig. 29. The leading decay component of decay time 29.4 ns is perfectly consistent with that in PL decay in Fig. 28. In addition, there is slower decay process which overestimates the fit above 60-70 ns and must be due to the delayed recombination process arising in the transport stage of scintillator mechanism.

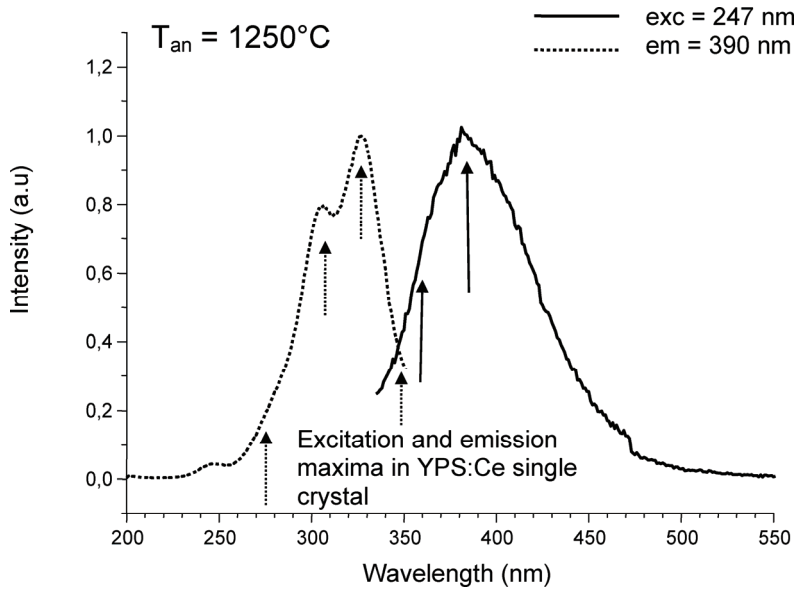


Fig. 24. PL (ex=247 nm) and PLE (em=390nm) spectra of YPS:Ce/SiO₂ A10 sample at RT.

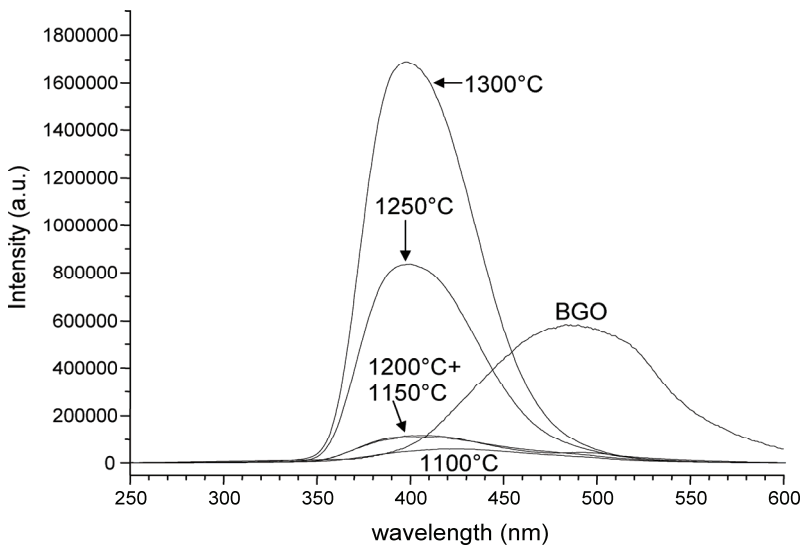


Fig. 25. RL spectra of LPS:Ce/SiO₂ nanocomposite sample annealed at different temperatures given in the figure. Excitation X-ray, 40 kV.

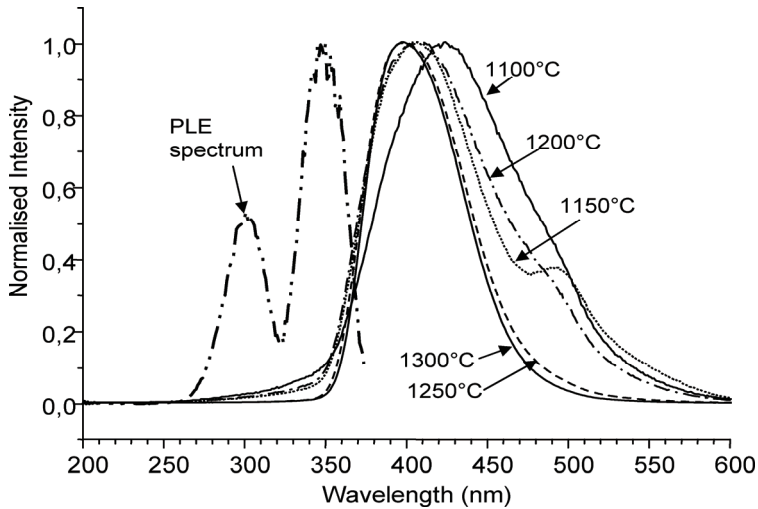


Fig. 26. Normalized RL spectra of LPS:Ce/SiO₂ nanocomposite samples from Fig. 25. Excitation X-ray, 40 kV. PLE spectrum for $T_{an}=1300^{\circ}\text{C}$ and $em=410\text{ nm}$ is shown as well

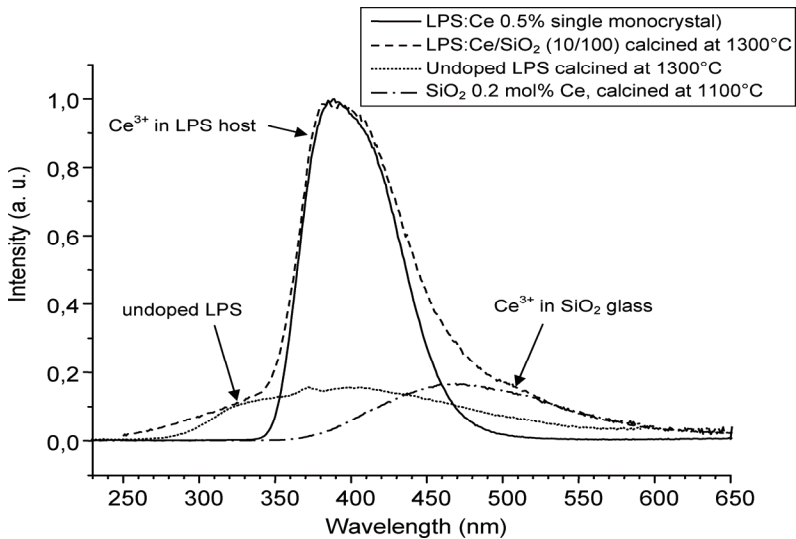


Fig. 27. Radioluminescence spectra (excitation X-ray, 40 kV) of LPS:Ce single crystal, LPS:Ce/SiO₂ nanocomposite, undoped LPS powder and SiO₂:Ce glass. The latter three samples were made by an analogous sol-gel route, single crystal was grown by Czochralski method (Feng et al., 2010)

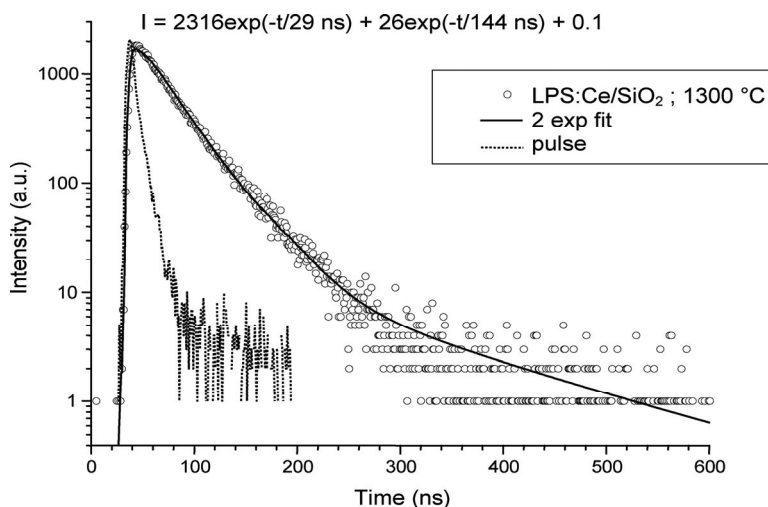


Fig. 28. PL decay of LPS:Ce/SiO₂ nanocomposite sample. Ex=300 nm, em=410 nm. Solid line is the fit $I(t)$ given in the figure.

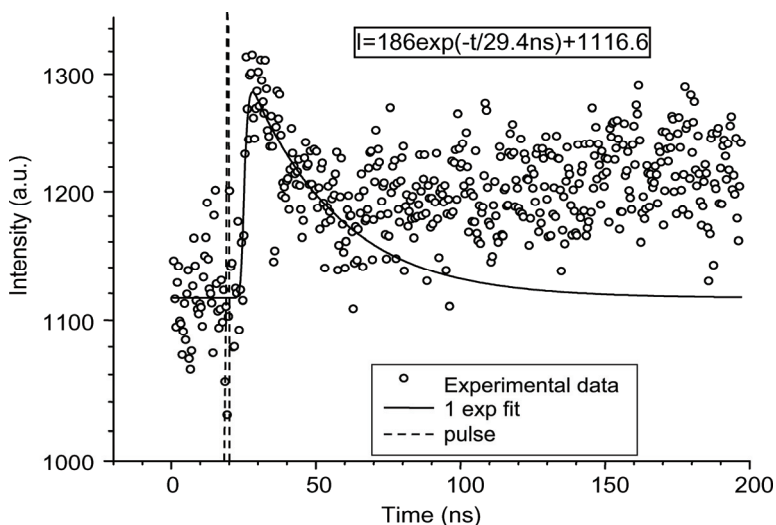


Fig. 29. Scintillation decay of LPS:Ce/SiO₂ nanocomposite sample. Excitation by picosecond X-ray pulse, for technical details see (Yanagida et al., 2010).

Following the procedure carried out at the Ce-doped silicate glasses (Chiodini et al., 2002) the samples of SiO₂/Lu₂Si₂O₇ nanocomposites annealed at 1000°C were rapidly heat-treated at temperature between 1600-2000 °C. This rapid thermal treatment (RTT) consisted of 30 seconds heating period in the hydrogen-oxygen flame. The characterization by XRD showed that they remain amorphous after such a treatment. RL spectra of the samples show that the

RTT strongly influences the shape, position and intensity of RL spectrum (Fig. 30). In (Chiodini et al., 2002) strong increase of scintillation efficiency was reported at Ce-doped silicate glass after RTT treatment. In our case, similar conclusion can be drawn for the highest RTT temperature of 2000 °C, when the spectrum remains low energy shifted compared to the situation in the powder nanocomposite annealed at 1250-1300 °C (Fig. 26). This is consistent with the fact that LPS nanophase crystallized in the latter case while remaining amorphous after RTT procedure. RTT probably helps to form better SiO₂ glass host which provides higher efficiency for charge carrier transport in the scintillation mechanism.

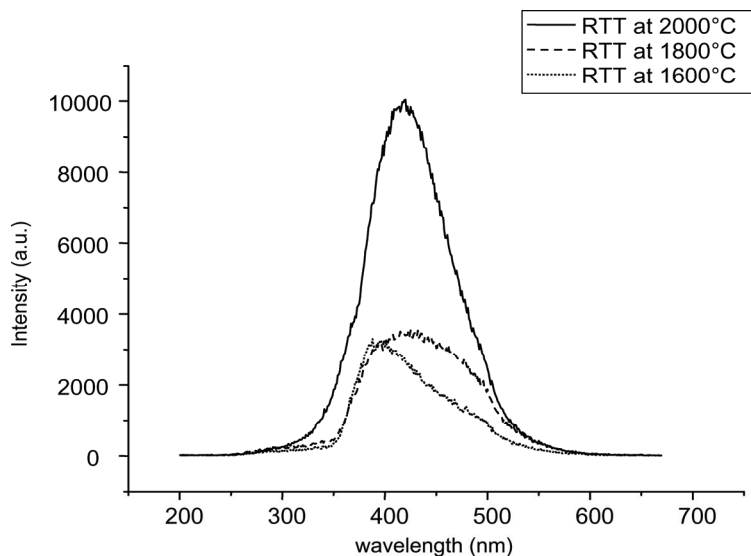


Fig. 30. RL spectra of LPS:Ce/SiO₂ nanocomposite sample after application of RTT procedure, the temperature of which is given in the legend

4. Conclusions

Sol-gel method has been successfully used for preparation of Ce-doped yttrium (YPS) and lutetium (LPS) pyrosilicates in powder form and of composite materials (REPS:Ce)_{0.1}-(SiO₂)_{0.9}, RE=Y,Lu. XRD measurements showed that the crystallization of YPS take the place at 1100°C in the case of pure powder sample while, in the case of nanocomposites, it is shifted to the range of 1200-1300°C. Moreover, in the latter case, it is accompanied by simultaneous crystallization of SiO₂ matrix leading to non-transparent samples. Nevertheless, this drawback (cristobalite formation, loss of transparency) could be partially overcome by RTT, because the kinetics of cristobalite formation is very slow. TEM images of (REPS:Ce)_{0.1}-(SiO₂)_{0.9}, RE=Y,Lu revealed the regular round shapes nanoparticles in the silica matrix. Its average size increases with the temperature of heat treatment from 30 nm (heat-treated at 1100°C) to 100 nm (heat-treated at 1300°C).

Luminescence spectra of powder YPS:Ce were found low energy shifted in comparison to the single crystal analogue which might be due to extensive perturbation of Ce³⁺ centers by

the grain surface and structural flaws. LPS:Ce emission characteristics showed to be closer to the bulk single crystal.

Photo- and radioluminescence spectra of YPS:Ce and LPS:Ce crystallized nanophase in SiO₂ host appeared very similar to their bulk single crystal analogs. Slightly shortened Ce³⁺ decay times in REPS:Ce/SiO₂ can indicate the effect of small size of REPS:Ce nanospheres and different refractive index of surrounding medium. RTT leaves the pyrosilicate phase amorphous although the luminescence efficiency increases noticeably, small low energy shift of Ce³⁺ spectrum is consistent with the amorphous character of REPS host. RTT procedure indicates the possibility to obtain transparent bulk optical elements with scintillating REPS:Ce nanophase, but more experimental work has to be done to achieve good transparency and crack-free samples.

5. Acknowledgement

The support of Grant Agency of AS CR, project KAN300100802 is gratefully acknowledged. Thanks are due to A. Beitlerova, R. Kucerkova and V. Jary for luminescence measurements. V.Tyrpekl and I.Jakubec are acknowledged for SEM, TEM and HRTEM photographs. CRYTUR Ltd. and P. Horodysky are acknowledged for technical help in the experiments.

6. References

- Becquerel, H. (1896). Sur les Radiations Invisibles Emises par les Corps Phosphorescents. *Comptes-Rendus Hebdomadaires des Séances de l'Académie des Sciences*, Vol. 122, pp. 501-503.
- Bihari, B.; Eilers, H. & Tissue, B. M. (1997). Spectra and Dynamics of Monoclinic Eu₂O₃ and Eu³⁺:Y₂O₃ Nanocrystals. *Journal of Luminescence*, Vol. 75, No. 1, (July 1997), pp. 1-10, ISSN 0022-2313
- Bretheau-Raynal, F.; Tercier, N. & Blanzat, B. (1980). Synthesis and Spectroscopic Study of Lutetium Pyrosilicate Single Crystals Doped with Trivalent Europium. *Materials Research Bulletin*, Vol. 15, No. 5, (May 1980), pp. 639-646, ISSN 0025-5408
- Brinker, C. J. & Scherer, G. W. (1990). *Sol-Gel Science: The Physics and Chemistry of Sol-Gel Processing*, Academic Press, ISBN 978-0121349707, San Diego
- Chen, W.; Zhang, J., Wescott, S. L., Joly, A. G., Malm, J.-O. & Bovin, J.-O. (2006). The Origin of X-Ray Luminescence from CdTe Nanoparticles in CdTe/BaFBr:Eu²⁺ Nanocomposite Phosphors. *Journal of Applied Physics*, Vol. 99, No. 3, (1 Feb 2006), p. 034302 (5 pages), ISSN 0021-8979
- Chiodini, N.; Fasoli, M., Martini, M., Rosetta, E., Spinolo, G., Vedda, A., Nikl, M., Solovieva, N., Baraldi, A. & Capelletti, R. (2002). High-Efficiency SiO₂:Ce³⁺ Glass Scintillators. *Applied Physics Letters*, Vol. 81, No. 23 (2 Dec 2002), pp. 4374-4376, ISSN 0003-6951
- Coetsee, E.; Swart, H. C. & Terblans, J. J. (2007). Cathodoluminescence Degradation of Y₂SiO₅:Ce Thin Films. *Journal of Vacuum Science and Technology A*, Vol. 25, No. 4, (July 2007), pp. 1226-1230, ISSN 0734-2101
- Cooke, D. W.; McClellan, K. J., Bennett, B. L., Roper, J. M., Whittaker, M. T., Muenchausen, R. E. & Sze, R. C. (2000). Crystal Growth and Optical Characterization of Cerium-Doped Lu_{1.8}Y_{0.2}SiO₅, *Journal of Applied Physics*, Vol. 88, No. 12, (15 Dec 2000), pp. 7360-7362, ISSN 0021-8979
- Cooke, D. W.; Lee, J.-K., Bennett, B. L., Groves, J. R., Jacobsohn, L. G., McKigney, E. A., Muenchausen, R. E., Nastasi, M., Sickafus, K. E., Tang, M. J. & Valdez, A. (2006).

- Luminescent Properties and Reduced Dimensional Behavior of Hydrothermally Prepared $Y_2SiO_5:Ce$ Nanophosphors. *Applied Physics Letters*, Vol. 88, No. 10, (6 Mar), p. 103108 (3 pages), ISSN 0003-6951
- Curie, M. (1898). Rayons Emises par les Composés de l'Uranium et du Thorium, *Comptes-Rendus Hebdomadaires des Séances de l'Académie des Sciences*, Vol. 126, pp. 1101-1103
- Dias, W.; Glasser, F. P., Gunwardane, R. P. & Howie, R. A. (1990). The Crystal Structure of δ -Yttrium Pyrosilicate, δ - $Y_2Si_2O_7$. *Zeitschrift für Kristallographie*, Vol. 191, No. 1-2, (January 1990), pp. 117-123, ISSN 0044-2968
- Feng, H.; Ding, D., Li, H., Lu, S., Pan, S., Chen, X. & Ren, G. (2010). Growth and Luminescence Characteristics of Cerium-Doped Yttrium Pyrosilicate Single Crystal. *Journal of Alloys and Compounds*, Vol. 489, No. 2, (21 Jan 2010), pp. 645-649, ISSN 0925-8388
- Goldburt, E. T.; Kulkarni, B., Bhargava, R. N., Taylor, J. & Libera, M. (1997). Size Dependent Efficiency in Tb Doped Y_2O_3 Nanocrystalline Phosphor. *Journal of Luminescence*, Vol. 72-74, (June 1997), pp. 190-192, ISSN 0022-2313
- Gonzalez-Ortega, J. A.; Tejada, E. M., Perea, N., Hirata, G. A., Bosze, E. J. & McKittrick, J. (2005). White Light Emission from Rare Earth Activated Yttrium Silicate Nanocrystalline Powders and Thin Film. *Optical Materials*, Vol. 27, No. 7, (April 2005), pp. 1221-1227, ISSN 0925-3467
- Greskovich, C. & Duclos, S. (1997). Ceramic Scintillators. *Annual Review of Materials Science*, Vol. 27, (August 1997), pp. 69-88, ISSN 0084-6600
- Holloway, P. H.; Trottier, T. A., Abrams, B., Kondoleon, C., Jones, S. L., Sebastian, J. S., Thomes, W. J. & Swart, H. (1999). Advances in Field Emission Displays Phosphors. *Journal of Vacuum Science and Technology B*, Vol. 17, No. 2, (March 1999), pp. 758-764, ISSN 1071-1023
- Jiao, H.; Wei, L. Q., Zhang, N., Zhong, M. & Jing, X. P. (2007). Melting Salt Assisted Sol-Gel Synthesis of Blue Phosphor $Y_2SiO_5:Ce$. *Journal of the European Ceramic Society*, Vol. 27, No. 1, (2007), pp. 185-189, ISSN 0955-2219
- Johnson, J. A.; Schweizer, S., Henke, B., Chen, G., Woodford, J., Newman, P. J. & Macfarlane, D. R. (2006). Eu-Activated Fluorochlorozirconate Glass-Ceramic Scintillators. *Journal of Applied Physics*, Vol. 100, No. 3, (1 Aug 2006), p. 034701 (5 pages), ISSN 0021-8979
- Kang, Y. C.; Lenggoro, I. W., Park, S. B. & Okuyama, K. (1999). $Y_2SiO_5:Ce$ Phosphor Particles 0.5 - 1.4 μm in Size with Spherical Morphology. *Journal of Solid State Chemistry*, Vol. 146, No. 1, (August 1999), pp. 168-175, ISSN 0022-4596
- Krell, A.; Klimke, J. & Hutzler, T. (2009). Transparent Compact Ceramics: Inherent Physical Issues. *Optical Materials*, Vol. 31, No. 8, (June 2009), pp. 1144-1150, ISSN 0925-3467
- Leonyuk, H. I.; Belokoneva, E. L., Bocelli, G., Righi, L., Shvanskii, E. V., Henrykhson, R. V., Kulman, N. V. & Kozhbakhteeva, D. E. (1999). High-Temperature Crystallization and X-Ray Characterization of Y_2SiO_5 , $Y_2Si_2O_7$ and $LaBSiO_5$. *Journal of Crystal Growth*, Vol. 205, No. 3, (September 1999), pp. 361-367, ISSN 0022-0248
- Létant, S. E. & Wang, T.-F. (2006a). Study of Porous Glass Doped with Quantum Dots or Laser Dyes under Alpha Irradiation. *Applied Physics Letters*, Vol. 88, No. 10, (6 Mar 2006), p. 103110 (3 pages), ISSN 0003-6951
- Létant, S. E. & Wang, T.-F. (2006b). Semiconductor Quantum Dot Scintillation under γ -Ray Irradiation. *Nano Letters*, Vol. 6, No. 12, (December 2006), pp. 2877-2880, ISSN 1530-6984

- Liddell, K. & Thompson, D. P. (1986). X-Ray Diffraction Data for Yttrium Silicates. *British Ceramic Transactions and Journal*, Vol. 85, No. 1, (January-February 1986), pp. 17-22, ISSN 0266-7606
- Louis, C.; Bazzi, R., Flores, M.A., Zheng, W., Lebbou, K., Tillement, O., Mercier, B., Dujardin, C. & Perriat, P. (2003). Synthesis and Characterization of $Gd_2O_3:Eu^{3+}$ Phosphor Nanoparticles by a Sol-Lyophilization Technique. *Journal of Solid State Chemistry*, Vol. 173, No. 2, (July 2003), pp. 335-341, ISSN 0022-4596
- Marsh, P. J.; Silver, J., Vecht, A. & Newport, A. (2002). Cathodoluminescence Studies of Yttrium Silicate: Cerium Phosphors Synthesised by a Sol-Gel Process. *Journal of Luminescence*, Vol. 97, No. 3-4, (June 2002), pp. 229-236, ISSN 0022-2313
- Meijerink, A.; Schipper, W. J. & Blasse, G. (1991). Photostimulated Luminescence and Thermally Stimulated Luminescence of $Y_2SiO_5:Ce, Sm$. *Journal of Physics D*, Vol. 24, No. 6, (June 1991), pp. 997-1002, ISSN 0022-3727
- Melcher, C. L.; Manente, R. A., Peterson, C. A. & Schweitzer, J. S. (1993). Czochralski Growth of Rare Earth Oxyorthosilicate Single Crystals. *Journal of Crystal Growth*, Vol. 128, No. 1-4 Part 2, (1 March 1993), pp. 1001-1005, ISSN 0022-0248
- Meltzer, R. S.; Jang, K. W., Hong, K. S., Sun, Y. & Feofilov, S. P. (1997). Optical Dephasing of Rare Earth Ions in Mixed Crystalline and Size-Restricted Systems. *Journal of Alloys and Compounds*, Vol. 250, No. 1-2, (20 March, 1997) pp. 279-286, ISSN 0925-8388
- Meltzer, R. S.; Feofilov, S. P., Tissue, B. & Yuan, H. B. (1999). Dependence of Fluorescence Lifetimes of $Y_2O_3:Eu^{3+}$ Nanoparticles on the Surrounding Medium. *Physical Review B*, Vol. 60, No. 20, (15 November 1999), pp. R14012-R14015, ISSN 1098-0121
- Mercier, B.; Dujardin, C., Ledoux, G., Luis, C., Tillement, O. & Perriat, P. (2004). Observation of the Gap Blueshift on $Gd_2O_3:Eu^{3+}$ Nanoparticles. *Journal of Applied Physics*, Vol. 96, No. 1, (1 July 2004), pp. 650-653, ISSN 0021-8979
- Mercier, B.; Dujardin, C., Ledoux, G., Louis, C., Tillement, O. & Perriat, P. (2006). Confinement Effects in Sesquioxides. *Journal of Luminescence*, Vol. 119-120, (July-October 2006) pp. 224-227, ISSN 0022-2313
- Mercier, B.; Ledoux, G., Dujardin, C., Nicolas, N., Masenelli, B., M'elinon, P. & Bergeret, G. (2007). Quantum Confinement Effect on Gd_2O_3 Clusters. *Journal of Chemical Physics*, Vol. 126, No. 4, (28 January 2007), p. 044507 (7 pages), ISSN 0021-9606
- Muenchausen, R. E.; Jacobsohn, L. G., Bennet, B. L., McKigney, E. A., Smith, J. F., Valdez, J. A. & Cooke, D. W. (2007). Effects of Tb Doping on the Photoluminescence of $Y_2O_3:Tb$ Nanophosphors. *Journal of Luminescence*, Vol. 126, No. 2, (October 2007), pp. 838-842, ISSN 0022-2313
- Niznansky, D. & Rehspringer, J. L. (1995). Infrared Study of SiO_2 Sol to Gel Evolution and Gel Aging. *Journal of Non-Crystalline Solids*, Vol. 180, No. 2-3, (January 1995), pp. 191-196, ISSN 0022-3093
- Niznansky, D.; Lančok, A., Hutlová, A., Bursik, J. & Rehspringer, J.-L. (2001). Preparation of $Y_3Fe_5O_{12}$ Nanocomposites by Sol-Gel Method: Influence of Modifiers. *International Journal of Inorganic Materials*, Vol. 3, No. 6, (September 2001), pp. 479-483, ISSN 1466-6049
- Pauwels, D.; Le Masson, N., Viana, B., Kahn-Harari, A., van Loef, E. V. D., Dorenbos, P. & van Eijk, C. W. E. (2000). A novel Inorganic Scintillator: $Lu_2Si_2O_7:Ce^{3+}$ (LPS). *IEEE Transactions on Nuclear Science*, Vol. 47, No. 6, (December 2000), pp. 1787-1790, ISSN 0018-9499

- Pedrini, C.; Moine, B., Gacon, J. C. & Jacquier, B. (1992). One- and Two-Photon Spectroscopy of Ce³⁺ Ions in LaF₃-CeF₃ Mixed Crystals. *Journal of Physics: Condensed Matter*, Vol. 4, No. 24, (15 June 1992), pp. 5461-5470, ISSN 0953-8984
- Pidol, L.; Viana, B., Bessière, A., Galtayries, A., Dorenbos, P. & Ferrand, B. (2007). High Efficiency of Lutetium Silicate Scintillators, Ce-Doped LPS and LYSO Crystals for Medical Applications. *Materials Science Forum*, Vol. 555, (2007), pp. 371-376, ISSN 0255-5476
- Redhammer, G. J. & Roth, G. (2003). β -Y₂Si₂O₇, A New Thortveitite-Type Compound, Determined at 100 and 280 K. *Acta Crystallographica C*, Vol. 59, No. 10, (October 2003), pp. i103-i106, ISSN 0108-2701
- Röntgen, W. C. (1896). On a New Kind of Rays. *Science*, Vol. 3, No. 59, (14 February 1896), pp. 227-231.
- Shibuya, K.; Koshimizu, M., Murakami, H., Muroya, Y., Katsumura, Y. & Asai, K. (2004). Development of Ultra-Fast Semiconducting Scintillators Using Quantum Confinement Effect. *Japanese Journal of Applied Physics*, Vol. 43, Part 2, No. 10B, (15 October 2004), pp. L1333-L1336, ISSN 0021-4922
- Soetebier, F. & Umland, W. (2002). Crystal Structure of Lutetium Disilicate Lu₂Si₂O₇. *Zeitschrift für Kristallographie - New Crystal Structure*, Vol. 217, No. 1, (2002), p. 22 , ISSN 1433-7266
- Sokolnicki, J. & Guzik, M. (2009). Synthesis and Photoluminescence of Nanocrystalline Lutetium Pyrosilicate Doped with Ce³⁺. *Optical Materials*, Vol. 31, No. 6, (April 2009), pp. 826-830, ISSN 0925-3467
- Suzuki, H.; Tombrello, T. A., Melcher, C. L. & J. S. Schweitzer, J. S. (1992). UV and Gamma-Ray Excited Luminescence of Cerium-Doped Rare-Earth Oxyorthosilicates, *Nuclear Instruments and Methods in Physics Research Section A: Accelerators, Spectrometers, Detectors and Associated Equipment*, Vol. 320, No. 1-2, (15 August 1992), pp. 263-272, ISSN 0168-9002
- Takagi, K. & Fukazawa, T. (1983). Cerium-Activated Gd₂SiO₅ Single Crystal Scintillator. *Applied Physics Letters*, Vol. 42, No. 1, (1 January 1983), pp. 43-45, ISSN 0003-6951
- Tissue, B. M. (1998). Synthesis and Luminescence of Lanthanide Ions in Nanoscale Insulating Hosts. *Chemistry of Materials*, Vol. 10, No. 10, (October 1998), pp. 2837-2845, ISSN 0897-4756
- Vakhidov, S. A.; Ibragimova, E. M., Nuritdinov, I., Rakov, A. F. & Ikramov, G. I. (1981). Self-Trapped Particles in Complex Oxide Crystals. *Physica Status Solidi B*, Vol. 106, No. 1, (July 1981), pp. 31-35, ISSN 0370-1972
- van Eijk, C. W. E. (2002). Inorganic Scintillators in Medical Imaging. *Physics in Medicine and Biology*, Vol. 47, No. 8, (21 April 2002), pp. R85-R106, ISSN 0031-9155
- Weber, M. J. (2002). Inorganic Scintillators: Today and Tomorrow. *Journal of Luminescence*, Vol. 100, No. 1-4, (December 2002), pp. 35-45, ISSN 0022-2313
- Yan, C.; Zhao, G., Hang, Y., Zhang, L. & Xu, J. (2006). Czochralski growth and crystal structure of cerium-doped Lu₂Si₂O₇ scintillator. *Materials Letters*, Vol. 60, No. 16, (July 2006), pp. 1960-1963, ISSN 0167-577X
- Yanagida, T.; Fujimoto, Y., Yoshikawa, A., Yokota, Y., Kamada, K., Pejchal, J., Kawaguchi, N., Ishizu, S., Fukuda, K., Suyama, T., Uchiyama, K., Mori, K., Kitano, K. & Nikl, M. (2010). Development and Performance Test of Picosecond Pulse X-Ray Excited Streak Camera System for Scintillator Characterization. *Applied Physics Express*, Vol. 3, No. 5, (May 2010), pp. 056202 (3 pages), ISSN 1882-0778

Atomic Scale Study of Deformation and Failure Mechanisms in Ceramic-Reinforced Metal-Matrix Composites

Avinash M. Dongare¹ and Bruce LaMattina²

¹*Materials Science and Engineering, North Carolina State University*

²*Rutgers, The State University of New Jersey
USA*

1. Introduction

One of the long-standing problems in materials research has been the development and improvement of materials capable of withstanding ballistic/blast impact. These materials, often referred to as blast and penetration resistant materials (BPRMs), require the ability to mitigate damage and dissipate energy and momentum. These materials are designed to stop fragments and/or projectiles while preventing behind armor debris or spall. Functionally graded ceramic particle reinforced metal-matrix composites (MMCs) are an emerging class of materials that show significant promise for applications in protective structures due to their improved damage mitigation response in addition to their superior strength, stiffness and wear resistance. The improved damage mitigation is attributed to the compositional/structural gradients introduced through the variation of the concentration of the reinforcing ceramic particles (SiC, Al₂O₃, etc.) in the matrix [Mortensen & Suresh, 1995; Suresh & Mortensen, 1997]. These functionally graded materials show promise to reduce the need for layered structures that are susceptible to delamination and the formation of axial cracks initiated at the interface of the ceramic and the more ductile backing material. The mechanisms responsible for plastic deformation and failure of these metal-matrix composites, however, are complex and are affected by multiple factors, such as the distribution and location/size of the reinforcing particles, grain size in the metal-matrix, the structural characteristics of the interface between the particles and matrix grains, and loading conditions [Li & Ramesh, 1998, Li et al., 2007]. The design and optimization of BPRM nanocomposite materials can be significantly accelerated by improvements in the understanding of the deformation and failure mechanisms under conditions of ballistic impact. An optimized design of these materials, therefore, requires a fundamental understanding of the links between the length scales (particle size/distribution, layer thickness) and properties (structure, chemistry, etc.) of these composites that enable enabling a combination of high strength and good ductility, and improved failure resistance in impact environments.

While there has been significant progress toward understanding the behavior of these materials, there are still major knowledge gaps to be filled with respect to the identification and characterization of the elementary processes responsible for plastic deformation and

failure. **These knowledge gaps are attributed to the inability to fully integrate theory, models, and experiments because of disparate time scales and the heterogeneous nature of these materials.** The time scales of the processes in these experiments can range from picoseconds to micro-seconds and the length scales can range from nanometers to micrometers [Remington et al., 2004]. These small time scales of the processes make it difficult to identify and characterize the elementary processes responsible for plastic deformation and failure using experiments alone. The molecular dynamics (MD) simulation technique has the ability to provide the atomic level structural information on the relevant micromechanisms at the time-scales of the spall experiments and may be instrumental in physical interpretation of experimental observations [Dongare et al., 2010a]. The applicability of MD simulations as an analysis/predictive tool, however, relies on the accuracy of the interatomic potentials to model the interactions between atoms in the system. The complex heterogeneity arises from the multicomponent interactions that results in complex bonding characteristics at the metal-ceramic interfaces. This heterogeneity limits the applicability of the MD technique due to inavailability of interatomic potentials capable of providing an accurate description of the structural and energy characteristics of metal-ceramic interfaces at the atomic scale. A new class of interatomic potentials referred as the angular dependent Embedded Atom Method (A-EAM) [Dongare et al., 2009a; Dongare et al., 2009b] has been recently developed that extends the ability of MD simulations to MMCs by combining the potentials conventionally used for metals with those conventionally used for ceramics in one functional form.

This chapter provides an overview of the current availability of interatomic potentials to investigate deformation and failure behavior in metal-matrix composites at the atomic scales using MD simulations in Section 2. An in-depth discussion on the formulation of interatomic potentials for complex metal-ceramic interactions is provided in Section 3 and an example parameterization is provided in Section 4. The applicability the A-EAM is demonstrated by investigating the strengthening and failure behavior of Si-particle reinforced Al-matrix nanocrystalline composites at high strain rates in Section 5.

2. Interatomic potentials for Molecular Dynamics simulations

The MD simulations study the evolution of the system as a function of time using classical atomistic models defined as interatomic potentials [Allen & Tildesley (1987)]. The interatomic potentials, $U(\vec{r}_1, \vec{r}_2, \dots, \vec{r}_N)$, describe the dependence of the potential energy of a system of N atoms as a function of the positions \vec{r}_i of the atoms. The Born-Oppenheimer approximation states that the electrons adjust to the changing atomic positions since they move much faster than atomic nuclei. This allows the exclusion of interactions for electrons in interatomic potentials and the potential energy can be defined based on atomic positions. Thus, to run a MD simulation, only the details of the interatomic interactions need to be specified in addition to the initial coordinates of the atoms in the system and boundary conditions. This is an important advantage that enables MD simulations to be treated as computer experiments and are therefore capable of discovering new physical phenomena or processes like real experiments. In addition, the analysis of the results provides complete information of the phenomena of interest at atomic-scale resolution. This predictive power of the MD method, however, is limited by the high computational cost of the simulations,

that leads to the severe limitations on time and length scales accessible for the simulation. While the current state-of-art MD simulations boast up to 10^{12} atoms (~ 10 micron size cubic samples) using hundreds of thousands of processors on one of the world-largest supercomputers [Germann & Kadau, 2008], the duration of most of the simulations in the area of materials research do not exceed tens of nanoseconds. The length-scales and the time scales of the MD simulations is largely defined by the computational efficiency of the interatomic potentials used to define the interatomic interactions.

The interatomic potentials typically are analytical functions that define the energy of an atom based on the coordinates of its neighboring atoms. The parameters of the analytical functions are chosen to describe properties of the material system as observed experimentally (crystal structure, cohesive energy, density, elastic constants, phase transformations, etc.) or as predicted using *ab initio* simulations where experimental data is not available. Metals and metallic alloys have been studied using the embedded atom method (EAM) [Daw & Baskes, 1984; Foiles, 1985; Johnson, 1988] potentials, whereas covalently bonded systems have been studied using the Stillinger – Weber (SW) potential [Stillinger & Weber, 1985; Ding & Anderson, 1986] for Si and Ge, Tersoff potential [Tersoff, 1988a, 1988b] for Si and C, and the Brenner potential [Brenner, 1990] for hydrocarbon systems. Each of these potentials has a unique functional form and underlying physical concept that allows them to model distinguishing characteristics of the material system. For example, the EAM potential uses an embedding energy term that simulates the effect of an atom embedded in an electron density in metals. The SW potential uses an explicit angular term that stabilizes the diamond cubic lattice for Si and Ge. The Tersoff potential uses a bond order interaction (which includes an angular dependence) that defines the strength of a bond based on the surrounding environment for Si, Ge, and C. These unique functional forms and concepts limit the transferability of these potentials from metallic systems to covalent systems and vice versa and hence limits the atomistic studies to pure systems or alloys with similar bonding characteristics. The modified embedded atom method (MEAM) potential [Baskes, 1992] is an attractive potential to model mixed metal-covalent systems as it includes parameterization for many cubic metals, as well as Si, Ge, C, H, N, and O. However, the formulation uses a many-body angular screening function as a cutoff mechanism that makes the potential computationally expensive. In addition, the parameterization of the mixed cross interactions in mixed systems also requires an adjustment of the parameters of the pure components [Thijsse, 2005] that will require testing the performance of the potentials for the pure systems.

The applicability of MD simulations to investigate deformation and failure micromechanisms in ceramic particle reinforced MMCs requires development of new computationally efficient interatomic potentials that are able to accurately reproduce the structural and energy characteristics of the metal matrix, the ceramic phase, as well as the metal-ceramic interface. An easier solution would be to design new alloy potentials by combining the well-established and thoroughly tested potentials developed for pure components within a unified approach. A number of studies have focused on the relationships between various potentials to justify this unified approach. For example, a potential for the Pt-C system was developed with an analytical form that reduces to the bond-order Brenner potential for C and an EAM-like potential for Pt [Albe et al., 2002]. Similar connections between the EAM formalisms and the bond-order scheme of the Tersoff potential [Brenner, 1989] and between the SW and MEAM potentials [Thijsse, 2002] have

been discussed. These studies suggest that despite the apparent distinctions between the functional forms and underlying physical arguments used in the description of interatomic bonding in metallic and covalent systems, a unified approach is feasible.

This chapter discusses the idea of developing a unified interatomic potential for systems with mixed type of bonding is extended to combine the EAM potential for metals with the SW potential commonly used in simulations of Si [Dongare et al., 2009a] and the Tersoff potential for Si and C [Dongare et al., 2009b]. The combined Angular-dependent EAM (A-EAM) potential incorporates a description of the angular dependence of the interatomic interactions into the framework of the EAM potential to make it compatible with the SW/Tersoff potentials. The A-EAM potential retains all the properties of the pure components as predicted by the original SW/Tersoff and EAM potentials and therefore eliminates the need for extensive testing for pure systems. In addition, the scope of the potential parameterization is limited to cross-interaction between the components. An example of the parameterization of the cross-interaction in the A-EAM potential is given for the Al-Si system here to study the micromechanisms related to deformation and failure of functionally graded Si reinforced Al-matrix composites (A359 alloy). Experimentally, the as-cast Al-Si (A359) alloy consists of a dendritic microstructure containing fine Si particles (wt % ~ 9 % Si) [Li et al., 1998, 2007]. The EAM potential for Al in the form suggested in Ref. [Mishin et al., 1999] is chosen as it provides a good description of the unstable and stable stacking fault energies and the surface and grain boundary energies in Al. In addition, the advantage of this potential is in the simplicity of the functional form and the availability of parameterizations for many metals, allowing for an easy implementation for a broad range of alloy systems. For pure Si, the original parameterization of SW potential [Stillinger & Weber, 1985] is used as it has been found to provide a good description of the crystalline, liquid, and amorphous phases of Si. The choice of the EAM and SW potentials renders the A-EAM potential to be computationally efficient and also provides an accurate description of the pure systems. The functional formulation of the A-EAM potential and the parameterization for the Al/Si cross-interactions are described in Section 3 below.

3. The Angular-dependent Embedded Atom Method (A-EAM)

A unified alloy potential based on a reformulation of the EAM and SW potentials in a compatible functional form is discussed in this section. A reformulation of the conventional EAM potential into a form that includes three-body terms in the expression for the total electron density function is presented first, followed by the description of an approach for incorporation of the angular dependence compatible with the SW potential.

3.1 Reformulation of the EAM potential

In the EAM potentials [Daw & Baskes, 1984; Foiles, 1985; Johnson, 1988], the energy of an atom is expressed as

$$E_i = \frac{1}{2} \sum_{j \neq i} \phi_{ij}(r_{ij}) + F_i(\rho_i) \quad (1)$$

where r_{ij} is the distance between atoms i and j , $\phi_{ij}(r_{ij})$ is the pair energy term defined as a function of the interatomic distance, $F_i(\rho_i)$ is the embedding energy term defined as a function of the electron density ρ_i at the position of atom i , and the summation is over all

atoms interacting with atom i . The electron density ρ_i is calculated as a sum of the partial electron density contributions from the neighboring atoms,

$$\rho_i = \sum_{j \neq i} f_j(r_{ij}) \quad (2)$$

where $f_j(r_{ij})$ is the partial electron density contribution from atom j at the location of atom i . Since only interatomic distances r_{ij} are needed to calculate the energy and forces in the system, the EAM calculations are nearly as simple and computationally efficient as the ones with pair potentials. The lack of explicit three-body terms, however, makes the conventional EAM inappropriate for covalently bonded materials.

To make the connections to SW or Tersoff potentials and to allow for the introduction of the angular dependence of the interatomic interactions, the linear sum of partial electron density contributions in Eq. (2) can be expressed through the sum of products of partial electron densities,

$$\rho_i = \left(\left[\sum_{j \neq i} f_j(r_{ij}) \right]^2 \right)^{1/2} = \left(\sum_{k \neq i} \sum_{j \neq i} f_j(r_{ij}) f_k(r_{ik}) \right)^{1/2} \quad (3)$$

The sum on the right hand side of the above equation includes two-body terms with identical pairs of atoms ($j = k$) and three-body terms ($j \neq k$) that can be separated from each other. The three-body terms can be written in the form of a sum over unique triplets of atoms (i, j, k) [Thijssse, 2002]:

$$\rho_i = \left\{ \sum_{j \neq i} [f_j(r_{ij})]^2 + 2 \sum_{j, k \in T_i} f_j(r_{ij}) f_k(r_{ik}) \right\}^{1/2} \quad (4)$$

where in the first (two-body) term under the square root, the summation is over all atoms interacting with atom i , and in the second (three-body) term under the square root, the summation is over all pairs of atoms j and k that form unique triplets with atom i . This formulation includes an explicit dependence on triplets of neighboring atoms and, as shown in Section 3.2, allows for incorporation of the angular dependence of the interatomic interactions in a form compatible with SW potential. Alternatively, the three-body terms can be written in a form of the “bond order” dependence:

$$\rho_i = \left\{ \sum_{j \neq i} [f_j(r_{ij})]^2 + \sum_{j \neq i} f_j(r_{ij}) \sum_{k \neq i, j} f_k(r_{ik}) \right\}^{1/2} \quad (5)$$

This formulation can be used to design an angular-dependent EAM potential compatible with the Tersoff potential [Dongare et al., 2009b].

3.2 Reformulation of the SW potential

The energy of an atom in a system described by SW potential [Stillinger & Weber, 1985] is defined as

$$E_i = \frac{1}{2} \sum_{j \neq i} U_2(r_{ij}) + \sum_{j, k \in T_i} U_3(\vec{r}_i, \vec{r}_j, \vec{r}_k) \quad (6)$$

The potential consists of a two-body (U_2) and a three-body (U_3) term, with the summation of the three-body terms being taken over all atom pairs j and k that form unique triplets with atom i . The two-body term has a Lennard-Jones form terminated at a distance r_c by a cut-off function:

$$U_2(r_{ij}) = A \left[B \left(\frac{r_{ij}}{\sigma} \right)^{-p} - \left(\frac{r_{ij}}{\sigma} \right)^{-q} \right] \exp \left[\frac{\sigma}{r_{ij} - r_c} \right] \quad (7)$$

The three-body term is defined as

$$U_3(\vec{r}_i, \vec{r}_j, \vec{r}_k) = \lambda \varepsilon \exp \left[\frac{\gamma \sigma}{r_{ij} - r_c} + \frac{\gamma \sigma}{r_{ik} - r_c} \right] (\cos \theta_{jik} + 1/3)^2 \text{ for } r_{ij} < r_c, r_{ik} < r_c \quad (8)$$

where θ_{jik} is an angle between vectors \vec{r}_{ij} and \vec{r}_{ik} originating from atom i and directed to atoms j and k . The parameters $A, B, p, q, \lambda, \varepsilon, \sigma, \gamma$, and r_c are adjustable parameters that are chosen to reproduce the properties of crystalline, liquid, and amorphous phases, as well as surface structures for Si. The sum of the three-body terms in Eq. (8) can be rewritten in a form of embedding energy,

$$E_i(\rho_i) = \sum_{j, k \in T_i} U_3(\vec{r}_i, \vec{r}_j, \vec{r}_k) = \frac{\lambda \varepsilon}{2(f_e^{Si})^2 \rho_i^2} \quad (9)$$

where the electron density and partial electron density contributions are defined as

$$\rho_i = \left(2 \sum_{j, k \in T} f_{ij}(r_{ij}) f_{ik}(r_{ik}) (\cos \theta_{jik} + 1/3)^2 \right)^{1/2} \quad (10)$$

$$f_{ij}(r_{ij}) = f_e^{Si} \exp \left(\frac{\gamma \sigma}{r_{ij} - r_c} \right) \quad (11)$$

where f_e^{Si} is an adjustable parameter that cancels out in Eq. (9) for pure Si. Note that in the expression for the electron density given by Eq. (10), the partial electron density contributions are defined by the type of the atoms forming the bond, $f_{ij}(r_{ij})$, rather than the type of the neighboring atom, $f_j(r_{ij})$, as in the original EAM, Eq. (2). This notation allows the definition of electron density contributions to be different for a bond formed by mixed species. In addition, the definition also allows for the incorporation of complex effects such as a charge transfer between species by defining different contributions to the electron density from two interacting atoms at the locations of these atoms, i.e. $f_{ij}(r_{ij}) \neq f_{ji}(r_{ij})$ for atoms i and j of different type [Dongare et al., 2009a]. This definition provides more flexibility in fitting the potential to the experimental data and the results of *ab initio*

calculations, as discussed in Section 4, where an example of the parameterization procedure for cross-interactions is given for Al-Si system.

3.3 Angular-dependent EAM compatible with SW potential

The reformulation of the three-body term of the SW potential in the functional form of the EAM embedding function, Eq. (9) with the inclusion of the first (two-body) term under the square root in Eq. (4) can be used to write a combined electron density as

$$\rho_i = \left\{ (1 - \delta_i) \sum_{j \neq i} (f_{ij}(r_{ij}))^2 + 2 \sum_{j,k \in T_i} f_{ij}(r_{ij}) f_{ik}(r_{ik}) (\cos \theta_{jik} + 1/3)^{c_i} \right\}^{1/2} \quad (12)$$

Two parameters, δ_i and c_i , are added to ensure that the combined electron density given by Eq. (12) reduces to the conventional EAM potential for pure metals and to the original SW potential for pure Si. For metals, $\delta_i = c_i = 0$ excludes the angular dependence and includes the radial contributions to electron density, thus, yielding the original EAM potential. For Si, $\delta_i = 1$ and $c_i = 2$ transform the electron density function into the three-body function of the SW potential, Eq. (10), that retains the angular dependence. The combined potential that reduces to the conventional SW and EAM potentials for pure components can be then formulated:

$$E_i = \frac{1}{2} \sum_{j \neq i} \phi_{ij}(r_{ij}) + F_i \left[\left\{ (1 - \delta_i) \sum_{j \neq i} (f_{ij}(r_{ij}))^2 + 2 \sum_{j,k \in T_i} f_{ij}(r_{ij}) f_{ik}(r_{ik}) (\cos \theta_{jik} + 1/3)^{c_i} \right\}^{1/2} \right] \quad (13)$$

Here, the form of the two-body term of the SW potential, $\phi_{ij}(r_{ij}) = U_2(r_{ij})$. As will be discussed in the next sections, the parameterization of the A-EAM potential for Al-Si interactions does not require an angular dependence of the electron density function for metal atoms. As a result, the computational efficiency of the evaluation of the A-EAM potential can be improved by rewriting the total electron density function in a form that does not involve the summation over triplets of neighboring atoms around a metal atom:

$$E_i = \frac{1}{2} \sum_{j \neq i} \phi_{ij}(r_{ij}) + F_i \left[\left\{ (1 - \delta_i) \sum_{j \neq i} f_{ij}(r_{ij}) + c_i \sum_{j,k \in T_i} f_{ij}(r_{ij}) f_{ik}(r_{ik}) (\cos \theta_{jik} + 1/3)^2 \right\}^{n_i} \right] \quad (13a)$$

Similarly to Eq. (13), the parameters are set to $\delta_i = c_i = 0$ for metals (the triplet contribution to electron density is eliminated) and $\delta_i = 1$ and $c_i = 2$ for Si (the radial contribution to the electron density is eliminated). The additional parameter n_i is equal to 1 for metals and 1/2 for Si. While in this work we use the formulation of the A-EAM potential given by Eq. (13a), the alternative formulation of Eq. (13) is useful when an angular dependence needs to be included in the electron density of metal atoms in order to provide an adequate representation of the interatomic interactions in metal-Si alloys.

The functional form and parameters of the embedding energy functions, $F_i(\rho_i)$, as well as the pair energy and partial electron density functions for the interactions between atoms of the same type are directly defined by the original EAM and SW potentials and do not need

to be adjusted in the alloy potential. The fitting of the alloy potential, therefore, is limited to finding the optimum parameters for the pair energy term, $\phi_{ij}(r_{ij})$, and the partial electron density contributions, $f_{ij}(r_{ij})$, for cross-interactions between atoms of different type. The angular dependence of interatomic interactions is incorporated into the alloy potential given by Eqs. (13) and (13a) in a form that is compatible with SW potential. Thus, this potential is referred to as the angular-dependent embedded atom method (A-EAM) potential.

4. A-EAM Potential for Si-particle reinforced Al-matrix composites

To test the ability of the combined A-EAM potential to reproduce the properties of systems with mixed metallic-covalent bonding, in this section we provide an example of parameterization of the potential for Al-Si systems. The formulation of the A-EAM potential, given by Eq. (13a), implies that the presence of a Si atom contributes to the electron density of a neighboring metal atom only through the two-body term of the electron density function that does not have the angular dependence. On the other hand, the presence of a metal atom contributes to the electron density of a neighboring Si atom through the three-body (triplet interaction) term of the electron density function.

For Al-Si cross-interactions, the pair energy term is defined as:

$$\phi_{ij}(r_{ij}) = A_C \exp \left[-\alpha_C \left(\frac{R_M}{r_{ij} - R_M} \right) \right] \left(\frac{r_{ij}}{\sigma_C} \right)^{-P_C} - B_C \exp \left[-\beta_C \left(\frac{R_M}{r_{ij} - R_M} \right) \right] \left(\frac{r_{ij}}{\sigma_C} \right)^{-Q_C} \quad (14)$$

where A_C , B_C , α_C , β_C , σ_C , R_M , P_C , and Q_C are fitting parameters. It should be noted that the partial electron density contributions $f_{ij}(r_{ij})$ are defined based on type of bond i.e. Si-Si, Al-Al, and Al-Si. The functional form for the partial electron density attributed to an Al-Si bond is given by

$$f_{ij}^{Al-Si}(r_{ij}) = f_{ij}^{Si-Al}(r_{ij}) = f_e^{Al-Si} \exp \left\{ -\gamma_C^{Al-Si} \left(\frac{R_M}{r_{ij} - R_M} \right) \right\} \quad (15)$$

Since there are no stable AlSi alloys (in the solid phase) observed experimentally, the parameters for the electron density function and the pair energy function for Al-Si cross-interactions, given by Eqs. (14)-(15), are selected based on the results of DFT calculations performed for several representative Al-Si bulk alloy structures. Since the number of the energy and structural parameters evaluated in DFT calculations exceeds the number of the fitting parameters, the fitting procedure is not aimed at reproducing the exact values of the material properties predicted in the DFT calculations. Rather, the results of the DFT calculations and the experimental data on the enthalpy of mixing of liquid Al-Si solutions [Kanibolotsky et al., 2002] are considered together as a target in the optimization of the overall agreement. Although several sets of parameters were obtained that provided a good agreement (less than 10 % deviation) with DFT results, the prediction of the enthalpy of mixing of the liquid alloy was the true test to study material behavior in extreme environments (high temperatures, pressures, and strain rates). The final parameter set chosen was found to provide an overall satisfactory description of the DFT results in addition to excellent prediction of the mixing behavior of the liquid alloy.

The plots of the embedding energy, the pair energy, and the partial electron density for Si (red lines) and Al (green lines) are shown in Fig. 1.(a), (b), and (c) respectively. The plots of the the pair energy functions and the partial electron density functions and are shown by the dashed blue lines in Fig. 1.(b), and (c), respectively. Thus, according to Eq. (2) and the plots in Fig. 1., the presence of Al atoms in the neighborhood of a Si atom causes a reduction in the partial electron density at the location of a Si atom and a reduced pair energy and therefore results in the weakening of the strength of the Si-Si interactions. This weakening

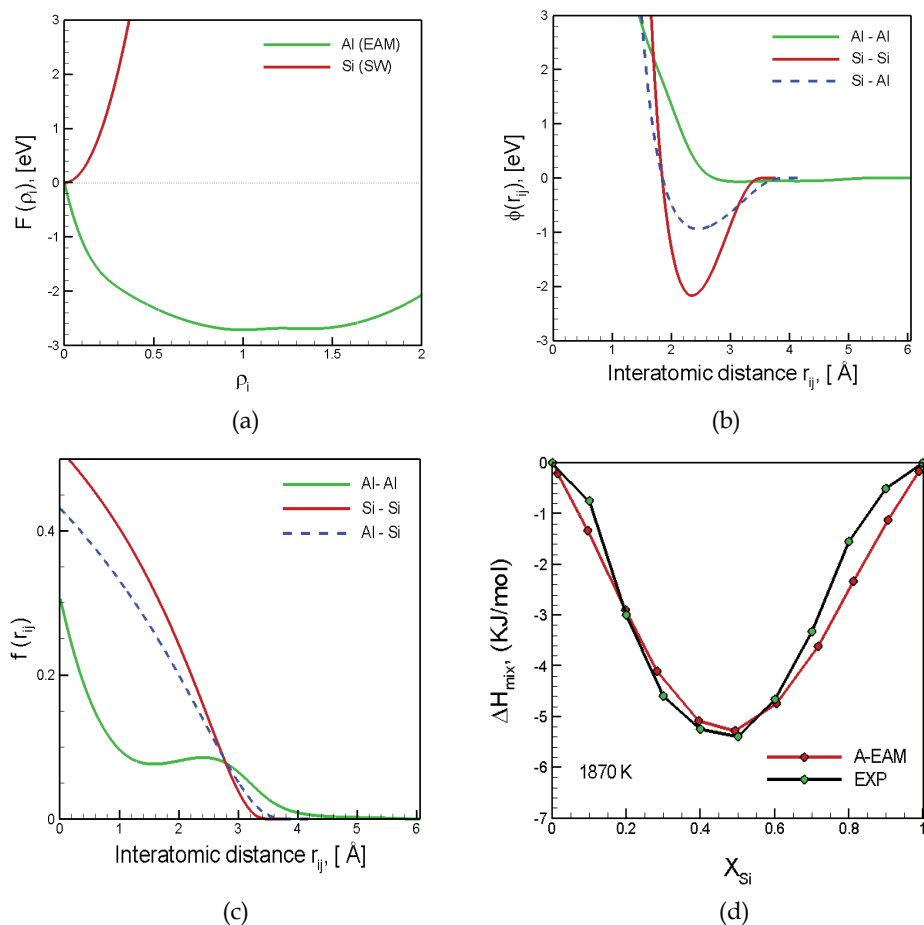


Fig. 1. Plots of the (a) embedding energy functions, (b) pair energy functions, and (c) partial electron density contributions for EAM Al (green line) and SW Si (red line) in the A-EAM formulation. The fitting of the cross-interactions is limited to the Al-Si pair energy and the Al-Si partial electron density contributions (dashed blue line) in (b) and (c), respectively. The enthalpy of mixing of liquid Al-Si alloy at 1870 K as predicted by the A-EAM potential (red line) is shown in (d) in comparison to experimental data [Kanibolotsky et al., 2002] (black line).

increases the tolerance of the local configuration in Si to deviations from the perfect diamond lattice structure in the presence of Al atoms. This observation is consistent with the results of recent DFT calculations which show a weakening of the Si-Si bonds at Al/Si interface [Nakayama et al., 2006]. The prediction of the experimental dependence of the enthalpy of mixing for the liquid Al-Si alloy at 1870 K by the A-EAM potential is shown in Fig. 1.(d) in comparison to that obtained using experiments [Kanibolotsky et al., 2002]. The plot shows excellent agreement of the prediction using the A-EAM potential that shows a minimum of -5.36 kJ/mol at a concentration of 49 at. % Si with experimental data exhibiting a minimum of -5.4 kJ/mol at a composition of 50 at. % Si. The accurate prediction of the mixing behavior across the composition range and the overall prediction of structural characteristics and energetics from DFT calculations enables the A-EAM to predict the relevant intermixing/melting behavior at Al/Si interfaces in extreme environments such as shock loading and radiation damage. More details of the fitting procedure and a quantitative analysis of the performance of the A-EAM potential in comparison to DFT calculations is provided elsewhere [Dongare et al., 2011].

5. Deformation and failure behavior of MMCs at high strain rates

MD simulations with the newly developed A-EAM Al/Si potential are used to investigate the strengthening and failure behavior of functionally graded Al/Si composites. Experimentally, the as-cast Al-Si (A359) alloy consists of a dendritic microstructure containing fine Si particles (wt % ~ 9 % Si) [Li et al., 2007]. While it is beyond the capabilities of MD simulations to model length scales that incorporate the gradation in composition as observed experimentally, the response of the material at local regions with different compositions can be investigated individually using MD simulations. Nanocrystalline Al/Si systems with varying volume fractions of Si grains are used as the first approximations of the local microstructure in the functionally graded Al/Si alloy. The initial Al/Si nanocrystalline systems with an average grain size of 6 nm and containing 43 grains are created using the Voronoi construction method [Derlet & Van Swygenhoven 2003]. The distribution of the Si grains is chosen at random with random grain orientations depending on the desired composition of the nanocomposites. To study the effect of volume fraction, five Al/Si nanocrystalline systems are created with volume fractions of ~ 5 %, ~ 16 %, ~ 28 %, ~ 35 %, and ~40% Si. The volume fraction is defined as the percentage of Si grains in the nanocrystalline Al/Si system. To facilitate easy comparison, the nanocrystalline composites of different compositions are created with the same grain morphologies and the same grain orientations. Periodic boundary conditions are used in all the three directions. The as-created systems are first relaxed to have zero pressure, and then equilibrated at 300 K for 100 ps. The elements of the atomic-level stress tensor are calculated as

$$\sigma_{\alpha\beta}(i) = -\frac{1}{\Omega_0} \left[\frac{1}{2} \sum_j F_{ij}^{\alpha\beta} + M_i v_i^\alpha v_i^\beta \right] \quad (15)$$

where α and β label the Cartesian components, Ω_0 is the atomic volume, F_{ij} is the force on atom i due to atom j , M_i is the mass of atom i , and v_i is the velocity of atom i . The strain (ϵ) calculated here is the engineering strain and the mean stress (σ_m) is calculated as

$$\sigma_m = (\sigma_x + \sigma_y + \sigma_z) / 3 \quad (16)$$

where σ_x , σ_y , and σ_z are the stresses averaged over the entire system in the X, Y, and Z directions, respectively.

The common neighbor analysis (CNA) [Honeycutt & Andersen, 1987 in addition to coordination number (CN) is used to identify local deformations in the FCC and diamond-cubic lattice. The initial nanocrystalline Al/Si systems with an average grain size of 6 nm are shown in Fig. 2. with the atoms colored according to the CNA/CN values. The contour for the Al atoms colored according to the CNA/CN characterization is as follows: the green atoms represent bulk fcc stacking, the red colored atoms represent local hexagonal close-packed order (stacking faults), the yellow atoms represent a coordination greater than 12, the light blue atoms represent a coordination of 12 other than fcc, and the dark blue atoms represent a coordination less than 12. The contour for the Si atoms colored according to the CNA/CN characterization is as follows: the purple atoms represent the tetrahedral bonding in the diamond cubic lattice, the white atoms represent coordination greater than 4, and the dark blue atoms represent a coordination of less than 4. The time step for all of the MD simulation runs was chosen to be 4 fs. The temperature was allowed to evolve during the deformation process.

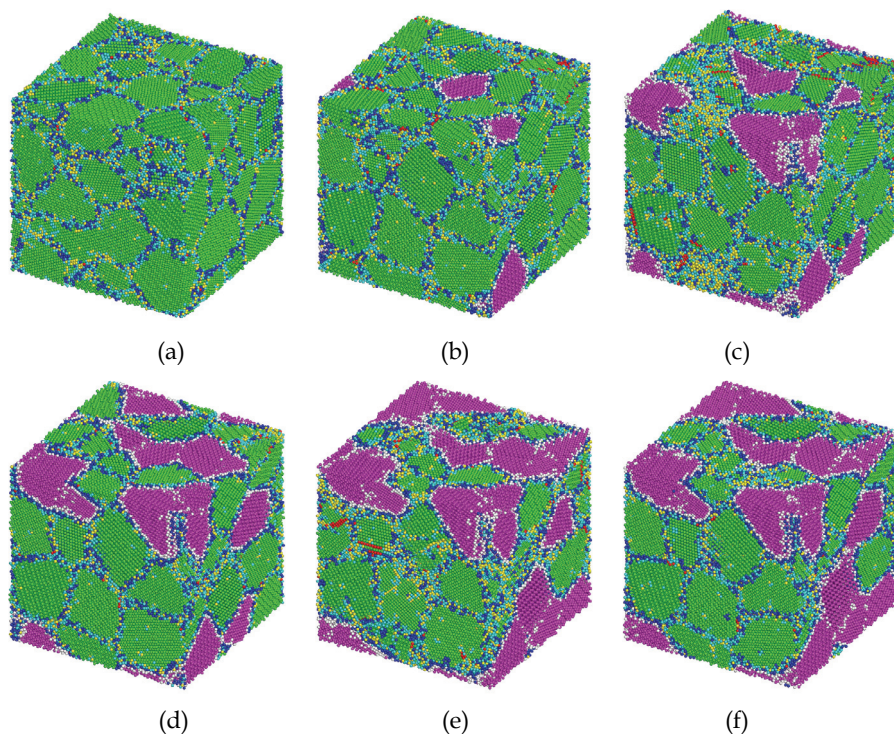


Fig. 2. The initial configuration of nanocrystalline Al/Si systems with an average grain size of 6 nm and a total of 43 grains and each atom is colored according to the CNA/CN values. The compositions (volume fractions) are : (a) pure Al, (b) ~ 5 % Si, (c) ~ 16 % Si, (d) ~ 28 % Si, (e) ~ 35 % Si and (f) ~ 40 % Si.

5.1 Strengthening behavior of the Al/Si nanocrystalline composite

At the macro scale, the strengths of materials are typically analyzed using the commonly used phenomenological yield criteria such as von Mises and Tresca [Hertzberg, 1996[29]. While, these criteria have been found to be appropriate to study deformation behavior in metals under quasi-static loading conditions, recent MD simulations suggest that several effects result in asymmetries in the tensile and compressive strengths and render these criteria to be inappropriate under dynamic loading conditions [Dongare et al., 2010a[30] ; Dongare et al., 2010b. As a result, the MD simulations of uniaxial stress loading were carried out to compute the flow stress of the composite at high strain rates. Deformation simulations were carried out at constant strain rate by deforming the sample in the loading direction while maintaining zero stress conditions in the lateral directions. The scaling parameter in the loading directions is chosen so as to achieve a strain rate of 10^9 s^{-1} . For each nanocrystalline system, three deformation simulations are carried out independently for loading in the X, Y, and Z directions to eliminate the effect of loading direction on the orientation of the Si grains in the composite.

The stress-strain curves obtained for the composite with a volume fraction of $\sim 35\%$ Si are plotted in Fig. 3.(a) and (b) for loading in tension and compression, respectively. The curves are initially linear and lie on top of each other up to the yield point, after which they start to deviate from elastic behavior. The flow stress (σ_f) is defined as the peak value of the stress in the stress-strain curve [Dongare et al., 2010b; Dongare et al., 2010c]. It can be seen from Fig. 3. that the nanocrystalline composite is stronger in compression than in tension. The flow stress for the nanocrystalline Al/Si composite for various compositions are tabulated in Table 1 for conditions of uniaxial tensile stress and uniaxial compressive stress loading at a constant strain rate of 10^9 s^{-1} .

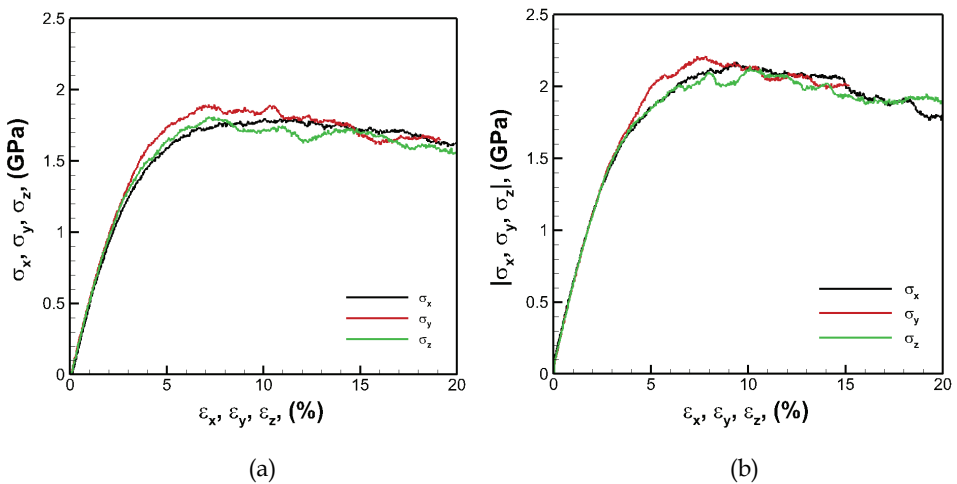


Fig. 3. Stress-strain curves for deformation of nanocrystalline Al/Si sample containing $\sim 35\%$ Si grains under loading conditions of (a) uniaxial tensile stress, and (b) uniaxial compressive stress. The three curves represent the deformation in X, Y and Z directions. Here ϵ_x , ϵ_y , and ϵ_z are the engineering strains in the X, Y, and Z directions, respectively.

Si Grains (wt. %)	Flow Stress (GPa) in (Tension/Compression)			
	σ_f^x	σ_f^y	σ_f^z	σ_f^{av}
0.00	1.750/1.835	1.689/1.846	1.694/1.536	1.711/1.739
4.65	1.665/1.851	1.718/1.901	1.737/1.859	1.707/1.870
16.28	1.493/1.738	1.572/1.741	1.530/1.785	1.532/1.755
27.91	1.848/2.166	2.113/2.294	1.926/2.258	1.962/2.239
34.88	1.801/2.173	1.896/2.211	1.812/2.139	1.836/2.174
39.53	2.049/2.411	2.171/2.456	2.042/2.451	2.087/2.439

Table 1. Calculated values of flow (peak) stress during uniaxial tensile/compressive deformation of nanocrystalline Al/Si composites with an average grain size of 6 nm and varying Si volume fraction at a constant strain rate of 10^9 s⁻¹.

The snapshots for the nanocrystalline Al system at 10% strain are shown in Fig. 4.(a) for conditions of tensile loading and in Fig. 4.(b) for conditions of compressive loading at a strain of 10 %. Intermediate snapshots of composite containing ~ 35 % Si grains are shown in Fig. 4.(c) for conditions of tensile loading and in Fig. 4.(d) for conditions of compressive loading at a strain of 10 % with the atoms colored according to the CNA/CN characterization. The snapshots do not show significant dislocation activity in the nanocrystalline Al and the Al/Si composite due to the small grain size (6 nm) of the nanocrystalline systems. While no dislocations are observed in the Si grains, it can be seen that the presence of the reinforcing phase does not significantly alter the dislocation density of the Al grains. The higher strengths in the composite are therefore attributed to reduced grain boundary rotation/sliding at the Al/Si grain boundaries. The fraction of Al/Si grain boundaries increases with increasing fractions of Si grains and therefore results in higher strength of the nanocrystalline composite.

The average values of the flow stress in tension and compression are plotted in Fig. 5.(a) as a function of Si composition. While there are some deviations, the plot shows a general trend that the flow stress values increase with increasing Si fraction. The deviations in the trend are attributed to the small system size and the small number of grains. The asymmetry in the strength of the nanocomposites in tension and compression is plotted in Fig. 5.(b) for various Si compositions. The strength asymmetry for the pure nanocrystalline Al system is predicted to be very small (~ 1.6 %) and addition of Si results in an increase in the asymmetry as the Si composition in the nanocomposites increases. The higher asymmetry in the strength values at higher volume fractions results from the limited grain boundary rotation/sliding behavior of the Al/Si grain boundaries in compression as compared to tension as observed for pure nanocrystalline systems at higher strain rates [Dongare et al., 2010b; Dongare et al., 2010c]. These results are consistent with results from MD simulations using the MEAM potential which suggest that the inclusion of Si particles reduces the relative motion of the Al grains by suppressing both sliding/shearing along the grain boundaries and dislocation nucleation from the boundaries that results in enhanced strengths of the Al-Si nanocomposites [Ward et al., 2006].

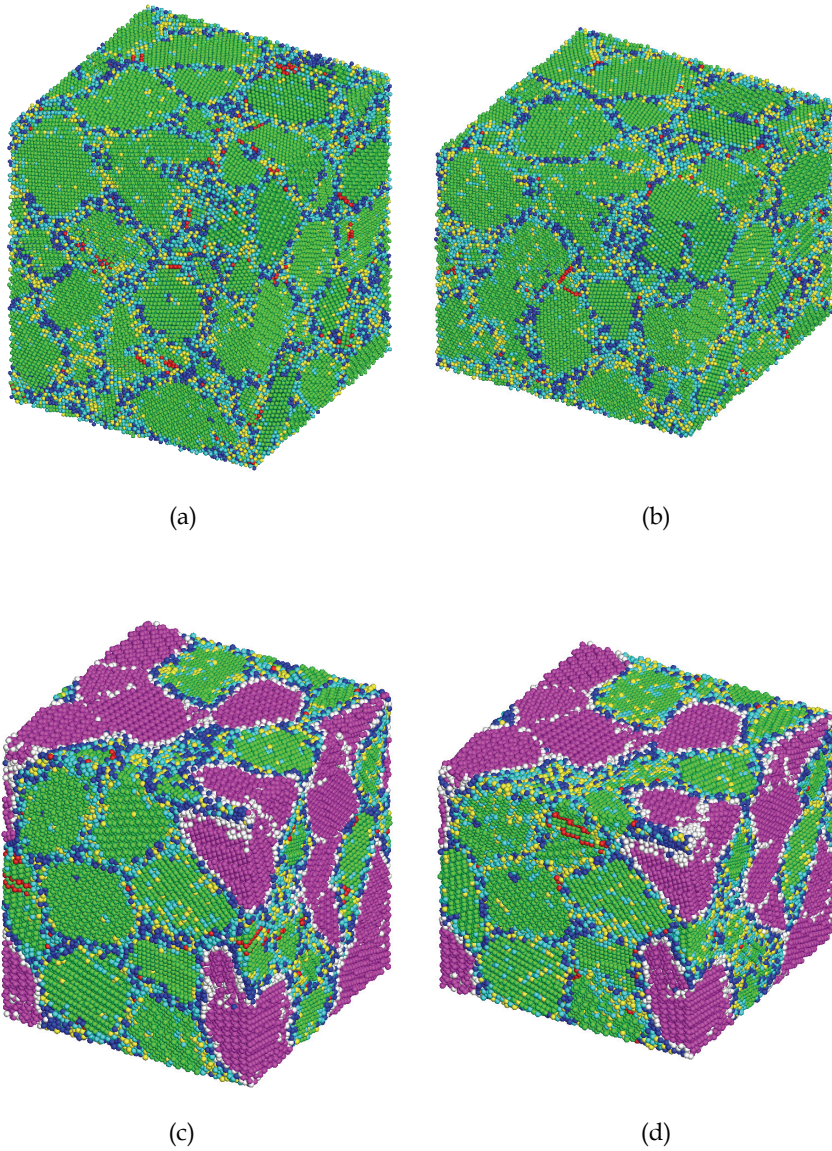


Fig. 4. Snapshots of the nanocrystalline Al system at a strain of 10 % in (a) tensile loading and (b) Compressive loading. The nanocrystalline Al/Si system with a volume fraction of ~40% Si at the same strain are shown in (c) for tensile loading, and in (d) for compressive loading. The atoms are colored according to the CNA/CN contour as indicated in Fig. 2.

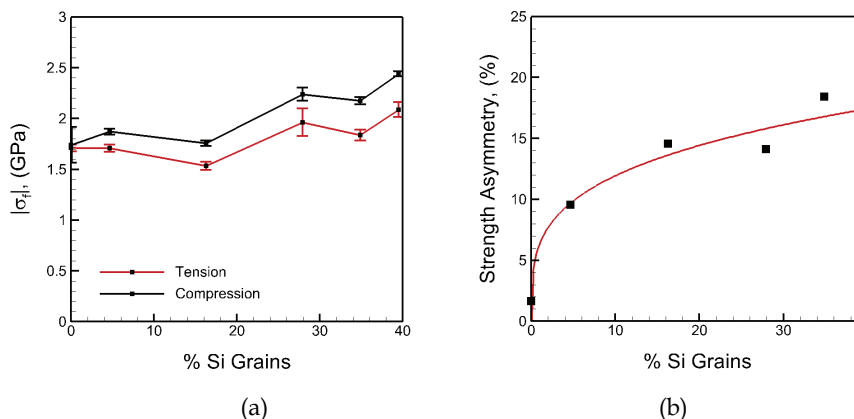


Fig. 5. (a) Calculated flow stress curves for deformation of nanocrystalline Al/Si sample for various volume fractions of Si. The red colored curve corresponds to tensile loading conditions and the black curve corresponds to compressive loading conditions.

5.2 Failure behavior of the Al/Si nanocrystalline composite

The failure behavior of nanocomposites formed by adding Si particles to Al nanocrystalline materials has been investigated using molecular dynamics simulations with the MEAM potential [Ward et al., 2006]. These results suggest that failure initiates by the nucleation of a void at the interface between the Al/Si grains. Experimental studies of deformation and failure of the A359 alloy at high strain rates also suggest that the fracture propagates along the interdendritic network of Si [Li et al., 2007]. A valid test of the A-EAM potential, therefore, is to study the micromechanisms related to ductile failure in nanocrystalline Al/Si composites consisting of an embedded Si nanocrystal in a nanocrystalline Al matrix. Deformation is carried out under conditions of uniaxial expansion ($\epsilon_x = \epsilon_y = 0$, and $\epsilon_z = \epsilon$) at a constant strain rate of 10^9 s^{-1} to relate to experimental dynamic loading conditions of dynamic failure [Dongare et al., 2009c]. Three deformation simulations are carried out independently for loading in the X, Y, and Z directions to eliminate the effect of loading direction on the orientation of the Si grains in the composite.

The stresses averaged over the entire system in the X, Y, and Z direction and the are plotted in Fig. 6.(a) as a function of engineering strain (ϵ) for uniaxial tensile strain loading in the Z direction. The evolution of mean stress (σ_m) as a function of engineering strain (ϵ) in the loading direction is plotted in Fig. 6.(b) as obtained in the three simulation runs during uniaxial tensile strain loading independently in the X, Y, and Z directions. The stress-strain curves in Fig. 6 show three stages of deformation. The first stage corresponds to elastic deformation of the nanocrystalline system leading to a linear evolution of the curves for σ_x , σ_y , and σ_z up to the yield point. Continued deformation results in deviation from linearity due to GB sliding/rotation processes that are accommodated by the nucleation of dislocations [Dongare et al., 2009c]. Continued deformation results in an increase in the stress to a peak value after which, nucleation of voids results in the relaxation of stresses as indicated by a sharp drop in the stresses in the X, Y, and Z directions as shown in Fig. 6.(a).

The stress state transitions to an almost hydrostatic stress condition ($\sigma_x \sim \sigma_y \sim \sigma_z$), resulting in a sharp drop in the stress values and mean stress values until a minimum is reached.

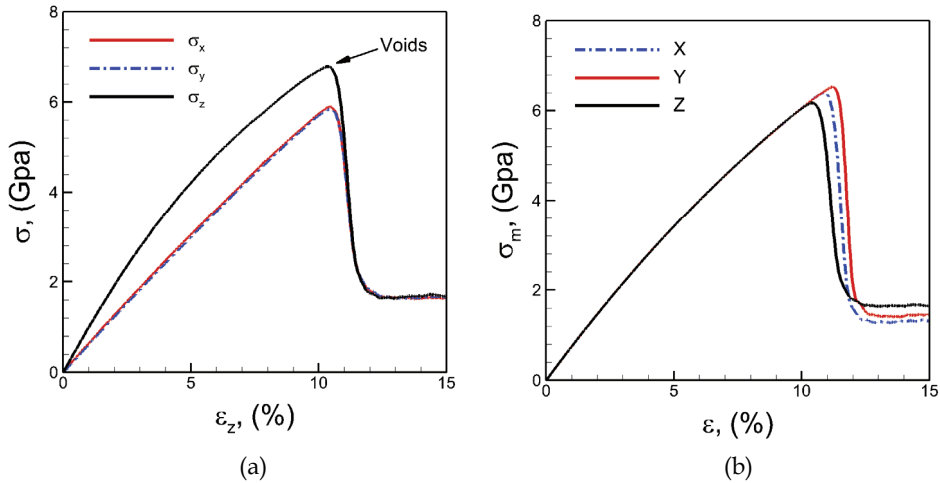


Fig. 6. (a) Plots of stresses in X, Y, and Z direction as a function of strain (ϵ_z) during tensile deformation under conditions of uniaxial strain at a strain rate of 10^9 s^{-1} . (b) Evolution of mean stress σ_m during uniaxial tensile strain loading independently in the X, Y, and Z directions at a strain rate of 10^9 s^{-1} .

Continued deformation results in the stress state to transition back to that corresponding to uniaxial strain.

Intermediate snapshots of a section of the system are illustrated in Fig. 7. with the atoms colored according to CAN/CN contour. The snapshot in Fig. 7.(a) corresponds to a time just before the peak in the stress value ($\epsilon \sim 9.0 \%$). A single void is observed to nucleate at a grain boundary interface between the embedded Si nanocrystal and the neighboring Al grains in Fig. 7.(b). Also, there is relatively little dislocation activity at the GB interface between the Al/Si grains. This indicates that void nucleation cannot be attributed to a dislocation pile-up process, but rather results from the mechanical separation/sliding at the Al/Si grain boundary interface. The creation of the void is accommodated by the shearing of the nearby atoms leading to the formation of a disordered shell of atoms around the void as shown in Fig. 7.(c). Continued deformation increases the size of this shell of disordered atoms around the voids and the void shape changes to near spherical as shown in Fig. 7.(b)-(d). Although a few dislocations are observed to propagate into the grains surrounding the void, most of the material surrounding the void consists of disordered atoms and void growth is observed to occur by the shearing of the disordered regions. The creation of disordered atoms surrounding the void increases until a minima in stresses is reached in Fig. 6. This minima in stresses corresponds to the snapshot shown in Fig. 7.(e). A transition in the stress state back to that corresponding to uniaxial strain conditions results in a slower growth rate of the void that is accompanied by the recrystallization of the surrounding disordered regions. The recrystallization of the disordered region around the void is attributed to the increased temperature of the system due to nucleation and growth of the void [Dongare et al., 2009c]. The results from these MD simulations thus agree with those predicted by the MEAM potential [Ward et al., 2006] that the failure of the nanocomposite is initiated by the nucleation of the void at the Al/Si interface.

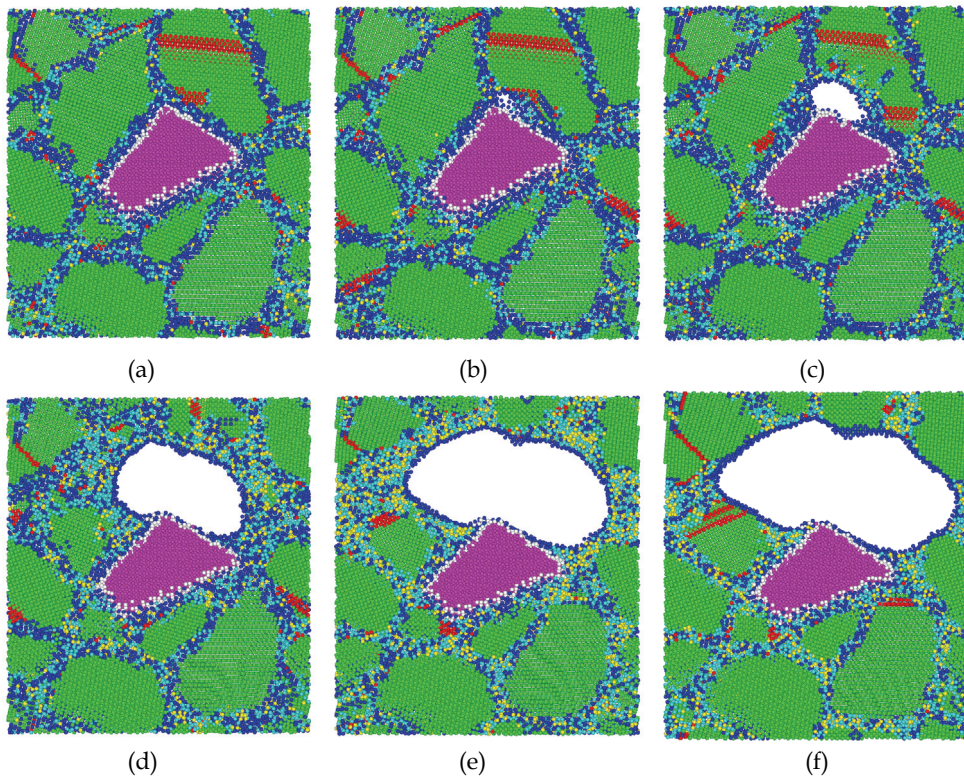


Fig. 7. Snapshots of a section of the system at (a) 90 ps ($\epsilon_z \sim 0.09$), (b) 100 ps ($\epsilon_z \sim 0.10$), (c) 105 ps ($\epsilon_z \sim 0.105$), (d) 110 ps ($\epsilon_z \sim 0.11$), (e) 120 ps ($\epsilon_z \sim 0.12$), and (d) 150 ps ($\epsilon_z \sim 0.15$), showing the nucleation and growth of the void under conditions of uniaxial tensile strain at a constant strain rate of 10^9 s^{-1} . The atoms are colored according to CNA/CN contour.

The value of the maximum mean tensile stress in Fig. 6.(b) can be compared to the peak spall pressure during spallation experiments. The plots suggest that the spall strength changes slightly for the nanocrystalline Al/Si composite with a change in loading direction. Intermediate snapshots of a section of the system at a strain of $\epsilon = 11\%$ during loading under conditions of uniaxial tensile strain in the X direction, the Y direction, and the Z direction are shown in Fig. 8.(a), (b), and (c), respectively at a constant strain rate of 10^9 s^{-1} . The snapshots suggest that failure (nucleation of void) initiates along the Al/Si grain boundary interface. Thus, the embedding of a Si nanocrystal results in the initiation of failure at the Al/Si interface irrespective of the loading conditions. These results suggest that the failure resistance behavior of these metal-matrix composites is dependent on the characteristics of the metal-ceramic interfaces in the nanocomposites. More work is needed to be done to obtain the links between the length scales (particle size/distribution, layer thickness) and properties (structure, chemistry, etc.) of these composites for enabling high strength behavior and improved failure resistance so as to allow for an optimized microstructural design of the MMnCs for use in extreme environments.

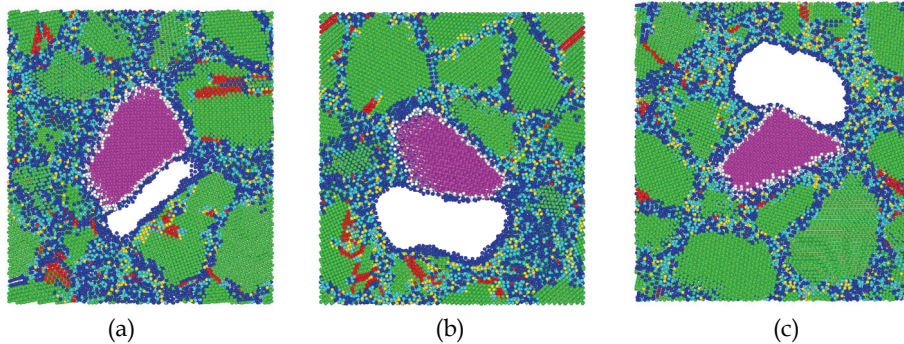


Fig. 8. Sectional snapshots of the nanocrystalline Al/Si system showing initiation of failure along the Al/Si grain boundary interface at a strain of $\epsilon = 11\%$ during loading under conditions of uniaxial tensile strain in (a) X direction ($\epsilon_z = \epsilon_y = 0$, and $\epsilon_x = \epsilon$), (c) Y direction ($\epsilon_x = \epsilon_z = 0$, and $\epsilon_y = \epsilon$), and (b) Z direction ($\epsilon_x = \epsilon_y = 0$, and $\epsilon_z = \epsilon$), at a constant strain rate of 10^9 s^{-1} . The atoms are colored according to CNA/CN contour.

6. Conclusion

A new angular-dependent EAM interatomic potential is developed that allows for the study of metal-ceramic interfaces at the atomic scale. The A-EAM potential is obtained by combining the EAM potential for Al with the SW potential for Si. The A-EAM potential retains the original functional forms and parameters and therefore all the properties of the pure components as predicted by the original SW and EAM potentials. The formulation of the A-EAM potential limits the parameterization to only the cross-interaction between the Al-Si components. An example parameterization is demonstrated for the Al/Si system based on the results of DFT calculations performed for artificial bulk Al/Si alloys and the compositional dependence of the enthalpy of mixing in liquid Al-Si alloys at 1870 K. Large scale molecular dynamics simulations using the A-EAM potential are carried out to study the strengthening behavior of the ceramic (Si) particle reinforced nanocrystalline metal (Al) matrix composites for varying volume fractions of the ceramic phase. The results suggest that the strength of the nanocrystalline composite increases with an increase in the volume fraction of the ceramic phase. The nanocrystalline composite is observed to be stronger in compression loading as compared to tensile loading and this strength asymmetry is observed to increase with increasing volume fraction of the ceramic phase. The microscopic mechanisms related dynamic failure predicted using MD simulations suggest that failure initiates at the metal-ceramic interface. These results suggest that the performance of the nanocomposites in extreme environments can be improved by a tailored design of a metal-ceramic interfaces in the nanocomposite. Future work will therefore focus on a fundamental understanding of the effect of the structure, size and distribution of the reinforcing ceramic phase that will enable high strengths of the nanocomposite in extreme environments.

7. Acknowledgment

This work has been done during AMD's tenure as a National Research Council (NRC) Research Associate funded by the US Army Research Office.

8. References

- Albe K., Nordlund K., and Averback R. S. (2002). Modeling the metal-semiconductor interaction: Analytical bond-order potential for platinum-carbon. *Phys. Rev. B*, Vol. 65, No. 19, pp. 195124, ISSN: 1098-0121
- Allen M. P., Tildesley D. J. (1987). *Computer simulation of liquids*, Clarendon Press, ISBN: 0198556454, Oxford
- Baskes M.I. (1992). Modified embedded-atom potentials for cubic materials and impurities. *Phys Rev B*; Vol. 46, No. 5, pp. 2727-2742, ISSN: 0163-1829
- Brenner D. W. (1989). Relationship between the embedded-atom method and Tersoff potentials. *Phys. Rev. Lett.*, Vol. 63, No. 9, pp. 1022-1022, ISSN: 0031-9007
- Brenner D. W. (1990). Empirical potential for hydrocarbons for use in simulating the chemical vapor deposition of diamond films. *Phys. Rev. B*, Vol. 42, No. 15, pp. 9458-9471, ISSN: 0163-1829
- Daw M. S. and Baskes M. I. (1984). Embedded-atom method: Derivation and application to impurities, surfaces, and other defects in metals. *Phys. Rev. B*, Vol. 29, No. 12, pp. 6443-6453, ISSN: 1098-0121
- Derlet P. M. and Van Swygenhoven H. (2003). Atomic positional disorder in fcc metal nanocrystalline grain boundaries. *Phys. Rev. B*, Vol. 67, No. 1, pp. 014202, ISSN: 1098-0121
- Ding K. and Andersen H. (1986). Molecular-dynamics simulation of amorphous germanium. *Phys. Rev. B*, Vol. 34, No. 10, pp. 6987-6991, ISSN: 0163-1829
- Dongare A. M., Neurock M., and Zhigilei L. V. (2009). Angular-dependent embedded atom method potential for atomistic simulations of metal-covalent systems. *Phys. Rev. B*, 80, No. 18, pp. 184106, ISSN: 1098-0121
- Dongare A. M., Zhigilei L. V., Rajendran A. M., and LaMattina B. (2009). Atomic scale modeling of multi-component interactions in nanocomposites, *Compos. Part B - Eng.*, Vol. 40, No. 6, pp. 461-467, ISSN: 1359-8368
- Dongare A. M., Rajendran A. M., LaMattina B., Zikry M. A., and Brenner D. W. (2009). Atomic scale simulations of ductile failure micromechanisms in nanocrystalline Cu at high strain rates. *Phys. Rev. B*, Vol. 80, No. 10, pp. 104108, ISSN: 1098-0121
- Dongare A. M., Rajendran A. M., LaMattina B., Zikry M. A., and Brenner D. W. (2010). Atomic scale study of plastic-yield criterion in nanocrystalline metals using molecular dynamics simulations. *Metall. Mater. Trans. A*, Vol. 41A, No. 2, pp. 523 - 531, ISSN: 1073-5623
- Dongare A. M., Rajendran A. M., LaMattina B., Zikry M. A., and Brenner D. W. (2010). Tension-Compression Asymmetry in Nanocrystalline Cu: High Strain Rate vs Quasi-Static Deformation. *Comp. Matl. Sci.*, Vol. 49, No. 2, pp. 260 -265, ISSN: 0927-0256
- Dongare A.M., Rajendran A. M., LaMattina B., Zikry M. A., and Brenner D. W. (2010). Atomic scale studies of spall behavior in nanocrystalline Cu. *J. Appl. Phys.*, Vol. 108, No. 11, pp. 113518, ISSN: 0021-8979
- Dongare A.M., Irving D. L., Rajendran A. M., LaMattina B., Zikry M. A., and Brenner D. W. (2011). *Physical Rev. B*, In review.
- Foiles S. M. (1985). Application of the embedded-atom method to liquid transition metals. *Phys. Rev. B*, Vol. 32, No. 32, pp. 3409-3415, ISSN: 0163-1829
- Germann TC, Kadau, K (2008). Trillion-atom molecular dynamics becomes a reality. *Int. J. Mod. Phys. C*, Vol. 19, No. 9, pp. 1315-1319, ISSN: 0129-1831
- Hertzberg R. W. (1996). *Deformation and fracture mechanics of engineering materials*, 4th ed., Wiley, ISBN: 0471012149, New York (NY), USA

- Honeycutt D. J. and Andersen H. C. (1987). Molecular dynamics study of melting and freezing of small Lennard-Jones clusters. *J. Phys. Chem.*, Vol. 91, No. 19, pp. 4950-4963, ISSN: 0022-3654
- Johnson R. A. (1988). Analytic nearest-neighbor model for fcc metals. *Phys. Rev. B*, Vol. 37, No. 37, pp. 3924-3931, ISSN: 0163-1829
- Kanibolotsky D. S., Bieloborodova O. A., Kotova N. V. and Lisnyak V. V. (2002). Thermodynamic properties of liquid Al-Si and Al-Cu alloys. *J. Therm. Anal. Calorim.*, Vol. 70, No. 3, pp. 975-983, ISSN: 1418-2874
- Li Y., and Ramesh K. T. (1998). Influence of particle volume fraction, shape, and aspect ratio on the behavior of particle-reinforced metal-matrix composites at high rates of strain. *Acta Mater.*, Vol. 46, No. 6, pp. 5633-5646, ISSN: 1359-6454
- Li Y., Ramesh K. T., Chin E. S. C. (2007). Plastic Deformation and failure in A359 aluminum and an A359-SiCp MMC under quasistatic and high-strain-rate tension. *J of Compos Mater.*, Vol. 41, No. 1, pp. 27-40, ISSN: 0021-9983.
- Mishin Y., Farkas D., Mehl M. J., and Papaconstantopoulos D. A. (1999). Interatomic potentials for monoatomic metals from experimental data and ab initio calculations. *Phys. Rev. B*, Vol. 59, No. 5, pp. 3393-3407, ISSN: 1098-0121
- Mortensen A., and Suresh S. (1995). Functionally graded metals and metal-ceramic composites: Part 1 Processing. *Int. Mat. Rev.*, Vol. 40, No. 6, pp. 239-265, ISSN: 0950-6608.
- Nakayama T., Itaya S., and Murayama D. (2006). Nano-scale view of atom intermixing at metal/semiconductor interfaces. *J. Phys.: Conf. Ser.: 7th International Conference on New Phenomena in Mesoscopic Structures/5th International Conference on Surfaces and Interfaces of Mesoscopic Devices*, Vol. 38, pp. 216-219, Maui, HI, Nov 27-Dec 02, 2005, ISSN: 1742-6588
- Remington B. A., Bazan G., Belak J., Bringa E., Caturla M., Colvin J. D., Edwards M. J., Glendinning S. G., Ivanov D. S., Kad B., Kalantar D. H., Kumar M., Lasinski B. F., Lorenz K. T., McNaney J. M., Meyerhofer D. D., Meyers M. A., Pollaine S. M., Rowley D., Schneider M., Stölken J. S., Wark J. S., Weber S. V., Wolfer W. G., Yaakobi B., and Zhigilei L. V. (2004). Materials science under extreme conditions of pressure and strain rate. *Metall. Mater. Trans. A* Vol. 35, No. 9, pp. 2587-2607, ISSN: 1073-5623
- Stillinger F. H. and Weber T. A. (1985). Computer simulation of local order in condensed phases of silicon. *Phys. Rev. B* 31 5262-5271, ISSN: 0163-1829
- Suresh S., and Mortensen A. (1997). Functional graded metals and metal-ceramic composites: Part 2 Thermomechanical Behavior. *Int. Mat. Rev.*, Vol. 42, No. 3, pp. 85-116, ISSN: 0950-6608
- Tersoff J. (1988). New empirical approach for the structure and energy of covalent systems. *Phys. Rev. B*, Vol. 37, No. 12, pp. 6991-7000, ISSN: 0163-1829
- Tersoff J. (1988). Empirical interatomic potential for carbon, with applications to amorphous carbon. *Phys. Rev. Lett.*, Vol. 61, No. 25, pp. 2879-2882, ISSN: 0031-9007
- Thijssse B.J. (2005). Silicon potentials under (ion) attack: Towards a new MEAM model. *Nucl Instrum Meth B*; Vol. 228, Sp. Iss. SI, pp. 198-211, ISSN: 0168-583X
- Thijssse B. J. (2002). Relationship between the modified embedded-atom method and Stillinger-Weber potentials in calculating the structure of silicon. *Phys. Rev. B*, Vol. 65, No. 19, pp. 195207, ISSN: 1098-0121
- Ward D.K., Curtin W.A. and Qi Y. (2006), Mechanical behavior of aluminum-silicon nanocomposites: A molecular dynamics study. *Acta Mater.*, Vol.54, No. 17, pp. 4441-4451, ISSN: 1359-6454

Functionalized Graphene Nanocomposites

Paula A. A. P. Marques, Gil Gonçalves, Sandra Cruz, Nuno Almeida,
Manoj K. Singh, José Grácio and Antonio C.M. Sousa
*Nanotechnology Research Division, Centre of Mechanical Technology and Automation
(TEMA), University of Aveiro
Portugal*

1. Introduction

Graphene is one of the most exciting materials being investigated today, not only out of academic curiosity but also for its potential applications. Graphene, a single layer of carbon packed in a hexagonal lattice, with a carbon-carbon distance of 0.142 nm is the first truly two-dimensional crystalline material, which is stable at room conditions. Graphene has displayed a variety of intriguing properties including high electron mobility at room temperature ($250,000 \text{ cm}^2/\text{Vs}$) exceptional thermal conductivity ($5000 \text{ W m}^{-1} \text{ K}^{-1}$) and superior mechanical properties with Young's modulus of 1TPa (Singh, Joung et al. 2011). Thus, graphene sheets offer extraordinary electronic, thermal and mechanical properties and are expected to find a variety of applications, such as sensors, batteries, supercapacitors, hydrogen storage systems and as reinforcement fillers of nanocomposites (Soldano C., Mahmood et al. 2010).

The joint award of the 2010 Physics Nobel Prize to Andre Geim and Konstantin Novoselov, as stated by the Royal Swedish Academy (2010), "for groundbreaking experiments regarding the two-dimensional material graphene", highlights the importance of this single atomic layer of carbon. This discovery is considered a breakthrough in the nanotechnology era, bringing the concept of single atomic component closer to reality.

Even before the studies of Novoselov and Geim, efforts had been carried out to prepare very thin graphite or graphene layers, since interesting properties were expected (Boehm 2010), but there were experimental difficulties in isolating single layers in such a way that electrical measurements could be performed on them, and there were doubts that this was practically possible. Graphene discovery marked the onset of experimental physics on graphene, which then made it relevant to revisit successfully all other methods to produce graphene which had reputedly failed in the past four decades.

So far, the original top-down approach of mechanical exfoliation using the Scotch-tape method has produced the highest quality samples, but the method is neither high throughput nor high-yield, the probability of finding individual graphene sheets of good quality is often low. In order to exfoliate a single sheet, van der Waals attraction between exactly the first and second layers must be overcome without disturbing any subsequent sheets (Allen, Tung et al. 2010). Many studies emerged over the last years with alternatives to mechanical exfoliation including chemical vapour deposition (Zhao, Rim et al. 2011), epitaxial growth (Ushio S, Arata Yoshii et al. 2011), carbon nanotube cutting (Janowska,

Ersen et al. 2009), chemical exfoliation (Wang, Robinson et al. 2009) and direct sonication (Lotya, Hernandez et al. 2009). Each of these methods presents both advantages and disadvantages, dealing with cost and scalability. At the moment, the reduction of graphene derivatives such as graphene oxide stands out as the primary strategy that can yield bulk amounts of graphene-like sheets that, albeit not defect-free, are highly processable.

Particularly attractive is the availability of bulk quantities of graphene as both colloidal dispersions and powders, which enables the possible fabrication of many carbon-based materials. The fact that such large amounts of graphene are somehow easily produced via the reduction of graphene oxide – oxygenated graphene sheets covered with epoxy, hydroxyl and carboxyl groups – offers tremendous opportunities for access to functionalized graphene-based nanocomposites. From the chemical point of view, the presence of oxygen functionalities at graphene oxide surface is very interesting since they provide reactive sites for chemical modification using known carbon surface chemistry. In this frame graphene oxide, because of its easier production and dispersion as well as simple chemical functionalization if compared to graphene, is emerging as a versatile material for applications in nanoscience and nanotechnology (Melucci, Treossi et al. 2010).

This chapter addresses the preparation, characterization and potential applications of graphene-based nanocomposites prepared using chemical strategies, which have been particularly relevant in our research group at TEMA. Special attention will be dedicated to graphene oxide precursor as a building block for the preparation of these nanocomposites. Interesting and promising applications for these materials are also discussed.

2. Graphene oxide

Graphene oxide (GO) has received the attention of a considerable number of researchers as it retains much of the properties of the highly valued super material pure graphene, but it is much easier, and cheaper, to make in bulk quantities; easier to process; and its significant oxygen content has been demonstrated to be very attractive to grow chemical structures at its surface.

2.1 Preparation methods

Chemical exfoliation is an important technique to produce graphene oxide for multifunctional materials. The most interesting advantages of this method are its low-cost and massive scalability. Graphite is the starting material and the technique can be easily scaled up to produce gram quantities or larger of “chemically derived graphene” dispersed in a liquid.

It all started in 1859, when Brodie (Brodie 1860) made the first attempt to produce graphene (at that time known as graphite oxide) using chemical exfoliation. Through adding potassium chlorate (KClO_3) to a mixture of graphite with nitric acid (HNO_3) an increase in the graphite mass was detected. The analysis of the obtained product revealed the presence of mainly hydrogen, oxygen and carbon.

Forty years later Staudenmaier (Staudenmaier 1898) achieved a 2:1 C:O ratio in the graphite oxidation by acidizing further the reaction medium. Hummers e Offeman (Hummers and Offeman 1958) used potassium permanganate (KMnO_4) in a sulfuric acid (H_2SO_4) medium and achieved similar oxidation levels of Staudenmaier’s method.

The first single sheet of GO obtained by chemical exfoliation was based in the use of graphite oxide, which is easily dispersed in water. The exfoliation is accomplished due to

the strength of interactions between water and the oxygen-containing (epoxide and hydroxyl) functionalities introduced into the basal plane during oxidation. The hydrophilicity leads water to readily intercalate between the sheets and disperse them as individuals. Mechanical stirring or sonication is employed in order to break the bonds between the carbon layers. The latter allows for a faster and more effective cleavage, as the cavitation of bubbles generated by ultrasonic fields produces shock waves that break apart the graphite flakes.

However there are limitations, mechanical and chemical exfoliation do not allow an absolute control over the graphene layer number, also the quality of the GO 2D crystal framework tends to be lower than graphene, hindering its performance in several applications mainly in the electronic area. These defects in the crystalline network are mainly noticed in the chemical exfoliations due to ample surface modification. In addition the ultrasonication tends to create bigger structural damages in the GO (Stankovich, Dikin et al. 2006; Gilje, Han et al. 2007; Paredes, Villar-Rodil et al. 2008).

Our research group has mainly used the top-down approach to prepare GO sheets from the referred chemical exfoliation of graphite. We followed the methodology suggested by Hummers and Offeman (Hummers and Offeman 1958) with minor modifications. This method involves the addition of concentrated H_2SO_4 (50 mL) into a 250 mL flask filled with graphite (2 g) at room temperature. The flask is cooled to $0\text{ }^\circ\text{C}$ in an ice bath, followed by slow addition of KMnO_4 (7 g); the flask is then allowed to warm to room temperature. After the temperature is raised to $35\text{ }^\circ\text{C}$ in a water bath, and the mixture is stirred with a Teflon-coated magnetic stirring bar for 2 h. The reaction mixture is then cooled in an ice bath, followed by the addition of distilled water in excess to the mixture. H_2O_2 (30 wt % in water) is next added until the gas evolution ceases. The resultant brown yellowish suspension is intensively washed by filtration. Firstly is washed with a diluted solution of HCl (0.1 mol dm^{-3}) and then with distilled water. The resulting slurry is re-suspended in distilled water and then centrifuged at 3.000 rpm until neutral pH.

The resulting material is dried by lyophilization in order to obtain a non agglomerated powder. The characterization of this nanomaterial, referred as graphene oxide (GO) is presented in the following section.

2.2 Characterization of GO sheets

As already referred, GO contains a variety of reactive oxygen functional groups, which renders it a good candidate for use in a wide variety of applications through well known chemical functionalizations.

The detailed structure of GO is still under discussion - since it depends on the chemical oxidation process used to its preparation. Because of this, models for the GO structure proposed in the literature differ considerably; this particular issue is discussed in considerable detail in a critical review by Daniel R. Dreyer (Dreyer, Park et al. 2010).

Meanwhile, the structure of GO can be simplistically assumed to be a graphene sheet bonded to oxygen in the form of hydroxyl (C-OH), ketonic species (C=O), carboxyl (COOH), epoxide (C-O-C) and various C-O and C=O containing chemical species such as lactol, peroxide, dioxolane, anhydride and ether (Acik, Lee et al. 2010).

The FTIR spectrum of GO nanosheets obtained from the methodology described in section 2.1 show the presence of these groups together with sp^2 -hybridized C=C (in-plane vibrations) (Figure 1). This figure also includes the spectra of thermally reduced GO (at $1050\text{ }^\circ\text{C}$ during 30 s in Argon atmosphere) identified as GTR and chemically reduced GO with

hydrazine (at 100 °C during 24 h) identified as GHR. In these cases, some residual bands at ~ 1720 , 1227, and 1070 cm^{-1} are still detected, showing that even after the application of reduction processes, some residual oxygen groups are still present. It should be noted that all spectra show a band at 1620 cm^{-1} , which can be attributed to aromatic carbon double bonds.

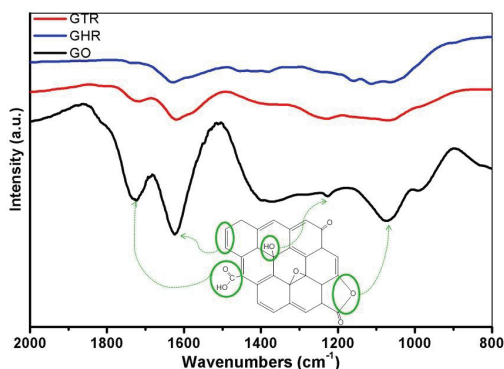


Fig. 1. FTIR spectra of as-prepared graphene oxide (GO), thermally reduced (GTR) and chemically reduced (GHR) GO. Reprinted (adapted) with permission from (Goncalves, Marques et al. 2009) Copyright 2011 American Chemical Society.

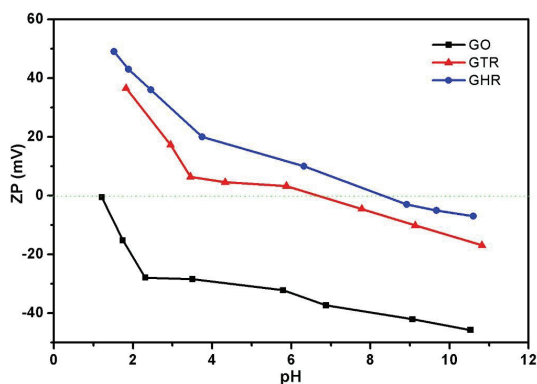


Fig. 2. Zeta potential of aqueous suspensions of as-prepared GO, thermally reduced (GTR) and chemically reduced (GHR) GO in function of pH. Reprinted with permission from (Goncalves, Marques et al. 2009) Copyright 2011 American Chemical Society.

Zeta potential measurements done in aqueous solutions of the previous mentioned samples (GO, GTR and GHR) in function of pH are important to determine the surface charge of the sheets (Figure 2). The results show that GO sheets are highly negatively charged with an average value equal to -35 mV at pH range between 3 and 9. This value is attributed to the presence of the above-described oxygen species at the surface of GO. On the contrary, GTR and GHR show positive zeta potential values near zero for the same pH range, which is indicative of the lower charge density of this type of graphene. The thermal and chemical

treatments of the GO sheets resulted in the reduction and almost complete elimination of the oxygen functionalities at the surfaces of these materials.

The presence of the oxygen functional groups at GO surface is responsible for its hydrophilicity, on contrary to graphene that is hydrophobic. The aqueous solutions of the as-prepared GO are then stable for long periods of time, showing a characteristic brown colour (Figure 3a).

The SEM images of GO reveal translucent sheets with wrinkles and folds as exemplified in Fig.3b. The thickness of these individual GO sheets measured by AFM show an average thickness around 1.8 nm for most GO sheets that is larger than the value of 0.8 nm referred for a single-layer graphene (Novoselov, Geim et al. 2004). Considering that the presence of the oxygen-containing functional groups on both sides of the GO surfaces increases their thickness with respect to nonfunctionalized graphene sheets, we may consider that most of these GO sheets consist of two or three layers of graphene. This result demonstrates the efficiency of the chemical treatment applied to exfoliate graphite into separate graphene sheets.

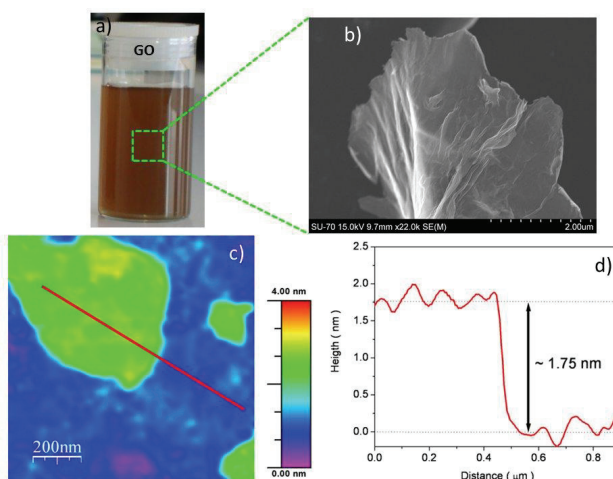


Fig. 3. a) Photographic image of an aqueous colloidal suspension of GO; b) SEM micrograph of graphene oxide sheet; c) Topographic view of contact-mode AFM scan of GO deposited on SiO₂ glass; and d) Height profile through the line shown in image (c). Reprinted (adapted) with permission from (Goncalves, Marques et al. 2009) Copyright 2011 American Chemical Society.

A more accurate analysis of the quality and crystallinity of GO sheets can be obtained by HR-TEM analysis. Figure 4a shows a bright-field TEM image of GO sheet attached to a copper grid. The suspended graphene membranes presented here consist of single layer or bilayer sheets with average dimensions of 2 μm. The HR-TEM image (Fig. 4b) clearly shows two-layered graphene (two graphene layers separated by 0.40 ± 0.02 nm) this is marked by green dotted area in Fig. 4b. A 2D fast Fourier transform (FFT) (Fig. 4c) was performed in the region indicated by a red box in Fig. 4b – this figure clearly shows the crystalline nature of bilayer graphene sheet. The corresponding HR-TEM image also reveals the honeycomb structure of graphene sheet (Fig. 4d).

The as-synthesized GO exhibits optical absorption in the visible and near-infrared range (Fig. 4e). The maximum absorbance at ~ 230 nm could originate from π - π^* transition of aromatic sp^2 domains (Novoselov, Geim et al. 2004) whereas a minor peak at ~ 320 nm was attributable to n - π^* transitions of C=O (Luo, Lu et al. 2009).

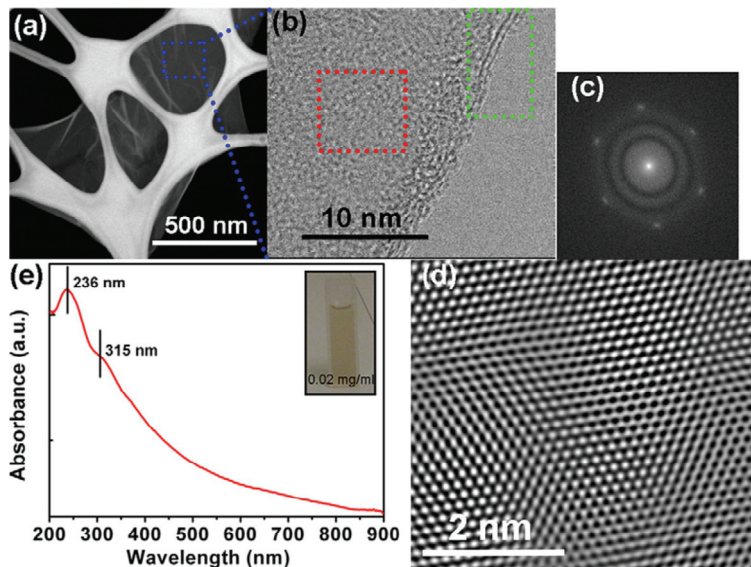


Fig. 4. (a) Bright-field TEM image of suspended GO sheet on carbon grid. (b) HR-TEM image of the blue dotted area denoted in a. (c) 2D FFT performed in the region indicated with red box exhibiting perfect crystallinity of GO sheet. (d) HR-TEM image reveals honeycomb structure of graphene sheet performed at the area denoted by red dotted line. (e) UV-vis absorbance spectra of GO solution in water. Inset shows the colour of the GO solution (0.02 mg/mL). Reprinted with permission from (Singh, Singh et al. 2011) Copyright 2011 American Chemical Society.

Recently, flow cytometry was presented as an alternative tool for analysis of size distribution and intrinsic fluorescence of GO sheets (Singh, Singh et al. 2011). Flow cytometry is a technique that integrates light scattering and fluorescence signals emanated from a group of cells or particles in the path of laser beam, thereby generating extensive statistical data on size, shape and internal characteristics of individual cells within the population. The method has found wide applications in biological research in view of its predilection for multi-parameter analysis at the single-cell level. Flow cytometry usually characterizes cells or particles with typical size range between 0.5 and 70 μm . Scatter signals evoked by submicron nano-sized particles are obligatorily gated along with the background noise, thereby blurring the distinction between noise and signal, which precludes flow cytometric analysis of nanoparticles unless particles are aggregated to larger dimension or have been made fluorescent.

In this work, it is report for the first time, that scatter signals generated by native single or few-layer GO sheets in a flow cytometer are gated distinctly apart from the background sheath fluid noise, thus enabling extensive analysis of size distribution and characterization

of fluorescence properties of individual GO sheets in the population. The results show that GO sheets are asymmetric in size and are endowed with intrinsic fluorescence detectable through the three fluorescence channels (FL1, FL2 and FL3) in the flow cytometer. Flow cytometer may, therefore, prove to be an indispensable tool in graphene research, which can have applications in exploring biomedical potential of this new material in miscellaneous areas like imaging, graphene-cell interaction as well as drug delivery.

3. Functionalization of graphene sheets

Due to the interest of using graphene as reinforcement filler of polymer matrixes to create multifunctional materials, a variety of methods for the graphene surface modification have been developed. Among other factors, the nature of the bonding interaction at the interface between the filler and the matrix has significant implications for the final composite properties, and most dispersion methods produce composites that are non-covalent assemblies where the polymer matrix and the filler interact through relatively weak dispersive forces. However, there is growing research focus on introducing covalent linkages between graphene based filler and the supporting polymer to promote stronger interfacial bonding, as will be presented in the following section entitled organic functionalization of graphene sheets.

On the other hand, graphene-based sheets have been utilized as burgeoning supports to disperse and stabilize nanoparticles, it is expected that such 2D carbon sheets may be appropriated candidates as nanoscale substrates in obtaining nanoparticle films. Metallic nanoparticles play an important role in wide number of applications such as surface-enhanced Raman scattering (SERS), display devices, catalysis, microelectronics, light emitting diodes, photovoltaic cells and also in medical or biological applications. Moreover, nanoparticles show changes in its electronic, optical and catalytic properties depending on the method of synthesis (Hodes 2007). Insertion of the nanoparticles on the graphene based matrix is an important study for the exploration of their properties and applications, examples of these materials will be included on section 3.2 entitled "inorganic functionalization of graphene sheets".

On the account of the importance of using graphene oxide to prepare graphene based materials, we will focus on two main types of functionalization: organic and inorganic.

3.1 Organic functionalization of graphene sheets

Concerning organic functionalization, we will discuss the importance of GO surface modification with organic moieties in order to disperse it in a polymeric matrix. As an example we will discuss in more detail the GO surface functionalization with an atom transfer polymerization initiator (ATRP) and subsequent poly(methylmethacrylate) (PMMA) chains growth via living/controlled polymerization yielding a nanocomposite soluble in organic medium. Polymerizations from surfaces, also known as SIP (surface initiated polymerization), have been widely used in the preparation of nanocomposites. In this context, living/controlled radical polymerization mechanisms, such as ATRP, offer the possibility of preparing multifunctional materials with good control over the polymer molecular weight, polydispersity index, composition and end group functionality. The interest of this organic functionalization of GO sheets lies in their potential to be homogeneously dispersed in polymeric dense matrices promoting good interfacial adhesion, of particular relevance in stress transfer to the fillers.

The organic functionalization of GO can be made by two distinct approaches, or by covalent or non-covalent bonds. In addition to other factors, the nature of the interaction at the interface of filler has significant implications on the enhancement of the final properties of the nanocomposites. For example the establishment of covalent bonds between graphene and polymeric matrices allows a more effectively tensions dissipation when the material is under strain which is quite important when talking about mechanical reinforcements. However it should be noted that the covalent functionalization of graphene creates discrete zones of discontinuity on sp^2 hybridized network not allowing the electron conduction, which has significant implications in reducing the conductivity of nanocomposites. In this case the non-covalent functionalization of graphene, through weak interactions minimizes this effect because it does not interfere in any destruction of aromatic structure of graphene.

3.1.1 Covalent functionalization

The covalent functionalization of carbon nanomaterials is usually preceded by an oxidation of the graphitic matrix with strong acids and oxidants in order to obtain oxygen functional groups that serve as precursors for the anchoring of organic molecules desired. As stated above the GO is characterized by being highly functionalized by oxygen groups reaching the C/O ratio of 2:1.

The availability of functional groups allows the use of various approaches already developed in organic chemistry in order to functionalize the GO (Figure 5). In terms of chemical reactions, acetylation is among the most common approaches to promote covalent binding of organic precursor molecules with functional groups at the surface of GO (Loh, Bao et al. 2010).

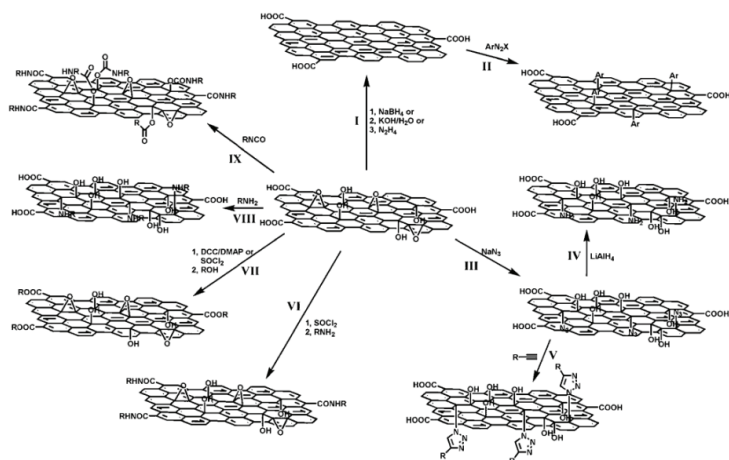


Fig. 5. Schematic representation showing various covalent functionalization chemistry of graphene or GO. I: Reduction of GO into graphene. II: Covalent surface functionalization via diazonium reaction (ArN_2X). III: Functionalization of with sodium azide. IV: Reduction of azide functionalized GO with $LiAlH_4$. V: Functionalization of azide functionalized GO through click chemistry ($R-CH \equiv CH / CuSO_4$). VI: Modification of GO with long alkyl chains by the acylation reaction. VII: Esterification of GO VIII: Nucleophilic ring-opening reaction of GO. IX: Functionalization of GO with organic isocyanates. (Loh, Bao et al. 2010) Reproduced by permission of The Royal Society of Chemistry (RSC).

The organic functionalization of GO allows the formation of stable colloidal solutions in several different solvents increasing the manipulation and processing of GO (water, acetone, ethanol, 1-propanol, ethylene glycol, dichloromethane, pyridine, DMF (dimethylformamide), THF (tetrahydrofuran), DMSO (dimethylsulfoxide), NMP (N-methyl pyrrolidone), acetonitrile, hexane, diethyl ether and toluene (Park, An et al. 2009; Rao, Biswas et al. 2009; Dreyer, Park et al. 2010), furthermore it also improves the molecular and atomic interfacial interactions between the graphene and solvents.

Stankovich et al demonstrated the surface functionalization of GO with aliphatic and aromatic isocyanates derivatives through formation of amide and carbamate esters with carboxylic groups and hydroxyl, respectively, on the surface of GO (Stankovich, Piner et al. 2006). The results show that these new hybrid materials allow the formation of stable colloidal solutions in various polar aprotic solvents such as dimethylformamide, N-methyl-2-pyrrolidone, dimethylsulfoxide or hexamethylphosphoramide.

Another approach that allows the addition of new functional groups on the surface of GO is silanization (Yang, Li et al. 2009; Hou, Su et al. 2010). Yang et al. described the covalent bond of 3-aminopropyltriethoxysilane (APTS) on the surface of GO, through S_N2 nucleophilic reactions between the epoxy groups of the surface of GO and the amine groups of APTS. This type of modification has a special interest in the dispersion of functionalized GO in different solvents (polar or non-polar), this is due to the fact that the family of silanes provide a wide range of terminal functional groups.

The functionalization of GO via carboxylic acids is one of the most common approaches and is possible by prior activation of these groups through various agents such as thionyl chloride ($SOCl_2$) (Niyogi, Bekyarova et al. 2006; Liu, Xu et al. 2009; Zhang, Huang et al. 2009; Karousis, Economopoulos et al. 2010; Zhuang, Chen et al. 2010), 1-ethyl-3-(3-dimethylaminopropyl)-carbodiimide (EDC) (Liu, Robinson et al. 2008), N, N'-dicyclohexylcarbodiimide (DCC) (Veca, Lu et al. 2009) and 2-(7-aza-1H-benzotriazole-1-yl)-1,1,3,3-tetramethyluronium hexafluorophosphate (Hatu) (Mohanty and Berry 2008). Subsequent addition of nucleophilic species, such as amines and hydroxyl, allow the formation of covalent bonds with functional groups of the graphene oxide through formation of amide or ester groups.

Another strategy for surface functionalization of GO is through the use of epoxide groups on the surface of graphitic planes, which can easily be modified on certain conditions through reactions of ring-opening. The preferred mechanism for this type of reaction involves a nucleophilic attack of amines to α -carbon. The study performed by Wang et al based on this methodology allowed the surface modification of GO with octadecylamine (Wang, Chia et al. 2008). Another author used the same procedure to establish links between an ionic liquid with terminal amine groups and epoxide groups at the surface of graphene oxide. This surface modification is of particular interest when attempting to disperse the GO in polar solvents (Yang, Shan et al. 2009).

A referred one of the main reasons for the surface modification of GO with organic moieties is that it enables a seamless integration with molecular polymeric matrixes. In this sense there is a range of approaches already described by several authors that allow the controlled growth of polymer chains at the surface of GO.

A well-known mechanism for the controlled growth of polymer chains on the surface of GO polymerization is atom transfer radical polymerization (ATRP). Usually in such cases the free carboxylic groups of GO are converted to acyl groups, which upon treatment with diols (ethylene glycol), yield graphene sheets rich in hydroxyl groups. These hydroxyl groups at

the surface of GO allows the establishment of covalent bonds with initiator agent of ATRP polymerization, which are usually compounds with terminal bromine groups (2-bromo-2-methylpropionyl bromide or α -bromoisobutyryl-bromide). After the addition of the initiating agent to the surface of GO is possible to perform the controlled growth of polymer chains via ATRP (Figure 6). Another approach is the surface modification of carboxylic groups of GO with diamines through the formation of amide groups, allowing the functionalization of GO with terminal amine groups, that also able to establish chemical bonds with the ATRP initiators (Fang, Wang et al. 2009; Lee, Dreyer et al. 2010).

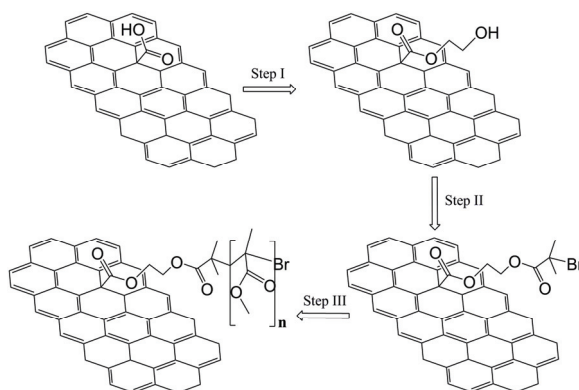


Fig. 6. Schematic representation of the ATRP reaction mechanism for the surface modification of GO with PMMA .

In our work we performed the surface modification of GO with PMMA polymers chains via ATRP in order to test it as a reinforcement of a PMMA matrix (Goncalves, Marques et al. 2010) following the scheme in Fig.6.

After the GO modification with the PMMA chains, hereafter referred as GPMMA, it turned hydrophobic and as a result soluble in chloroform as can be seen in the inset of Figure 7a. It should be also notice that this solution is clearly darker than the original GO in aqueous solution (Fig.3a) indicating the conversion of GO to GPMMA. Figure 7 depicts the TEM image of the GPMMA sample where some dark features can be observed. The high magnification image (Fig. 7b) of the area denoted by the square region in Fig. 7a, clearly shows these dark spots as opposed to what is observed for pristine GO. The presence of such spots can be attributed to polymer brushes and has been observed by other authors with different polymers as described elsewhere (Yang, Wang et al. 2009; Fang, Wang et al. 2010). According to Yang et al. (Yang, Wang et al. 2009), in solution the grafted polymer chains are extended due to their solubility in the solvent, however, after drying the polymer chains collapse onto the surface of the GO sheets forming nanosized domains that may correspond to the dark spots observed.

The characterization of GPMMA by infrared spectroscopy showed an increase of the intensity of the carbonyl band combined with appearance of characteristic bands of $-\text{CH}_2$ at 2850 and 2920 cm^{-1} in the infrared spectrum confirming the presence of PMMA polymer chains at GO surface. In Raman spectrum there was a decrease of intensity of the characteristic D (1330 cm^{-1}) and G (1590 cm^{-1}) bands of graphene in relation to what is normally observed for GO, which is associated with surface defects created during the surface treatments (Fang, Wang et al. 2010).

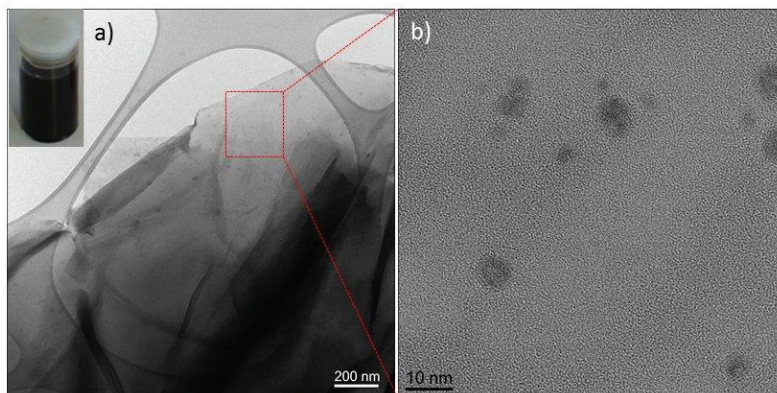


Fig. 7. a) TEM image of the GPMMA sample; b) high magnification image of the area denoted by the square region is shown in a). Inset in Fig. 7a show the photographic image of GPMMA in chloroform. (Goncalves, Marques et al. 2010) Reproduced (adapted) by permission to The Royal Society of Chemistry.

To further understand the surface of GPMMA AFM studies in friction mode were performed on these sheets. It is known that the adhesion force (F_{ad}) and the friction coefficient (μ) of a material depend on its atomic structure and can be calculated by the following equation $F_L = \mu (F_N + F_{ad})$, where F_L is the lateral force, also known as friction force, and F_N the normal force. From the graphics inserted in Fig. 8 it is possible to see the different

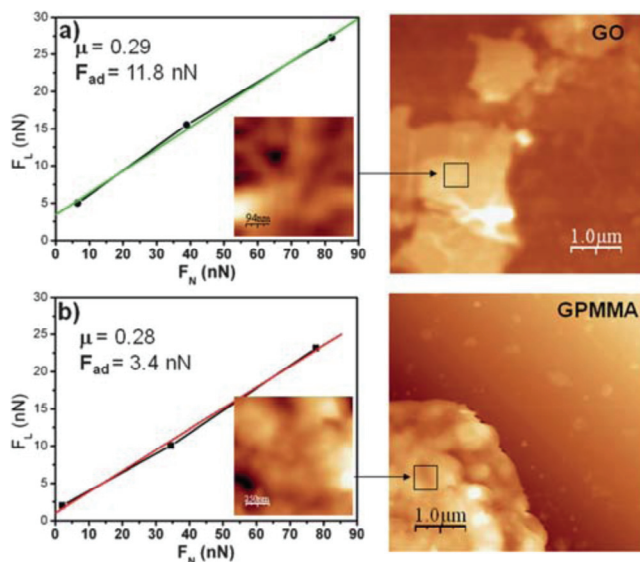


Fig. 8. A graphical representation of lateral versus normal forces determined by the AFM analysis in friction mode and contact-mode AFM topography images of (a) GO and (b) GPMMA (Goncalves, Marques et al. 2010) Reproduced by permission to The Royal Society of Chemistry.

response of the materials (GO and GPMMA) by applying three different normal forces. The results show that the friction coefficients are relatively similar in both samples. However, the adhesion force is three times higher in the case of the GO sheets ($F_{ad} \text{ GO} = 11.8 \text{ nN}$ and $F_{ad} \text{ GPMMA} = 3.4 \text{ nN}$). These results can be attributed to the different chemical surface of GPMMA which results in different atomic interactions with the AFM cantilever. Careful analysis of the graphs shows a linear relationship between the normal and lateral forces which point to a homogeneous distribution of the polymer chains at the GO surface. These results are in agreement with an effective modification of the GO surface with the ATRP initiator and subsequent uniform polymerization, as previously discussed. The study of the effect of the incorporation of this GPMMA in a PMMA matrix is discussed in section 4.1.

3.1.2 Non-covalent functionalization

GO can also form various multifunctional materials through non-covalent bonds, either of the Van der Waals or ionic type, this property is mainly due to the fact that its surface is negatively charged due to the presence of oxygen functional groups, in addition to its graphitic structure with delocalized π orbital that allow π - π interaction type.

This type of functionalization has some advantages in certain areas, such as chemical sensors and biomedical materials. In this context, several materials, such as polymers (Hu, Wang et al. 2010; Liu, Tao et al. 2010; Liu, Yang et al. 2010), surfactants (Hao, Qian et al. 2008; Xu, Bai et al. 2008; Liang, Wu et al. 2009), polyelectrolytes (Hasin, Alpuche-Aviles et al. 2010; Qi, Pu et al. 2010; Tian, Meziani et al. 2010) and biomolecules (Lu, Yang et al. 2009; Patil, Vickery et al. 2009; Husale, Sahoo et al. 2010; Laaksonen, Kainlauri et al. 2010; Wu, Shao et al. 2010) can be used to functionalize the surface of GO (Figure 9).

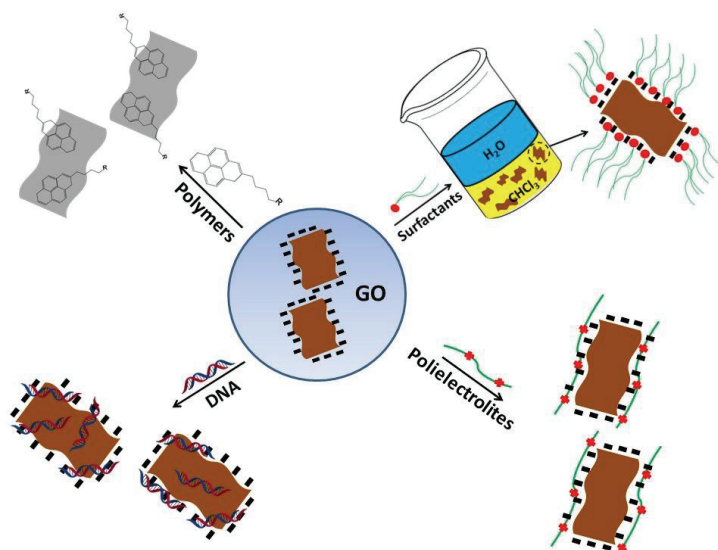


Fig. 9. Schematic representation of non-covalent functionalization of GO through surfactants, polyelectrolytes, polymers and DNA.

Recent studies indicate a growing interest to functionalize graphene with various types of biomolecules such as DNA, proteins and enzymes in order to obtain functional materials with a wide range of applications in nano-electronics and biotechnology.

For example, adsorption of DNA biomolecules on the surface of graphene is enabled due to non-covalent interactions (electrostatic/hydrogen bonding) between the primary amines of the single-stranded DNA and the carboxylic groups of the GO and by the π - π stacking interactions involving both purine and pyrimide bases of DNA. The results demonstrate that these systems are stable in aqueous solutions for several months at concentrations below 2.5 mg/mL (Patil, Vickery et al. 2009). This approach was also developed for chains of double-stranded DNA, yet the results showed that the aqueous suspensions of graphene were less stable, probably due to the pairing of helices limiting interactions with the hydrophilic surface of GO.

3.2 Inorganic functionalization of graphene sheets

Graphene is an interesting substrate for the immobilization of inorganic nanoparticles. The dispersion of metal nanoparticles on graphene sheets potentially provides a new way to develop catalytic, magnetic, and optoelectronic materials. In the last years, the ability of combining well with metallic nanoparticles producing nanocomposites with promising applications such as chemical sensors, energy and hydrogen storage systems and catalysts, among others, has captured the interest of a number of researchers; the advantage, beyond the already mentioned characteristics of graphene, is that we can add specific properties associated to the inorganic nanoparticles like magnetic, optical, electrical, catalytic and others (Hassan, Abdelsayed et al. 2009; Kamat 2009).

The majority of the publications related to the preparation and applications of this new class of graphene based nanocomposites uses noble metals like gold (Goncalves, Marques et al. 2009; Hong, Bai et al. 2010), platinum (Si and Samulski 2008), palladium (Scheuermann, Rumi et al. 2009) and silver (Shen, Shi et al. 2010); however, there is also a growing interest in the use of other metals like, iron, copper, tin and cobalt.

Some of the published papers about the preparation of graphene/metal nanocomposites makes use of organic spacers, like octadecylamine, to anchor the metallic nanoparticles to the graphene surface or organic solvents such as tetrahydrofuran, methanol, and ethylene glycol (Muszynski, Seger et al. 2008). However, the in situ synthesis of the metal nanoparticles in the presence of GO has received particular attention, since it allows the controlled growth of the nanoparticles on the graphene surface through the use of precursors of the metallic molecules that are then reduced by the addition of reducing agents and reducing GO at the same time. In this context, for the preparation of Au/graphene nanocomposites by in situ synthesis, we have shown that the presence of oxygen functional groups at GO surface are fundamental for the nucleation and growth of gold nanoparticles (Goncalves, Marques et al. 2009).

3.2.1 Gold/graphene nanocomposites

Gold was selected for its unique optical and surface properties that attract a great deal of attention because of their potential applications in catalysis, optics, and nanobiotechnology.

The synthesis of Au/graphene nanocomposites was based on the reduction of gold(III) complex by sodium citrate. Typically, 2.5 mL of a GO aqueous suspension (1.5 mg/mL) was added to 50 mL of HAuCl₄ solution (0.24 mmol dm⁻³). The resultant suspension was aged

during 30 min to promote the interaction of gold ions with the graphene surface. After that, the solution was heated until 80 °C, after which 940 μL of sodium citrate ($0.085 \text{ mol dm}^{-3}$) was added dropwise. The reaction was kept at these conditions during one hour.

The resultant nanocomposite was washed with distilled water using centrifugation (3000 rpm) to remove the free gold nanoparticles that formed in solution. The final nanocomposite was dried by lyophilization.

The SEM and TEM analysis of the resulting material shows a homogeneous distribution of gold nanoparticles at graphene surface with an average particle size of $21.3 \pm 1.8 \text{ nm}$ (Fig. 10a and b). The thin structure of the graphene sheet and smooth surface are confirmed and some corrugation is detected, suggesting a flexible structure of the graphene sheets. The dispersion of the gold nanoparticles on the 2D sheet of carbon can be visualized also in the AFM image in Fig.10c. The AFM analysis further confirms the ability to attain a uniform distribution of $\sim 20 \text{ nm}$ diameter gold nanoparticles anchored on the graphene sheets. The corrugated nature of the graphene sheets is also evident by this analysis.

The nucleation of gold nanoparticles at GO surfaces should be mainly governed by the presence of oxygen groups at GO which contribute to an overall negatively charged surface as confirmed by zeta potential measurements (see section 2.2). To study the influence of the presence of the oxygen functionalities at the GO surface we applied the previously described methodology using reduced graphene sheets. In this case almost no gold nanoparticles were detected at graphene surface.

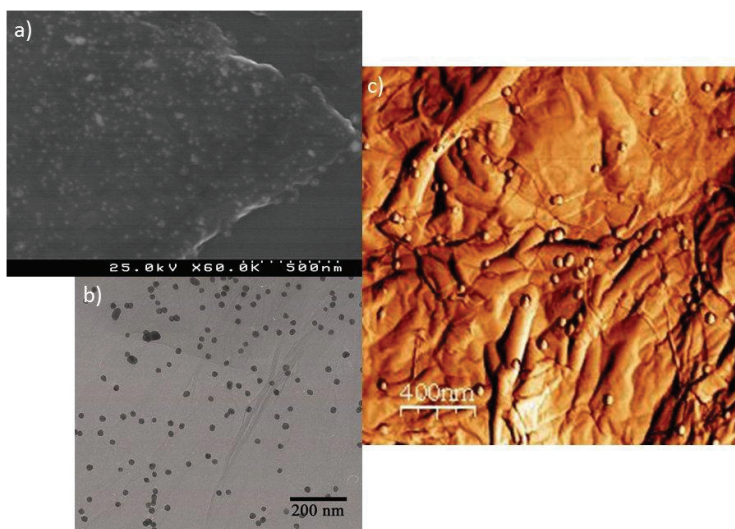


Fig. 10. a) SEM, b) TEM and c) AFM images of gold/graphene nanocomposite prepared from GO.

Although it is not possible to make a distinction between the roles of each oxygen group (carbonyl, carboxylic, or other) present at GO surface on the nucleation of Au nanoparticles, it is supposed that the overall oxygen functional groups are responsible for a previous attachment of the free gold (III) ions in solution because of electrostatic interactions. The initial step of the experimental reaction, which ages the solution containing gold ions in the

presence of graphene, has this main propose. Afterwards, the addition of the reducing agent (citrate ion) to the precursor solution promotes the subsequent reduction of gold (III) ions, enabling the growth of gold nanoparticles at the graphene surface. The scheme presented in Figure 11 illustrates the reaction steps involved in the above described process.

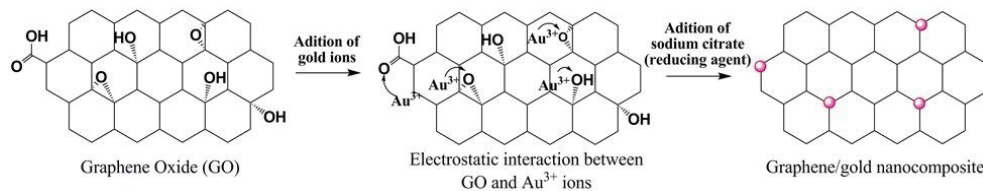


Fig. 11. Schematic representation of the possible mechanism of nucleation of gold nanoparticles at functionalized graphene surface.

3.2.2 Silver/graphene nanocomposites

Like Au nanoparticles, the Ag nanoparticles have excellent optical, electric and biological properties; in addition silver has antibacterial properties which are very important for biomedical applications.

A desire to exploit the unique association of Ag nanoparticles to graphene sheets led us to explore the synthesis of Ag nanoparticles on GO matrix. Silver nanoparticles were synthesized on the surface of GO sheet by the simultaneous reduction of Ag^+ and GO in the presence of simple reducing agent, hydrazine hydrate ($\text{N}_2\text{H}_4\cdot\text{H}_2\text{O}$). Both the Ag^+ and GO were reduced and Ag^+ was nucleated onto graphene.

Figure 12 shows the TEM image of few layers-thick graphene sheets where the nucleation of

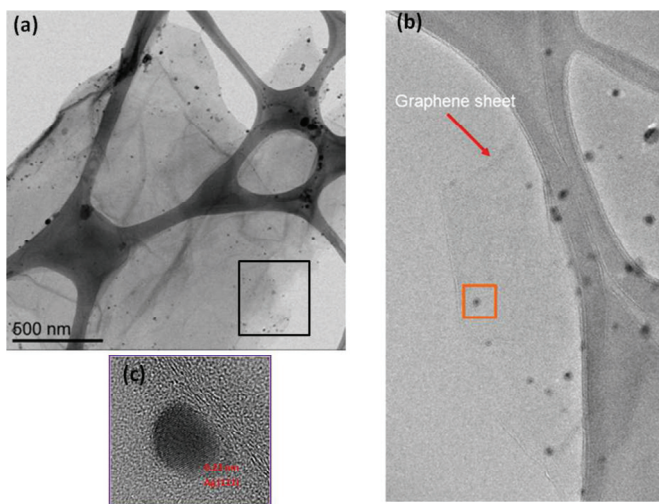


Fig. 12. (a) shows bright field TEM image of Ag/ graphene sheet (b) HRTEM image of Ag/graphene sheet performed on the area denoted by black square region (a). (c) HR TEM image of single crystal Ag nanoparticle on graphene sheet which shows the characteristic (111) plane of Ag.

Ag onto graphene is demonstrated. These results clearly exhibited (Fig.12) the ultra-thin nature of reduced graphene sheet with ripples. We have also investigated the oxygen rich sites of GO which behave as a receptor sites for Ag⁺, and integrate the Ag preventing the aggregation of Ag nanoparticles. Das et al. also demonstrated the synthesis of Ag nanoparticles (of average size 5-25 nm) in an aqueous suspension of GO for antimicrobial activity (Das, Sarma et al. 2011). The incorporation of Ag nanoparticles into the graphene sheets prevents the agglomeration of nanoparticles and privileges the nucleation over growth, this combined effect led to the good particle density and monodispersity observed in the Ag/graphene sample.

4. Applications of graphene nanocomposites

Functionalized graphene has been considered as one of the next-generation nanofillers for polymer nanocomposites due to its outstanding physical properties and low fabrication cost in comparison with that of carbon nanotubes. Improvements of mechanical, electrical and thermal properties of the resulting materials are expected. In this section we show an example of good integration of the previously modified graphene with PMMA chains in a PMMA matrix.

The association of noble metal nanoparticles to graphene sheets is still an unexplored field of research with huge potentialities. Here, we also present one example of the potentialities of Au/graphene nanocomposite as substrate for SERS analysis.

4.1 Graphene modified with PMMA as polymer matrix reinforcement

To assess the compatibility between the previously discussed GPMMA nanosheets with PMMA matrix, nanocomposite films with 0.5, 1 and 3% (w/w) of GPMMA dispersed in PMMA were prepared. PMMA films without fillers and PMMA films with 1% (w/w) of GO were also prepared for comparison. These films were prepared by solvent casting method as discussed by G. Gonçalves et al (Goncalves, Marques et al. 2010)

The mechanical behaviour of the composite films was studied by nanoindentation and uniaxial tensile tests. Figure 13a displays typical loading–unloading curves for pure PMMA

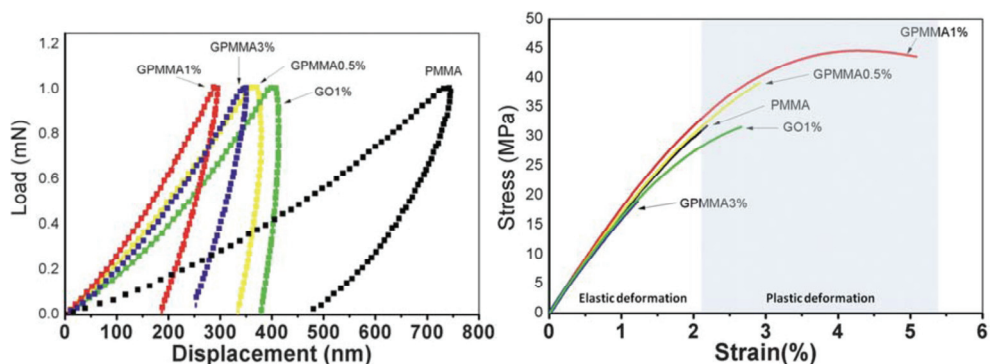


Fig. 13. a) Load-displacement nanoindentation curves of PMMA films with and without graphene fillers; b) Stress–strain dependencies of PMMA films with and without graphene fillers. (Goncalves, Marques et al. 2010) Reproduced by permission to The Royal Society of Chemistry.

films and for the films prepared using 0.5, 1 and 3% (w/w) of GPMMA and 1% of GO which shows that incorporation of fillers into the PMMA matrix increases the resistance to penetration by the nanoindenter.

For the pure PMMA film, the maximum indentation depth at the maximum load of 1.0 mN was 760 nm which was reduced to 420 nm upon addition of 1% (w/w) of GO. This reduction was even more significant for the series of films prepared with GPMMA fillers: 0.5% (w/w), maximum depth 380 nm; 3% (w/w) maximum depth 350 nm; 1% (w/w), maximum depth 290 nm. The results obtained for loads of 1% (w/w) for GO and GPMMA show that the reinforcement effect of GPMMA is significantly more effective due to the surface modification and subsequent increased adhesion with the polymer matrix.

Furthermore, the results obtained for the films prepared with GPMMA show that 1% (w/w) loading yields the stiffest nanocomposite films.

Further confirmation of the tensile properties of the composite films was conducted by performing uniaxial tensile tests. A set of five measurements on five different strips was performed on each sample for statistical accuracy. The stress-strain curves of pure PMMA films as well as for films prepared using 0.5, 1 and 3% (w/w) of GPMMA, and 1% of GO are presented in Fig.13b. At very low stresses and strains, all the samples behave as a linear elastic solid with Young's modulus varying between 18.7 MPa for pure PMMA and 21.8 MPa for films prepared with 1% (w/w) of GPMMA (the highest value obtained). Films prepared with 1% (w/w) of GPMMA also showed plastic regime characterized by average values of uniform and ultimate elongations of 4.0% and 4.8% respectively for a relatively high level of flow stress (42.0 MPa at break). For this condition, the material exhibits elasto-plastic deformation and reasonable ductility. Such mechanical improvements could be attributed to the efficient load transfer between graphene sheet and the PMMA matrix. This kind of polymer matrix could be very interesting for load bearing applications. However, increasing the concentration of GPMMA to about 3% (w/w) deteriorated the mechanical behaviour of the overall composite film. This may be due to the agglomeration of graphene sheets creating defects in the PMMA matrix composite. Concerning the films prepared with 1% GO in the PMMA matrix, the Young's modulus, tensile strength and elongation at break values determined are comparatively lower than the ones obtained for 0.5%, and 1% GPMMA in the PMMA matrix. This indicates that GO sheets do not establish appropriate interfaces with the PMMA matrix. So there might be a lack of load transfer from matrix to GO sheets which directly reflects the mechanical behaviour of the overall composite. Young's modulus and tensile strength values for the film with 1% GO are even smaller than the values obtained for PMMA film prepared without fillers. Moreover, the elongation at break for 1% GO in the PMMA matrix is 2.7%, which is slightly higher than that for pure PMMA (2.3%). This can be explained the presence of graphene sheets which are known for their elasto-plastic behaviour.

From the previous discussion it is obvious that the GO modification with PMMA via ATRP acts as a reinforcement agent of the PMMA matrix. This strategy can be further exploited to grow a large range of polymers from the GO surface only by changing the monomer, for example styrene (Fang, Wang et al. 2009; Fang, Wang et al. 2010; Lee, Dreyer et al. 2010), 2-(dimethylamine) ethyl methacrylate (DMAEMA) (Yang, Wang et al. 2009), butylacrylate (Lee, Dreyer et al. 2010; Li, Liu et al. 2010) are just some of the monomers already used. The versatility of this mechanism also allows the controlled growth of copolymers; if the free radical polymerization remains active, it will allow the growth of another polymer chain just by shifting to the desired monomer.

4.2 Nobel metal/Graphene nanocomposites as SERS substrates

Surface enhanced Raman scattering (SERS) occurs when molecules are adsorbed on nanostructured surfaces, nanoparticles, or rough electrodes of noble metals and it is one of the most powerful microanalytical techniques with single-molecule capabilities and chemical specificity. Different types of SERS substrates have been developed involving either pure or supported nanostructured metals, mostly gold and silver. SERS technique has been implemented widely by a broad scientific research community for chemical and biological sensing and measurements. This technique combines the capability of molecular fingerprinting with ultrahigh sensitivity (Liu, Cao et al. 2010). Increases in the intensity of the Raman signal have been observed by factors up to 10^6 , reaching in particular cases the single-molecule detection level. This remarkable enhancement provides high sensitivity and gives an opportunity for the development of ultrasensitive analytical methods for chemical and biochemical detection (Alvarez-Puebla and Liz-Marzan 2010). Numerous applications have demonstrated the potential of SERS for the label-free detection of various analytes. More recently, SERS is increasingly used as a readout method for the selective and sensitive detection of proteins and oligonucleotides. (Schlucker 2009) For SERS it is critical to have a good substrate to obtain a good enhancement. The development and use of highly reproducible substrates is critical in the advancement of SERS as a mainstream spectroscopic technique. This is particularly important in studies of large, complex molecules such as DNA or proteins, because the SERS signal in these molecules already depends significantly on molecular conformation, orientation, and binding specificity to the substrate surface (Barhoumi, Zhang et al. 2008).

Traditionally, the SERS substrate is based on a rough surface of a noble metal such as Ag, Au, Cu, and so on. To make a rough metal surface for SERS, relatively complex methods are used like electrochemical ways by successive oxidation-reduction cycles, depositing a thin film using vacuum evaporation methods, nanosphere lithography with the assistance of micro-nano-fabrication techniques, etc. No matter which method is used, the fabrication process is difficult to control, reproduce, or keep clean, which leads to the low activity of SERS. Also, the enhanced efficiency is often quite different for different metals. Silver is thought to be the best one, but it is expensive and easily oxidized, which will decrease the enhanced efficiency. Besides, metals usually have a bad biological compatibility. Therefore, it is necessary to develop new substrates for Raman enhancement. A material that meets the requirements of being inexpensive and easy to obtain, effective and can be used directly, chemically inert, and biocompatible should be exploited.

Graphene is a very promising material for the use as a SERS substrate. Graphene itself was recently reported by Ling X et al, to induce a clear Raman enhancement effect on adsorbed molecules. (Ling, Xie et al. 2010) From the data presented by these authors, much stronger Raman signals of the molecules on graphene compared with those on the SiO₂/Si substrate were obtained, and the appearance of the Raman signals for molecules on graphene when soaking in solutions with very low concentrations clearly suggests that a Raman enhancement effect exists on the surface of graphene. As a result of the Raman enhancement on the surface of graphene, it is possible to obtain the Raman signals from very few molecules. This enhancement was attributed to the charge transfer between graphene and the molecules, which result in a chemical enhancement.

More recently, Yu X. et al (Yu, Cai et al. 2011) showed that mildly reduced GO (MR-GO) nanosheets can significantly increase the chemical enhancement of the main peaks by up to

1 order of magnitude for adsorbed Rhodamine B (tested molecule), in comparison to mechanical exfoliated graphene. The observed enhancement factors can be as large as $\sim 10^3$ and show clear dependence on the reduction time of GO, indicating that the chemical enhancement can be steadily controlled by specific chemical groups. It was shown that the highly electronegative oxygen species, which can introduce a strong local electric field on the adsorbed molecules, are responsible for the large enhancement. In contrast, the local defects generated by the chemical reduction show no positive correlation with the enhancement. Most importantly, the dramatically enhanced Raman spectra of RhB molecules on MR-GO nanosheets reproduce all important spectral fingerprints of the molecule with a negligible frequency shift. Such a unique noninvasive feature, along with the other intrinsic advantages, such as low cost, light weight, easy availability, and flexibility, makes the MR-GO nanosheets very attractive for a variety of practical applications.

Our research team has shown that graphene/gold nanocomposites prepared by in situ growth of gold nanoparticles in the presence of GO sheets are potential substrates for SERS in particular for single gold nanoparticle SERS studies (Goncalves, Marques et al. 2009). The combination of gold nanoparticles and graphene may confer a unique electron or energy transfer mechanism between both phases that allows the SERS observation. Lately other groups have also referred to the potential of using gold, palladium and silver nanoparticles associated with graphene as SERS substrates. (Wang, Ni et al. 2010) These studies highlight the importance of the development and study of possible applications of these nanocomposites as optical nanosensors.

We have tested the potential application of the gold/graphene nanocomposite as substrate for SERS. SERS was tested for Rhodamine 6G (R6G) using a laser source of 1064 nm. Figure 14 shows the Raman spectrum obtained for R6G adsorbed at the surface of the Au/graphene nanocomposite, together with the one obtained for R6G adsorbed at a single graphene surface, the Raman spectrum of solid R6G is also presented for comparison. The Raman spectrum of R6G adsorbed at a single graphene substrate (GO in Fig. 14) shows only a large broadband in the 1600-1300 cm^{-1} region, composed by the so-called G and D peaks of graphene. A good SERS signal was obtained for R6G adsorbed at gold/graphene nanocomposite (GAu in Fig. 14)

The SERS spectrum (GAu in Fig. 14) shows a selective enhancement of bands when compared to the Raman of solid R6G. The SERS signals observed at 1308, 1360, and 1504 cm^{-1} are assigned to the aromatic C-C stretching vibrations of R6G molecule, according to literature reports on the SERS of R6G. The SERS spectrum obtained for R6G in the graphene/gold nanocomposite (in the range 1300-1550 cm^{-1}) is similar to the R6G SERS spectra found in the literature using different types of gold substrates such as gold nanochains, gold-coated 3D ordered colloidal crystal films, Au-coated ZnO nanorods, or mechanically ruptured nanoporous gold (Goncalves, Marques et al. 2009).

At present, the evaluation of the detection limits is being conducted.

5. Outlook and challenges

Within a short time of being available in bulk quantities, graphene oxide have become highly versatile, inexpensive building blocks for the development of several advanced materials with applications having as the limit only the imagination.

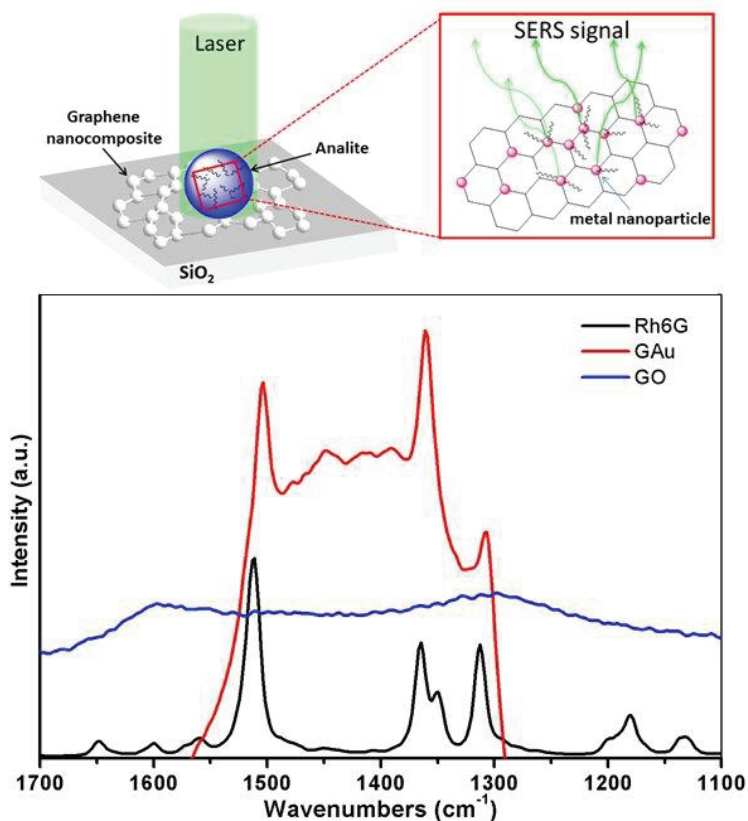


Fig. 14. SERS spectrum of Rh6G adsorbed at the surface of Au/graphene nanocomposite (GAu) and Raman spectra of Rh6G adsorbed at a single graphene sheet (GO) and of solid Rh6G (Rh6G). The inset shows a schematic representation of the SERS phenomena. Reprinted (adapted) with permission from (Goncalves, Marques et al. 2009) Copyright 2011 American Chemical Society.

Current results have indicated that GO is an interesting platform to build different nanocomposites with very promising properties for different areas of application. The above mentioned outstanding properties of GO inspired us to explore the potential of multi-functional GO based materials. The future development of GO based nanocomposites that may function as SERS substrates of high activity and investigation of the SERS active nanocomposites as probes for biodetection is one of our goals. It is our aim to increase the knowledge that concerns the chemistry required for graphene/gold and silver nanoparticles applied to the preparation of SERS active substrates. It is predictable to modulate the surface of the nanocomposites in order to make them specific to a given molecule and, in this way, contribute to the development of manageable SERS sensors for the selective detection of biomolecules in targeted research.

We have shown the importance of the previous surface modification of graphene with PMMA chains in order to improve its dispersion in the polymer matrix. The organic

functionalization of GO is special relevant for its interaction with polymers. The suitable modification of the nano-filler by the careful control of the atomic surface chemistry can generate a perfect integration of all components on polymeric matrixes. This allows the combination between the reinforcements and the polymeric matrices to develop multifunctional materials with increased electrical, thermal, mechanical properties or reduction of the penetration of gases. However some challenges remain in order to scale up the synthesis of these modified fillers in order to find real application of the resulting materials. One interesting area of research that we are developing uses graphene fillers as mechanical reinforcement of PMMA based bone cements since GO is also biocompatible.

To achieve these goals it is of fundamental importance to control the synthesis of GO sheets and develop adequate methods to modify their surface in order to tune its properties for the desired applications.

6. Acknowledgments

The authors P. A. A. P. Marques and M. K. Singh would like to thank the Ciência Program, FCT. G. Gonçallves thanks the PhD grant from INL (International Iberian Nanotechnology Laboratory). Sandra Cruz and Nuno Almeida thanks FCT for the PhD grants, respectively SFRH/BD/68598/2010 and SFRH/BD/70300/2010.

We also thank the facility RNME - Pole University of Aveiro, FCT Project REDE/1509/RME/2005.

7. References

- Acik, M., Lee, G., Mattevi, C., Chhowalla, M., Cho, K. and Chabal, Y. J. (2010). Unusual infrared-absorption mechanism in thermally reduced graphene oxide. *Nat Mater*, Vol.9, No.10: pp.840-845,ISSN 1476-1122
- Allen, M. J., Tung, V. C. and Kaner, R. B. (2010). Honeycomb Carbon: A Review of Graphene. *Chemical Reviews*, Vol.110, No.1: pp.132-145,ISSN 0009-2665
- Alvarez-Puebla, R. A. and Liz-Marzan, L. M. (2010). SERS-based diagnosis and biodetection. *Small*, Vol.6, No.5: pp.604-610,ISSN
- Barhoumi, A., Zhang, D., Tam, F. and Halas, N. J. (2008). Surface-Enhanced Raman Spectroscopy of DNA. *Journal of the American Chemical Society*, Vol.130, No.16: pp.5523-5529,ISSN 0002-7863
- Boehm, H.-P. (2010). Graphene—How a Laboratory Curiosity Suddenly Became Extremely Interesting. *Angewandte Chemie International Edition*, Vol.49, No.49: pp.9332-9335,ISSN 1521-3773
- Brodie, B. (1860). Sur le poids atomique du graphite. *Ann Chem Phys*, No.59: pp.466-472,ISSN
- Das, M. R., Sarma, R. K., Saikia, R., Kale, V. S., Shelke, M. V. and Sengupta, P. (2011). Synthesis of silver nanoparticles in an aqueous suspension of graphene oxide sheets and its antimicrobial activity. *Colloids and Surfaces B: Biointerfaces*, Vol.83, No.1: pp.16-22,ISSN 0927-7765
- Dreyer, D. R., Park, S., Bielawski, C. W. and Ruoff, R. S. (2010). The chemistry of graphene oxide. *Chemical Society Reviews*, Vol.39, No.1: pp.228-240,ISSN 0306-0012
- Fang, M., Wang, K. G., Lu, H. B., Yang, Y. L. and Nutt, S. (2009). Covalent polymer functionalization of graphene nanosheets and mechanical properties of composites. *Journal of Materials Chemistry*, Vol.19, No.38: pp.7098-7105,ISSN 0959-9428

- Fang, M., Wang, K. G., Lu, H. B., Yang, Y. L. and Nutt, S. (2010). Single-layer graphene nanosheets with controlled grafting of polymer chains. *Journal of Materials Chemistry*, Vol.20, No.10: pp.1982-1992,ISSN 0959-9428
- Gilje, S., Han, S., Wang, M., Wang, K. L. and Kaner, R. B. (2007). A chemical route to graphene for device applications. *Nano Letters*, Vol.7, No.11: pp.3394-3398,ISSN 1530-6984
- Goncalves, G., Marques, P., Barros-Timmons, A., Bdkin, I., Singh, M. K., Emami, N. and Gracio, J. (2010). Graphene oxide modified with PMMA via ATRP as a reinforcement filler. *Journal of Materials Chemistry*, Vol.20, No.44: pp.9927-9934,ISSN 0959-9428
- Goncalves, G., Marques, P., Granadeiro, C. M., Nogueira, H. I. S., Singh, M. K. and Gracio, J. (2009). Surface Modification of Graphene Nanosheets with Gold Nanoparticles: The Role of Oxygen Moieties at Graphene Surface on Gold Nucleation and Growth. *Chemistry of Materials*, Vol.21, No.20: pp.4796-4802,ISSN 0897-4756
- Hao, R., Qian, W., Zhang, L. H. and Hou, Y. L. (2008). Aqueous dispersions of TCNQ-anion-stabilized graphene sheets. *Chemical Communications*, No.48: pp.6576-6578,ISSN 1359-7345
- Hasin, P., Alpuche-Aviles, M. A. and Wu, Y. Y. (2010). Electrocatalytic Activity of Graphene Multi layers toward I-/I³⁻(-): Effect of Preparation Conditions and Polyelectrolyte Modification. *Journal of Physical Chemistry C*, Vol.114, No.37: pp.15857-15861,ISSN 1932-7447
- Hassan, H. M. A., Abdelsayed, V., Khder, A. E. R. S., AbouZeid, K. M., Ternier, J., El-Shall, M. S., Al-Resayes, S. I. and El-Azhary, A. A. (2009). Microwave synthesis of graphene sheets supporting metal nanocrystals in aqueous and organic media. *Journal of Materials Chemistry*, Vol.19, No.23: pp.3832-3837,ISSN 0959-9428
- Hodes, G. (2007). When Small Is Different: Some Recent Advances in Concepts and Applications of Nanoscale Phenomena. *Advanced Materials*, Vol.19, No.5: pp.639-655,ISSN 1521-4095
- Hong, W., Bai, H., Xu, Y., Yao, Z., Gu, Z. and Shi, G. (2010). Preparation of Gold Nanoparticle/Graphene Composites with Controlled Weight Contents and Their Application in Biosensors. *The Journal of Physical Chemistry C*, Vol.114, No.4: pp.1822-1826,ISSN 1932-7447
- Hou, S. F., Su, S. J., Kasner, M. L., Shah, P., Patel, K. and Madarang, C. J. (2010). Formation of highly stable dispersions of silane-functionalized reduced graphene oxide. *Chemical Physics Letters*, Vol.501, No.1-3: pp.68-74,ISSN 0009-2614
- Hu, H. T., Wang, X. B., Wang, J. C., Wan, L., Liu, F. M., Zheng, H., Chen, R. and Xu, C. H. (2010). Preparation and properties of graphene nanosheets-polystyrene nanocomposites via in situ emulsion polymerization. *Chemical Physics Letters*, Vol.484, No.4-6: pp.247-253,ISSN 0009-2614
- Hummers, W. S. and Offeman, R. E. (1958). PREPARATION OF GRAPHITIC OXIDE. *Journal of the American Chemical Society*, Vol.80, No.6: pp.1339-1339,ISSN 0002-7863
- Husale, S., Sahoo, S., Radenovic, A., Traversi, F., Annibale, P. and Kis, A. (2010). ssDNA Binding Reveals the Atomic Structure of Graphene. *Langmuir*, Vol.26, No.23: pp.18078-18082,ISSN 0743-7463
- Janowska, I., Ersen, O., Jacob, T., Vennégues, P., Bégin, D., Ledoux, M.-J. and Pham-Huu, C. (2009). Catalytic unzipping of carbon nanotubes to few-layer graphene sheets

- under microwaves irradiation. *Applied Catalysis A: General*, Vol.371: pp.22-30,ISSN 0926-860X
- Kamat, P. V. (2009). Graphene-Based Nanoarchitectures. Anchoring Semiconductor and Metal Nanoparticles on a Two-Dimensional Carbon Support. *The Journal of Physical Chemistry Letters*, Vol.1, No.2: pp.520-527,ISSN 1948-7185
- Karousis, N., Economopoulos, S. P., Sarantopoulou, E. and Tagmatarchis, N. (2010). Porphyrin counter anion in imidazolium-modified graphene-oxide. *Carbon*, Vol.48, No.3: pp.854-860,ISSN 0008-6223
- Laaksonen, P., Kainlauri, M., Laaksonen, T., Shchepetov, A., Jiang, H., Ahopelto, J. and Linder, M. B. (2010). Interfacial Engineering by Proteins: Exfoliation and Functionalization of Graphene by Hydrophobins. *Angewandte Chemie-International Edition*, Vol.49, No.29: pp.4946-4949,ISSN 1433-7851
- Lee, S. H., Dreyer, D. R., An, J. H., Velamakanni, A., Piner, R. D., Park, S., Zhu, Y. W., Kim, S. O., Bielawski, C. W. and Ruoff, R. S. (2010). Polymer Brushes via Controlled, Surface-Initiated Atom Transfer Radical Polymerization (ATRP) from Graphene Oxide. *Macromolecular Rapid Communications*, Vol.31, No.3: pp.281-288,ISSN 1022-1336
- Li, G. L., Liu, G., Li, M., Wan, D., Neoh, K. G. and Kang, E. T. (2010). Organo- and Water-Dispersible Graphene Oxide-Polymer Nanosheets for Organic Electronic Memory and Gold Nanocomposites. *Journal of Physical Chemistry C*, Vol.114, No.29: pp.12742-12748,ISSN 1932-7447
- Liang, Y. Y., Wu, D. Q., Feng, X. L. and Mullen, K. (2009). Dispersion of Graphene Sheets in Organic Solvent Supported by Ionic Interactions. *Advanced Materials*, Vol.21, No.17: pp.1679-+,ISSN 0935-9648
- Ling, X., Xie, L., Fang, Y., Xu, H., Zhang, H., Kong, J., Dresselhaus, M. S., Zhang, J. and Liu, Z. (2010). Can graphene be used as a substrate for Raman enhancement? *Nano Letters*, Vol.10, No.2: pp.553-561,ISSN
- Liu, F., Cao, Z., Tang, C., Chen, L. and Wang, Z. (2010). Ultrathin diamond-like carbon film coated silver nanoparticles-based substrates for surface-enhanced Raman spectroscopy. *ACS Nano*, Vol.4, No.5: pp.2643-2648,ISSN
- Liu, J. Q., Tao, L., Yang, W. R., Li, D., Boyer, C., Wuhler, R., Braet, F. and Davis, T. P. (2010). Synthesis, Characterization, and Multilayer Assembly of pH Sensitive Graphene-Polymer Nanocomposites. *Langmuir*, Vol.26, No.12: pp.10068-10075,ISSN 0743-7463
- Liu, J. Q., Yang, W. R., Tao, L., Li, D., Boyer, C. and Davis, T. P. (2010). Thermosensitive Graphene Nanocomposites Formed Using Pyrene-Terminal Polymers Made by RAFT Polymerization. *Journal of Polymer Science Part a-Polymer Chemistry*, Vol.48, No.2: pp.425-433,ISSN 0887-624X
- Liu, Z., Robinson, J. T., Sun, X. M. and Dai, H. J. (2008). PEGylated nanographene oxide for delivery of water-insoluble cancer drugs. *Journal of the American Chemical Society*, Vol.130, No.33: pp.10876-+,ISSN 0002-7863
- Liu, Z. B., Xu, Y. F., Zhang, X. Y., Zhang, X. L., Chen, Y. S. and Tian, J. G. (2009). Porphyrin and Fullerene Covalently Functionalized Graphene Hybrid Materials with Large Nonlinear Optical Properties. *Journal of Physical Chemistry B*, Vol.113, No.29: pp.9681-9686,ISSN 1520-6106
- Loh, K. P., Bao, Q. L., Ang, P. K. and Yang, J. X. (2010). The chemistry of graphene. *Journal of Materials Chemistry*, Vol.20, No.12: pp.2277-2289,ISSN 0959-9428

- Lotya, M., Hernandez, Y., King, P. J., Smith, R. J., Nicolosi, V., Karlsson, L. S., Blighe, F. M., De, S., Wang, Z., McGovern, I. T., Duesberg, G. S. and Coleman, J. N. (2009). Liquid Phase Production of Graphene by Exfoliation of Graphite in Surfactant/Water Solutions. *Journal of the American Chemical Society*, Vol.131, No.10: pp.3611-3620,ISSN 0002-7863
- Lu, C. H., Yang, H. H., Zhu, C. L., Chen, X. and Chen, G. N. (2009). A Graphene Platform for Sensing Biomolecules. *Angewandte Chemie-International Edition*, Vol.48, No.26: pp.4785-4787,ISSN 1433-7851
- Luo, Z., Lu, Y., Somers, L. A. and Johnson, A. T. C. (2009). High Yield Preparation of Macroscopic Graphene Oxide Membranes. *Journal of the American Chemical Society*, Vol.131, No.3: pp.898-899,ISSN 0002-7863
- Melucci, M., Treossi, E., Ortolani, L., Giambastiani, G., Morandi, V., Klar, P., Casiraghi, C., Samori, P. and Palermo, V. (2010). Facile covalent functionalization of graphene oxide using microwaves: bottom-up development of functional graphitic materials. *Journal of Materials Chemistry*, Vol.20, No.41: pp.9052-9060,ISSN 0959-9428
- Mohanty, N. and Berry, V. (2008). Graphene-Based Single-Bacterium Resolution Biodevice and DNA Transistor: Interfacing Graphene Derivatives with Nanoscale and Microscale Biocomponents. *Nano Letters*, Vol.8, No.12: pp.4469-4476,ISSN 1530-6984
- Muszynski, R., Seger, B. and Kamat, P. V. (2008). Decorating Graphene Sheets with Gold Nanoparticles. *The Journal of Physical Chemistry C*, Vol.112, No.14: pp.5263-5266,ISSN 1932-7447
- Niyogi, S., Bekyarova, E., Itkis, M. E., McWilliams, J. L., Hamon, M. A. and Haddon, R. C. (2006). Solution properties of graphite and graphene. *Journal of the American Chemical Society*, Vol.128, No.24: pp.7720-7721,ISSN 0002-7863
- Novoselov, K. S., Geim, A. K., Morozov, S. V., Jiang, D., Zhang, Y., Dubonos, S. V., Grigorieva, I. V. and Firsov, A. A. (2004). Electric field effect in atomically thin carbon films. *Science*, Vol.306, No.5296: pp.666-669,ISSN 0036-8075
- Paredes, J. I., Villar-Rodil, S., Martinez-Alonso, A. and Tascon, J. M. D. (2008). Graphene oxide dispersions in organic solvents. *Langmuir*, Vol.24, No.19: pp.10560-10564,ISSN 0743-7463
- Park, S., An, J. H., Jung, I. W., Piner, R. D., An, S. J., Li, X. S., Velamakanni, A. and Ruoff, R. S. (2009). Colloidal Suspensions of Highly Reduced Graphene Oxide in a Wide Variety of Organic Solvents. *Nano Letters*, Vol.9, No.4: pp.1593-1597,ISSN 1530-6984
- Patil, A. J., Vickery, J. L., Scott, T. B. and Mann, S. (2009). Aqueous Stabilization and Self-Assembly of Graphene Sheets into Layered Bio-Nanocomposites using DNA. *Advanced Materials*, Vol.21, No.31: pp.3159-+,ISSN 0935-9648
- Qi, X. Y., Pu, K. Y., Zhou, X. Z., Li, H., Liu, B., Boey, F., Huang, W. and Zhang, H. (2010). Conjugated-Polyelectrolyte-Functionalized Reduced Graphene Oxide with Excellent Solubility and Stability in Polar Solvents. *Small*, Vol.6, No.5: pp.663-669,ISSN 1613-6810
- Rao, C. N. R., Biswas, K., Subrahmanyam, K. S. and Govindaraj, A. (2009). Graphene, the new nanocarbon. *Journal of Materials Chemistry*, Vol.19, No.17: pp.2457-2469,ISSN 0959-9428
- Scheuermann, G. M., Rumi, L., Steurer, P., Bannwarth, W. and Mühlaupt, R. (2009). Palladium Nanoparticles on Graphite Oxide and Its Functionalized Graphene Derivatives as Highly Active Catalysts for the Suzuki–Miyaura Coupling Reaction.

- Journal of the American Chemical Society*, Vol.131, No.23: pp.8262-8270,ISSN 0002-7863
- Schlucker, S. (2009). SERS microscopy: nanoparticle probes and biomedical applications. *Chemphyschem*, Vol.10, No.9-10: pp.1344-1354,ISSN
- Shen, J., Shi, M., Li, N., Yan, B., Ma, H., Hu, Y. and Ye, M. (2010). Facile synthesis and application of Ag-chemically converted graphene nanocomposite. *Nano Research*, Vol.3, No.5: pp.339-349,ISSN 1998-0124
- Si, Y. and Samulski, E. T. (2008). Exfoliated Graphene Separated by Platinum Nanoparticles. *Chemistry of Materials*, Vol.20, No.21: pp.6792-6797,ISSN 0897-4756
- Singh, S. K., Singh, M. K., Nayak, M. K., Kumari, S., Grácio, J. J. A. and Dash, D. (2011). Size distribution analysis and physical/fluorescence characterization of graphene oxide sheets by flow cytometry. *Carbon*, Vol.49, No.2: pp.684-692,ISSN 0008-6223
- Singh, V., Joung, D., Zhai, L., Das, S., Khondaker, S. I. and Seal, S. (In Press). Graphene Based Materials: Past, Present and Future. *Progress in Materials Science*, Vol.In Press, Accepted Manuscript,ISSN 0079-6425
- Soldano C., Mahmood and E., D. (2010). Production, properties and potential of graphene. *Carbon*, Vol.48, No.8: pp.2127-2150,ISSN 0008-6223
- Stankovich, S., Dikin, D. A., Dommett, G. H. B., Kohlhaas, K. M., Zimney, E. J., Stach, E. A., Piner, R. D., Nguyen, S. T. and Ruoff, R. S. (2006). Graphene-based composite materials. *Nature*, Vol.442, No.7100: pp.282-286,ISSN 0028-0836
- Stankovich, S., Piner, R. D., Nguyen, S. T. and Ruoff, R. S. (2006). Synthesis and exfoliation of isocyanate-treated graphene oxide nanoplatelets. *Carbon*, Vol.44, No.15: pp.3342-3347,ISSN 0008-6223
- Staudenmaier, L. (1898). Verfahren zur Darstellung der Graphitsäure. *Berichte der deutschen chemischen Gesellschaft*, Vol.31, No.2: pp.1481-1487,ISSN 1099-0682
- Tian, L. L., Mezziani, M. J., Lu, F. S., Kong, C. Y., Cao, L., Thorne, T. J. and Sun, Y. P. (2010). Graphene Oxides for Homogeneous Dispersion of Carbon Nanotubes. *Acs Applied Materials & Interfaces*, Vol.2, No.11: pp.3217-3222,ISSN 1944-8244
- Ushio S, Arata Yoshii, Naoto Tamai, Noboru Ohtani and Kaneko, T. (2011). Wide-range temperature dependence of epitaxial graphene growth on 4H-SiC (0 0 0 -1): A study of ridge structures formation dynamics associated with temperature. *Journal of Crystal Growth*, Vol.318, No.1: pp.590-594
- Veca, L. M., Lu, F. S., Mezziani, M. J., Cao, L., Zhang, P. Y., Qi, G., Qu, L. W., Shrestha, M. and Sun, Y. P. (2009). Polymer functionalization and solubilization of carbon nanosheets. *Chemical Communications*, No.18: pp.2565-2567,ISSN 1359-7345
- Wang, H., Robinson, J. T., Li, X. and Dai, H. (2009). Solvothermal Reduction of Chemically Exfoliated Graphene Sheets. *Journal of the American Chemical Society*, Vol.131, No.29: pp.9910-9911,ISSN 0002-7863
- Wang, S., Chia, P. J., Chua, L. L., Zhao, L. H., Png, R. Q., Sivaramakrishnan, S., Zhou, M., Goh, R. G. S., Friend, R. H., Wee, A. T. S. and Ho, P. K. H. (2008). Band-like transport in surface-functionalized highly solution-processable graphene nanosheets. *Advanced Materials*, Vol.20, No.18: pp.3440+,ISSN 0935-9648
- Wang, Y., Ni, Z., Hu, H., Hao, Y., Wong, C. P., Yu, T., Thong, J. T. L. and Shen, Z. X. (2010). Gold on graphene as a substrate for surface enhanced Raman scattering study. *Applied Physics Letters*, Vol.97, No.16: pp.163111,ISSN

- Wu, P., Shao, Q. A., Hu, Y. J., Jin, J. A., Yin, Y. J., Zhang, H. and Cai, C. X. (2010). Direct electrochemistry of glucose oxidase assembled on graphene and application to glucose detection. *Electrochimica Acta*, Vol.55, No.28: pp.8606-8614,ISSN 0013-4686
- Xu, Y. X., Bai, H., Lu, G. W., Li, C. and Shi, G. Q. (2008). Flexible graphene films via the filtration of water-soluble noncovalent functionalized graphene sheets. *Journal of the American Chemical Society*, Vol.130, No.18: pp.5856+,ISSN 0002-7863
- Yang, H. F., Li, F. H., Shan, C. S., Han, D. X., Zhang, Q. X., Niu, L. and Ivaska, A. (2009). Covalent functionalization of chemically converted graphene sheets via silane and its reinforcement. *Journal of Materials Chemistry*, Vol.19, No.26: pp.4632-4638,ISSN 0959-9428
- Yang, H. F., Shan, C. S., Li, F. H., Han, D. X., Zhang, Q. X. and Niu, L. (2009). Covalent functionalization of polydisperse chemically-converted graphene sheets with amine-terminated ionic liquid. *Chemical Communications*, No.26: pp.3880-3882,ISSN 1359-7345
- Yang, Y. F., Wang, J., Zhang, J., Liu, J. C., Yang, X. L. and Zhao, H. Y. (2009). Exfoliated Graphite Oxide Decorated by PDMAEMA Chains and Polymer Particles. *Langmuir*, Vol.25, No.19: pp.11808-11814,ISSN 0743-7463
- Yu, X., Cai, H., Zhang, W., Li, X., Pan, N., Luo, Y., Wang, X. and Hou, J. G. (2011). Tuning Chemical Enhancement of SERS by Controlling the Chemical Reduction of Graphene Oxide Nanosheets. *ACS Nano*: pp.null-null,ISSN 1936-0851
- Zhang, X., Huang, Y., Wang, Y., Ma, Y., Liu, Z. and Chen, Y. (2009). Synthesis and characterization of a graphene-C60 hybrid material. *Carbon*, Vol.47, No.1: pp.334-337,ISSN 0008-6223
- Zhao, L., Rim, K. T., Zhou, H., He, R., Heinz, T. F., Pinczuk, A., Flynn, G. W. and Pasupathy, A. N. (2011). Influence of copper crystal surface on the CVD growth of large area monolayer graphene. *Solid State Communications*, Vol.151, No.7: pp.509-513,ISSN 0038-1098
- Zhuang, X. D., Chen, Y., Liu, G., Li, P. P., Zhu, C. X., Kang, E. T., Neoh, K. G., Zhang, B., Zhu, J. H. and Li, Y. X. (2010). Conjugated-Polymer-Functionalized Graphene Oxide: Synthesis and Nonvolatile Rewritable Memory Effect. *Advanced Materials*, Vol.22, No.15: pp.1731+,ISSN 0935-9648

Part 3

Human and Bioapplications

Biofunctional Composites of Polysaccharides Containing Inorganic Nanoparticles

Ana L. Daniel-da-Silva and Tito Trindade
*Department of Chemistry and CICECO, University of Aveiro
Portugal*

1. Introduction

In the last years, a variety of biopolymers have been investigated as soft matrices to accommodate inorganic nanoparticles (Darder et al., 2007; Dias et al., 2011). Innovation in Nanomedicine has been a major driving force to create new bionanocomposites because these materials bring together the intrinsic functionalities of inorganic nanoparticles and the biointerfaces offered by polymers of natural origin. On one hand, this type of hybrid materials can be designed to perform a specific function, depending on the characteristics of the loaded inorganic nanoparticles and, on the other hand, the composite can be easily adapted to biosystems due to the potential biocompatibility and low-toxicity of the biopolymer matrix.

In view of the large number of available polymers to produce such bionanocomposites this chapter has focus on the use of polysaccharides derived from natural sources, i.e. polymeric carbohydrate structures, that have been intensely investigated in the context of bio-applications. As such, cellulose, that together with lignin forms the ubiquitous composite wood, will be only briefly mentioned in specific contexts. Since synthesis conditions play a determinant role in the performance of the final materials, the chemical strategies for the production of bulk and nanodispersed bionanocomposites will be reviewed. Depending on the type of envisaged bioapplication, aspects related to the performance of the polysaccharide will be highlighted. These include relevant biochemical interactions with the surroundings and, the biofunctionality of the nanocomposite that results from the conjugated action of both the biopolymer and the inorganic nanofillers.

Recent years have witnessed the implementation of new therapeutics, clinical diagnostic techniques and disease preventive strategies that directly emerge from Nanotechnology (Sakamoto et al., 2010; Seigneuric et al., 2010). Therefore this chapter concludes with illustrative examples of bionanocomposites whose properties are of great interest in bio-applications such as magnetic nanocarriers for drug delivery and antimicrobial composites based on nanometals. As a final note, the challenging field comprising the development of multifunctional bionanocomposites will be put in perspective.

2. Relevant properties of polysaccharides for bio-applications

The polysaccharides most commonly used for preparing bionanocomposites are summarized in Table 1 and Fig. 1. They can be classified according to their ionic character

(neutral, anionic, cationic) and they bring different properties and chemical functionalities to the nanocomposites. The polysaccharides indicated in Table 1 derive from natural sources, hence presenting advantages in terms of biodegradability, low-toxicity and low cost. An exhaustive description of the properties of the polysaccharides is out of the scope of this chapter and can be found in the references included in Table 1.

Ionic character	Polysaccharide	Source	Functional Groups	Reference
Neutral	Agarose	Marine red algae	OH	(Nijenhuis, 1997)
	Dextran	Produced by lactic acid bacteria	OH	(Heinze et al., 2006)
	Pullulan	Produced by yeast-like fungus	OH	(Singh et al., 2008)
	Starch	Green plants	OH	(Le Corre et al., 2010)
Anionic	Alginate	Brown algae	OH, COO ⁻	(Augst et al., 2006)
	Carrageenans	Red seaweeds	OH, OSO ₃ ⁻	(Campo et al., 2009)
	Gum Arabic	Acacia trees	OH, COO ⁻	(Ali et al., 2009)
	Heparin	Animal tissues	OH, OSO ₃ ⁻	(Rabenstein, 2002)
	Hyaluronan	Animal tissues	OH, COO ⁻	(Gaffney et al., 2010)
Cationic	Chitosan	Shellfish and fungi cell wall	OH, NH ₃ ⁺	(Rinaudo, 2006)

Table 1. Polysaccharides commonly used in the preparation of bionanocomposites.

Polysaccharides have been used as composite matrices due to several characteristics of relevance for biological and medical applications, namely:

i. Biocompatibility

Polysaccharides are very often incorporated into nanocomposites aiming to improve their biocompatibility, namely because they are hydrophilic, and administered in approved conditions, are non-toxic. For example, the intravenous administration of less biocompatible nanoparticles may elicit a response from the immune system that results in their uptake by macrophages, rendering them useless. Heparin, a polysaccharide with anticoagulant properties, has shown to be effective as a coating agent to increase the biocompatibility of several materials (Kemp & Linhardt, 2010) including carbon nanotubes (Murugesan et al., 2006) and metal nanoparticles (Kemp et al., 2010). Also dextran and carboxydextran coated magnetite nanoparticles have been commercialized as contrast agents for magnetic resonance imaging of liver tumors. Other nanocomposite systems are currently under clinical investigations (Corot et al., 2006).

ii. Biofunctionalization

Polysaccharides have specific functional chemical groups in their structure (Table 1) and as such they can serve as a springboard for the creation of multimodal and multifunctional systems through the addition of reactive and bioactive groups at the composites surface,

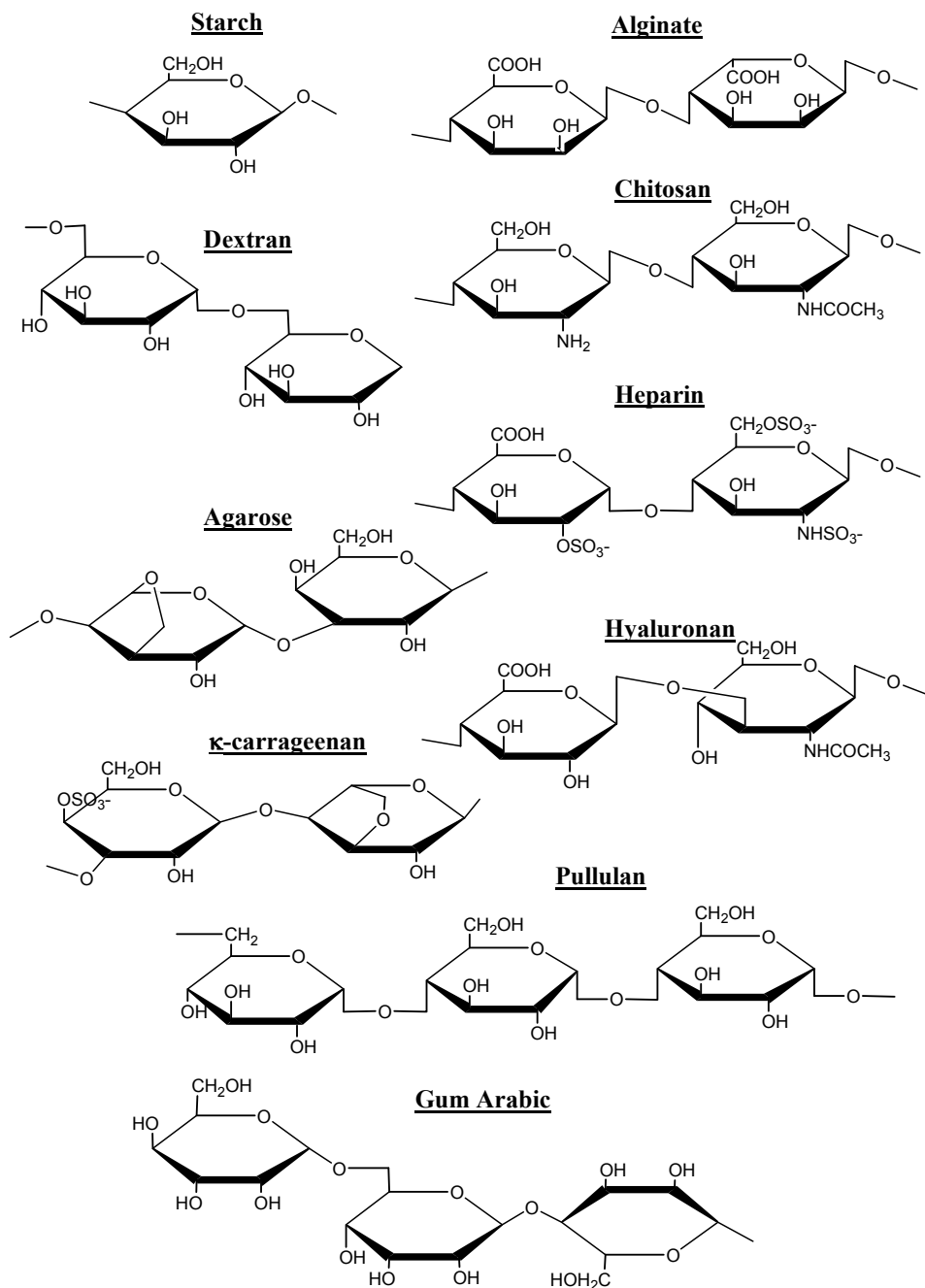


Fig. 1. Chemical structures of polysaccharides commonly employed in the preparation of nanocomposites for biomedical applications.

which further augments the range of applications. For example, hydrogels of κ -carrageenan containing magnetic nanoparticles were chemically modified by carboxymethylation of the polymer chains and further coupled to an antibody envisaging applications as targeted local nanodelivery system (Daniel-da-Silva et al., 2009).

iii. Sensitivity to external stimuli

Overall polysaccharides form gels that respond to physiological changes in temperature and pH or even to mechanical stress. This property has been explored in the preparation of composite systems for remotely triggered applications including bioadhesives and drug delivery, amongst others. Chitosan for instance, due to its excellent biocompatibility and mechanical properties (it forms films with high mechanical strength and elasticity) is a very attractive polysaccharide for applications such as wound dressing and tissue repair. Very recently it was found out that nanocomposite films of chitosan with gold nanorods can bound to biological tissues by activation of the embedded nanoparticles with a near-infrared (NIR) laser device (Matteini et al., 2010). This outcome represents an opportunity for the development of remotely activated bioadhesives useful for applications where suturing may be hardly feasible such as for poorly accessible or delicate body regions. Alginate (Brulé et al., 2011) and chitosan (Hu et al., 2007) were used in the preparation of magnetic composite hydrogels for magnetically triggered drug release. The application of a high-frequency magnetic field caused a local increase of the temperature of the embedded magnetic nanoparticles that induced structural changes in the polysaccharide matrix, thus leading to a controlled and enhanced release of an encapsulated drug.

3. Inorganic nanoparticles

This section summarizes relevant properties of inorganic nanoparticles (magnetic, metal and luminescent nanoparticles) employed as dispersed phases in the preparation of functional bionanocomposites.

3.1 Magnetic nanoparticles

Iron oxide nanoparticles are by far the most extensively investigated magnetic nanoparticles for biomedical (*in vivo* and *in vitro*) applications due to their particular magnetic properties and low toxicity. Most commonly are magnetite (Fe_3O_4) and maghemite ($\gamma\text{-Fe}_2\text{O}_3$), the latter results from the topotactic oxidation of magnetite, and both phases exhibit the inverse spinel crystal structure. Other magnetic nanoparticles include metal alloy nanoparticles (e.g. FePt, FeCo, and CoPt_3) (Behrens et al., 2006; Gu et al., 2003; Martins et al., 2007) and metallic nanoparticles (e.g. Co and Ni) (D. Guo et al., 2008; Zeisberger et al 2007). However at the present stage these nanoparticles are limited to *in vitro* applications due to toxicological concerns.

Unlike bulk magnetite (a ferrimagnetic material composed by multiple magnetic domains and that exhibits a permanent magnetization in the absence of a magnetic field) Fe_3O_4 nanoparticles smaller than *ca.* 30 nm contain a single magnetic domain and exhibit superparamagnetic behavior (Fig. 2a). The magnetization curve of superparamagnetic nanoparticles does not exhibit hysteresis loop (Fig. 2b) which means that in the absence of an external magnetic field these particles have zero magnetization and less tendency to agglomerate. This is a key feature for some bio-applications as the magnetic properties and the particles bio-distribution depends strongly on the aggregation of the nanoparticles. Another important feature of superparamagnetic nanoparticles for Nanomedicine is their

ability to dissipate heat when exposed to an external ac field (magnetic hyperthermia) a property that is currently being explored for the treatment of cancer. More detailed description of the physical phenomena subjacent to bio-applications of iron oxide nanoparticles can be found elsewhere (Daniel-da-Silva et al., 2011; Laurent et al., 2008). The biomedical and biotechnological applications of magnetic nanoparticles and their composites include magnetic separation, medical imaging, drug delivery and cancer hyperthermia (Dias et al., 2011; Laurent et al., 2008; Tartaj, 2011) and will be described in section 5 of this chapter. The properties required for the magnetic nanoparticles differ according to the application envisaged and are strongly dependent on the particle size and shape. Thus, a number of synthetic strategies have been developed for the synthesis of magnetic nanoparticles with uniform morphology, narrow size distribution and tailored properties, as extensively reviewed elsewhere (Dave & Gao, 2009; Jeong et al., 2007; Laurent et al., 2008; Lu et al., 2007).

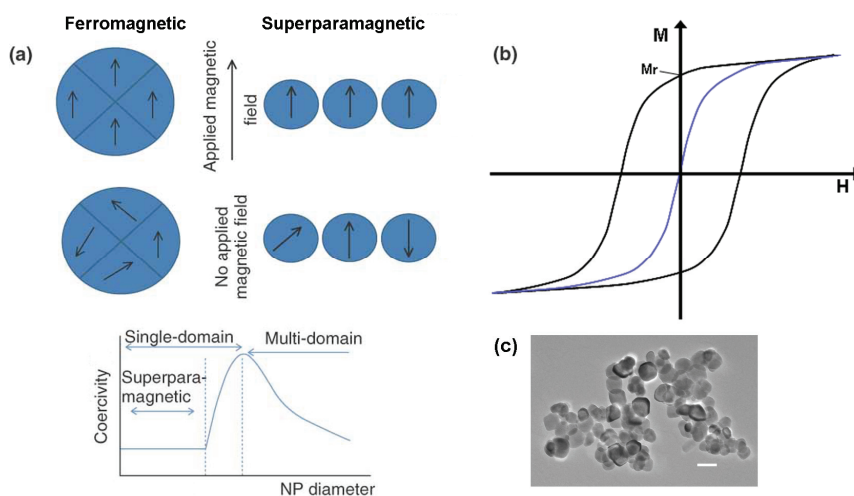


Fig. 2. (a) Under a magnetic field, the magnetic moment of the domains of a ferromagnetic particle and single-domain superparamagnetic particles are aligned. After removal of the magnetic field, ferromagnetic particles maintain a net magnetization (adapted and reproduced from Dave & Gao, 2009, with permission of John Wiley & Sons, Inc., Copyright 2009, John Wiley & Sons, Inc.). (b) Typical magnetization curves of ferromagnetic (black line) and superparamagnetic (blue line) particles. Superparamagnetic nanoparticles show no remanent magnetization (M_r). (c) TEM image of magnetic Fe_3O_4 nanoparticles prepared by co-precipitation method (scale bar 100nm).

3.2 Metal nanoparticles

Silver nanoparticles and composites have been extensively studied for biotechnological and biomedical applications (e.g. wound dressing, water treatment) mostly due to the well-known antimicrobial activity of silver (Pradeep & Anshup, 2009; Rai et al., 2009). In addition, silver nanoparticles exhibit a size and shape-dependent surface plasmon resonance band (Cobley et al., 2009) that is sensitive to the surrounding conditions, a property that is being explored for applications as biosensors (Fan et al., 2010; Le Guével et al., 2009). Silver

nanoparticles also find application in analytical tools such as surface enhanced Raman scattering (SERS) and metal enhanced fluorescence (Nair & Laurencin, 2007; X. S. Shen et al 2009).

Typically Ag nanoparticles are prepared by chemical methods that involve the reduction of silver ions in the presence of sodium borohydride (Nair & Laurencin, 2007) or citric acid, among others. Further chemical treatments can be employed to modify the surface of the nanoparticles in order to promote colloidal stability and/or make the particles compatible with specific environments. Although these methods are simple and effective, the presence of residual amounts of the reducing (or stabilizers) agents may raise toxicological and environmental concerns, limiting the application of these nanoparticles. In this context, some polysaccharides with reducing action are being currently investigated for the development of more friendly strategies of synthesis and surface modification of metal nanoparticles (V. K. Sharma et al., 2009), as detailed in section 4 of this chapter.

Colloidal gold has been used as a therapeutic since remote times, for example it is reported that Paracelsus (15th century) used to prescribe a purple Au colloid, known as *Aurum Potable*, to rejuvenate, as was believed, the human body (Pradeep et al., 2009). The recent interest in Au nanoparticles for biomedical applications relies mostly on their tunable and environment sensitive optical properties. Gold nanospheres exhibit an absorption band (surface plasmon resonance (SPR) band) that is sensitive to the composition, size, shape, inter-particle distance and environment of the nanoparticles (V. Sharma et al., 2009). The sensitivity of the SPR band is in the basis of the application of gold nanoparticles for biological labeling, imaging, sensing and diagnostic (Boisselier & Astruc, 2009; Sperling et al., 2008). When gold nanoparticles absorb light at the wavelength of the SPR band, the dissipation of the energy originates a local increase of the temperature, an effect that is being explored in several applications, including photothermally triggered drug release (Timko et al., 2010) and cancer hyperthermia (Jain et al., 2007). In addition gold nanoparticles have anti-angiogenic properties (i.e. they inhibit the formation and growth of new blood vessels from existing ones) and their application as anti-angiogenic agents in the treatment of cancer is under investigation (Bhattacharya & Mukherjee, 2008).

The most common synthetic method of gold nanoparticles involves the reduction of Au(III) to Au(0), usually starting from HAuCl₄ complexes and using citrate or borohydride as reducing agent (Daniel & Astruc, 2004). Making use of the strong affinity of sulfur donor ligands to gold, capping agents such as alkanethiols are frequently employed to modify the Au nanoparticles' surfaces. Besides spherical nanoparticles, it is possible to vary the size and shape of gold nanoparticles using appropriate synthetic techniques (Busbee et al., 2003; Grzelczak et al., 2008; V. Sharma et al., 2009). The control of the morphology of gold nanoparticles is an important feature because the surface plasmon resonance (SPR) band is shape dependent. For important therapeutic applications it is convenient to shift the maximum of the SPR band into the biological near-infrared (NIR) window (650-1100 nm) where the absorption and scattering of body tissues is minimal and therefore the penetration into living tissues is much deeper than that of visible light. The shift of the plasmon band to NIR region can be achieved with gold nanoshells or by increasing the morphological anisotropy of NPs as in the case of gold nanorods (Fig. 3).

3.3 Luminescent inorganic nanoparticles

A variety of photoluminescent inorganic nanoparticles have been investigated for several bio-applications including as optical biomarkers and biosensors (Burns et al., 2006; Jorge et

al. 2007). In this context, nanoparticles of semiconductors (quantum dots: QDs), nanosized lanthanide compounds and doped amorphous particles, namely of SiO_2 , are of special relevance. Luminescent nanoparticles appear as an alternative to conventional organic dyes in bioanalysis by photoluminescence (Fig. 4), as the latter have limitations, such as a narrow range of absorption wavelengths, broad emission bands and reduced photostability. However, all these systems have advantages and limitations, relative to each other, depending on the context of application. In fact a number of fluorophores of distinct chemical nature, including a variety of surface functionalized QDs, are already available commercially for biolabeling.

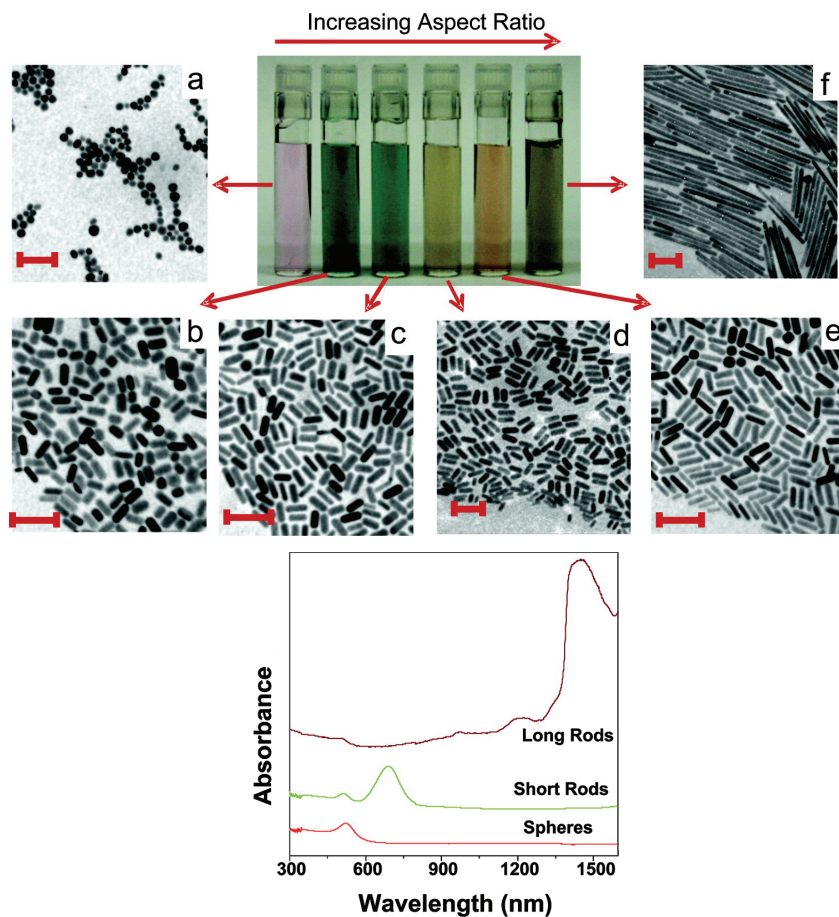


Fig. 3. Top: Photographs of aqueous solutions of gold nanorods with variable aspect ratio and corresponding TEM images (scale bar 100 nm). Aspect ratio varies from 1.3 to 5 for short rods (TEMs a-e) and 20 (TEM f) for long rods. Bottom: Optical spectra of gold spherical nanoparticles (8 nm size), short and long rods (aspect ratio of 3 and 20 respectively). Reprinted adapted with permission from (Murphy et al., 2008). Copyright 2008 American Chemical Society.

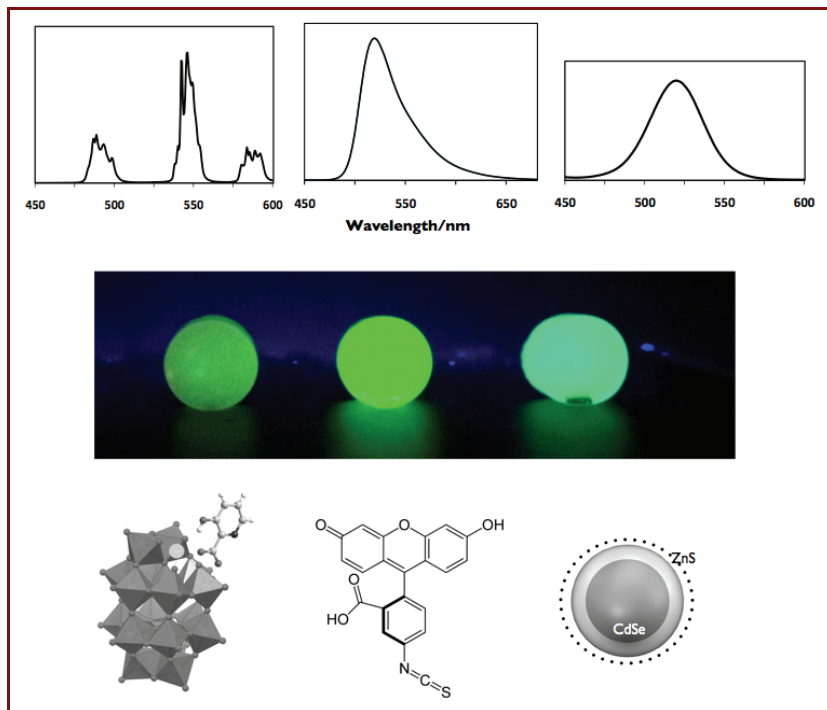


Fig. 4. Upper panel, left to right: Photoluminescence emission spectra (intensity in a.u.) for: i) $K_{11}[Tb_2(\alpha-P_2W_{17}O_{61})(picOH)_7] \cdot 20H_2O$ polyoxometalate powders (excitation at 320 nm) showing the emission bands due to the intra-f transitions of the lanthanide; ii) fluorescein isothiocyanate (ethanolic solution), an organic fluorophore commonly used in flow cytometry (excitation at 350 nm); iii) Organically capped quantum dots of CdSe overlaid by ZnS ($d_{core} \sim 2.8$ nm, toluene solution), showing the corresponding excitonic emission band. The middle panel shows photographs of UV light irradiated (325 nm) *k*-carrageenan gels containing the fluorophores that are schematically represented in the bottom panel.

Quantum dots are nanosized particles of semiconductors that exhibit quantum size effects due to three dimensional confinement of the charge carriers (Steigerwald & Brus, 1990). As a consequence, the electronic structure of the semiconductor develops from bands of energy into discrete energy levels as the particle size decreases and approaches the molecular dimensions, increasing the band gap of the semiconductor. Noteworthy, the particle size dependent absorption and emission of light observed for a number of materials have been exploited in several applications with great emphasis in nanobiotechnology. Quantum dots of CdSe and InP (typical dimensions 1.5-6 nm) have been of special interest as fluorescent biolabels because their size dependent and bright emission can be precisely tuned across the visible spectrum or, by using narrow band gap materials such as PbS or PbSe, light emission can be extended to NIR. These materials are prepared as colloidal core-shell nanoparticles whose cores (e.g. CdSe, InP) have the surfaces coated with shells of a wide band gap semiconductor, normally ZnS (Dabbousi et al., 1997). An outer layer of organic ligands confers colloidal stability to these particulate systems and also allows surface exchange

reactions for specific purposes such as biofunctionalized tags. In comparison to conventional dyes, QDs are remarkable stable against photobleaching and because they absorb in a wider wavelength region, distinct sized QDs can be excited simultaneously to originate emission bands that depend on the particles size. This interesting feature allows multicolor optical coding using QDs as biotags and in biotracking procedures for several clinical applications. However, toxicity concerns associated to QDs limit their use in a number of applications. Luminescence of lanthanide ions, in particular for those in the centre of the series, is an iconic feature that has developed intense research in their compounds. The fluorescence observed in these materials, for example when excited in the UV region, arises from $f \rightarrow f$ transitions that occur in the lanthanide ion, whose chemical environment can vary from coordinating ligands in solution to solid networks (Granadeiro et al., 2009). Efficient emission requires that non-radiate mechanisms in the material are less relevant as compared to the lanthanide emission. The luminescence observed in these compounds, namely of Eu(III) and Tb(III), prompted the development of a number of photoactive devices, which include some appliances of general use such as fluorescent tubes and color monitors. Luminescent nanoparticles of lanthanide compounds can be also useful fluorophores in clinical applications that benefit from long fluorescence lifetimes. Additionally, these systems exhibit sharp emission bands strongly shifted from the excitation line wavelength (large Stokes shifts).

Encapsulation of fluorescent NPs serve multipurposes and can be performed using diverse matrices. Silica encapsulation and polymer encapsulation have been extensively used. Silica encapsulation normally involves the growth of SiO_2 shells, very often following the hydrolysis of tetraethylortosilicate precursor, in the presence of the above mentioned fluorophores. The literature offers a number of examples of nanoparticles comprising amorphous silica encapsulating fluorophores, these include organic dyes (Ow et al., 2005), lanthanide complexes (Granadeiro et al., 2010; Soares-Santos et al., 2003), gold clusters (Guével et al., 2011) and quantum dots (Darbandi et al., 2005), among other luminescent systems (Burns et al., 2006). Silica coating of fluorophores provides a large surface area for which a number of functionalization procedures that are well known in chemistry can be directly applied. In this way, versatile chemical strategies for silica derivatization can be adapted according to the envisaged bioapplication. Additionally, photobleaching of the fluorophore can be limited by the protective silica shells which is of special relevance for bioanalysis in physiological medium. Earlier reports on the adsorption of organic dyes at silica surfaces point to other possibilities among the immense field of silica nanocomposites (G. Wu et al., 1997).

As it happens with a silica coating, several fluorophores can be encapsulated in a variety of polymers though in these cases, and depending on the type of polymer, biocompatibility issues need to be considered. Synthetic polymers have been investigated aiming to produce fluorescent nanocomposite particles that form the basis to produce multifunctional systems (e.g. fluorescent and magnetic). Hydrophobic colloidal nanoparticles have been frequently used as fillers for *in situ* polymerization in miniemulsions that depending on the synthetic route led to nanocomposites as stable aqueous emulsions (Esteves et al., 2005) or homogeneous spin-coated films (Esteves et al., 2007). A number of polymers have been investigated in this context. For example, polyacrylates and derived co-polymers were used to produce fluorescent nanocomposite particles with great interest for cancer imaging and targeting (X. Gao et al., 2004).

The development of bionanocomposites comprising a natural polymer matrix incorporating inorganic fluorophores has been less exploited. Examples include the synthesis of chitosan beads incorporating CdSe/ZnS QDs that have been previously surface modified with 3-mercaptopropionic acid; the free carboxylic groups of this acid were then cross-linked to the amino groups of chitosan forming a composite with 11.8% quantum yield (Nie et al., 2006). Biodegradable nanocomposites comprising QDs in poly(D,L- lactide-co-glycolide) nanospheres have been investigated as fluorophores with improved efficiency for intracellular delivery, which remains a strong limitation on the use of naked QDs for cell labeling and imaging of cytoplasmic targets (Kim et al., 2008). Multifunctional polysaccharide based microspheres have been prepared using a fluorescent/magnetic poly(styrene-maleic anhydride) composite (0.15-0.7 μm) that could be conjugated via surface anhydride groups to heparin. The composite contained an Eu(III) phthalate complex as the fluorophore and nanosized magnetite as the magnetic driver (Qiu et al., 2005). The development of multifunctional nanocomposite particles is currently an active research field that calls for a variety of chemical strategies that includes the design of innovative nanocomposites (Corr et al., 2008).

4. Preparative chemical strategies for polysaccharide based nanocomposites

Herein we will draw our attention on the synthetic approaches for the production of bionanocomposites comprising a matrix of a polysaccharide and inorganic nanoparticles as dispersed phases. Overall the strategies for the preparation of polysaccharide based nanocomposites include the encapsulation of the preformed inorganic nanoparticles in the biopolymer (*ex situ*) or the *in situ* synthesis of the nanoparticles in the presence of the biopolymers. The synthesis *in situ* allows a more intimate dispersion of the nanoparticles within the polymer matrix. However the control over size and shape of nanoparticles synthesized in the presence of polymers still remains a challenge. *In situ* synthesized nanoparticles are generally size polydispersed which may limit the application of the composites since most of the properties of the inorganic nanoparticles are size and shape dependent (section 3). To overcome these limitations, the biopolymer encapsulation of preformed nanoparticles is an interesting alternative.

Polysaccharide nanocomposites can be in the form of macroscopic networks ("bulk nanocomposites") or confined to smaller dimensions in the micron and submicron range. Due to their reduced dimensions, nanoparticulate systems may offer unique advantages for biomedical applications such as cellular internalization. In this section, we will briefly describe relevant preparative strategies to obtain polysaccharide composite nanoparticles with controlled size and narrow size distribution.

4.1 Bulk nanocomposites

Ex situ strategies for the preparation of functional polysaccharide nanocomposites consist generally in the encapsulation of preformed inorganic nanoparticles by the biopolymer. Due to the hydrophilic nature of polysaccharides, firstly the nanoparticles are dispersed in water and then, the encapsulation can be performed by the homogeneous mixing of the nanoparticles hydrosol with an aqueous solution of the biopolymer. This route has been extensively used for the preparation of functional nanocomposites of chitosan (Liu & Huang, 2010; Matteini et al., 2010), alginate (Brulé et al., 2011; Marsich et al., 2011), dextran

(Hong et al., 2009) and gum arabic (Banerjee & Chen, 2007) amongst other polymers, containing dispersed inorganic phases, such as magnetic (e.g. iron oxides) and optical active (e.g. gold) nanoparticles. The development of bionanocomposites using this strategy relies, as expected, on the ability to produce nanoparticles with the required functionality (optical, magnetic or biological) and with the required chemical moieties at their surfaces. This aspect is not only relevant to enable chemical compatibility between the composite components but can be crucial to guarantee the aimed performance of the material.

In situ strategies for the preparation of the polysaccharide nanocomposites described here consist on the synthesis of the inorganic nanofillers in the presence of the polysaccharide. In aqueous solutions, most of the polysaccharides, due to their specific functional groups (Table 1), have the ability to interact with positive metal ions via electron rich oxygen atoms. In some of the cases, metal ions act as crosslinkers of the polysaccharide chains and promote the formation of a hydrogel network. For example, carrageenans form gels in the presence of monovalent and divalent cations due to the formation of a double helical configuration and helix aggregation (Stephen, 1995). The guluronic acid units of the polysaccharide alginate can pack forming a network with cavities simulating “egg box” in the presence of divalent cations (Braccini & Perez, 2001). The polymer network can be used as a template for the growth of diverse nanostructures, including magnetic and metal nanoparticles. Each cavity of the network is used for the nucleation of the nanoparticles and acts as a constrained environment that limits the growth of the *in situ* generated particles. The functional groups of the biopolymer will define the affinity towards specific metallic ions and may determine the morphology and the chemical properties of the resulting inorganic phase.

4.1.1 Magnetic nanoparticles

Amongst the several experimental routes developed for the synthesis of magnetic iron oxide nanoparticles (Dave & Gao, 2009; Jeong et al., 2007; Laurent et al., 2008; Lu et al., 2007), some require organic solvents and high temperature, conditions which are incompatible with the hydrophilic nature and thermal properties of most of natural polysaccharides. Thus, the polysaccharide-assisted growth of magnetic iron oxide nanoparticles has been mostly performed using chemical routes that require mild conditions such as the co-precipitation process. This method consists basically in the co-precipitation of a stoichiometric mixture of ferrous and ferric salts in aqueous media under basic conditions and in the absence of oxygen. It is a simple method that yields large amount of nanoparticles, although it does not allow for a fine control over the particle size.

Carrageenan was successfully employed as a colloidal stabilizer in the synthesis of superparamagnetic Fe_3O_4 nanoparticles via the co-precipitation method (Daniel-da-Silva et al., 2007; Jones et al., 2000). Besides preventing the spontaneous agglomeration of the nanoparticles, carrageenan induced the formation of smaller particles, when compared to conventional co-precipitation synthesis and allowed to control the chemical stability of the Fe_3O_4 towards oxidation, by careful choice of carrageenan type and concentration (Daniel-da-Silva et al., 2007). This is an important outcome since maghemite, the product that results in this case from the oxidation of magnetite, has lower saturation magnetization than magnetite.

Magnetic iron oxide nanoparticles have been also synthesized in the presence of other polysaccharides such as starch (D. K. Kim et al., 2003), alginate (Morales et al., 2008; Naik et al., 2005), dextran (Dou et al., 2008) and chitosan (Hernandez et al., 2009), using the co-precipitation method. The presence of starch molecules limited the size of the Fe_3O_4

nanoparticles to 6 nm and the agglomeration of the coated nanoparticles was controlled upon the cleavage of the glycosidic bonds of the polymer, which allowed preparing magnetic composite particles with average size smaller than commercially available dextran-coated magnetic nanoparticles. The starch coated Fe_3O_4 nanoparticles were biocompatible and tested for *in vivo* monitoring of the brain of rats using MRI (D. K. Kim et al., 2003). The formation of Fe_3O_4 nanoparticles within preformed dextran hydrogel beads (Dou et al., 2008) resulted in superparamagnetic composite particles with magnetization saturation values comparable to those of Fe_3O_4 nanoparticles prepared via typical coprecipitation routes, which renders these materials interesting for applications in the biomedical field. The formation of magnetite nanoparticles within chitosan using the coprecipitation route was found to be dependent on the concentration of this polysaccharide (Hernandez et al., 2009). Above a chitosan content of 3 wt%, a non magnetic iron hydroxide was formed instead of magnetite. The slow diffusion of OH-species through the viscous polymer medium was pointed out as a possible explanation for the observed effect.

4.1.2 Metal nanoparticles

Silver and gold nanoparticles are usually synthesized following chemical routes that involve the reduction of metal ions in the presence of a stabilizing agent to prevent the aggregation of the nanoparticles. Polysaccharides, due to their ability to coordinate to metal ions can act as stabilizing agents. The polymer-metal ion complex can then be reduced under mild conditions, resulting in the formation of particles with smaller size and narrower size distribution than those obtained in the absence of polymer. Once the reduction occurred, the polysaccharide chains impair the aggregation of the nanoparticles. Chitosan (Božanić et al., 2010; Travan et al., 2009), starch (Raveendran et al., 2006), gum arabic (Gils et al., 2010) and alginate (Jaouen et al., 2010) are some examples of polysaccharides that were reported as stabilizing agents for the synthesis of metal nanoparticles.

In addition to their ability to complex metal ions, polysaccharides may also exhibit reducing properties and thus can play the role of reducing and stabilizing agent in the synthesis of metal nanoparticles. This dual function of the polysaccharide can be an advantage in the clean synthesis of metal nanoparticles since it avoids the incorporation of interfering and, eventually harmful, chemicals that limit the use of metal composites for bio-applications. Following this strategy, Au and Ag nanoparticles were successfully prepared using chitosan (Huang & Yang, 2004; Laudenslager et al., 2008), heparin (Y. Guo & Yan, 2008; Huang & Yang, 2004; Kemp et al., 2009b) and hyaluronan (Kemp et al., 2009b).

Gold and silver nanoparticles prepared using carboxymethyl chitosan (CMC) exhibited similar particle size distribution than those prepared using chitosan (Laudenslager et al., 2008) despite CMC has a higher reported metal chelation capacity than chitosan. However the ability of the two polymers to stabilize the particles varied and particles prepared using CMC evidenced more aggregation. The reduced cross-linking ability of CMC compared to chitosan was pointed out as a possible explanation for the reported differences.

The use of heparin as reducing/stabilizing agent was found to control the size distribution of gold nanoparticles, and the particle size decreased with increasing heparin concentration (Y. Guo & Yan, 2008). Silver and gold nanoparticles prepared using hyaluronan showed wider particle size distribution than those prepared in heparin (Kemp et al., 2009b). The resulting heparin based metal nanocomposites retained its anticoagulant activity and anti-inflammatory properties as confirmed by *in vitro* and *in vivo* tests (Kemp et al., 2009a). The use of the polysaccharide heparin as simultaneously reducing and stabilizing agent avoided the need of intermediate purification steps to remove any traces of harmful reagents.

4.2 Composite nanoparticles

The use of polysaccharide nanoparticles has its roots in drug delivery research as nanocarriers for local targeted drug delivery applications (Liu et al., 2008). The application of polysaccharides nanoparticles was further extended to other biomedical contexts such as medical imaging and hyperthermia. This can be achieved upon the inclusion of inorganic nanoparticles that confer new functionalities to the resulting composite nanoparticles.

Polysaccharide composite nanoparticles from tens to hundreds of nanometers in diameter can be prepared using emulsification techniques. For example, chitosan nanoparticles carrying CdTe quantum dots and magnetite nanoparticles, with an average size of 100 nm, were prepared using water-in-oil (w/o) microemulsions (Li et al., 2007). The composite particles showed superparamagnetic and fluorescent properties favourable for multimodal imaging and were tested for pH controlled drug release for *in vitro* conditions. Thermo-sensitive magnetite/ κ -carrageenan nanogels with an average size of 50 nm and narrow size distribution were also prepared using w/o microemulsions (Fig. 5) (Daniel-da-Silva et al., 2009). The magnetic nanogels exhibited superparamagnetic properties at room temperature and have shown thermo-sensitive behavior in the temperature range 37-45°C which is necessary for thermal controlled delivery applications. The nanogels were successfully conjugated to an antibody via a carbodiimide mediated reaction, and after surface carboxymethylation, showing the potential of these nanocomposites for local targeting drug delivery.

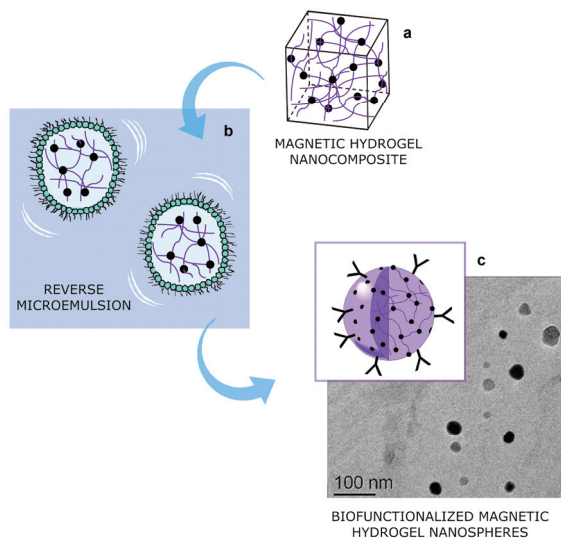


Fig. 5. Scheme of the synthetic steps involved in the preparation and bioconjugation of magnetic κ -carrageenan composite hydrogel nanoparticles. Magnetic bulk nanocomposite is first prepared (a) and then confined to nano-reactors using microemulsions (b). Composite nanoparticles are conjugated to an antibody after surface carboxymethylation (c). TEM image of composite nanoparticles shows an inner darker core that indicates the presence of magnetic nanoparticles (Reprinted adapted with permission from (Daniel-da-Silva et al., 2009). Copyright 2009 IOP Publishing Ltd).

5. Bio-applications of polysaccharide based nanocomposites

The most representative bio-applications of polysaccharide based nanocomposites and some illustrative examples of bionanocomposite systems from literature are listed in table 2.

Applications		Bionanocomposites	References
Biotechnological	Bioseparation	Fe ₃ O ₄ /dextran Fe ₃ O ₄ /gum arabic Fe ₃ O ₄ /chitosan	(Heebøll-Nielsen et al., 2004) (Batalha et al., 2010) (Liu et al., 2009)
	Biolabeling & Biosensing	Au, Ag/chitosan Au, Ag/alginate QDs/chitosan	(Santos Jr. et al., 2004; Wei et al., 2009) (Lim et al., 2010; Saha et al., 2009) (Tan & Zhang, 2005)
	Antimicrobial	Ag/chitosan Ag/hyaluronan	(Potara et al., 2011; Travan et al., 2009) (Kemp et al., 2009a)
Biomedical	Clinical Imaging	Fe ₃ O ₄ /dextran	(Chachuat & Bonnemain, 1995; Corot et al., 2006)
	Drug Delivery	Fe ₃ O ₄ /alginate Fe ₃ O ₄ /chitosan Fe ₃ O ₄ /heparin	(Brulé et al., 2011) (Hu et al., 2007) (Khurshid et al., 2009)
	Cancer Hyperthermia	Fe ₃ O ₄ /chitosan Fe ₃ O ₄ /pullulan acetate	(Zhao et al., 2009) (Gao et al., 2010)

Table 2. Examples of bio-applications of polysaccharide based nanocomposites.

5.1 Biotechnological applications

5.1.1 Bioseparation

Several polysaccharides have been explored for the surface coating or encapsulation of magnetic nanoparticles envisaging applications in bioseparation processes (Dias et al., 2011). The polysaccharides protect the inner magnetic core and provide functional moieties for further modification with other specific ligands. For example dextran coated magnetic nanoparticles functionalized with different ligands were tested for the separation of lectins from legume extracts, using high-gradient magnetic separation technique (Heebøll-Nielsen et al., 2004). Gum Arabic coated iron oxide nanoparticles were functionalized with triazine ligands with specificity towards antibodies and successfully used for the antibody immobilization (Batalha et al., 2010).

Due to the intrinsic ability of the polysaccharides to coordinate to metal ions, polysaccharide based magnetic nanocomposites have been explored in magnetically assisted water purification (Ambashta & Sillanpää, 2010; Liu et al., 2009). Polysaccharides offer the advantage of being low-cost biosorbents capable of removing trace levels of heavy metal ions. Their combination with magnetic nanoparticles delivers materials with large surface and that can be conveniently separated from wastewater by magnetic separation.

5.1.2 Biolabeling and biosensing

Luminescent inorganic nanoparticles such as quantum dots are promising for the *ex vivo* detection of biomarkers (Jaiswal & Simon, 2003; Wu & Bruchez, 2003). However their use in *in vivo* conditions raises toxicological concerns. The encapsulation of quantum dots in polysaccharides such as alginate, chitosan and dextran sulfate was found to prevent the leakage of the nanocrystals from the microcapsules (Gaponik et al., 2003). More recently it has been confirmed by *in vitro* cell tests that the use of chitosan for the encapsulation of CdSe/ZnS quantum dots improves considerably the biocompatibility of these nanoparticles (Tan & Zhang, 2005), rendering materials with potential application in *in vivo* optical biodetection.

SERS spectroscopy is a well-established analytical technique that permits detection of molecular adsorbates at the surface of silver and gold surfaces. With the development of new instrumental tools and materials platforms, this vibrational spectroscopic method appeared as a powerful method for single molecule detection. It is gaining attention as bioanalytical tool as it can be used to extract information from complex samples such as biological fluids, living tissues and cells (Abalde-Cela et al., 2010). Gold and silver chitosan and alginate nanocomposites were successfully used as substrates in trace analysis using SERS (Saha et al., 2009; Santos Jr. et al., 2004; Wei et al., 2009). Also cellulose of vegetable and bacterial origin were investigated as matrices to fabricate composites containing Ag nanoparticles that allowed the development of handy and sensitive SERS substrates (Marques et al., 2008). The use of the polysaccharides confers flexibility and portability to the substrate which is essential for extending the applications of this technique.

Hydrogel composites containing nanometals have been also reported for the construction of optical biosensors. For example, gold chitosan and alginate nanocomposites have shown good results as glucose sensing platforms (Du et al., 2007; Lim et al., 2010). Alginate hydrogel has shown to provide a protective medium for the bioreceptor glucose oxidase (Lim et al., 2010).

5.1.3 Antimicrobials

The use of silver and silver salts in commercial products for antimicrobial purposes is relatively widespread. However studies from the last decade have revealed that silver nanoparticles have improved antibacterial properties than bulk silver and that even nanomolar concentrations of silver nanoparticles can be more effective than micromolar concentrations of silver ions (Kong & Jang, 2008), thus leading to an increased interest on materials comprising nano-silver. In this context, a number of polysaccharide based silver nanocomposites have been reported (Liu & Huang, 2010; Kemp et al., 2009a; Travan et al., 2009; Vimala et al., 2010). These materials exhibit antimicrobial activity and may be considered for applications in wound dressings and for water purification purposes. In this context bacterial cellulose offers several possibilities and the antimicrobial activity of the derived silver nanocomposites has been reported (Pinto et al., 2009). The polysaccharide plays an important role in these materials as stabilizer, preventing the aggregation of the nanoparticles. Moreover, polysaccharide nanocomposites may show a synergistic antibacterial activity and exhibit higher antibacterial activity than their separated components as recently observed for chitosan-silver nanocomposites (Potara et al., 2011). Also, despite the growing use of silver nanomaterials, the potential implications for human health and the environment are not completely clarified (Marambio-Jones & Hoek, 2010).

The immobilization of silver nanoparticles in polysaccharide gels might be a promising strategy to respond to these toxicity concerns, by preventing the cell internalization of silver nanoparticles without affecting the antimicrobial activity (Travan et al., 2009).

5.2 Biomedical applications

5.2.1 Clinical imaging

Magnetic iron oxides are currently used as contrast agents in magnetic resonance imaging (MRI) (Corot et al., 2006). The commercially available compositions include dextran and carboxymethyl-dextran coated iron oxide nanoparticles (Endorem® and Resovist®, respectively) and other polysaccharide based compositions are under evaluation (Shen et al., 2003). The polysaccharide coating increases the blood circulation time and improves the efficiency of the detection of cancer cells. Moreover, the functional groups of the polysaccharide allow for further bioconjugation for specific cell targeting.

5.2.2 Drug delivery

Magnetic polysaccharide nanocomposites are useful nanocarriers for magnetically driven drug delivery. The polysaccharide matrix stabilizes the encapsulated bioactive molecules, preventing their loss or degradation during the delivery, while the magnetism of the carrier makes possible to target drug to specific sites upon the application of a magnetic field, minimizing any side-effects. Alginate, heparin and gum arabic are some examples of polysaccharides that were investigated in the preparation of magnetic composites for drug delivery (Dias et al., 2011).

Polysaccharides that form networks sensitive to environment changes (e.g. temperature, mechanical stress) when combined with inorganic nanophases with magnetic and/or optical functionalities afford composite materials of interest for remotely triggered drug delivery (Timko et al., 2010). The local increase of the temperature promoted by magnetic nanoparticles, if activated by an alternating magnetic field, or by gold nanoparticles, if activated by adequate optical radiation, originates structural changes in a thermosensitive polysaccharide and the modulated release of an encapsulated drug. This triggering approach has been investigated in alginate (Brulé et al., 2011) and chitosan (Hu et al., 2007) magnetic nanocomposites and in gold nanocomposites comprising thermosensitive synthetic polymers (Shiotani et al., 2007). The advantage of this strategy is that it can provide on demand drug release profiles, according to the needs of each patient.

5.2.3 Cancer hyperthermia

Hyperthermia is a type of cancer treatment in which specific areas of the body undergo a local increase of the temperature to damage and kill cancer cells, or to make cancer cells more sensitive to the effects of other therapies (radiotherapy or chemotherapy). The local increase of the temperature can be achieved exposing magnetic nanoparticles to an alternating magnetic field (magnetic hyperthermia). Alternatively thermal ablation can be obtained exposing gold nanoparticles or nanoshells to near-infrared light. (Cherukuri et al., 2010; Sakamoto et al., 2010).

The challenge of hyperthermia is heating locally, at the tumor site, without affecting the surrounding healthy tissue (Cherukuri et al., 2010). If the nanoparticles possess a specific targeting agent the efficiency of the treatment can be increased. The encapsulation of the nanoparticles using polysaccharides appears as a useful strategy for the biofunctionalization

of the nanoparticles with adequate targeting moieties. Chitosan (Zhao et al., 2009) and pullulan acetate (Gao et al., 2010) coated magnetic nanoparticles were investigated for magnetic hyperthermia.

6. Concluding remarks and future trends

In the last decades increasing attention has been devoted to the combination of inorganic nanoparticles with polysaccharides, to benefit from the advantages of both composite components. A number of formulations of such bionanocomposites exhibit magnetic, optical and antimicrobial functionalities of interest for biotechnological and biomedical applications that have been investigated to the present. The performance of those materials strongly relies on earlier steps of the chain production, which emphasises the relevance of preparative strategies that take in consideration the envisaged applications. Although *ex situ* preparations are still of great interest, namely due to their simplicity in terms of composite preparation, other more elaborate strategies that bring together concepts from materials design and chemical synthesis have proved to add great value in new biofunctional composites. In this respect, it will never be over emphasized that the use of polysaccharides in composite synthesis that mimic natural processes is currently a big challenge but that points to unprecedented consequences in terms of high performance materials fabrication. Additionally, it is an approach that in some aspects may help to overcome limitations on the use of nanocomposites due to toxicological concerns. From the recent attempts to find new methods of early-diagnosis of diseases and more effective therapies a new generation of multifunctional nanostructured materials is emerging. Bionanocomposites specifically designed to incorporate multiple functional nanoparticles are attractive materials for the development of integrated platforms merging functions such as targeting, imaging and therapy in one system. It is expectable that medicine platforms based on multifunctional bionanocomposites will enable better detection of the disease across a number of diagnosis techniques and simultaneous treat and monitoring the response to the therapy.

7. Acknowledgments

A. L. Daniel-da-Silva acknowledges FCT, FSE and POPH for funding. The authors thank FCT/FEDER: PTDC/QUI/67712/2006 and NANO/NMED-SD/0140/2007, that provided opportunities to develop some topics discussed in this work.

8. References

- Abalde-Cela, S., Aldeanueva-Potel, P., Mateo-Mateo, C., Rodríguez-Lorenzo, L., Alvarez-Puebla, R. A., & Liz-Marzán, L. M. (2010). Surface-enhanced Raman scattering biomedical applications of plasmonic colloidal particles. *Journal of the Royal Society Interface*, 7, pp. S435-S450.
- Ali, B. H., Ziada, A., & Blunden, G. (2009). Biological effects of gum arabic: a review of some recent research. *Food and Chemical Toxicology*, 47, pp. 1-8.
- Ambashta, R. D., & Sillanpää, M. (2010). Water purification using magnetic assistance: a review. *Journal of Hazardous Materials*, 180, pp. 38-49.
- Augst, A. D., Kong, H. J., & Mooney, D. J. (2006). Alginate hydrogels as biomaterials. *Macromolecular Bioscience*, 6, pp. 623-633.

- Banerjee, S. S., & Chen, D-H. (2007). Fast removal of copper ions by gum arabic modified magnetic nano-adsorbent. *Journal of Hazardous Materials*, 147, pp. 792-799.
- Batalha, I. L., Hussain, A., & Roque, A. C. A. (2010). Gum arabic coated magnetic nanoparticles with affinity ligands specific for antibodies. *Journal of Molecular Recognition*, 23, pp. 462-471.
- Behrens, S., Bönneemann, H., Matoussevitch, N., Gorschinski, A., Dinjus, E., Habicht, W., Bolle, J., Zinoveva, S., Palina, N., Hormes, J., Modrow, H., Ahr, S., & Kemper, V. (2006). Surface engineering of Co and FeCo nanoparticles for biomedical application. *Journal of Physics Condensate Matter*, 18, pp. S2543-S2561.
- Bhattacharya, R., & Mukherjee, P. (2008). Biological properties of naked metal nanoparticles. *Advanced Drug Delivery Reviews*, 60, pp. 1289-1306.
- Boisselier, E., & Astruc, D. (2009). Gold nanoparticles in nanomedicine: preparations, imaging, diagnostics, therapies and toxicity. *Chemical Society Reviews*, 38, pp. 1759-1782.
- Božanić, D. K., Trandafilović, L. V., Luyt, A. S., & Djoković, V. (2010). Green synthesis and optical properties of silver-chitosan complexes and nanocomposites. *Reactive and Functional Polymers*, 70, pp. 869-873.
- Braccini, I., & Perez, S. (2001). Molecular basis of Ca²⁺ induced gelation in alginates and pectins: the egg-box model revisited. *Biomacromolecules*, 2, pp.1089-1096.
- Brulé, S., Levy, M., Wihelm, C., Letourneur, D., Gazeau, F., Ménager, C., & Le Visage, C. (2011). Doxorubicin release triggered by alginate embedded magnetic nanoheaters: a combined therapy. *Advanced Materials*, 23, pp. 787-790.
- Burns, A., Ow, H., & Wiesner, U. (2006). Fluorescent core-shell silica nanoparticles: towards "Lab on a Particle" architectures for nanobiotechnology. *Chemical Society Reviews*, 35, pp. 1028-1042.
- Busbee, B. D., Obare, S. O., & Murphy, C. J. (2003). An improved synthesis of high-aspect-ratio gold nanorods. *Advanced Materials*, 15, pp. 414-416.
- Campo, V. I., Kawano, D. F., Braz da Silva Jr, D., & Carvalho, I. (2009). Carrageenan: biological properties, chemical modifications and structural analysis - a review. *Carbohydrate Polymers*, 77, pp. 167-80.
- Chachuat, A., & Bonnemain, B. (1995). European clinical experience with Endorem. A new contrast agent for liver MRI in 1000 patients. *Radiology*, 35, pp. S274-S276.
- Cherukuri, P., Glazer, E. S., & Curley, S. A. (2010). Targeted hyperthermia using metal nanoparticle. *Advanced Drug Delivery Reviews*, 62, pp. 339-345.
- Cobley, C. M., Skrabalak, S. E., Campbell, D. J., & Xia, Y. (2009). Shape-controlled synthesis of silver nanoparticles for plasmonic and sensing applications. *Plasmonics*, 4, pp. 171-179.
- Corot, C., Robert, P., Idée, J.-M., & Port M. (2006). Recent advances in iron oxide nanocrystal technology for medical imaging. *Advanced Drug Delivery Reviews*, 58, pp. 1471-1504.
- Corr, S. A., Rakovich, Y. P., & Gun'ko, Y. K. (2008). Multifunctional magnetic-fluorescent nanocomposites for biomedical applications. *Nanoscale Research Letters*, 3, pp. 87-104.
- Dabbousi, B. O., Rodriguez-Viejo, J., Mikulec, F. V., Heine, J. R., Mattoussi, H., Ober, R., Jensen, K. F. & Bawendi, M. G. (1997). (CdSe)ZnS Core-Shell Quantum Dots: Synthesis and Characterization of a Size Series of Highly Luminescent Nanocrystallites. *Journal of Physics Chemistry B*, 101, pp. 9463-9475.
- Daniel, M.-C., & Astruc, D. (2004). Gold nanoparticles: assembly, supramolecular chemistry, quantum-size-related properties, and applications toward biology, catalysis and nanotechnology. *Chemical Reviews*, 104, pp. 293-346.

- Daniel-da-Silva, A. L., Silva, N. J. O., Gil, A. M., & Trindade, T. (2011). Biocomposites containing magnetic nanoparticles, In: *Nanocomposite particles for bio-applications – Materials and Biointerfaces*, T. Trindade and A. L. Daniel-da-Silva, pp. 165-192, Pan Stanford Publishing Pte Lda, ISBN 9814267783, Singapore.
- Daniel-da-Silva, A. L., Fateixa, S., Guiomar, A. J., Costa, B. F. O., Silva, N. J. O., Trindade, T., Goodfellow, B. J., & Gil, A. M. (2009). Biofunctionalized magnetic hydrogel nanospheres of magnetite and kappa-carrageenan. *Nanotechnology*, 20, 355602, pp. 1-10. doi: 10.1088/0957-4484/20/35/355602
- Daniel-da-Silva, A. L., Trindade, T., Goodfellow, B. J., Costa, B. F. O., Correia, R. N. & Gil, A. M. (2007). *In situ* synthesis of magnetite nanoparticles in carrageenan gels. *Biomacromolecules*, 8, pp. 2350-2357.
- Darbandi, M., Thomann, R. & Nann, T. (2005). Single Quantum Dots in Silica Spheres by Microemulsion Synthesis. *Chemistry of Materials*, 17, pp. 5720-5725.
- Darder, M., Aranda, P., & Ruiz-Hitzky, E. (2007) Bionanocomposites: a new concept of ecological, bioinspired and functional hybrid materials. *Advanced Materials*, 19, pp. 1309-1319.
- Dave, S. R., & Gao, X. (2009). Monodisperse magnetic nanoparticles for biodetection, imaging, and drug delivery: a versatile and evolving technology. *WIREs Nanomedicine and Nanobiotechnology*, 1, pp. 583-609.
- Dias, A. M. G. C., Hussain, A., Marcos, A. S., & Roque, A. C. A. (2011). A biotechnological perspective on the application of iron oxide magnetic colloids modified with polysaccharides. *Biotechnology Advances*, 29, pp. 142-155.
- Dou, H., Xu, B., Tao, K., Tang, M. and Sun, K. (2008). The one-pot synthesis of dextran-based nanoparticles and their application in in-situ fabrication of dextran-magnetite nanocomposites, *Journal of Materials Science: Materials in Medicine*, 19, pp. 2575-2580.
- Du, Y., Luo, X-L., Xu, J-J. & Chen, H-Y. (2007). A simple method to fabricate a chitosan-gold nanoparticles film and its application in glucose biosensor. *Bioelectrochemistry*, 70, pp. 342-347.
- Esteves, A. C. C., Bombalski, L., Trindade, T., Matyjaszewski, K., & Barros-Timmons, A. (2007). Polymer grafting from CdS quantum dots via AGET ATRP in miniemulsion. *Small*, 3, pp. 1230-1236.
- Esteves, A. C. C., Barros-Timmons, A., Monteiro, T. & Trindade, T. (2005). Polymer encapsulation of CdE (E = S, Se) quantum dot ensembles via in situ radical polymerization in miniemulsion. *Journal of Nanoscience and Nanotechnology*, 5, pp. 766-771.
- Fan, M., Thompson, M., Andrade, M. L., & Brolo, A. G. (2010). Silver nanoparticles on a plastic platform for localized surface plasmon resonance biosensing. *Analytical Chemistry*, 82, pp. 6350-6352.
- Gaffney, J., Matou-Nasri, S., Grau-Olivares, M., & Slevin, M. (2010). Therapeutic applications of Hyaluronan. *Molecular BioSystems*, 6, pp. 437-443.
- Gao, F., Cai, Y., Zhou, J., Xie, X., Ouyang, W., Zhang, Y., Wang, X., Zhang, X., Wang, X., Zhao, L., & Tang, J. (2010). Pullulan acetate coated magnetite nanoparticles for hyper-thermia: preparation, characterization and in vitro experiments. *Nano Research*, 3, pp. 23-31.
- Gao, X., Yuanyuan, C., Levenson, R. M., Chung, L. W. K., & Nie, S. (2004). *In vivo* cancer targeting and imaging with semiconductor quantum dots. *Nature Biotechnology*, 22, pp. 969-976.

- Gaponik, N., Radtchenko, I. L., Gerstenberger, M.R., Fedutik, Y. A., Sukhorukov, G. B., & Rogach, A. L. (2003). Labeling of biocompatible polymer microcapsules with near-infrared emitting nanocrystals. *Nanoletters*, 3, pp. 369-372.
- Gils, P. S., Ray, D., & Sahoo, P. K. (2010). Designing of silver nanoparticles in gum arabic based semi-IPN hydrogel. *International Journal of Biological Macromolecules*, 46, pp. 237-244.
- Granadeiro, C. M., Ferreira, R. A. S., Soares-Santos, P. C. R., Carlos, L. D., & Nogueira, H. I. S. (2009). Lanthanopolyoxometalates as Building Blocks for Multiwavelength Photoluminescent Organic-Inorganic Hybrid Materials. *European Journal of Inorganic Chemistry*, 34, pp. 5088-5095.
- Granadeiro, C. M., Ferreira, R. A. S., Soares-Santos, P. C. R., Carlos, L. D., Trindade, T., & Nogueira, H. I. S. (2010). Lanthanopolyoxotungstates in silica nanoparticles: multi-wavelength photoluminescent core/shell materials. *Journal of Materials Chemistry*, 20, pp. 3313-3318.
- Grzelczak, M., Pérez-Juste, J., Mulvaney, P., & Liz-Marzán, L. M. (2008). Shape control in gold nanoparticles synthesis. *Chemical Society Reviews*, 37, pp. 1783-1791.
- Gu, H., Ho, P. L., Tsang, K. W. T., Wang, L. & Xu, B. (2003). Using bifunctional magnetic nanoparticles to capture vancomycin-resistant enterococci and other gram-positive bacteria at ultralow concentration. *Journal of American Chemical Society*, 125, pp. 15702-15703.
- Guével, X. L., Hotzer, B., Jung, G., & Schneider, M. (2011). NIR-emitting fluorescent gold nanoclusters doped in silica nanoparticles. *Journal of Materials Chemistry*, 21, pp. 2974-2981.
- Guo, D., Wu, C., Li, X., Jiang, H., Wang, X. & Chen, B. (2008). In vitro cellular uptake and cytotoxic effect of functionalized nickel nanoparticles on leukemia cancer cells. *Journal of Nanoscience and Nanotechnology*, 8, pp. 2301-2307.
- Guo, Y., & Yan, H. (2008). Preparation and characterization of heparin-stabilized gold nanoparticles. *Journal of Carbohydrate Chemistry*, 27, pp. 309-319.
- Heebøll-Nielsen, A., Dalkiae, M., Hubbuch, J. J., & Thomas, O. R. T. (2004). Superparamagnetic adsorbents for high-gradient magnetic fishing of lectins out of legume extracts. *Biotechnology and Bioengineering*, 87, pp. 311-323.
- Heinze, T., Liebert, T., Heublein, B., & Hornig, S. (2006). Functional polymers based on dextran. *Advances in Polymer Science*, 205, pp. 199-291.
- Hernandez, R., Zamora-Mora, V., Sibaja-Ballester, M., Vega-Baudrit, J., Lopez, D., & Mijangos, C. (2009). Influence of iron oxide nanoparticles on the rheological properties of hybrid chitosan ferrogels. *Journal of Colloid and Interface Science*, 339, pp. 53-59.
- Hong, R. Y., Li, J. H., Qu, J. M., Chen, L. L., & Li, H. Z. (2009). Preparation and characterization of magnetite/dextran nanocomposite used a precursor of magnetic field. *Chemical Engineering Journal*, 150, pp. 572-580.
- Hu, S-H., Liu, T-Y., Liu, D-M., & Chen, S-Y. (2007). Controlled Pulsatile Drug Release from a Ferrogel by a High-Frequency Magnetic Field. *Macromolecules*, 40, pp. 6786-6788.
- Huang, H., & Yang, X. (2004). Synthesis of polysaccharide-stabilized gold and silver nanoparticles: a green method. *Carbohydrate Research*, 339, pp. 2627-2631.
- Jain, P. K., El-Sayed, I. H., & El-Sayed, M. A. (2007). Au nanoparticles target cancer. *Nano Today*, 2, pp. 18-29.
- Jaiswal, J. K. & Simon, S. M. (2003). Long-term multiple colour imaging of live cells using quantum dot bioconjugates. *Nature Biotechnology*, 21, pp. 47-51.

- Jaouen, V., Brayner, R., Lantiat, D., Steunou, N., & Coradin, T. (2010). In situ growth of gold colloids within alginate films. *Nanotechnology*, 21, 185605.
- Jeong, U., Teng, X., Wang, Y., Yang, H., & Xia, Y. (2007). Superparamagnetic colloids: controlled synthesis and niche applications. *Advanced Materials*, 19, pp. 33-60.
- Jones, F., Cölfen, H. & Antonietti, M. (2000). Iron oxyhydroxide colloids stabilized with polysaccharides. *Colloid Polymer Science*, 278, pp. 491-501.
- Jorge, P., Martins, M. A., Trindade, T., Santos, J. L., & Farahi, F. (2007). Optical Fiber Sensing Using Quantum Dots. *Sensors*, 7, pp. 3489-3534.
- Kemp, M. M., Kumar, A., Clement, D., Ajayan, P., Mousa, S., & Linhardt, R. J. (2009a). Hyaluronan- and heparin-reduced silver nanoparticles with antimicrobial properties. *Nanomedicine (Lond)*, 4, pp. 421-429.
- Kemp, M. M., Kumar, A., Mousa, S., Park, T.-J., Ajayan, P., Kubotera, N., Mousa, S. A., & Linhardt, R. J. (2009b). Synthesis of gold and silver nanoparticles stabilized with glycosaminoglycans having distinctive biological activities. *Biomacromolecules*, 10, pp. 589-595.
- Kemp, M. M., & Linhardt, R. J. (2010). Heparin based nanoparticles. *WIREs Nanomedicine and nanobiotechnology*, 2, pp. 77-87.
- Khurshid, H., Kim, S. H., Bonder, M. J., Colak, L., Ali, B. H., Shah, S. I., Kiick, K. L., & Hadjipanayis, G. C. (2009). Development of heparin-coated magnetic nanoparticles for targeted drug delivery applications. *Journal of Applied Physics*, 105, 07B308.
- Kim, B. Y. S., Jiang, W., Oreopoulos, J., Yip, C. M., Rutka, J. T., & Chan, W. C. W., (2008). Biodegradable quantum dot nanocomposites enable live cell labeling and imaging of cytoplasmic targets. *Nano Letters*, 8, pp. 3887-3892.
- Kim, D. K., Mikhaylova, M., Wang, F. H., Kehr, J., Bjelke, B., Hang, Y., Tsakalakos, T. & Muhammed, M. (2003). Starch-coated superparamagnetic nanoparticles as MRI contrast agents. *Chemistry of Materials*, 15, pp. 4343-4351.
- Kong, H., & Jang, J. (2008). Antibacterial properties of novel poly(methyl methacrylate) nanofiber containing silver nanoparticles. *Langmuir*, 24, pp. 2051-2056.
- Laudenslager, M. J., Schiffman, J. D., & Schauer, C. L. (2008). Carboxymethyl chitosan as a matrix materials for platinum, gold and silver nanoparticles. *Biomacromolecules*, 9, pp. 2682-2685.
- Laurent, S., Forge, D., Port, M., Roch, A., Robic, C., Elst, L. V., & Muller, R. N. (2008). Magnetic iron oxide nanoparticles: synthesis, stabilization, vectorization, physicochemical characterizations, and biological applications. *Chemical Reviews*, 108, pp. 2064-2110.
- Le Corre, D., Bras, J., & Dufresne, A. (2010). Starch nanoparticles: a review. *Biomacromolecules*, 11, pp. 1139-1153.
- Le Guével, X., Wang, F. Y., Stranik, O., Nooney, R., Gubala, V., McDonagh, C., & MacCraith, B. D. (2009). Synthesis, stabilization and functionalization of silver nanoplates for biosensor applications. *Journal of Physics and Chemistry C* 37, pp. 16380-16386.
- Li, L., Chen, D., Zhang, Y., Deng, Z., Ren, X., Meng, X., Tang, F., Ren, J., & Zhang, L. (2007). Magnetic and fluorescent multifunctional chitosan nanoparticles as a smart drug delivery systems. *Nanotechnology*, 18, 405102.
- Lim, S. Y., Lee, J. S., & Park, C. B. (2010). In situ growth of gold nanoparticles by enzymatic glucose oxidation within alginate gel matrix. *Biotechnology and Bioengineering*, 105, pp. 210-214.
- Liu, B.-S., & Huang, T.-B. (2010). Nanocomposites of genipin-crosslinked chitosan/silver nanoparticles-structural reinforcement and antimicrobial properties. *Macromolecular Bioscience*, 8, pp. 932-941.

- Liu, X., Hu, Q., Fang, Z., Zhang, X., & Zhang, B. (2009). Magnetic chitosan nanocomposites: a useful recyclable tool for heavy metal ion removal. *Langmuir*, 25, pp. 3-8.
- Liu, Z., Jiao, Y., Wang, Y., Zhou, C., & Zhang, Z. (2008). Polysaccharide-based nanoparticles as drug delivery systems. *Advanced Drug Delivery Reviews*, 60, pp. 1650-1662.
- Lu, A-H., Salabas, E. L., & Schüth, F. (2007). Magnetic nanoparticles: synthesis, protection, functionalization and application. *Angewandte Chemie International Edition*, 46, pp. 1222-1244.
- Marambio-Jones, C., & Hoek, E. M. V. (2010). A review of the antibacterial effects of silver nanomaterials and potential implications for human health and the environment. *Journal of Nanoparticle Research*, 12, pp. 1531-1551.
- Marques, P. A. A. P., Nogueira, H. I. S., Pinto, R. J. B., Neto, C. P., & Trindade, T. (2008). Silver-bacterial cellulosic sponges as active SERS substrates. *Journal of Raman Spectroscopy*, 39, pp. 439-443.
- Marsich, E., Travan, A., Donati, I., Di Luca A, Benincasa, M., Crosera, M., & Paoletti, S. (2011). Biological response of hydrogels embedding gold nanoparticles. *Colloids and Surfaces B: Biointerfaces*, 83, pp. 331-339.
- Martins, M. A., Neves, M. C., Esteves, A. C. C., Girginova, P. I., Guiomar, A. J., Amaral, V. A. & Trindade, T. (2007). Biofunctionalized ferromagnetic CoPt₃/polymer nanocomposites. *Nanotechnology*, 18, 215609.
- Matteini, P., Ratto, F., Rossi, F., Centi, S., Dei, L., & Pini, R. (2010). Chitosan films doped with gold nanorods as laser-activatable hybrid bioadhesives. *Advanced Materials*, 22, pp. 4313-4316.
- Morales, M. A., Finotelli, P. V., Coaquira, J. A. H., Rocha-Leão, M. H. M., Diaz-Aguila, C., Baggio-Saitovitch, E. M. & Rossi, A. M. (2008). *In situ* synthesis and magnetic studies of iron oxide nanoparticles in calcium-alginate matrix for biomedical applications. *Materials Science & Engineering C-Biomimetic and Supramolecular Systems*, 28, pp. 253-257.
- Murphy, C. J., Gole, A. M., Stone, J. W., Sisco, P. N., Alkilany, A. M., Goldsmith, E., & Baxter, S. C. (2008). Gold nanoparticles in biology: beyond toxicity to cellular imaging. *Accounts of Chemical Research*, 41, pp. 1721-1730.
- Murugesan, S., Park, T.-J., Yang, H., Mousa, S., & Linhardt, R. J. (2006). Blood compatible carbon nanotubes-nanobased neoproteoglycans. *Langmuir*, 22, pp. 3461-3463.
- Naik, R., Senaratne, U., Powell, N., Buc, E. C., & Tsoi, G. M. (2005). Magnetic properties of nanosized iron oxide particles precipitated in alginate hydrogels, *Journal of Applied Physics*, 97, 10J313.
- Nair, L. S., & Laurencin, C. T. (2007). Silver nanoparticles: synthesis and therapeutic applications. *Journal of Biomedical Nanotechnology*, 3, pp. 301-316.
- Nie Q., Tan, W. B., & Zhang, Y. (2006). Synthesis and characterization of monodisperse chitosan nanoparticles with embedded quantum dots. *Nanotechnology*, 17, pp. 140-144.
- Nijenhuis, K. (1997). Thermoreversible networks - viscoelastic properties and structure of gels. *Advances in Polymer Science*, 130, pp. 194-202.
- Ow, H., Larson, D. R., Srivastava, M., Baird, B. A., Webb, W. W., & Wiesner, U. (2005). Bright and stable core-shell fluorescent silica nanoparticles. *Nano Letters*, 5, pp. 113-117.
- Pinto, R. J. B., Marques, P. A. A. P., Neto, C. P., Trindade, T., Daina, S., & Sadocco, P. (2009). Antibacterial activity of nanocomposites of silver and bacterial or vegetable cellulosic fibers. *Acta Biomaterialia*, 5, pp. 2279-2289.

- Potara, M., Jakab, E., Damert, A., Popescu, O., Canpean, V., & Astilean, S. (2011). Synergistic antibacterial activity of chitosan-silver nanocomposites on *Staphylococcus aureus*. *Nanotechnology*, 22, 135101.
- Pradeep, T., & Anshup (2009). Noble metal nanoparticles for water purification: A critical review. *Thin Solid Films*, 517, pp. 6441–6478.
- Qiu, G., Xu, Y., Zhu, B., & Qiu, G. (2005). Novel, fluorescent, magnetic, polysaccharide-based microsphere for orientation, tracing, and anticoagulation: preparation and characterization. *Biomacromolecules*, 6, pp. 1041-1047.
- Rabenstein, D. L. (2002). Heparin and heparin sulphate: structure and functions. *Natural Product Reports*, 19, pp. 312-331.
- Rai, M., Yadav, A., & Gade, A. (2009). Silver nanoparticles as a new generation of antimicrobials. *Biotechnology Advances*, 27, pp. 76-83.
- Raveendran, P., Fu, J., & Wallen, S. L. (2006). A simple and green method for the synthesis of Au, Ag and Au-Ag alloy nanoparticles. *Green Chemistry*, 8, pp. 34-38.
- Rinaudo, M. (2006). Chitin and chitosan: properties and applications. *Progress in Polymer Science*, 31, pp. 603-632.
- Saha, S., Pal, A., Pande, S., Sarkar, S., Panigrahi, S., & Pal, T. (2009). Alginate gel-mediated photochemical growth of mono- and bimetallic gold and silver nanoclusters and their application to surface-enhanced raman scattering. *Journal of Physics Chemistry C*, 113, pp. 7553-7560.
- Sakamoto, J. H., van de Ven, A. L., Godin, B., Blanco, E., Serda, R., Grattoni, A., Ziemys, A., Bouamrani, A., Hu, T., Ranganathan, S. I., De Rosa, E., Martinez, J. O., Smid, C. A., Buchanan, R. M., Lee, S.-Y., Srinivasan, S., Landry, M., Meyn, A., Tasciotti, E., Liu, X., Decuzzi, P., & Ferrari, M. (2010). Enabling individualized therapy through nanotechnology. *Pharmacological Research*, 62, pp. 57-89.
- Santos Jr., D. S., Goulet, P. J. G., Pieczonka, N. P. W., Oliveira Jr., O. N., & Aroca, F. (2004). Gold nanoparticle embedded, self-sustained chitosan films as substrates for surface-enhanced raman scattering. *Langmuir*, 20, pp. 10273-10277.
- Seigneuric, R., Markey, L., Nuyten, D. S. A., Dubernet, C., Evelo, C. T. A., Finot, E., & Garrido, C. (2010). From Nanotechnology to Nanomedicine: Applications to Cancer Research. *Current Molecular Science*, 10, pp. 640-652.
- Sharma, V. K., Yngard, R. A., & Lin, Y. (2009). Silver nanoparticles: green synthesis and their antimicrobial activities. *Advances in Colloid and Interface Science*, 145, pp. 83-96.
- Sharma, V., Park, K., & Srinivasarao, M. (2009). Colloidal dispersion of gold nanorods: Historical background, optical properties, seed-mediated synthesis, shape separation and self-assembly. *Materials Science and Engineering R*, 65, pp. 1-38.
- Shen, F., Poncet-Legrand, C., Somers, S., Slade, A., Yip, C., Duft, A. M., Winnik, F. M., & Chang, P. L. (2003). Properties of a novel magnetized alginate for magnetic resonance imaging. *Biotechnology and Bioengineering*, 83, pp. 282-292.
- Shen, X. S., Wang, G. Z., Hong, X., & Zhu, W. (2009). Nanospheres of silver nanoparticles: agglomeration, surface morphology control and application as SERS substrates. *Physical Chemistry Chemical Physics*, 11, pp. 7450-7454.
- Shiotani, A., Mori, T., Nidome, T., Nidome, Y., & Katayama, Y. (2007). Stable incorporation of gold nanorods into *N*-Isopropylacrylamide hydrogels and their rapid shrinkage induced by near-infrared laser irradiation. *Langmuir*, 23, pp. 4012-4018.
- Singh, R. S., Saini, G. K., & Kennedy, J. F. (2008). Pullulan: microbial sources, production and applications. *Carbohydrate Polymers*, 73, pp. 515-531.
- Soares-Santos, P. C. R., Nogueira, H. I. S., Felix, V., Drew, M. G. B., Ferreira, R. A. S., Carlos, L. D., & Trindade, T. (2003). Novel lanthanide luminescent materials based on

- complexes of 3-hydroxypicolinic acid and silica nanoparticles. *Chemistry of Materials*, 15, pp. 100-108.
- Sperling, R. A., Gil, P. R., Zhang, F., Zanella, M., & Parak, W. J. (2008). Biological applications of gold nanoparticles. *Chemical Society Reviews*, 37, pp. 1896-1908.
- Steigerwald, M. L., & Brus, L. E. (1990). Semiconductor crystallites: a class of large molecules. *Accounts of Chemical Research*, 23, pp. 183-188.
- Piculell, L. (1995). Gelling carrageenans, In: *Food Polysaccharides and their applications*, Stephen, A. M., pp. 205-244, Marcel Dekker Incorporation, ISBN 0824793536, New York.
- Tan, W. B., & Zhang, Y. (2005). Surface modification of gold and quantum dot nanoparticles with chitosan for bioapplications. *Journal of Biomedical Materials Research*, 75A, pp. 56-62.
- Tartaj, P. (2011). Bio-applications of functionalized magnetic nanoparticles and their nanocomposites, In: *Nanocomposite particles for bio-applications - Materials and Biointerfaces*, T. Trindade and A.L. Daniel-da-Silva, pp. 217-247, Pan Stanford Publishing Pte Lda, ISBN 9814267783, Singapore.
- Timko, B. P., Dvir, T., & Kohane, D. S. (2010). Remotely triggerable drug delivery systems. *Advanced Materials*, 22, pp. 4925-4943.
- Travan, A., Pelillo, C., Donatei, I., Marsich, E., Benincasa, M., Scarpa, T., Semeraro, S., Turco, G., Gennaro, R., & Paoletti, S. (2009). Non-cytotoxic silver nanoparticle-polysaccharide nanocomposites with antimicrobial activity. *Biomacromolecules*, 10, pp. 1429-1435.
- Vimala, K., Mohan, Y. M., Sivudu, K. S., Varaprasad, K., Ravindra, S., Reddy, N. N., Padma, Y., Sreedhar, B., & MohanaRaju, K. (2010). Fabrication of porous chitosan films impregnated with silver nanoparticles: a facile approach for superior antibacterial application. *Colloids and Surfaces B: Biointerfaces*, 76, pp. 248-258.
- Wei, D., Qian, W., Wu, D., & Xia, Y. (2009). Synthesis, properties, and surface enhanced raman scattering of gold and silver nanoparticles in chitosan matrix. *Journal of Nanoscience and Nanotechnology*, 9, pp. 2566-2573.
- Wu, G., Koliadima, A., Her, Y., & Matijevic, E. (1997). Adsorption of dyes on nanosized modified silica particles. *Journal of Colloid and Interface Science*, 195, pp. 222-228.
- Wu, X., & Bruchez, M. P. (2003). Immunofluorescent labeling of cancer marker Her2 and other cellular targets with semiconductor quantum dots. *Nature Biotechnology*, 21 pp. 41-46.
- Zeisberger, M., Dutz, S., Müller, R., Hergt, R., Matoussevitch, N., & Bönnemann, H. (2007). Metallic cobalt nanoparticles for heating applications. *Journal of Magnetism and Magnetic Materials*, 311, pp. 224-227.
- Zhao, D. I., Wang, X-X., Zeng, X-W., Xia, Q-S., & Tang, J-T. (2009). Preparation and inductive heating property of Fe₃O₄-chitosan composite nanoparticles in an AC magnetic field for localized hyperthermia. *Journal of Alloy Compounds*, 477, pp. 739-743.

Applications of Antimicrobial Polymer Nanocomposites in Food Packaging

Aryou Emamifar
University of Kurdistan
Iran

1. Introduction

The demand for minimally processed, easily prepared and ready-to-eat 'fresh' food products, globalization of food trade, and distribution from centralized processing pose major challenges for food safety and quality. Recently, extensive studies have been conducted to develop non-thermal processing techniques (PEF, HHP, IR, UV, US) as replacements for thermal processing in order to keep the freshness of food along with extending its shelf life. Although some of these technologies are capable of decontaminating of food, they are energy-intensive and require costly equipment; hence, their yet relatively limited commercial applications. However, the use of proper packaging technology to minimize food losses and provide safe and sound food products has always been the focus of food packaging. Nanotechnology has potential to influence the packaging sector greatly. Nanoscale innovations in the forms of pathogen detection, active packaging, antimicrobial packaging and barrier formation are poised to elevate food packaging to new heights. This chapter lays foundations for the role of antimicrobial polymer nanocomposites in food packaging (Emamifar et al., 2010; Brody et al., 2008). This chapter briefly describes new food packaging and focus mainly on the applications of nanotechnology in food packaging. Effort will be made to considerable extent to explore the potential of using antimicrobial polymer metal nanocomposites for food packaging industry. Moreover, the antimicrobial performance of the most common nanoparticles based on zinc oxide, titanium oxide and nanosilver applied directly to plastic films, will be described. This chapter also demonstrates the effect of nanocomposite packaging containing Ag and ZnO on the shelf life of fresh orange juice and on inactivation of *Lactobacillus plantarum* in orange juice as a case study.

2. Innovative food packaging

Traditional food packaging is meant for mechanical supporting of otherwise non-solid food, and protecting food from external influences. This principal function of packaging involves retardation of deterioration, extension of shelf-life, and maintenance of quality and safety of packaged food. Packaging protects from environmental influences causing deterioration of foods and beverages such as heat, light, the presence or absence of moisture, oxygen, pressure, enzymes, spurious odors, microorganisms, insects, dirt and dust particles, gaseous emissions, and so on. Prolonging shelf-life involves application of various strategies such as

temperature control; moisture control; addition of chemicals such as salt, sugar, carbon dioxide, or natural acids; removal of oxygen; or a combination of these with effective packaging (Restuccia et al., 2010). In recent years, new food-packaging systems have been developed as a response to trends in consumer preferences towards mildly preserved, fresh, tasty and convenient food products with a prolonged shelf-life. In addition, changes in retail practices, such as centralization of activities (e.g. preparation of retail packs of fresh meat and sliced vegetables) and the globalization of markets resulting in longer distribution distances, present major challenges to the food-packaging industry to develop packaging concepts that extend shelf-life while maintaining the safety and quality of the packaged food. Traditional systems are reaching their limits with regard to further extension of shelf-life of packaged food. To provide this shelf-life extension, and to improve the quality, safety and integrity of the packaged food, innovative active and intelligent packaging concepts are being developed. Active and intelligent packaging may be defined as follows:

Active packaging changes the condition of the packaged food to extend shelf-life or improve food safety or sensory properties, while maintaining the quality of the packaged food.

Intelligent packaging systems monitor the condition of packaged foods to give information about the quality of the packaged food during transport and storage (De Kruijf et al., 2002).

Important examples of active packaging include oxygen scavengers, carbon dioxide emitters/absorbers, moisture absorbers, ethylene absorbers, ethanol emitters, flavor releasing/absorbing systems and antimicrobial containing films and for Intelligent packaging include time-temperature indicators, leakage indicators and freshness indicators (Ozdemir et al., 2004).

2.1 Antimicrobial food packaging

Antibacterial agents are of relevance to a number of industrial sectors including environmental, food, synthetic textiles, packaging, healthcare, medical care, as well as construction and decoration. They can be broadly classified into two types, organic and inorganic. Organic antibacterial materials are often less stable particularly at high temperatures and/or pressures compared to inorganic antibacterial agents. This presents a potential obstacle for the product formulation. As a consequence, inorganic materials such as metal and metal oxides have attracted lots of attention over the past decade due to their ability to withstand harsh process conditions (Zhang et al., 2007). Antimicrobial packaging is a form of active packaging (Appendini & Hotchkiss, 2002). Antimicrobial food packaging materials have to extend the lag phase and reduce the growth rate of microorganisms in order to extend shelf life and to maintain product quality and safety. The need to package foods in a versatile manner for transportation and storage, along with the increasing consumer demand for fresh, convenient, and safe food products presages a bright future for AM Packaging. However, more information is required on the chemical, microbiological and physiological effects of these systems on the packaged food especially on the issues of nutritional quality and human safety. So far, research on AM packaging has focused primarily on the development of various methods and model systems, whereas little attention has been paid to its preservation efficacy in actual foods. Research is essential to identify the types of food that can benefit most from AM packaging materials (Suppakul et al., 2003). Antimicrobial packaging can take several forms including:

1. Addition of sachets pads containing volatile antimicrobial agents into packages.
2. Incorporation of volatile and non-volatile antimicrobial agents directly into polymers.

3. Coating or adsorbing antimicrobials onto polymer surfaces.
4. Immobilization of antimicrobials to polymers by ion or covalent linkages.
5. Use of polymers that are inherently antimicrobial (Appendini & Hotchkiss, 2002).

Among the active packaging applications, the incorporation of antimicrobials is receiving considerable attention as a means of extending the bacterial lag phase, slowing the growth rate of micro-organisms and maintaining food quality and safety.

Direct addition of antimicrobials (organic acids or their respective acid anhydrides, spice extracts, chelating agents, metals, enzymes, bacteriocins, etc.) could result in some loss of activity because of leaching into the food matrix, and cross-reaction with other food components such as lipids or proteins. Therefore, the use of packaging films containing antimicrobial agents could be more efficient, by a controlled migration of the compound into the food, not only allowing for initial inhibition of undesirable micro-organisms, but also residual activity over time, during the transport and storage of food during distribution (Mauriello et al., 2005). Combinations of more than one antimicrobial incorporated into packaging have also been investigated. For example, it is hypothesized that compounds active against Gram-positive bacteria (i.e. lysozyme. Combined with chelating agents (i.e. EDTA. can target Gram-negative bacteria. Addition of EDTA to edible films containing nisin or lysozyme, however, had little inhibition effect on *E. coli* and *Salmonella typhimurium*. The rationale for incorporating antimicrobials into the packaging is to prevent surface growth in foods where a large portion of spoilage and contamination occurs. For example, intact meat from healthy animals is essentially sterile and spoilage occurs primarily at the surface. This approach can reduce the addition of larger quantities of antimicrobials that are usually incorporated into the bulk of the food. Many antimicrobials are incorporated at 0.1–5% w/w of the packaging material, particularly films. Antimicrobials may be incorporated into polymers in the melt or by solvent compounding. Thermal polymer processing methods such as extrusion and injection molding may be used with thermally stable antimicrobials such as metals (Appendini & Hotchkiss, 2002). Antimicrobials that cannot withstand the processing temperatures of the polymers are often coated onto the materials, which require surface functionalisation to improve the adhesion of the coatings. Surface immobilization requires the presence of functional groups on both the antimicrobial and the polymer and also spacer molecules that link the polymer surface to the active agent (Radheshkumar & Münstedt, 2006).

2.2 Nanotechnology applications for food packaging

Nanotechnology focuses on the characterization, fabrication, and manipulation of biological and nonbiological structures smaller than 100 nm. Structures on this scale have been shown to have unique and novel functional properties. Consequently, interest and activities in this research area have greatly increased over the past years. According to the National Nanotechnology Initiative (2006), Nanotechnology is the understanding and control of matter at dimensions of roughly 1 to 100 nanometers, where unique phenomena enable novel applications. Encompassing nanoscale science, engineering and technology, nanotechnology involves imaging, measuring, modeling, and manipulating matter at this length scale (Weiss et al., 2006). Nanotechnology recently introduced in the food packaging industry can potentially provide solutions to food packaging challenges such as short shelf life (Emamifar et al., 2010). Nanotechnology derived food packaging materials are the

largest category of current nanotechnology applications for the food sector. The main applications for food contact materials (FCMs) including:

1. FCMs incorporating nanomaterials to improve packaging properties (flexibility, gas barrier properties, temperature/moisture stability).
2. "Active" FCMs that incorporate nanoparticles with antimicrobial or oxygen scavenging properties.
3. "Intelligent" food packaging incorporating nanosensors to monitor and report the condition of the food.
4. Biodegradable polymer-nanomaterial composites (Chaudhry et al., 2008).

2.2.1 Nanocomposites food packaging

Polymer composites are mixtures of polymers with inorganic or organic fillers with certain geometries (fibers, flakes, spheres, particulates). The use of fillers which have at least one dimension in the nanometric range (nanoparticles) produces polymer nanocomposites. Three types of fillers can be distinguished, depending on how many dimensions are in the nanometric range. Isodimensional nanoparticles, such as spherical silica nanoparticles or semiconductor nanoclusters, have three nanometric dimensions. Nanotubes or whiskers are elongated structures in which two dimensions are in the nanometer scale and the third is larger. When only one dimension is in the nanometer range, the composites are known as polymer-layered crystal nanocomposites, almost exclusively obtained by the intercalation of the polymer (or a monomer subsequently polymerized) inside the galleries of layered host crystals (Azeredo, 2009). There are three common methods used to process nanocomposites: solution method, *in situ* or interlamellar polymerization technique, and melt processing. The solution method can be used to form both intercalated and exfoliated nanocomposite materials. In the solution method, the nanocomposite clay is first swollen in a solvent. Next, it is added to a polymer solution, and polymer molecules are allowed to extend between the layers of filler. The solvent is then allowed to evaporate. The *in situ* or interlamellar method swells the fillers by absorption of a liquid monomer. After the monomer has penetrated in between the layers of silicates, polymerization is initiated by heat, radiation, or incorporation of an initiator. The melt method is the most commonly used method due to the lack of solvents. In melt processing, the nanocomposite filler is incorporated into a molten polymer and then formed into the final material (Brody et al., 2008). Nanocomposite packages are predicted to make up a significant portion of the food packaging market in the near future. Research on use of nanocomposites for food packaging began in the 1990s. Most of the research has involved the use of montmorillonite clay as the nanocomponent in a wide range of polymers such as polyethylene, nylon, polyvinyl chloride, and starch. Many nanocomposite food packages are either already in the marketplace or being developed. The majority of these are targeted for beverage packaging. In large part, the impetus for this predicted growth is the extraordinary benefits nanoscience offers to improve food packages. (Brody et al., 2008). Recent advances in the field of nanotechnology, particularly the ability to prepare highly ionic metal oxide nanoparticulates of any size and shape, may lead to the development of new antibacterial agents (Jones et al., 2008). Antimicrobially active packaging based on metal nanocomposites is a new generation of nano food packaging which are made by incorporating metal nanoparticles into polymer films. The high performance of nanoparticles is due to their high surface area/volume ratio, which is the main reason for increasing antimicrobial activity of metal nanoparticles (Emamifar et al.,

2010). The metal and metal oxide nanomaterials commonly used as antimicrobial agents are silver (Ag), gold (Au), zinc oxide (ZnO), silica (SiO₂), titanium dioxide (TiO₂), alumina (Al₂O₃) and iron oxides (Fe₃O₄, Fe₂O₃). The antimicrobial properties of nano-zinc oxide and magnesium oxide have recently been discovered. Compared to nanosilver, the nanoparticles of zinc oxide and titanium dioxide are expected to provide a more affordable and safe food packaging solutions in the future (Chaudhry et al., 2008).

2.2.2 Antimicrobial mechanisms of nanomaterials

The antimicrobial activity of nanoparticles may be related to several mechanisms. The nanoparticles can either directly interact with the microbial cells, e.g. interrupting transmembrane electron transfer, disrupting/penetrating the cell envelope, or oxidizing cell components, or produce secondary products (e.g. reactive oxygen species (ROS) or dissolved heavy metal ions) that cause damage (Fig 1.) (Li et al., 2008). Antimicrobial mechanisms of the major nanomaterials are discussed as followed:

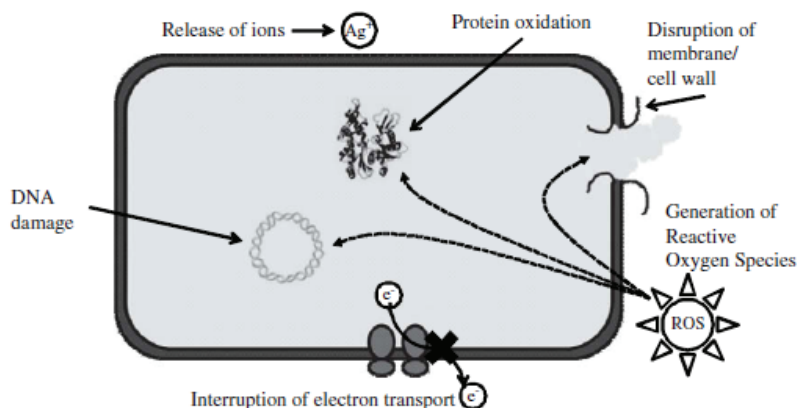


Fig. 1. Various mechanisms of antimicrobial activities exerted by nanomaterials

TiO₂

Titanium dioxide (TiO₂) is non-toxic and has been approved by the American Food and Drug Administration (FDA) for use in human food, drugs, cosmetics and food contact materials. Currently there is considerable interest in the self-disinfecting property of TiO₂ for meeting hygienic design requirements in food processing and packaging surfaces. Bactericidal and fungicidal effects of TiO₂ on *E. coli*, *Salmonella choleraesuis*, *Vibrio parahaemolyticus*, *Listeria monocytogenes*, *Pseudomonas aeruginosa*, *Staphylococcus aureus*, *Diaporthe actinidiae* and *Penicillium expansum* have been reported. Application of TiO₂ photocatalytic disinfection for drinking water production was investigated. The development of TiO₂-coated or incorporated food packaging and food preparing equipment has also received attention. Chawengkijwanich & Hayata, 2008 concluded that the TiO₂-coated film could reduce the microbial contamination on the surface of solid food products and thus reduce the risks of microbial growth on fresh-cut produce (Chawengkijwanich & Hayata, 2008). Adams et al., 2006 studied the toxic effects associated with TiO₂ water suspensions using two model bacterial species, Gram-negative *E. coli* and Gram positive *B.*

subtilis. They suggested that the antibacterial activity of TiO₂ towards both Gram negative and Gram positive bacterial species is significantly greater ($p < 0.05$) in the presence of light than in the dark, and this difference was more pronounced for *B. subtilis*. Specifically, the degree of inhibition for *B. subtilis* was 2.5-fold greater in the presence than in the absence of light, compared to 1.8-fold for *E. coli*. The greater inhibition in the presence of light supports the notion that the antibacterial activity of TiO₂ was related to photocatalytic ROS production. While cell death with TiO₂ was less pronounced in the dark, it still occurred, indicating that an additional mechanism is involved. Similar results have been reported from mammalian cytotoxicity studies, where TiO₂ exerted oxidative stress in the dark under non-photocatalytic conditions (Adams et al., 2006).

ZnO

The antibacterial activity of ceramic powders has attracted attention as a new technique that can substitute for conventional methods using organic agents. Ceramic powders of zinc oxide (ZnO), calcium oxide (CaO) and magnesium oxide (MgO) were found to show marked antibacterial activity (Yamamoto, 2001). The advantage of using these inorganic oxides as antimicrobial agents is that they contain mineral elements essential to humans and exhibit strong activity even when administered in small amounts (Sawai & Yoshikawa, 2004). Jin et al., 2009 studied several approaches (powder, film, PVP capped and coating) for the application of nano-ZnO in food systems and concluded that nano-ZnO exhibits antimicrobial effects against *L.monocytogenes* and *S.enteritidis* in liquid egg white and in culture media. ZnO has found many applications in daily life such as in drug delivery, cosmetics, and medical devices due to its strong antimicrobial effect on a broad spectrum of microorganisms. Moreover, it is currently listed by FDA as a generally recognized as safe (GRAS) material. Antimicrobial effects of ZnO nanoparticles may be attributed to several mechanisms: 1) induction of oxidative stress due to ROS generation especially interior or out of cell H₂O₂ which leads to interaction with proteins, DNA, and lipids causing death ; 2) membrane disorganization due to accumulation of ZnO nanoparticles in the bacterial membrane and also their cellular internalization; 3) release of Zn ions that may be responsible for antimicrobial activity by binding to the membrane of microorganisms. However, the toxicity of ZnO nanoparticles is not directly related to their entering into the cell, rather their intimate contact onto the cell causes changes in the microenvironment in the vicinity of the organism-particle contact area to either increase metal solubilization or to generate ROS, that may ultimately damage cell membrane . Moreover, the toxicity of ZnO nanoparticles is not only affected by the light via ROS production, but may also happen in the dark although its mechanism is not yet defined (Emamifar et al., 2010). The generation of highly reactive species such as OH[·], H₂O₂ and O₂²⁻ is explained as follows. Since ZnO with defects can be activated by both UV and visible light, electron-hole pairs (e⁻h⁺) can be created. The holes split H₂O molecules (from the suspension of ZnO) into OH⁻ and H⁺. Dissolved oxygen molecules are transformed to superoxide radical anions (O₂⁻), which in turn react with H⁺ to generate (HO₂[·]) radicals, which upon subsequent collision with electrons produce hydrogen peroxide anions (HO₂⁻). They then react with hydrogen ions to produce molecules of H₂O₂. The generated H₂O₂ can penetrate the cell membrane and kill the bacteria. Since, the hydroxyl radicals and super oxides are negatively charged particles, they cannot penetrate into the cell membrane and must remain in direct contact with the outer surface of the bacteria; however, H₂O₂ can penetrate into the cell (Padmavathy & Vijayaraghavan, 2008). It can be assumed that the concentration of H₂O₂ generated from the

surface increases with decreasing particle size, because the number of ZnO powder particles per unit volume of powder slurry increases with decreasing particle size. Based on the above, the increase in antibacterial activity is assumed to be due to the increase in H₂O₂ generated from the surface of ZnO on reducing the particle size of the powder samples. For ZnO powders, the influence of particle size on *S. aureus* was less than that on *E. coli*. The structures and chemical compositions of the cell surface of the bacteria used in this study are quite different. Thin layers of lipid A, lipopolysaccharide and peptidoglycan are present on the cell surface of *E. coli*, whereas there is only a peptidoglycan layer for *S. aureus*. However, the differences in antibacterial action towards *S. aureus* and *E. coli* are assumed to be due to the different sensitivities towards H₂O₂ (Yamamoto, 2001). Overall, the preliminary findings suggest that ZnO nanoparticles can be used externally to control the spreading of bacterial infections. It would be interesting to determine if any derivatives of ZnO nanoparticles with various chemical groups or bioagents are more effective at eliminating various microorganisms. In the prevention and control of bacterial spreading and infections, the main target is the cell wall structure. The cell wall of most pathogenic bacteria is composed of surface proteins for adhesion and colonization, and components such as polysaccharides and teichoic acid that protect against host defences and environmental conditions. These components are charged macromolecules; therefore, specific interactions to disrupt their main function and location may be triggered by introducing specific groups on the surface of the nanoparticles. It has been reported that certain long-chain polycations coated onto surfaces can efficiently kill on contact both Gram-positive and Gram-negative bacteria (Jones et al., 2008).

Ag

Silver has been in use since time immemorial in the form of metallic silver, silver nitrate, silver sulfadiazine for the treatment of burns, wounds and several bacterial infections. But due to the emergence of several antibiotics the use of these silver compounds has been declined remarkably. Nanotechnology is gaining tremendous impetus in the present century due to its capability of modulating metals into their nanosize, which drastically changes the chemical, physical and optical properties of metals. Metallic silver in the form of silver nanoparticles has made a remarkable comeback as a potential antimicrobial agent. The use of silver nanoparticles is also important, as several pathogenic bacteria have developed resistance against various antibiotics. Hence, silver nanoparticles have emerged up with diverse medical applications ranging from silver based dressings, silver coated medicinal devices, such as nanogels, nanolotions, etc (Rai et al., 2009). Silver has also been long known to have microbial inhibition. The antimicrobial activity of these nanoparticles may be related to several mechanisms including, induction of oxidative stress due to generation of reactive oxygen species (ROS) which may cause the degradation of the membrane structure of the cell, release of ions from the surface of nanoparticles that has been reported to cause bacterial death due to binding to cell membrane. However, the mechanism of toxicity is still only partially understood (Emamifar et al., 2011). Silver nanoparticles can damage cell membranes of microorganisms by forming "pits" on their surfaces. Moreover, they may penetrate into the cells to cause DNA damage (Morones et al., 2005). Silver ions released from the surface of these nanoparticles can interact with thiol groups in protein to induce bacterial inactivation, condensation of DNA molecules, and loss of their replication ability (Emamifar et al., 2010). Based on electron spin resonance (ESR) measurements, Kim et al., 2007 observed that the antimicrobial mechanism of Ag nanoparticles is related to the

formation of free radicals and the subsequent free radical-induced membrane damage. Treatment with nano-Ag destabilized the outer membrane of bacteria. This indicates that nano-Ag can disrupt the outer membrane barrier components such as lipopolysaccharide or porins, culminating in the perturbation of the cytoplasmic membrane. Although the detailed mechanism by which nanoparticles with a diameter of 10 nm can penetrate and disrupt the membranes remains to be determined, electron microscopy and optical imaging results suggest that nano-Ag penetrate the outer and inner membranes of the treated Gram negative bacteria, with some nanoparticles being found intracellularly. Nano-Ag elicited a rapid collapse of proton motive force. This was also indicated by the observation that nano-Ag induced a massive loss of intracellular potassium. As expected, nano-Ag also decreased the cellular ATP levels, apparently resulting from the collapse of membrane potential. The rapid and complete depletion of ATP may be also indicative of a stimulation of hydrolysis of residual ATP. It is conceivable that this dissipation of bacterial membrane potential and reduction of ATP levels by nano-Ag may culminate in loss of the cell viability. In addition, nano-Ag and Ag⁺ ions in the form of AgNO₃ appear to share a similar membrane-targeting mechanism of action. The effective concentrations of nano-Ag and Ag⁺ ions are at nanomolar and micromolar levels, respectively. Nano-Ag appear to be significantly more efficient than Ag⁺ ions in mediating their antimicrobial activities (Lok et al., 2006). Yoon et al., 2007 observed that *B. subtilis* was more sensitive than *E. coli* to the nanoparticles, meaning that *E. coli* was more resistive to nanoparticles than *B. subtilis* was. They concluded that the lower sensitivities of *E. coli* as compared to *B. subtilis* is that the outer membrane of Gram-negative bacteria such as *E. coli* is predominantly constructed from tightly packed lipopolysaccharide (LPS) molecules, which provide an effective resistive barrier against nanoparticles (Yoon et al., 2008).

2.2.3 Polymer nanocomposites with enhanced photocatalytic antimicrobial properties

Modification of polymeric matrices to prevent growth or reduce adhesion of detrimental microorganisms is a highly desired objective. Hence, there is a significant interest in the development of antimicrobial biomaterials for application in the health and biomedical devices, food, and personal hygiene industries. Among several possibilities currently explored, titania (TiO₂) can be spot out as a potential candidate for polymer modification with a significant number of advantages. TiO₂ works under UV light excitation with energy above the corresponding band gap (ca. 3.2 eV) forming energy-rich electron-hole pairs. Once at the surface of the material, such charge carriers are able to interact with microorganisms rendering biocidal properties to the corresponding polymer-based nanocomposite films. A point of relevance is the control of the TiO₂ polymorphism ensuring the presence of the anatase form, the one with biocidal capability, as well as to control primary particle size in the nanometer range, a fact that would limit scattering events among other things. Novel hybrid or nanocomposite organo-inorganic materials that combine attractive qualities of dissimilar oxide and polymer components are not simply physical blends (vide supra) but can be broadly defined as complex materials having both organic and inorganic constituents intimately mixed. The scale of mixing or, in other words, the degree of homogeneity would influence or even command the properties of the nanocomposite solid materials when the component mixture is adequately reached, typically at the nanometer range. In particular, the optimization of the component contact has been shown to be crucial in order to render TiO₂-containing polymer nanocomposites with outstanding biocidal properties. Another

point of importance to improve the performance of TiO₂-containing nanocomposite systems concerns the optimization of light absorption and the adequate handling of subsequent charge (electron-hole) pair creation and annihilation processes. This task has been typically attempted by controlling the morphological-structural-defect characteristics of the oxide and/or by extending its absorption power into the visible region through a doping process (Kubacka et al., 2009). Metal doping has long been known to be one of the most effective ways to change the intrinsic band structure of TiO₂, and consequently, to improve its visible light sensitivity as well as increase its photocatalytic activity under UV irradiation.

Among various dopants, noble metals (especially Ag) have received much attention for this purpose. Among various dopants, noble metals (especially Ag) have received much attention for this purpose. It is generally believed that Ag nanoparticles enhances photoactivity of TiO₂ by lowering the recombination rate of its photo-excited charge carriers and/or providing more surface area for adsorption. Visible light absorption by surface plasmon resonance of Ag nanoparticles is also thought to induce electron transfer to TiO₂ resulting in charge separation and thus activation by visible light (Akhavan, 2009). A route to simultaneously influence both light absorption and charge handling is based on the so-called plasmonic photosystems. As detailed above, TiO₂ is excited by near-UV irradiation and a metal such as Ag shows a very intense localized surface plasmon (LSP) absorption band in the near-UV-visible region. Adequate handling of the LPS resonance can allow extending the absorption light into the visible region of the electromagnetic spectrum and, due to the enhancement of the electric near-field in the vicinity of the Ag, would allow boosting the excitation of electron-hole pairs. An overall improvement of the oxide-polymer nanocomposite performance upon excitation on a region ranged from the near-UV (above ca. 280 nm) to the visible light (below ca. 500-525 nm) can be thus envisaged through a plasmonic effect. This would yield highly efficient systems, with improved performance with respect to TiO₂-alone nanocomposites, and having the potential of working under sunlight and/or diffuse artificial light typical of human environments. A last point to mention is the concomitant degradation of the polymer matrix by effect of the charge carriers; this has been proved to be limited by addition of small amounts of titania, typically below 5 wt. % (Kubacka et al., 2009). On the other hand high release level of silver, especially for silver based bulk materials, leads to shortening the effective life of antibacterial activity. If Ag nanoparticles and nanostructures with high antibacterial activities are immobilized on porous matrixes, the release time of silver can be delayed for a long time so that these kinds of silver-supported materials will be of great potentials for bactericidal application (Akhavan, 2009). Yao et al., 2007, demonstrated that Ag, as a typical antimicrobial metal, could be homogeneously deposited onto the surface of TiO₂ photocatalyst thin films under UV light illumination. The amount of Ag deposited was controllable as desired by controlling only the UV irradiation time. The Ag/TiO₂-coated silicon catheters possessed significant bactericidal activity against *E. coli*, *P. aeruginosa*, and *S. aureus* under dark conditions. In addition, the self-cleaning property of Ag/TiO₂ thin films was confirmed on decomposition of MB dye with a certain amount of deposited Ag under UV light illumination. Thus, Ag/TiO₂ coating of silicon catheters is believed to be useful and reusable as an antimicrobial coating for medical devices against nosocomial infections. We are currently examining the photocatalytic antibacterial effect of TiO₂-coated and Ag/TiO₂-coated catheters and their safety for clinical applications (Yao et al., 2008).

3. Preparation antimicrobial nanocomposite films containing Ag and ZnO

As a case study a laboratory trial by Emamifar et al., 2010, was conducted to producing antimicrobial nanocomposite films containing Ag and ZnO. Film grade LDPE resin pellets were directly mixed with each of the antimicrobial agents including P105 powder (a combination of 95% TiO₂ powder, with an average particle diameter of about 250 nm, which acts as a base for doping of nanosilver plus 5% metal nanosilver with particle diameters of about 10 nm) and ZnO nanoparticle powder with an average particle diameter of about 70 nm (Figs 2a, b) separately and the mixture was fed into a twin-screw extruder machine to be cut into masterbatch nano-granules. Proper amounts of masterbatch resins were then added to pure LDPE resin pellets into a single-screw blowing machine to fabricate the final nanocomposite film (50 μm thick) with the desired nanomaterial concentrations (0.25 and 1% for nano-ZnO & 1.5 and 5% for P105). Dispersion quality of nanomaterials into the polymer matrix film was monitored using the Transmission Electron Microscope (Philips CM 200 kV, The Netherlands). Figs (3a, b, c, d) show TEM images of nanocomposites LDPE containing different concentrations of P105 and ZnO nanoparticles. As shown in Figs (3a, b), P105 particles are well distributed in the polymer matrix. However, a slight agglomeration is observed by increasing the concentration of particle powders to 5%. The TEM image of nanocomposite LDPE+0.25% nano-ZnO indicates that the particles are well dispersed in the polymer matrix exhibiting nanometer-scale aggregates ranging from 10 to 200 nanometers with an average size of 70 nm (Fig 3. c). As the nano-ZnO content increases to 1%, the quantity of the agglomerates increases and their size becomes more uneven (Fig 3. d).

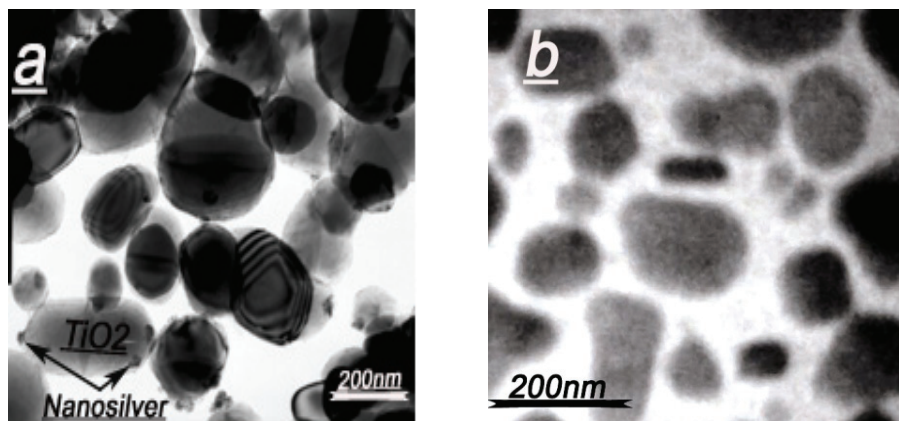


Fig. 2. TEM micrograph of a: P105 and b: nano-ZnO

4. Applications of antimicrobial polymer nanocomposites for fresh orange juice packaging

Orange juice is one of the most globally accepted fruit products. Demand for natural orange juice with high quality in terms of nutritional value, physicochemical properties and sensory characteristics with minimal or no heat treatment has increased considerably (Bull et al., 2004; Souza et al., 2004). Natural orange juice, even kept under refrigeration, has a short shelf-life due to increasing microbial spoilage (Emamifar et al., 2010). Therefore, Emamifar

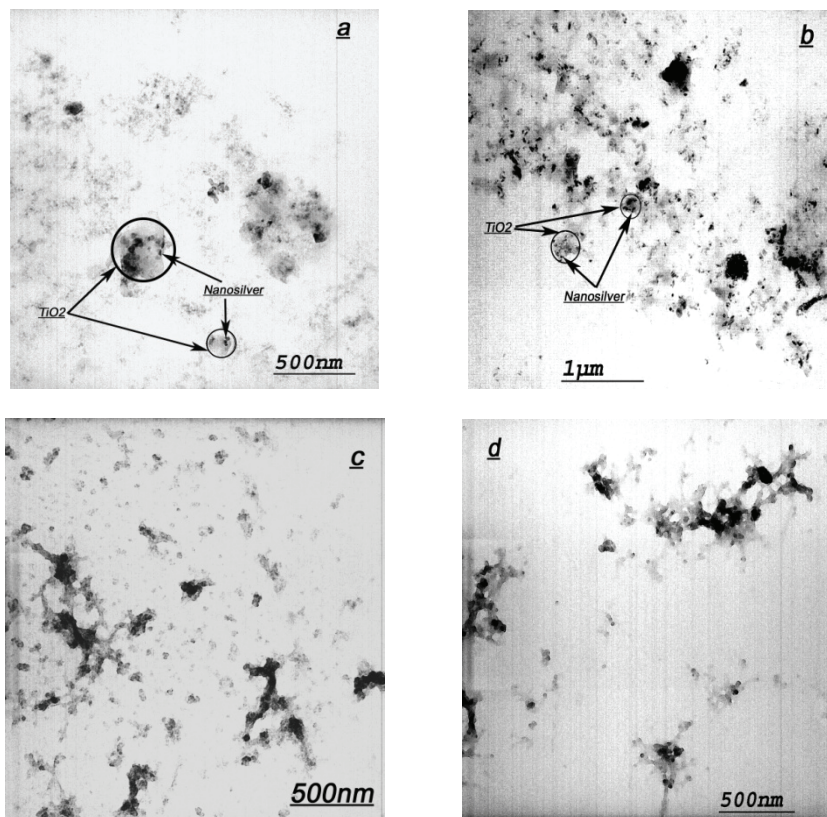


Fig. 3. TEM micrograph of antimicrobial nanocomposites LDPE film. **a:** LDPE+1.5% P105, **b:** LDPE+5% P105, **c:** LDPE+0.25% nano-ZnO, **d:** LDPE+1% nano-ZnO.

et al. 2010 evaluated the capabilities of ZnO and Ag nanoparticles filled LDPE nanocomposite packaging as a new approach to preservation and prolonging shelf life of orange juice by using an antimicrobial nanocomposite (0.25 and 1% for nano-ZnO & 1.5 and 5% for P105) and pure LDPE films 15×10 cm in size, similar to Doypack packaging commonly used for packaging fruit juice. The packages were immediately wrapped in aluminum foil and sanitized at 95°C for 2 min. After cooling and under a sterile laboratory hood, 175 ml of fresh orange juice was poured into each package and sealed by the heat sealer. Packages containing orange juice were stored in dark and cool conditions (4°C). The samples were evaluated in duplicate for their microbiological and sensory characteristics immediately after packaging and after 7, 28, and 56 days of storage.

Mean initial population immediately after packaging was determined to be 4.93 log cfu/ml for yeast and moulds and 4.83 log cfu/ml for total aerobic bacteria in orange juice. The variations in the population of yeast and moulds and total aerobic bacteria are shown in Table 1. In packages made from pure LDPE, the mean population of yeast and moulds increased whereas that of total aerobic bacteria decreased after 7 days of storage. It can be observed that yeast and moulds are better adapted to orange juice under refrigeration than

Film type	Storage time (day)	Fungi (log cfu/ml)	Total Aerobic Bacteria (log cfu/ml)
LDPE pure	0	4.94 ^{ij} ± 0.05	4.84 ^{fg} ± 0.07
	7	5.08 ^h ± 0.08	4.65 ^{hi} ± 0.05
	28	6.26 ^{cd} ± 0.02	5.27 ^d ± 0.06
	56	6.47 ^b ± 0.14	6.35 ^a ± 0.06
LDPE+1.5%P105	0	4.94 ^{ij} ± 0.03	4.83 ^{fg} ± 0.02
	7	4.51 ^k ± 0.07	4.65 ^{hi} ± 0.05
	28	5.74 ^f ± 0.04	4.85 ^{fg} ± 0.05
	56	6.16 ^d ± 0.05	5.76 ^c ± 0.16
LDPE+5%P105	0	4.94 ^{ij} ± 0.05	4.84 ^{fg} ± 0.06
	7	4.36 ^l ± 0.05	4.16 ^k ± 0.05
	28	5.43 ^g ± 0.08	4.54 ^j ± 0.05
	56	6.02 ^e ± 0.02	5.66 ^c ± 0.06
LDPE+0.25% nano-ZnO	0	4.95 ⁱ ± 0.03	4.83 ^{fg} ± 0.05
	7	4.85 ^j ± 0.03	4.62 ^{ij} ± 0.05
	28	5.97 ^e ± 0.03	4.90 ^f ± 0.10
	56	6.30 ^c ± 0.04	5.72 ^c ± 0.08
LDPE+1% nano-ZnO	0	4.90 ^{ij} ± 0.03	4.83 ^{fg} ± 0.01
	7	4.93 ^{ij} ± 0.03	4.75 ^{gh} ± 0.05
	28	6.15 ^{sc} ± 0.03	5.100 ^e ± 0.01
	56	6.59 ^a ± 0.12	6.150 ^b ± 0.01

Table 1. Effect of packaging containing Ag and ZnO nanoparticles (mean ± SD) on the fungi, and total aerobic bacteria population, during 56 days storage at 4°C.

bacteria. In the LDPE +5% P105 sample, significance decreases were observed over 7 days of storage in total count and yeast and moulds population compared with LDPE +0.25% nano-ZnO packages and LDPE pure packages containing the same concentration of nano-ZnO. Table 1 shows that the level of population of yeast and moulds and total count increased to 6.47 log cfu/ml and 6.37 log cfu/ml, respectively, after 28 days of storage in LDPE pure packages. The shelf life of fresh orange juice is defined as the time to reach a microbial population of 6 log cfu/ml (Raccach & Mellatdoust, 2007). The mean population of total

aerobic bacteria and yeast and moulds remained below 6 log cfu/ml after identical storage times in all the packages except for the LDPE +1% nano-ZnO one. By increasing nano-ZnO concentration to 1%, the antimicrobial activity of the film decreased (Table 1).

This is due to the agglomeration of nanoparticles during the processing of the film (Fig 3. d). In contrast, by increasing the nanosilver concentration, the antimicrobial activity of the film increased (Table 1). The reduced antimicrobial activity of ZnO powder might be related to the increasing particle size, which might decrease the generation of H₂O₂ from the surface of ZnO powder (Yamamoto, 2001). No significant differences were observed in total aerobic bacteria between LDPE +1.5% P105 and LDPE +0.25% nano-ZnO packages, whereas LDPE +1.5% P105 showed a higher antifungal activity compared with LDPE+0.25% nano-ZnO after 28 days of storage. It appears that antifungal activity of nanocomposites containing nanosilver is significantly ($p<0.05$) higher than that of nano-ZnO. Sawai et al., 2004 have concluded that ZnO, CaO, and MgO powders have satisfactory antimicrobial effects against broad spectrum microorganisms but that ZnO has a poor antimicrobial effect on *Saccharomyces cerevisiae* and other yeast and moulds compared with bacteria.

Based on our results (Table 1), the antimicrobial effect of Ag nanoparticles is much higher than that of ZnO nanoparticles. However, it seems that LDPE+5% P105 has a significantly ($p<0.05$) higher antimicrobial activity compared with other nanocomposites over 28 days of storage for orange juice at 4°C. This is while previous studies have shown a shelf life of up to 14 days for natural, cold orange juice (4°C) (Bull et al., 2004). Yeast, moulds and bacteria exhibit different levels of susceptibility to antimicrobial nanoparticles. The shelf life of natural orange juice has been observed to depend mainly on yeast growth in cold storage (Zanoni et al., 2005). Microbial population increased with increasing storage time to 56 days in all the test packages, indicating the limited effect of long storage time on natural orange juice preservation. However, LDPE +5% P105 packaging has a significantly less loading level at this storage time than other packaging materials. Fig.4. shows the change of sensory attributes of natural orange juice packed in different packages. The high similarity observed in color attribute scores of the packages after 28 days of cold storage ($p<0.05$) indicates that the change in the color of the samples is still invisible. These results correlated well with the values of browning index presented in Table 1. Odor attribute is greatly influenced by microbial growth and may lead to fermentation in orange juice during storage. After 28 days of storage, a significant difference is observed between the odor of orange juice packed in the test packages and that in pure package except for the one containing 1% nanoZnO. Changes in the taste of packed orange juice during 28 days of storage show the positive effect of nanoantimicrobial packaging. It is obvious that there is a significant difference between LDPE +0.25% nano-ZnO packaging and other nanosilver packaging materials, the lowest score being associated with LDPE +1% nano-ZnO and pure LDPE. The sensory panelists recognized LDPE +0.25% nano-ZnO film followed by LDPE +5% P105 and LDPE +1.5% P105 as the best packaging material in terms of overall acceptability. It is noteworthy that changing orange juice flavor during storage is not only due to the growth of microorganisms but also to heating, storage time, and the common chemical interactions that occur in stored juices (Parish, 1998; Haugaard et al., 2002). Souza et al., 2004 reported that lower storage temperatures of unpasteurized orange juice gave rise to a higher sensory acceptance than the the higher temperatures for 72h. Leizeron et al., 2005 reported that the sensorial shelf life of orange juice is equal to half its microbial and 2/3 its chemical shelf life.

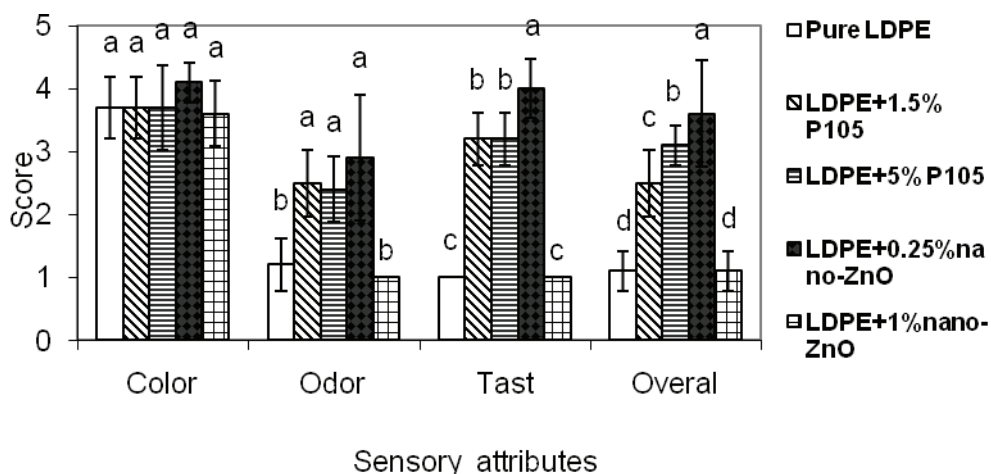


Fig. 4. Sensory attributes of orange juice that is stored in antimicrobial nanocomposite and pure packages

5. Effect of nanocomposite packaging containing Ag and ZnO on inactivation of *Lactobacillus plantarum* in orange juice

Acidophilic microorganisms have been shown to be the major contaminants of citrus juices, especially, lactic acid bacteria and yeasts. *Lactobacillus plantarum* is capable of growing over a wide pH range and spoiling minimally processed or fresh fruit juices owing to its aciduric nature, producing a “butter” off-flavor and swelling of packages. Antimicrobial food packaging materials have to extend the lag phase and reduce the growth rate of microorganisms in order to extend shelf life and to maintain product quality and safety (Emamifar et al. 2011). Emamifar et al. 2011, continued their studied using nanocomposite packaging containing Ag and ZnO on inactivation of *Lactobacillus plantarum* in orange juice. The growth curve of *L. plantarum* was studied and results showed that the stationary phase was reached after 8 h of incubation at 37°C under 5% CO₂ atmosphere (Fig. 5). The survivor curves showed the relationship between microbial population and OD versus time of incubation.

Sterilized orange juice was inoculated with *L. plantarum* at 8.5 log cfu/ml and packaged in antimicrobial and pure LDPE films similar to **Section 4**. Packages containing inoculated orange juice were stored in dark and cool conditions (4°C) and microbial counts of the samples were evaluated immediately after packaging and after 7, 28, 56, 84 and 112 days of storing. Mean initial microbial population immediately after packaging was determined to be 8.5 log cfu/ml in orange juice. The variations in the *L. plantarum* numbers during storage, are shown in Fig. 5. In all of packages, the mean population increased after 7 days of storage. In the LDPE +5% P105 samples, significance decreases ($p < 0.05$) were observed over 7 days of storage in *L. plantarum* numbers compared with LDPE +0.25% nano-ZnO packages and LDPE pure packages containing the same concentration of nano-ZnO. According to Fig. 5, the level of microbial population increased to 8.82 log cfu/ml after 56 days of storage in

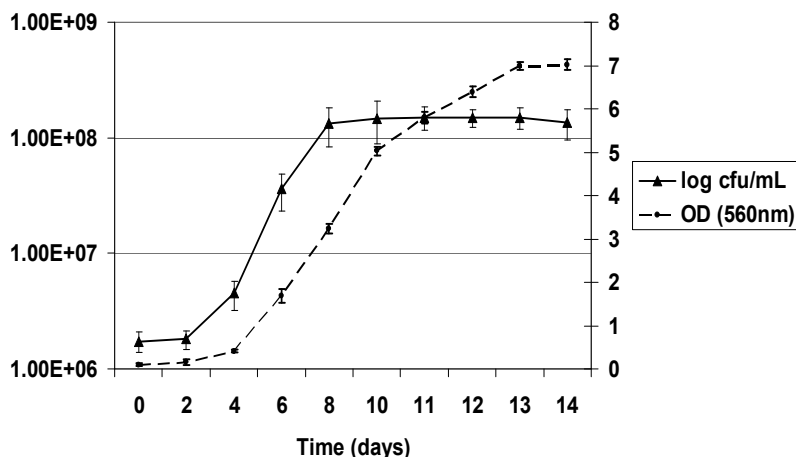


Fig. 5. The survivor curves of *Lactobacillus plantarum*

LDPE pure packages which is higher than that of in LDPE +5% P105 (8.23 log cfu/ml), LDPE +1.5% P105 (8.48 log cfu/ml), LDPE +0.25% nano-ZnO (8.56 log cfu/ml), and LDPE +1% nano-ZnO (8.73 log cfu/ml). No significant differences were observed in *L. plantarum* populations between LDPE +1.5% P105 and LDPE +0.25% nano-ZnO packages, after 56 days of storage. Microbial population increased with increasing storage time to 56 days and then decreased up to 112 days of storage in all the test packages. However, microbial growth in LDPE +5% P105, LDPE +1.5% P105, LDPE+0.25% nano-ZnO, and LDPE+1% nano-ZnO compared with pure LDPE packages, showed a higher reduction up to 112 days storage at 4°C, respectively. Packages containing nanosilver had lower ($P < 0.05$) bacterial populations compared packages containing nano-ZnO (Fig. 6). The LDPE +5% P105 packages had a significantly less loading level for 112 days of storage than other packages.

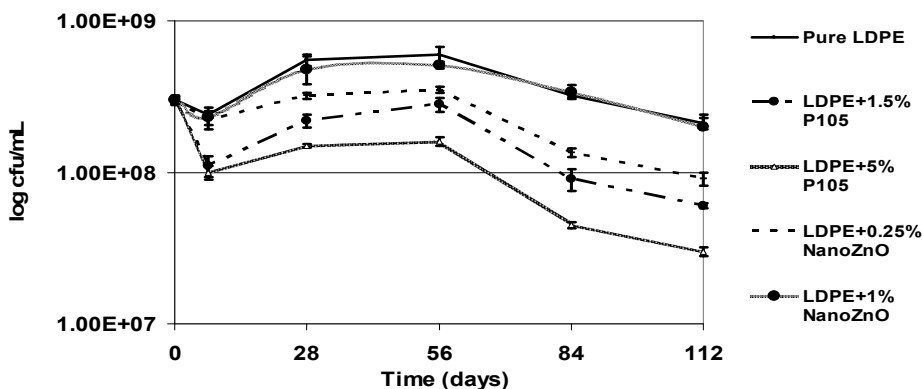


Fig. 6. Effect of packaging containing Ag and ZnO nanoparticles on the population of *L. plantarum* during 112 days of storage at 4°C.

6. Metal ions releasing measurement

The quantities of silver and Zinc ions in orange juice after 112 days of storage are shown in Table 2. The quantity of silver ions migrating into orange juice after 112 days, is less than its allowable concentration (10 ppm). It has been reported that silver ions at as low concentrations as 10^{-9} moles $^{-1}$ have an antimicrobial effect in water (Damm et al., 2006). Moreover, the quantity of Zinc ions indicated a higher rate of Zn migration than that of silver but as Zinc is proved to be a GRAS compound for food applications, its low concentration is in the acceptable range for food consumers (Jin et al., 2009).

Concentration ions (μgL^{-1})	Storage Time (days)	Film type			
		LDPE+ 1.5% P105	LDPE+ 5% P105	LDPE+ 0.25% nano-ZnO	LDPE+ 1% nano-ZnO
Silver	28	ND ^a	0.1 ± 0.003		
	56	ND	0.11 ± 0.005		
	84	ND	0.13 ± 0.005		
	112	ND	0.15 ± 0.002		
Zinc	28			0.16 ± 0.007	0.11 ± 0.005
	56			0.26 ± 0.006	0.13 ± 0.004
	84			0.48 ± 0.002	0.30 ± 0.005
	112			0.68 ± 0.002	0.54 ± 0.005

Table 2. The quantity of Ag and Zn ions (mean \pm SD) released from nanocomposite LDPE films containing Ag and ZnO nanoparticles in orange juice after 112 days of storage at 4°C.

7. Conclusion

This study showed that application of LDPE nanocomposite packaging materials containing Ag and ZnO nanoparticles is a new approach for preserving and extending the microbial shelf life of fresh orange juice at 4°C. The quality of the packaging film including good dispersion of nanomaterials in the polymer matrix free from agglomeration was shown to be very effective on the antimicrobial effects of these packaging materials. Application of packages containing nano-ZnO prolonged the shelf life of fresh orange juice up to 28 days without any negative effects on sensorial parameters. Nanosilver had a higher antimicrobial activity on *L. plantarum*, yeast and moulds compared with ZnO nanoparticles, especially for

longer storage times. These results would help the industry for combining pasteurization with antimicrobial nanocomposite packages that resulted in developing of cost-effective pasteurization method to control microorganisms in orange juice and to preserve the desirable qualities of it.

8. Acknowledgment

I gratefully acknowledge considerable assistance from Parastoo Samadi (Master of Engineering in Food Science).

9. References

- Adams, L. K.; Lyon, D. Y. & Alvarez, P. J. J. (2006). Comparative eco-toxicity of nanoscale TiO₂, SiO₂, and ZnO water suspensions. *Water Research*, Vol.40, No.19, (November 2006), pp. 3527-3532, ISSN 0043-1354
- Akhavan, O. (2009). Lasting antibacterial activities of Ag-TiO₂/Ag/a-TiO₂ nanocomposite thin film photocatalysts under solar light irradiation. *Journal of Colloid and Interface Science*, Vol.336, No.1, (August 2009), pp. 117-124, ISSN 0021-9797
- Appendini, P. & Hotchkiss, J. H. (2002). Review of antimicrobial food packaging. *Innovative Food Science and Emerging Technologies*, Vol.3, No.2, (June 2002), pp. 113-126, ISSN 1466-8564
- Azeredo, H. M. C. (2009). Nanocomposites for food packaging applications. *Food Research International*, Vol.42, No.9, (November 2009), pp. 1240-1253, ISSN 0963-9969
- Brody, A.; Bugusu, B.; Han, J. H.; Sand, C. K. & Machugh, T. H. (2008). Inovative food packaging solutions. *Journal of Food Science*, Vol.73, No.8, (October 2008), pp. 107 - 116, ISSN 1750-3841
- Bull, M. K., Zerdin, K., Goicoechea, D., Paramanandhan, P., Stockman, R., Sellahewa, J. Et al. (2004). The effect of high pressure processing on the microbial, physical and chemical properties of Valencia and Navel orange juice. *Innovative Food Science and Emerging Technology*, Vol.5, No.2, (June 2004), pp. 135-149, ISSN 1466-8564
- Chaudhry, Q. S., M.; Blackburn, J.; Ross, B.; Boxall, A. & Castle, L. (2008). Applications and implications of nanotechnologies for the food sector. *Food Additives & Contaminants*, Vol.25, No.3, (March 2008), pp. 241-258, ISSN 1464-5122
- Chawengkijwanich, C. & Hayata, Y. (2008). Development of TiO₂ powder-coated food packaging film and its ability to inactivate Escherichia coli in vitro and in actual tests. *International Journal of Food Microbiology*, Vol.123, No.3, (April 2008), pp. 288-292, ISSN 0168-1605
- Damm, C., Neumann, M., & Münstedt, H. (2005). Properties of nanosilver coatings on polymethyl methacrylate. *Soft Materials*, Vol. 3, No.2,3, (May 2005), pp. 71-88, ISSN 1539-4468
- De Kruijff, N.; Van Beest, M.; Rijk, R.; Sipilainen-Malm, T.; Losada, P. P. & De Meulenaer, B. (2002). Active and intelligent packaging: applications and regulatory aspects. *Food Additives & Contaminants*, Vol. 19, No.4, (April 2002), pp. 144-162, ISSN 1464-5122
- Emamifar, A., Kadivar, M., Shahedi, M. & Solaimanianzad, S. (2010). Evaluation of nanocomposite packaging containing Ag and ZnO on the shelf life of fresh orange

- juice. *Innovative Food Science & Emerging Technologies.*, Vol. 11, No.4, (October 2010), pp. 742–748, ISSN 1466-8564
- Emamifar, A., Kadivar, M., Shahedi, M. & Solaimanianzad, S. (2011). Effect of nanocomposite packaging containing Ag and ZnO on inactivation of *Lactobacillus plantarum* in orange juice. *Food Control*, Vol. 22, No.3,4, (March-April 2011), pp. 408-413, ISSN 0956-7135
- Haugaard, V. K., Weber, C. J., Danielsen, B., & Bertelsen, G. (2002). Quality changes in orange juice packed in materials based on polylactate. *European Food Research and Technology*, Vol. 214, No.5, (November 2002), pp. 423–428, ISSN 1438-2385
- Jin, T., Sun, D., Su, J. Y., Zhang, H., & Sue, H. J. (2009). Antimicrobial efficacy of zinc oxide quantum dots against *Listeria monocytogenes*, *Salmonella enteritidis*, and *Escherichia coli* O157:H7. *Journal of Food Science*, Vol. 74, No.1, (Jan-Feb 2009), pp. 46-52, ISSN 1750-3841
- Jones, N.; Ray, B.; Ranjit, K. T. & Manna, A. C. (2008). Antibacterial activity of ZnO nanoparticle suspensions on a broad spectrum of microorganisms. *FEMS Microbiology Letters*, Vol. 279, No.1, (February 2008), pp. 71–76, ISSN 1574-6968
- Kim, Y. M.; Kuk, E.; Yu, K. N.; Kim, J. H.; Park, S. J. & Lee, H. J. (2007). Antimicrobial effects of silver nanoparticles. *Nanomedicine: Nanotechnology, Biology, and Medicine*, Vol. 3, No.1, (March 2007), pp. 95– 101, ISSN 1549-9634
- Kubacka, A. C., M. L.; Serrano, C.; Fernández-García, M.; Ferrer, M. & Fernández-García, M. (2009). Plasmonic nanoparticle/polymer nanocomposites with enhanced photocatalytic antimicrobial properties. *The Journal of Physical Chemistry C*, Vol. 113, No.21, (May 2009), pp. 9182–9190, ISSN 1932-7455
- Leizeron, S., & Shimoni, E. (2005). Stability and sensory shelf Life of orange juice pasteurized by continuous ohmic heating. *Journal of Agriculture and Food Chemistry*, Vol. 53, No.10, (May 2005), pp. 4012-4018, ISSN 1520-5118
- Li, Q., Mahendra, S.; Lyon, D. Y.; Brunet, L.; Liga, M. V.; Li, D. & Alvarez, P. J. J. (2008). Antimicrobial nanomaterials for water disinfection and microbial control: Potential applications and implications. *Water Research*, Vol. 42, No.18, (November 2008), pp. 4591-4602, ISSN 0043-1354
- Lok, C. N., Ho, C. M.; Chen, R.; He, Q. Y.; Yu, W. Y.; Sun, H.; Tam, P. K. H.; Chiu, J. F. & Che, C. M. (2006). Proteomic analysis of the mode of antibacterial action of silver nanoparticles. *Journal of Proteome Research*, Vol. 5, No.4, (April 2006), pp. 916-924, ISSN 1535-3907
- Morones, J. R.; Elechiguerra, J. L.; Camacho, A.; Holt, K.; Kouri, J. B.; Ramírez, J. T. & Yacaman, M. J. (2005). The bactericidal effect of silver nanoparticles. *Nanotechnology*, Vol. 16, No.10, (October 2010), pp. 2346–2353, ISSN 1361-6528
- Mauriello, G. D. L., E.; La Storia, A.; Villani, F. & Ercolini, D. (2005). Antimicrobial activity of a nisin-activated plastic film for food packaging. *Letters in Applied Microbiology*, Vol. 41, No.6, (December 2005), pp. 464–469, ISSN 1472-765X
- Ozdemir, M., Floros, J. D. (2004). Active food packaging technologies. *Critical Reviews in Food Science and Nutrition*, Vol. 44, No.3, (October 2010), pp. 185–193, ISSN 1040-8398

- Parish, M. E. (1998). Orange juice quality after treatment by thermal pasteurization or Isostatic High Pressure. *Lebensmittel Wissenschaft und Technologie*, Vol. 31, No.5, (August 1998), pp. 439-442, ISSN, 0023-6438
- Padmavathy, N. & Vijayaraghavan, R. (2008). Enhanced bioactivity of ZnO nanoparticles – an antimicrobial study. *Science and Technology Advanced Materials*, Vol. 9, No.3, (September 2008), pp. 1-7, ISSN 1878-5514
- Raccach, M. & Mellatdoust, M. (2007). The effect of temperature on microbial growth in orange juice. *Journal of Food Processing and Preservation*, Vol. 31, No.2, (April 2007), pp. 129-142, ISSN 1745-4549
- Radheshkumar, C. & Münstedt, H. (2006). Antimicrobial polymers from polypropylene/silver composites-Ag⁺ release measured by anode stripping voltammetry. *Reactive and Functional Polymers*, Vol. 66, No.7, (July 2006), pp. 780-788, ISSN 1381-5148
- Rai, M.; Yadav, A. & Gade, A. (2009). Silver nanoparticles as a new generation of antimicrobials. *Biotechnology Advances*, Vol. 27, No.1, (Jan-Feb 2009), pp. 76-83, ISSN 0734-9750
- Restuccia, D.; Spizzirri, U. G.; Parisi, O. I.; Cirillo, G.; Curcio, M.; Iemma, F.; Puoci, F.; Vinci, G. & Picci, N. (2010). New EU regulation aspects and global market of active and intelligent packaging for food industry applications. *Food Control*, Vol. 21, No.11, (November 2010), pp. 1425-1435, ISSN 0956-7135
- Sawai, J. & Yoshikawa, T. (2004). Quantitative evaluation of antifungal activity of metallic oxide powders (MgO, CaO and ZnO) by an indirect conductimetric assay. *Journal of Applied Microbiology*, Vol. 96, No.4, (April 2004), pp. 803-809, ISSN 1365-2672
- Suppakul, P.; Miltz, J.; Sonneveld, K. & Bigger, S. W. (2003). Active packaging technologies with an emphasis on antimicrobial packaging and its applications. *Journal of Food Science*, Vol. 68, No.2, (April 2004), pp. 408-420, ISSN 1750-3841
- Souza, M. C. C., Benassi, M. T., Meneghel, R. F. A., & Silva, R. S. S. F. (2004). Stability of unpasteurized and refrigerated orange juice. *Brazilian Archives of Biology and Technology*, Vol. 47, No.3, (July 2004), pp. 391-397, ISSN, 1516-8913
- Weiss, J.; Takhistov, P. & McClements, D. J. (2006). Functional materials in food nanotechnology. *Journal of Food Science*, Vol.71, No.9, (Nov-Dec 2006), pp. 107-116, ISSN, 1750-3841
- Yamamoto, O. (2001). Influence of particle size on the antibacterial activity of zinc oxide. *International Journal of Inorganic Materials*, Vol. 3, No.7, (November 2001), pp. 643-646, ISSN, 1466-6049
- Yao, Y.; Ohko, Y.; Sekiguchi, Y.; Fujishima, A. & Kubota, Y. (2008). Self-sterilization using silicone catheters coated with Ag and TiO₂ nanocomposite thin film. *Journal of Biomedical Materials Research Part B: Applied Biomaterials*, Vol.85B, No.2, (May 2008), pp. 453-460, ISSN 1552-4981
- Yoon, K. Y. H., B. J.; Park, J. H. & Hwang, J. (2007). Susceptibility constants of Escherichia coli and Bacillus subtilis to silver and copper nanoparticles. *Science of the Total Environment*, Vol.373, No.2-3, (January 2007), pp. 572-575, ISSN, 0048-9697

- Zanoni, A., Pagliarini, E., Galli, A., & Laureati, M. (2005). Shelf-life prediction of fresh blood orange juice. *Journal of Food Engineering*, Vol.70, No.4, (October 2005), pp. 512-517, ISSN, 0260-8774
- Zhang, L.; Jiang, Y.; Ding, Y.; Povey, M. & York, D. (2007). Investigation into the antibacterial behaviour of suspensions of ZnO nanoparticles (ZnO nanofluids). *Journal of Nanoparticle Research*, Vol.9, No.3, (June 2007), pp. 479-489, ISSN 1388-0764

Functional Polymer Nanocomposite Materials from Microfibrillated Cellulose

Philippe Tingaut, Christian Eyholzer and Tanja Zimmermann
Swiss Federal Laboratories for Materials Science and Technology (EMPA)
Switzerland

1. Introduction

In line with recent environmental policies, increased attention has been paid to the development of bio-based nanocomposite materials for several industrial applications, such as automotive, construction, packaging or medical applications. Thus, much effort has been devoted to the use of natural fibers in composite materials as an alternative to conventional inorganic fillers, traditionally used to reinforce thermoplastic matrices (*i.e.*, glass fibers, aramid or carbon fibers, for instance). (Eichhorn, 2006; Pandey, et al., 2005) Hence, natural fibers present very attractive properties such as low cost, renewability, biodegradability and low density. (Bledzki & Gassan, 1999; Samir, et al., 2005)

Cellulose is the most abundant biopolymer on earth, and is present in natural fibers such as wood, cotton or hemp, as well as in a wide variety of living species, such as animals, plants and bacteria. This linear polymer is composed of β -1,4 linked glucopyranose units, with polymer chains associated by hydrogen bonds forming bundles of fibrils, also called microfibrillar aggregates, where highly ordered regions (*i.e.*, crystalline phases) alternate with disordered domains (*i.e.*, amorphous phases). (Samir, Alloin & Dufresne, 2005) In the last decades, the production of cellulose nanofibers from different sources has gained a tremendous success. Hence, apart from the already mentioned advantages related to natural fibers, cellulosic nanoelements also possess very high strength and stiffness, therefore making them excellent reinforcing agents for nanocomposites. As will be discussed later in detail, two main types of cellulose nanofibers can be produced: the Cellulose nanowhiskers (CNW) and Microfibrillated cellulose (MFC). These natural fillers differ from their size and crystallinity, but the highest aspect ratios are usually found for MFC.

In the past decade, the EMPA Wood Laboratory has acquired a strong experience in the production, functionalization and use of MFC for a wide range of applications, including adhesives, packaging or medical applications. Consequently, this book chapter will specifically address the elaboration of functional nanocomposite materials using MFC as reinforcing agent. A first section will present the production and properties of MFC. In a second section, the chemical modification of MFC will be presented, therefore highlighting the possibility to tailor the surface polarity of the cellulosic fillers. Finally, a third section will address the elaboration of nanocomposite materials from unmodified and functionalized MFC.

2. Cellulose nanofibers

As stated in the Introduction part, cellulosic nanoelements are mainly divided into two main families, which are the CNW and MFC. We will thus present these nanofibers in terms of preparation and morphological properties, with an emphasis on MFC.

2.1 Cellulose Nanowhiskers (CNW)

CNW, also called cellulose nanocrystals, are usually isolated from cellulose fibers through an acid treatment. This simple process involves an acid hydrolysis of the biomass using concentrated sulfuric acid (H_2SO_4), which removes disordered or paracrystalline regions of cellulose and leaves crystalline regions intact. After this treatment, cellulose nanocrystals with a rod-like morphology are produced. The geometrical dimensions of these nanoparticles depend on the starting cellulose source, resulting in CNW with widths in the nanometer scale and lengths from nanometer to micrometer scale. An example of CNW isolated from Microcrystalline Cellulose is presented in Fig. 1.

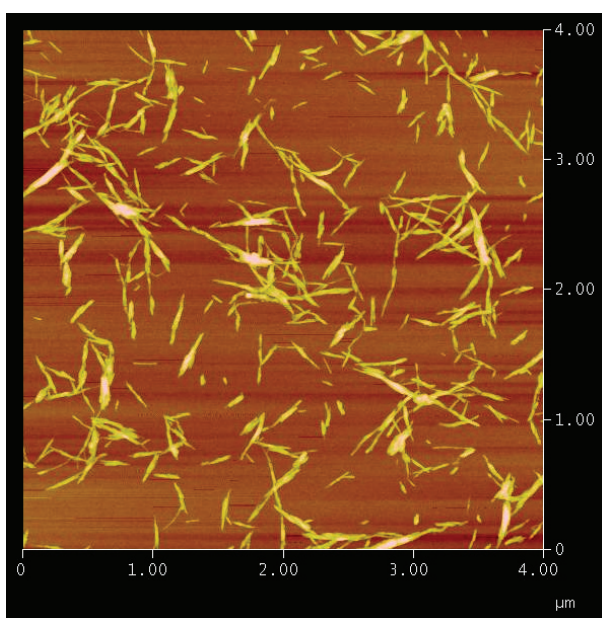


Fig. 1. AFM image of CNW

2.2 Microfibrillated Cellulose (MFC)

As compared with CNW, MFC consists of long, flexible and entangled cellulose nanofibers. MFC can be prepared from different raw materials and preparation processes, the characteristics of the resulting nanofibers being dependant on these two parameters. Wood constitutes the most important source of cellulose nanofibers, however research on other potentially suitable cellulose-based materials is in progress, especially in developing countries where agricultural wastes are underutilized. For this reason, cellulose sources coming from agricultural by-products have already successfully been tested for the

production of MFC, such as wheat straw, sugar beat pulp, potato pulp or bagasse.(Siro & Plackett, 2010)

Concerning the production of MFC, several mechanical treatments have been used, such as a two-steps process including a refining and a high-pressure homogenization steps, cryocrushing, and grinding methods. Developed in 1983 by Turbak *et al.*, the homogenization technology allows the production of a network of interconnected cellulose microfibrils, with diameters from 10 to 100 nm and aspect ratios from 50 to 100.(Boldizar, et al., 1987; Gardner, et al., 2008; Turbak, et al., 1983; Zimmermann, et al., 2004) Without any cellulose pre-treatment, the two-steps mechanical process has usually led to the obtention of MFC with the smallest diameters.(Zimmermann, Pöhler & Geiger, 2004) Nevertheless, in order to decrease the high energy consumption associated with such processes, chemical (Habibi, et al., 2006; Iwamoto, et al., 2007; Lasseuguette, et al., 2008) and enzymatic (Henriksson & Berglund, 2007; Janardhnan & Sain, 2006; Paakko, et al., 2007) pre-treatments together with subsequent mechanical processes have also led to the preparation of cellulose nanofibers with diameters between 5 and 30 nm. In the EMPA Wood laboratory, MFC is obtained from cellulose fibers after a two-step mechanical disintegration process, consisting of an initial refining step followed by a high pressure homogenization step. Fig. 2 presents an example of MFC isolated from oat straw cellulose powder in our laboratory.

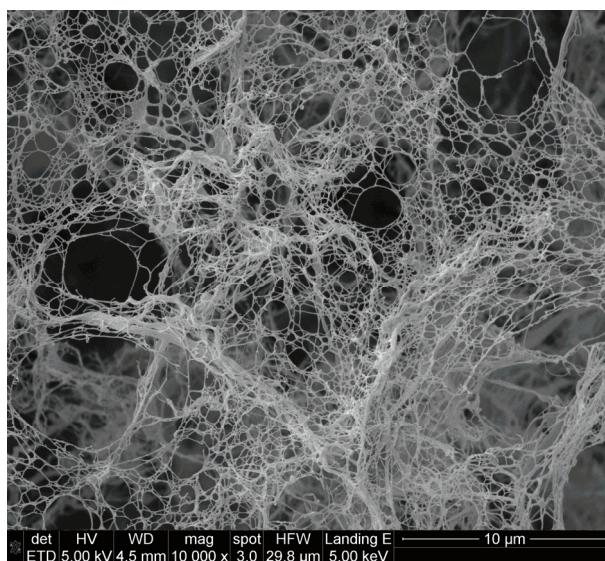


Fig. 2. SEM image of MFC mechanically isolated from oat straw cellulose powder

3. Limitations of MFC in composite applications

Nevertheless, despite all previously stated advantages, MFC suffers from its strong hydrophilic character which causes two critical issues, namely the hornification during drying and agglomeration of MFC in non-polar matrices during compounding.

Irreversible agglomeration of cellulose during drying is called hornification and is explained by the formation of additional hydrogen bonds between amorphous parts of the cellulose

fibrils during drying. (Young 1994; Hult et al. 2001) The formation of these bonds is related to the amount of water removed, and does not depend directly on temperature. As in the crystalline parts of cellulose, water cannot break the formed hydrogen bonds of hornified cellulose during rewetting. (Eyholzer, et al., 2010a) For this reason, isolation of MFC is preferentially done by mechanical disintegration of never dried pulp in aqueous suspension of low cellulose concentration (1 to 2 % w/w). The consequences are high storage volumes and shipping costs, as well as a decrease in storage life of the product due to bacterial degradation.

Moreover, in order to match the targeted property improvements, the natural fibers must be homogeneously dispersed in the polymeric matrix, which is non-trivial. Hence, due to its strong hydrophilic character and high aspect ratio, MFC tends to flocculate through hydrogen bonding. In general, the dispersion of hydrophilic MFC in apolar solvents, as well as its further homogeneous incorporation in most common apolar thermoplastic polymers, is challenging. A non homogeneous dispersion of the filler in the polymer matrix is often obtained, thus decreasing the final mechanical properties of the nanocomposite material. (Hubbe, et al., 2008) For these reasons, the preparation of nanocomposite materials from MFC has often been restricted to water soluble polymers, (Dufresne & Vignon, 1998; Lu, et al., 2008b; Zimmermann, Pöhler & Geiger, 2004; Zimmermann, Pöhler & Schwaller, 2005) latexes, (Samir, et al., 2004) acrylic and phenol-formaldehyde resin through a fiber impregnation process, (Iwamoto, Nakagaito & Yano, 2007; Nakagaito & Yano, 2008; Nakagaito & Yano, 2004; Nakagaito & Yano, 2005), or poly(lactic acid) under specific compounding conditions. (Iwatake, et al., 2008; Nakagaito, et al., 2009; Suryanegara, et al., 2009) As compared with neat matrices, the incorporation of MFC led to an increase in mechanical properties such as bending and tensile strength, (Iwatake, Nogi & Yano, 2008; Nakagaito, Fujimura, Sakai, Hama & Yano, 2009; Nakagaito & Yano, 2004; Suryanegara, Nakagaito & Yano, 2009; Zimmermann, Pöhler & Geiger, 2004) Young's modulus, (Iwatake, Nogi & Yano, 2008; Nakagaito & Yano, 2008; Nakagaito & Yano, 2005; Zimmermann, Pöhler & Geiger, 2004; Zimmermann, Pöhler & Schwaller, 2005), as well as thermal stability. (Dufresne & Vignon, 1998; Iwatake, Nogi & Yano, 2008; Lu, Wang & Drzal, 2008b; Nakagaito, Fujimura, Sakai, Hama & Yano, 2009; Samir, Alloin, Paillet & Dufresne, 2004; Suryanegara, Nakagaito & Yano, 2009) Moreover, recent studies have highlighted the possibility to prepare optically transparent nanocomposites by impregnating MFC with an acrylic resin. (Iwamoto, Nakagaito & Yano, 2007)

Nevertheless, the hydrophilic character of MFC constitutes a major obstacle for its use in composite applications. In order to tackle this problem, one strategy involves the chemical modification of MFC's surface hydroxyl groups, in order to prevent hornification phenomena and/or decrease the nanofiber surface hydrophilicity.

4. Chemical modification of MFC

In the past decades, the chemical modification of MFC has received a significant interest from the scientific community. Thus, many reactions have already been performed in order to permanently modify the surface properties of the nanofibers (*i.e.*, surface polarity), involving the use of the TEMPO oxidative agent, (Lasseguette, Roux & Nishiyama, 2008; Saito, et al., 2006) silane reagents, (Andresen, et al., 2006; Gousse, et al., 2004; Gousse, et al., 2002; Grunert & Winter, 2002; Lu, et al., 2008a) isocyanates, (Nair, et al., 2003; Siqueira, et al., 2009) poly(ϵ -caprolactone), (Habibi & Dufresne, 2008) or anhydrides. (Cavaille, et al., 1997;

Ifuku, et al., 2007; Kim, et al., 2002; Nogi, et al., 2006; Sassi & Chanzy, 1995; Stenstad, et al., 2008)

In our laboratory, we have been particularly interested in developing simple and efficient modification pathways that could be potentially suitable for the modification of MFC at industrial scale. In this section, we will present two examples of chemical modifications which were envisaged to improve the nanofibers' properties in polar and non polar environments.

4.1 Carboxymethylation of MFC

Partial carboxymethylation of the MFC hydroxyl groups has been envisaged to overcome hornification during drying, with the aim to prepare dry, water-redispersible MFC (Fig. 3).

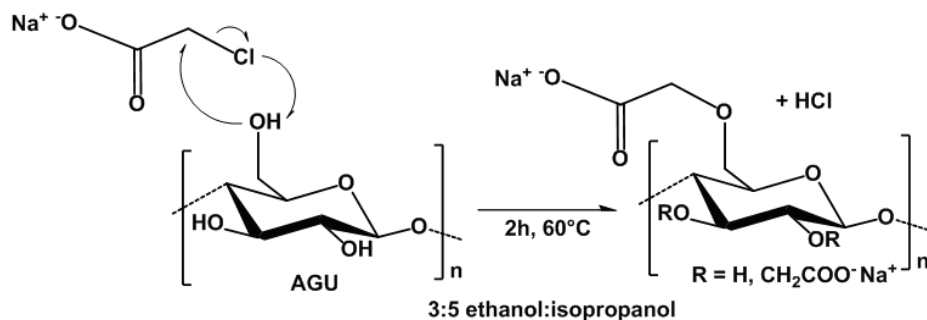


Fig. 3. Carboxymethylation of MFC

The success of the reaction was monitored using different characterization techniques, such as Fourier-Transformed Infrared Spectroscopy (FTIR) and Solid-State NMR spectroscopy. Finally, the impact of the modification on the properties of the modified MFC was evaluated, such as redispersion properties in water and crystallinity.

Two sets of experiments were compared. Unmodified and chemically modified MFC were dried to a powder from an aqueous suspension, and then redispersed in water. Finally, a drop of these suspensions was freeze-dried and the morphology of the resulting nanofibers was assessed using Scanning Electron Microscopy (SEM). Fig. 4 presents the crystallinity values, SEM and redispersion test images of these two samples. Results indicated that the crystalline structure of MFC was partially affected by the treatment, but a crystallinity of 49% could still be remained. But most importantly, differences were noted concerning the dispersion properties and morphology of these two samples. After 1h, a complete sedimentation of the unmodified MFC was observed, and the SEM characterization revealed large aggregates which were not dispersed in the suspension. These results confirmed the hornification problem of unmodified MFC. On the other hand, a stable and transparent suspension was obtained for the carboxymethylated MFC, a network of nanofibers with overall diameters below 100 nm being observed by SEM after freeze drying. Moreover, by varying the Degree of Substitution (DS), other morphological and dispersion properties of MFC could be obtained (not shown here).

In conclusion, these results confirmed the possibility to prepare dry, redispersable MFC with the carboxymethylation reaction, which is strongly interesting for composite applications.

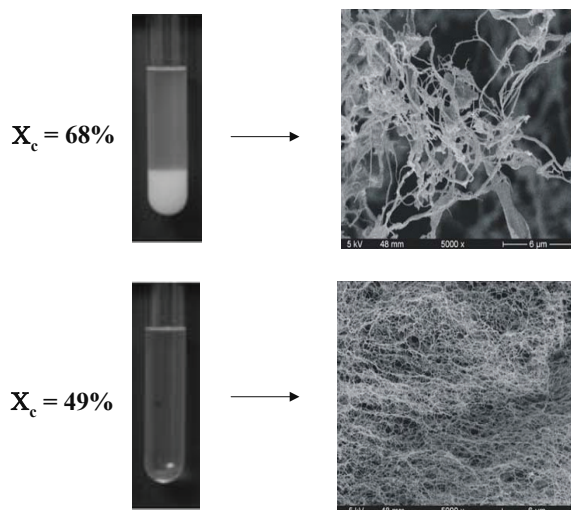


Fig. 4. Crystallinity (X_c), redispersion tests in water (0.2% w/w, 1h) and SEM images of unmodified and carboxymethylated MFC

4.2 Acetylation of MFC

In another approach, the acetylation of MFC has been envisaged to decrease the nanofibers hydrophilicity, and further improve the chemical affinity between MFC and non-polar environments (Fig. 5).

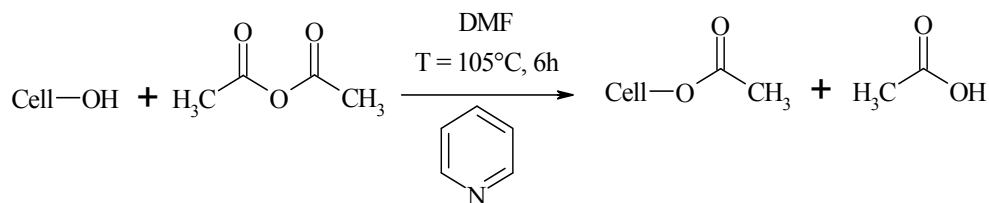


Fig. 5. Chemical modification of MFC with Acetic Anhydride

The acetylation reaction has been monitored spectroscopically, and the kinetics of the reaction was obtained by plotting the evolution of the DS against reaction time (Figure 6). As shown in this graph, the DS increased rapidly during the first 60 min, suggesting that the reaction occurred primarily on easily accessible surface hydroxyl groups (OH). On the other hand, the reaction rate gradually slowed down up to 180 min, with DS ranging from 0.37 to 0.41. This behavior was associated with the modification of less accessible surface OH groups which may be located deeper in the nanofibers, as well as steric hindrance induced by grafted acetyl groups on fiber surfaces, thus affecting the reaction rate.

In parallel, the dispersion properties of unmodified and acetylated MFC were examined in CHCl_3 , a solvent of low polarity (Fig. 6). All nanofibers were first manually dried to a powder form and redispersed afterwards in CHCl_3 . Unmodified MFC could not be dispersed, as a result of strong hornification during drying. However, the suspensions of

acetylated MFC showed varying degrees of stability, which were dependent on DS. Stable suspensions were observed for acetylated MFC with a DS above 0.18, the suspensions being increasingly homogeneous with the modification rate. This behavior was associated with the increasing amount of acetyl moieties on the cellulose surface, thus limiting the interactions between adjacent microfibrils. However, a total flocculation was observed for MFC with a DS of 0.13, which was associated with an incomplete acetylation of the nanofibers surface. These innovative results confirm that the acetyl groups prevent the interactions between nanofibers, and suggest that a minimum DS is required to efficiently disperse dried MFC in CHCl_3 . This finding is of great interest from an economical point of view, as the acetylation treatment would also provide powdered MFC, reducing significantly the transportation costs.

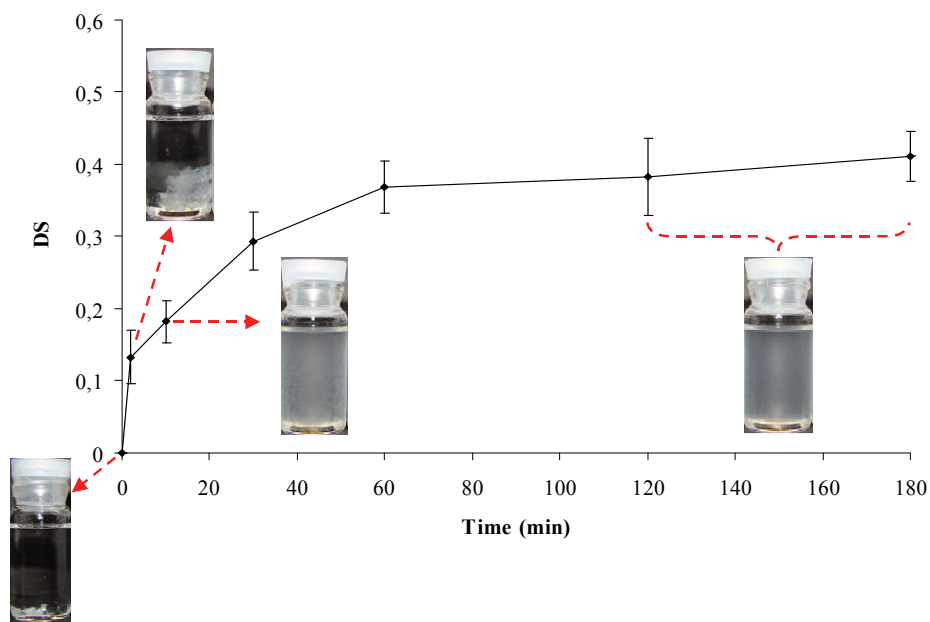


Fig. 6. Evolution of DS as function of reaction time. Photographs indicated by red arrows display the stability of the suspension in CHCl_3

5. Elaboration of nanocomposites from MFC

As stated in the previous sections, our activities in the EMPA Wood Laboratory have been dealing with the reinforcement of polar and non polar polymer matrices for many applications. In this section, examples of nanocomposites reinforced with unmodified and chemically modified MFC will be presented, and the envisaged applications of the resulting nanocomposites will be addressed for all of them. Two polymer matrices were envisaged, namely the hydrophilic Hydroxypropyl Cellulose (HPC) and the hydrophobic Poly(lactic acid) polymers. Unmodified and functionalized MFC were both used as reinforcing agents, and the impact of the modification on the resulting composite properties was evaluated. All nanocomposite films were prepared using a solvent casting approach, a simple and efficient method commonly used at laboratory scale for the preparation of composite materials.

5.1 HPC nanocomposites

HPC is a highly interesting cellulose derivative which has been extensively analyzed, regarding its ability to form liquid crystalline (LC) mesophases (Werbowyj & Gray, 1976; Werbowyj & Gray, 1980) and its compatibility with cellulosic nanofibers.(Johnson, et al., 2009; Zimmermann, Pöhler & Geiger, 2004). Therefore, we envisaged to reinforce HPC using unmodified and carboxymethylated MFC, and we studied the impact of drying these nanofibers on their reinforcing potentials in HPC composites.(Eyholzer, et al., 2010b) The carboxymethylated nanofibers being not susceptible to hornification problems, the preservation of their ability to reinforce matrices in powder form would be highly beneficial from a practical and industrial point of view.

The polymer matrix was reinforced with either never-dried (aq) or dried and redispersed (s) nanofibers. All composite films had a filler content of 20% (w/w) and were characterized by dynamic mechanical analysis (DMA). The viscoelastic responses of all composites studied are presented in Fig. 7.

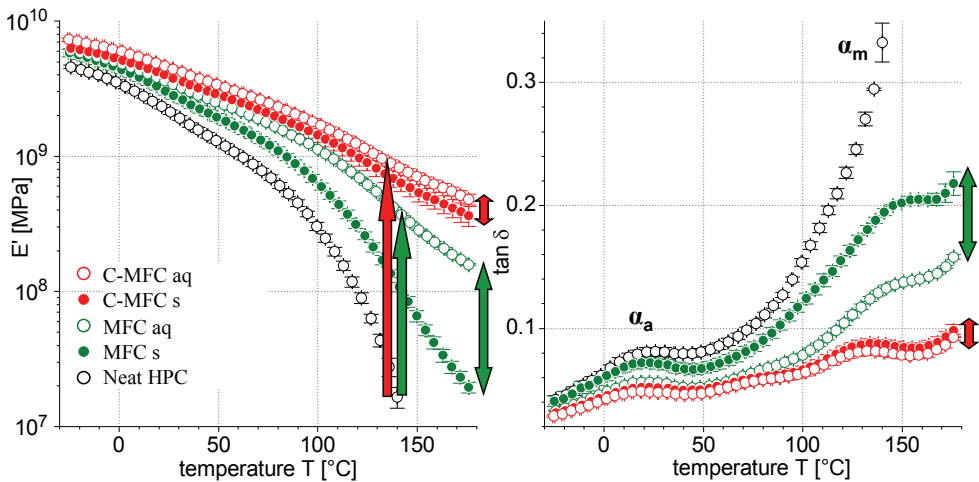


Fig. 7. Temperature dependence of the Storage modulus (E') (left) and $\tan \delta$ (right) for neat HPC (black) and its nanocomposites reinforced with 20% (w/w) of unmodified (green) and carboxymethylated (red) MFC. (aq: never-dried, s: dried and redispersed)

5.1.1 Neat HPC

The neat HPC films (black) show three regions that are separated by two relaxations, α_a and α_m , both involving large-scale molecular motions. (Pizzoli, et al., 1991) In the first region ranging from -30 to 20°C, the films exhibit a very high storage modulus which is in the range of several GPa. At these temperatures, the bulk HPC consists of essentially three distinct phases: a crystalline phase, a disordered isotropic amorphous phase and a phase of intermediate order which was described as a frozen anisotropic amorphous phase.(Pizzoli, Scandola & Ceccorulli, 1991; Rials & Glasser, 1988; Wojciechowski, 2000) At 20 °C, a first transition can be observed, indicated by the peak in the $\tan \delta$ curve. This Tg-like transition was attributed to the α_a relaxation, denoting a devitrification process of the disordered amorphous phase. The second region between 20 and 130 °C is characterized by a relatively

large drop in storage modulus, exhibiting a remarkable softening of the films. Around 130 °C a second T_g-like transition occurs with a strong increase in the tan δ intensity, known as the α m relaxation. (Pizzoli, Scandola & Ceccorulli, 1991) In the third region above 130 °C, the storage modulus decreases drastically and the neat HPC films start to flow. At these temperatures, the flexible side chains of HPC act like an internal plasticizer, allowing the rather stiff main chains some mobility. To avoid plastic deformation of the neat HPC films in tensile geometry, we limited data acquisition to 140 °C for this reference sample.

5.1.2 Viscoelastic properties of composites reinforced with never-dried (aq) and dried and redispersed (s) nanofibers

To allow easier comparison, green and red curves denote composites reinforced with unmodified and carboxymethylated MFC, respectively. Open and filled circles correspond to nanocomposites reinforced with never-dried (aq) and dried and redispersed (s) MFC. For all composites studied, the storage modulus of the composite films increased with fiber loadings regardless of the treatment. Below the α a relaxation at -20 °C, the increase in storage modulus was generally small. At 75 °C, after the α a relaxation, this increase became more pronounced. However, the strongest increase in E' compared with neat HPC was observed at 140 °C, after the α m relaxation. This later increase in storage modulus was associated with the formation of a highly rigid percolating network of fibrils. (Dalmas, et al., 2007) The rigidity of this network arises from strong hydrogen bonds and entanglements between the fibrils. Clearly, the tan δ intensity of all composites was reduced over the whole temperature range but most pronounced in the high temperature region above 130 °C. This decrease in tan δ is commonly associated with the increased volume fraction of the filler in the composites. However, it can be observed that the decrease in tan δ intensity depends on the filler type, becoming more pronounced for the functionalized MFC. This suggests that the presence of the fillers, together with the resulting percolating networks, promoted different degrees of segmental restrictions of the molecular motion of HPC chains, leading to an increase in E' and a decrease in tan δ . The efficiency of these segmental restrictions may depend on surface chemistry (i.e. the availability of carboxylate groups COO⁻), surface area to volume ratio and aspect ratio of the filler. (Johnson, Zink-Sharp, Renneckar & Glasser, 2009) As carboxymethylation prior to mechanical disintegration enhances the isolation of fibrils, (Eyholzer, Bordeanu, Lopez-Suevos, Rentsch, Zimmermann & Oksman, 2010a) this might lead to the production of fibrils which are favorable in terms of the above mentioned properties compared to unmodified nanofibers, and therefore account for more efficient segmental restriction of HPC molecular motion.

Nevertheless, a clear difference was observed between the films containing unmodified and carboxymethylated MFC. For all temperatures studied, storage modulus values of HPC reinforced with dried and redispersed (s) unmodified MFC were clearly lower than its never-dried analogues. This effect can be attributed to the hornification of MFC upon drying as described earlier, leading to a reduction of the fiber's aspect ratio and the prevention of a percolating network formation. In contrast, films containing dried and redispersed carboxymethylated MFC showed an almost identical response as those containing the never-dried fibers in the whole temperature range.

In conclusion, carboxymethylated MFC can be dried and redispersed in water without affecting its mechanical performance in nanocomposite applications.

5.2 PLA nanocomposites

Poly(lactic acid) (PLA) is a hydrophobic biopolymer, soluble in chloroform, and is considered biodegradable and biocompostable. This thermoplastic polymer can be synthesized from natural resources (*e.g.* starch or corn) and shows high strength and stiffness. Therefore, PLA has gained strong interests in several fields of applications, such as food packaging, automotive or medicine. (Garlotta, 2001) Its reinforcement with natural fibers has already been reported in literature, but few studies report the use of cellulose nanofibers, such as MFC as filler reinforcement in PLA matrices. Moreover, the same limitations have often been pointed out, such as aggregation of the filler and a lack of compatibility at the fiber-matrix interface. (Iwatake, Nogi & Yano, 2008; Mathew, et al., 2005)

In this context, we proposed to reinforce PLA with acetylated MFC, as it was shown earlier that such nanofibers display excellent dispersion properties in CHCl_3 , a PLA solvent. (Tingaut, et al., 2010) In addition to an improved filler dispersion as compared with unmodified MFC, an improved fiber/matrix interface was therefore expected due to the grafting of hydrophobic acetyl moieties on the surface of the nanofibers. PLA bionanocomposites with tunable properties were prepared using unmodified and acetylated MFC (with DS ranging from 0 to 0.77), with MFC contents from 2.5 to 17 wt%. The resulting nanocomposites were characterized in terms of filler dispersion and mechanical properties.

The quality of filler dispersion in the PLA matrix was visually evaluated assessing the transparency of the resulting films. Similar differences were observed among all filler contents tested, and therefore only photographs corresponding to nanocomposites reinforced with 10 wt% MFC are presented in Fig. 8. As compared with the neat PLA film, nanocomposite films were less translucent, but different behaviors were obtained depending on the DS. The addition of unmodified MFC led to a film off-white in color, with the appearance of MFC aggregates as white dots all over the film. When acetylated MFC was used, the presence of aggregates progressively vanished with an increase in DS, and the films became increasingly translucent. These observations suggest that the MFC dispersion in the PLA film was significantly improved by the surface grafting of acetate groups, and correlate with the improved dispersion of acetylated MFC in CHCl_3 .

The mechanical properties of the composites were evaluated using tensile tests measurements (Fig. 9). As it can be seen, in general, the presence of the MFC had a strong

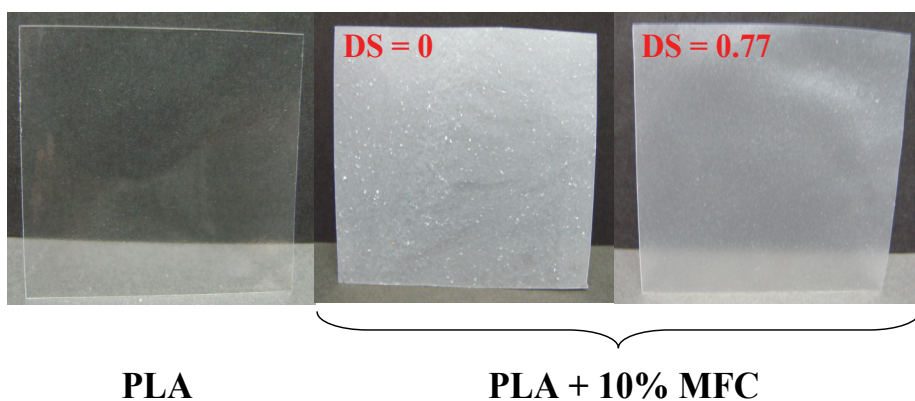


Fig. 8. Optical micrographs of neat PLA and its nanocomposites reinforced with 10% (w/w) of unmodified and acetylated MFC

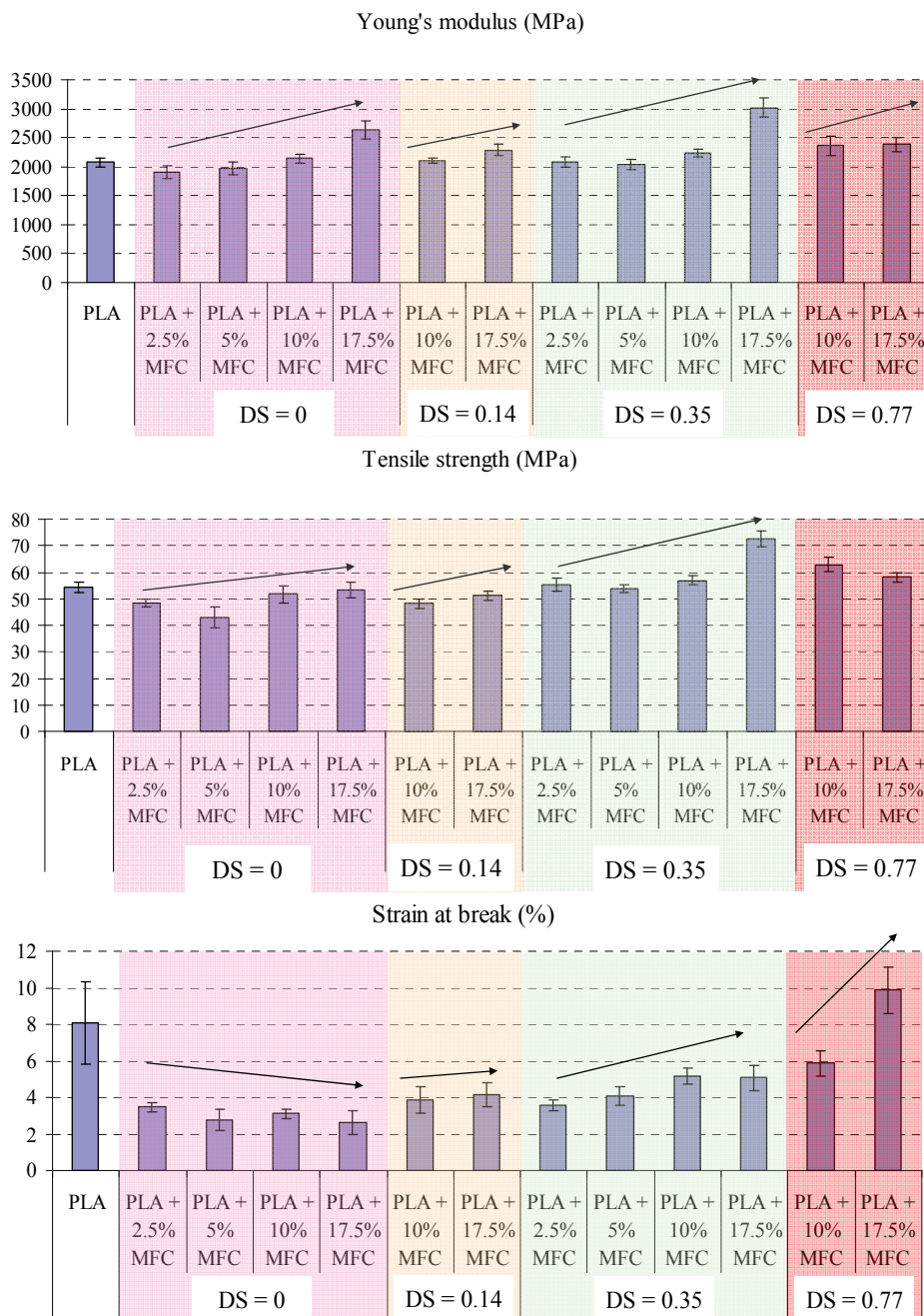


Fig. 9. Evolution of the Modulus of Elasticity (Young's modulus), Tensile strength and Strain at break as function of MFC content and DS

influence on the Modulus of elasticity (E'), Tensile strength (σ) and Strain at break (ϵ) of the resulting nanocomposites.

As compared with neat PLA, a gradual increase in E' and σ was noted upon the incorporation of nanofibers, whatever the type of fibrils used. This reinforcing effect might result from the formation of a stiff hydrogen bonded cellulose network above a percolation threshold. (Dufresne & Vignon, 1998; Siqueira, Bras & Dufresne, 2009) But most interestingly, the DS significantly altered the reinforcement of nanocomposites. Hence, at the same filler content, higher E' and σ were systematically measured for nanocomposites reinforced with nanofibers with a DS of 0.35. This behavior was attributed to an improved dispersion and/or compatibility between the bulk PLA and the modified MFC at this particular modification rate, and suggests that an optimum DS is required to elaborate nanocomposite materials with higher mechanical properties. Surprisingly, nanocomposites reinforced with MFC having a DS of 0.77 did not present the highest mechanical properties, for which the best chemical affinity towards the hydrophobic PLA matrix would be expected. These findings suggest that a combination of the DS, which will adjust the chemical affinity of the microfibrils to the matrix, and the filler content are essential in order to achieve a good polymer-matrix interaction.

Finally, the DS seemed to have a strong influence on ϵ . As compared with neat PLA, a progressive decrease in ϵ was measured upon filler content for nanocomposites reinforced with unmodified MFC, as expected. These results are in agreement with the increased stiffness of the materials with the MFC content. However, different results were obtained when acetylated MFC was used. Hence, ϵ progressively increased not only with the filler content, but also with the DS of the nanofibers. These results might be associated with a disruption of the fiber network upon the introduction of acetyl moieties on MFC, therefore increasing the strain at break of the materials. However, additional experiments are needed to validate this hypothesis.

In conclusion, PLA bionanocomposite materials with enhanced properties (*i.e.*, transparency, mechanical properties) were obtained as compared with those reinforced with unmodified MFC. Other properties could also be improved with the acetylated nanofibers, such as the hygroscopicity and thermal stability (not shown here). But most importantly, all these properties could be tailored by adjusting both the DS and the amount of MFC.

6. Conclusion

As demonstrated across this book chapter, Microfibrillated cellulose (MFC) is an excellent candidate for composite applications. Nevertheless, this highly promising natural material also suffers from its strong hydrophilic character, therefore leading to few drawbacks, namely the hornification phenomena upon drying, high shipping cost, susceptibility to biodegradation, as well as the lack of compatibility with non polar matrices.

We have here demonstrated that all these issues could be easily tackled through a chemical approach. Hence, the chemical modification of the cellulose hydroxyl groups clearly highlighted the possibility to use MFC in both dry or wet forms in composite applications, whatever the polarity of the matrix.

In aqueous environments, bionanocomposites from hydroxypropyl cellulose (HPC) with dried and redispersed carboxymethylated MFC powders were prepared. In general, the mechanical response of these composites was independent of whether the fibrils were dried

or not prior to compounding. On the other hand, MFC without carboxylate groups showed a strong decrease of its reinforcing potential when dried before mixing with HPC due to hornification. In conclusion, these results demonstrated that carboxymethylated MFC in powder form has a high potential for polymer reinforcement with increased shelf life and easier handling compared to conventional MFC.

In hydrophobic environments, novel bionanocomposites were synthesized from PLA and acetylated MFC, with the objective of demonstrating that the final nanocomposite properties could be tailored through a careful control of the DS. It was shown that a DS above 0.18 prevented hornification upon drying. This was possible since the grafted acetyl groups allowed reduced hydrogen bonding between cellulose microfibrils. Moreover, we demonstrated that the resulting powdered nanofibers were easily redispersed in chloroform, a PLA solvent of low polarity, leading to very stable suspensions. These nanofibers were used to reinforce PLA through a solvent casting approach in chloroform. We showed that MFC with increasing DS provided more translucent nanocomposites versus unmodified MFC. Concerning the mechanical properties, regardless of the microfibril type, increasing amounts of MFC provided higher modulus of elasticity (E') and Tensile strength (σ). However and most interestingly, higher E' and σ values were measured for nanocomposites reinforced with acetylated MFC as compared with those reinforced with unmodified nanofibers, which was associated with an improved dispersion and/or compatibility at the fiber/matrix interface. We conclude that the possibility to redisperse dried acetylated MFC in a non polar solvent, such as chloroform, is very promising from an economical point of view, and opens up new opportunities for the development of novel nanocomposites materials using non polar matrices.

Thus, the chemical modification of MFC with simple and efficient methods constitutes a great industrial interest because the modified nanofibers can be stored in dry form, improving their durability against bacteria and reducing transportation costs.

7. References

- Andresen, M., Johansson, L. S., Tanem, B. S. & Stenius, P. (2006). Properties and characterization of hydrophobized microfibrillated cellulose. *Cellulose*, 13, 6, 665-677.
- Bledzki, A. K. & Gassan, J. (1999). Composites reinforced with cellulose based fibres. *Progress in Polymer Science*, 24, 2, 221-274.
- Boldizar, A., Klason, C., Kubat, J., Naslund, P. & Saha, P. (1987). Prehydrolyzed Cellulose as Reinforcing Filler for Thermoplastics. *International Journal of Polymeric Materials*, 11, 4, 229-262.
- Cavaille, J. Y., Chanzy, H., Fleury, E. & Sassi, J. F. Surface-modified cellulose microfibrils, method for making same, and use thereof as a filler in composites materials. WO9712917 1997.
- Dalmas, F., Cavaille, J. Y., Gauthier, C., Chazeau, L. & Dendievel, R. (2007). Viscoelastic behavior and electrical properties of flexible nanofiber filled polymer nanocomposites. Influence of processing conditions. *Composites Science and Technology*, 67, 5, 829-839.
- Dufresne, A. & Vignon, M. R. (1998). Improvement of starch film performances using cellulose microfibrils. *Macromolecules*, 31, 8, 2693-2696.

- Eichhorn, S. J. (2006), Useful insights into cellulose nanocomposites using Raman spectroscopy, In: *Cellulose Nanocomposites: Processing, Characterization, and Properties*, 63-77, Amer Chemical Soc, 0097-6156, Washington.
- Eyholzer, C., Bordeanu, N., Lopez-Suevos, F., Rentsch, D., Zimmermann, T. & Oksman, K. (2010a). Preparation and characterization of water-redispersible nanofibrillated cellulose in powder form. *Cellulose*, 17, 1, 19-30.
- Eyholzer, C., Lopez-Suevos, F., Tingaut, P., Zimmermann, T. & Oksman, K. (2010b). Reinforcing effect of carboxymethylated nanofibrillated cellulose powder on hydroxypropyl cellulose. *Cellulose*, 17, 4, 793-802.
- Gardner, D. J., Oporto, G. S., Mills, R. & Samir, M. (2008). Adhesion and surface issues in cellulose and nanocellulose. *Journal of Adhesion Science and Technology*, 22, 5-6, 545-567.
- Garlotta, D. (2001). A literature review of poly(lactic acid). *Journal of Polymers and the Environment*, 9, 2, 63-84.
- Gousse, C., Chanzy, H., Cerrada, M. L. & Fleury, E. (2004). Surface silylation of cellulose microfibrils: preparation and rheological properties. *Polymer*, 45, 5, 1569-1575.
- Gousse, C., Chanzy, H., Excoffier, G., Soubeyrand, L. & Fleury, E. (2002). Stable suspensions of partially silylated cellulose whiskers dispersed in organic solvents. *Polymer*, 43, 9, 2645-2651.
- Grunert, M. & Winter, W. T. (2002). Cellulose nanocrystal reinforced cellulose acetate butyrate nanocomposites. *Abstracts of Papers of the American Chemical Society*, 223, 240-PMSE.
- Habibi, Y., Chanzy, H. & Vignon, M. R. (2006). TEMPO-mediated surface oxidation of cellulose whiskers. *Cellulose*, 13, 6, 679-687.
- Habibi, Y. & Dufresne, A. (2008). Highly filled bionanocomposites from functionalized polysaccharide nanocrystals. *Biomacromolecules*, 9, 7, 1974-1980.
- Henriksson, M. & Berglund, L. (2007). Structure and properties of cellulose nanocomposite films containing melamine formaldehyde. *Journal of Applied Polymer Science*, 106, 4, 2817-2824.
- Hubbe, M. A., Rojas, O. J., Lucia, L. A. & Sain, M. (2008). Cellulosic Nanocomposites: A Review. *Bioresources*, 3, 3, 929-980.
- Ifuku, S., Nogi, M., Abe, K., Handa, K., Nakatsubo, F. & Yano, H. (2007). Surface modification of bacterial cellulose nanofibers for property enhancement of optically transparent composites: Dependence on acetyl-group DS. *Biomacromolecules*, 8, 6, 1973-1978.
- Iwamoto, S., Nakagaito, A. N. & Yano, H. (2007). Nano-fibrillation of pulp fibers for the processing of transparent nanocomposites. *Applied Physics a-Materials Science & Processing*, 89, 2, 461-466.
- Iwatake, A., Nogi, M. & Yano, H. (2008). Cellulose nanofiber-reinforced polylactic acid. *Composites Science and Technology*, 68, 9, 2103-2106.
- Janardhan, S. & Sain, M. (2006). Isolation of cellulose microfibrils - an enzymatic approach. *BioResources*, 1, 2, 176-188.
- Johnson, R. K., Zink-Sharp, A., Rennecker, S. H. & Glasser, W. G. (2009). A new bio-based nanocomposite: fibrillated TEMPO-oxidized celluloses in hydroxypropylcellulose matrix. *Cellulose*, 16, 2, 227-238.
- Kim, D. Y., Nishiyama, Y. & Kuga, S. (2002). Surface acetylation of bacterial cellulose. *Cellulose*, 9, 3-4, 361-367.
- Lasseguette, E., Roux, D. & Nishiyama, Y. (2008). Rheological properties of microfibrillar suspension of TEMPO-oxidized pulp. *Cellulose*, 15, 3, 425-433.

- Lu, J., Askeland, P. & Drzal, L. T. (2008a). Surface modification of microfibrillated cellulose for epoxy composite applications. *Polymer*, 49, 5, 1285-1296.
- Lu, J., Wang, T. & Drzal, L. T. (2008b). Preparation and properties of microfibrillated cellulose polyvinyl alcohol composite materials. *Composites Part A: Applied Science and Manufacturing*, 39, 5, 738-746.
- Mathew, A. P., Oksman, K. & Sain, M. (2005). Mechanical properties of biodegradable composites from poly lactic acid (PLA) and microcrystalline cellulose (MCC). *Journal of Applied Polymer Science*, 97, 5, 2014-2025.
- Nair, K. G., Dufresne, A., Gandini, A. & Belgacem, M. N. (2003). Crab shell chitin whiskers reinforced natural rubber nanocomposites. 3. Effect of chemical modification of chitin whiskers. *Biomacromolecules*, 4, 6, 1835-1842.
- Nakagaito, A. N., Fujimura, A., Sakai, T., Hama, Y. & Yano, H. (2009). Production of microfibrillated cellulose (MFC)-reinforced polylactic acid (PLA) nanocomposites from sheets obtained by a papermaking-like process. *Composites Science and Technology*, 69, 7-8, 1293-1297.
- Nakagaito, A. N. & Yano, H. (2004). The effect of morphological changes from pulp fiber towards nano-scale fibrillated cellulose on the mechanical properties of high-strength plant fiber based composites. *Applied Physics a-Materials Science & Processing*, 78, 4, 547-552.
- Nakagaito, A. N. & Yano, H. (2005). Novel high-strength biocomposites based on microfibrillated cellulose having nano-order-unit web-like network structure. *Applied Physics a-Materials Science & Processing*, 80, 1, 155-159.
- Nakagaito, A. N. & Yano, H. (2008). The effect of fiber content on the mechanical and thermal expansion properties of biocomposites based on microfibrillated cellulose. *Cellulose*, 15, 4, 555-559.
- Nogi, M., Ifuku, S., Abe, K., Handa, K., Nakagaito, A. N. & Yano, H. (2006). Fiber-content dependency of the optical transparency and thermal expansion of bacterial nanofiber reinforced composites. *Applied Physics Letters*, 88, 13.
- Paakko, M., Ankerfors, M., Kosonen, H., Nykanen, A., Ahola, S., Osterberg, M., Ruokolainen, J., Laine, J., Larsson, P. T., Ikkala, O. & Lindstrom, T. (2007). Enzymatic hydrolysis combined with mechanical shearing and high-pressure homogenization for nanoscale cellulose fibrils and strong gels. *Biomacromolecules*, 8, 6, 1934-1941.
- Pandey, J. K., Kumar, A. P., Misra, M., Mohanty, A. K., Drzal, L. T. & Singh, R. P. (2005). Recent advances in biodegradable nanocomposites. *Journal of Nanoscience and Nanotechnology*, 5, 4, 497-526.
- Pizzoli, M., Scandola, M. & Ceccorulli, G. (1991). Dielectric and mechanical loss processes in hydroxypropylcellulose. *Plastics Rubber and Composites Processing and Applications*, 16, 4, 239-244.
- Rials, T. G. & Glasser, W. G. (1988). Thermal and Dynamic Mechanical-Properties of Hydroxypropyl Cellulose Films. *Journal of Applied Polymer Science*, 36, 4, 749-758.
- Saito, T., Nishiyama, Y., Putaux, J. L., Vignon, M. & Isogai, A. (2006). Homogeneous suspensions of individualized microfibrils from TEMPO-catalyzed oxidation of native cellulose. *Biomacromolecules*, 7, 6, 1687-1691.
- Samir, M., Alloin, F. & Dufresne, A. (2005). Review of recent research into cellulosic whiskers, their properties and their application in nanocomposite field. *Biomacromolecules*, 6, 2, 612-626.
- Samir, M., Alloin, F., Paillet, M. & Dufresne, A. (2004). Tangling effect in fibrillated cellulose reinforced nanocomposites. *Macromolecules*, 37, 11, 4313-4316.

- Sassi, J. F. & Chanzy, H. (1995). Ultrastructural Aspects of the Acetylation of Cellulose. *Cellulose*, 2, 2, 111-127.
- Siqueira, G., Bras, J. & Dufresne, A. (2009). Cellulose Whiskers versus Microfibrils: Influence of the Nature of the Nanoparticle and its Surface Functionalization on the Thermal and Mechanical Properties of Nanocomposites. *Biomacromolecules*, 10, 2, 425-432.
- Siro, I. & Plackett, D. (2010). Microfibrillated cellulose and new nanocomposite materials: a review. *Cellulose*, 17, 3, 459-494.
- Stenstad, P., Andresen, M., Tanem, B. S. & Stenius, P. (2008). Chemical surface modifications of microfibrillated cellulose. *Cellulose*, 15, 1, 35-45.
- Suryanegara, L., Nakagaito, A. N. & Yano, H. (2009). The effect of crystallization of PLA on the thermal and mechanical properties of microfibrillated cellulose-reinforced PLA composites. *Composites Science and Technology*, 69, 7-8, 1187-1192.
- Tingaut, P., Zimmermann, T. & Lopez-Suevos, F. (2010). Synthesis and Characterization of Bionanocomposites with Tunable Properties from Poly(lactic acid) and Acetylated Microfibrillated Cellulose. *Biomacromolecules*, 11, 2, 454-464.
- Turbak, A. F., Snyder, F. W. & Sandberg, K. R. (1983). Microfibrillated Cellulose, A New Cellulose Product: Properties, Uses and Commercial Potential. *Journal of Applied Polymer Science: Applied Polymer Symposium*, 37, 815-827.
- Werbosy, R. S. & Gray, D. G. (1976). Liquide crystalline structure in aqueous hydroxypropylcellulose solutions. *Molecular Crystals and Liquid Crystals*, 34, 4, 97-103.
- Werbosy, R. S. & Gray, D. G. (1980). Ordered phase formation in concentrated hydroxypropylcellulose solutions. *Macromolecules*, 13, 1, 69-73.
- Wojciechowski, P. (2000). Thermotropic mesomorphism of selected (2-hydroxypropyl)cellulose derivatives. *Journal of Applied Polymer Science*, 76, 6, 837-844.
- Zimmermann, T., Pöhler, E. & Geiger, T. (2004). Cellulose fibrils for polymer reinforcement. *Advanced Engineering Materials*, 6, 9, 754-761.
- Zimmermann, T., Pöhler, E. & Schwaller, P. (2005). Mechanical and morphological properties of cellulose fibril reinforced nanocomposites. *Advanced Engineering Materials*, 7, 12, 1156-1161.

Versatile Nanocomposite Formulation System of Non-Steroidal Anti-Inflammatory Drugs of the Arylalkanoic Acids

Mohamed R. Berber^{1,2}, Inas H. Hafez², Keiji Minagawa², Takeshi Mori³ and Masami Tanaka⁴

¹*Department of Chemistry, Faculty of Science, Tanta University*

²*Institute of Technology and Science, The University of Tokushima*

³*Department of Applied Chemistry, Kyushu University, Fukuoka*

⁴*Faculty of Pharmaceutical Sciences, Tokushima Bunri University*

¹*Egypt*

^{2,3,4}*Japan*

1. Introduction

Nanotechnology has shown tremendous promise in target-specific delivery of drugs in the body. Although passive and active targeted-drug delivery has addressed a number of important issues, additional properties that can be included in nanocarrier systems to enhance the bioavailability of drugs at the disease site, and especially upon cellular internalization, are very important.

Upon the support of nanotechnology, scientists in hybrid research field could deal with the combination of different substances from macroscopic to molecular level, and create novel materials with intentional functionalities. Thus, the hybridization technology can be adapted to create efficient drug nanocarriers. Hybridized drug-carriers can be made from a variety of organic and inorganic materials including biodegradable polymers and inorganic clays. The selection of material for development of nanoparticle carriers is mainly dictated by the desired diagnostic or therapeutic goal, type of payload, material safety profile, and the route of administration.

Among the various approaches for exploiting developments in drug nanotechnology, layered double hydroxide (LDH) materials offer some unique advantages, as their medical properties support their different pharmaceutical applications. By the introduction of drug-LDH nanocomposite platform, the delivery system becomes an active participant rather than passive vehicle in the optimization of drug-therapy.

In this chapter, we are going to focus on the intercalation chemistry of LDH, the different LDH nanocomposites formulation strategies, and the physical and chemical properties of drug-LDH nanocomposites. In addition, we discuss the different drug-LDH pharmaceutical applications such as drug solubility, dissolution behavior, and the delivery of some non-steroidal anti-inflammatory drugs (NSAIDs) to its active target-sites.

2. Layered double hydroxides (LDHs)

Driven by the high promise for new nanotechnological applications and our belief that development of biomedical science demands new advanced materials, clays are of particular interest. An interesting category of clay materials is (LDHs).

2.1 Structure of LDHs

LDHs are a family of natural and synthetic compounds having a general formula of $[M^{II}_1-xM^{III}_x(OH)_2](Y^{n-})_{x/n} \cdot yH_2O$, where M^{II} and M^{III} represent divalent and trivalent metal ions respectively, and Y^{n-} is the anion between the layers. M^{II} can be for example Mg^{2+} , Ca^{2+} , Zn^{2+} , Co^{2+} , Cu^{2+} ; and M^{III} can be Al^{3+} , Cr^{3+} , Co^{3+} , Fe^{3+} , Mn^{3+} . The interlayer anion Y^{n-} can be Cl^- , NO_3^- , CO_3^{2-} , or organic anions (Bocclair *et al.*, 1999). LDHs are also known as hydrotalcite-like compounds due to their structural similarities to hydrotalcite mineral, or known as anionic clays. They consist structurally of brucite-like sheet with hexagonal-shaped crystallite layers as shown in the scanning electron micrograph (SEM) of Figure 1. This structured-shape is formed by the edge sharing of $[Mg(OH)_6]$ octahedral as displayed in the schematic illustration of Figure 2. The net positive charge of LDH is due to a partial substitution of M^{2+} by M^{3+} ; typically, the substitution leads to values of x in the range of 0.2 to 0.33. This positive charge is effectively dispersed uniformly across each layer (Rives, 2002). Anions are attracted into the interlayer space along with water molecules, balancing the overall positive charge with a negative one of equal magnitude. LDH materials appear in nature and can be readily prepared in the laboratory. In nature, they are formed from the weathering of basalts (Bail *et al.*, 1987) or precipitation in saline water sources (Frost & Erickson, 2004). All natural LDH minerals have a structure similar to hydrotalcite, which has the formula $[Mg_6Al_2(OH)_{16}]CO_3 \cdot 4H_2O$ (Cavani *et al.*, 1991). Unlike clays, however, layered double hydroxides are not discovered in large scale.

2.2 Preparation techniques of LDHs

LDH can be prepared in the laboratory by different techniques. Coprecipitation (Miyata, 1980), anion exchange (Liu *et al.*, 2006), glycerol-effected exchange (Carlino, 1997), reconstruction (Geraud *et al.*, 2007) and homogeneous precipitation (Ogawa & Kaiho, 2002). Coprecipitation is perhaps the most widely used technique of LDH. In this method, LDH is precipitated by adding a base to a stirred aqueous solution containing the metals salts (M^{II} and M^{III}) and the desired anion. A 50 wt% solution of alkali hydroxide was found to be effective in the precipitation of pure LDH materials without impurities at the pH range 8.0-10.0. LDH systems generally prefer carbonate to most other anions. Thus, carbonate and carbon dioxide must be rigorously excluded from the medium in case of anions other than carbonate. The metal hydroxide layers nucleate and grow under stirring. Aging of the formed LDH precipitate is preferable to improve the crystallinity of LDH materials which is considered as an effective property in the stabilization of the beneficial intercalated anions. The aging process of LDH is often used as a post-treatment method and it usually performed by hydrothermal or microwave treatment techniques (Miyata, 1980).

2.3 Identification of LDHs and their nanocomposites

LDHs can be identified by different techniques: Powder X-ray diffraction (PXRD) is a very useful tool to analyze the crystalline structure, lattice parameters, crystal morphology, and crystal size of LDHs. This application is based on the fact that an X-ray diffraction is unique for each crystalline substance. The reflections of LDH are indexed to a hexagonal lattice

(Zou *et al.*, 2007) with rhombohedral 3R symmetry. The peaks of LDH from the lower angle to the high angle are the diffraction by planes (003), (006), (009), etc. Thus, the cell parameter c (the thickness of one layer consisting of a brucite-like sheet and one interlayer) of LDH is usually estimated as $3d_{003}$ or $d_{003} + 2d_{006} + 3d_{009}$, and the cell parameter a (the mean closest metal-metal distance within a layer) can be easily calculated from the 110 reflection ($a = 2d_{110}$). XRD measurement is based on Bragg's law: $n\lambda = 2d \sin \theta$, where λ is the wavelength

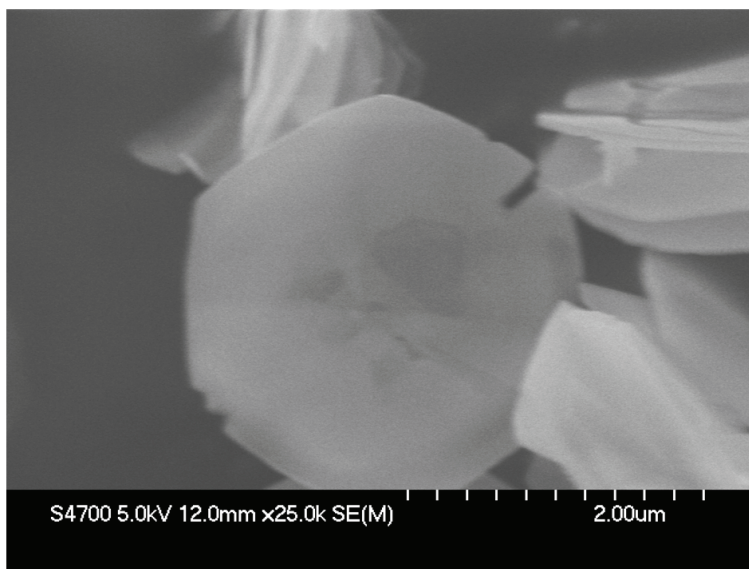


Fig. 1. SEM image of a hexagonal-shaped crystallite layer of Mg-Al LDH

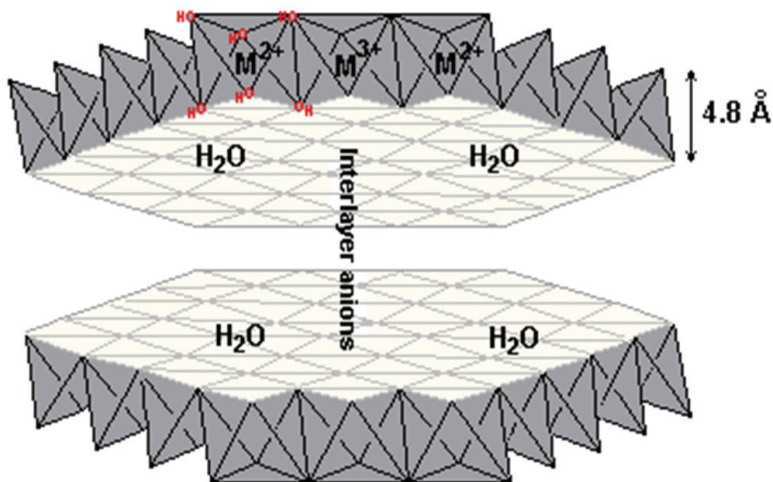


Fig. 2a. Schematic illustration of the brucite-like sheet structure of LDH; Horizontal view with a layer thickness of 4.8Å.

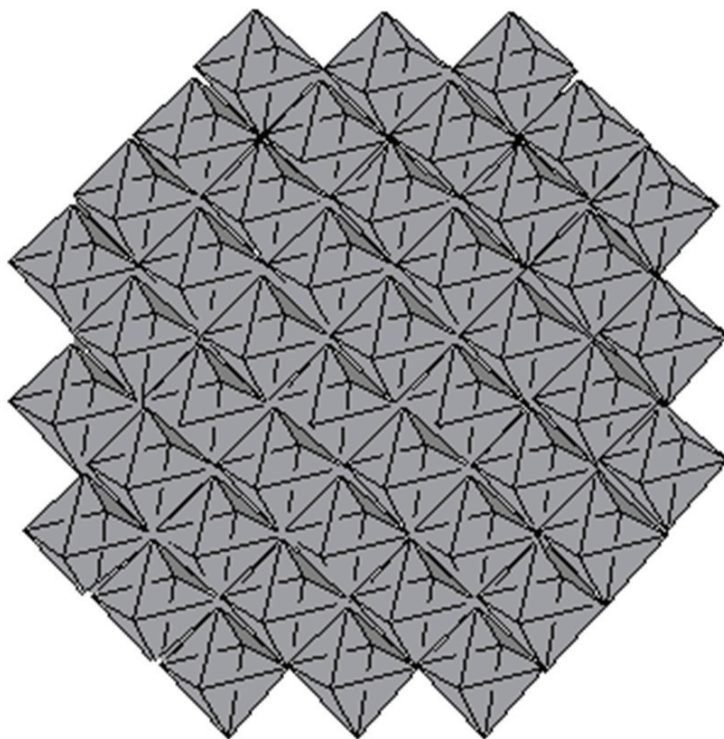


Fig. 2b. Schematic illustration of the brucite-like sheet structure of LDH; Vertical view.

of the incident X-ray beam, d is the spacing between each lattice, θ is the angle between the incident X-ray beam and the reflecting crystal plan, and n is an integer representing the order of the reflection (in practice, taken to be 1). Fourier transform infrared spectroscopy (FTIR): FTIR has been used as a tool for the evaluation of a molecule's structure by studying the vibration change occurring from the excitation of the bonds. In LDH, FTIR is used to determine the presence or absence of particular active agents in the interlayer, and to check that LDH layer material matches the expected spectrum. Since functional groups absorb at characteristic frequencies of infrared radiation, many compounds can be identified using only their spectra. Higher-quality scans of FTIR can be performed to give detailed information about the interlayer environment, to indicate the presence or absence of key functional groups in the system, to illustrate the relative orderliness of the hydroxide layers, and to determine the extent of ordering of water in the sample. We can also use FTIR to determine how much contamination (e.g. how much carbonate) is present in the system; if the LDH parent was a nitrate. We can also semi-quantitatively determine the extent of intercalation of our anion of interest. In addition, we can obtain detailed information about the extent of distortion that the intercalated anions undergo by comparing the spectra of the original compounds with those of the intercalated LDHs. Accordingly, FTIR provided valuable information on the ordering of these anions in the interlayer. Thermal analysis: the thermal gravimetric analysis (TGA) of LDH is used to determine the thermal stability of the layered materials and also the thermal stability of the intercalated anions. Elemental

analysis for carbon, hydrogen, and nitrogen (CHN) presents a useful technique of determining the percentage of the intercalated compound where LDH does not contain these elements. Scanning electron microscopy (SEM) and transmittance electron microscopy (TEM) are used to describe the structure morphology and crystal growth of LDH, and to provide useful information about the particle size of the LDH-composite materials.

2.4 Properties of LDH

LHDs display unique physical and chemical properties surprisingly close to the properties of clay minerals. The most interesting properties can be summarized as follows: a- High specific surface area, that varies from a few m^2/g to $\sim 100 \text{ m}^2/\text{g}$. This property is useful in the pharmaceutical applications, gas-adsorption and purification techniques. The synthetic route of LDH has a great influence on its adsorption capacity (Malherbe *et al.*, 1997). b- Memory effect, which allows a reconstruction process of LDH after calcination of the original structure by contact with solutions containing the desired anions. The calcination-reconstruction technique of LDH was used to prepare advanced nanocomposite materials of different anions. c- Anion-exchange property, this property was used to construct efficient bionanocomposites compounds of nucleosides (Choy *et al.*, 2001; Lotsch *et al.*, 2001), DNA (Minagawa *et al.*, 2009; Xu *et al.*, 2007), amino acids (Aisawa *et al.*, 2006; Ajat *et al.*, 2008; Chen *et al.*, 2009; Reinholdt & Kirkpatrick, 2006; Wei *et al.*, 2007) fatty acids (Nhlapo *et al.*, 2008), sugars (Aisawa *et al.*, 2003), drugs (Ladewig *et al.*, 2009; Li *et al.*, 2009; Tammaro *et al.*, 2007; Trikeriotis & Ghanotakis, 2007; Xia *et al.*, 2008; Zhang *et al.*, 2009a, 2009b) and vitamins (Choy *et al.*, 2004; Hwang *et al.*, 2001; Tronto *et al.*, 2004), through an anion-exchange mechanism of the interlayer anion of the original LDH. The exchange capacity of LDH was found to depend on the interlayer anion type. Usually LDH- NO_3 nanoparticles are used in the exchange process where LDH has low affinity to the interlayer anion NO_3 (Yahaya *et al.*, 2003). d- Biomedical properties, LDH possess excellent biomedical properties such as chemical inertness, null toxicity, biocompatibility, and antacidic and antipyretic properties. Consequently, they can be used as drug matrixes, drug stabilizers during storage and drug delivery. All in all, the previously mentioned properties of LDH raise the interest of LDH applications in the different biomedical fields especially the pharmaceutical one.

3. Non-steroidal anti-inflammatory drugs (NSAIDs)

Many drugs used for pharmacotherapy, while having a beneficial action, can also exhibit side-effects that may limit their clinical application. Therefore, there has been a long desire to achieve safe and selective delivery of drugs to target areas in the body in order to maximize the therapeutic potential and minimize the undesired side-effects. NSAIDs (Chart 1) are classified base on their chemical structure including: Salicylic acid derivatives (e.g. aspirin), Fenamic acid derivatives (e.g. Flufenamic acid), Acetic acid derivatives (e.g. Sulindac) and Propionic acid derivatives (e.g. Naproxen, Flurbiprofen, Suprofen, and Indoprofen).

NSAIDs are drugs with analgesic and antipyretic effects. They also produce anti-inflammatory effects when administrated in high doses. NSAIDs act by interfere with cyclooxygenase enzyme which control the production of prostaglandins responsible for inflammation and pain. However, prostaglandins have other vital functions, such as protecting the stomach from indigestion and ulcers, thus NSAIDs can have undesirable side effects in the gastrointestinal track and in some cases in the cardiovascular system.

Herein, we are going to cover the LDH nanocomposites of NSAIDs of the arylalkanoic acids derivatives. However most of NSAIDs are facing some administration problems such as low water solubility, non-target adsorption and local gastrointestinal irritation that is called direct contact effect. Thus, there is a need in-the-art for nanocomposite formulation technology to overcome the previously mentioned problems and to medicate the problems associated with prior conventional formulations such as milling and microcoating.

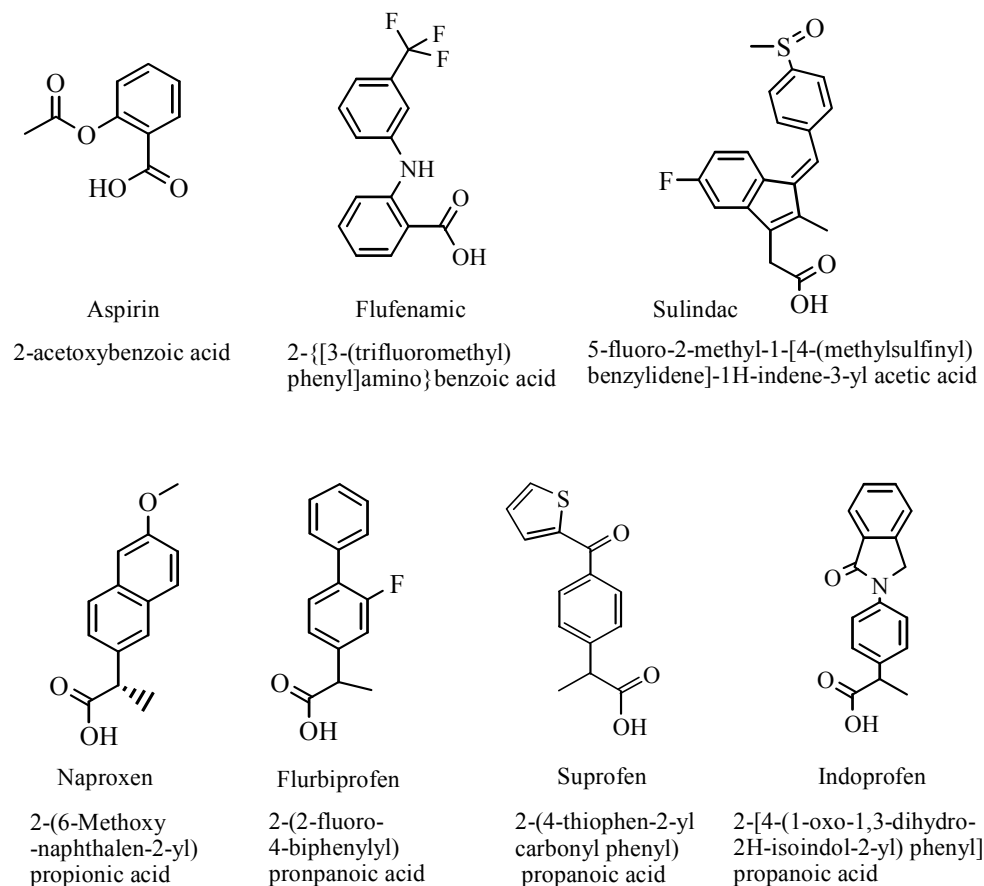


Chart 1

3.1 Physicochemical properties of NSAIDs

During drug substance development the molecules are screened in nanomolar receptor assays. The molecules with the best receptor binding are selected for further pre-clinical investigations. Already at this stage, solubility is of critical importance because it estimates the poorly defined drug substances and emphasizes the drug pharmacological and toxicological profiling.

When going into humans, sufficient and well characterized solubility becomes even more critical. The solubility or dissolution of the dose ranges in the various biophysiological media to which the drug substance or formulated drug substance is expected to be reproducible and remain unchanged for the final development and eventually marketing. It is well accepted today throughout the scientific community that drug substance solubility and especially aqueous drug substance solubility is an issue for the drug discovery as well as the early and late stage pharmaceutical development process and therefore needs to be addressed perfectly during compound design and optimization.

Most of NSAIDs have low solubility or completely insoluble. To achieve a pharmacological activity of NSAIDs, the molecules must in general exhibit certain solubility in physiological intestinal fluids to be present in the dissolved state at the site of absorption. The aqueous insolubility of NSAIDs is a major indicator for the drug activity in the intestinal fluids and its potential contribution to bioavailability issues. From literature, solubility or dissolution of NSAIDs can be mainly altered on two levels, through material engineering of the drug substance or through formulation approaches. Whatever route is taken to enhance or modify the solubility and/or dissolution, it needs to be a commercially viable process (Amidon *et al.*, 1995; Lipinski *et al.*, 1997; Lipinski, 2000). Furthermore, most classical NSAIDs have a carboxylic acid group. This acidic group can impart local gastrointestinal irritation through the direct contact with mucous membrane (Davies & Wallace, 1997; Emre, 1998). Therefore, the physicochemical properties of NSAIDs should be addressed and controlled carefully through an advanced formulation system.

3.2 Formulation strategies of NSAIDs

3.2.1 Preliminary routes

The initial drug discovery screening is typically performed with the amorphous forms of substances in organic solvents such as dimethylsulphoxide (Semin *et al.*, 2005). These formulations of high-energy forms of the substance are sufficient for the receptor and efficacy screen, but neglect any solubility characteristics of the substance at this stage and therefore cannot allow for a relevant biopharmaceutical (i.e. absorption) assessment. For the continuation of the early drug discovery program, sufficient concentration of the amorphous or crystalline drug dissolved in aqueous test media is needed for appropriate *in vitro* and *in vivo* testing. When the solubility of substances in aqueous media is limited, simple and effective formulation strategies are required.

3.2.2 Conventional formulations

Particle size reduction is one of the first investigated strategies. Milling is used for particle size reduction; accordingly a particle size of about 200 nm has been achieved (Markus *et al.*, 2008). However this formulation strategy raised only the drugs surface area for rapid dissolution using complicated and technically challenging processes. Later on, formulations with solubilizing agents like cyclodextrins or micellar systems were evaluated (Mura *et al.*, 1995). Other systems that used solvent- or surfactant-based formulations (e.g. micro-emulsions) or solid dispersions with polyethylene glycol and with polyvinylpyrrolidone required substantial development times and might be limited due to potential excipient-related toxicity or unwanted effects on the test system (Bettinetti & Mura, 1994; Melani *et al.*, 1995; Mitchell *et al.*, 2003; Mura *et al.*, 2001, 2003; Pignatello *et al.*, 2002; Uekama *et al.*, 2006). Upon that, drug-nanotechnology becomes a requirement.

Drug-delivery systems using nano- and microparticles show a clear potential for various diseases treatment. In view of advantages, the ability to target specific locations, the ability to reduce the quantity of drug that needs to be delivered to attain a particular concentration level in the vicinity of the target, and the ability to decrease the concentration of the drug at non-target sites. As a consequence, the controlled drug delivery became one of the fastest growing technologies of the pharmaceutical market.

3.2.3 Clay hybrid formulations

The strategy of using clay materials in drug formulation has been raised in the last century (Miyata, 1975). Several reports have evaluated the effect of the clay materials in pharmacy including biopharmaceutical objectives, modification of drug liberation, pharmacological targets to avoid or to diminish adverse effects and chemical factors. Summarizing, clays were found in solid forms of administration (tablets, capsules, granulates and dusts), liquid (suspensions and emulsions) and semisolids (ointment, pastes). In the all cases, clays fulfilled a series of chemical (stability and purity), physical (water texture, content, particles dimensions) and toxicological requirements (non-toxic, security and microbiological purity) (Flesken *et al.*, 2007). In particular, the effect of clay minerals on drug solubility has received a great deal of attention. For example, the complexation of the analgesic indomethacin drug with smectite enhanced the drug-skin penetration rate and increased the drug stability as well as drug water solubility (Ito *et al.*, 2001). Also, the hybridization of the poor water soluble itraconazole with smectites led to a remarkable improvement of the drug water solubility and bioavailability (Park *et al.*, 2004). Furthermore, the intercalation of 5-fluorouracil into montmorillonite diminished the drug side effects through its slow release from the hybrid materials (Lin *et al.*, 2002).

3.2.4 LDH nanocomposite formulations

The work of LDH clay materials in the field of health and pharmacy has started in the last years. Several papers have emphasized the effect of the use of LDH nanomaterials as a drug carrier. Tronto *et al.* (Tronto *et al.*, 2001) intercalated a variety of anions of pharmaceutical interest, such as salicylate, citrate, glutamate and aspartate, using two different synthesis methods, a direct one (coprecipitation) and an indirect one (anion exchange of dodecylsulfate-LDH). Bingxin *et al.* (Bingxin *et al.*, 2004) showed that the release of the intercalated NSAID fenbufen from LDH nanocomposites is a slow process, especially in the case of Mg/Al intercalated materials.

Recently, we described a new approach of improving drug solubility and absorption in the gastrointestinal track by using LDH nanoparticles as a drug carrier (Berber *et al.* 2008). In this work, the NSAIDs naproxen and flurbiprofen were chosen as models of poorly soluble drugs. Here, we study in details the effect of LDH nanocomposite structure on potential pharmaceutical properties of NSAIDs such as dissolution behavior, drug delivery and drug release. In addition, we emphasize the effect of LDH nanocomposite formulation technique on drug incorporation efficiency, drug preservation into the layered structure of LDH and drug thermal stability after the composite formation. For these investigations, we select some different drugs of NSAIDs such as Aspirin (ASP), Flufenamic acid (FFA), Sulindac (SUL), Suprofen (SUP) and Indoprofen (IND).

4. New experimental investigations

4.1 Materials and drugs used

Magnesium nitrate hexahydrate, aluminum nitrate nanohydrate and ASP (purity = 99.5, 98, and 99.5% respectively; Wako Pure Chemical Industries, Ltd.), FFA, SUL, NAP, FLU, SUP and IND high grades were purchased from Sigma Chemical Co., and used as received. All solutions were prepared using deionized water (18.2 M Ω /cm, produced from Milli-Q Grandient ZMQG000kt).

4.2 Nanocomposite formulations of the selected drugs

4.2.1 Synthesis of MgAl-NO₃ LDH

To a 200 mL three-necked round flask containing 30 mL of 1.0 M sodium nitrate solution was added dropwise a 50 mL solution of 8.538 g (0.0333 M) of magnesium nitrate hexahydrate and 6.249 g (0.01666 M) of aluminum nitrate nanohydrate (metal ions molar ratio of Mg²⁺/Al³⁺ = 2) with constant magnetic stirring. During the metal ion addition, the pH of the suspension was kept constant at 8.0 by adding appropriate amounts of 2.0 M KOH solution. The final volume of the preparation medium was augmented to 100 mL by deionized water. The resultant suspension was stirred at 70 °C for 24 h under N₂ flow. At the end of the reaction, the formed MgAl LDH material was collected by filtration (0.45 μ m Millipore membrane), washed several times with deionized water, and finally freeze-dried.

4.2.2 Coprecipitation technique of drug-LDH

To a 200 mL three-necked round flask, 1.0 g of the target drug was dissolved in 60 mL deionized water by adjusting the solution pH to 8.0 using 2.0 M KOH solution. A 30 mL aqueous solution containing 8.538 g Mg (NO₃)₂ · 6H₂O and 0.73 g Al (NO₃)₃ · 9H₂O (M²⁺/M³⁺ molar ratio = 2) was added dropwise with constant stirring to the drug solution. During the metal ion addition, the pH of the suspension was kept constant at 8.0 by adding appropriate amounts of 2.0 M KOH solution. The final volume of the preparation medium was augmented to 100 mL by deionized water. The resultant suspension was stirred at 70°C for 24 h under N₂ flow. At the end of the reaction, the formed drug-LDH material was collected by filtration (0.45- μ m Millipore membrane), washed several times by 0.1 M KOH solution and subsequently deionized water until a negative test was obtained for drug in the washing medium. A UV spectrophotometer (U-3210, Hitachi, Japan) was used to check for the presence of drug (ASP, FFA, SUL, NAP, FLU, SUP and IND) in the washing medium at 235 nm, 288.0 nm, 254.0 nm, 230.5 nm, 247.0 nm, 300.4 nm and 279.0 nm respectively. Finally, the collected drug-LDH material was freeze-dried.

4.2.3 Anion-exchange technique of drug-LDH

In a 100 mL round flask was dissolved 2.0 g of drug in 100 mL of deionized water by adjusting the solution pH to 8.0 using 2.0 M KOH solution. To the drug solution was added 1.0 g of NO₃-LDH with constant stirring. The reaction mixture was stirred at 40 °C for 7 days. After the reaction completed, the drug-LDH material was collected, washed and dried as described above in the coprecipitation technique.

4.2.4 Reconstruction technique of drug-LDH

In order to prepare drug-LDH composites by reconstruction technique, the prepared NO₃-LDH sample was calcined at 500 °C for 4.0 h under N₂ flow. Depending on the memory

character of LDH, 1.0 g of the calcined LDH was dispersed in a 100 mL aqueous solution containing 1.0 g drug. The resultant suspension was stirred at 40 °C for 48 h. The obtained drug-LDH was collected, washed and finally dried as described above in the coprecipitation technique.

4.3 Characterization of the prepared composites

X-ray powder diffraction patterns were recorded on a Rigaku X-ray diffractometer using CuK α radiation at $\lambda=1.5405 \text{ \AA}$. The measurement was performed in the 2θ range $1.5-70^\circ$ with a 2θ scanning step of 0.02° , a scanning step time of 5 s, a filament intensity of 40 mA, and a voltage of 150 kV. Infrared spectra (KBr disk method) were recorded on a Bio-Rad FTS 3000MX FT-IR spectrophotometer with a TGS detector in the wavenumber range of $4000-500 \text{ cm}^{-1}$ by accumulating 16 scans at 4 cm^{-1} resolution. Thermogravimetric analysis (TGA) was conducted with a Shimadzu thermogravimetric analyzer (TGA-50, TA-60WS) using a platinum cell with a heating rate of $10 \text{ }^\circ\text{C}/\text{min}$, under a N_2 flow of $20 \text{ mL}/\text{min}$. The scanning electron micrographs (SEM) were captured by a Hitachi FE-SEMS-4700 microscope.

5. Results and discussion

5.1 The effect of preparation technique on drug incorporation ratio

The amount of drug incorporated into LDH was calculated by using a UV quantitative method as follows. A known amount of the composite material was dissolved in 10.0 mL of 1.0 M HCl solution. The obtained solution was diluted using a phosphate buffer of pH 7.4. The drug concentration was determined from the UV-absorption peak. The drug incorporation ratio was expressed by the percentage of drug weight intercalated into a unit weight of composite. The UV method was also used to check the integrity of the target drug after the intercalation process.

Successfully, all the studied synthetic techniques showed drug-LDH composites; however the amounts of the incorporated drugs were different. The coprecipitation technique showed the highest loading ratio, while reconstruction method showed the lowest one as noted in Table 1.

	ASP	FFA	SUL	NAP	FLU	SUP	IND
Coprecipitation technique	53	58	45	52 ^a	49 ^a	49	51
Anion exchange technique	45	42	31	43	41	40	37
Reconstruction technique	25	19	20	23 ^a	21 ^a	17	18

Table 1. The determined incorporation ratios (%), ^a(Berber *et al.*, 2008)

With no doubt, the preparation technique of LDH-composites affected the incorporation process of the drugs into LDH. In the coprecipitation process, the reaction medium contained the metals and the drug anion, accordingly LDH possesses high affinity to upload the drug anions and form ordered structure. In the anion exchange process, LDH is already constructed with its exchangeable inorganic anion, thus the exchange process is affected by the affinity of LDH layers to the drug charge and its size. This kind of stacking usually disturbs the layered structure of LDH. In the reconstruction process, the metal oxides of the

calcined LDH have the ability to recognize its original structure; as a consequence there is a high priority to reconstruct LDH layered structure of with the inorganic anions; especially atmospheric CO_2 .

The X-ray patterns of Figure 3 confirmed the effect of the preparation technique on drug incorporation ratio. The absence of original LDH basal spacing peaks (pattern a) from pattern b and c indicated a successful synthesis of drug-LDH composites with single phase incorporation. The strong diffraction peaks of pattern b reflected a good crystallinity and a high ordered structure of drug-LDH composites prepared by coprecipitation technique. In the case of reconstruction technique, pattern d showed two (003) peaks style; one of low intensity at lower angle corresponding to the intercalated drug and the other for the CO_3 -LDH with an interlayer distance 7.6\AA . This means, the interlayer gallery of LDH contained both the drug with low content and carbonate with high content. Consequently, the method of drug incorporation has a profound influence on the drug incorporation ratio.

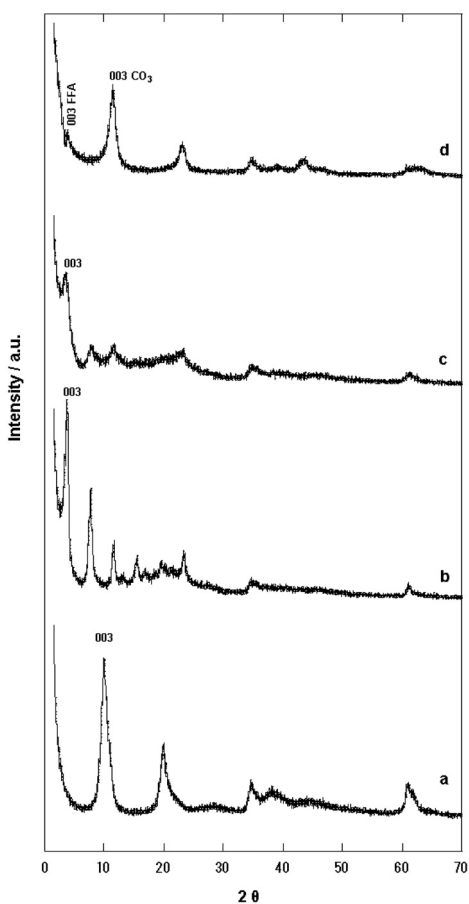


Fig. 3. X-ray diffraction patterns of NO_3 -LDH (a), FFA-LDH coprecipitation (b), FFA-LDH anion exchange (c) and FFA-LDH reconstruction (d).

5.2 Nanocomposite structure of drug-LDH materials

The scanning electron microscopy was used to investigate the nanocomposite structure of the prepared materials. Figure 4 displays the SEM images of the synthesized NO_3 -LDH material and FFA-LDH composites. Image a (inset) shows uniform and regular hexagonal platelets characteristic for LDH particles. The regularity of the LDH particles confirmed the good crystallinity recorded by X-ray measurement (X-ray section). The LDH particles size was recorded in the nanoscale. When the LDH was calcined, the hexagonal platelet structure disappeared (image b) as LDH particles lost their morphology. In the case of drug-LDH composites (images c, d and e), such LDH regular structure was demolished, and aggregates composed of small nanoparticles were observed. This aggregation process is probably due to a hydrophobic interaction of the LDH surface-adsorbed drug. The aggregates of image (e) were different from those of images (c) and (d). The aggregates were smaller in size and some regular LDH particles were observed. This difference is probably due to the applied preparation technique and the memory effect of LDH which recognize the original structure. The SEM images of the other drug-LDH materials were also recorded in the nanoscale and showed similar behaviors. Conclusively, the recorded SEM images confirmed the nanocomposite structure of synthesized drug-LDH materials.

5.3 X-ray analysis of drug-LDH nanocomposites

Figure 5 shows the XRD patterns of LDH, its calcined form and SUP-LDH nanocomposites prepared by previously mentioned synthetic methods. Pattern A indicated the formation of NO_3 form of LDH with sharp and symmetric $(00l)$ reflections. Using Bragg's law ($n\lambda = 2d \sin \theta$), the basal spacing was calculated to be 8.9 Å. As a result of intercalation of SUP, the basal d-spacing was expanded to 22.6 Å. The SUP-LDH nanocomposite interlayer distance was calculated by subtracting the inorganic layer thickness (4.8 Å) (Miyata, 1975) from the d_{003} -spacing. The determined value was 17.8 Å irrespective to the preparation technique.

The interlayer distance of SUP-LDH was larger than SUP molecular length (12.8 Å). However LDH attaches its interlayer anions through an electrostatic interaction (Costantino *et al.*, 1998), we speculated that SUP molecules were stacked into LDH as a monolayer of a staggered interdigitated arrangement through the attachment of SUP carboxyl groups with the LDH positive layers, as schematically drawn in Figure 6.

Anion exchange technique (pattern c), showed a monophasic drug-LDH nanocomposites. The NO_3 anions are fully replaced by the drug anions, showing that NO_3 is a good leaving group. The asymmetric broadening of the basal reflections (003 and 006) is typical of LDH composite materials with turbostratic disorder (Warren & Bodenstein, 1966; Hines *et al.*, 1997). This result clearly showed that the mechanism of anion-exchange disturbed the stacking process of the drug into the LDH layers.

Unlike coprecipitation and anion-exchange techniques, the metal oxides resulted from the calcination step are subjected to a reconstruction process. The X-ray (pattern e) showed a biphasic nanocomposites consist of the drug-LDH (lower angle; $d_{003} = 22.6$ Å) and CO_3 -LDH (higher angle; $d_{003} = 7.6$ Å). The small amount of the intercalated drug indicated that LDH prefers to memorize its original structure (small interlayer distance) rather than incorporating large anions. In addition, carbonate anions seems to have a high priority to produce an ordered LDH structure than other anions.

To avoid reproduction of numerous X-ray diffractions, it will suffice to describe the results obtained for the other drug-LDH nanocomposites. The X-ray analysis confirmed the formation of ASP-LDH, FFA-LDH, SUL-LDH and IND-LDH nanocomposites. The X-ray patterns were generally similar to those of SUP-LDH nanocomposites. The differences were observed in the d-spacing and the interlayer distance as schematically drawn in Figure 6.

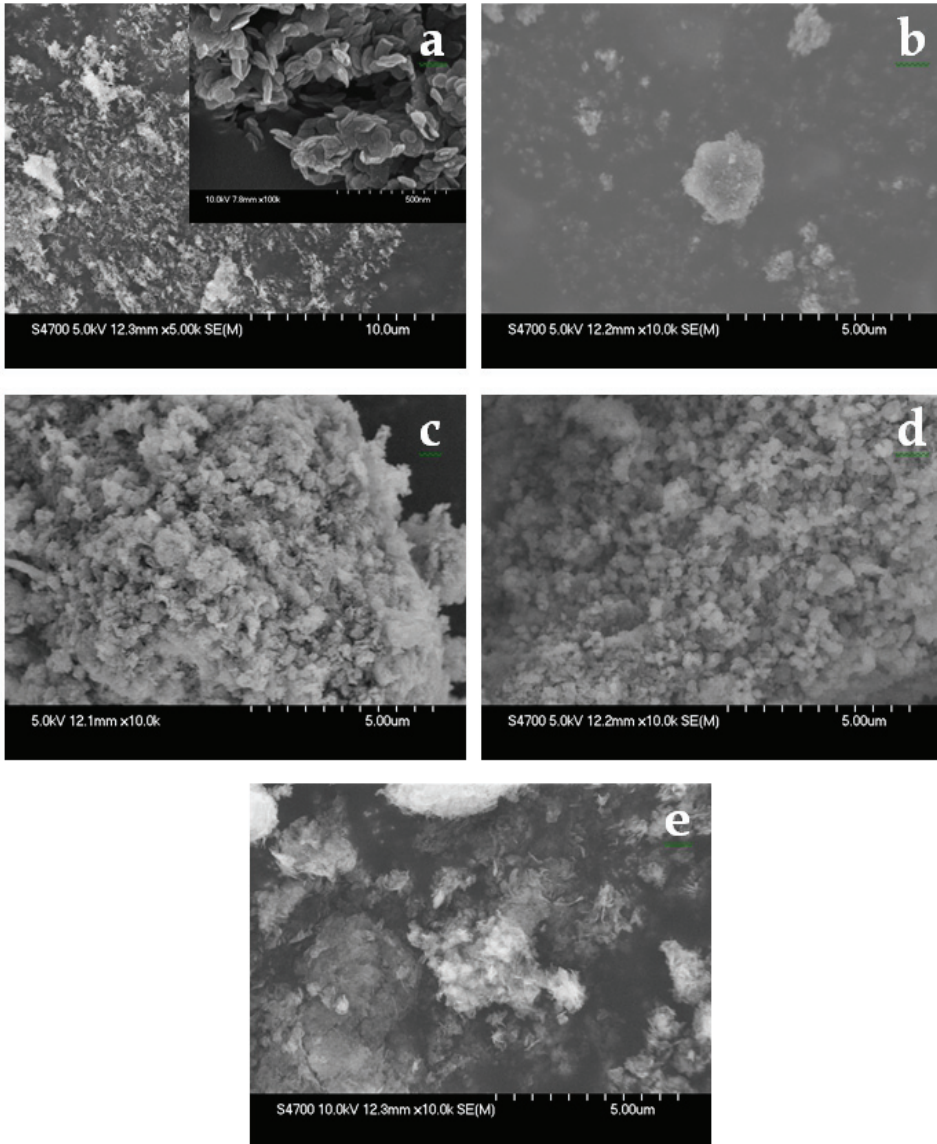


Fig. 4. SEM images of NO₃-LDH (a), LDH calcined (b), FFA-LDH coprecipitation (c), FFA-LDH anion exchange (d) and FFA-LDH reconstruction (e).

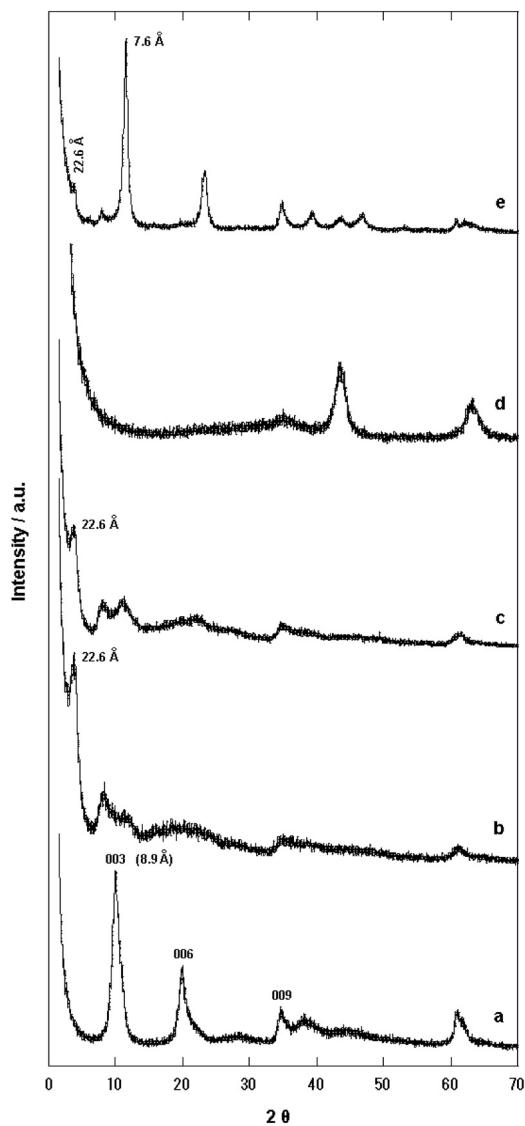


Fig. 5. X-ray diffraction patterns of $\text{NO}_3\text{-LDH}$ (a), SUP-LDH coprecipitation (b), SUP-LDH anion exchange (c), calcined LDH (d) and SUP-LDH reconstruction (e).

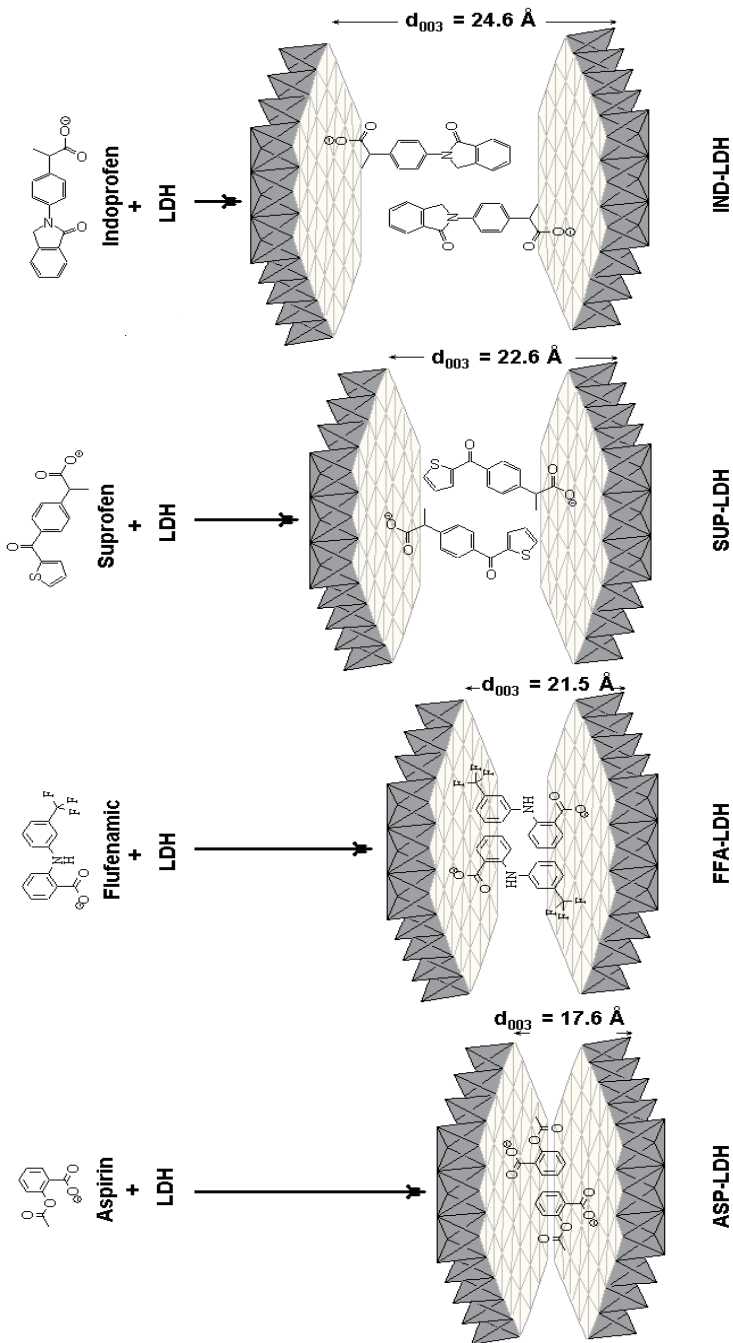


Fig. 6. Schematic illustration of intercalation process of some NSAIDs.

Accordingly, it is concluded that drug-LDH nanocomposites are produced with a high order structure, single phase incorporation of the drug with a high loading ratio in the case of coprecipitation technique.

5.4 Infrared spectra of drug-LDH nanocomposites

Drug-LDH nanocomposites were further characterized by FT-IR spectroscopy to verify the presence of the intercalated drugs and to gather information about the nanocomposites' molecular structure. For example, the infrared spectra of SUP-LDH nanocomposites which were prepared by different techniques are displayed in Figure 7. Figure 7a exhibited the characteristic bands of NO_3 -LDH, in particular the lattice vibration modes ($\nu_{\text{M-O-M}}$, $\nu_{\text{M-O}}$) at 550, 630, and 780 cm^{-1} (Lin *et al.*, 2006) and the asymmetric stretching band of the interlayer nitrate (ν_{NO_3}) at 1365 cm^{-1} as well as the vibration modes of the hydroxyl groups of LDH layers; bending at 960 cm^{-1} , deformation at 1610 cm^{-1} and stretching at 3440 cm^{-1} (Olanrewaju *et al.*, 2000). The FT-IR spectrum of SUP (Figure 7b) showed complex features below 1520 cm^{-1} , which can be attributed to the bending and stretching of aromatic rings, carbon-carbon, carbon-sulfur, and carbon-oxygen bonds. The stretching vibration band of COOH group was detected at 1740 cm^{-1} . The weak stretching vibration modes of SUP alkyl groups ($\nu_{\text{C-H}}$) were detected between 3060 and 2870 cm^{-1} .

As a result of intercalation of SUP into LDH, new bands are emerged such as symmetric and asymmetric modes of COO^- at 1560 and 1670 cm^{-1} , respectively, besides the characteristic bands of SUP and LDH. The intensities of the emerged bands suggested a dependence on the amount of the intercalated drug. The bands were sharp in the case of coprecipitation and anion exchange techniques, respectively, indicating a high loading ratio of the drug into the LDH gallery. The lack of the inorganic anions in the interlayer indicated the formation of monophasic drug-LDH nanocomposites. On the other side, the reconstruction technique (spectrum e) showed the valence vibration of carbonate anion at 1410 cm^{-1} (Del Arco *et al.*, 1993) beside the characteristic bands of SUP, confirming the formation of biphasic nanocomposites. The presence of carbonate band in spite of the precautions taken during the preparation process indicates the high selectivity of LDH for carbonate anion (Miyata, 1980). The weak bands of the drug reflected its low interlayer contribution. In conclusion, the molecular structure information of drug-LDH nanocomposites indicated that drug molecules are intercalated into LDH gallery with different ratios depending on loading technique and are combined with LDH layers through electrostatic interactions.

5.5 Pharmaceutical properties of NSAIDs and their LDH nanocomposites

5.5.1 Drug thermal stability

An important pharmaceutical use of LDH compounds could be drug stabilizing during storage. The active ingredient was protected by the laminar structure. In the case of the used drugs, photodecarboxylation was prevented because of the interaction of the carboxylate groups of NSAIDs and the positive layer charges. During storage, the layers of LDH supply a well-defined and relatively hydrophobic microenvironment for these guest molecules, accordingly LDH controlled the guest hydrolysis and photoreactivity (Cavani *et al.*, 1991; Costantino & Nocchetti, 2001). Figure 8 shows the TGA and differential thermal analysis curves of LDH, SUP, and SUP-LDH prepared by coprecipitation technique.

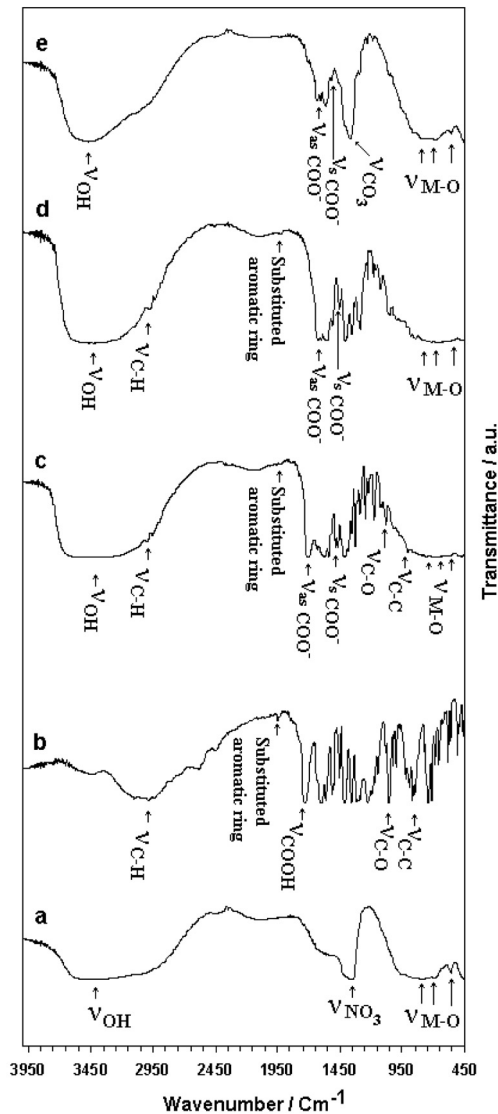


Fig. 7. Infrared spectra of LDH- NO_3 (a), SUP drug (b), SUP-LDH prepared by coprecipitation technique (c), SUP-LDH prepared by anion-exchange technique (d), and SUP-LDH prepared by reconstruction technique (e).

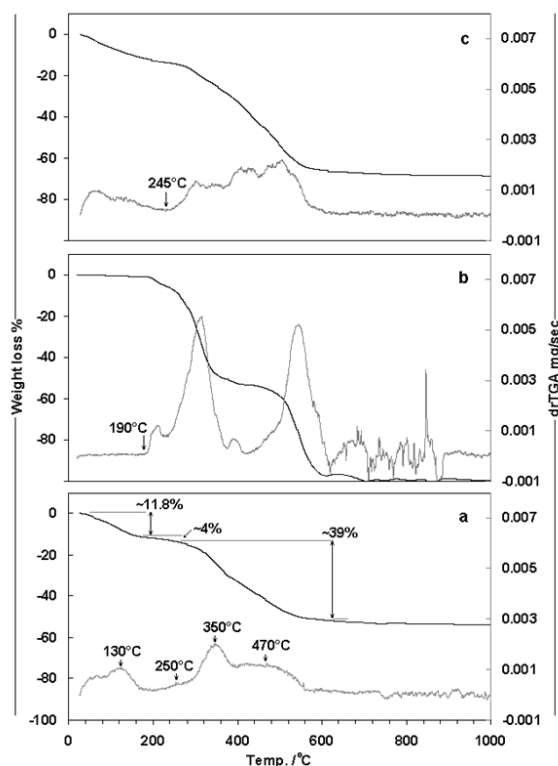


Fig. 8. Thermogravimetric analysis and differential curves of LDH-NO₃ (a), SUP drug (b), and SUP-LDH prepared by coprecipitation technique (c).

In the case of LDH (Figure 8a), the weight loss was observed to proceed mainly in three steps: ~11.8% starting from 90 °C, reaching maximum at 130 °C and ended at 170 °C (the loss of the physically adsorbed water molecules) (Darder *et al.*, 2005), ~4% from 170 to 270 °C (the loss of the interlayer water molecules), and ~39% from 270 to 620 °C (the dehydroxylation process and the decomposition of the interlayer anions) (Lopez *et al.*, 1997). The formation of MgO and MgAl₂O₄ oxides was observed in the TGA residue by measuring X-ray diffraction (Figure 9). The resultant oxides were in agreement with previous literature data (Labajos *et al.*, 1992).

After the intercalation of SUP into LDH, the TGA curve (Figure 8c) was significantly changed. The amount of interlayer water was decreased, probably due to the hydrophobic nature of the intercalated SUP. The overall weight loss was increased from 55% to 67% in the final stage. The onset temperature of drug decomposition shifted to a higher value (from 190 °C to 245 °C). Similar changes were also observed in the TGA curves of the samples prepared by anion-exchange and reconstruction techniques. The differences were observed in the reduced weight loss which was related to the small content of the intercalated drug and the presence of carbonate as an interlayer component beside the drug in the case of reconstruction techniques. Accordingly, the stability of SUP was promoted against the thermal decomposition after the LDH nanocomposite formulation.

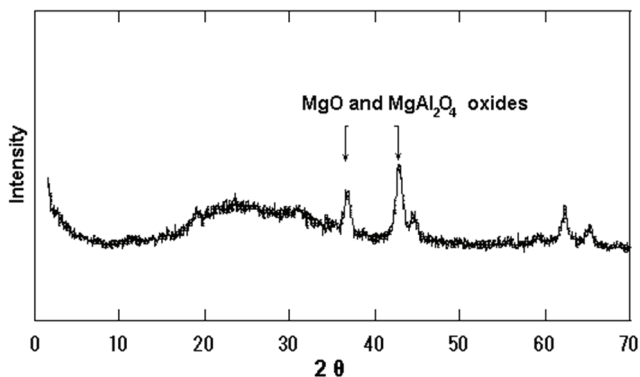


Fig. 9. X-ray pattern of TGA residue of LDH-NO₃

5.5.2 Drug delivery of NSAIDs and their LDH nanocomposites

The dissolution experiments of the pure drugs and drug-LDH nanocomposites was monitored in the following buffer mediums: buffer A as a simulated stomach solution (a 100 mL solution mixture of 100.0 mM HCl and 100.0 mM KCl; a few drops of 10.0 mM HCl solution was used to adjust the solution pH at 2.0), buffer B as a simulated duodenum solution (a 100 mL solution mixture of 100.0 mM NaHCO₃ and 100.0 mg NaCl; a few drops of 50.0 mM HCl solution was used to adjust the solution pH at 6.0), and buffer C as a simulated small intestine solution (a 100 mL solution mixture of 100.0 mM NaHCO₃ and 100.0 mg NaCl; a few drops of 50.0 mM HCl solution was used to adjust the solution pH at 8.0). The anionic buffer composition was defined on the basis of literature data (Vatier *et al.*, 1992; White, 1980). By considering both of the usual daily doses of the selected drugs and the drug ratio incorporated into LDH, the release experiments were conducted with sufficient amounts of drugs-LDH nanocomposites to study the effect of LDH on drug-release properties and to ensure a good therapeutic effect. Consequently, the release experiments were performed as follows: In a round-bottom flask, a sample of 100.0 mg of drug or 200.0 mg of drug-LDH nanocomposite was dispersed in 100 mL of buffer solution, which was maintained at 36.8±0.1°C with constant agitation of 80 rpm. At appropriate time intervals, a 1.0 mL sample solution was withdrawn from the release medium and filtered by using a 0.45 µm Millipore filter unit to remove the insoluble particles. The filtrate was diluted and assayed for UV measurement. The removed aliquot was immediately replenished by the same volume of the used buffer, which was equilibrated at the same reaction temperature. The dissolution experiment of each sample in each buffer was performed in duplicates (Berber *et al.*, 2010).

Figure 10 (upper panel) shows the solubility of SUP drug powder at the different mediums. The solubility was very small in buffer A (~ 6%), due to the acidic character of SUP. The drug was completely dissolved during 30 min (buffer B) and 25 min (buffer C), due to deprotonation of carboxylic acid group at high pH(s). These observations indicate the uncontrollable dissolution of SUP in the gastrointestinal tract after administration. Figure 10 (lower panel) shows the release of SUP from LDH nanocomposite prepared by coprecipitation technique. Significant change in the amount of drug dissolved was observed with time progress. Around 32%, 53% and 71% was released in a controlled process during

12 h in buffer A, B and C, respectively. The release of the intercalated SUP depended on both medium anionic species and LDH nanocomposite properties. However, LDH possesses an anion exchange selectivity for carbonate than chloride (Kaneyoshi & Jones, 1998; Miyata, 1983; Wang *et al.*, 2009), the release of the drug in buffers B and C was higher than in buffer A. Additionally, the layered molecular structure of LDH limited the intercalation of the drug in two-dimensional directions. Such kind of stacking process prevents the crystallization of the drug into the gallery of LDH. As a consequence, the drug was released in an amorphous form suitable for dissolution.

The release studies of the other drugs LDH nanocomposites showed similar behaviors and changes as SUP did before and after LDH nanocomposite formation. The differences were observed only in the amounts released and releasing times. The improved release properties of the other drug-LDH nanocomposites were also related to the medium anionic species and LDH nanocomposite properties.

The question arises now: How LDH supports a controlled release process of the intercalated drug? With no doubt the exchange mechanism is the key answer. The phase boundary formed between the internal zone (drug-LDH; large d-spacing) and the external zone (exchanged LDH; small d-spacing) during the medium anion exchange process decreased the amount of drug released with time progress, consequently a controlled behavior was obtained (Kaneyoshi & Jones, 1998). At this stage and from the observations of release data, we can say that LDH nanocomposite platform enhanced the solubility of NSAIDs and diminished the drug high local concentration through a controlled release process. Furthermore, LDH material lowered the direct gastrolesivity of the NSAIDs drugs through its barrier properties.

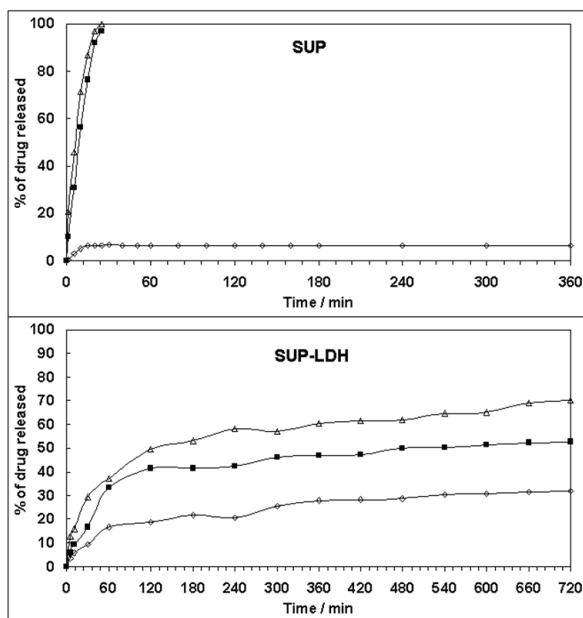


Fig. 10. Release profile of pure SUP (upper panel) and SUP-LDH nanocomposites (lower panel) in buffer A (\diamond), buffer B (\blacksquare) and buffer C (Δ). panel

6. Prospects for the future of LDH

With no doubt, one of the most important advances of science and technology is the birth of nanocomposites materials. From the many significant research achievements in the past decade and the many potential practical applications, it is assumed that the prospects for nanocomposite research are very bright indeed. From commercial, industrial, and scientific point of views, clay nanocomposites are of particular interest due to their previously discussed properties. At present, even though a great deal of work on LDH materials has been carried out, still more remains to be done in order to exploit completely their potential applications.

Regarding information required for developing LDH nanocomposite science, three specific areas of research seem particularly important. The first is the optimization of present synthetic techniques or the innovation of new methodologies; however uniform LDH nanoparticles are not synthesized yet, and literature data strongly emphasized the effect of LDH nanoparticle size and its distribution ratio on the applications of LDH. In this regard, high quality basic research should be the foundation of our discipline. The directions of the basic science of LDH nanocomposites should remain open, driven by the flow of the scientific inquiry to prepare more advanced nanocomposites. Another area of focus is the establishment of new tools for the characterization of nanocomposites. It is well known that X-ray analysis is the only standard technique for the identification of clay nanocomposites. Sometimes during the analysis, peaks related to specific groups are identified by using IR spectroscopy but not by X-ray spectroscopy. Hence, much more research should be directed towards the innovation of new sensitive measurement techniques. Still another direction to consider for future LDH nanocomposite research might be the stacking mechanism of the bioactive compounds into the layers during the nanocomposite formation. Some nanocomposites are suggested to be produced in a monolayer stacking process while others are formed through a bilayer stacking process. In fact, the complete understanding of the interaction mechanism between the bioactive anions and the inorganic layers in addition to the exfoliation mechanism of the layers during the nanocomposite formation are important issues of research and will help in the preparation of more advanced nanocomposites.

Because we believe that the future of the nano-dimensional LDHs carries new innovations of utilization in the different fields, professional organizations such as high ranked universities and academic institutes are encouraged to sponsor and to focus on the LDH nanocomposite research.

7. References

- Aisawa, S.; Hirahara, H.; Ishiyama, K.; Ogasawara, W.; Umetsu, Y. & Narita, E. (2003). Sugar-anionic clay composite materials: intercalation of pentoses in layered double hydroxide, *J. Solid State Chem.*, 174 (2), 342-348.
- Aisawa, S.; Sasaki, S.; Takahashi, S.; Hirahara, H.; Nakayama, H. & Narita, E. (2006). Intercalation of amino acids and oligopeptides into Zn-Al layered double hydroxide by coprecipitation reaction, *J. Phys. Chem. Solids*, 67 (5-6), 920-925.
- Ajat, M. M. M.; Yusoff, K. & Hussein, M. Z. (2008). Synthesis of glutamate- zinc-aluminium-layered double hydroxide nanobiocomposites and cell viability study, *Curr. Nanosci.*, 4 (4), 391-396.

- Amidon, G. L.; Lennernäs, H.; Shah, V. P. & Crison, J. (1995). A theoretical basis for a biopharmaceutical drug classification: The correlation of in vitro drug product dissolution and in vivo bioavailability, *Pharm. Res.* 12 (3), 413-420.
- Bail, C. L.; Thomassin, J.-H. & Touray, J.-C. (1987). Hydrotalcite-like solid solutions with variable SO_4^{2-} and CO_3^{2-} contents at 50° C, *Phys. Chem. Minerals*, 14 (4), 377-382.
- Berber, M. R.; Hafez, I. H.; Minagawa, K.; Mori, T. & Tanaka M. (2010). Nanocomposite formulation system of lipid-regulating drugs based on layered double hydroxide: synthesis, characterization and drug release properties, *Pharm. Res.*, 27 (114), 2394-2401.
- Berber, M. R.; Minagawa, K.; Katoh, M.; Mori, T. & Tanaka, M. (2008). Nanocomposites of 2-arylpropionic acid drugs based on Mg-Al layered double hydroxide for dissolution enhancement, *Eur. J. Pharm. Sci.*, 35 (4), 354-360.
- Bettinetti, G. P. & Mura, P. (1994). Dissolution properties of naproxen in combination with polyvinylpyrrolidone, *Drug Dev. Ind. Pharm.*, 20 (8), 1353-1366.
- Bingxin, L.; Jing, H.; Evans, D. G. & Xue, D. (2004). Inorganic layered double hydroxides as a drug delivery system—intercalation and in vitro release of fenbufen, *Appl. Clay Sci.*, 27 (3-4), 199-207.
- Bocclair, J. W.; Braterman, P. S.; Brister, B. D. & Yarberry, F. (1999). Layer anion interactions in magnesium aluminum layered double hydroxides intercalated with cobalticyanide and nitroprusside, *Chem. Mater.*, 11(8), 2199-2204.
- Carlino, S. (1997). The intercalation of carboxylic acids into layered double hydroxides: a critical evaluation and review of the different methods, *Solid State Ionics*, 98 (1-2), 73-84.
- Cavani, F.; Trifiro, F. & Vaccari, A. (1991). Hydrotalcite-type anionic clays: preparation, properties and applications, *Catal. Today*, 11 (2), 173-301.
- Chen, Q.; Shi, S.; Liu, X.; Jin, L. & Wei, M. (2009). Studies on the oxidation reaction of cysteine in a confined matrix of layered double hydroxides, *Chem. Eng. J.*, 153 (1-3), 175-182.
- Choy, J. H. & Son, Y. H. (2004). Intercalation of vitamer into LDH and their controlled release properties, *Bull. Korean Chem. Soc.*, 25 (1), 122-126.
- Choy, J.-H.; Kwak, S.-Y.; Park, J.-S. & Jeong, Y.-J. (2001). Cellular uptake behavior of [γ - ^{32}P] labeled ATP-LDH nanohybrids, *J. Mater. Chem.*, 11 (6), 1671-1674.
- Costantino, U.; Marmottini, F.; Nocchetti, M. & Vivani, R. (1998). New synthetic routes to hydrotalcite-like compounds: characterization and properties of the obtained materials, *Eur. J. Inorg. Chem.*, 10, 1439-1446.
- Costantino, U.; Nocchetti, M. (2001). *Layered double hydroxides. Present and future* (V. Rives Ed.), Nova Sci. Pub. Co., Inc. New York, pp. 383-412.
- Darder, M.; Blanco, M. L.; Aranda, P.; Leroux, F. & Hitzky, E. R. (2005). Bio-nanocomposites based on layered double hydroxides, *Chem. Mater.*, 17 (8), 1969-1977.
- Davies, N. M. & Wallace, J. L. (1997). Non-steroidal anti-inflammatory drug-induced gastrointestinal toxicity: new insights into an old problem, *J. Gastroenterol.*, 32 (1), 127-133.
- Del Arco, M.; Martin, C.; Martin, I.; Rives, V. & Trujillano, R. (1993). A FTIR spectroscopic study of surface acidity and basicity of mixed Mg, Al-oxides obtained by thermal decomposition of hydrotalcite, *Spectrochim. Acta A: Mol. Spect.*, 49 (11), 1575-1582.

- Emre, M. (1998). The gastroprotective effects of tizanidine: an overview, *Curr. Ther. Res.*, 59 (1), 2-12.
- Flesken, N., A.; Toshkov, I.; Naskar, J.; Tyner, K. M.; Williams, R. M.; Zipfel, W. R.; Giannelis, E. P. & Nikitin, A. Yu. (2007). Toxicity and biomedical imaging of layered nanohybrids in the mouse, *Toxicol. Pathol.*, 35 (6), 804-810.
- Frost, R. L. & Erickson, K. L. (2004). Thermal decomposition of synthetic hydrotalcites reevesite and pyroaurite, *J. Therm. Anal. Calorim.*, 76 (1), 217-225.
- Geraud, E.; Bouhent, M.; Derriche, Z.; Leroux, F.; Prevot, V. & Forano, C. (2007). Texture effect of layered double hydroxides on chemisorption of Orange II, *J. Phy. Chem. Solids*, 68 (5-6), 818-823.
- Hines, D. R.; Seidler, G. T.; Treacy, M. M. J. & Solin, S. A. (1997). Random stacking of a commensurate guest layer in an ordered host: NiAl layer-double-hydroxides, *Solid State Commun.*, 101 (11), 835-839.
- Hwang, S. H.; Han, Y. S. & Choy, J. H. (2001). Intercalation of functional organic molecules with pharmaceutical, cosmeceutical and nutraceutical functions into layered double hydroxides and zinc basic salts, *Bull. Korean Chem. Soc.*, 22 (9), 1019-1022.
- Ito, T.; Sugafuji, T.; Maruyama, M.; Ohwac, Y. & Takahashic, T. (2001). Skin penetration by indomethacin is enhanced by use of an indomethacin/smectite, complex *J. Supramol. Chem.*, 1 (4-6), 217-219.
- Kaneyoshi, M. & Jones, W. (1998). Exchange of interlayer terephthalate anions from a Mg-Al layered double hydroxide: formation of intermediate interstratified phases, *Chem. Phys. Lett.*, 296 (1-2), 183-187.
- Labajos, F. M.; Rives, V. & Ulibarri, M. A. (1992). Effect of hydrothermal and thermal treatments on the physicochemical properties of Mg-Al hydrotalcite-like materials, *J. Mater. Sci.*, 27 (6), 1546-1552.
- Ladewig, K.; Xu, Z. P. & Lu, G. Q. (2009). Layered double hydroxide nanoparticles in gene and drug delivery, *Expert Opin. Drug Delivery*, 6 (9), 907-922.
- Li, F.; Jin, L.; Han, J.; Wei, M. & Li, C. (2009). Synthesis and controlled release properties of prednisone intercalated Mg-Al layered double hydroxide composite, *Ind. Eng. Chem. Res.*, 48 (12), 5590-5597.
- Lin, F. H.; Lee, Y. H.; Jian, C. H.; Wong, J. M.; Shieh, M. J. & Wang, C. Y. (2002). A study of purified montmorillonite intercalated with 5-fluorouracil as drug carrier, *Biomaterials*, 23 (9), 1981-1987.
- Lin, Y.; Wang, J.; Evans, D. G. & Li, D. (2006). Layered and intercalated hydrotalcite-like materials as thermal stabilizers in PVC resin, *J. Phys. Chem. Solids*, 67 (5-6), 998-1001.
- Lipinski, C. A. (2000). Drug-like properties and the causes of poor solubility and poor permeability, *J. Pharmacol. Toxicol. Met.*, 44 (1), 235-249.
- Lipinski, C. A.; Lombardo, F.; Dominy, B. W. & Feeney, P. J. (1997). Experimental and computational approaches to estimate solubility and permeability in drug discovery and development settings, *Adv. Drug Delver. Rev.*, 23 (1-3), 3-25.
- Liu, Z.; Ma, R.; Osada, M.; Iyi, N.; Ebina, Y.; Takada, K. & Sasaki, T. (2006). Synthesis, anion exchange, and delamination of Co-Al layered double hydroxide: assembly of the exfoliated nanosheet/polyanion composite films and magneto-optical studies, *J. Am. Chem. Soc.*, 128 (14), 4872-4880.

- Lopez, T.; Bosch, P.; Asomoza, M.; Gomez, R. & Ramos, E. (1997). DTA-TGA and FTIR spectroscopies of sol-gel hydrotalcites: aluminum source effect on physicochemical properties, *Mat. Lett.*, 31 (3-6), 311-316.
- Lotsch, B.; Millange, F.; Walton, R. I. & O'Hare, D. (2001). Separation of nucleoside monophosphates using preferential anion exchange intercalation in layered double hydroxides, *Solid State Sci.*, 3 (8), 883-886.
- Malherbe, F.; Forano, C. & Besse, J. P. (1997). Use of organic media to modify the surface and porosity properties of hydrotalcite-like compounds, *Micropor. Mesopor. Mater.*, 10 (1-3), 67-84.
- Markus, V.; Klaus, K. & Jennifer, B. D. (2008). Dissolution enhancement of fenofibrate by micronization, cogrinding and spray-drying: comparison with commercial preparations, *Eur. J. Pharm. Biopharm.*, 68 (2), 283-288.
- Melani, F.; Bettinetti, G. P.; Mura, P. & Manderioli, A. (1995). Interaction of naproxen with α -, β -, and γ -hydroxypropyl cyclodextrins in solution and in the solid state, *J. Incl. Phenom. Macro. Chem.*, 22 (2), 131-143.
- Minagawa, K.; Aoki, Y.; Berber, M. R.; Mori, T. & Tanaka, M. (2009). DNA as a Component of ER Materials, *J. Phys.: Conf. Ser.*, 149(1), 012023(1-4).
- Mitchell, S. A.; Reynolds, T. D. & Dasbach, T. P. (2003). A compaction process to enhance dissolution of poorly water-soluble drugs using hydroxypropyl methylcellulose, *Int. J. Pharm.*, 250 (1), 3-11.
- Miyata, S. (1975). The syntheses of hydrotalcite-like compounds and their structures and physico-chemical properties-I: The systems Mg^{2+} - Al^{3+} - NO_3^- , Mg^{2+} - Al^{3+} - Cl^- , Mg^{2+} - Al^{3+} - ClO_4^- , Ni^{2+} - Al^{3+} - Cl^- and Zn^{2+} - Al^{3+} - Cl^- . *Clays Clay Miner.*, 23 (1), 369-370.
- Miyata, S. (1980). Physico-chemical properties of synthetic hydrotalcites in relation to composition, *Clays Clay Miner.*, 28 (1), 50-56.
- Miyata, S. (1983). Anion exchange properties of hydrotalcite-like compounds, *Clays Clay Miner.*, 31 (4), 305-311.
- Mura, P.; Bettinetti, G. P.; Faucci, M. T.; Sorrenti, M. & Negri, A. (2001). Interaction of naproxen with crystalline and amorphous methylated β -cyclodextrin in the liquid and solid state, *Supramol. Chem.*, 12 (4), 379-389.
- Mura, P.; Bettinetti, G. P.; Melani, F. & Manderioli, A. (1995). Interaction between naproxen and chemically modified β -Cyclodextrins in the Liquid and Solid State, *Eur. J. Pharm. Sci.*, 3 (6), 347-355.
- Mura, P.; Zerroukb, N.; Menninia, N.; Maestrellia, F. & Chemtob, C. (2003). Development and characterization of naproxen-chitosan solid systems with improved drug dissolution properties, *Eur. J. Pharm. Sci.*, 19 (1), 67-75.
- Nhlapo, N.; Motumi, T.; Landman, E.; Verryn, S. M. C. & Focke, W. W. (2008). Surfactant-assisted fatty acid intercalation of layered double hydroxides, *J. Mater. Sci.*, 43 (3), 1033-1043.
- Ogawa, M. & Kaiho, H. (2002). Homogeneous precipitation of uniform hydrotalcite particles, *Langmuir*, 18(11), 4240-4242.
- Olanrewaju, J.; Newalkar, B. L.; Mancino, C. & Komarneni, S. (2000). Simplified synthesis of nitrate form of layered double hydroxide, *Mater. Lett.*, 45 (6), 307-310.
- Park, M.; Shim, I. K.; Jung, E. Y. & Choy, J. H. (2004). Modification of external surface of laponite by silane grafting, *J. Phys. Chem. Solids*, 65 (2-3), 499-501.

- Pignatello, R.; Bucolo, C.; Spedalieri, G.; Maltese, A. & Puglisi, G. (2002). Flurbiprofen-loaded acrylate polymer nanosuspensions for ophthalmic application, *Biomaterials*, 23 (15), 3247-3255.
- Reinholdt, M. X. & Kirkpatrick, R. J. (2006). Experimental investigations of amino acid-layered double hydroxide complexes: Glutamate-hydroxalite, *Chem. Mater.*, 18 (10), 2567-2576.
- Rives, V. (2002). Characterization of layered double hydroxides and their decomposition products, *Mater. Chem. Phys.*, 7(1-3), 19-25.
- Semin, D. J.; Malone, T. J.; Paley, M. T. & Woods, P. W. (2005). A novel approach to determine water content in DMSO for a compound collection repository, *J. Biomol. Screen.* 10 (6), 568-572.
- Tammaro, L.; Costantino, U.; Bolognese, A.; Sammartino, G.; Marenzi, G.; Calignano, A.; Tete, S.; Mastrangelo, F.; Califano, L. & Vittoria, V. (2007). Nanohybrids for controlled antibiotic release in topical applications, *Int. J. Antimicrob. Agents*, 29 (4), 417-423.
- Trikeriotis, M. & Ghanotakis, D. F. (2007). Intercalation of hydrophilic and hydrophobic antibiotics in layered double hydroxides, *Int. J. Pharm.*, 332 (1-2), 176-184.
- Tronto, J.; Crepaldi, E. L.; Pavan, P. C.; De Paula, C. C. & Valim, J. B. (2001). Organic anions of pharmaceutical interest intercalated in magnesium aluminum LDHs by two different methods, *Mol. Cryst. Liq. Cryst.*, 356, 227-237.
- Tronto, J.; Sanchez, K. C.; Crepaldi, E. L.; Naal, Z. K.; Stanlei, I. & Valim, J. B. (2004). Synthesis, characterization and electrochemical study of layered double hydroxides intercalated with 2-thiophenecarboxylate anions, *J. Phys. Chem.*, 65 (2-3), 493-498.
- Uekama, K.; Imai, T.; Maeda, T.; Irie, T.; Hirayama, F. & Otagir, M. (2006). Improvement of dissolution and suppository release characteristics of flurbiprofen by inclusion complexation with heptakis (2,6-di-O-methyl) - β -cyclodextrin, *J. Pharm. Sci.*, 74 (8), 841-845.
- Vatier, J.; Malikova-Sekera, E.; Vitre, M. T. & Mignon, M. (1992). An artificial stomach-duodenum model for the in-vitro evaluation of antacids, *Aliment. Pharmacol. Ther.*, 6 (4), 447-458.
- Wang, S. L.; Liu, C. H.; Wang, M. K.; Chuang, Y. H. & Chiang, P. N. (2009). Arsenate adsorption by Mg/Al-NO₃ layered double hydroxides with varying the Mg/Al ratio. *Appl Clay Sci.*, 43 (1), 79-85.
- Warren, B. E. & Bodenstein, P. (1966). The shape of two-dimensional carbon black reflections, *Acta Cryst.*, 20, 602-605.
- Wei, M.; Guo, J.; Shi, Z.; Yuan, Q.; Pu, M.; Rao, G. & Duan, X. (2007). Preparation and characterization of L-cystine and L-cysteine intercalated layered double hydroxides, *J. Mater. Sci.*, 42 (8), 2684-2689.
- White, J. F. (1980). Bicarbonate-dependent chloride absorption in small intestine: ion fluxes and intracellular chloride activities, *J. Membrane Biol.*, 53 (2), 95-107.
- Xia, S.-J.; Ni, Z.-M.; Xu, Q.; Hu, B.-X. & Hu, J. (2008). Layered double hydroxides as supports for intercalation and sustained release of antihypertensive drugs, *J. Solid State Chem.*, 181 (10), 2610-2619.
- Xu, Z. P.; Walker, T. L.; Liu, K.-I.; Cooper, H. M.; Lu, G. Q. M. & Bartlett, P. F. (2007). Layered double hydroxide nanoparticles as cellular delivery vectors of supercoiled plasmid DNA, *Int. J. Nanomed.*, 2 (2), 163-174.

- Yahaya, A. H.; Bin-Hussein, M. Z. & Seh, W. S. (2003). Ion exchange study of carbonate, nitrate and dioctyl sulfosuccinate with anthraquinone-2-sulphonate encapsulated in inorganic layered structures, *J. Phys. Chem. Solids*, 64 (7), 1113-1118.
- Zhang, H.; Pan, D. & Duan, X. (2009). Synthesis, characterization, and magnetically controlled release behavior of novel core-shell structural magnetic ibuprofen-intercalated LDH nanohybrids, *J. Phys. Chem. C.*, 113 (28), 12140-12148.
- Zhang, H.; Pan, D.; Zou, K.; He, J. & Duan, X. (2009). A novel core-shell structured magnetic organic-inorganic nanohybrid involving drug-intercalated layered double hydroxides coated on a magnesium ferrite core for magnetically controlled drug release, *J. Mater. Chem.*, 19 (19), 3069-3077.
- Zou, K.; Zhang, H. & Duan, X. (2007). Studies on the formation of 5-aminosalicylate intercalated Zn-Al layered double hydroxides as a function of Zn/Al molar ratios and synthesis routes, *Chem. Eng. Sci.*, 62 (7), 2022-2031.

Dendrimers in Anti-HIV Therapy

Volha Dzmitruk¹, Dzmitry Shcharbin¹,
Elzbieta Pedziwiatr-Werbicka² and Maria Bryszewska²

¹*Institute of Biophysics and Cell Engineering of NASB*

²*University of Lodz*

¹*Belarus*

²*Poland*

1. Introduction

Human immunodeficiency virus (HIV), a retrovirus that was clinically detected in 1980 and demonstrated to be the causative agent of acquired immunodeficiency syndrome (AIDS), had resulted in over 25 million deaths by 2005. Currently, more than 33 million people are HIV-positive, and approximately 2.6 million people were newly infected and 1.8 million died of AIDS-related disorders in 2009. Antiretroviral therapy (ART), available from the mid-1990s, greatly improves the quality of life for HIV-infected persons and reduces mortality. However, there are several limitations to obtaining recovery from HIV infection including drug resistance, high rate of viral mutations, limited number of targets, low bioavailability of some compounds, presence of viral reservoirs and severe side-effects. The inability of standard highly active anti-retroviral therapy (HAART) drugs to penetrate some cells ensures that virus replication continues, although the common viral load can be reduced to undetectable levels [Finzi, 1997]. In addition, owing to the high cost and complexity of current HIV therapies, fewer than 5% of HIV infected patients worldwide receive antiretroviral treatment, and in underdeveloped countries access to such drugs is severely restricted. Therefore, development of preventive and therapeutic vaccines represents a tremendous challenge to AIDS researchers. In Europe the elaboration of new therapies is one of the main goals and several studies have concerned nanotechnology, with gene therapy being proposed as a good alternative that can efficiently inhibit gene expression in a sequence-specific manner. Dendrimers, a new class of polymeric molecules, are potential candidates for developing preventive antiretroviral vaccines where the delivery vehicles have low level cytotoxicity and targeted action. The aim of this chapter is to summarize studies concerning dendrimers and their application as therapy against HIV-1.

2. HIV-1 pandemic. Fail of HAART. The necessity of a new therapy approach

Conventional antiretroviral therapy consists of a combination of antiviral drugs to decrease the mortality of HIV-1 infected patients [Palella et al., 1998], with the mixture of drugs interfering with various stages of the virus life cycle at one time. Therefore, antiretroviral therapies (ART) are targeted to block key steps of the viral replication cycle: binding and fusing to the target host CD4 T-cell, reverse transcription of the viral RNA, and integration

of viral DNA into host DNA. For a better understanding of novel approaches such as dendrimer based therapies, a brief description of the viral life cycle is required.

The first step in the viral life cycle is attachment, fusion of the viral envelope and consequent entry into an immune cell. CD4 receptors bind the viral surface protein gp120, enabling further interaction with co-receptor proteins, predominantly CCR5 and CXCR4 [Eckert et al., 2001]. After CD4-virus binding, conformational changes in gp120 initiate fusion of the two membranes by reorientation of the transmembrane protein gp41. This step is a target for preventive therapy and drugs, and several HIV entry inhibitors are the subject of clinical trials. Among them, Enfuvirtide, Sifurvitide (blocks the surface envelope glycoprotein 41 of HIV-1, already approved) [Lalezari et al., 2003], Aplaviroc, Vicriviroc and Maraviroc are host co-receptor CCR5 antagonists [Liu et al., 1996; Dean et al., 1996], AMD11070 (CXCR4 antagonist, in phase II clinical trials) [De Clercq, 2003; Hendrix et al. 2004] and other associated entry and fusion drugs are being developed and await approval [Esté & Telenti, 2007].

Viral reverse transcriptase copies the single-stranded RNA into double-stranded DNA. RT inhibitors are divided into two fundamentally different groups: nucleosides (NRTI) and non-nucleosides (NNRTI); AZV was approved six years after the discovery of HIV-1. The NTRIs represent nucleosides, mimic natural ones and are capable of competing with them. Activity, effectiveness and toxicity are highly dependent on the design of the NTRI. NNRTIS were developed to fight the virus selectively. Being approved, RTs reduce the viral load effectively, but toxicity, pharmacokinetics, drug clearance, dosing, cost and drug adherence are limiting factors, and multiple resistance remains the main obstacle [Basavapathruni & Anderson, 2007]. Delivering RTs using non-toxic vehicles can greatly improve the clinical effect.

Once synthesized, the viral DNA is incorporated into a pre-integration complex to be transported to the nucleus. Viral proteins facilitate transportation and integration of the DNA chain into the host genome. At the late phase, mRNAs are produced and move out of nucleus to undergo translation and protein synthesis. After viral particle budding, viral DNA leaves the cell via exocytosis.

The genome of HIV is encoded by single-stranded RNA [Turner & Summers, 1999]. However, HAART prevents HIV-1 infected patients from making a complete recovery [Sekaly, 2008], and this therapy is associated with dangerous side-effects including mitochondrial toxicity and myopathy [Scruggs & Dirks Naylor, 2008], lipodystrophy [Mallewa et al., 2008] associated with insulin resistance and lipid abnormalities [Mallon, 2007], and induced liver injury [Inductivo-Yu & Bonacini, 2008]. Therefore, new approaches to treating HIV-positive individuals are required that are selective and impact only infected cells, or have no effects on healthy cells. Treatment systems that can cross the blood-brain barrier would be advantageous, and gene therapy [Strayer et al., 2008] or delivery using nanostructures could be realistic alternatives.

3. Gene therapy: mechanism of RNA interference

Gene therapy is a technique for replacing mutant genes in cells and tissues, and has been utilized for disorders such as Alzheimer's disease and Parkinson's syndrome [Kelly, 2007]. The ability to repair genes within a cell is a new potential approach for treatment of cells and tissues that possess abnormal gene patterns. Gene therapy is based on two conceptually

different approaches. The first, called up-regulation, suggests delivery of nucleic acids or corresponding constructs for expression of the gene of interest under the control of an appropriate promoter, resulting in increased target activity, i.e. in production of a protein playing the role of a drug. The other approach concerns the delivery of oligomeric genetic materials such as antisense oligodeoxynucleotides or siRNA (short interfering RNA) that cause a decrease in the target activity, resulting in inhibition of harmful mRNA expression and/or synthesis of harmful proteins. Referred to as down-regulation or gene silencing, this approach became key to the development of anti-cancer and anti-HIV vaccines.

RNA interference (RNAi) was first used in plants as a tool for changing the color of petunias [Napoli et al. 1990; Sen & Blau, 2006]. RNAi as a gene silencing tool has wide therapeutic applications and can be utilized in animal cells [Guo & Kemphues, 1995]. Three mechanisms can be applied within a cell, depending on the type of effector molecules: antisense single-stranded oligonucleotides (ODN), double-stranded antisense small interfering RNA (siRNA) and ribozymes.

RNA interference is based on the ability of ODN, siRNA and ribozymes to stimulate specific degradation of an mRNA target with a sequence complementary to one or two strands of ODN, siRNA and ribozymes. When long double-stranded RNA enters a cell, it undergoes cleavage by endonucleases, resulting in short 19-21 bp double-stranded fragments with two protruding nucleotides at the 3'-ends of the strands. These short duplexes, called siRNA, form within a complex with protein catalytic structures causing directed degradation of complementary target mRNA. RNA interference is used to regulate gene expression and as a method for investigating functional genomics in eukaryotes. As for other nucleic acids, one of the main limitations of RNA interference for gene therapy concerns delivery of ODN or siRNA into cells.

4. Barriers and vectors for delivering nucleic acids

To explain the necessity for nucleic acid delivery systems, the barriers to nucleic acid delivery within organisms need to be discussed. Normally, introduction of free nucleic acid is accompanied by its enzymic degradation in the organism. Furthermore, RNAi effectors are unable to cross biological membranes readily owing to their strong negative charge, inducing poor cellular uptake. Therefore, delivery agents should maintain the biological activity of drugs and promote cell penetrating activities so that the process of RNAi is efficient; this necessitates the existence of vectors for nucleic acid packing and transport. Vectors aid nucleic acid delivery to zones necessary for its localization and provide efficient intracellular transport, predominantly to the nucleus. Viral vectors are efficient but shortcomings include high immunogenicity and carcinogenicity in vivo [Mulligan, 1993; Briand & Kahn, 1993]. Compared to viral systems, synthetic (non-viral) systems are characterized by lower efficiency but higher flexibility and safety [Eliyahu et al., 2005]. Normally, packing of nucleic acids is provided by electrostatic interaction of the anionic phosphate groups with positive charges on the synthetic vector, resulting in complex formation.

Nucleic acid complexes with liposomes and various cationic linear polymers are the most widely used non-viral vectors. Complexes with liposomes are called lipoplexes, and those with linear polymers are called polyplexes. However, the development of nanotechnology led to the appearance of new nanocomposites for gene delivery – dendrimers [Eliyahu et al., 2005].

5. Dendrimers as new class of nanoparticles for drug and gene delivery

The application of nanotechnology in biology and medicine induced the appearance of new devices, supramolecular systems, structures, complexes and composites. Dendrimers (from the Greek "dendron" - tree and "meros" - branch) are excellent examples of nanotechnological composites [Newkome et al., 1986; Tomalia, 1995; Fischer & Vogtle, 1999]. They are globular in shape, with a topological structure formed by monomeric subunit branches diverging to the sides from the central nucleus (Fig. 1). Properties of synthesized macromolecules can be precisely assigned in advance by choosing appropriate monomers and functional groups [Newkome et al., 1986; Tomalia, 1995; Fischer & Vogtle, 1999; Bosman et al., 1999]. The following features can be distinguished in dendrimers: (i) multivalent surface containing numerous potentially active sites; (ii) envelopes surrounding the nucleus; (iii) the nucleus with attached dendrons.

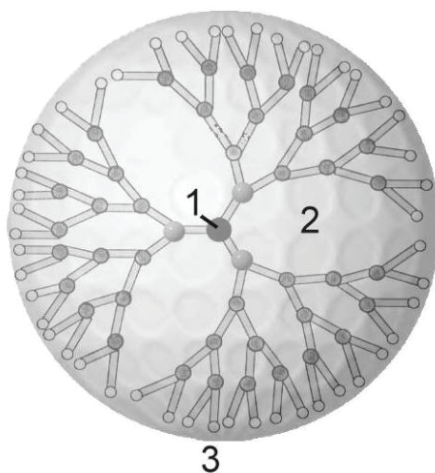


Fig. 1. Dendrimer structure. 1) Nucleus, 2) Internal cavities, 3) Surface groups.

Two main strategies have been used during dendrimer synthesis: a divergent method, in which dendron growth begins from the nucleus, and a convergent method in which already finished dendrimer branches join the nucleus. According to the divergent method proposed by the Tomalia and Vogtle groups [Tomalia, 1995; Fischer & Vogtle, 1999], dendrimer synthesis includes association of monomeric modules in a radial structure, from one branch to another, following definite rules. In particular, the dendrimer increases in size from one layer to another (from one generation to the next). According to the convergent method proposed by Hawker and Frechet [Hawker & Frechet, 1990], branches join the nucleus at the final stage of the process and form the dendrimer, and are grown first in the course of dendrimer synthesis.

An interesting property of dendrimers is the dependence of their solution viscosity on molecular mass, which differs from that for linear polymers [Frechet, 1994]. Solution viscosity for linear polymers is described by the exponential function $\eta \sim C^N$, where C is polymer concentration and N is the exponential parameter ($1 < N < 10$), but the viscosity of dendrimer solutions is described by the linear function $\eta = \eta_0(1 + k\phi)$, where k is a constant

and ϕ is the disperse phase volume fraction. Therefore, on increasing dendrimer generation (molecular mass), at a certain point the viscosity in solution begins to decrease. This effect is the result of globular dimensions of high dendrimer generations [Matthews et al., 1998].

With regard to modifications, over 100 types of dendrimers have been synthesized, although there are five common families.

Polyamide amine (PAMAM) dendrimers [Tomalia, 1995] are based on the ethylenediamine nucleus, and their branches are designed from methyl acrylate and ethylenediamine. Half generations of PAMAM dendrimers have surface carboxyls, while complete generations have surface amino groups. At present, there is an abundant choice of PAMAM dendrimers with various types of surface groups. Polypropyleneimine (PPI) dendrimers [Matthews et al., 1998] are based on the butylenediamine nucleus and polypropyleneimine monomers. Besides PPI, another popular abbreviation of these dendrimers is DAB (diaminobutyl), based on the name of the nucleus, and these are commercially available. Phosphorus dendrimers were synthesized by the Majoral and Caminade group [Majoral et al., 2002]. Phosphorus atoms are present in the nucleus and branches of these dendrimers. Carbosilane dendrimers are based on a silicon nucleus and have ammonium or amino groups at the periphery [Ortega et al., 2006]. Polylysine dendrimers are based on the amino acid lysine and have polylysine branches and surface groups [Vlasov, 2006], and these are commercially available.

The architecture and properties of dendrimers depends on the generation. Low generations of dendrimers have an open, flattened and asymmetric shape, but as the generation increases the structure becomes globular and densely packed at the periphery. Inside dendrimers there are empty cavities where small therapeutic molecules can be entrapped and safely transported to targets. Another important feature of dendrimers is monodispersity. The classical polymerization process is usually random and produces molecules of different sizes, whereas the size and molecular mass of dendrimers can be specifically controlled during synthesis.

Dendrimers possess many functional end groups, which are responsible for high solubility and reactivity. Long chain molecules with many reaction sites interact with dendrimers by wrapping around them, as normally happens for single- or double-stranded nucleic acids. These properties make dendrimers suitable for targeting, microarray systems, and catalysis and drug delivery systems [Matthews et al., 1998].

6. Dendrimers themselves as anti-HIV therapeutic agents

Dendrimers are anti-HIV therapeutic agents. PAMAM polyanionic phenyldicarboxylic acid (BRI6195) and naphthylsulfonic acid (BRI2923) terminated dendrimers were synthesized as inhibitors of the viral replication cycle in different strains of HIV-1 and in various cell lines including those that display reverse transcription resistance. Suppression provided by such macromolecules is based on the interaction with the envelope protein gp120, which prevents the first steps of cell infection, i.e. binding to host-cells. Owing to the different cell penetration rates of BRI6195 and BRI2923 compounds, the latter was demonstrated to exhibit another antiviral activity during reverse transcription and integration steps. Unfortunately, it has been found that some gp120 mutations display inconsistency, preventing the described PAMAM dendrimers from completely and successfully curing patients after treating cells [Witvrouw, 2000].

A new class of polycationic molecules called "VIOLOGEN" was synthesized and investigated by Asaftei and De Clercq as candidate antiviral drugs [Asaftei & De Clercq, 2010]. They represented dendrimers with bipyridiniumhexafluorophosphate end groups consisting of viologen units, synthesized with a phenyl- or benzyl-type core, carrying between one and 90 charges per molecule. Inhibition of HIV-1 replication of some constituents in MT-4 cells were demonstrated at $EC_{50}=0.26\pm 0.08 \mu\text{M}$, $SI=75.7$. Investigation of the activity of compounds on peripheral blood mononuclear cells (PBMC) demonstrated their inability to interfere with the viral life cycle, showing that the mechanism of HIV-1 inhibition concerned dendrimers and heparin sulfate interaction. Therefore, it was concluded that viologen compounds block the electrostatic interaction of cell surfaces and viral particles. Polycationic dendrimers were tested in two steric architectures: spheroidal and comb-branched. This demonstrated that spherical branched organization is an advanced property of dendrimeric molecules. Spherical forms of "VIOLOGEN" bound to the viral envelope better than comb-branched dendrimers, indicating increased efficacy against the virus. Moreover, the intensity of viral activity correlated with surface charges, i.e. a lack of charges reduced attempts to stop HIV-1 replication in cells [Asaftei & De Clercq, 2010].

The scientific group led by Prof. Majoral [Pérez-Anes et al., 2010] is developing multivalent cationic galactosylceramide (GalCer) dendritic analogs with antiviral activity (inhibition of HIV-1 entry into the host-cell), based on treating epithelial cells with a lack of CD4 receptors. The HIV virus targets immune cells via a specific interaction between gp120 and the amino-terminal immunoglobulin domain of CD4 [Ho et al., 1995]. Therefore, it was supposed that the presence of this receptor was the determining factor for cells to absorb small viral particles. However, the human immunodeficiency type 1 virus was subsequently found to bind to CD4 (-) cells. Widely expressed at cell surfaces, glycosphingolipid GalCer plays the role of an alternative receptor for gp120 [Yahi et al., 1994], explaining why success of infection depends on GalCer/gp120 interaction in cells with a blocked or absent CD4 (+)-mediated pathway. The first attempt to use this concept was in 2000, when multivalent polysulfated PPI glycodendrimers were tested as binding antagonists of the virus. Results indicated similar inhibitory and cytotoxicity properties as dextran sulfate [Kensinger et al., 2004]. More recent *in vitro* studies have demonstrated that HIV-1 inhibitory properties of compounds, based on phosphonic acid terminated dendrimers and N-hexadecylamino lactitol moieties, make them promising anti-HIV drug candidates. However, their low therapeutic indices in cellular studies required scientists to modify the stability of assemblies *in vitro*.

Another attempt to uncover novel antiviral dendrimers resulted in scientists using the disaccharide cellobiose as a terminal layer of polylysine dendrimers generation 3. Further sulfation of the terminating groups allowed them to interact with the viral surface electrostatically, particularly with the positively charged envelope glycoprotein gp120. Polylysine dendrimers exhibited antiviral activity as high as that of approved drugs, maintaining low level cytotoxicity and revealing additional anticoagulant properties. Very low level anti-HIV-1 activity and anticoagulant activities responsible for uncontrolled bleeding are substantial shortcomings of this method [Han et al., 2010].

The so-called "Trojan horse", *in vitro* studies of HIV treatments with low cytotoxicity, is the new concept in HIV research. Such an approach has demonstrated that a polylysine dendrimer-based container is the optimal choice for initiating cytotoxic mechanisms

comprising proteins penetrating cells to inhibit the chymotrypsin-like activity of proteasomes. The "Trojan horse" includes small cytotoxic molecules as functioning agents conjugated with a "steric cap", and a relatively big carrier to avoid immediate entry into the catalytic hollow of proteasomes. The effect is thought to be activated by viral proteases via cleavage of the linkage between the agent and nanoparticle, although further investigations are required to validate this type of approach [Buckley et al., 2011].

At present there is only one product based on dendrimers on the market. The product, VivaGel®, is produced by Starpharma and protects against sexually transmitted diseases and human immunodeficiency virus (HIV). It is a vaginal microbicide gel under development for the prevention of sexually transmitted infections (STIs) including genital herpes and HIV infection. The VivaGel® product concept is designed to offer a safe, convenient and affordable means for women to protect themselves from infection with genital herpes and HIV during sex. Surveys demonstrate that there is substantial demand in North America and Europe for such a product, with an estimated billion dollar market for STI prevention products in the developed world.

7. Potential revolution in gene delivery: dendrimers as gene carriers in anti-HIV therapy

No dendrimer-based delivery systems are approved or the subject of clinical trials for HIV-1 treatment as an application of gene therapy. Nevertheless, numerous studies are currently underway to develop vectors based on dendrimeric polymers for improved delivery of approved drugs and nucleic acids, as this is a promising approach that can potentially overcome all known safety issues. There are several reviews concerning the application of nanotechnology [Neves et al., 2010; Mallipeddi & Rohan, 2010; Sharma & Garg, 2010], but none provides total and complete descriptions of associated problems. This sub-section has, as far as possible, attempted to summarize all attempts to elaborate effective nucleic acid carriers by applying various types of dendrimers, generations and with different modifications.

HAART antiviral therapy has critical side effects and does not provide complete recovery from infection. Furthermore, some medical components often included in drug cocktails for antiviral chemotherapy (for example NRTIs) cause intensified neuropathological disorders [Cherry et al., 2003] that can lead to nervous system degradation. Targeting familiar drug molecules directly to infected cells would improve their safety.

Dendrimer-based carriers were developed to support, rationalize and improve drug efficiency, avoiding consequences observed for pure drugs that were administered without special carriers. Polymolecular compounds were proposed as a delivery system. Nanogel particles consisting of PEG- (polyethylene glycol) and Pluronic-PEI- (polyethylenimine) biodegradable networks, i.e. star PEG-g-PEI and PAMAM-PEI-g-PEG, were synthesized and investigated in terms of drug delivery analysis. Recent studies have shown that the phosphorylate-modified nucleoside analogs zidovudine (AZT) and didanosine (ddI) coupled with nanogels were effective in terms of cellular uptake and had increased and upgraded target selectivity. Moreover, the process of mtDNA depletion, responsible for neuropathy reinforcing, was reduced threefold by administering NRTIs with nanocarriers rather than using a pure NRTI injection [Vinogradov et al., 2010]. Such vectors were demonstrated to be a promising tool for reaching viral reservoirs in the central nervous system (CNS) and were capable of crossing the blood-brain barrier [McGee et al., 2006].

When cells infected with HIV-1 can be killed in a targeted manner, mature non-proliferating active macrophages in the organism can reproduce viral particles, and this is one reason for the failure of existing therapies. Development of non-toxic targeting nanocarriers could be vital in overcoming this problem.

Modified PPI dendrimers have been used for the aim of targeted delivery into cells involved in highly conserved retention, and mannosylated PPI dendrimers possess double the effect in terms of viral attack, improving biological properties of drugs and displaying antiviral activity themselves owing to specific binding and their penetrating ability via cell receptors [Dutta & Jain, 2007]. As demonstrated for complexes of coupled tuftsin and zidovudine, antiretroviral activity of each separate compound was not enough for them to be considered anti-HIV agents in isolation, but when conjugated they represent a good method and are likely to enter phase I clinical trials [Fridkin et al., 2005]. Modifying dendrimers with tuftsin revealed them as the most biocompatible carriers, demonstrating striking results in studies concerning infected macrophages [Dutta et al., 2007]. Tuftsin is a tetrapeptide (Thr-Lys-Pro-Arg) related to macrophage activation, and it binds specifically to macrophages, monocytes and polymorphonuclear leukocytes. Its covalent conjugation with 5 generation PPI dendrimers increases entrapment (49.3%) of Efavirenz into the internal cavities of the transmitting agent, compared with 37.5% entrapment efficiency for unmodified dendrimers. Such vehicles significantly prolong release of the non-nucleoside reverse transcriptase inhibitor Efavirenz through controlled drug administration. This delivery system also provides 34-fold increased cellular uptake and more than 7-fold augmented anti-HIV activity compared with pure drugs without carriers [Dutta et al., 2008].

PPI dendrimers are characterized as good binding agents for antisense oligodeoxynucleotides, resulting in compact complexes with close to neutral charge. Amino-terminated dendrimers of second, third and fourth generations can produce dendriplexes suitable for cell transfection and to release cargos in a time-dependent manner [Pedziwiatr-Werbicka et al., 2011]. Only first stage results have been published so far, but this should not minimize the importance and potential of such an approach.

The most studied PAMAM dendrimers have the potential to inhibit viral replication by blocking interaction of the Tat peptide and transacting responsive element (TAR) RNA. This process is essential for the production of full-length viral transcripts and proliferation of the virus. Establishment of new drugs that disrupt this binding within cells is a new concept for anti-HIV-1 therapeutics. [Zhao et al., 2004].

Carbosilane dendrimers containing ammonium or amine groups at their periphery are nanocarriers that are appropriate vectors for successful gene therapy against HIV-1. They are water-soluble and polycationic, and effectively bind small nucleic acid chains. After complete dendriplex formation, antiviral oligodeoxynucleotides (ODN) were immune to the actions of their binding proteins [Shcharbin et al., 2007; Chonco et al., 2007], and the inhibitory effect of viral replication in cells in the presence of human plasma was increased by 25-30%, similar to that for naked ODNs. In order to conserve the biological ability of siRNA to have a role in the RNA interference process inside infected lymphocytes, second generation amino-terminated carbosilane dendrimers (2G-NN8 and 2G-NN16) were tested, resulting in formation of strong complexes with siRNAs (siP24, siNEF and siGAG1 [Shcharbin et al., 2011]. These are antisense to HIV regions responsible for p24, nef and gag protein expression, respectively, with diameters between 300 and 370nm, protection against RNase digestion, low cytotoxicity at therapeutic concentrations (sufficient to 40% HIV

inhibition), and comparatively good ability to inhibit viral replication in peripheral blood mononuclear cells and human leukemia T lymphocytes. Gradual hydrolysis of the interior carbon-silicon bonds leads to time delayed cargo liberation (4-24 hours), which would be important for treatment as the necessary amounts of siRNA and ODNs would be decreased and the effect is believed to be longer [Weber et al., 2008]. 2G-NN16 dendrimers coupled with antiviral siRNA have been demonstrated to cross the blood-brain barrier (BBB) in an in vitro model, making the possibility of conducting gene therapy using dendrimer-based delivery in human astrocytes and to fight viruses within CNS cells a more realistic option. Transfection with infected and non-infected human astrocytoma cells did not result in significant cytotoxicity when treated with up to 24 μ M/ml dendriplexes, while sequence-specific down-regulation of the housekeeping gene GAPDH was observed, indicating the ability of siRNA to exert its biological function. At the same time, inhibition of X4-HIV NL4-3 and R5-HIV strains of HIV-1 by dendriplexes was 80% as effective as treating cells with naked siRNA. In spite of numerous positive results for carbosilane dendrimers as a delivery system in in vitro studies, this approach is still at the pre-clinical experimental stage. Theoretically, dendriplexes did not have sufficiently small-scale diameters to penetrate deeply into brain issues, but in practice transcytosis through the blood-brain barrier was demonstrated. Furthermore, structural and functional alterations of BBB occur during HIV infection [Jiménez et al., 2010]. Injection of pure dendrimers causes a high rate of cell death due to electrostatic interactions of polycationic surface groups and negatively charged cell membranes, although this has no effect on pivotal properties of dendritic cells (mature and immature) in terms of linking adaptive and innate immunities [Pion et al., 2010].

8. Conclusion

Dendrimers are nanomaterials with great potential to be anti-HIV therapies of the future. However, despite potential applications, at present there is only one product based on dendrimers available on the market. This product, VivaGel® (Starpharma, Australia), protects against sexually transmitted diseases and human immunodeficiency virus. Systematic studies concerning dendrimers are required for the development of new dendrimer-based antiretroviral drugs.

9. Acknowledgment

This work was supported by project MNT-ERA NET 2007 (funded by National Centre for Research and Development Nr ERA-NET-MNT/01/2009).

10. References

- Asaftei, S., De Clercq, E. (2010). "Viologen" dendrimers as antiviral agents: the effect of charge number and distance. *Journal of Medicinal Chemistry*, Vol. 53, pp. 3480-3488, ISSN 0022-2623.
- Basavapathruni, A., Anderson, K.S. (2007). Reverse transcription of the HIV-1 pandemic. *FASEB Journal*, Vol. 21, pp. 3795-3808, ISSN 0892-6638.

- Bosman, A.W., Janssen, H.M., Meijer, E.W. (1999). About Dendrimers: structure, physical properties, and applications. *Chemical Reviews*, Vol. 99, pp. 1665-1688, ISSN 0009-2665.
- Briand, P., and Kahn, A. (1993). Values and limits of adenoviral vectors for gene transfer *in vivo*. *Pathologie et Biologie (Paris)*, Vol. 41, pp. 663-671, ISSN 0369-8114.
- Buckley, D.L., Corson, T.W., Aberle, N., Crews, C.M. (2011). HIV protease-mediated activation of sterically capped proteasome inhibitors and substrates. *Journal of American Chemical Society*, Vol. 133, pp. 698-700, ISSN 0002-7863.
- Cherry, C.L., McArthur, J.C., Hoy, J.F., Wesselingh, S.L. (2003). Nucleoside analogues and neuropathy in the era of HAART. *Journal of Clinical Virology*, Vol. 26, pp. 195-207, ISSN 1386-6532.
- Chonco, L., Bermejo-Martín, J.F., Ortega, P., Shcharbin, D., Pedziwiatr, E., Klajnert, B., de la Mata, F.J., Eritja, R., Gómez, R., Bryszewska, M., Muñoz-Fernandez, M.A. (2007). Water-soluble carbosilane dendrimers protect phosphorothioate oligonucleotides from binding to serum proteins. *Organic & Biomolecular Chemistry*, Vol. 5, pp. 1886-1893, ISSN 1477-0520.
- De Clercq, E. (2003). The bicyclam story. *Nature Review Drug Discovery*, Vol. 2, pp.581-587, ISSN 1474-1776.
- Dean, M., Carrington, M., Winkler, C., Huttley, G.A., Smith, M.W., Allikmets, R., Goedert, J.J., Buchbinder, S.P., Vittinghoff, E., Gomperts, E., Donfield, S., Vlahov, D., Kaslow, R., Saah, A., Rinaldo, C., Detels, R., O'Brien, S.J. (1996). Genetic restriction of HIV-1 infection and progression to AIDS by a deletion allele of the CKR5 structural gene. Hemophilia Growth and Development Study, Multicenter AIDS Cohort Study, Multicenter Hemophilia Cohort Study, San Francisco City Cohort, ALIVE Study. *Science*, Vol. 273, pp. 1856-1862, ISSN 0036-8075.
- Dutta, T., Agashe, H.B., Garg, M., Balakrishnan, P., Kabra, M., Jain, N.K. (2007). Poly (propyleneimine) dendrimer based nanocontainers for targeting of efavirenz to human monocytes/macrophages *in vitro*. *Journal of Drug Targeting*, Vol. 15, pp. 89-98, ISSN 1061-186X.
- Dutta, T., Garg, M., Jain, N.K. (2008). Targeting of efavirenz loaded tuftsin conjugated poly(propyleneimine) dendrimers to HIV infected macrophages *in vitro*. *European journal of pharmaceutical sciences*, Vol. 34, pp. 181-189, ISSN 0928-0987.
- Dutta, T., Jain, N.K. (2006). Targeting potential and anti-HIV activity of lamivudine loaded mannosylated poly (propyleneimine) dendrimer. *Biochimica et Biophysica Acta*, Vol. 1770, pp. 681-686, ISSN 0006-3002.
- Eckert, D.M., Kim, P.S. (2001) Mechanisms of viral membrane fusion and its inhibition. *Annual Review of Biochemistry*, Vol. 70, pp. 777-810, ISSN 1545-4509.
- Eliyahu, H., Barenholz, Y., and Domb, A. J. (2005). Polymers for DNA Delivery. *Molecules*, Vol. 10, pp. 34-64. ISSN 1420-3049.
- Esté, J.A., Telenti, A. (2007). HIV entry inhibitors. *Lancet*, Vol. 370, pp. 81-88, ISSN 0140-6736.
- Finzi, D. (1997). Identification of a reservoir for HIV-1 in patients on highly active antiretroviral therapy. *Science*, Vol. 278, pp. 1295-1300, ISSN 0036-8075.
- Fischer, M. Vogtle, F. (1999). Dendrimers: From Design to Application - A. Progress Report. *Angewandte Chemie International Edition*, Vol. 38, pp. 884-905, ISSN 0570-0833.

- Frechet, J.M. (1994). Functional polymers and dendrimers: reactivity, molecular architecture, and interfacial energy. *Science*, Vol. 263, pp. 1710-1715, ISSN 0036-8075.
- Fridkin, M., Tsubery, H., Tzeheval, E., Vonsover, A., Biondi, L., Filira, F., Rocchi, R. (2005). Tuftsin-AZT conjugate: potential macrophage targeting for AIDS therapy. *Journal of Peptide Science*, Vol. 11, pp. 37-344, ISSN 1075-2617.
- Guo, S., Kemphues, K. J. (1995). Par-1, a gene required for establishing polarity in *C. elegans* embryos, encodes a putative Ser/Thr kinase that is asymmetrically distributed. *Cell*, Vol. 81, pp. 611-620, ISSN 0092-8674.
- Han, S., Yoshid, D., Kanamoto, T., Nakashima, H., Uryu, T., Yoshida T. (2010). Sulfated oligosaccharide cluster with polylysine core scaffold as a new anti-HIV dendrimer. *Carbohydrate Polymers*, Vol. 80, pp. 1111-1115, ISSN 0144-8617.
- Hawker, C.J., Frechet, J.M.J. (1990). Preparation of Polymers with Controlled Molecular architecture. A New Convergent Approach to Dendritic Macromolecules. *Journal of the American Chemical Society*, Vol. 112, pp. 7638-7647, ISSN 0002-7863.
- Hendrix, C.W., Collier, A.C., Lederman, M.M., Schols, D., Pollard, R.B., Brown, S., Jackson, J.B., Coombs, R.W., Glesby, M.J., Flexner, C.W., Bridger, G.J., Badel, K., MacFarland, R.T., Henson, G.W., Calandra, G., AMD3100 HIV Study Group (2004). Safety, pharmacokinetics, and antiviral activity of AMD3100, a selective CXCR4 receptor inhibitor, in HIV-1 infection. *Journal of Acquired Immune Deficiency Syndromes*, Vol. 37, pp. 1253-1262, ISSN 1077-9450.
- Ho, D.D., Neumann, A. U., Perelson, A. S., Chen, W., Leonard, J. M., Markowitz, M. (1995). Rapid turnover of plasma virions and CD4 lymphocytes in HIV-1 infection. *Nature*, Vol. 373, pp. 123-126, ISSN 0028-0836.
- Inductivo-Yu, I., Bonacini, M. (2008). Highly active antiretroviral therapy-induced liver injury. *Current drug safety*, Vol. 3, pp. 4-13, ISSN 1574-8863.
- Jiménez, J.L., Clemente, M.I., Weber, N.D., Sanchez, J., Ortega, P., de la Mata, F.J., Gómez, R., García, D., López-Fernández, L.A., Muñoz-Fernández, M.A. (2010). Carbosilane dendrimers to transfect human astrocytes with small interfering RNA targeting human immunodeficiency virus. *BioDrugs*, Vol. 24, pp. 331-343, ISSN 1173-8804.
- Kelly, E.B. (2007). *Gene therapy. Health and medical issues today*, Greenwood Publishing Group, ISBN 031-333-760-8, UK.
- Kensinger, R.D., Catalone, B.J., Krebs, F.C., Wigdahl, B., Schengrund, C.L. (2004). Novel polysulfated galactose-derivatized dendrimers as binding antagonists of human immunodeficiency virus type 1 infection. *Antimicrobial Agents and Chemotherapy*, Vol. 48, pp. 1614-1623, ISSN 0066-4804.
- Lalezari, J.P., Henry, K., O'Hearn, M., Montaner, J.S., Piliero, P.J., Trottier, B., Walmsley, S., Cohen, C., Kuritzkes, D.R., Eron, J.J. Jr, Chung, J., DeMasi, R., Donatucci, L., Drobnos, C., Delehanty, J., Salgo, M.; TORO 1 Study Group (2003). Enfuvirtide, an HIV-1 fusion inhibitor, for drug-resistant HIV infection in North and South America. *New England Journal of Medicine*, Vol. 348, pp. 2175-2185, ISSN 0028-4793.
- Liu, R., Paxton, W.A., Choe, S., Ceradini, D., Martin, S.R., Horuk, R., MacDonald, M.E., Stuhlmann, H., Koup, R.A., Landau, N.R. (1996). Homozygous defect in HIV-1 coreceptor accounts for resistance of some multiply-exposed individuals to HIV-1 infection. *Cell*, Vol. 86, pp. 367-377, ISSN 0092-8674.

- Majoral, J.P., Caminade, A.M., Laurent, R., Sutra, P. (2002). Phosphorus-containing dendrimers. From material science to biology. *Heteroatom Chemistry*, Vol. 13, pp. 474-485, ISSN 1098-1071.
- Mallewa, J.E., Wilkins, E., Vilar, J., Mallewa, M., Doran, D., Back, D., Pirmohamed, M. (2008). HIV-associated lipodystrophy: a review of underlying mechanisms and therapeutic options. *Journal of Antimicrobial Chemotherapy*, Vol. 62, pp. 648-660, ISSN 0305-7453.
- Mallipeddi, R., Rohan, L.C. (2010). Progress in antiretroviral drug delivery using nanotechnology. *International Journal of Nanomedicine*, Vol. 5, pp. 533-547, ISSN 1176-9114.
- Mallon, P.W. (2007). Pathogenesis of lipodystrophy and lipid abnormalities in patients taking antiretroviral therapy. *AIDS Reviews*, Vol. 9, pp. 3-15, ISSN 1139-6121.
- Matthews, O.A., Shipway, A.N., Stoddart, J.F. (1998). Dendrimers – Branching out from Curiosities into New Technologies. *Progress in Polymer Science*, Vol. 23, pp. 1-56. ISSN 0079-670023.
- McGee, B., Smith, N., Aweeka, F. (2006). HIV pharmacology: barriers to the eradication of HIV from the CNS. *HIV Clinical Trials*, Vol. 7, pp. 142-153, ISSN 1528-4336.
- Mulligan, R. C. (1993). The basic science of gene therapy. *Science*, Vol. 260, pp. 926-932. ISSN 0036-8075.
- Napoli, C., Lemieux, C., Jorgensen, R. (1990). Introduction of a chimeric chalcone synthase gene into petunia results in reversible co-suppression of homologous genes in trans. *Plant Cell*, Vol. 2, pp. 279-289, ISSN 1040-4651.
- Neves, J., Amiji, M.M., Bahia, M.F., Sarmiento, B. (2010). Nanotechnology-based systems for the treatment and prevention of HIV/AIDS. *Advanced Drug Delivery Reviews*, Vol. 62, pp. 458-477, ISSN 0169-409X.
- Newkome, G.R., Yao, Z.Q., Baker, G.R., Gupta, V.K., Russo, P.S., Saunders, M.J. (1986). Chemistry of micelles series. Part 2. Cascade molecules. Synthesis and characterization of a benzene[9]3-arborol. *Journal of American Chemical Society*, Vol. 108, pp. 849-850, ISSN 0002-7863.
- Ortega, P., Bermejo, J.F., Chonco, L., de Jesus, E., de la Mata, F. J., Fernandez, G. , Flores, J., Gomez, R., Serramia, M.J., Munoz-Fernandez, M.A. (2006). Novel water soluble carbosilane dendrimers: synthesis and biocompatibility. *European Journal of Inorganic Chemistry*, Vol. 7, pp. 1388-1396, ISSN 1099-0682.
- Palella, F.J. Jr, Delaney, K.M., Moorman, A.C., Loveless, M.O., Fuhrer, J., Satten, G.A., Aschman, D.J., Holmberg, S.D. (1998). Declining morbidity and mortality among patients with advanced human immunodeficiency virus infection. HIV Outpatient Study Investigators. *New England Journal of Medicine*, Vol. 338, pp. 853-860, ISSN 0028-4793.
- Pedziwiatr-Werbicka, E., Ferenc, M., Zaborski, M., Gabara, B., Klajnert, B., Bryszewska, M. (2011). Characterization of complexes formed by polypropylene imine dendrimers and anti-HIV oligonucleotides. *Colloids and Surfaces B: Biointerfaces*, Vol. 83, pp. 360-366, ISSN 0927-7765.
- Pérez-Anes, A., Stefaniu, C., Moog, C., Majoral, J.P., Blanzat, M., Turrin, C.O., Caminade, A.M., Rico-Lattes, I. (2010). Multivalent cationic GalCer analogs derived from

- first generation dendrimeric phosphonic acids. *Bioorganic & Medicinal Chemistry*, Vol. 18, pp. 242-248, ISSN 0968-0896.
- Pion, M., Serramia, M.J., Diaz, L., Bryszewska, M., Gallart, T., García, F., Gómez, R., de la Mata, F.J., Muñoz-Fernandez, M.Á. (2010). Phenotype and functional analysis of human monocytes-derived dendritic cells loaded with a carbosilane dendrimer. *Biomaterials*, Vol. 31, pp. 8749-8758, ISSN 0142-9612.
- Scruggs, E.R., Dirks Naylor, A.J. (2008). Mechanisms of zidovudine-induced mitochondrial toxicity and myopathy. *Pharmacology*, Vol. 82, pp. 83-88, ISSN 0031-7012.
- Sekaly RP. (2008). The failed HIV Merck vaccine study: a step back or a launching point for future vaccine development? *Journal of Experimental Medicine*, Vol. 205, pp. 7-12, ISSN 0022-1007.
- Sen, G.L., Blau, H.M. A brief history of RNAi: the silence of the genes. *FASEB Journal*, Vol. 20, pp. 1293-1299, ISSN 0892-6638.
- Sharma, P., Garg, S. (2010). Pure drug and polymer based nanotechnologies for the improved solubility, stability, bioavailability and targeting of anti-HIV drugs. *Advanced Drug Delivery Reviews*, Vol. 62, pp. 491-502, ISSN 0169-409X.
- Shcharbin, D., Pedziwiatr, E., Chonco, L., Bermejo-Martín, J.F., Ortega, P., de la Mata, F.J., Eritja, R., Gómez, R., Klajnert, B., Bryszewska, M., Muñoz-Fernandez, M.A. (2007). Analysis of interaction between dendriplexes and bovine serum albumin. *Biomacromolecules*, Vol. 8, pp. 2059-2062, ISSN 1525-7797.
- Shcharbin, D., Pedziwiatr, E., Nowacka, O., Kumar, M., Zaborski, M., Ortega, P., de la Mata, F.J., Gómez, R., Muñoz-Fernandez, M.A., Bryszewska, M. (2011). Carbosilane dendrimers NN8 and NN16 form a stable complex with siGAG1. *Colloids and Surfaces B: Biointerfaces*, Vol. 83, pp. 388-391, ISSN 0927-7765.
- Strayer, D.S., Akkina, R., Bunnell, B.A., Dropulic, B., Planelles, V., Pomerantz, R.J., Rossi, J.J., Zaia, J.A. (2005). Current status of gene therapy strategies to treat HIV/AIDS. *Molecular Therapy*, Vol. 11, pp. 823-842, ISSN 1525-0016.
- Tomalia, D.A. (1995). Dendrimer molecules. *Scientific American*, Vol. 272, pp. 62-66. ISSN 0036-8733.
- Turner, B.G., Summers, M.F. (1999). Structural biology of HIV. *Journal of Molecular Biology*, Vol. 285, pp. 1-32, ISSN 0022-2836.
- Vinogradov, S.V., Poluektova, L.Y., Makarov, E., Gerson, T., Senanayake, M.T. (2010). Nano-NRTIs: Efficient Inhibitors of HIV Type-1 in Macrophages with a Reduced Mitochondrial Toxicity, *Antiviral Chemistry & Chemotherapy*, Vol. 21, pp. 1-14, ISSN 0956-3202.
- Vlasov, G.P. (2006). Starlike branched and hyperbranched biodegradable polymer systems as DNA carriers, *Russian Journal of Bioorganic Chemistry*, Vol. 32, pp. 205-218, ISSN 1068-1620.
- Weber, N., Ortega, P., Clemente, M.I., Shcharbin, D., Bryszewska, M., de la Mata, F.J., Gómez, R., Muñoz-Fernández, M.A. Characterization of carbosilane dendrimers as effective carriers of siRNA to HIV-infected lymphocytes. *Journal of Controlled Release*, Vol. 132, pp. 55-64, ISSN 0168-3659.
- Witvrouw, M., Fikkert, V., Pluymers, W., Matthews, B., Mardel, K., Schols, D., Raff, J., Debyser, Z., De Clercq, E., Holan, G., Pannecouque, C. (2000). Polyanionic (i.e., polysulfonate) dendrimers can inhibit the replication of human immunodeficiency

virus by interfering with both virus adsorption and later steps (reverse transcriptase/integrase) in the virus replicative cycle. *Molecular Pharmacology*, Vol. 58, pp. 1100-1108, ISSN 0026-895X.

- Yahi, N., Sabatier, J.M., Nickel, P., Mabrouk, K., Gonzalez-Scarano, F., Fantini, J. (1994). Suramin inhibits binding of the V3 region of HIV-1 envelope glycoprotein gp120 to galactosylceramide, the receptor for HIV-1 gp120 on human colon epithelial cells. *Journal of Biological Chemistry*, Vol. 269, pp. 24349-24353, ISSN 0021-9258.
- Zhao, H., Li, J., Xi, F., Jiang, L. (2004). Polyamidoamine dendrimers inhibit binding of Tat peptide to TAR RNA. *FEBS Letters*, Vol. 563, 241-245, ISSN 0014-5793.